Doktorand:

MARKO LAVRENČIČ

NUMERIČNI POSTOPKI ZA NELINEARNE STATIČNE IN DINAMIČNE ANALIZE LUPINSKIH SISTEMOV RAZLIČNIH VELIKOSTI

DOKTORSKA DISERTACIJA

NUMERICAL PROCEDURES FOR NONLINEAR STATIC AND DYNAMIC ANALYSES OF SHELL SYSTEMS OF VARIOUS SIZES

DOCTORAL DISSERTATION

Ljubljana, 2020

Univerza
v Ljubljani

Fakulteta
*za gradbeništvo
in geodezijo*

Mentor: prof. dr. Boštjan Brank

Poročevalci za oceno doktorske disertacije:

- prof. dr. Gordan Jelenić, Univerza na Reki

- doc. dr. Miha Brojan, UL FS

- prof. dr. Peter Betsch, Karlsruhe Institute of Technology

- prof. dr. Jože Korelc, UL FGG

ERRATA

Page	Line	Error	Correction

BIBLIOGRAPHIC-DOCUMENTALISTIC INFORMATION AND ABSTRACT

Abstract

The topics of the thesis are mixed(-hybrid) finite element formulations for shell-like structures, and implicit time-stepping schemes that preserve basic constants of the motion. The considered finite elements are based on two geometrically exact shell models, in particular, large rotation inextensible-director model and rotation-less extensible-director model. The performance of the current state-of-the-art mixed(-hybrid) shell finite element formulations is assessed by studying a large number of numerical examples. Some novel "near optimal" mixed-hybrid shell finite element formulations are proposed that allow for large solution steps, show near optimal convergence characteristics and display little sensitivity to mesh distortion. As for the non-linear shell elasto-dynamics, we revisit implicit dynamic schemes that belong to the groups of generalized-α methods and energy-conserving/decaying and momentum-conserving methods. We compare their spectral characteristics, the tendency to overshoot and their accuracy. By performing a set of numerical tests for numerically stiff nonlinear shell-like examples, we assess how these features extend to nonlinear elasto-dynamics. We illustrate the ability of the considered schemes to dissipate the energy, to fully or approximately conserve the angular momentum, and we estimate the order of accuracy for nonlinear problems by error indicators. Novel energy-conserving/decaying and momentum-conserving schemes are derived for the previously introduced novel mixed-hybrid shell formulations. The numerical examples demonstrate that the robustness and efficiency of the novel static formulations can be prolonged to dynamics. The final part of the thesis is related to the application of the derived formulations. In particular, the shell buckling process is studied by applying numerically dissipative schemes. The ability of these schemes to handle complex buckling and post-buckling processes is assessed. It is demonstrated that controlled numerical dissipation of higher structural frequencies is absolutely necessary for an efficient simulation of a post-buckling response. Finally, we apply the derived procedures to study the problem of surface wrinkling on curved stiff-shell/soft-core substrates, including the transition between the wrinkling modes.

BIBLIOGRAFSKO-DOKUMENTACIJSKA STRAN IN IZVLEČEK

Izvleček

Tema disertacije so mešani(-hibridni) končni elementi za lupine in integracijske sheme za dinamiko, ki ohranjajo osnovne konstante gibanja. Obravnavani končni elementi temeljijo na dveh geometrijsko točnih teorijah lupin: na modelu z velikimi rotacijami in neraztegljivim smernikom ter modelu brez rotacij z raztegljivim smernikom. Učinkovitost najsodobnejših mešanih(-hibridnih) končnih elementov za lupine je ocenjena na podlagi velikega števila numeričnih primerov. Predlagamo tudi nove, »skoraj optimalne« hibridne-mešane formulacije, ki omogočajo račun dolgih obtežnih korakov, izkazujejo skoraj optimalno konvergenco in so neobčutljive na popačenje mreže. Narejen je pregled implicitnih dinamičnih shem za nelinearno elastodinamiko, ki spadajo med posplošene α metode in metode, ki ohranjajo (oziroma kontrolirano zmanjšujejo) energijo in ohranjajo gibalno in vrtilno količino. Primerjamo njihove spektralne lastnosti, nagnjenost k močni prekoračitvi analitične rešitve in njihovo natančnost. Z računom niza primerov, kjer rešujemo numerično toge nelinearne enačbe za lupine, ocenimo, kako se te lastnosti prenesejo v nelinearno elastodinamiko. Prikažemo sposobnost obravnavanih shem za kontrolirano disipacijo energije in zmožnost ohranjanja vrtilne količine, s kazalniki napake pa ocenimo njihovo natančnost za nelinearne primere. Izpeljemo sheme, ki ohranjajo/disipirajo energijo ter ohranjajo gibalno in vrtilno količino za hibridno-mešane formulacije lupin. Numerični primeri kažejo, da se robustnost in učinkovitost novih statičnih formulacij prenese tudi v dinamiko. Zaključni del disertacije je povezan z aplikacijo izpeljanih formulacij. Z numerično disipativnimi implicitnimi shemami proučujemo proces uklona lupin. Ocenimo sposobnost teh shem za opis zapletenih procesov uklona, tudi v postkritičnem območju, in pokažemo, da je numerična disipacija višjih frekvenc nujno potrebna za učinkovito dinamično simulacijo teh procesov. Na koncu izpeljane postopke uporabimo še za proučevanje površinskega gubanja ukrivljenih in tankih lupin na mehkih jedrih, vključno s preskoki uklonskih oblik.

ZAHVALA

Najprej se zahvaljujem mentorju prof. Boštjanu Branku za vse nasvete in usmeritve. Pokazal mi je pozitiven pristop do raziskovalnega dela in mi odprl vrata v zanimiv svet numerične mehanike in končnih elementov.

Za dodeljena finančna sredstva, ki so mi omogočila študij, se zahvaljujem Javni agenciji za raziskovalno dejavnost Republike Slovenije.

Sodelavcem Andjelki, Blažu in Tomu, s katerimi sem si med študijem delil pisarno, se zahvaljujem za pomoč in prijateljske pogovore. Hvala tudi vsem ostalim sodelavcem in prijateljem, ki so pripomogli k dobremu vzdušju na fakulteti in zunaj nje.

Celotni družini, še posebej pa staršem se zahvaljujem za izkazano podporo in privzgojene vrednote, ki so me usmerile na zastavljeno življenjsko pot.

Posebna zahvala pa gre tebi, Katja, da mi stojiš ob strani že vse od začetka študija. Hvala ti za vso ljubezen in podporo. Hvala tudi tebi, Oskar, da mi že več kot pol leta s smehom polepšaš vsak dan.

»This page is intentionally blank«

TABLE OF CONTENT

Lavrenčič, M. 2020. Numerical Procedures for Nonlinear Static and Dynamic Analyses of Shell Systems of Various Sizes.
PhD Th. Ljubljana, UL FGG, Third cycle doctoral study Built Environment.

IX

LIST OF FIGURES

XII

Lavrenčič, M. 2020. Numerical Procedures for Nonlinear Static and Dynamic Analyses of Shell Systems of Various Sizes.
PhD Th. Ljubljana, UL FGG, Third cycle doctoral study Built Environment.

KAZALO SLIK

LIST OF TABLES

KAZALO PREGLEDNIC

LIST OF ABBREVIATIONS AND SYMBOLS

General abbreviations

DOF	Degree of freedom
FEM	Finite Element Method
SDOF	Single degree of freedom

Variational formulations

ANS	Assumed Natural Strain technique
EAS	Enhanced Assumed Strain technique
HR	Hellinger-Reissner functional
HW	Hu-Washizu functional
MITC	Mixed Interpolation of Tensorial Components

ANS and EAS finite elements

MITC4	Element with transverse shear ANS
MITC4+	Element with transverse shear ANS and membrane ANS
EAS4	Element with membrane EAS with 4 parameters
EAS5	Element with membrane EAS with 5 parameters
EAS7	Element with membrane EAS with 7 parameters
QKQ-3	Dynamic formulation (ED1) of MITC4 with reduced-order kinematics (tangential displacements are neglected), large shear modulus (acting as penalty parameter to mimic quasi-Kirchhoff kinematics), and elastic foundation
RM-5	Dynamic formulation (ED1) of MITC4, and elastic foundation

Mixed-hybrid finite elements

HR	Hybrid element with HR functional for membrane, bending and transverse shear
HR-M	Hybrid element with HR functional for membrane
HR-MB	Hybrid element with HR functional for membrane and bending
HR-MS	Hybrid element with HR functional for membrane and transverse shear
HW	Hybrid element with HW functional for membrane, bending and transverse shear
HWEAS	Extension of HW element with membrane (2), bending (2) and transverse shear (2) EAS (with 6 parameters in total)
+HR	Extension of HR element with membrane ANS
+HR-MS	Extension of HR-MS element with membrane ANS
+HW	Extension of HW element with membrane ANS

Rotation algorithms

T	Additive update of rotations (with total rotation vector)
TQ	T algorithm with quaternions
I	Multiplicative-additive update of rotations (with incremental rotation vector)
IQ	I algorithm with quaternions
M	Multiplicative update of rotations (with iterative rotation vector)
MQ	M algorithm with quaternions

Implicit dynamic time stepping schemes

BAM	Wood-Bossak-Zienkiewicz-α scheme
ED1	First-order accurate Energy-Decaying scheme
EDMC1	First-order accurate Energy-Decaying Momentum Conserving scheme
EDMC2	Second-order accurate Energy-Decaying Momentum Conserving scheme
EMC	Energy Momentum Conserving scheme
GAM	Chung-Hulbert-α scheme
HHT	Hiberlt-Huges-Taylor-α scheme
JWH	Jansen-Whiting-Hulbert-α scheme
NMD	First-order Newmark scheme with dissipation
NTR	Newmark Trapezoidal Rule
G-α	Group of generalized alpha schemes (GAM, BAM, HHT, JWH)
NG-α	Group of the following schemes: GAM, BAM, HHT, NTR, NMD

»This page is intentionally blank«

1   INTRODUCTION

Let us begin the exposition by introducing the topics that are later addressed in detail and by providing the motivation behind the research that was undertaken. A brief state-of-the-art is given on the topics of shell finite elements, mixed formulations, shell dynamics and shell stability problems. The goals of the thesis and the methodology are presented and finally an outline of the rest of the manuscript is given.

1.1   Motivation

Shell structures and shell systems are used in various engineering and technological fields, including civil engineering. The reason for their frequent use in engineering and technology lies mainly in their innumerable possibilities for curved shapes and in their ability to carry transversal loading primarily by the in-plane action [128]. This makes them attractive also for other fields of science, e.g. medicine, biology, nanotechnology, etc.

For the numerical solving of nonlinear problems in engineering, the finite element method is currently the most frequently used. It translates a mathematical description of an engineering problem into a system of nonlinear equations (with space-discrete values of variables as the unknowns), which is then solved using Newton's iterative method, e.g. [41]. If the problem at hand is of dynamic nature, the system of nonlinear equations also becomes time dependent. Hence, besides a spatial discretization, we also need a temporal discretization in connection with an effective time stepping scheme. Modern time integration schemes for nonlinear structural dynamics are based on the requirements that they must be able to algorithmically conserve some physical quantities during the dynamic motion. These are, for example, the total energy of the system, the linear and the angular momentum, the inelastic material dissipation and similar. Such schemes can then be modified to numerically dissipate the frequencies of higher orders, which are, due to the spatial discretization, distorted and therefore unrealistic.

Shell structure is characterized as a three-dimensional body with thickness dimension much smaller than span-wise dimensions. Consequently, its behavior can be approximated by an idealized two-dimensional continuum. The difficulties that arise in the numerical modeling of the nonlinear response of shells and shell systems are mostly related to the exact description of kinematics, especially large rotations, material nonlinearity and inelasticity, exact description of transverse shear stresses and the prevention of various parasitic stresses (i.e. locking), e.g. [164]. These requirements are not only the consequences of the applied computational model, but are also directly connected to the underlying physical characteristics of the shell structure [128]. Shell finite elements are of many types, since many shell elements are intended to simulate specific problems. Recently, various new numerical formulations for the analysis of shells have been derived. We should mention some of them: (a) geometrically simple, hybrid finite elements, that show, despite simple geometry, great robustness and good accuracy in solving various nonlinear shell problems, (b) finite elements with kinematics capable of using complex 3d nonlinear and inelastic material models, (c) isogeometric finite elements that are geometrically compatible with other computer modeling tools used in CAD (Computer Aided Design) and BIM (Building Information System) technologies, (d) finite elements with a precise description of the transverse stresses, which is important for composite-laminate problems, and (e) finite elements

specially derived for specific purposes such as, for example, analysis of curved nano structures, emerging of wrinkling patterns, etc.

Note that the meaning of the term "hybrid" is hereinafter adopted from a definition presented by Crisfield [42]. He termed the elements with all degrees of freedom (displacement-like and additional non-displacement-like) specified at nodes as mixed. He further termed the elements that condense the non-displacement-like degrees of freedom at the element level as hybrid or mixed-hybrid. This terminology is not universally accepted as some publications correlate terms mixed and hybrid with other meanings.

Shell structures can be found in a variety of shapes and sizes. An assortment of phenomena ranging from mega size (e.g., buckling of thin steel silos [76] or the behavior of reinforced concrete cooling towers), through micro size (e.g. wrinkling of solid films on soft cores [31]), all the way to the nano size (e.g. deformation and removal of nano structures), can be simulated with shell finite elements. Thus, a need is recognized to provide efficient finite element tools that can be used in the analysis of shell structures across the entire spectrum.

1.2   Background

1.2.1   Shell mixed-hybrid formulations

From the first works by e.g. Kirchoff [84], Love [112], Reissner [129], Mindlin [117] and many others, the theory in the field of plate and shell structures has been continuously developed. With the advent of computer power and the ever growing demand for more detailed results, attention has focused mainly on theories that are given in a form, suitable for efficient computer implementation, such as the geometrically exact shell theory, presented by Simo and Fox [140], [141], [142]. The displacement-based finite elements have since been improved using various techniques, and many works aimed at developing a low-order (4-noded) optimal nonlinear shell finite element. The development of such an element is still of great practical interest, since accurate and efficient shell elements play an essential role for successful nonlinear analysis.

The pure displacement-based shell finite element developed from the geometrically exact shell theory gives a too stiff response due to shear and membrane locking. Different techniques have been proposed to mitigate these unwanted effects. The mixed and hybrid formulations are a possible approach, which will be the focus of our work. These elements are usually based on a multifield variational principle and treat the displacement, stress and/or strain fields as independent.

Significant amount of work in the field of hybrid formulations was done by Pian, starting with [125]. The first very successful 4-node plane stress hybrid finite element was a result of his continuous work in this field and was proposed by Pian and Sumihara [126]. They proposed to use Hellinger–Reissner variational principle in the formulation of hybrid stress elements. The proposed concept of assuming independent stress resultant interpolations for membrane and bending components was improve in [140] and [141], where it was used also in combination with the Assumed Natural Strain concept for the treatment of transverse shear strains [48].

The Assumed Natural Strain (ANS) concept was applied to shells by Dvorkin an Bathe [48], who proposed a formulation that removes the transverse shear locking by assuming an independent interpolation field of transverse shear strains over the element. Betsch and Stein [15] proposed an ANS treatment for normal strains that help avoid the transverse normal locking in 6- and 7-parameter shell formulations. Choi and Paik [36] proposed a new four node shell element that avoids the shear and membrane locking problems. A family of new ANS shell elements was later proposed in [98] that aimed to alleviate the membrane and shear locking. The same task was also undertaken by Ko et al., first in [87] and later in [89] and [88], to arrive at the shell formulation that is free from locking and exhibits superior convergence properties even when applied to distorted meshes; see [89] for linear and [90] for nonlinear version of the element. The element is an extension of the nonlinear version of the popular MITC4 (Mixed Interpolation of Tensorial Components) element [48] and was denoted by the authors as MITC4+.

The concept of the Enhanced Assumed Strain (EAS) is another possible mixed approach that was proposed by Simo et al. in [143] and further developed in [139]. The EAS plate and shell formulations were further investigated by Andelfinger and Ramm [2], who elaborated on their equivalence to the Hellinger-Reissner elements from [126]. Different enhancements for the membrane and bending parts of the strains, e.g. [17], [22], or also the transverse shear strains, e.g. [12], [34], [127], have been proposed since. For the 5-parameter, large rotation shell model, the membrane strain enhancement has proven to be the most valuable, while other formulations do not justify the added computational cost, see [22].

Although a very successful formulation was proposed by Simo et al. in [140], [142], the development of an effective hybrid elements has continued since then. Wagner and Gruttmann [159] proposed a mixed-hybrid Hu-Washizu (HW) type nonlinear 4-node shell element that allows for large load increments and requires substantially less iterations than other shell formulations. The formulation has been further developed to include also the EAS strains [60] and the thickness strains [85], allowing to incorporate 3d constitutive equations. Gruttmann and Wagner further developed a linear version of effective hybrid Hellinger-Reissner (HR) type shell elements [59] that can be straightforwardly extended to nonlinear regime, e.g. [103]. Note that all the mentioned elements apply the ANS [48] for the transverse shear strains on top of the proposed formulation.

Different representations of strains and stress resultants were explored in [165] and [166], where the HR and HW elements were developed in skew coordinates, and in [168], where the strains were formulated in contravariant coordinates. We have recently expanded the HW formulation to include also the ANS for the membrane strains in [104]. A similar task was performed in [107], where we followed the same guidelines and expanded also the HR formulation. In Chapter 2 of this manuscript we chose, out of the above-mentioned element formulations, a group of the most prominent ones and subjected them to extensive tests in order to deliver a straightforward comparison of their performance and finally derive the "optimal" ones.

1.2.2   Implicit shell dynamics

The goal of the numerical time stepping schemes for nonlinear structural dynamics is to provide a sufficiently precise solution in time for the problem under consideration. There are several classifications of the schemes, among which the most conventional is the division into explicit and implicit. Implicit schemes generally exhibit better computational stability, compared to explicit ones [67]. They also allow for longer time steps, are more precise, but also more computationally expensive. Classical implicit schemes in structural dynamics belong to the Newmark family [118]. Among them, the trapezoidal rule strictly preserves the total energy for linear systems, and the mid-point rule conserves linear and angular momentum for a general nonlinear problem.

It has been proven desirable and often necessary for the implicit schemes to possess some numerical damping. The numerical dissipation is favorable if it helps to avoid adverse effects of spurious higher frequency modes on the numerical solution. High frequencies are an artefact of the spatial discretization and do not reflect the high frequencies of the original continuum problem. As shown e.g. in [121], extremely fine mesh is needed for an accurate representation of short waves in elastic continuum. Because such meshes are not an option for structural dynamics, the numerical dissipation of poorly represented short waves, associated with high-frequency modes, is desirable. Besides the spatial discretization, the high-frequency error depends also on the underlying mechanical model and the choice of the time step. Namely, for a dissipative scheme, large time steps generally increase numerical dissipation in the low-frequency range.

Single-step collocation schemes with numerical damping have been proposed as an extension of the Newmark method. Such schemes are e.g. Wilson-θ method [163], ρ- family of algorithms [10], various well-established α-methods [38], [65], [77], [170], and some more recent versions [80], [81] (collectively called the generalized-α (G-α) methods), among many others. More recently, attention has been turned also to dissipative composite time integration schemes with several sub-steps in the time step, such as e.g. the Bathe method [7], [120].

For linear dynamics, the unconditional stability of the time-stepping schemes is well defined by the spectral radius [67]. For nonlinear dynamics, the algorithmic stability is rather related to energy, as already recognized in [11], [68]. In this sense, a significant progress in implicit schemes for nonlinear elasto-dynamics was made when Simo and Tarnow [146], [145] introduced a scheme that conserves the total mechanical energy of the system for free motions, as well as linear and angular momentum. They also emphasized that the conservation of the physical constants of the motion of the underlying nonlinear continuous system should be a desirable feature of the time integration algorithm. The Energy-Momentum Conserving scheme (denoted here as EMC) is basically the mid-point rule with the algorithmic stresses conveniently derived to satisfy the requirement of energy conservation. Thus, the scheme is "backward-engineered" in order to preserve the important qualitative feature of the governing equations [18]. The energy-momentum conserving algorithm was later applied for the dynamics of various nonlinear structural models by Simo et al. and others: for rigid-bodies [147], beams [138], trusses [96], shells [146], [23], [134], [18] and solids [181], [53], [16]. More recently, it has been extended for mixed formulations [13], [119] and multi-physics problems, e.g. for electro-elastic-dynamics, thermo-mechanical dynamics, etc.

Although the energy-momentum conserving scheme [145] fulfils the energy criterion for nonlinear elasto-dynamics, it proves to be unstable for some nonlinear applications. Because it is non-dissipative, it does not damp any vibrations, which makes it inefficient for snap-through and buckling problems, as presented for dynamic buckling of shells in [102] and [108]. In such cases, the energy-momentum conserving scheme computes highly oscillatory responses of a purely numerical origin. The nonlinearities provide a mechanism for transferring energy from low to high frequency regime, so that numerical solutions show never ending (intense) oscillations. For the dynamics of complex nonlinear systems, like shells, numerical dissipation seems to be indispensable. However, conservation of energy and high frequency dissipation cannot coexist, unless energy is transferred from high to low frequency modes, which has no physical basis. Nevertheless, [97] proposed a dissipative constrained G-α scheme that conserves energy and momenta. Because of the energy constraint, higher modes are dissipated, whereas the total energy of the system remains constant because the algorithm makes an unphysical transfer of energy from the artificial high modes to the low modes [18].

Thus, the need to controllably dissipate the total mechanical energy of the system served as motivation to extend the energy-momentum conserving scheme so that it includes algorithmic dissipation. A series of first-order and second-order energy-decaying (ED) schemes that fulfil the energy stability criterion have been proposed, with some of them being able to conserve angular momentum and some not. For the first- and second-order energy-decaying schemes, we refer to e.g. [3], [4], [5], [26], [51], [132]. Let us mention that the energy-momentum conserving scheme was analyzed in [146] and [13], and that the energy-decaying schemes of the first-order were analyzed in [4] and [26] and compared with the energy-decaying schemes of the second-order in [5].

Application of the above-mentioned schemes to the pure displacement-based shell elements is not without difficulties, although it is a standard task that many of the commercially available software enable. However, it is probably due to implementation difficulties that none of the high-performing shell elements in combination with the energy-decaying schemes have yet been formulated. Betsch and Janz recently applied the HW formulation [159] to the EMC scheme, whereas the energy-decaying scheme was applied to mixed EAS formulations by Gebhardt and Rolfes [50]. In Chapter 4 of this manuscript we develop two formulations that combine the positive features of the "optimal" shell quadrilaterals presented in Chapter 2 with the energy-decaying momentum-preserving scheme presented in Chapter 3.

1.2.3   Shell stability in dynamics

A systematic understanding of buckling of shell-like systems, including the development and evolution of buckling pattern, e.g. [155], [30], [100], [183], calls for computational procedures that can go far beyond the buckling initiation into the post-buckling regime. To handle this kind of instability by static analysis, one must use the path-following method, e.g. [41], which can decrease the load when tracing the equilibrium path. The static analysis may be extended by directly jumping to the critical points, e.g. [172], [93], and by switching from the primary equilibrium path to the secondary ones (called branch-switching), e.g. [160], [173], in order to investigate different possible ways of shell post-buckling behavior and to get an idea of the most realistic one.

It is sometimes difficult to compute complete shell buckling process by the path-following method, e.g. [149], [150]. Moreover, jumping to the critical points and branch-switching is cumbersome, and it is robust only for some simple shell problems, e.g. [58]. For this reason, one can turn to quasi-static analysis, known as dynamic relaxation, where the static problem is replaced, for the purposes of numerical solution only, by an artificial dynamic problem with damping (i.e. viscous) and inertia forces, e.g. [154]. Another way to compute the shell buckling process is by defining the problem as a nonlinear structural dynamic one, and exploiting explicit time stepping schemes to compute the solution. Let us mention some recent examples of explicit dynamic buckling analyses of shells: cylinders were studied by [92] and [162], silos by [76], creased shells by [123], and steel tanks by [46]. Let us further mention that the idea of studying shell buckling and post-buckling by structural dynamics goes back to 1980's, see e.g. [136], [40], [133], [66].

In this manuscript we aim to apply the implicit dynamic time stepping schemes to compute shell-buckling phenomena, which is a considerably less common approach, despite the fact that implicit schemes are generally more stable and accurate than explicit ones, and can use larger time steps. Some remarks on common implicit schemes in structural dynamics have already been presented above, and a more detailed description is given in Chapter 3. Schemes from the families of generalized-α and energy-decaying methods will be applied to tackle the difficult shell stability problems.

The majority of the applied schemes enable user-controlled numerical (i.e. algorithmic) dissipation in the high-frequency range, which has been recognized as desirable and often necessary. The need to remove the high frequency modes is the error accumulated in these modes. On one hand, the error is a direct consequence of the spatial discretization of infinite-dimensional structural system. On the other hand, the error in the high-frequency range also depends on the underlying mechanical (i.e. physical) model, because some mechanical models tend to produce more high-frequency modes than others. For example, the introduction of rotations into structural models, e.g. [72], [75], [25], may improve element conditioning properties (and diminish the number of stiffness matrix eigenvalues with large values) in statics, which is also reflected in dynamics. Contrary to the spurious higher modes, it is very important that the introduced numerical damping has little effect in the low-frequency range, e.g. [80]. Otherwise, the application of the scheme with numerical damping for buckling simulation might lead to missing out some buckling modes, e.g. [116].

1.2.4   Wrinkling of curved shell-core substrate

Surface wrinkling exhibits some unique deformation patterns that can be found in diverse natural systems, ranging from biology to geology, as well as in various engineering systems. Regardless of the context or parameter setting in which the wrinkle patterns are observed (natural/engineered, flat/curved, length-scale, external stimuli, etc.), they develop, due to the stress, relaxation associated with the loss of stability. As such, wrinkling is traditionally understood as a sign of failure. Just recently, we have seen the introduction of so-called active materials that exploit mechanical instabilities as a platform for advanced functionality and superior physical properties. Examples are active control of adhesion [35], active control of wetting to achieve hydro-phobicity/-philicity [39], active control of aerodynamic drag [155], etc.

A systematic understanding of the loss of stability and the wrinkling pattern evolution in these systems requires analyses that reach deep into the post-buckling regime, where, unfortunately, practically no analytical calculations on curved geometry are possible. The common approach is therefore to perform a numerical nonlinear static stability analysis, which usually includes the path-following methods and branch switching algorithms, see e.g. [42], [173], [149], [150]. For problems where such methods fail, nonlinear structural dynamics can be used, see e.g. [102]. Explicit schemes are preferred because they always give results, but they may not be accurate. Implicit schemes, on the other hand, are more accurate but more difficult to implement. The above-mentioned common methods have been applied in several articles on the wrinkling of elastic films adhering to thick substrates in various curved geometry settings, including cylindrical [182], [173], spherical [148], spheroidal [156] and toroidal [184]. In this manuscript we will focus only on cylindrical and spherical systems.

In the analysis of cylindrical shell-substrate composite systems, axial and/or radial loading was applied to trigger wrinkling. For example, the deformations of stiff cylinders attached to elastic substrates and limited to radial wrinkling were studied [110], [33], [100]. The wrinkling of anisotropic films on cylindrical substrates was investigated by Yin and Chen [177] to find an effective way to fabricate 3D (helical) gear-like structures. They analyzed the effects of geometric and material parameters on the wavelength and inclination of wrinkles. In [124] Patricio et al. investigated the wrinkling of stiff-shell/soft-core cylindrical fibers with mismatches in length and radius, as well as critical conditions for the initiation of wrinkling along the fiber axis or wrinkling along the fiber circumference. They found that stiffer and thicker shell tends to wrinkle along the circumference, while thinner and softer shell tends to wrinkle along the length. The theoretical stability and pattern evolution on these cylindrical systems due to differential volumetric growth were investigated by Jia et al. [78]. They found that during post-buckling, depending on the geometric and material parameters, multiple morphological transitions occur, which lead to the formation of square, hexagonal and labyrinthine wrinkles. Furthermore, Zhao et al. [182] reported a combined experimental and theoretical investigation of the same system that was subjected to axial compression. They showed that regardless of the system properties, the first wrinkling mode is always axisymmetric and periodic along the longitudinal axis of the cylinder. Their theoretical findings were extended by Xu and Potier-Ferry [173], who performed numerical analyses on axially compressed cylinders on substrates in a static framework by applying pseudo-dynamic regularization. They identified a parameter that predicts the type of wrinkling to occur.

In the analysis of spherical core-shell systems, Cao et al. [32] performed experiments on microscopic spheres and performed related numerical simulations in Abaqus [1]. Both results showed that either hexagonal or labyrinthine dimple patterns will emerge, depending on the properties of the analyzed system. These results were confirmed by micro-scale experiments in [29] and [178], as well as macro-scale experiments in [30] and [155]. 3D finite elements were used in a numerical study performed in [111], where they showed that the sphere first buckles into a dimple pattern, which gradually evolves into a labyrinthine pattern through subsequent bifurcations. In [151] they confirmed these results by implementing a reduced model, which preserves only radial displacements. Furthermore, Veldin et al. [156] used similar reduced procedure to predict the characteristic wrinkling pattern at initial post-buckling. In a recent work, Xu et al. [174] performed experimental and numerical investigation on micro-scale spheres, where they proposed the validity of a parameter that was previously derived for cylinders, also for spheres.

In this work, we recognize the implicit dynamics as a suitable setting in which to address the difficult problem of surface wrinkling of soft-core-stiff-film composites. To analyze these problems, we apply several schemes from the class of generalized-α methods [49] and the energy-decaying methods [4].

1.3   The goals of the thesis

The main goal of the thesis is to further advance the available knowledge and tools for the shell finite element analysis. The particular goals fit the main goal and can be summarized as follows:

- Extensive review of existing mixed-hybrid, ANS and EAS formulations for geometrically exact shell models. Proposal of an "optimal" four-node element.
- Review and assessment of some existing, one-step, implicit time integration schemes for structural dynamics that fall into the classes of generalized-α and energy-momentum conserving/decaying schemes. Extension of a new generalized-α scheme, recently proposed for structural dynamics by Kadapa et al. [80], to shell formulation.
- Derivation of energy-momentum conserving/decaying scheme for mixed-hybrid shell formulations.
- Application of the derived formulations for shell stability problems, including buckling and surface wrinkling phenomena.

1.4   Methodology

All the derived finite elements and dynamic schemes are implemented using AceGen and AceFEM environments, see [94] and [95]. They are available as add-ons in commercial software Wolfram Mathematica [169].

AceGen enables automatic finite element code generation by exploiting the abilities of Wolfram Mathematica, performing automatic differentiation of large expressions and algorithms as well as automatic code generation. AceFEM is a finite-element analysis environment. The combined use of both enabled us to implement different finite element formulations quickly and efficiently and to extensively test the derived formulations.

1.5   The outline of the thesis

In addition to Chapter 1, where we introduce the topics of interest, the thesis consists of 6 chapters.

In Chapter 2, we present two shell models and then focus on the mixed formulations for shells. An extensive review of some of the most prominent formulations is presented, where we address several theoretical and numerical aspects that have to be carefully considered in the design of a high-performance element. Finally, the performance of the chosen mixed, low-order finite element formulations is investigated on a set of benchmark problems. A closer look at three nearly optimal quadrilateral finite elements for geometrically exact inextensible-director shell model is taken and their weak and strong spots are highlighted.

Chapter 3 is devoted to structural dynamics. We revisit some existing time-stepping schemes that fall either into the class of the generalized-α or the energy-decaying methods. We perform a systematic comparison of their characteristics for linear dynamics and we study how these features extend to nonlinear dynamics by performing a set of numerical tests on examples of shell structure.

In Chapter 4, we present a novel mixed variational formulation that incorporates the energy-decaying momentum-conserving time stepping scheme. Previously identified high-performance mixed-hybrid shell finite elements from Chapter 2 are extended to the transient regime, where their robustness is preserved. The proposed temporal discretization allows to controllably dissipate the total energy of the system and ensures conservation of momenta.

In Chapter 5, the implicit dynamic time-stepping schemes with numerical dissipation are applied to study the shell buckling process. We assess the ability of these schemes to handle complex buckling and post-buckling processes of thin shells. Furthermore, we show that high-frequency numerical dissipation is necessary for an efficient implicit dynamic simulation of stability problems.

Chapter 6 is devoted to wrinkling analysis of curved shell-core composites. We propose computational models for predicting the surface wrinkling that are based on the shell models presented in Chapters 4 and 5 and use implicit dynamic schemes. We apply these models to the problems of axially compressed cylindrical composites and spherical composites subjected to external pressure. We show that the proposed computational models predict wrinkling patterns that are in good agreement with the experimental and other numerical results from the available references.

Conclusions and possible guidelines for future work are drawn in Chapter 7.

We would like to point out to the reader that the notation is not necessarily transferred from one chapter to another, unless specifically stated in the text. However, the notation is consistent within each chapter.

2   OVERVIEW AND COMPARISON OF MIXED LOW-ORDER FINITE ELEMENTS FOR GEOMETRICALLY EXACT SHELL MODELS

Chapter abstract

Development of accurate, robust and efficient finite elements for the analysis of shell structures has been one of the key tasks in computational mechanics of shells. This chapter is devoted to the mixed shell formulations. Due to a great variety of mixed formulations and despite their flexibility, several theoretical and numerical aspects have to be carefully considered in the design of a high-performance element. The present chapter aims to provide the basis for methodological analysis and comparison of such aspects. A critical review of the state-of-the-art methods is given with regard to the treatment of large rotations, variational formulations and the selection of interpolation spaces. Finally, the performances of the chosen mixed, low-order finite element formulations are investigated on a set of benchmark problems, where we evaluate their robustness, speed, mesh distortion sensitivity and convergence properties. Note that this chapter includes parts of our article [104], book chapter [103] and yet unpublished article [107].

2.1   Chapter introduction

Development of a low-order (4-node) "optimal" nonlinear shell finite element is of great practical interest. Such an element should: (i) pass the basic tests, (ii) show nearly optimal convergence behavior, (iii) display low sensitivity to mesh distortion, (iv) allow for large solution steps, and (v) be computationally fast. It should maintain these favorable properties irrespective of the type of shell problem categorized by geometry, loading and boundary conditions.

It is furthermore understood that such an element should also be equipped with efficient description of large rotations. Thus, in this chapter we compare several possible implementation strategies that more or less effectively equip the model with large rotation description. They include a parametrization using a rotation matrix or rotation quaternion and three possible rotation update methods.

It is understood that a pure displacement-based formulation cannot fulfill all of the above listed criterions. Thus, our attention is focused on the mixed and mixed-hybrid formulations that fall in the families of assumed natural strain (ANS), enhanced assumed strain (EAS), hybrid Hu-Washizu-based (HW) or hybrid Hellinger-Reissner-based (HR) formulations. In the following sections we will describe the implementation details for 15 mixed or mixed-hybrid shell formulations that allow for an independent interpolation of strains and/or stresses and we will compare their numerical performance.

As a starting point, two shell models are used: 5-parameter, large rotation, inextensible director model, see e.g. [139], [24], and 6-parameter, rotation-less, extensible director model, see e.g. [17]. For the 6-parameter model, only one finite element version will be investigated which applies the ANS technique for transverse shear [48] and normal strains [15]. As for the 5-parameter model, we will implement two elements based on the ANS formulation. The first one modifies only the transverse shear strain interpolation [48] (we denote it as MITC4), while the second one modifies also the membrane strain field [89] (we denote it as MITC4+). Numerical examples in [89], [90], [91], [104] and our numerical experiments demonstrate that MITC4+ shows nearly optimal rate of convergence (also for nonlinear

problems), and displays incredibly little sensitivity to mesh distortion. However, its weak spots are: (i) pure membrane (i.e. in-plane) deformations, and (ii) very large bending deformations accompanied by small membrane deformations (such problem is, e.g., deployable ring presented in the section with numerical examples). In these cases, the ANS enhancement of the membrane behavior has only a minor effect, which is revealed by practically identical behavior of MITC4+ and MITC4. Thus, for the two mentioned shell problem types, MITC4+ does not remove membrane locking.

From the family of enhanced assumed strain (EAS) formulations, we will focus only on those that improve the membrane field of the strains. Adopted from [22] and [12], we will implement formulations with 4, 5 or 7 independent strain parameters, denoted here as EAS4, EAS5 and EAS7, respectively. We will show that the number of parameters strongly influences their behavior and determines how many of the above listed favorable properties are possessed by a specific formulation.

From the hybrid formulations we will focus on the formulations derived by Wagner and Gruttmann, who proposed in [159] a Hu-Washizu type nonlinear 4-node shell element, denoted here as HW. We will further implement also the formulation from [60] that additionally employs the EAS type interpolations for the independent strains, denoted as HWEAS, and the one based on the Hellinger-Reissner functional from [59], denoted here as HR. We argue that these formulations all have the last two (plus the first one) of the above listed favorable properties of the "optimal" shell finite element. Numerical examples in [59], [60], [159] and our numerical experiments show that they are very fast, can use large solution steps, and have good convergence behavior for regular meshes. However, they are sensitive to mesh distortion, which is their weak spot. They do not remove the membrane locking for distorted meshes.

We show in this chapter that new formulations can be obtained by straightforwardly merging some of the existing ones in a way that preserves the positive features of their predecessors. This is proved by the superior performance of the elements that synergize the positive features of the membrane ANS treatment and the hybrid HW or HR formulation. Our extensive numerical tests, partly presented in Section 2.5, demonstrate that the resulting elements possess all five of the above listed favorable properties of the "optimal" shell finite element, while no weak spots of their predecessors are present.

In the rest of the chapter we first present our version of the geometrically exact, inextensible-director shell model. In the following section, we describe the implementation details for the displacement-based formulations. The interpolations for mixed and mixed-hybrid element formulations are presented next, followed by an extensive set of numerical examples where we demonstrate their behavior and elaborate on their properties.

2.2   Geometrically exact shell models

In this section, the basic features of the geometrically nonlinear, large rotation, inextensible-director shell theory are presented. Its more detailed description is given in seminal works [140], [142], and many later works, see, e.g., [25], [28], [47], [74], [98], [159], [164] (among others) and references therein. Moreover, the rotation-less, extensible director shell theory is presented, where the rotations are replaced by the difference vector. For further details on this kind of theories we refer to [17], [144].

2.2.1   Inextensible-director shell theory

The shell is modelled as a surface equipped with an inextensible one-director field that is embedded in the 3d space with fixed orthonormal basis $\boldsymbol{e}_i$, $i = 1,2,3$. The position vector to the material point at the shell initial configuration is given as:

$$\boldsymbol{X}(\xi^1,\xi^2,\zeta) = \boldsymbol{X}_0(\xi^1,\xi^2) + \zeta\boldsymbol{D}(\xi^1,\xi^2), \quad \zeta \in [-t/2, t/2], \quad (\xi^1,\xi^2) \in \mathcal{A}, \quad \|\boldsymbol{D}\| = 1 \qquad (2.1)$$

where ξ^1, ξ^2 are convected curvilinear coordinates, ζ is through-the-thickness coordinate, $\boldsymbol{X}_0(\xi^1,\xi^2)$ is shell mid-surface, $\boldsymbol{D}(\xi^1,\xi^2)$ is normal-to-the-surface vector field of unit length that is called director, t is shell thickness, and $\mathcal{A}$ is the domain of mid-surface parametrization. Let the shell director be represented as

$$\boldsymbol{D}(\xi^1,\xi^2) = \boldsymbol{\Lambda}_0(\xi^1,\xi^2)\boldsymbol{e}_3, \qquad (2.2)$$

where $\boldsymbol{\Lambda}_0(\xi^1,\xi^2)$ is tensor field that can be called initial rotation. The basic kinematic assumption of the theory defines the position vector in the deformed configuration of the shell, which assumes that the displacements vary linearly through the thickness and that the director is inextensible:

$$\boldsymbol{x}(\xi^1,\xi^2,\zeta) = \underbrace{[\boldsymbol{X}_0(\xi^1,\xi^2) + \boldsymbol{u}(\xi^1,\xi^2)]}_{\boldsymbol{x}_0(\xi^1,\xi^2)} + \zeta\boldsymbol{d}(\xi^1,\xi^2), \quad \|\boldsymbol{d}\| = 1 \qquad (2.3)$$

Note that hereinafter we will omit writing arguments on functions and functionals for the sake of brevity, and we will refrain from explicitly mentioning vector and tensor fields. In (2.3), $\boldsymbol{d}$ is the director at deformed configuration, which is not necessarily perpendicular to the deformed surface, and $\boldsymbol{u}$ is mid-surface displacement. Furthermore, let

$$\boldsymbol{d} = \boldsymbol{\Lambda}\boldsymbol{e}_3, \qquad (2.4)$$

be the shell director at the deformed configuration, where $\boldsymbol{\Lambda}$ is rotation, which rotates $\boldsymbol{e}_3$ into $\boldsymbol{d}$ without a drill and is parametrized with rotational parameters collected in $\boldsymbol{\vartheta}$. With (2.1) and (2.3), the covariant bases at the initial and deformed configurations are

$$\boldsymbol{G}_\alpha = \frac{\partial \boldsymbol{X}}{\partial \xi^\alpha}, \qquad \boldsymbol{R}_\alpha = \frac{\partial \boldsymbol{X}_0}{\partial \xi^\alpha} = \boldsymbol{G}_\alpha|_{\zeta=0}, \qquad \boldsymbol{G}_3 = \boldsymbol{R}_3 = \boldsymbol{D},$$
$$\alpha = 1,2 \qquad (2.5)$$
$$\boldsymbol{g}_\alpha = \frac{\partial \boldsymbol{x}}{\partial \xi^\alpha}, \qquad \boldsymbol{r}_\alpha = \frac{\partial \boldsymbol{x}_0}{\partial \xi^\alpha} = \boldsymbol{g}_\alpha|_{\zeta=0}, \qquad \boldsymbol{g}_3 = \boldsymbol{r}_3 = \boldsymbol{d},$$

respectively. Vectors $\boldsymbol{R}_\alpha$ span the tangent plane at the mid-surface point at the initial configuration and the dual base vectors $\boldsymbol{R}^i$ and $\boldsymbol{r}^i$ are defined through relationships $\boldsymbol{R}^i \cdot \boldsymbol{R}_j = \delta_j^i$ and $\boldsymbol{r}^i \cdot \boldsymbol{r}_j = \delta_j^i$, where δ_j^i is a Kronecker symbol. The out-of-mid-surface dual base vectors $\boldsymbol{G}^\alpha$ and $\boldsymbol{g}^\alpha$ are defined in the same way. For thin shell problems, which present a vast majority of shell problems, one can justify geometric approximation $\boldsymbol{G}_\alpha \approx \boldsymbol{R}_\alpha$ and $\boldsymbol{G}^\alpha \approx \boldsymbol{R}^\alpha$, which we also apply in this work. Our numerical experiments confirm that for thin and moderately thick shells such an approximation has a negligible effect on numerical results.

With (2.1)-(2.5), the Green-Lagrange strain tensor can be derived as

$$\boldsymbol{E} = \frac{1}{2}\big(\boldsymbol{g}_i \cdot \boldsymbol{g}_j - \boldsymbol{G}_i \cdot \boldsymbol{G}_j\big)\boldsymbol{G}^i \otimes \boldsymbol{G}^j = E_{ij}\boldsymbol{G}^i \otimes \boldsymbol{G}^j \approx E_{ij}\boldsymbol{R}^i \otimes \boldsymbol{R}^j. \qquad (2.6)$$

Strains E_{ij} in (2.6) can be expanded as $E_{ij} = \varepsilon_{ij} + \zeta\kappa_{ij} + (\zeta)^2\rho_{ij}$, with $\varepsilon_{33} = \kappa_{33} = \rho_{\alpha3} = \rho_{3\alpha} = \rho_{33} = 0$. It is very common that strains $E_{\alpha\beta}$ are truncated after the linear term, and that the transverse shear strains $E_{\alpha3} = E_{3\alpha}$ are truncated after the constant term, see e.g. [140], [142]. Our numerical experiments confirm that such truncation has an insignificant effect on the results, which is why it is

also applied in this work. We will work with $E_{\alpha\beta} \approx \varepsilon_{\alpha\beta} + \zeta\kappa_{\alpha\beta}$ and $E_{\alpha 3} \approx \varepsilon_{\alpha 3}$, where $\varepsilon_{\alpha\beta}$, $\kappa_{\alpha\beta}$, $\varepsilon_{\alpha 3}$ are the membrane, bending and transverse shear strains, respectively, defined as

$$\varepsilon_{\alpha\beta} = \frac{1}{2}\left(\boldsymbol{r}_\alpha \cdot \boldsymbol{r}_\beta - \boldsymbol{R}_\alpha \cdot \boldsymbol{R}_\beta\right), \qquad 2\varepsilon_{\alpha 3} = \gamma_\alpha = \boldsymbol{r}_\alpha \cdot \boldsymbol{d} - \boldsymbol{R}_\alpha \cdot \boldsymbol{D},$$
$$\kappa_{\alpha\beta} = \frac{1}{2}\left(\boldsymbol{r}_\alpha \cdot \boldsymbol{d}_{,\beta} + \boldsymbol{r}_\beta \cdot \boldsymbol{d}_{,\alpha} - \boldsymbol{R}_\alpha \cdot \boldsymbol{D}_{,\beta} - \boldsymbol{R}_\beta \cdot \boldsymbol{D}_{,\alpha}\right),$$
(2.7)

where $(\circ)_{,\alpha} = \partial(\circ)/\partial\xi^\alpha$. For the finite element implementation of the theory, it proves convinient to introduce at the mid-surface point an orthonormal basis $\hat{\boldsymbol{e}}_i$ such that $\hat{\boldsymbol{e}}_3 \equiv \boldsymbol{D}$, $\hat{\boldsymbol{e}}_1 \perp \hat{\boldsymbol{e}}_3$, $\|\hat{\boldsymbol{e}}_1\| = 1$, and $\hat{\boldsymbol{e}}_2 = \hat{\boldsymbol{e}}_3 \times \hat{\boldsymbol{e}}_1$. Thus, the initial rotation matrix for that point is simply

$$\boldsymbol{\Lambda}_0 = [\hat{\boldsymbol{e}}_1, \hat{\boldsymbol{e}}_2, \boldsymbol{D}]. \tag{2.8}$$

The strains can be given with respect to such orthonormal basis by using (2.7) and by applying the following transformations

$$\hat{\varepsilon}_{ab} = \varepsilon_{\alpha\beta}(\hat{\boldsymbol{e}}_a \cdot \boldsymbol{R}^\alpha)(\hat{\boldsymbol{e}}_b \cdot \boldsymbol{R}^\beta), \quad \hat{\kappa}_{ab} = \kappa_{\alpha\beta}(\hat{\boldsymbol{e}}_a \cdot \boldsymbol{R}^\alpha)(\hat{\boldsymbol{e}}_b \cdot \boldsymbol{R}^\beta), \quad \hat{\gamma}_a = \gamma_\alpha(\hat{\boldsymbol{e}}_a \cdot \boldsymbol{R}^\alpha), \quad a = 1,2 \tag{2.9}$$

Energy conjugated to the Green-Lagrange shell strains in (2.7) and (2.9) are the second Piola-Kirchhoff shell stress resultants. The shell membrane, moment and transverse shear tensors, $\boldsymbol{n}$, $\boldsymbol{m}$ and $\boldsymbol{q}$, respectively, can be resolved with respect to the basis $\hat{\boldsymbol{e}}_i$ as

$$\boldsymbol{n} = \hat{n}_{ab}\hat{\boldsymbol{e}}_a \otimes \hat{\boldsymbol{e}}_b, \qquad \boldsymbol{m} = \hat{m}_{ab}\hat{\boldsymbol{e}}_a \otimes \hat{\boldsymbol{e}}_b, \qquad \boldsymbol{q} = \hat{q}_a(\hat{\boldsymbol{e}}_a \otimes \boldsymbol{D} + \boldsymbol{D} \otimes \hat{\boldsymbol{e}}_a). \tag{2.10}$$

In order to simplify the notation, the strain and stress resultant vectors are introduced as

$$\boldsymbol{\epsilon} = [\hat{\varepsilon}_{11}, \hat{\varepsilon}_{22}, 2\hat{\varepsilon}_{12}]^T, \quad \boldsymbol{\kappa} = [\hat{\kappa}_{11}, \hat{\kappa}_{22}, 2\hat{\kappa}_{12}]^T, \quad \boldsymbol{\gamma} = [\hat{\gamma}_1, \hat{\gamma}_2]^T,$$
$$\boldsymbol{n} = [\hat{n}_{11}, \hat{n}_{22}, \hat{n}_{12}]^T, \quad \boldsymbol{m} = [\hat{m}_{11}, \hat{m}_{22}, \hat{m}_{12}]^T, \qquad \boldsymbol{q} = [\hat{q}_1, \hat{q}_2]^T. \tag{2.11}$$

As for the material model, the usual choice is the stress-resultant version of the Saint-Venant-Kirchhoff isotropic hyperelastic material model. It takes into account the assumption of the zero normal stress in the thickness direction, which reflects in $\hat{n}_{33} = \hat{m}_{33} = 0$. It is suitable for shell problems with large elastic displacements and large rotations, but small strains. For the inextensible director shell theory, such a choice leads to the following constitutive relations

$$\boldsymbol{n} = \boldsymbol{C}^m \boldsymbol{\varepsilon}, \qquad \boldsymbol{m} = \boldsymbol{C}^b \boldsymbol{\kappa}, \qquad \boldsymbol{q} = \boldsymbol{C}^s \boldsymbol{\gamma}, \qquad \boldsymbol{C}^m = t\bar{\bar{\boldsymbol{C}}}, \qquad \boldsymbol{C}^b = t^3/12\bar{\bar{\boldsymbol{C}}}, \tag{2.12}$$

where $\bar{\bar{\boldsymbol{C}}}$ is the standard plane-stress constitutive matrix

$$\bar{\bar{\boldsymbol{C}}} = \frac{E}{(1-\nu^2)}\begin{bmatrix} 1 & \nu & 0 \\ \nu & 1 & 0 \\ 0 & 0 & \frac{1-\nu}{2} \end{bmatrix}, \quad \boldsymbol{C}^s = c\frac{Et}{2(1+\nu)}\begin{bmatrix} 1 & 0 \\ 0 & 1 \end{bmatrix}, \tag{2.13}$$

E is elastic modulus, ν is Poissons ratio and c is shear correction factor, which is set to 5/6.

Let the shell be loaded by (mid-surface) pressure and body loads, which are both included in $\bar{\boldsymbol{b}}$, and boundary forces $\bar{\boldsymbol{t}}$. For this type of loading, the potential energy functional reads as

$$\Pi(\boldsymbol{u}, \boldsymbol{d}) = \Pi_{\text{int}}(\boldsymbol{u}, \boldsymbol{d}) - \Pi_{\text{ext}}(\boldsymbol{u}, \boldsymbol{d}) =$$
$$\int_M \frac{1}{2}\left(\boldsymbol{\varepsilon} \cdot \boldsymbol{C}^m \boldsymbol{\varepsilon} + \boldsymbol{\kappa} \cdot \boldsymbol{C}^b \boldsymbol{\kappa} + \boldsymbol{\gamma} \cdot \boldsymbol{C}^s \boldsymbol{\gamma}\right) dA - \left(\int_M \boldsymbol{u} \cdot \bar{\boldsymbol{b}} \, dA + \int_{\Gamma_{\bar{t}}} \boldsymbol{u} \cdot \bar{\boldsymbol{t}} \, ds\right), \tag{2.14}$$

where M is initial mid-surface of the shell, and $\Gamma_{\bar{t}}$ is part of its boundary with prescribed forces. The shell is in equilibrium when the potential energy functional is at its minimum. The necessary condition is

$$\delta\Pi(\boldsymbol{u}, \boldsymbol{d}; \delta\boldsymbol{u}, \delta\boldsymbol{d}) = \int_M \left(\delta\boldsymbol{\varepsilon} \cdot \boldsymbol{C}^m \boldsymbol{\varepsilon} + \delta\boldsymbol{\kappa} \cdot \boldsymbol{C}^b \boldsymbol{\kappa} + \delta\boldsymbol{\gamma} \cdot \boldsymbol{C}^s \boldsymbol{\gamma}\right) dA - \delta\Pi_{\text{ext}}(\delta\boldsymbol{u}, \delta\boldsymbol{d}) = 0, \tag{2.15}$$

where $\delta\Pi$ is variation of potential energy, which is obtained as $\delta\Pi = \frac{d}{d\omega}\Pi(\boldsymbol{u} + \omega\delta\boldsymbol{u}, \boldsymbol{\vartheta} + \omega\delta\boldsymbol{\vartheta})|_{\omega=0}$, where ω is a scalar parameter, $\delta\boldsymbol{u}$ and $\delta\boldsymbol{d} = \frac{d}{d\omega}\boldsymbol{d}(\boldsymbol{\vartheta} + \omega\delta\boldsymbol{\vartheta})|_{\omega=0}$ are the kinematically admissible variations of $\boldsymbol{u}$ and $\boldsymbol{d}$, $\delta\Pi_{\text{ext}}$ is variation of external loading potential, and $\delta\boldsymbol{\varepsilon}, \delta\boldsymbol{\kappa}$ and $\delta\boldsymbol{\gamma}$ are vectors of variations of membrane, bending and transverse shear strains. Their components need to be defined with respect to the $\hat{\boldsymbol{e}}_i$ basis. Therefore, the strain variations with respect to the curvilinear coordinates, which are

$$\delta\varepsilon_{\alpha\beta} = \frac{1}{2}\left(\delta\boldsymbol{u}_{,\alpha} \cdot \boldsymbol{r}_\beta + \boldsymbol{r}_\alpha \cdot \delta\boldsymbol{u}_{,\beta}\right), \qquad \delta\gamma_\alpha = \delta\boldsymbol{u}_{,\alpha} \cdot \boldsymbol{d} + \boldsymbol{r}_\alpha \cdot \delta\boldsymbol{d},$$

$$\delta\kappa_{\alpha\beta} = \frac{1}{2}\left(\delta\boldsymbol{u}_{,\alpha} \cdot \boldsymbol{d}_{,\beta} + \boldsymbol{r}_\alpha \cdot \delta\boldsymbol{d}_{,\beta} + \delta\boldsymbol{u}_{,\beta} \cdot \boldsymbol{d}_{,\alpha} + \boldsymbol{r}_\beta \cdot \delta\boldsymbol{d}_{,\alpha}\right), \tag{2.16}$$

need to be transformed to the $\hat{\boldsymbol{e}}_i$ basis by using the rules given in (2.9).

Either the weak form of the problem (2.15) or the potential energy functional (2.14) represent the starting point for the finite element implementation of the theory if the implementation is based on the interpolations of displacement and director, i.e. $\boldsymbol{u}$ and $\boldsymbol{d}$. It is well documented, however, that such a straightforward implementation produces formulations, which suffer critically from the shear locking and also from the membrane locking, see e.g. [17], [48], [60], [90], [104]. A variety of approaches can be applied to avoid locking, and to improve robustness and speed of numerical formulations. Those that replace the potential energy functional (2.14) with the mixed functionals that allow for an independent interpolations of strains and/or stresses will be assessed below for the quadrilateral shell finite element.

2.2.2   Large rotations description

Large rotation $\boldsymbol{\Lambda}$, introduced in (2.4), is part of a special group of orthogonal transformations $\boldsymbol{\Lambda} \in SO(3)$ $(\boldsymbol{\Lambda}^{-1} = \boldsymbol{\Lambda}^T, \det\boldsymbol{\Lambda} = 1)$ and rotates $\boldsymbol{e}_3$ into $\boldsymbol{d}$ without a drill. In addition, we can define the tangent space to $SO(3)$, as $T_X SO(3)$, see [115], [176], where $X \in \{T, I, M\}$ corresponds to points during the Newton-Raphson procedure at which the plane can be defined, see Figure 2.1. Rotation $\boldsymbol{\Lambda}$ can be parametrized in different ways, see e.g. [14], [25], [28], [71], [142], [164] for detailed discussions on this topic. However, before a parametrization, let us decompose $\boldsymbol{\Lambda}$ into two rotations, where one of them is the initial rotation $\boldsymbol{\Lambda}_0$ that is known from the initial geometry, see (2.2) and (2.8). This allows to express $\boldsymbol{d}$ as

$$\boldsymbol{d} = \boldsymbol{\Lambda}_0\widetilde{\boldsymbol{\Lambda}}(\boldsymbol{\vartheta}_T)\boldsymbol{e}_3 = \widetilde{\boldsymbol{\Lambda}}(\boldsymbol{\theta}_T)\boldsymbol{\Lambda}_0\boldsymbol{e}_3 = \widetilde{\boldsymbol{\Lambda}}(\boldsymbol{\theta}_T)\boldsymbol{D}, \tag{2.17}$$

where $\widetilde{\boldsymbol{\Lambda}}$ is the rotation that is parametrized by either $\boldsymbol{\vartheta}_T$ or $\boldsymbol{\theta}_T$. We choose to parametrize $\widetilde{\boldsymbol{\Lambda}}$ with the rotation vector, and in this case $\boldsymbol{\vartheta}_T$ and $\boldsymbol{\theta}_T$ are called total material and spatial rotation vector, respectively (which is emphasized by index T). For the parametrization with the material rotation vector, the following formula of Rodrigues applies, see e.g. [140]

$$\widetilde{\boldsymbol{\Lambda}}(\boldsymbol{\vartheta}_T) = \cos\vartheta_T\mathbf{I} + \frac{\sin\vartheta_T}{\vartheta_T}\widehat{\boldsymbol{\vartheta}}_T + \frac{1 - \cos\vartheta_T}{\vartheta_T^2}\boldsymbol{\vartheta}_T\otimes\boldsymbol{\vartheta}_T, \tag{2.18}$$

where $\mathbf{I}$ is identity matrix, $\vartheta_T = \|\boldsymbol{\vartheta}_T\|$, $\widehat{\boldsymbol{\vartheta}}_T\boldsymbol{b} = \boldsymbol{\vartheta}_T \times \boldsymbol{b}$ for $\forall\boldsymbol{b}$ for the skew-symmetric matrix $\widehat{\boldsymbol{\vartheta}}_T \in T_T SO(3)$, and $\otimes$ denotes the tensor product. Because $\boldsymbol{\vartheta}_T$ rotates $\boldsymbol{e}_3$ into $\boldsymbol{d}$ without a drill, it has only two nonzero components. The drilling component is zero, which simplifies the expression for the deformed shell director into

$$\boldsymbol{d} = \boldsymbol{\Lambda}_0 \widetilde{\boldsymbol{\Lambda}}(\boldsymbol{\vartheta}_T) \boldsymbol{e}_3 = \boldsymbol{\Lambda}_0 \left(\cos\vartheta_T \boldsymbol{e}_3 + \frac{\sin\vartheta_T}{\vartheta_T} \boldsymbol{\vartheta}_T \times \boldsymbol{e}_3 \right). \tag{2.19}$$

The variation of (2.19) is $\delta\boldsymbol{d} = \mathbf{A}(\boldsymbol{\vartheta}_T)\delta\boldsymbol{\vartheta}_T$, where $\delta\boldsymbol{\vartheta}_T$ is variation of the rotation vector (with two non-zero components), and $\mathbf{A}(\boldsymbol{\vartheta}_T)$ is 3×2 matrix. At $\vartheta_T = k\pi$, $k = 1,2,\cdots$, $\mathbf{A}(\boldsymbol{\vartheta}_T)$ has two linear-dependent rows and the mapping between the director vector variation and the corresponding rotation vector variation is no longer a bijection, see [25], [74].

In order to avoid singularity problems in computations because the bijection is lost at $\vartheta_T = \pi$, one can replace rotation $\boldsymbol{\Lambda}_0$ in (2.19), which is related to the initial configuration, with rotation $\boldsymbol{\Lambda}_n$, which is related to a shell configuration between the initial one and the current one. From the computational point of view, the most convenient choice is to associate $\boldsymbol{\Lambda}_n$ with the last computed equilibrium configuration in the framework of the incremental-iterative Newton-Raphson procedure that is used to solve discrete version of the weak form of the nonlinear equilibrium equations. Let subscripts $n, n-1, \dots, 0$, denote computed equilibrium configurations that are set in order from the last one towards the first one. With this notation, the shell director at the last computed equilibrium configuration is $\boldsymbol{d}_n = \boldsymbol{\Lambda}_n \boldsymbol{e}_3$, where $\boldsymbol{\Lambda}_n$ is computed as $\boldsymbol{\Lambda}_n = \boldsymbol{\Lambda}_{n-1}\widetilde{\boldsymbol{\Lambda}}(\boldsymbol{\vartheta}_{I,n})$, where $\boldsymbol{\vartheta}_{I,n}$ is known incremental rotation vector (which is emphasized by index I) that rotates the shell director from configuration $n-1$ into configuration n and $\boldsymbol{\Lambda}_{n-1}$ is known rotation at configuration $n-1$. By using (2.18), rotation $\boldsymbol{\Lambda}_n$ can be computed as

$$\boldsymbol{\Lambda}_n = \boldsymbol{\Lambda}_{n-1}\left(\cos\vartheta_{I,n}\mathbf{I} + \frac{\sin\vartheta_{I,n}}{\vartheta_{I,n}}\widehat{\boldsymbol{\vartheta}}_{I,n} + \frac{1 - \cos\vartheta_{I,n}}{\vartheta_{I,n}^2}\boldsymbol{\vartheta}_{I,n}\otimes\boldsymbol{\vartheta}_{I,n} \right), \tag{2.20}$$

where $\widehat{\boldsymbol{\vartheta}}_{I,n} \in T_I SO(3)$. Shell director at the current deformed configuration can thus be expressed as

$$\boldsymbol{d} = \boldsymbol{\Lambda}_n \widetilde{\boldsymbol{\Lambda}}(\boldsymbol{\vartheta}_I) \boldsymbol{e}_3 = \boldsymbol{\Lambda}_n \left(\cos\vartheta_I \boldsymbol{e}_3 + \frac{\sin\vartheta_I}{\vartheta_I} \boldsymbol{\vartheta}_I \times \boldsymbol{e}_3 \right), \tag{2.21}$$

where $\boldsymbol{\vartheta}_I$ is the current incremental rotation vector. Eq. (2.21) resembles Eq. (2.19), except that the reference configuration for the rotation vector is different: in (2.19), we have the total rotation vector measured from the initial (undeformed) configuration, and in (2.21), we have the incremental rotation vector measured from the last computed equilibrium configuration. Moreover, in (2.19) we have initial rotation $\boldsymbol{\Lambda}_0$ and in (2.21) we have the rotation from the last equilibrium configuration $\boldsymbol{\Lambda}_n$. The variation of $\boldsymbol{d}$ in (2.21) is now $\delta\boldsymbol{d} = \mathbf{A}(\boldsymbol{\vartheta}_I)\delta\boldsymbol{\vartheta}_I$, where $\delta\boldsymbol{\vartheta}_I$ is the variation of the incremental rotation vector (with two non-zero components), and $\mathbf{A}(\boldsymbol{\vartheta}_I)$ is matrix with singularity at $\vartheta_I = \| \boldsymbol{\vartheta}_I \| = k\pi$, $k = 1,2,\cdots$, see [25]. In practice, this singularity does not present a problem, because the norm of the incremental rotation vector is always (much) smaller than π.

Furthermore, the singularity can also be avoided by replacing rotation $\boldsymbol{\Lambda}_0$ in (2.19), with rotation $\boldsymbol{\Lambda}_{n+1}^{k-1}$, which is related to (in generally) non-converged shell configuration at the last iteration. Let superscripts $k-1, k-2, \dots, 0$ denote computed iterations inside the last increment of the Newton-Raphson procedure. We can write the shell director at the last computed iteration as $\boldsymbol{d}_{n+1}^{k-1} = \boldsymbol{\Lambda}_{n+1}^{k-1}\boldsymbol{e}_3$, where $\boldsymbol{\Lambda}_{n+1}^{k-1}$ is known. Using the same analogy as for the incremental rotation vector, the latter can be computed as $\boldsymbol{\Lambda}_{n+1}^{k-1} = \boldsymbol{\Lambda}_{n+1}^{k-2}\widetilde{\boldsymbol{\Lambda}}(\boldsymbol{\vartheta}_{M,n+1}^{k-1})$, where $\boldsymbol{\vartheta}_{M,n+1}^{k-1}$ is known iterative rotation vector that rotates the shell director from configuration $k-2$ into configuration $k-1$, which are both (in general) non-converged. Following the development in (2.20), the skew-symmetric tensor is defined as $\widehat{\boldsymbol{\vartheta}}_{M,n+1}^{k-1} \in T_M SO(3)$ and the shell director at the current deformed configuration can be expressed as

$$d = \Lambda_{n+1}^{k-1}\widetilde{\Lambda}(\boldsymbol{\vartheta}_M)\boldsymbol{e}_3 = \Lambda_{n+1}^{k-1}\left(\cos\vartheta_M\boldsymbol{e}_3 + \frac{\sin\vartheta_M}{\vartheta_M}\boldsymbol{\vartheta}_M \times \boldsymbol{e}_3\right), \tag{2.22}$$

where $\boldsymbol{\vartheta}_M$ is the current iterative rotation vector. Eq. (2.22) resembles Eqs. (2.19) and (2.22), but with the reference configuration set in the last computed increment. The variation of $\boldsymbol{d}$ again follows the same guidelines as presented above. We note that index M comes from the fact that in the case of iterative rotation vector, the rotations are always updated multiplicatively, as opposed to the incremental and total vectors, where the update is either additive-multiplicative (additive inside a single increment and multiplicative between the increments) or purely additive.
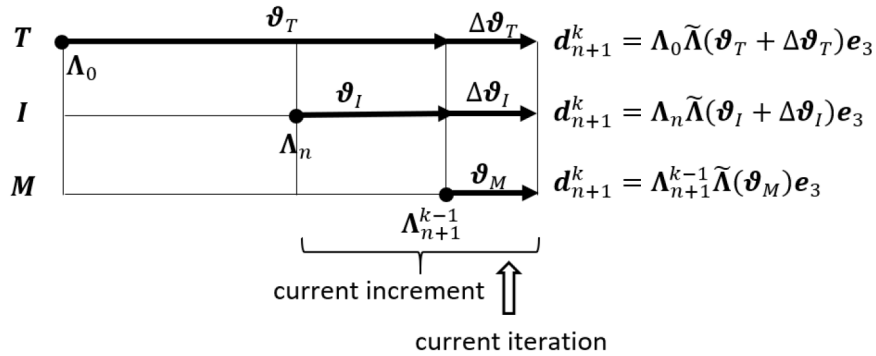
Figure 2.1: Visualization of rotation schemes *T*, *I* and *M*. Thick arrow denotes where the rotation update happens.
Slika 2.1: Vizualizacija različnih rotacijskih shem *T*, *I* in *M*. Odebeljene puščice predstavljajo, kje se zgodi posodobitev rotacij.

2.2.2.1   Algorithm T

The shell director position is described by the second expression in Eq. (2.19), and the total rotation vector is updated additively. When the norm of the total rotation vector reaches π, this description has an unwanted singularity.

2.2.2.2   Algorithm TQ

The shell director position is described by rewriting the first expression in Eq. (2.19) using quaternions, which helps to maintain numerical orthogonality of the current rotation. To this end, the initial rotation $\Lambda_0 = \left[\Lambda_{0,ij}\right], i,j = 1,2,3$, is conveyed to the rotation quaternion $\hat{q}_0$ by using the standard relations as (see e.g. [187])

$$q_0 = \frac{1}{2}\sqrt{\mathrm{tr}\Lambda_0 + 1}, \qquad \boldsymbol{q}_0 = \frac{1}{4q_0}\begin{bmatrix}\Lambda_{0,32} - \Lambda_{0,23}\\ \Lambda_{0,13} - \Lambda_{0,31}\\ \Lambda_{0,21} - \Lambda_{0,12}\end{bmatrix}, \qquad \hat{q}_0 = \begin{bmatrix}q_0\\ \boldsymbol{q}_0\end{bmatrix}, \qquad q_0 \in \mathbb{R}, \boldsymbol{q}_0 \in \mathbb{R}^3. \tag{2.23}$$

Relations (2.23) are applicable only for $\mathrm{tr}\Lambda_0 + 1 > 0$. If this inequality is not satisfied, the algorithm should be modified following standard procedures. The rotation quaternion that corresponds to rotation $\widetilde{\Lambda}(\boldsymbol{\vartheta})$ from (2.19), with the total rotation vector $\boldsymbol{\vartheta}$, can be obtained as (see e.g. [187])

$$\hat{q} = \left[cos\left(\frac{\vartheta}{2}\right), \frac{\boldsymbol{\vartheta}}{\vartheta}sin\left(\frac{\vartheta}{2}\right)\right]^T = [q, \boldsymbol{q}]^T. \tag{2.24}$$

By combining $\hat{q}_0$ from (2.23) and $\hat{q}$ from (2.24), one can get the rotation quaternion $\bar{\hat{q}}_{tot}$ that corresponds to the rotation $\mathbf{\Lambda}_0\widetilde{\mathbf{\Lambda}}(\boldsymbol{\vartheta})$ from (2.19)

$$\hat{q}_{tot} = \hat{q}_0 \circ \hat{q}, \qquad \bar{\hat{q}}_{tot} = \frac{\hat{q}_{tot}}{\|\hat{q}_{tot}\|}, \tag{2.25}$$

where $\circ$ denotes the quaternion multiplication. The shell director in the current configuration $\boldsymbol{d}$ is obtained by applying the quaternion algebra as

$$\hat{d} = [0, \boldsymbol{d}]^T = \bar{\hat{q}}_{tot} \circ [0, \boldsymbol{e}_3]^T \circ \bar{\hat{q}}^*_{tot}, \tag{2.26}$$

where $\bar{\hat{q}}^*_{tot}$ represents the conjugate pair of $\bar{\hat{q}}_{tot}$, defined as

$$\bar{\hat{q}}^*_{tot} = \left[\bar{\hat{q}}_{tot,1}, -\bar{\hat{q}}_{tot,2}, -\bar{\hat{q}}_{tot,3}, -\bar{\hat{q}}_{tot,4}\right]^T, \tag{2.27}$$

where $\bar{\hat{q}}_{tot,k}, k = 1,2,3,4$, is a component of $\bar{\hat{q}}_{tot}$. Our numerical computations show that the use of quaternions in order to compute the current shell director produces better convergence in comparison with the direct application of the second expression from Eq. (2.19). We attribute this to the fact that numerical orthogonality of the current rotation is more accurately preserved by quaternion multiplication than by rotation matrix multiplication.

2.2.2.3 Algorithms I and IQ

These algorithms avoid the singularity that appears in Algorithms T and TQ. The singularity is avoided not theoretically, but practically (in computations) by using the incremental rotation vector. In Algorithm I, the shell director is described by incremental rotation vector $\boldsymbol{\vartheta}_I$ and expression (2.21).

Moreover, in order to improve the convergence, expression (2.21) can be rewritten using quaternions which can maintain numerical orthogonality of rotation. This approach will be called algorithm IQ. The procedure is the same as explained in Section 2.2.2.2 above, except that subscript 0 is replaced by subscript n and the total rotation vector ϑ is replaced by incremental rotation vector $\boldsymbol{\vartheta}_I$.

2.2.2.4 Algorithms M and MQ

These algorithms again avoid the singularity in a practical way. In Algorithm M, the shell director is described by iterative rotation vector $\boldsymbol{\vartheta}_M$ and expression (2.22).

In order to improve the convergence and numerical orthogonality of rotations, expression (2.22) can again be rewritten using quaternions. This will be called algorithm MQ. The procedure is the same as explained in Section 2.2.2.2 above, except that subscript 0 is replaced by subscript $n + 1$, superscript $k - 1$ is added and the total rotation vector $\boldsymbol{\vartheta}$ is replaced by iterative rotation vector $\boldsymbol{\vartheta}_M$.

2.2.3 Extensible director shell theory

In this section, we show that a modification of the inextensible director shell model described above leads to an extensible director shell model with no rotational degrees of freedom. The latter considerably facilitates the finite element implementation with respect to the inextensible director one.

In the extensible director shell theory, the shell is modelled as a surface equipped with an extensible one-director field. The position vector to the material point at the shell initial configuration is still of the form given in (2.1). However, the basic kinematic assumption differs from the one adopted in the inextensible director theory. Namely, the position vector to the material point at the shell deformed configuration is for the extensible director theory defined as

$$x(\xi^1, \xi^2, \zeta) = \underbrace{[X_0(\xi^1, \xi^2) + u(\xi^1, \xi^2)]}_{x_0(\xi^1, \xi^2)} + \zeta\, d(\xi^1, \xi^2), \qquad d = D + w, \qquad (2.28)$$

where d is an extensible shell director, not necessarily of unit length, and w is the difference vector, see Figure 2.2.
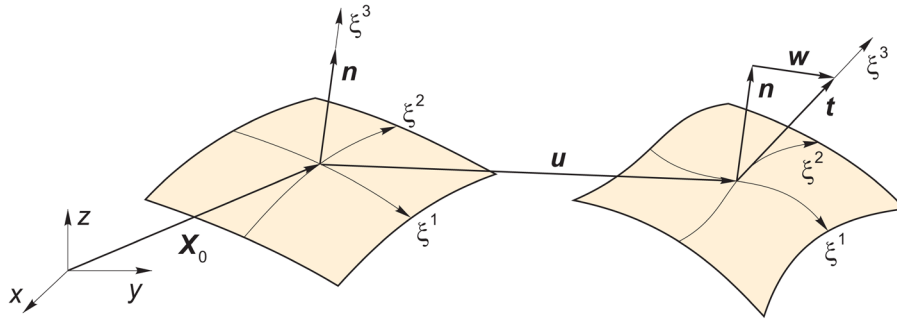
Figure 2.2: Extensible director shell model kinematics.
Slika 2.2: Kinematika modela lupine z raztegljivim smernikom.

The introduction of the difference vector allows for the derivation of a rotation-less shell theory. Note that we use the same notation for the current shell director for both inextensible- and extensible-shell models, see (2.2) and (2.28), which will enable avoiding repeating similar expressions. The components of the Green-Lagrange strain tensor with respect to the basis R^i are obtained by using (2.28) in (2.5)-(2.7). These components vary quadratically trough the thickness, i.e. $E_{ij} = \varepsilon_{ij} + \zeta\kappa_{ij} + (\zeta)^2\rho_{ij}$, where $\kappa_{33} = \rho_{\alpha3} = \rho_{3\alpha} = \rho_{33} = 0$. In the same manner as in Section 2.2.1, we apply truncation of the strains $E_{\alpha\beta}$ after the linear term, and truncation of the transverse shear strains $E_{\alpha3} = E_{3\alpha}$ after the constant term. Note that in some studies on extensible shell theory, the linear part of the transverse shear strains was not neglected. However, our numerical experiments show that retaining the linear part of the transverse shear strains has practically no effect on results. Moreover, such experiments show that taking into account all the terms of E_{ij} considerably increases the computational time for an insignificant change in results. The above-mentioned truncation leads to the membrane, bending and transverse shear strains, which can be expressed as in (2.7) with d defined as in (2.28). In addition, the through-the-thickness normal strain appears

$$\varepsilon_{33} = \frac{1}{2}\left(x_{,3} \cdot x_{,3} - X_{,3} \cdot X_{,3}\right) = \frac{1}{2}\left(d \cdot d - \underbrace{D \cdot D}_{1}\right). \qquad (2.29)$$

where $(\circ)_{,3} = \partial(\circ)/\partial\zeta$, and its transformation to the orthonormal basis $\hat{e}_i$, leads simply to $\hat{\varepsilon}_{33} = \varepsilon_{33}$. The transformation of the rest of the strains is performed as shown in (2.9). These strains and the energy conjugate second Piola-Kirchhoff stress resultants are collected in the following vectors

$$\begin{aligned}
\bar{\boldsymbol{\varepsilon}} &= [\hat{\varepsilon}_{11}, \hat{\varepsilon}_{22}, \hat{\varepsilon}_{33}, 2\hat{\varepsilon}_{12}]^{\mathrm{T}}, & \boldsymbol{\kappa} &= [\hat{\kappa}_{11}, \hat{\kappa}_{22}, 2\hat{\kappa}_{12}]^{\mathrm{T}}, & \boldsymbol{\gamma} &= [\hat{\gamma}_1, \hat{\gamma}_2]^{\mathrm{T}}, \\
\bar{\boldsymbol{n}} &= [\hat{n}_{11}, \hat{n}_{22}, \hat{n}_{33}, \hat{n}_{12}]^{T}, & \boldsymbol{m} &= [\hat{m}_{11}, \hat{m}_{22}, \hat{m}_{12}]^{T}, & \boldsymbol{q} &= [\hat{q}_1, \hat{q}_2]^{T}.
\end{aligned} \qquad (2.30)$$

Note that both $\bar{\boldsymbol{\varepsilon}}$ and $\bar{\boldsymbol{n}}$ have one component more than the corresponding vectors of the inextensible director shell model, see (2.11). For $\boldsymbol{\kappa}$ and $\boldsymbol{\gamma}$ in (2.30), expressions (2.7) and (2.9) apply, except that the current shell director is now described in a rotation-less manner by the second expression from (2.28).

As for the material model, we will use the isotropic Saint-Venant-Kirchhoff hyperelasticity, specialized for the extensible director shell theory. Forces $\bar{\boldsymbol{n}}$ relate to strains $\bar{\boldsymbol{\varepsilon}}$ as $\bar{\boldsymbol{n}} = \bar{\boldsymbol{C}}^m \bar{\boldsymbol{\varepsilon}}$, where $\bar{\boldsymbol{C}}^m = t\bar{\boldsymbol{C}}$, and $\bar{\boldsymbol{C}}$ is a part of the standard 3d constitutive matrix

$$\bar{\boldsymbol{C}} = \frac{E}{(1+v)(1-2v)} \begin{bmatrix} 1-v & v & v & 0 \\ v & 1-v & v & 0 \\ v & v & 1-v & 0 \\ 0 & 0 & 0 & \dfrac{1-2v}{2} \end{bmatrix}. \tag{2.31}$$

For the moments and transverse shear forces, however, the constitutive relations remain the same as for the inextensible director model, i.e. $\boldsymbol{m} = \boldsymbol{C}^b \boldsymbol{\kappa}$, and $\boldsymbol{q} = \boldsymbol{C}^s \boldsymbol{\gamma}$, with $\boldsymbol{C}^b$ and $\boldsymbol{C}^s$ defined as in (2.12) and (2.13).

The virtual work equation is a functional of displacement and difference vector and their variations (the former are compliant with boundary conditions and the latter are kinematically admissible)

$$\delta\Pi(\boldsymbol{u}, \boldsymbol{w}; \delta\boldsymbol{u}, \delta\boldsymbol{w}) = \int_M (\delta\bar{\boldsymbol{\varepsilon}}^T \bar{\boldsymbol{n}} + \delta\boldsymbol{\kappa}^T \boldsymbol{m} + \delta\boldsymbol{\gamma}^T \boldsymbol{q})\, dA - \delta\Pi_{\text{ext}}(\delta\boldsymbol{u}, \delta\boldsymbol{w}) = 0. \tag{2.32}$$

The vectors of strain variations, $\delta\boldsymbol{\varepsilon}$, $\delta\boldsymbol{\kappa}$ and $\delta\boldsymbol{\gamma}$, which are functionals of $\boldsymbol{u}$, $\boldsymbol{w}$ and their variations, are defined with respect to the basis $\hat{\boldsymbol{e}}_i$. Thus, the strain variations, defined with respect to the convected basis $\boldsymbol{R}^i$, which are

$$\delta\varepsilon_{\alpha\beta} = \frac{1}{2}\big(\delta\boldsymbol{u}_{,\alpha} \cdot \boldsymbol{x}_{0,\beta} + \boldsymbol{x}_{0,\alpha} \cdot \delta\boldsymbol{u}_{,\beta}\big), \qquad \delta\gamma_\alpha = \delta\boldsymbol{u}_{,\alpha} \cdot \boldsymbol{d} + \boldsymbol{x}_{0,\alpha} \cdot \delta\boldsymbol{w}, \qquad \delta\varepsilon_{33} = \delta\boldsymbol{w} \cdot \boldsymbol{d}\,,$$

$$\delta\kappa_{\alpha\beta} = \frac{1}{2}\big(\delta\boldsymbol{u}_{,\alpha} \cdot \boldsymbol{d}_{,\beta} + \boldsymbol{x}_{0,\alpha} \cdot \delta\boldsymbol{w}_{,\beta} + \delta\boldsymbol{u}_{,\beta} \cdot \boldsymbol{d}_{,\alpha} + \boldsymbol{u}_{,\beta} \cdot \delta\boldsymbol{w}_{,\alpha}\big), \tag{2.33}$$

have to be transformed to the basis $\hat{\boldsymbol{e}}_i$ by using the rules given in (2.9) and applying $\delta\hat{\varepsilon}_{33} = \delta\varepsilon_{33}$.

By inserting the constitutive relations into the virtual work equation (2.32), the weak form of the boundary value problem for the extensible director shell theory is obtained. The corresponding potential energy reads

$$\Pi(\boldsymbol{u}, \boldsymbol{w}) = \int_M \frac{1}{2}\big(\bar{\boldsymbol{\varepsilon}}^T \bar{\boldsymbol{C}}^m \bar{\boldsymbol{\varepsilon}} + \boldsymbol{\kappa}^T \boldsymbol{C}^b \boldsymbol{\kappa} + \boldsymbol{\gamma}^T \boldsymbol{C}^s \boldsymbol{\gamma}\big)\, dA - \Pi_{\text{ext}}(\boldsymbol{u}, \boldsymbol{w}) \tag{2.34}$$

where Π_{ext} is potential of external loading, and strains in (2.34) are functionals of $\boldsymbol{u}$ and $\boldsymbol{w}$. The mid-surface displacement $\boldsymbol{u}$ and the difference vector $\boldsymbol{w}$, which correspond to the minimum of the potential energy (2.34), are the solution of the weak form of the problem.

The equations of this section represent the fundamentals of an elastic (6-parameter), extensible director shell model. The first difference of this model with respect to the inextensible director one is that the former is rotation-less, which considerably simplifies its finite element implementation, especially for the shell dynamics formulations, e.g. [102]. Another difference is that it explicitly includes the through-the-thickness stretching. Because this stretching is taken into account by the difference vector only, the complete version of the through-the-thickness pre-integrated 3d constitutive relations cannot be applied.

It can be applied only for the relation between $\bar{\boldsymbol{n}}$ and $\bar{\boldsymbol{\varepsilon}}$. For the relation between $\boldsymbol{m}$ and $\boldsymbol{\kappa}$, however, the pre-integration of the plane-stress relations has to be adopted, as in the inextensible director theory.

2.3   Implementation for quadrilateral

2.3.1   Inextensible-director model interpolations

Let the initial mid-surface M be discretized by n_{el} non-overlapping isoparametric quadrilateral finite elements, such that $M \approx \bigcup_{e=1}^{n_{el}} A_e$. Over an element A_e, the initial mid-surface and shell director are approximated as

$$X_0^h(\xi, \eta) = \sum_{a=1}^{4} N_a(\xi, \eta) X_{0a}, \qquad \boldsymbol{D}^h = \sum_{a=1}^{n_4} N_a(\xi, \eta) \boldsymbol{D}_a, \qquad \|\boldsymbol{D}_a\| = 1, \qquad (2.35)$$

where subscript h denotes the approximation of a function of functional of the continuous shell model. Here, $(\cdot)_a$ are nodal values, and ξ, η are isoparametric coordinates that parametrize the element mid-surface and are interpreted as $\xi = \xi^1$ and $\eta = \xi^2$ over A_e. $N_a(\xi, \eta)$ are bilinear Lagrange interpolation functions defined over the bi-unit square $\mathcal{A}_e = [-1, 1] \times [-1, 1]$. Moreover, $\boldsymbol{D}_a$ is the exact normal to the shell mid-surface at node a. The deformed configuration over the element is approximated as

$$\boldsymbol{x}_0^h = \boldsymbol{X}_0^h + \boldsymbol{u}^h, \qquad \boldsymbol{u}^h(\xi, \eta) = \sum_{a=1}^{n_{en}} N_a(\xi, \eta) \boldsymbol{u}_a, \qquad \boldsymbol{d}^h = \sum_{a=1}^{n_{en}} N_a(\xi, \eta) \boldsymbol{d}_a. \qquad (2.36)$$

Note that the interpolation for the shell director vector in (2.36) demands the application of the above described finite rotation algorithms only at the nodes of the finite element. For this reason, the rotations and rotational parameters are needed only at the nodes. For example, for Algorithms T and TQ, one has $\boldsymbol{d}_a = \boldsymbol{d}_a(\boldsymbol{\vartheta}_a)$, where $\boldsymbol{\vartheta}_a$ is nodal total rotation vector.

After considering the spatial discretization and the relations between the mesh and the element degrees-of-freedom, functional (2.14) becomes an assembly of finite element contributions with mesh nodal values as the unknowns

$$\Pi^h = \mathbb{A}_{e=1}^{n_{el}} \Pi^{e,h}(\boldsymbol{u}^h, \boldsymbol{d}^h) = \mathbb{A}_{e=1}^{n_{el}} \left(\Pi_{\text{int}}^{e,h}(\boldsymbol{u}^h, \boldsymbol{d}^h) - \Pi_{\text{ext}}^{e,h}(\boldsymbol{u}^h, \boldsymbol{d}^h) \right), \qquad (2.37)$$

where $\mathbb{A}$ denotes the finite-element-assembly operator, see, e.g., [6], [41], [42], [73], [171].

2.3.2   Extensible-director model interpolations

Over an element A_e, the initial mid-surface and shell director are approximated as in (2.36) and the displacement vector $\boldsymbol{u}$ is interpolated as in (2.36). However, the shell director and the difference vector for this 6-parameter shell model are interpolated differently, namely as

$$\boldsymbol{d}^h = \boldsymbol{D}^h + \boldsymbol{w}^h, \qquad \boldsymbol{w}^h(\xi, \eta) = \sum_{a=1}^{n_{en}} N_a(\xi, \eta) \boldsymbol{w}_a. \qquad (2.38)$$

After considering the spatial discretization and the relations between the mesh and the element degrees-of-freedom, functional (2.34) becomes an assembly of finite element contributions with mesh nodal values as the unknowns

$$\Pi^h = \mathbb{A}_{e=1}^{n_{el}} \Pi^{e,h}(\boldsymbol{u}^h, \boldsymbol{w}^h) \tag{2.39}$$

2.3.3 Transformations for element discretization

In the following, we will extensively use the transformation from the curvilinear bases $\boldsymbol{R}_\alpha, \alpha = \xi, \eta$ and $\boldsymbol{R}^\alpha, \alpha = \xi, \eta$ to the local Cartesian bases, with all the bases defined at the mid-surface of the element. Let G and C sub/super-scripts denote a Gauss point (2×2 Gaussian quadrature is applied) and element center-point, with the local Cartesian bases $\hat{\boldsymbol{e}}_{G,i}$ and $\hat{\boldsymbol{e}}_{C,i}$, respectively, given as

$$\hat{\boldsymbol{e}}_{G,3} = \frac{\boldsymbol{R}_\xi^{h,G} \times \boldsymbol{R}_\eta^{h,G}}{\left|\boldsymbol{R}_\xi^{h,G} \times \boldsymbol{R}_\eta^{h,G}\right|}, \qquad \hat{\boldsymbol{e}}_{C,3} = \frac{\boldsymbol{R}_\xi^{h,C} \times \boldsymbol{R}_\eta^{h,C}}{\left|\boldsymbol{R}_\xi^{h,C} \times \boldsymbol{R}_\eta^{h,C}\right|}, \tag{2.40}$$

and $\hat{\boldsymbol{e}}_1 \perp \hat{\boldsymbol{e}}_3$, and $\hat{\boldsymbol{e}}_2 = \hat{\boldsymbol{e}}_3 \times \hat{\boldsymbol{e}}_1$, see Figure 2.3. At the element center-point the transformation of the covariant or contravariant components of the strains or stress resultants to the corresponding Cartesian components is done using components of the following matrix

$$\mathbf{J}_C^C = \left[\mathbf{J}_{C\,\alpha\beta}^C\right], \qquad \mathbf{J}_{C\,\alpha\beta}^C = \boldsymbol{R}_\alpha^{h,C} \cdot \hat{\boldsymbol{e}}_{C,\beta}. \tag{2.40}$$

Replacing C by G in (2.40), one gets $\mathbf{J}_G^G$ for the transformation of covariant or contravariant components to the Cartesian components at the Gauss point. Furthermore, matrices $\mathbf{J}_C^G$ and $\mathbf{J}_G^C$ are defined as

$$\begin{aligned} \mathbf{J}_C^G = \left[\mathbf{J}_{C\,\alpha\beta}^G\right], \qquad \mathbf{J}_{C\,\alpha\beta}^G = \boldsymbol{R}_\alpha^{h,G} \cdot \hat{\boldsymbol{e}}_{C,\beta}, \\ \mathbf{J}_G^C = \left[\mathbf{J}_{G\,\alpha\beta}^C\right], \qquad \mathbf{J}_{G\,\alpha\beta}^C = \boldsymbol{R}_\alpha^{h,C} \cdot \hat{\boldsymbol{e}}_{G,\beta}. \end{aligned} \tag{2.41}$$
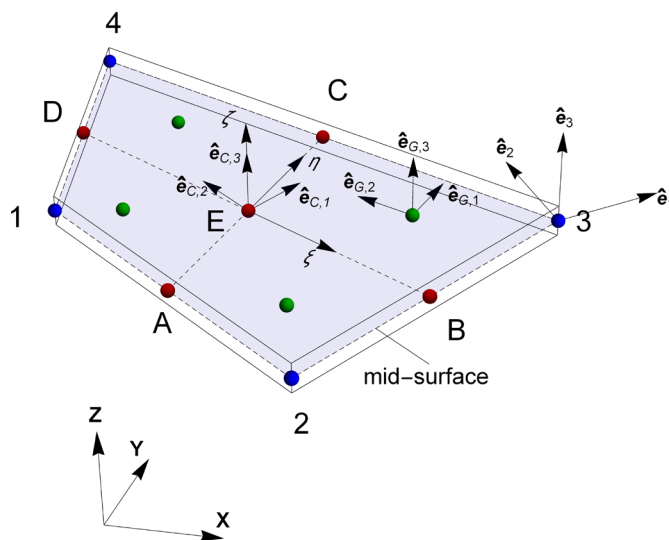
Figure 2.3: Shell quadrilateral finite element: coordinate systems and ANS points.
Slika 2.3: Štirivozliščni lupinasti končni element: koordinatni sistemi in ANS točke.

2.4 Mixed shell finite elements

In this section, we present shell formulations for four-node quadrilateral element that allow for independent interpolations of strains and/or stress resultants. Most of them rely on the Hu-Washizu variational principle, whereas some of them rely on the Hellinger-Reissner variational principle. The majority of the formulations are revisited, and some are novel. We will use the symbol $\tilde{\ }$ to denote the

strains and stress resultants with respect to the covariant or contravariant bases. When these strains are transformed to the local Cartesian coordinate, they get the symbol $\widehat{\widetilde{}}$ or simply $\widehat{}$.

2.4.1 Assumed natural strain (ANS) concept

The Assumed Natural Strain (ANS) concept is based on the application of the interpolations for the strains. Namely, at the collocation points of the element, the strains are evaluated by using the expressions from the theory, and these strains are further interpolated across the element by suitable functions. It was shown in [137] that the ANS concept falls under the class of the variational methods based on the Hu-Washizu principle. It was also shown in [137] that the variationally consistent internal forces are those that are orthogonal to the ANS strains. In practice, however, this is frequently not taken into account and in many ANS formulations the internal forces are computed from the constitutive relations, thus using variationally non-consistent internal forces.

In the shell finite element formulations, the ANS concept is widely used to avoid undesirable locking effects such as the transverse shear locking, the membrane locking and the through-the-thickness locking (the latter appears only in the extensible-director formulations).

2.4.1.1 ANS concept for transverse shear strains

In has been agreed that for the quadrilateral shell element, the most effective ANS interpolations for the transverse shear strains are those presented in [48], which assume that the covariant transverse shear strains are

$$\begin{bmatrix} \tilde{\gamma}_1 \\ \tilde{\gamma}_2 \end{bmatrix} = \frac{1}{2} \begin{bmatrix} (1-\eta)\gamma_1^A + (1+\eta)\gamma_1^C \\ (1-\xi)\gamma_2^D + (1+\xi)\gamma_2^B \end{bmatrix}, \tag{2.42}$$

where A, B, C and D are mid-side points, see Figure 2.3, at which the finite element approximation of the theoretical expression for transverse shear strains (2.7) are evaluated as

$$\gamma_\alpha^P = r_\alpha^h \cdot d^h - R_\alpha^h \cdot D^h, \qquad P = A, B, C, D. \tag{2.43}$$

The transformation from covariant strain (2.42) to the Cartesian coordinate system is given by

$$[\hat{\tilde{\gamma}}_1, \hat{\tilde{\gamma}}_2]^T = J_G^{G-1}[\tilde{\gamma}_1, \tilde{\gamma}_2]^T. \tag{2.44}$$

The inextensible-director isoparametric quadrilateral with interpolations (2.44) is frequently called MITC4, see e.g. [87], [88]. The application of ANS changes the functional $\Pi^{e,h}$ in (2.37) only slightly, because the orthogonality of the transverse shear stress resultant and the ANS transverse shear strains is assumed in the original Hu-Washizu functional. By using notation $\gamma^{ANS} = \left[\hat{\tilde{\gamma}}_1, \hat{\tilde{\gamma}}_2\right]^T$, the resulting functional can be written as

$$\Pi_{\text{MITC4}}^{e,h}(u^h, d^h) = \int_{A_e} \frac{1}{2}\left(\varepsilon^h \cdot C^m \varepsilon^h + \kappa^h \cdot C^b \kappa^h + \gamma^{ANS} \cdot C^s \gamma^{ANS}\right) dA - \Pi_{\text{ext}}^{e,h}(u^h, d^h) \tag{2.45}$$

integrated by 2×2 Gaussian quadrature. The same principle can also be applied to functional (2.39) for extensible director element formulation.

2.4.1.2   ANS concept for membrane strains

First in [87] and later in [89], Ko et al. presented a new shell quadrilateral denoted as MITC4+. The formulation alleviates the transverse shear locking by using an assumed strain field described in section 2.4.1.1, while the membrane locking is alleviated using an assumed membrane strain field, which was derived by adopting the ideas of [36] and [98]. The nonlinear version of the element is presented in [90]. The MITC4+ assumed covariant membrane strains are given as

$$\tilde{\varepsilon}_{11} = (-1 + \eta^2)\big(a_{\mathrm{B}}\varepsilon_{11}^{\mathrm{B}} + a_{\mathrm{D}}\varepsilon_{11}^{\mathrm{D}} + a_{\mathrm{E}}\varepsilon_{12}^{\mathrm{E}}\big) +$$
$$\frac{1}{2}(1 - 2a_{\mathrm{A}} - \eta + 2a_{\mathrm{A}}\eta^2)\varepsilon_{11}^{\mathrm{A}} + \frac{1}{2}(1 - 2a_{\mathrm{C}} + \eta + 2a_{\mathrm{C}}\eta^2)\varepsilon_{11}^{\mathrm{C}}, \tag{2.46}$$

$$\tilde{\varepsilon}_{22} = (-1 + \xi^2)\big(a_{\mathrm{A}}\varepsilon_{22}^{\mathrm{A}} + a_{\mathrm{C}}\varepsilon_{22}^{\mathrm{C}} + a_{\mathrm{E}}\varepsilon_{12}^{\mathrm{E}}\big) +$$
$$\frac{1}{2}(1 - 2a_{\mathrm{B}} + \xi + 2a_{\mathrm{B}}\xi^2)\varepsilon_{22}^{\mathrm{B}} + \frac{1}{2}(1 - 2a_{\mathrm{D}} - \xi + 2a_{\mathrm{D}}\xi^2)\varepsilon_{22}^{\mathrm{D}}, \tag{2.47}$$

$$\tilde{\varepsilon}_{12} = \frac{1}{4}(-\xi + 4a_{\mathrm{A}}\xi\eta)\varepsilon_{11}^{\mathrm{A}} + \frac{1}{4}(\xi + 4a_{\mathrm{C}}\xi\eta)\varepsilon_{11}^{\mathrm{C}} +$$
$$\frac{1}{4}(\eta + 4a_{\mathrm{B}}\xi\eta)\varepsilon_{22}^{\mathrm{B}} + \frac{1}{4}(-\eta + 4a_{\mathrm{D}}\xi\eta)\varepsilon_{22}^{\mathrm{D}} + (1 + a_{\mathrm{E}}\xi\eta)\varepsilon_{12}^{\mathrm{E}}, \tag{2.48}$$

where points A, B, C, D and E are shown in Figure 2.3, and the strains at these points are evaluated using expression from Eq. (2.7) as $\varepsilon_{\alpha\beta}^{\mathrm{P}} = 1/2\big(\boldsymbol{r}_\alpha^h \cdot \boldsymbol{r}_\beta^h - \boldsymbol{R}_\alpha^h \cdot \boldsymbol{R}_\beta^h\big)$, P = A, B, C, D, E. Note that $\tilde{\varepsilon}_{11}$ is quadratic in η, $\tilde{\varepsilon}_{22}$ is quadratic in ξ, and $\tilde{\varepsilon}_{12}$ is a bilinear function. For the theoretical background of interpolations (2.46)-(2.48) and the related low-sensitivity to mesh distortion, we refer to [89], [36] and [98]. The weighting factors that appear in the above expressions are

$$a_{\mathrm{A}} = \frac{c_\xi(c_\xi + 1)}{2d}, a_{\mathrm{B}} = \frac{c_\eta(c_\eta - 1)}{2d}, a_{\mathrm{C}} = \frac{c_\xi(c_\xi - 1)}{2d}, a_{\mathrm{D}} = \frac{c_\eta(c_\eta + 1)}{2d}, a_{\mathrm{E}} = \frac{2c_\xi c_\eta}{d}, \tag{2.49}$$

where c_ξ, c_η and d measure element distortion

$$c_\xi = \boldsymbol{m}^\xi \cdot \boldsymbol{x}_d, \qquad c_\eta = \boldsymbol{m}^\eta \cdot \boldsymbol{x}_d, \qquad d = c_\xi^2 + c_\eta^2 - 1. \tag{2.50}$$

They are defined as (note that notations $\boldsymbol{m}^\xi = \boldsymbol{m}^1$, $\boldsymbol{m}^\eta = \boldsymbol{m}^2$, $\boldsymbol{x}_\xi = \boldsymbol{x}_1$ and $\boldsymbol{x}_\eta = \boldsymbol{x}_2$ are applied, and that δ_β^α is Kronecker's delta):

$$\boldsymbol{x}_d = \frac{\partial^2 \boldsymbol{x}_0}{\partial\eta\partial\xi}, \qquad \boldsymbol{m}^\alpha \cdot \boldsymbol{x}_\beta = \delta_\beta^\alpha, \qquad \boldsymbol{m}^\alpha \cdot \boldsymbol{n} = 0,$$
$$\boldsymbol{x}_1 = \boldsymbol{r}_\xi^h\big|_{\eta=0}, \qquad \boldsymbol{x}_2 = \boldsymbol{r}_\eta^h\big|_{\xi=0}, \quad \boldsymbol{n} = \frac{\boldsymbol{x}_1 \times \boldsymbol{x}_2}{\|\boldsymbol{x}_1 \times \boldsymbol{x}_2\|}. \tag{2.51}$$

The weighting factors in (2.49) are configuration dependent and are updated at every solution increment. For solution increment $n + 1$, the converged configuration at solution increment n is used to compute vectors in (2.51) and factors in (2.49). An illustration of distortion vectors in (2.50) is given in Figure 2.4.

The covariant membrane strains (2.46)-(2.48) are transformed to the Cartesian strains at the Gauss point as

$$\big[\hat{\tilde{\varepsilon}}_{11}, \hat{\tilde{\varepsilon}}_{22}, 2\hat{\tilde{\varepsilon}}_{12}\big]^T = \mathbf{T}_G^{G-1}[\tilde{\varepsilon}_{11}, \tilde{\varepsilon}_{22}, 2\tilde{\varepsilon}_{12}]^T, \tag{2.52}$$

where the transformation matrix is

$$\mathbf{T}_G^G = \begin{bmatrix} \left(J_{G\,11}^G\right)^2 & \left(J_{G\,12}^G\right)^2 & J_{G\,11}^G J_{G\,12}^G \\ \left(J_{G\,21}^G\right)^2 & \left(J_{G\,22}^G\right)^2 & J_{G\,21}^G J_{G\,22}^G \\ 2J_{G\,11}^G J_{G\,21}^G & 2J_{G\,12}^G J_{G\,22}^G & J_{G\,11}^G J_{G\,22}^G + J_{G\,12}^G J_{G\,21}^G \end{bmatrix}, \tag{2.53}$$

and the resulting strains can be collected in a vector $\boldsymbol{\varepsilon}^{ANS} = \left[\hat{\tilde{\varepsilon}}_{11}, \hat{\tilde{\varepsilon}}_{22}, 2\hat{\tilde{\varepsilon}}_{12}\right]^{\mathrm{T}}$. The contribution of the elements to the potential energy functional reads as

$$\Pi_{\mathrm{MITC4+}}^{e,h}\left(\boldsymbol{u}^h, \boldsymbol{d}^h\right) = \int_{A_e} \frac{1}{2}\left(\boldsymbol{\varepsilon}^{ANS} \cdot \mathbf{C}^m \boldsymbol{\varepsilon}^{ANS} + \boldsymbol{\kappa}^h \cdot \mathbf{C}^b \boldsymbol{\kappa}^h + \boldsymbol{\gamma}^{ANS} \cdot \mathbf{C}^s \boldsymbol{\gamma}^{ANS}\right) dA - \Pi_{\mathrm{ext}}^{e,h}\left(\boldsymbol{u}^h, \boldsymbol{d}^h\right). \tag{2.54}$$
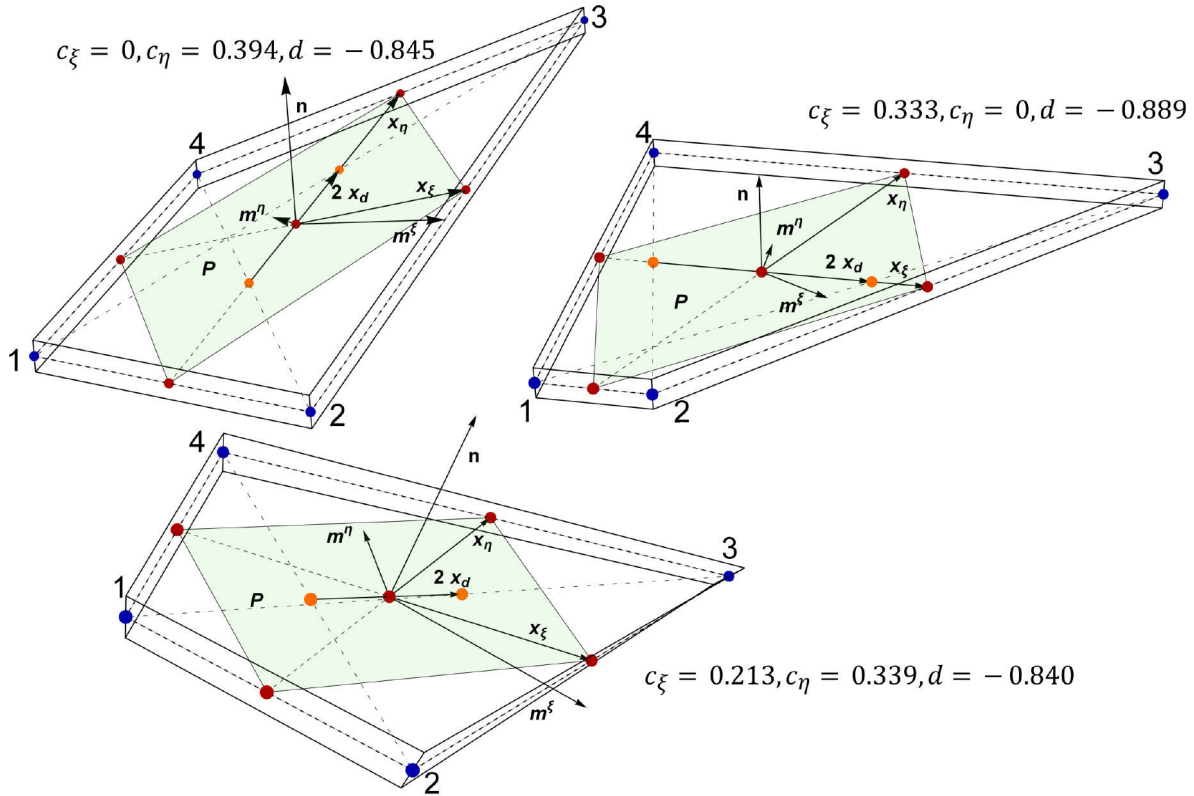
Figure 2.4: Distortion vectors for two in-plane distortions (top) and out-of-plane distortion (bottom).
Slika 2.4: Vektorji popačenja za dve ravninski popačenji (zgoraj) in izvenravninsko popačenje (spodaj).

2.4.1.3   ANS concept for transverse normal strain

For the extensible shell director model, assumed strain approach to avoid artificial thickness straining was proposed by Betsch and Stein in [15]. The assumed transverse normal strains are given by interpolating the transverse normal strains at element nodes as

$$\hat{\varepsilon}_{33}^{ANS} = \tilde{\varepsilon}_{33} = \sum_{a=1}^{n_{en}} N_a(\xi, \eta)\, \varepsilon_{33a}, \qquad \varepsilon_{33a} = \frac{1}{2}\left(\boldsymbol{d}_a \cdot \boldsymbol{d}_a - \underbrace{\boldsymbol{D}_a \cdot \boldsymbol{D}_a}_{1}\right). \tag{2.55}$$

By changing the membrane and through-the-thickness strains from (2.30) as $\bar{\boldsymbol{\varepsilon}}^{ANS} = \left[\hat{\varepsilon}_{11}, \hat{\varepsilon}_{22}, \hat{\varepsilon}_{33}^{ANS}, 2\hat{\varepsilon}_{12}\right]^{\mathrm{T}}$ and by taking into account the ANS concept for the transverse shear strains (which is applied by the same lines as presented in Section 2.4.1.1), the contribution of the element to the potential energy functional for the rotation-less shell formulation reads as (see (2.34))

$$\Pi_{\text{D-ANS}}^{e,h}(\boldsymbol{u}^h, \boldsymbol{w}^h) = \int_{A_e} \frac{1}{2} \left(\overline{\boldsymbol{\varepsilon}}^{ANS} \cdot \overline{\boldsymbol{C}}^m \overline{\boldsymbol{\varepsilon}}^{ANS} + \boldsymbol{\kappa}^h \cdot \boldsymbol{C}^b \boldsymbol{\kappa}^h + \boldsymbol{\gamma}^{ANS} \cdot \boldsymbol{C}^s \boldsymbol{\gamma}^{ANS} \right) dA - \Pi_{\text{ext}}^{e,h}(\boldsymbol{u}^h, \boldsymbol{w}^h). \quad (2.56)$$

2.4.2   Enhanced assumed strain (EAS) concept

The variational equations of the enhanced assumed strain (EAS) method can be derived from the Hu-Washizu functional combined with a reparameterization of the strain field such that

$$\boldsymbol{\epsilon}^{EAS} = \boldsymbol{\epsilon}^h + \hat{\tilde{\boldsymbol{\epsilon}}}, \quad (2.57)$$

where $\boldsymbol{\epsilon}^h$ is the Green-Lagrange strain tensor compatible to the displacement field and $\hat{\tilde{\boldsymbol{\epsilon}}}$ is the enhancing part of the strain field, which does not have to be continuous over the element domain. This is in contrast to the work of [143], where the displacement gradient was enhanced. Membrane, bending, shear and through-the-thickness strain can be enhanced by the EAS method, but it was shown (see e.g. [17], [22] for bending enhancement and [15], [34], [127] for transverse shear enhancement) that due to the additional numerical cost, the small improvement of the results is not always justified. In this work we focus only on the enhancement of the membrane part of the strains.

The contribution of the elements to the potential energy functional reads as

$$\Pi_{\text{EAS}}^{e,h}(\boldsymbol{u}^h, \boldsymbol{d}^h, \boldsymbol{\sigma}^{EAS}, \hat{\tilde{\boldsymbol{\epsilon}}}) =$$
$$\int_{A_e} \left(\frac{1}{2} \boldsymbol{\epsilon}^{EAS} \cdot (\boldsymbol{C} \, \boldsymbol{\epsilon}^{EAS}) + \boldsymbol{\sigma}^{EAS} \cdot \underbrace{\left(\boldsymbol{\epsilon}^h - \boldsymbol{\epsilon}^{EAS} \right)}_{\hat{\tilde{\boldsymbol{\epsilon}}}} \right) dA - \Pi_{\text{ext}}^{e,h}(\boldsymbol{u}^h, \boldsymbol{d}^h), \quad (2.58)$$

where $\boldsymbol{C} = \text{DIAG}[\boldsymbol{C}^m, \boldsymbol{C}^b, \boldsymbol{C}^s]$. The key assumption in the EAS formulation is the orthogonality condition between the stress field and the enhanced strain field $\int_{A_e} \boldsymbol{\sigma}^{EAS} \cdot \hat{\tilde{\boldsymbol{\epsilon}}} \, dA = 0$, which simplifies functional (2.58) to a simpler two-field functional

$$\Pi_{\text{EAS}}^{e,h}(\boldsymbol{u}^h, \boldsymbol{d}^h, \hat{\tilde{\boldsymbol{\epsilon}}}) = \int_{A_e} \left(\frac{1}{2} \boldsymbol{\epsilon}^{EAS} \cdot (\boldsymbol{C} \, \boldsymbol{\epsilon}^{EAS}) \right) dA - \Pi_{\text{ext}}^{e,h}(\boldsymbol{u}^h, \boldsymbol{d}^h), \quad (2.59)$$

where no independent stress resultants are present.

2.4.2.1   Membrane EAS formulations for shells

The enhancing membrane strains are interpolated with respect to the element-center contravariant base

$$\tilde{\boldsymbol{\varepsilon}} = \boldsymbol{\Gamma} \, \tilde{\boldsymbol{\alpha}}, \qquad \tilde{\boldsymbol{\varepsilon}} = [\tilde{\varepsilon}_{11}, \tilde{\varepsilon}_{22}, 2\tilde{\varepsilon}_{12}]^T, \quad (2.60)$$

where $\boldsymbol{\Gamma}$ is the interpolation tensor and $\tilde{\boldsymbol{\alpha}}$ the vector of the strain parameters of the element. The dimension of the interpolation tensor $\boldsymbol{\Gamma}$ depend on the chosen number of independent parameters $\tilde{\boldsymbol{\alpha}}$. The interpolation functions are chosen in such a way that the compatible strains are enriched or decoupled, see e.g. [12], [22], [2]. Namely, components ε_{11}^h and ε_{22}^h need to be enriched, while component ε_{12}^h is decomposed. This is done by looking at the polynomial space of the compatible membrane strains of the bilinear element, which is of the form

$$\varepsilon_{\alpha\beta}^h \in \text{span} \begin{bmatrix} 1 & 0 & 0 & \eta & 0 & 0 & 0 & \eta^2 & 0 & 0 \\ 0 & 1 & 0 & 0 & \xi & 0 & 0 & 0 & \xi^2 & 0 \\ 0 & 0 & 1 & 0 & 0 & \xi & \eta & 0 & 0 & \xi\eta \end{bmatrix}. \quad (2.61)$$

With the displacement-based strains $\boldsymbol{\varepsilon}^h$ expressed in the Gauss point Cartesian coordinate system, we need to transform $\tilde{\boldsymbol{\varepsilon}}$ from (2.60) to the same coordinates to get $\hat{\tilde{\boldsymbol{\varepsilon}}}$. In order to get element that passes the

patch test, it is assumed that $\tilde{\boldsymbol{\varepsilon}}$ are defined with respect to the contravariant base at element's center. To this end, the following transformation is applied (see e.g. [143])

$$\hat{\tilde{\boldsymbol{\varepsilon}}} = \begin{bmatrix} \hat{\tilde{\varepsilon}}_{11} \\ \hat{\tilde{\varepsilon}}_{22} \\ 2\hat{\tilde{\varepsilon}}_{12} \end{bmatrix} = \frac{j_C}{j_G} \mathbf{T}_G^{C-1} \tilde{\boldsymbol{\varepsilon}} = \frac{j_C}{j_G} \mathbf{T}_G^{C-1} \begin{bmatrix} \tilde{\varepsilon}_{11} \\ \tilde{\varepsilon}_{22} \\ 2\tilde{\varepsilon}_{12} \end{bmatrix}, \tag{2.62}$$

where $j = \|\boldsymbol{R}_\xi^h \times \boldsymbol{R}_\eta^h\|$. The transformation matrix $\mathbf{T}_G^C$ is defined in (2.53), but it is here assembled using components of $\boldsymbol{J}_G^C$.

Using 4, 5 or 7 independent parameters $\tilde{\boldsymbol{\alpha}}$, the membrane strains $\hat{\tilde{\boldsymbol{\varepsilon}}}$ are computed using expressions (2.60) and (2.62). Interpolation functions, discontinuous over element boundaries, are defined as

$$\boldsymbol{\Gamma} = \begin{bmatrix} \xi & 0 & 0 & 0 \\ 0 & \eta & 0 & 0 \\ 0 & 0 & \xi & \eta \end{bmatrix}, \qquad \boldsymbol{\Gamma} = \begin{bmatrix} \xi & 0 & 0 & 0 & 0 \\ 0 & \eta & 0 & 0 & 0 \\ 0 & 0 & \xi & \eta & \xi\eta \end{bmatrix}, \qquad \boldsymbol{\Gamma} = \begin{bmatrix} \xi & 0 & 0 & 0 & \xi\eta & 0 & 0 \\ 0 & \eta & 0 & 0 & 0 & \xi\eta & 0 \\ 0 & 0 & \xi & \eta & 0 & 0 & \xi\eta \end{bmatrix}, \tag{2.63}$$

for 4-, 5- and 7-parameter formulation, respectively, see e.g. [12], [22], [2].

For the shell formulation with ANS for the transverse shear strains and EAS for the membrane strains, the element functional reads simply as

$$\Pi_{\text{EAS}}^{e,h}(\boldsymbol{u}^h, \boldsymbol{d}^h, \hat{\tilde{\boldsymbol{\varepsilon}}}) =$$
$$\int_{A_e} \frac{1}{2}(\boldsymbol{\varepsilon}^{EAS} \cdot \boldsymbol{C}^m \boldsymbol{\varepsilon}^{EAS} + \boldsymbol{\kappa}^h \cdot \boldsymbol{C}^b \boldsymbol{\kappa}^h + \boldsymbol{\gamma}^{ANS} \cdot \boldsymbol{C}^s \boldsymbol{\gamma}^{ANS}) \, dA - \Pi_{\text{ext}}^{e,h}(\boldsymbol{u}^h, \boldsymbol{d}^h). \tag{2.64}$$

Additional parameters $\tilde{\boldsymbol{\alpha}}$ are condensed on the element level, thus yielding an element that has only nodal displacements and rotations as global degrees of freedom.

2.4.3 Hybrid Hellinger-Reissner (HR) formulations

The two-field Hellinger-Reissner functional was used in the development of some of the first mixed element formulations with very good properties, see e.g. [126], [141], [142]. It introduces the displacement and rotation field $\boldsymbol{u}^h, \boldsymbol{d}^h$ and the independent stress resultant field $\boldsymbol{\sigma}^{HR}$ as independent variables. The contribution of the element to the Hellinger-Reissner functional is

$$\Pi_{\text{HR}}^{e,h}(\boldsymbol{u}^h, \boldsymbol{d}^h, \boldsymbol{\sigma}^{HR}) = \int_{A_e} \left(\boldsymbol{\epsilon}^h \cdot \boldsymbol{\sigma}^{HR} - \frac{1}{2}\boldsymbol{\sigma}^{HR} \cdot \boldsymbol{C}^{-1}\boldsymbol{\sigma}^{HR} \right) dA - \Pi_{\text{ext}}^{e,h}(\boldsymbol{u}^h, \boldsymbol{d}^h), \tag{2.65}$$

where the independent stress resultants and displacement-derived strains are defined as

$$\boldsymbol{\sigma}^{HR} = [\boldsymbol{N}^{HR,T}, \boldsymbol{M}^{HR,T}, \boldsymbol{Q}^{HR,T}]^T, \qquad \boldsymbol{\epsilon}^h = [\boldsymbol{\varepsilon}^{h,T}, \boldsymbol{\kappa}^{h,T}, \boldsymbol{\gamma}^{h,T}]^T, \tag{2.66}$$

respectively. Note that $\boldsymbol{\sigma}^{HR}$ in (2.66) is comprised of a membrane, bending and shear parts. If the above definition is used, the potential energy functional of the element takes a full Hellinger-Reissner form. On the other hand, the HR functional can also be applied only for the membrane, bending or shear parts of the shell response, see e.g. [142], [167], because these parts are not coupled for isotropic shells.

Considering discontinuous interpolations for the membrane part only, the potential energy functional of the element is composed of the Hellinger-Reissner functional for the membrane stresses and the quadratic strain energy function of the displacement-based strains, for the bending and shear parts

$$\Pi_{\text{HR-M}}^{e,h}\left(\boldsymbol{u}^h, \boldsymbol{d}^h, \boldsymbol{\sigma}^{HR}\right) =$$

$$\int_{A_e} \left(\boldsymbol{\varepsilon}^h \cdot \boldsymbol{N}^{HR} - \frac{1}{2} \boldsymbol{N}^{HR} \cdot \boldsymbol{C}^{m-1} \boldsymbol{N}^{HR} + \frac{1}{2} \boldsymbol{\kappa}^h \cdot \left(\boldsymbol{C}^b \boldsymbol{\kappa}^h \right) + \frac{1}{2} \boldsymbol{\gamma}^h \cdot \left(\boldsymbol{C}^s \boldsymbol{\gamma}^h \right) \right) dA - \Pi_{\text{ext}}^{e,h}\left(\boldsymbol{u}^h, \boldsymbol{d}^h\right). \qquad (2.67)$$

A similar functional can be straightforwardly composed for a combination of independent membrane and bending or membrane and shear stress resultants.

A linear version of the formulation briefly presented here was first introduced in [59] and has its roots in the pioneering work of [126]. Other interpolations that use different number of independent stress parameters or different coordinate representations are also common in the literature. See e.g. [165] for a short history of the developed formulations and comparison between different coordinate representations, [180] for formulations with 9 or 7 parameters, and [9] for different interpolation of transverse shear stresses.

2.4.3.1   HR formulations for shells

The performance of a mixed-hybrid HR shell element depends on the interpolations chosen for the stress resultants. For plane stress quadrilaterals, "optimal" stress interpolation was derived in [126] (see, e.g., [179] for the discussion on optimality). Because the membrane and bending relations of the applied shell model enforce the zero through-the-thickness normal stress constraint, these interpolations retain the same level of optimality if applied to membrane forces and bending moments of shell quadrilateral, as is the case in [59], while the interpolations for the contravariant components of the transverse shear forces may be chosen in the linear manner (see [59])

$$\begin{bmatrix} \tilde{n}^{11} \\ \tilde{n}^{22} \\ \tilde{n}^{12} \end{bmatrix} = \begin{bmatrix} \bar{\beta}_1 + (\eta - \bar{\eta})\bar{\beta}_9 \\ \bar{\beta}_2 + (\xi - \bar{\xi})\bar{\beta}_{10} \\ \bar{\beta}_3 \end{bmatrix}, \qquad \begin{bmatrix} \tilde{m}^{11} \\ \tilde{m}^{22} \\ \tilde{m}^{12} \end{bmatrix} = \begin{bmatrix} \bar{\beta}_4 + (\eta - \bar{\eta})\bar{\beta}_{11} \\ \bar{\beta}_5 + (\xi - \bar{\xi})\bar{\beta}_{12} \\ \bar{\beta}_6 \end{bmatrix},$$

$$\begin{bmatrix} \tilde{q}^{13} \\ \tilde{q}^{23} \end{bmatrix} = \begin{bmatrix} \bar{\beta}_7 + (\eta - \bar{\eta})\bar{\beta}_{13} \\ \bar{\beta}_8 + (\xi - \bar{\xi})\bar{\beta}_{14} \end{bmatrix}. \qquad (2.68)$$

Here, $\bar{\beta}$-s are stress resultant parameters of the element, and $\bar{\xi}$ and $\bar{\eta}$ are constants that denote the coordinates of the center of gravity of the element and are defined as, see [141]

$$\bar{\xi} = \frac{1}{A_e} \int_{A_e} \xi \, dA, \qquad \bar{\eta} = \frac{1}{A_e} \int_{A_e} \eta \, dA. \qquad (2.69)$$

The setting of $\bar{\xi} = \bar{\eta} = 0$ corresponds to the original interpolations proposed in [126]. See supplement material of [159] or Appendix A for details on numerical implementation.

The contravariant components of stress resultants (2.68) and (2.69) need to be transformed to the Cartesian components that enter $\boldsymbol{\sigma}^{HR}$ in (2.65). For the element to pass the patch-test, each stress resultant should have a constant part. This is achieved if the transformation for the whole element is performed at one point of the element. For this purpose, the center-point is chosen, which leads to

$$\boldsymbol{\sigma}^{HR} = [\mathbf{1}_{8\times 8}, \mathbf{M}_\sigma]\boldsymbol{\beta}, \quad \mathbf{M}_\sigma = \text{DIAG}[\mathbf{N}_\sigma^m, \mathbf{N}_\sigma^b, \mathbf{N}_\sigma^s], \qquad (2.70)$$

where $\mathbf{1}_{8\times 8}$ is unit matrix, $\boldsymbol{\beta} = \left[\beta_1, \cdots, \beta_8, \bar{\beta}_9, \cdots, \bar{\beta}_{14}\right]^T$ (note that the first 8 components of $\boldsymbol{\beta}$ differ from $\bar{\beta}_1, \cdots, \bar{\beta}_8$ in (2.68) due to the transformation), and

$$\mathbf{N}_\sigma^m = \mathbf{N}_\sigma^b = \begin{bmatrix} \left(\mathsf{J}_{C\,11}^C\right)^2(\eta - \bar{\eta}) & \left(\mathsf{J}_{C\,21}^C\right)^2(\xi - \bar{\xi}) \\ \left(\mathsf{J}_{C\,12}^C\right)^2(\eta - \bar{\eta}) & \left(\mathsf{J}_{C\,22}^C\right)^2(\xi - \bar{\xi}) \\ \mathsf{J}_{C\,11}^C \mathsf{J}_{C\,12}^C(\eta - \bar{\eta}) & \mathsf{J}_{C\,21}^C \mathsf{J}_{C\,22}^C(\xi - \bar{\xi}) \end{bmatrix}, \qquad \mathbf{N}_\sigma^s = \begin{bmatrix} \mathsf{J}_{C\,11}^C(\eta - \bar{\eta}) & \mathsf{J}_{C\,21}^C(\xi - \bar{\xi}) \\ \mathsf{J}_{C\,12}^C(\eta - \bar{\eta}) & \mathsf{J}_{C\,22}^C(\xi - \bar{\xi}) \end{bmatrix}. \quad (2.71)$$

Matrices $\mathbf{N}_\sigma^m$, $\mathbf{N}_\sigma^b$ and $\mathbf{N}_\sigma^s$ contain the interpolation as well as the transformation from the covariant coordinate system to the local Cartesian coordinate system at the element center, which is done using components of $\boldsymbol{J}_C^C$. The detailed derivation of transformation is available in Appendix B .

To retain the same pattern of transformation, and to keep the components of all vectors in (2.65) in the same basis, the displacement-derived strains are also transformed via center-point as

$$\boldsymbol{\epsilon}^h = \bar{\mathbf{N}}_\epsilon \boldsymbol{\chi}, \qquad \boldsymbol{\chi} = \left[\varepsilon_{11}^h, \varepsilon_{22}^h, 2\varepsilon_{12}^h, \kappa_{11}^h, \kappa_{22}^h, 2\kappa_{12}^h, 2\varepsilon_{13}^h, 2\varepsilon_{23}^h\right]^T, \qquad \bar{\mathbf{N}}_\epsilon = \mathrm{DIAG}\left[\mathbf{T}_C^C, \mathbf{T}_C^C, \mathbf{J}_C^C\right]^{-1}. \quad (2.72)$$

Note that here the last two components in $\boldsymbol{\chi}$ can be replaced by ANS interpolations $\tilde{\gamma}_1$ and $\tilde{\gamma}_2$ from (2.42) and the membrane components in $\boldsymbol{\chi}$ can be replaced by the ANS interpolations from (2.46) – (2.48) such that

$$\boldsymbol{\epsilon}^{h+} = \bar{\mathbf{N}}_\epsilon^+ \boldsymbol{\chi}^+, \qquad \boldsymbol{\chi}^+ = \left[\tilde{\varepsilon}_{11}, \tilde{\varepsilon}_{22}, 2\tilde{\varepsilon}_{12}, \kappa_{11}^h, \kappa_{22}^h, 2\kappa_{12}^h, 2\tilde{\varepsilon}_{13}, 2\tilde{\varepsilon}_{13}\right]^T,$$
$$\bar{\mathbf{N}}_\epsilon^+ = \mathrm{DIAG}\left[\mathbf{T}_C^G, \mathbf{T}_C^G, \mathbf{J}_C^G\right]^{-1}, \tag{2.73}$$

in order to treat better the transverse shear locking and membrane locking, respectively. However, care must be taken when performing transformation of these quantities, as expressions (2.44) and (2.52) are no longer valid. Instead, we adopt here a transformation that relies on the components of $\mathbf{J}_C^G$, which are provided in (2.41), and matrix $\mathbf{T}_C^G$, which is obtained by using the components from (2.41) in place of those in (2.53).

As was mentioned before, a partial or incomplete HR functional can be considered for the element formulation. The direct advantage of this approach is a lower number of independent interpolation parameters, which results in a shorter element code. Thus, the dimensions of $\mathbf{N}_\sigma$ and $\boldsymbol{\beta}$ in (2.70) are changed. As is clear from (2.68), 5 parameters are used for the membrane, 5 for the bending and 4 for the shear stress resultant. For an element with the membrane and bending part of the HR functional, (2.70) changes to

$$\boldsymbol{\sigma}^{HR} = [\boldsymbol{n}^{HR,T}, \boldsymbol{m}^{HR,T}]^T = [\mathbf{1}_{6\times 6}, \mathbf{M}_\sigma]\boldsymbol{\beta}, \quad \mathbf{M}_\sigma = \mathrm{DIAG}[\mathbf{N}_\sigma^m, \mathbf{N}_\sigma^b], \tag{2.74}$$

where $\boldsymbol{\beta} = \left[\beta_1, \cdots, \beta_6, \bar{\beta}_9, \cdots, \bar{\beta}_{12}\right]^T$. Other partial HR formulations can be obtained by following the same procedure.

In all cases, the dditional parameters $\boldsymbol{\beta}$ are condensed on the element level, thus yielding an element that has only nodal displacements and rotations as global degrees of freedom.

2.4.4 Hybrid Hu-Washizu (HW) formulations

A number of different mixed variational formulations can be derived from the classical Hu-Washizu functional [161], which involves as independent variables the displacement and rotation field $\boldsymbol{u}^h, \boldsymbol{d}^h$, the independent stress resultant field $\boldsymbol{\sigma}^{HW}$ and the independent strain field $\boldsymbol{\epsilon}^{HW}$. The contribution of the element to the Hu-Washizu functional is

$$\Pi_{\text{HW}}^{e,h}(\boldsymbol{u}^h, \boldsymbol{d}^h, \boldsymbol{\epsilon}^{HW}, \boldsymbol{\sigma}^{HW}) = \int_{A_e} \left(\frac{1}{2} \boldsymbol{\epsilon}^{HW} \cdot \boldsymbol{C} \boldsymbol{\epsilon}^{HW} + \boldsymbol{\sigma}^{HW} \cdot \left(\boldsymbol{\epsilon}^h - \boldsymbol{\epsilon}^{HW} \right) \right) dA - \Pi_{\text{ext}}^{e,h}(\boldsymbol{u}^h, \boldsymbol{d}^h). \quad (2.75)$$

Hereinafter we only consider formulations based on the full Hu-Washizu functional, where the strains, stress resultants, and displacement-derived strains in (2.75) are

$$\boldsymbol{\epsilon}^{HW} = [\boldsymbol{\varepsilon}^{HW,T}, \boldsymbol{\kappa}^{HW,T}, \boldsymbol{\gamma}^{HW,T}]^T, \qquad \boldsymbol{\sigma}^{HW} = [\boldsymbol{n}^{HW,T}, \boldsymbol{m}^{HW,T}, \boldsymbol{q}^{HW,T}]^T,$$
$$\boldsymbol{\epsilon}^h = [\boldsymbol{\varepsilon}^{h,T}, \boldsymbol{\kappa}^{h,T}, \boldsymbol{\gamma}^{h,T}]^T. \qquad (2.76)$$

respectively. Note, however, that the Hu-Washizu functional can be also considered only for the membrane, bending or the transverse shear parts of the shell response.

Introducing $\boldsymbol{\alpha}$ and $\boldsymbol{\beta}$ as element strain and stress parameters vectors, respectively, the variation of $\Pi_{\text{HW}}^{e,h}$ is $\delta\Pi_{\text{HW}}^{e,h} = \frac{d}{d\omega} \Pi_{\text{HW}}^{e,h}(\boldsymbol{\Phi} + \omega\delta\boldsymbol{v}, \boldsymbol{\alpha} + \omega\delta\boldsymbol{\alpha} + \boldsymbol{\beta} + \omega\delta\boldsymbol{\beta})\big|_{\omega=0}$, where ω is a scalar parameter, $\boldsymbol{\Phi}$ is the vector of all nodal degrees of freedom, and $\delta\boldsymbol{\Phi}$, $\delta\boldsymbol{\alpha}$ and $\delta\boldsymbol{\beta}$ are admissible variations. The stationary point $\delta\Pi_{\text{HW}}^{e,h} = 0$ yields three equations that need to be linearized in order to be solved iteratively. The condensation of iterative vectors $\Delta\boldsymbol{\alpha}$ and $\Delta\boldsymbol{\beta}$ is performed from linearized equations. Inversion due to condensation is possible for the sequence $\{\Delta\boldsymbol{\alpha}, \Delta\boldsymbol{\beta}\}$ and it fails (due to singularity) if the vectors are interchanged. A similar procedure (only for vector $\Delta\boldsymbol{\beta}$) is performed for the HR elements from Section 2.4.3. For implementation details we refer to [45], [59], [60], [142] and [159].

2.4.4.1 HW formulations for shells

The independent stress resultants are interpolated with respect to the element-center Cartesian coordinate system, using the same vector of independent parameters $\boldsymbol{\beta}$ as shown in (2.68) – (2.71).

Two different interpolations are investigated for the contravariant components of shell strains with $\bar{\alpha}$-s as strain parameters of the element. The first interpolation is identical to the one presented in (2.68), as proposed in [159], with 14 independent $\bar{\alpha}$-s. For the second interpolation, 20 independent $\bar{\alpha}$-s are used, as proposed in [60], where the 6 additional $\bar{\alpha}$-s correspond to the EAS parameters.

In order to keep the components of vectors in scalar products in (2.75) in the same basis, the transformation of contravariant strains to the Cartesian strains is again performed at the center-point of element as

$$\boldsymbol{\epsilon}^{HW} = [\mathbf{1}_{8\times8}, \mathbf{M}_{\varepsilon}]\boldsymbol{\alpha}, \qquad (2.77)$$

where either

$$\boldsymbol{\alpha} = [\alpha_1, \cdots, \alpha_8, \bar{\alpha}_9, \cdots, \bar{\alpha}_{14}]^T, \mathbf{M}_{\varepsilon} = \text{DIAG}[\mathbf{N}_{\varepsilon}^{\text{m}}, \mathbf{N}_{\varepsilon}^{\text{b}}, \mathbf{N}_{\varepsilon}^{\text{s}}], \qquad (2.78)$$

or

$$\boldsymbol{\alpha} = [\alpha_1, \dots, \bar{\alpha}_{14}, \alpha_{15}, \dots, \alpha_{20}]^T, \mathbf{M}_{\varepsilon} = \left[\text{DIAG}[\mathbf{N}_{\varepsilon}^{\text{m}}, \mathbf{N}_{\varepsilon}^{\text{b}}, \mathbf{N}_{\varepsilon}^{\text{s}}], \text{DIAG}[\mathbf{N}_{\varepsilon}^{\text{m,EAS}}, \mathbf{N}_{\varepsilon}^{\text{b,EAS}}, \mathbf{N}_{\varepsilon}^{\text{s,EAS}}]\right], \quad (2.79)$$

are used for the element with 14 or 20 components of $\boldsymbol{\alpha}$, respectively. Here $\mathbf{N}_{\varepsilon}^{\text{s}} = \mathbf{N}_{\sigma}^{\text{s}}$, $\mathbf{N}_{\varepsilon}^{\text{m}} = \text{DIAG}[1,1,2]\mathbf{N}_{\sigma}^{\text{m}}$ and $\mathbf{N}_{\varepsilon}^{\text{b}} = \text{DIAG}[1,1,2]\mathbf{N}_{\sigma}^{\text{b}}$. The additional EAS interpolations are chosen in such a way that they are orthogonal to the independent stress interpolations

$$\mathbf{N}_{\varepsilon}^{\text{m,EAS}} = \mathbf{N}_{\varepsilon}^{\text{b,EAS}} = \frac{j_C}{j_G} \mathbf{T}_C^{C-1} \begin{bmatrix} \xi & 0 \\ 0 & \eta \\ 0 & 0 \end{bmatrix}, \qquad \mathbf{N}_{\varepsilon}^{\text{s,EAS}} = \frac{j_C}{j_G} \mathbf{J}_C^{C-1} \begin{bmatrix} \xi & 0 \\ 0 & \eta \end{bmatrix}, \qquad (2.80)$$

with j_C, $\mathbf{T}_C^C$ and $\mathbf{J}_C^C$ defined in the previous sections. Note that only one of the possibilities for the additional EAS interpolations is presented here. For more detail, we refer to [60], where this kind of transformation was initially proposed, and to Section 2.4.2 of this manuscript.

Note that the same transformation as in (2.72) must be applied to the displacement-derived strains, to retain the same pattern of transformation and to keep the components of all vectors in the same basis. The membrane and shear components in χ can again be replaced by the ANS interpolations as in (2.73) to better treat the transverse shear locking and membrane locking. In [104] it was demonstrated that it leads to near optimal quadrilateral.

The stress resultant interpolations (2.68) can be considered as optimal ones, while the strain interpolations are just one of the possibilities. Other suitable interpolations may be applied (e.g., with more parameters or/and with covariant strain components), which, however, produce only minor changes in results according to [166] and [168]. The changes in the interpolation of the displacement-derived strains χ in (2.73) have a much greater impact.

2.5   Numerical examples

In this section, we compare the performance of mixed rotation and rotation-less finite elements, listed in Tables 2.1 – 2.6. In these tables, the (variational) concepts for the membrane, bending, transverse shear and thickness-stretching parts are summarized for each element. Note that all the formulations use the ANS concept for the transverse shear. The finite rotation algorithms are summarized in Table 2.7.

Table 2.1: Controllers for adaptive load increments.
Preglednica 2.1: Kontrolerji za prilagajanje obtežnih inkrementov.

Example	$\Delta\lambda_{min}$	$\Delta\lambda_{max}$	$\Delta\lambda_{initial}$
2.5.1	10^{-5}	10^{-1}	$5\ 10^{-2}$
2.5.4.1	10^{-8}	$5\ 10^{-2}$	10^{-2}
2.5.4.2	10^{-8}	$5\ 10^{-2}$	10^{-2}
2.5.4.3	10^{-4}	10^{-1}	10^{-1}
2.5.4.4	10^{-8}	10^{-1}	10^{-2}
2.5.4.5	10^{-8}	$5\ 10^{-3}$	10^{-3}
2.5.4.6	10^{-8}	10^{-2}	10^{-2}
2.5.4.7	10^{-8}	$2\ 10^{-2}$	$5\ 10^{-2}$
2.5.4.8	10^{-8}	$2\ 10^{-1}$	$5\ 10^{-2}$
2.5.4.9	10^{-12}	10^{-4}	10^{-4}

The nonlinear examples presented below were computed by the load control by either constant or adaptive load increments. For the latter case, the incremental load multiplication factor at n-th increment was computed as $\Delta\lambda_n = B(I_o, I_{n-1})\Delta\lambda_{n-1}$, $\Delta\lambda_n \in [\Delta\lambda_{min}, \Delta\lambda_{max}]$ (the total value of the load multiplication factor was $\lambda_n = \lambda_{n-1} + \Delta\lambda_n$, $0 < \lambda_n \leq 1$). The adjustable factor B depended on I_0, which is the desired number of incremental iterations (set to 8 in all examples), and I_{n-1}, which is the number of iterations in the last converged increment

$$B = \begin{cases} 2 - \left(\dfrac{I_{n-1} - 1}{I_o - 1}\right)^2, & I_{n-1} < I_o \\ 1 - \dfrac{1}{2}\left(\dfrac{I_{n-1} - I_o}{N - I_o}\right)^2, & I_{n-1} \geq I_o \end{cases} \tag{2.81}$$

The maximum allowed number of iterations N was set to 15. The values of controllers for examples with adaptive load increments are given in Table 2.1. In all examples, the convergence was achieved when the norm of the iterative displacement vector was less than 10^{-8}.

Table 2.2: Considered ANS elements.
Preglednica 2.2: Obravnavani ANS elementi.

FE	Membrane	Bending	Shear	Reference
MITC4	Disp.	Disp.	ANS	[48]
MITC4+	ANS	Disp.	ANS	[89], [90]

Table 2.3: Considered EAS elements (the number of parameters is in brackets).
Preglednica 2.3: Obravnavani EAS elementi (število parametrov je v oklepajih).

FE	Membrane	Bending	Shear	Reference
EAS4	EAS (4)	Disp.	ANS	[2], [22]
EAS5	EAS (5)	Disp.	ANS	[12], [22]
EAS7	EAS (7)	Disp.	ANS	[2], [22]

Table 2.4: Considered HR elements (the number of parameters is in brackets).
Preglednica 2.4: Obravnavani HR elementi (število parametrov je v oklepajih).

FE	Membrane	Bending	Shear	Reference
HR-M	HR (5)	Disp.	ANS	[126], [142]
HR-MB	HR (5)	HR (5)	ANS	[126], [142]
HR-MS	HR (5)	Disp.	ANS & HR (4)	[59]
HR	HR (5)	HR (5)	ANS & HR (4)	[59]
+HR-MS	ANS+ & HR (5)	Disp.	ANS & HR (4)	[107]
+HR	ANS+ & HR (5)	HR (5)	ANS & HR (4)	[107]

Table 2.5: Considered HW elements (the number of parameters is in brackets).
Preglednica 2.5: Obravnavani HW elementi (število parametrov je v oklepajih).

FE	Membrane	Bending	Shear	Reference
HW	HW (10)	HW (10)	ANS & HW (8)	[159]
HWEAS	EAS (2) & HW (10)	EAS (2) & HW (10)	ANS & EAS (2) & HW (8)	[60]
+HW	ANS+ & HW (10)	HW (10)	ANS & HW (8)	[104]

Table 2.6: Considered rotation-less elements.
Preglednica 2.6: Obravnavani elementi brez rotacij.

FE	Membrane	Bending	Shear	Thickness stretch	Reference
D-ANS	Disp.	Disp.	ANS	ANS	[15]

Table 2.7: Finite rotation algorithms.
Preglednica 2.7: Algoritmi za rotacije v končnih elementih.

Rotation algorithm	Description
T	Additive update
TQ	Additive update using quaternions
I	Multiplicative-additive update
IQ	Multiplicative-additive update using quaternions
M	Multiplicative update
MQ	Multiplicative update using quaternions

2.5.1   Comparison of finite rotation algorithms

Four examples were chosen to evaluate the finite rotation algorithms from Table 2.7, implemented in the MITC4 formulation, see Table 2.2. The geometric and material data of the considered beams in Figure 2.5 are $L = 10, w = 1, t = 0.1, E = 12\ 10^{12}$ and $v = 0$. Three examples were performed by imposing different load cases on the initially straight cantilever beam. One load case produced planar rotations and the other two spatial rotations. The fourth example was performed on the cantilever beam of circular shape that underwent large spatial rotations. The mesh of 25×1 elements and adaptive control of load increments, see Table 2.1, were used for all four examples.
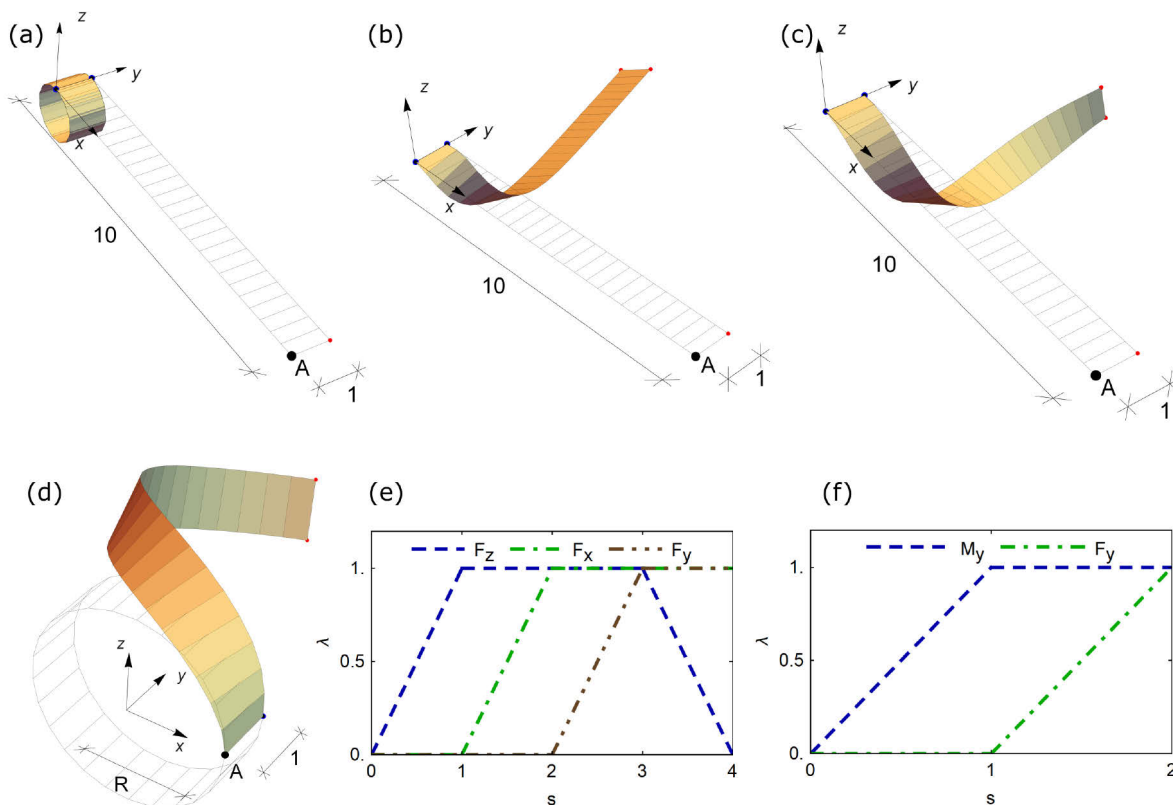
Figure 2.5: Large rotation tests. (a) Roll-up of a cantilever beam. (b) Cantilever beam under three forces. (c) Cantilever beam under moment and lateral force. (d) Circular beam under lateral force. (e) & (f) Load steps for tests (b) and (c), respectively.
Slika 2.5: Testi velikih rotacij. (a) Zavijanje konzole. (b) Konzola, obremenjena s tremi silami. (c) Konzola, obremenjena z momentom in prečno silo. (d) Krožni nosilec, obremenjen s prečno silo. (e) & (f) Obtežni režim za testa (b) in (c), v tem vrstnem redu.

In the first example, moment $M_y = 4\pi EI/L = 1256.6$ was applied at its free end, see Figure 2.5 (a). Large rotations of all the nodes were planar, see Table 2.8. The analytical solution predicts rolling of a beam into a complete circle for the end moment $2\pi EI/L$. Thus, the analytical free end rotation for the applied M_y is 720°, which is 95 % of the computed solution. Using a finer mesh of e.g. 100 elements resulted in the final rotation of 723°, which is 100.5% of the analytical solution. Figure 2.6 (a) shows the applied moment versus vertical displacement u_z at node A. The results are identical for the finite rotation algorithms from Table 2.7 and for the rotation-less formulation from Table 2.6, which is in Figure 2.6 denoted as D. For the latter, the moment was applied as proposed in [15]; at the free end, a linear through-the-thickness normal-pressure distribution was applied in deformed configuration, and such a load was used in the external virtual work.

In the second example, the free end was loaded by uniformly distributed forces $F_x = F_z = 300$, $F_y = 1200$ in four load steps, $s = 1, \cdots 4$, as seen in Figure 2.5 (e). With these load steps, we assured that the rotations were large and spatial, see Table 2.8. Namely, the examples with spatial rotations are more demanding for the finite rotation algorithms than the examples with planar rotations. Figure 2.5 (b) shows the final deformed configuration. Figure 2.6 (b) shows how the displacements at node A were changing during the load steps. The displacement response of all finite rotation algorithms from Table 2.7 and the rotation-less formulation (D) from Table 2.6 was identical.

In the third example, two load steps were used, see Figure 2.5 (f). First, moment $M_y = 2\pi EI/L = 628.3$ was incrementally applied at the free end. In the second load step, the moment was kept constant, and $F_y = 300$ was incrementally applied, which moved the rotations out of one plane, see Figure 2.5 (c) and Table 2.8. Regarding the moment loading, the following needs to be explained. The derived formulations allow to apply two external moments around two orthogonal axes. For T-algorithm, the applied incremental moment always rotates around x and y. This is not the case for the I- and M-algorithms, where the reference frame for rotations (and moments) is updated at each load increment and iteration, respectively. Thus, the applied incremental moments rotate around two axes of updated frame, which no longer coincide with x and y. The T-, I- and M-algorithms will give identical results only for incremental moments, which produce planar rotations (the case of the first load step). When the rotations are not planar (the case of the second load step), the results will not be the same. This is demonstrated in Figure 2.6 (c), where displacements at node A are given for the two load steps. In the first load step, the results are identical for all the algorithms, which is not the case in the second load step. While the difference between the T- and I-, M-algorithms is clearly visible, the difference between I- and M-algorithms is smaller, but still present.

In the fourth example, the initial configuration of the cantilever beam was a circle with radius $R = 2\pi/L$, see Figure 2.5 (d). Its free end was incrementally loaded by $F_y = 300$. Table 2.8 shows the final rotations, and Figure 2.6 (d) shows the displacements at node A.

The following can be concluded from the above examples:
i.   All finite rotation algorithms produce identical displacement response, see Figure 2.6, while the rotations differ for all algorithms. An exception is the third example with the load case, which includes moment and produces spatial rotations. For such a load case the T-, I- and M-algorithms

   naturally give different results, because the I- and M-algorithms make moment load to be configuration dependent. This cannot be removed for the I- and M-algorithms, designed for formulations with two rotational degrees of freedom. For this reason, we recommend caution when using them for problems with moments.

ii.   The difference in the final rotation is big when comparing the T-algorithm with the other two, see Table 2.8. If, however, we compare the I- and M-algorithms, the difference is very small. In both cases, the reference frame is updated during the computation, so the results are relatively close.

iii.   Even though the T-algorithm has singularity when the rotation norm at any node of the mesh is $k\pi$, $k = 1,2,\cdots$, see e.g. [25], it was able to step over the singular points, see Figure 2.5. Nevertheless, we do not recommend the use of the T-algorithms for problems where the nodal rotations norm is expected to exceed π.

iv.   In the third example, the I- and M-algorithms could not reach the final solution. They stopped at approximately $\lambda = 0.6$ and $\lambda = 0.1$, respectively, for $s = 2$. The algorithms with quaternions (IQ and MQ) did not have such problems. The reason is that by using the quaternion-based update procedure, the loss of orthogonality of the incremental rotation matrix (in a numerical sense) can be avoided, which makes the algorithms more robust.

v.   The rotation-less formulation (D) produces results that are almost identical to the finite rotation ones, see Figure 2.6. This indicates that the presented rotation-less formulation can handle well finite rotation problems.

vi.   Concerning the computational speed of rotation algorithms, we can conclude that the IQ-algorithm is generally the fastest, with the T-algorithm close in second place, see

vii.   Table 2.9. When the quaternion (Q) update is used, the T-algorithm becomes slower (see TQ), while the I- and M-algorithms become faster (see IQ and MQ). The latter is due to the fact that using the rotation matrix update, 9 values (3×3 rotation matrix) need to be stored, while using the quaternion update algorithm, the storage of 4 nodal values is required. Both the T- and TQ-algorithms do not require storage of any nodal values, but due to additional operations required by TQ, this algorithm is slower.

For the nonlinear examples in Section 2.5.4 below, the IQ and T algorithms were used.

Table 2.8: Final rotations at node A for examples from Figure 2.6.
Preglednica 2.8: Končne rotacije vozlišča A za primere s slike 2.6.

Rot.\Ex.	(a) All formulations	(b)			(c)			(d)		
		T	I	M	T	I	M	T	I	M
ϕ_x [°]	0	-39.3	-3.21	-3.18	14.2	-83.7	-83.1	-93.9	-89.32	-89.35
ϕ_y [°]	756.8	158	163.71	163.73	274.5	244.34	244.31	56.5	64.95	65.0
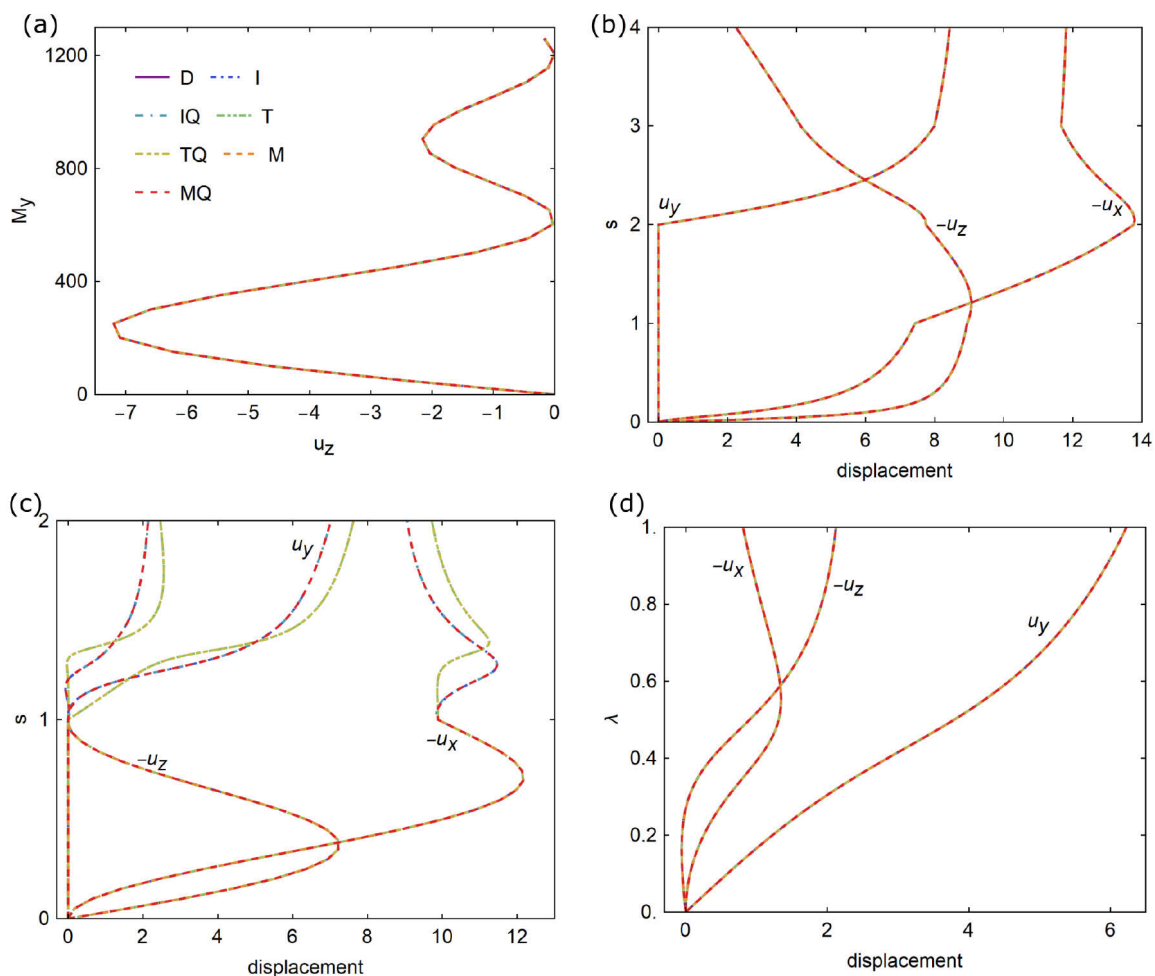
Figure 2.6: Load versus displacements for large rotation tests. (a) – (d) correspond to respective tests from Figure 2.5.

Slika 2.6: Obtežba v odvisnosti od pomika za teste velikih rotacij. (a)–(d) se nanašajo na pripadajoče teste s slike 2.5.

Table 2.9: Normalized CPU time for examples from Figure 2.6 for different finite rotation algorithms.
Preglednica 2.9: Normiran CPU čas za primere s slike 2.6 za različne rotacijske algoritme.

Alg.\Ex.	(a)	(b)	(c)	(d)
D	1.43	1.26	/	0.96
I	1.15	1.21	/	0.86
IQ	0.83	0.80	0.72	0.96
T	1	1	1	1
TQ	0.94	1.11	1.40	1.04
M	1.19	1.12	/	0.96
MQ	0.79	1.68	1.37	0.96

2.5.2   Basic tests

2.5.2.1   Patch test

Displacements for membrane test:
$u_x(x,y) = 10^{-3}(x + 1/2y)$,
$u_y(x,y) = 10^{-3}(1/2x + y)$,
$u_z(x,y) = 0$.

Displacements and rotations for bending test:
$u_z(x,y) = 5\,10^{-4}(x^2 + xy + y^2)$,
$\Phi_x(x,y) = 5\,10^{-4}(x + 2y)$,
$\Phi_y(x,y) = 5\,10^{-4}(2x + y)$

$a=40$, $b=20$, $t=0.1$, $E=10^6$, $v=0.3$

Load case	1		2	
Node	F_x	F_z	M_x	M_y
1	-20	-2	20	-10
2	0	0	20	10
3	0	0	-20	10
4	-20	0	-20	-10
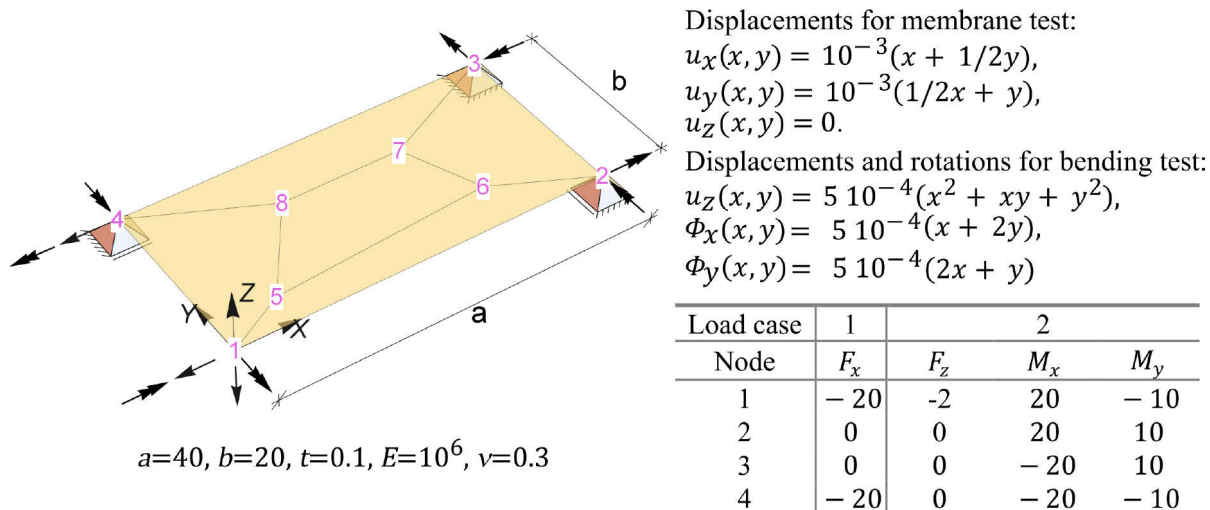
Figure 2.7: Patch test data.
Slika 2.7: Podatki za patch test.

All the formulations from Tables 2.2 – 2.6 pass two sets of membrane and bending patch tests, see e.g. [113]. The data for the first one are taken from [164]. Two arrangements of displacements and rotations are imposed at nodes $1-4$ in accordance with formulae from Figure 2.7. The exact solutions are constant membrane strains $\varepsilon_{xx} = \varepsilon_{yy} = 2\varepsilon_{xy} = 10^{-3}$ and constant curvatures $\kappa_{xx} = \kappa_{yy} = \kappa_{xy} = -10^{-3}$. Linear versions of all the formulations computed these exact values.

The data for the second set are taken from [159]. Two loading cases are imposed in accordance with the table in Figure 2.7. All formulations computed correct values of membrane forces $n_{xx} = 2, n_{yy} = n_{xy} = 0$ for load case 1 and moments $m_{xx} = m_{yy} = m_{xy} = 1$ for load case 2.

2.5.2.2 Conditioning number

We checked the conditioning number of the initial (i.e. linear) stiffness matrix for the derived formulations. To this end, we computed eigenvalues of stiffness matrix of a square element and distorted (curved) element, see Figure 2.8, with $a = 2, t = 0.02, E = 10^8, v = 0.3$. Moreover, the same was done for a simply supported plate with $t/a = 10^{-3}$, discretized with 100 elements, after [52].
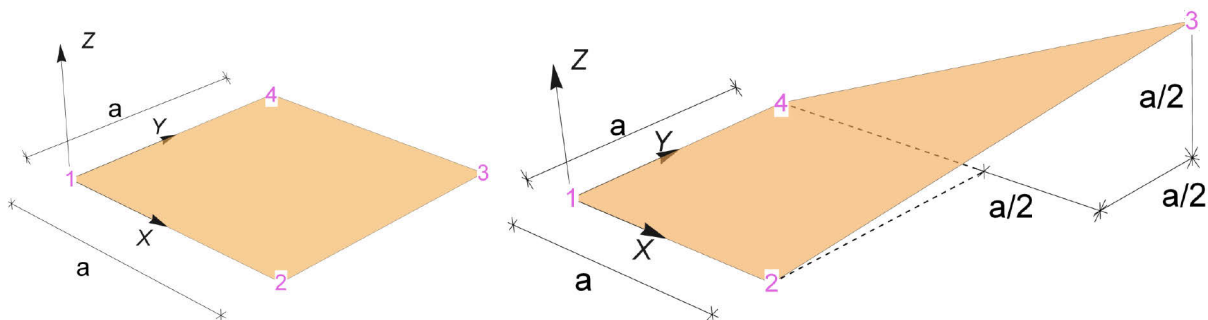
Figure 2.8: Elements for eigenvalue analysis.
Slika 2.8: Elementa za analizo lastnih vrednosti.

All the formulations have six zero eigenvalues that correspond to rigid body modes. The curves in Figure 2.9 (a) and (b) exhibit a jump at a certain deformation mode number. Lower eigenvalues (before the jump) are related to the bending-dominated modes, while higher eigenvalues (after the jump) are related to the stiffer membrane- and shear-dominated modes.
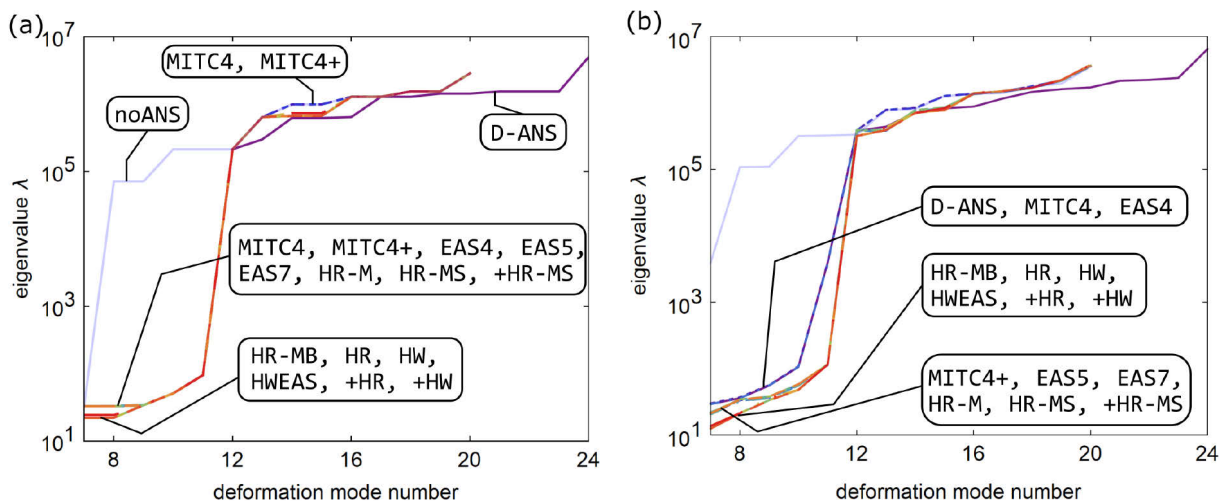
Figure 2.9: Eigenvalues of square (a) and distorted (b) element.
Slika 2.9: Lastne vrednosti kvadratnega (a) in popačenega (b) elementa.

The additional curve shows a rotation formulation without any ANS treatment, which differs considerably from other curves. One can conclude that the difference is due to shear locking remedies. The membrane locking remedies show a large influence on the distorted element values, see Figure 2.9 (b). The D-ANS, MITC4 and EAS4 elements show pollution of bending-dominated modes 7-11 by excessive membrane deformations. After the jump (deformation mode 12), the EAS4 element has identical modes as the EAS5, EAS7, HR-M and HR-MB elements, which are similar to those of the rest of elements. MITC4 and MITC4+ have the same membrane-dominated modes 13-15, but they differ from the rest of formulations.

Table 2.10 shows that the condition number of the stiffness matrix $C = \lambda_{max}/\lambda_{min}$ (here, λ is a non-zero eigenvalue) is of the same order for the considered formulations for all three tests. The rotation-less formulation does have larger C than the finite rotation ones, but not significantly. The maximal increasing factors (compared to the MITC4 formulation) are 1.75 and 1.24 for single-element and plate tests, respectively.

Table 2.10: Stiffness matrix condition number.

Preglednica 2.10: Koeficient pogojenosti togostnih matrik.

FE	Square element		Distorted element		Simply supported plate	
	$c \, 10^4$	$\dfrac{c}{c_{MITC4}}$	$c \, 10^4$	$\dfrac{c}{c_{MITC4}}$	$c \, 10^9$	$\dfrac{c}{c_{MITC4}}$
D-ANS	15.17	1.75	22.28	1.87	7.14	1.240
MITC4	8.67	1.00	11.93	1.00	5.75	1.000
MITC4+	8.67	1.00	17.65	1.45	5.75	1.000
EAS4	8.67	1.00	12.21	1.02	5.73	0.996
EAS5	8.67	1.00	16.22	1.36	5.73	0.996
EAS7	8.67	1.00	17.41	1.46	5.73	0.996
HR-M	8.67	1.00	16.82	1.41	5.73	0.996
HR-MB	12.86	1.48	29.06	2.44	5.73	0.997
HR-MS	8.67	1.00	16.82	1.41	5.73	0.996
HR	12.86	1.48	29.06	2.44	5.73	0.997
HW	11.70	1.35	26.52	2.22	5.74	0.997
HWEAS	12.86	1.48	29.04	2.43	5.73	0.997
+HR-MS	8.67	1.00	17.79	1.49	5.73	0.996
+HR	12.86	1.48	30.24	2.53	5.73	0.997
+HW	11.70	1.35	27.6	2.31	5.74	0.997

The simply supported plate example in Figure 2.10 shows the importance of the ANS treatment for the shear locking. The element without ANS is the only one producing different results, while the rest of the formulations behave the same. For a cylinder with the same material characteristics as the plate, height $L = 20$, radius $R = 10, t/R = 10^{-4}$, and discretized with 200 elements, the produced graph is similar to that in Figure 2.10, and the maximum increasing factor is 1.26. This also indicates that the finite rotation formulations are only slightly more robust (i.e. better conditioned) than the rotation-less formulation, for both flat and curved thin shells.
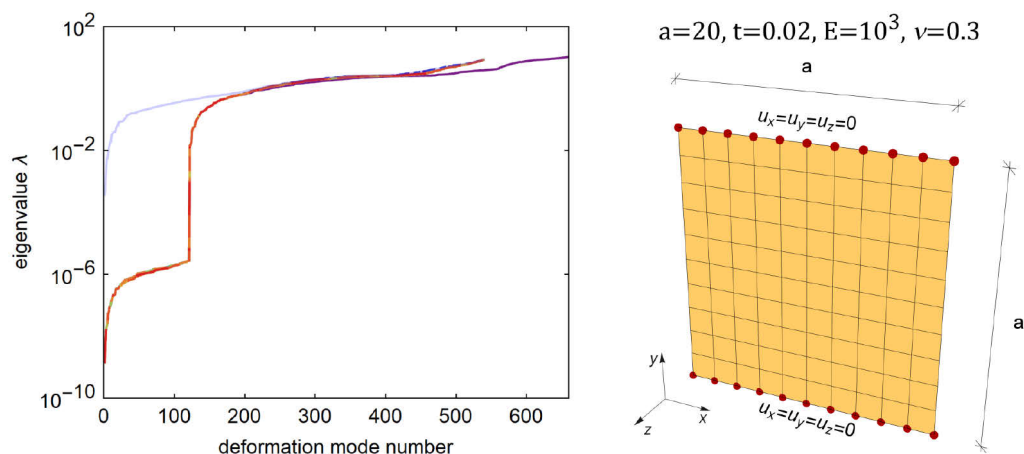
Figure 2.10: Simply supported plate eigenvalue analysis.
Slika 2.10: Členkasto podprta plošča za analizo lastnih vrednosti.

2.5.3 Linear tests

2.5.3.1 Cook's membrane

The membrane is clamped at one end and subjected to force $F = 1$ at the opposite end (the force is uniformly distributed along the edge), see Figure 2.11 (a). The data are $E = 1, \nu = 1/3$ and thickness $t = 1$. Nonlinear version of the example is presented in Section 2.5.4.1. This is a membrane problem test, which also incorporates the element distortion. This test primarily shows how well a formulation can handle the in-plane bending, where the in-plane shear dominates.
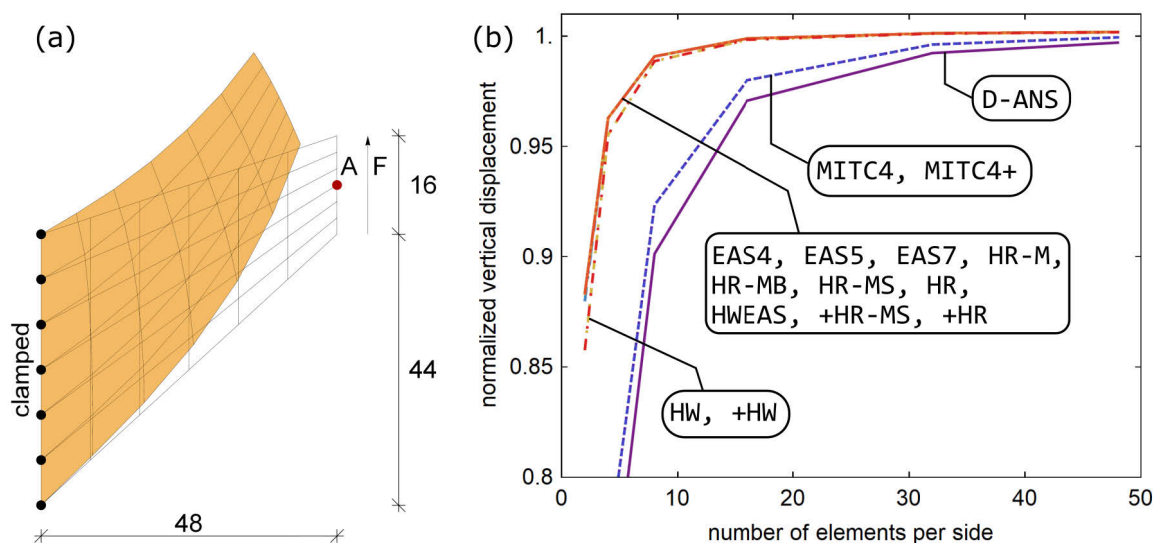
Figure 2.11: Cook's membrane: initial and deformed meshes for nonlinear analysis with MITC4 element (a), and linear convergence (b).

Slika 2.11: Cookova membrana: začetna in deformirana mreža za nelinearno analizo z MITC4 elementi (a) in linearna konvergenca (b).

Complete test results are shown in Table 2.11. Figure 2.11 (b) presents normalized vertical displacement at point A (with respect to the reference FE solution 23.91, taken from [141]) only for non-matching formulations. One can see that the EAS, HR and HW elements from Tables 2.3 – 2.5 exhibit very fast convergence, while the rotation-less element from Table 2.6 and the ANS elements from Table 2.2 converge much slower. The D-ANS formulation shows the poorest convergence. Thus, the EAS, HR or HW improvement of the membrane part of the shell response is very favorable for the (flat) membrane problems. On the other hand, the ANS treatment of the membrane part of the shell response does not show any improvement. The MITC4+ convergence matches exactly the MITC4, and +HR and +HW match exactly HR and HW. This is due to the fact that the membrane parts of the MITC4 and MITC4+ element formulations are identical for a flat geometry, see also [89].

Table 2.11: Cook's membrane: linear convergence.
Preglednica 2.11: Cookova membrana: linearna konvergenca.

FE\mesh	2x2	4x4	8x8	16x16	32x32	48x48
D-ANS	10.977	17.334	21.55	23.208	23.725	23.839
MITC4, MITC4+	11.845	18.299	22.079	23.43	23.818	23.896
EAS4, EAS5	21.05	23.016	23.689	23.883	23.94	23.953
EAS7, HR-M, HR-MB, HR-MS, HR, +HR-MS, +HR	21.129	23.022	23.689	23.883	23.94	23.953
HW, +HW	20.52	22.841	23.638	23.869	23.936	23.951
HWEAS	21.119	23.021	23.689	23.883	23.94	23.953

2.5.3.2 Raasch's hook

Raasch's hook is a curved beam-like shell, which consists of two arches with different radii of curvature, see Figure 2.12. It is clamped at one end and subjected to force F at the opposite end (the force is uniformly distributed along the edge). Two different width to thickness ratios are considered, $w/t = 10$ and $w/t = 10^2$, with $w = 20$, and forces $F = 1$ and $F = 1000$, respectively. The material data, $E = 3300$ and $\nu = 0.35$, are taken after [86]. The shell was analyzed with meshes of $(2N + 3N) \times N$ elements, with $N \in \{2, 4, 8, 16, 32, 48\}$. Here, N is the number of elements in the width direction, and $2N$ and $3N$ are the number of elements in the hook length direction in the first and second arch, respectively.
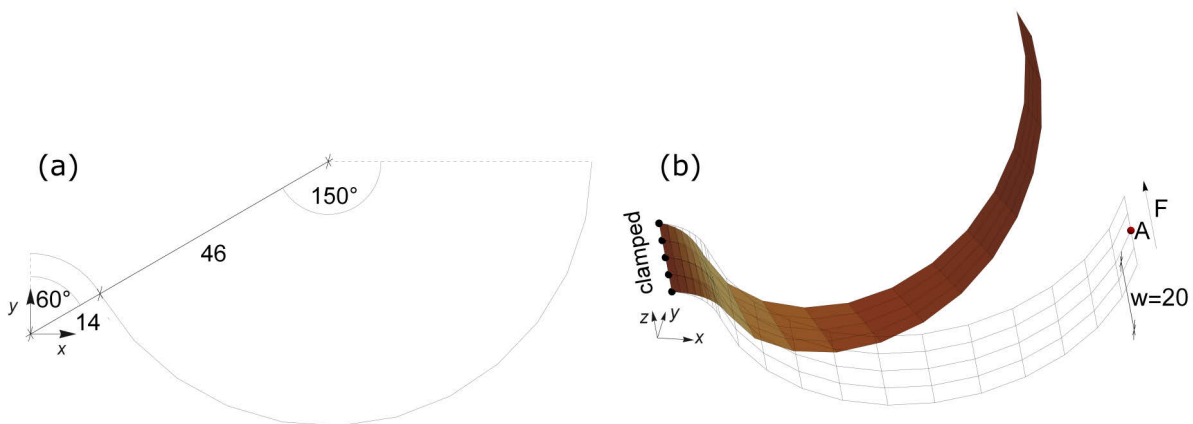
Figure 2.12: Raasch's hook: geometry (a) and initial and deformed meshes for nonlinear analysis with MITC4 element (b).
Slika 2.12: Raascheva kljuka: geometrija (a) ter začetna in deformirana mreža za nelinearno analizo z MITC4 elementom (b).

The results are presented in Figures 2.12 and 2.13, only for non-matching formulations, while complete results are given in Table 2.12. They show that the shell deforms in a combined membrane-bending manner. Figure 2.13 (a) presents the convergence of normalized displacement u_z at point A. For $w/t = 10$, the computed values are normalized with the reference displacement 5.02, which was obtained with Abaqus [1] for a mesh of $20 \times 144 \times 2$ 3D 20-node elements with reduced integration (C3D20R) [164]. For $w/h = 10^2$, the computed values are normalized with the reference displacement 4660, obtained by mesh of $20 \times 136 \times 2$ eight-node assumed-stress hybrid solid brick elements [86]. In general, the convergence of all the formulations is excellent and better than for Cook's problem. The convergence

is almost the same for all the formulations. It is interesting to note that the convergence for thicker shell is slower than for the thinner one and that the converged value slightly differs from the reference results.
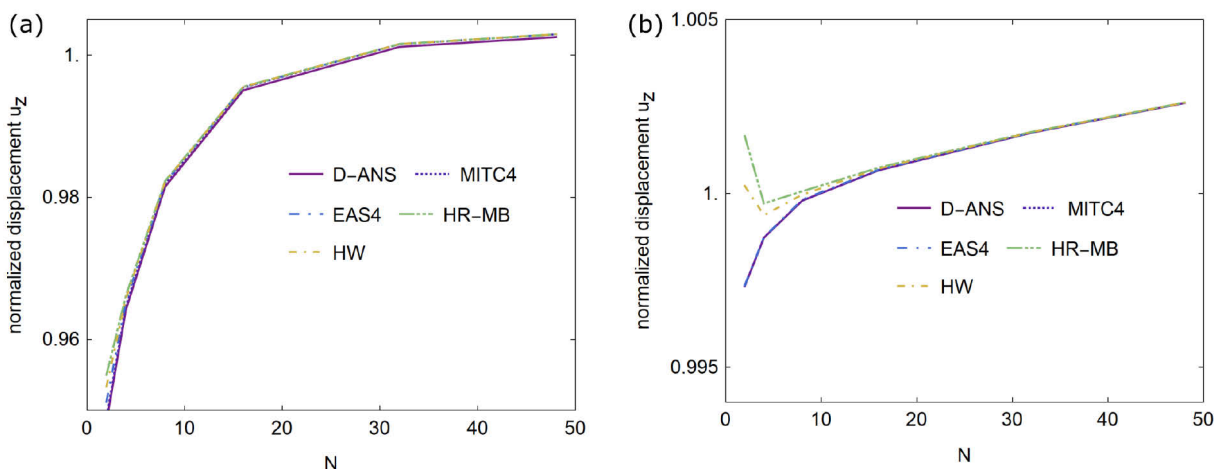
Figure 2.13: Raasch's hook: linear convergence for $w/t = 10$ (a) and $w/t = 10^2$ (b).
Slika 2.13: Raascheva kljuka: linearna konvergenca za $w/t = 10$ (a) in $w/t = 10^2$ (b).

Table 2.12: Raasch's hook: linear convergence for u_z for thick shell (top) and thin shell (bottom).
Preglednica 2.12: Raascheva kljuka: linearna konvergenca za u_z za debelo lupino (zgoraj) in tanko lupino (spodaj).

FE\N	2	4	8	16	32	48
$w/t = 10$						
D-ANS	4.758	4.837	4.924	4.992	5.023	5.030
MITC4, MITC4+	4.761	4.840	4.926	4.994	5.025	5.032
EAS4, EAS5, EAS7, HR-M, HR-MS, HR, +HR-MS, +HR	4.772	4.843	4.927	4.994	5.025	5.032
HR-MB, HR, HWEAS, +HR	4.791	4.848	4.928	4.995	5.025	5.032
HW, +HW	4.783	4.846	4.928	4.995	5.025	5.032
$w/t = 10^2$						
D-ANS, MITC4, MITC4+	4647.6	4654.1	4659	4663.1	4668.2	4672.2
EAS4, EAS5, EAS7, HR-M, HR-MS, HR, +HR-MS, +HR	4647.7	4654.1	4659.2	4663.2	4668.2	4672.2
HR-MB, HR, HWEAS, +HR	4667.7	4658.7	4660.3	4663.5	4668.3	4672.2
HW, +HW	4661	4657.1	4659.8	4663.3	4668.2	4672.2

2.5.4   Nonlinear tests

2.5.4.1   Cook's membrane

The data for the nonlinear Cook's membrane test are the same as for the linear one (see Figure 2.11), with Young's modulus changed to $E = 2$, as proposed in [139] for nonlinear version of this example. Adaptive control of load increments was used, see Table 2.1. Figure 2.14 (a) shows the convergence for nonlinear analysis of vertical displacement at node A and load $F = 1$. The graphs resemble those for linear analysis, see Figure 2.11. The HR, EAS and HW elements exhibit excellent convergence. On the other hand, MITC4, MITC4+ and D-ANS require a very fine mesh to converge. Figure 2.14 (b) shows

vertical displacement at node A versus applied load for a 4×4 mesh. The solution, referred to as ref., is for 48×48 mesh of HWEAS elements. The response for the EAS, HR and HW formulations is already close to the reference one, while MITC4, MITC4+ and D-ANS are quite away.
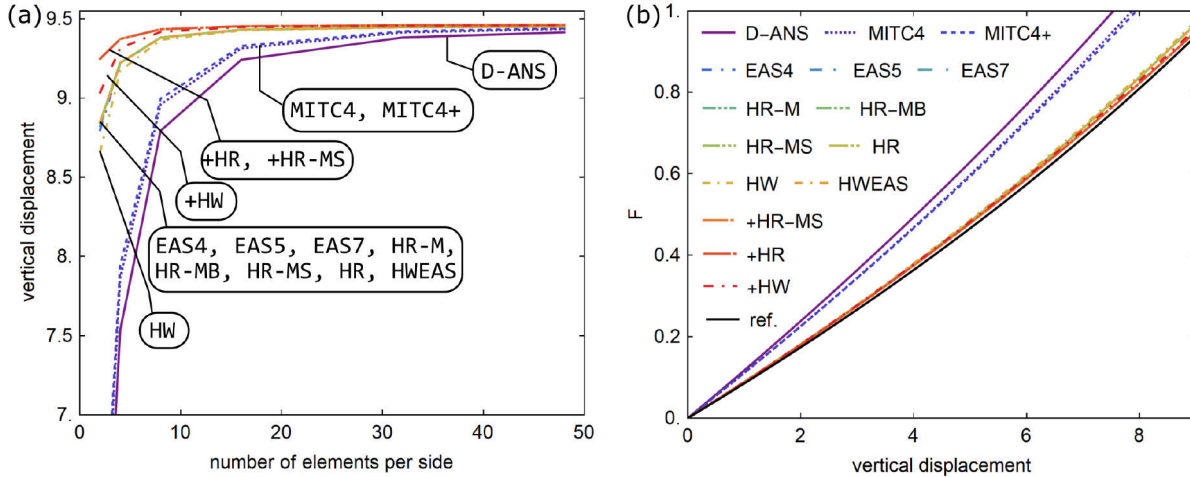
Figure 2.14: Cook's membrane: nonlinear convergence (a) and load versus displacement for 4×4 mesh (b).

Slika 2.14: Cookova membrana: nelinearna konvergenca (a) in obtežba v odvisnosti od pomika za 4×4 mrežo (b).

2.5.4.2   Raasch's hook

Ratio $w/t = 10^3$ was used and Poisson's ratio changed to $\nu = 0.3$, as proposed in [91], [90] and [104] for nonlinear version of the test, while the rest of the data were the same as in Section 2.5.3.2, see Figure 2.12. We used the same set of regular meshes. In addition, we also used a set of distorted meshes with pattern as shown in Figure 2.15. The ratio between the longest and the shortest element edge (in the length direction of the hook) L_{max}/L_{min} was set to 1.5 and 2 for first and the second arch, respectively. Adaptive control of load increments was used, see Table 2.1. This is a demanding test for shell formulations, especially for distorted meshes. This single curved shell exhibits membrane-bending deformations.

Figures 2.16 (a) and 2.17 (a) show convergence (for nonlinear analysis) for displacement u_z at point A for $F = F_z = 10^{-4}$. The computed converged solution, $u_z = 78.55$, was reached by all formulations for regular meshes (some of them needed very fine meshes) and by the majority for distorted meshes. In contrast to the linear version of the test, the differences are large. MITC4+ exhibits the best convergence and is in the same range as +HR-MS, +HR and +HW. MITC4, D-ANS and EAS4 perform worst. Mesh distortion significantly influences MITC4, D-ANS and EAS4, while having a minor effect on MITC4+, +HR-MS, +HR and +HW.

Figures 2.16 (b), (c) and 2.17 (b), (c) present the applied force versus displacement u_x at point A, shown in Figure 2.12, for two regular and two distorted meshes, see Figure 2.15. As the reference result, we adopt the solution computed with regular mesh of $(64 + 96) \times 32$ HWEAS elements. MITC4+, +HR-MS, +HR and +HW are superior; they provide excellent agreement with the reference solution already for mesh (b), and are almost insensitive to mesh distortion. MITC4, D-ANS and EAS4 perform worst;

they are far from the reference solution for mesh (b), and they show significant mesh-distortion sensitivity. They do not get very close to the reference solution even for fine distorted mesh, see Figure 2.17 (c). The other EAS formulations, as well as the HR and HW formulations, perform better. They are still quite sensitive to mesh distortion, but they reach the reference solution for a fine distorted mesh, see Figure 2.17 (c).

The results show that the description of membrane effects is of major importance for this test. The formulations with the displacement-based description of membrane effects (and even the EAS formulation with only four parameters, i.e. EAS4) show poor performance. The EAS formulations with 5 and 7 parameters (EAS5 and EAS7) perform better and yield identical results as the hybrid formulations without independent bending stress interpolations (HR-M and HR-MS). The group of the HR-MB, HR and HWEAS formulations also performs identically. However, the EAS, HR and HW formulations are all outperformed by the ANS treatment of membrane effects applied in MITC4+ as well as in +HR-MS, +HR and +HW. It is demonstrated that the applied ANS membrane treatment almost eliminates any sensitivity to mesh distortion. Note that this test (with curvature in one direction) also shows that the ANS treatment of membrane effects (MITC4+) is far more effective for nonlinear problems than for linear ones.

Table 2.13 shows the computational details of some of the selected formulations. It demonstrates that (of the selected elements) the +HW formulation is the most robust while at the same time computationally very fast. It does not require any back steps and on average less iterations to converge in a certain load increment.
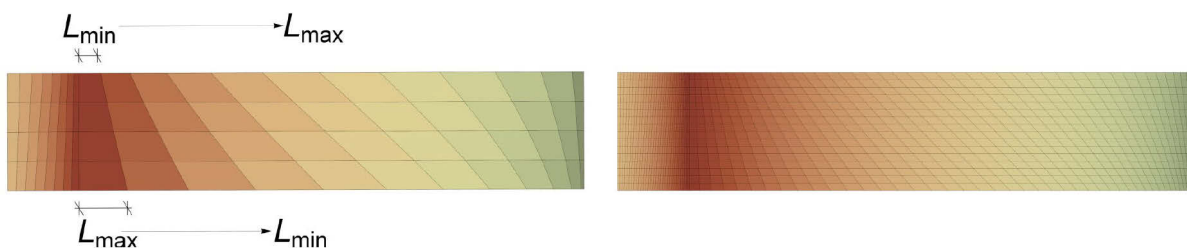
Figure 2.15: Raasch's hook: distorted meshes with $N = 4$ and $N = 16$.
Slika 2.15: Raascheva kljuka: pokvarjene mreže z $N = 4$ in $N = 16$.
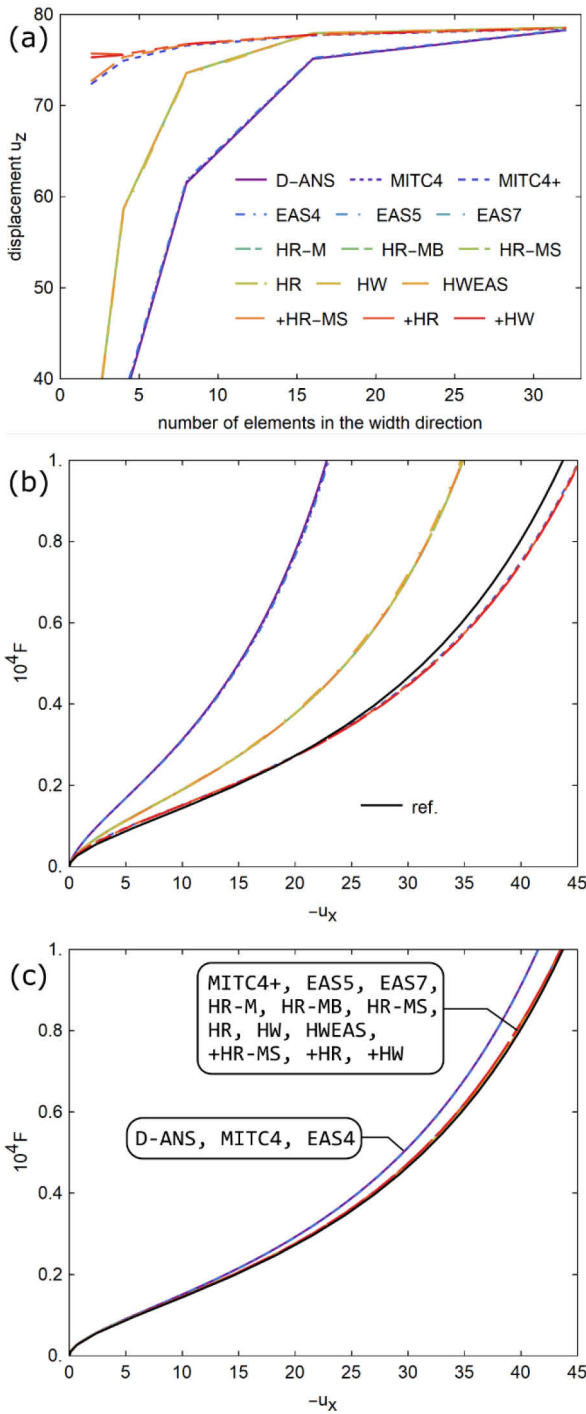
Figure 2.16: Raasch's hook, regular mesh: (a) nonlinear convergence, (b) $N = 4$ mesh, (c) $N = 16$ mesh.
Slika 2.16: Raascheva kljuka, običajna mreža: (a) nelinearna konvergenca, (b) mreža $N = 4$, (c) mreža $N = 16$.
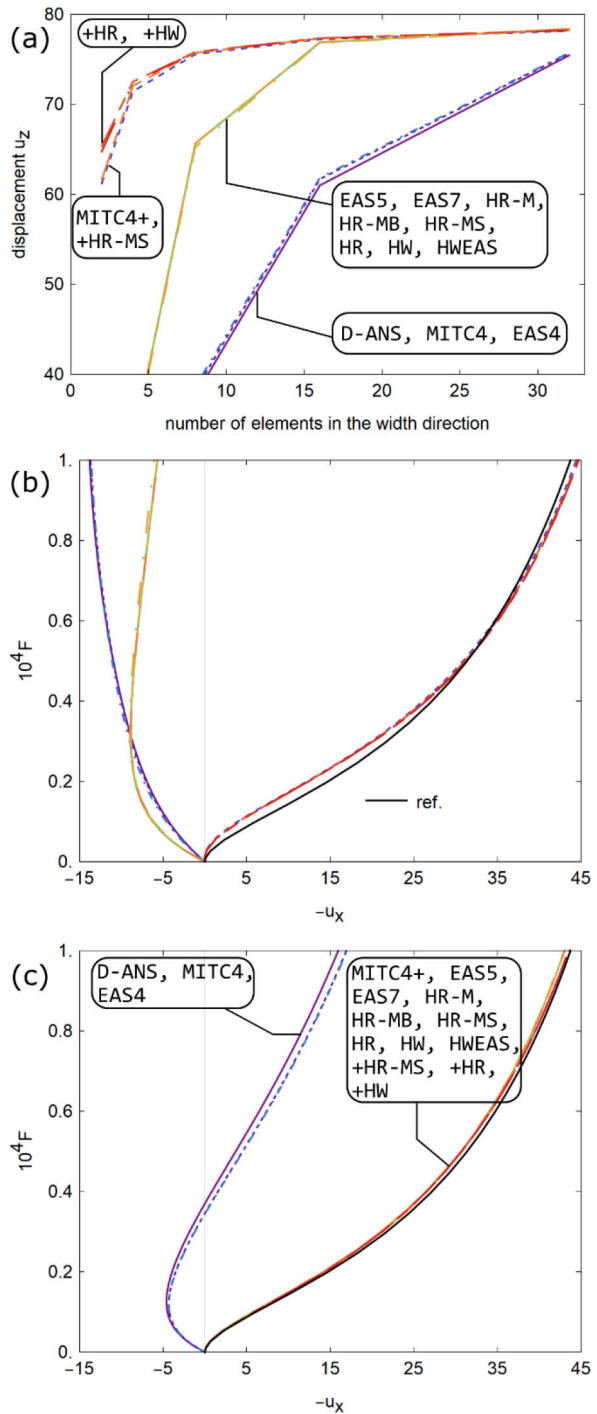
Figure 2.17: Raasch's hook, distorted mesh: (a) nonlinear convergence, (b) $N = 4$ mesh, (c) $N = 16$ mesh.
Slika 2.17: Raascheva kljuka, pokvarjena mreža: (a) nelinearna konvergenca, (b) mreža $N = 4$, (c) mreža $N = 16$.

Table 2.13: Raasch's hook: computational details for $F_z = 10^{-4}$ and $N = 16$ for regular mesh (top) and distorted mesh (bottom).

Preglednica 2.13: Raascheva kljuka: računske podrobnosti za $F_z = 10^{-4}$ in $N = 16$ za običajno mrežo (zgoraj) in pokvarjeno mrežo (spodaj).

FE	MITC4	MITC4+	HW	+HW
Displacement u_z ($\frac{u_z}{u_{z,ref}}$ [%])	75.12 (96)	77.66 (99)	77.87 (99)	77.73 (99)
Normalized CPU time	1.00	1.13	0.18	0.22
Req. no. of load increments	92	96	22	22
Total number of iterations	883	930	120	124
Number of back-steps	3	4	0	0
Displacement u_z ($\frac{u_z}{u_{z,ref}}$ [%])	61.68 (79)	77.19 (98)	76.77 (98)	77.29 (98)
Normalized CPU time	1.00	1.15	0.20	0.27
Req. no. of load increments	91	96	22	22
Total number of iterations	874	931	120	124
Number of back-steps	6	4	0	0

2.5.4.3 Hemisphere with a hole

We considered a hemispherical shell with a hole, which is subjected to alternating radial point forces P, as shown in Figure 2.18, see e.g. [152], [102]. The material and geometric data are $R = 10, E = 6.825\ 10^7, v = 0.3$, and $t = 0.04$. Due to the symmetry, we modelled only one quarter of the shell and applied symmetry boundary conditions. Both uniform and distorted meshes were used. The distorted mesh pattern has on the symmetry edges the ratio between the longest and the shortest element $L_{max}/L_{min} = 16$, with the in-between elements changing linearly from L_{min} to L_{max}. Adaptive control of load increments was applied, Table 2.1. This double curved shell at first exhibits large, almost inextensible deformations, which are followed by large membrane forces (including shear).
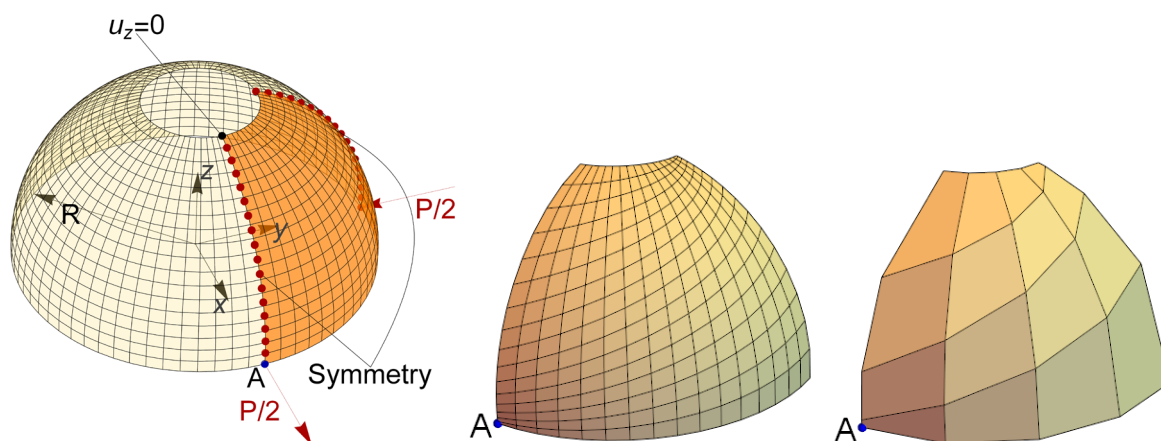
Figure 2.18: Hemispherical shell: problem data and distorted meshes.
Slika 2.18: Polkrožna lupina: podatki o problemu in pokvarjeni mreži.

Figures 2.19 (a) and 2.20 (a) show convergence (for nonlinear analysis) for displacement u_x at point A for $P = 400$. The converged displacement is $u_x = 4.07$, reached by all formulations for a regular 48×48 mesh. Convergence of MITC4+, +HR-MS, +HR-MBS and +HW is superior, whereas the convergence of D-ANS, MITC4 and EAS4 is the worst. Mesh distortion influences the convergence of

all the formulations. Nevertheless, the convergence of MITC4+, +HR-MS, +HR-MBS and +HW is still superior.

Figures F2.19 (b) and 2.20 (b) compare load-displacement curves for point A for regular and distorted 4×4 meshes, see Figure 2.18. As the reference solution, we adopt the one obtained by regular mesh of 48×48 HWEAS elements. For the coarse mesh, the group of MITC4+, +HR-MS, +HR-MBS and +HW performs best, and the group of D-ANS, MITC4 and EAS4 performs worst. The curves of the other formulations represent the third group; they are almost identical and lie between the solutions of the first two groups. Mesh distortion affects all the formulations, but the result can still be presented in three groups. Although not shown, the results of all formulations converge to the reference solution, for both regular and distorted meshes, for 16×16 elements (with only the first group of formulations being slightly away from the reference solution). The robustness and speed of the formulations are compared in

Table 2.14. A normalized CPU time shows that the hybrid formulations are computationally the fastest. This is partly due to the fact that they allow for very large load increments and require no back-steps. Note that +HR-MS, +HR-MBS and +HW are fast and can also provide reliable results already for coarse mesh.
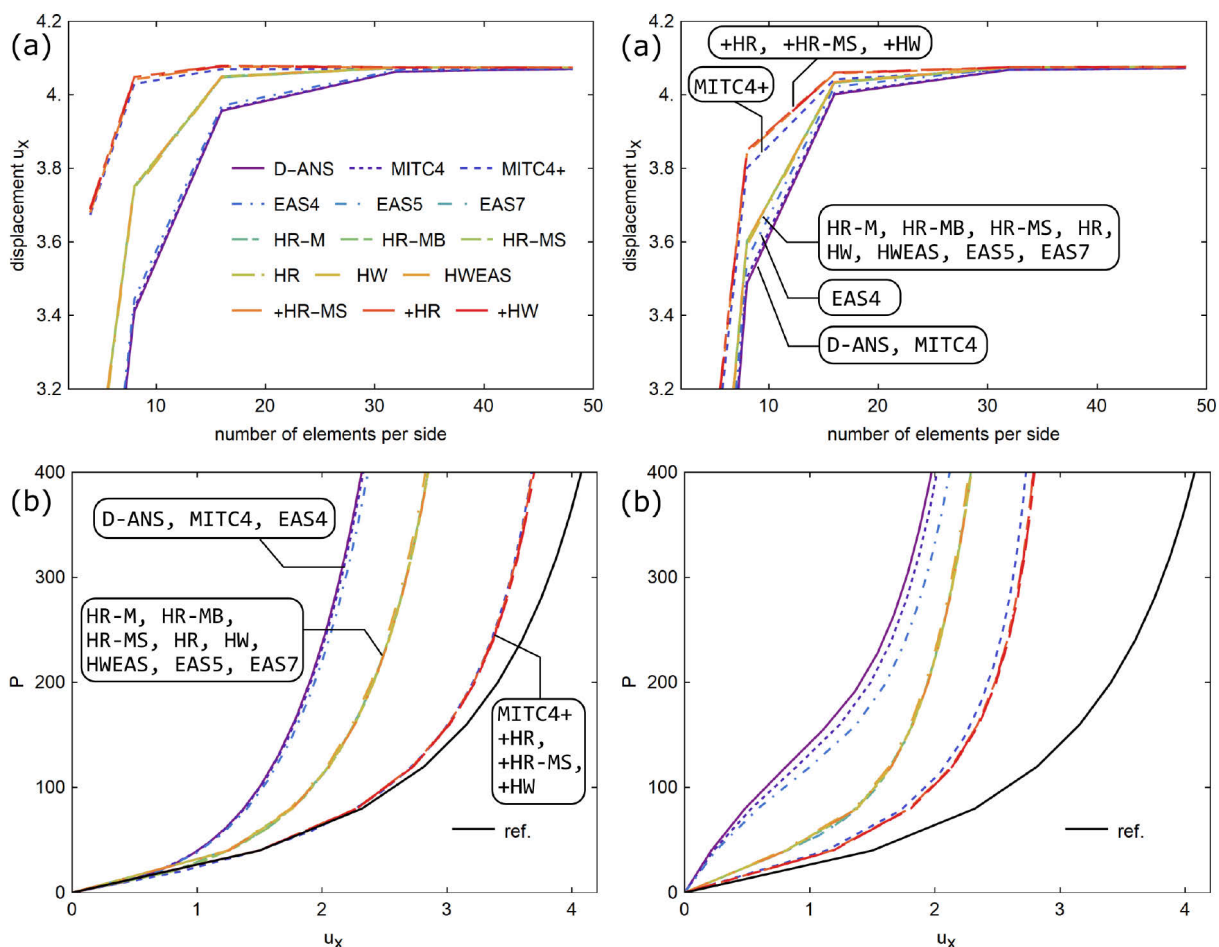
Figure 2.19: Hemispherical shell, regular mesh: (a) convergence, (b) displacement for 4×4 mesh.
Slika 2.19: Polkrožna lupina, običajna mreža: (a) konvergenca, (b) pomik za 4×4 mrežo.

Figure 2.20: Hemispherical shell, distorted mesh: (a) convergence, (b) displacement for 4×4 mesh.
Slika 2.20: Polkrožna lupina, pokvarjena mreža: (a) konvergenca, (b) pomik za 4×4 mrežo.

Table 2.14: Hemispherical shell: computational details for $P = 400$ for regular and distorted 16×16 mesh.
Preglednica 2.14: Polkrožna lupina: računske podrobnosti za $P = 400$ za običajno in pokvarjeno mrežo 16×16.

	Regular mesh				Distorted mesh			
FE	Req. no. of load increments	Total no. of iterations	Normalized CPU time	No. of back-steps	Req. no. of load increments	Total no. of iterations	Normalized CPU time	No. of back-steps
D-ANS	20	192	1.70	1	24	234	1.51	2
MITC4	16	150	1.00	1	16	151	1.00	1
MITC4+	16	152	1.46	1	16	152	1.22	1
EAS4	16	150	1.22	1	16	152	1.11	1
EAS5	16	152	0.76	1	16	151	1.20	1
EAS7	16	152	1.27	1	16	151	1.11	1
HR-M	14	122	1.32	2	13	109	0.89	1
HR-MB	14	118	1.19	2	13	119	0.82	1
HR-MS	10	55	0.49	0	10	55	0.49	0
HR	10	57	0.51	0	10	57	0.53	0
HW	10	57	0.76	0	10	57	0.44	0
HWEAS	10	57	0.78	0	10	57	0.51	0
+HR-MS	10	55	0.78	0	10	55	0.40	0
+HR	10	57	0.38	0	10	57	0.49	0
+HW	10	57	0.62	0	10	57	0.56	0

2.5.4.4   Twisted beam

We consider the twisted beam problem, shown in Figure 2.21, see also e.g. [164], [90], [91]. The beam with material data $E = 29\,10^6, \nu = 0.22$ and thickness $t = 0.0032$ is clamped at one edge and subjected to either in-plane or out-of-plane force, $P_Z = 0.1$ and $P_Y = 0.1$, respectively. Adaptive control of load increments was applied, see Table 2.1. The used mesh was 4×24. The reference solution was obtained by mesh of 12×72 HWEAS elements.
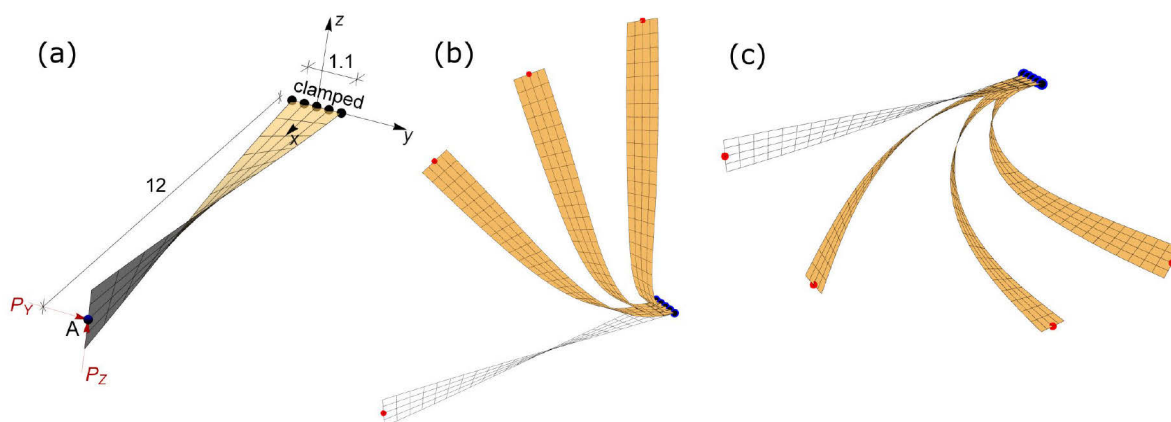
Figure 2.21: Twisted beam: (a) initial data; deformed configurations for the in-plane force (b), and out-of-plane load (c).
Slika 2.21: Zavit nosilec: (a) začetni podatki; deformirane konfiguracije za silo v ravnini (b) in silo izven ravnine (c).

Table 2.15: Twisted beam: computational details for $P = 0.1$ for in-plane and out-of-plane load case.

Preglednica 2.15: Zavit nosilec: računske podrobnosti za $P = 0.1$ za silo v ravnini in izven ravnine.

FE	In-plane loading			Out-of-plane loading		
	Req. no. of load increments	Normalized CPU time	No. of back-steps	Req. no. of load increments	Normalized CPU time	No. of back-steps
D-ANS	77	0.86	10	85	0.97	14
MITC4	66	1.00	13	84	1.00	11
MITC4+	73	1.38	14	80	1.14	8
EAS4	65	1.12	13	84	1.45	12
EAS5	79	1.18	11	87	1.42	10
EAS7	79	1.21	11	87	1.39	10
HR-M	220	4.39	70	189	3.73	56
HR-MB	225	4.01	77	195	4.18	61
HR-MS	14	0.18	0	14	0.21	0
HR	14	0.22	0	14	0.22	0
HW	14	0.21	0	14	0.22	0
HWEAS	14	0.21	0	14	0.25	0
+HR-MS	14	0.19	0	14	0.15	0
+HR	14	0.20	0	14	0.19	0
+HW	14	0.18	0	14	0.21	0
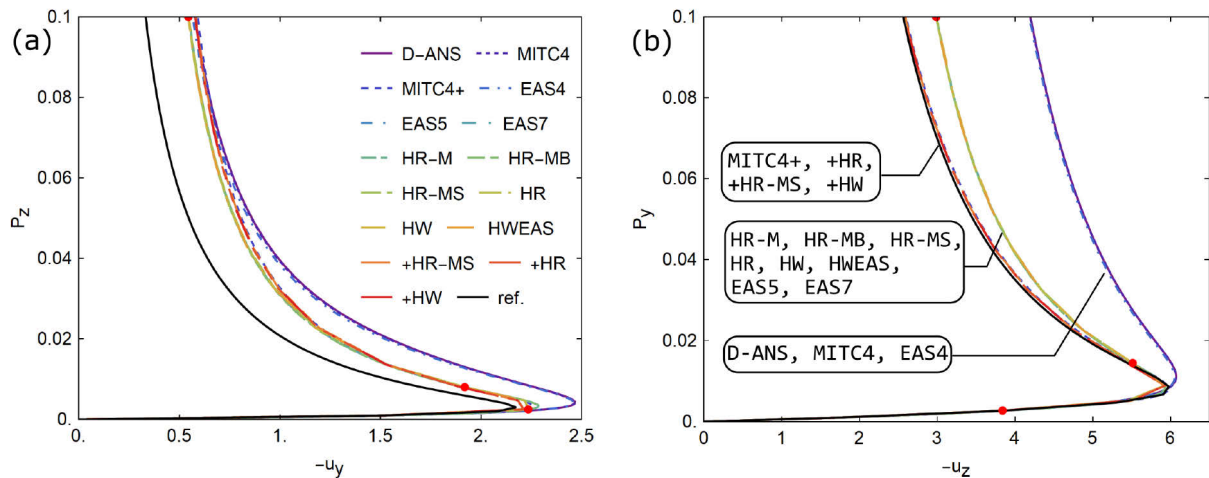
Figure 2.22: Twisted beam: Load-displacement curves for the in-plane (a) and the out-of-plane (b) load cases.
Red dots mark deformed configurations in Figure 2.21 (b) and (c).

Slika 2.22: Zavit nosilec: krivulje sila-pomik za obtežbo v ravnini (a) in izven ravnine (b). Rdeče točke
označujejo deformirane konfiguracije na sliki 2.21 (b) in (c).

In Figure 2.21 (b) and (c), we show deformed configurations for both load cases. These configurations are marked with red dots on the response curves in Figure 2.22, where load versus displacements at point A is shown. For the in-plane load case, see Figure 2.22 (a), all the formulations perform similarly (however, the results do not match the reference solution), except D-ANS, MITC4 and EAS4, which stand out in a negative way. For the out-of-plane load case, see Figure 2.22 (b), MITC4+, +HR-MS, +HR and +HW give the most accurate response (very close to the reference solution), whereas D-ANS, MITC4 and EAS4 again perform worst among the formulations. In Table 2.15, we compare robustness

and speed of the used formulation by the normalized CPU time and the number of load increments it took, to arrive to the final configuration. It can be observed again that all the (+)HR and (+)HW formulations, except HR-M and HR-MB, are the fastest. The former also compute the response using much larger steps and they require no back-steps in the solution procedure. The latter, on the other hand, require a large number of back-steps and very small load increments to arrive at the final configuration.

2.5.4.5 Hyperbolic paraboloid under edge load

We considered a hyperbolic paraboloid shell, with mid-surface defined as $z = x^2 - y^2$, with $(x, y) \in (-L/2, L/2)$ and $L = 1$. The shell thickness is $t = 0.001$. The material data are $E = 2\,10^{11}$ and $v = 0.3$. One edge of the shell is clamped and the other edges are free, see Figure 2.23 (a). The shell is loaded at the free edge, opposite to the clamped one, by a uniform line force $f = 400$. Two mesh densities are considered: a coarse mesh of 16×16 elements and a very fine mesh of 112×112 elements. In addition to the regular meshes, distorted meshes are considered as well, see Figure 2.23 (b). For a distorted mesh, the length of the element edge changes linearly with the ratio $L_{max}/L_{min} = 4$. Adaptive control of load increments was applied, see Table 2.1. With this example, we illustrate that mesh distortion introduces imperfections, which can have significant influence on results, if the bifurcation points are present on equilibrium path. A similar problem was presented in e.g. [8], [57], [109], however, the load was self-weight (the final free-edge displacement was roughly 10-times smaller than for the here-presented example), and the stability analysis was not of interest.
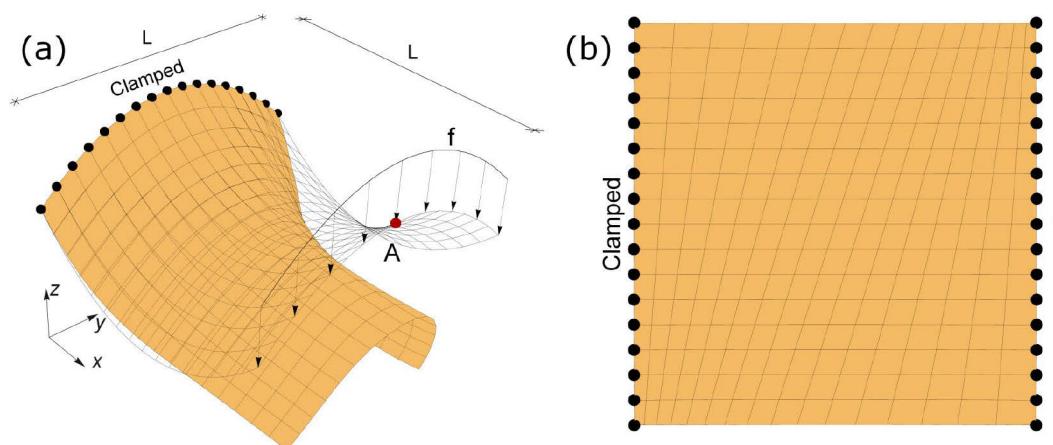
Figure 2.23: Hyperbolic paraboloid: (a) Initial and deformed configurations for MITC4 element, (b) distorted mesh pattern for 16×16 mesh.
Slika 2.23: Hiperbolični paraboloid: (a) začetna in deformirana konfiguracija za MITC4 element, (b) vzorec pokvarjene mreže za 16×16 mrežo.

The results are presented in Figures 2.24 and 2.25, where the displacements u_z and u_y at node A are given with respect to the load f_z, represented as the total resultant of the applied line force. Results for regular and distorted meshes are presented together on each of the response graphs. For a regular mesh (which is symmetrical with respect to the plane $y = 0$, see Figure 2.23 (b)), the horizontal displacement of node A was $u_y = 0$ at all times. Thus, the deformed configurations were symmetric with respect to the plane $y = 0$. However, a bifurcation point was reported for symmetrical meshes during the computations. The type of the bifurcation point was symmetric positive, see e.g. [150]. All the

formulations detected the bifurcation point for a 112×112 symmetrical mesh at approximately $f_z = 240$, see yellow dots in Figure 2.25. For a 16×16 symmetrical mesh, some formulations located it at approximately $f_z = 240$ (i.e. MITC4+, +HR-MS, +HR and +HW), others located it at much higher loads, at approximately $f_z = 400$, while D-ANS, MITC4 and EAS4 did not locate it at all for the applied range of the load, see Figure 2.24. This demonstrates that some formulations were precise with location of the bifurcation point already for the coarse mesh.
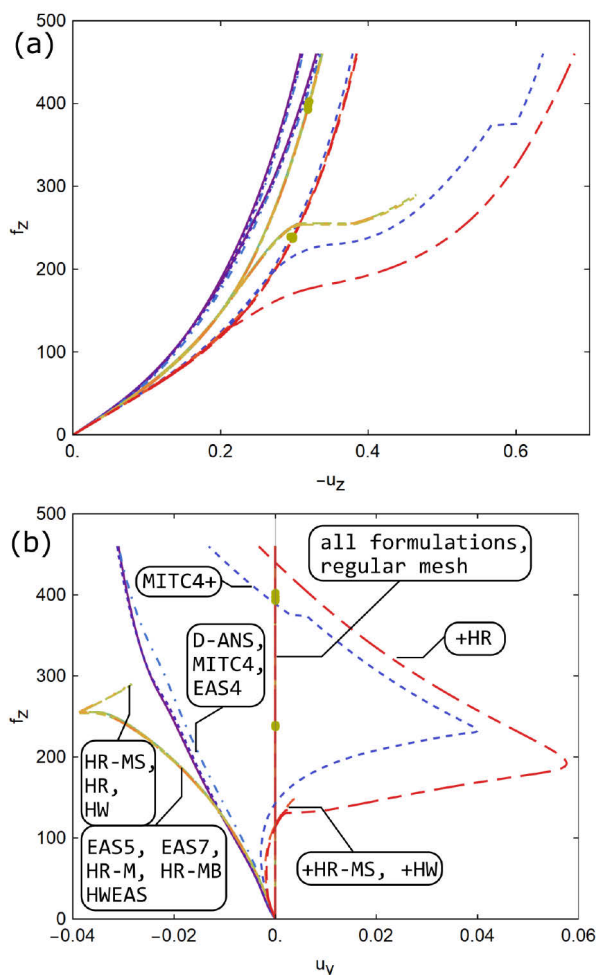
Figure 2.24: Load-displacement curves for 16×16
mesh. (a) displacement $-u_z$ (b) displacement u_y.
Slika 2.24: Krivulje sila-pomik za 16×16 mrežo. (a)
pomik $-u_z$ (b) pomik u_y.
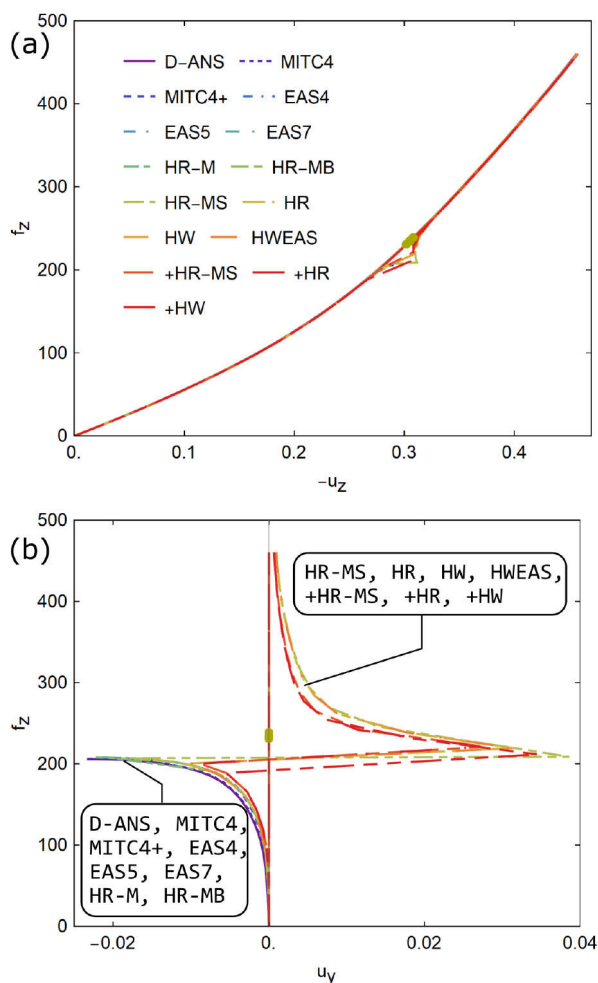
Figure 2.25: Load-displacement curves for 112×112
mesh. (a) displacement $-u_z$ (b) displacement u_y.
Slika 2.25: Krivulje sila-pomik za 112×112 mrežo.
(a) pomik $-u_z$ (b) pomik u_y.

Distorted mesh introduced small unsymmetrical imperfections, which broke the symmetry, see Figure 2.23 for initial and Figure 2.26 for deformed configurations. This resulted in vanishing of the bifurcation point. The results were not symmetric any more, i.e. u_y for node A was not zero. The $f_z - u_y$ curves for node A are given in Figure 2.24 (b) for the coarse mesh, and in Figure 2.25 (b) for the fine mesh. For the coarse mesh, the computed responses are quite different. The majority of the formulations predicted negative u_y at node A, some changed the initial sign but soon failed (+HR-MS and +HW), and some (+HR and MITC4+) changed the sign even two times. For the fine mesh, all the formulations gave very similar (almost identical) results for the solution branch below the bifurcation point. However, it is interesting to note that (+)HR-MS, (+)HR, (+)HW and HWEAS found also a solution branch above

the bifurcation point, probably due to their ability to take very large increments. Note i) that (+)HW jumped to the above branch already for a 64×64 mesh, (+)HWEAS and (+)HR for 80×80 mesh, (+)MR-MS for 112×112 mesh, while the other formulations did not jump to the above branch, even for 160×160 mesh; ii) that changing the distortion of the mesh by switching the location of longest and shortest element produces results that are identically symmetrical with respect to $u_y = 0$ in Figure 2.24 (b) and Figure 2.25 (b).
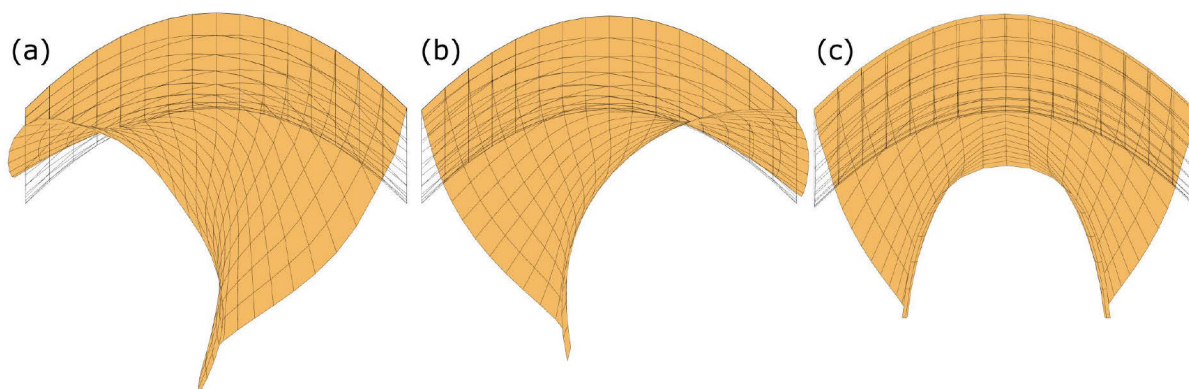
Figure 2.26: Hyperbolic paraboloid: final deformed configurations for 16×16 mesh. (a) MITC4+ distorted mesh, (b) HR-MS distorted mesh, (c) +HW regular mesh.
Slika 2.26: Hiperbolični paraboloid: končne deformirane konfiguracije za 16×16 mrežo. (a) MITC4+ pokvarjena mreža, (b) HR-MS pokvarjena mreža, (c) +HW običajna mreža.

2.5.4.6 Thin deployable ring

The data for this example are presented in Figure 2.27. The example has similarities with the snap-through-of-an-elastic-ring example, which was studied in e.g. [54] and computed by shell finite elements in [122]. We show the ability of the derived formulations to represent a deployment phenomenon, where the ring folds into three smaller rings with the radius of $1/3$ of the initial one, and by further increasing the load regains its initial configuration. We chose a ring with the following geometric and material data: $R = 500, H = 5$, thickness $t = 1, E = 2 \; 10^6, v = 0.3$. We considered two meshes of 60×1 and 400×1 elements. The rotation $\phi = \phi_x = 4\pi$ was imposed at one upper node, while the lower end of the ring was clamped, see Figure 2.27. Adaptive control of load increments was used, see Table 2.1. This example is a test for both the finite element formulations and the adopted finite rotation algorithm.

Figures 2.29 and 2.30 show the moment reaction M, at the node where the rotation is imposed, versus displacements u_y, u_z and rotation ϕ_x at the same node. It is interesting to note that all the formulations can handle this problem without any difficulties. Moreover, they behave almost in the same manner for the chosen meshes. Exceptions are MITC4 and MITC4+, which give slightly different response curves than the rest of formulations. Nevertheless, the +HR and +HW formulations were the most accurate, since their results with the coarse mesh were the closest to the converged results obtained with the fine mesh. In Figure 2.28, a sequence of deformed configurations is shown for a mesh of 400×1 HWEAS in order to present how the ring folds and unfolds. The configurations are connected by red dots to the curves in Figure 2.30. On the $M - \phi_x$ curve in Figures 2.29 (c) and 2.30 (c), there are four limit points and three points with $M = 0$. The second one of the latter points, located at $\phi_x = 2\pi$, is related to the

folded three-circles configuration. Note that the moment-displacement curves for $\phi_x \in [2\pi, 4\pi]$ are mirror images of the curves for $\phi_x \in [0, 2\pi]$, for performing mirroring over line $M = 0$ or for a sequence of two mirrorings over lines $M = 0$ and $u_y = 0$. Similarly, $M - \phi_x$ curves for $\phi_x \in [2\pi, 4\pi]$ are mirror images of the curves for $\phi_x \in [0, 2\pi]$, for a sequence of two mirrorings over lines $M = 0$ and $\phi_x = 2\pi$.
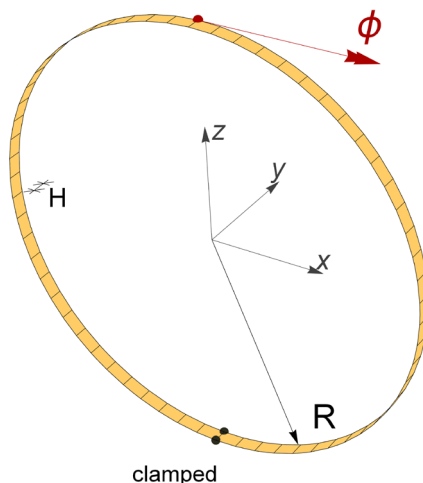
Figure 2.27: Thin deployable ring data.
Slika 2.27: Podatki za tanek zložljiv obroč.
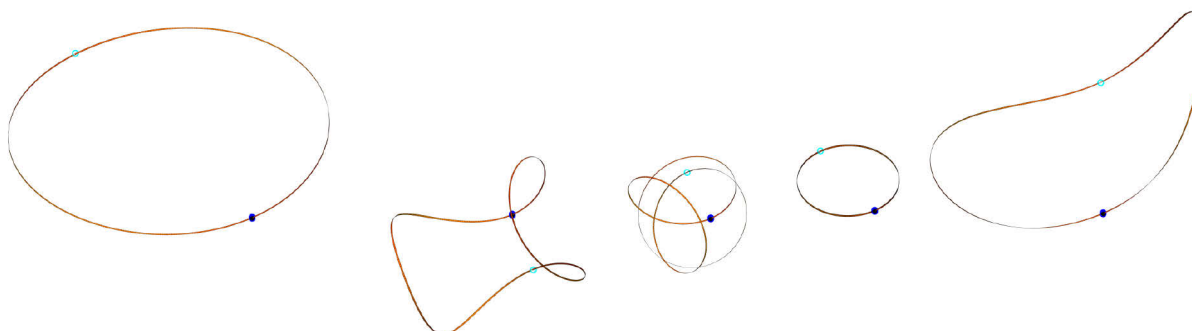
Figure 2.28: Thin deployable ring: Sequence of deformed configurations that correspond to the red dots in Figure 2.30.
Slika 2.28: Tanek zložljiv obroč: zaporedje deformiranih konfiguracij, ki se nanašajo na rdeče pike na sliki 2.30.
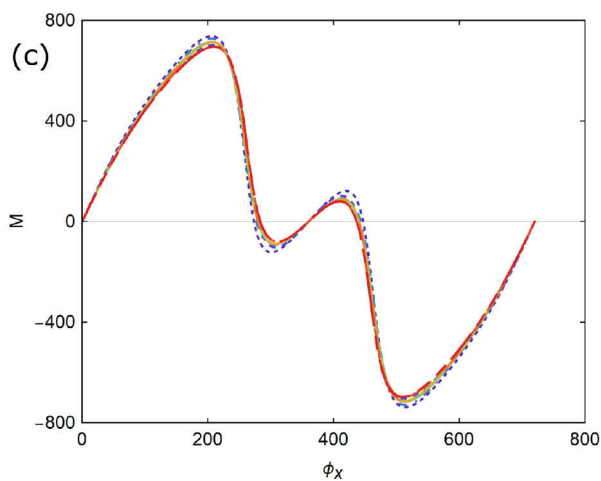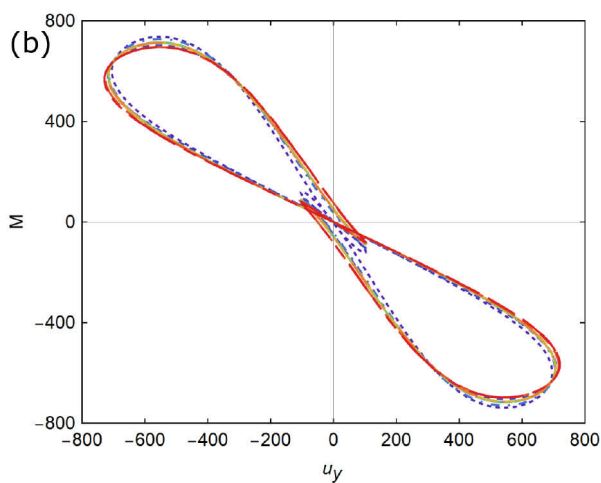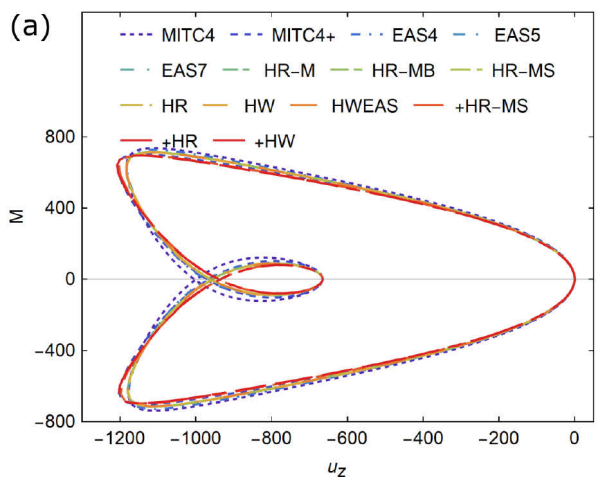
Figure 2.29: Thin deployable ring: Moment displacement and moment rotation curves for 60×1 mesh.

Slika 2.29: Tanek zložljiv obroč: krivulje moment-pomik in moment-rotacija za mrežo 60×1.
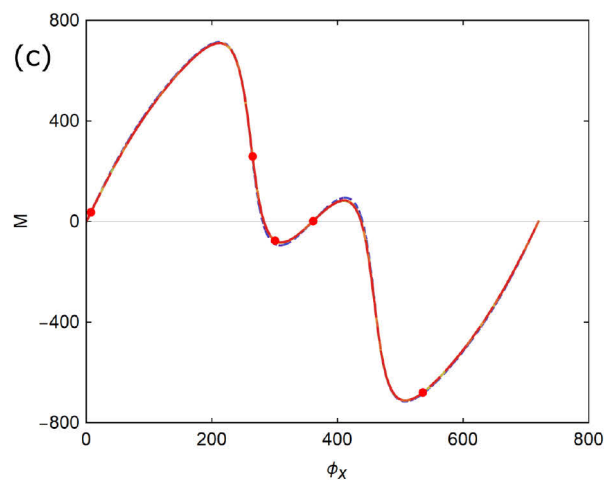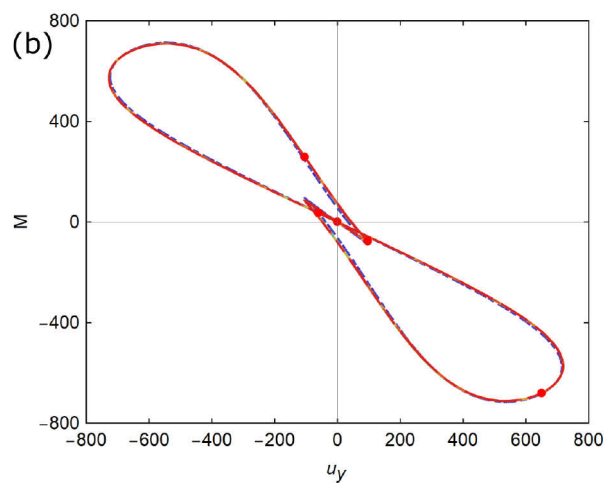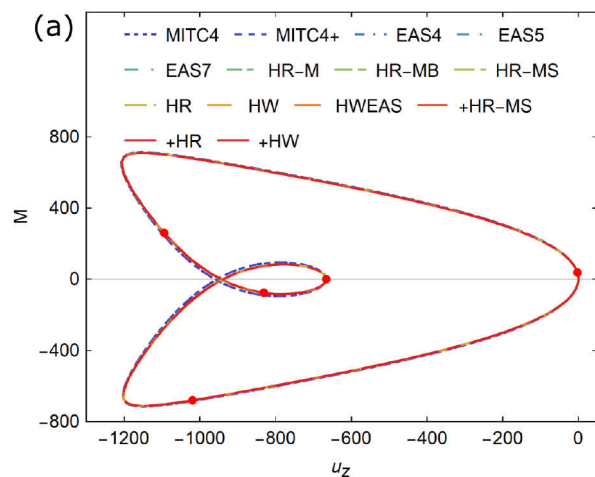
Figure 2.30: Thin deployable ring: Moment displacement and moment rotation curves for 400×1 mesh.

Slika 2.30: Tanek zložljiv obroč: krivulje moment-pomik in moment-rotacija za mrežo 400×1.

2.5.4.7   Cylindrical panel

In the four following tests, we apply only four shell formulations that we identify either as well-established (MITC4) or near optimal (MITC4+, HW, +HW).

Thin cylindrical panel, considered also in [90], is clamped at one edge and subjected to distributed moment $M = \lambda M_0$ along the opposite edge, see Figure 2.31. This is a pure bending test. Regular and distorted meshes shown in Figure 2.31 are used; the ratio $L_{min}/L_{max} = 1/12$.

$$L = 10,\ R = 20$$
$$t = \frac{R}{10000},\ \Phi = \frac{\pi}{6}$$
$$M_0 = 3.2\ 10^{-4}$$
$$E = 2.1\ 10^6,\ \nu = 0$$
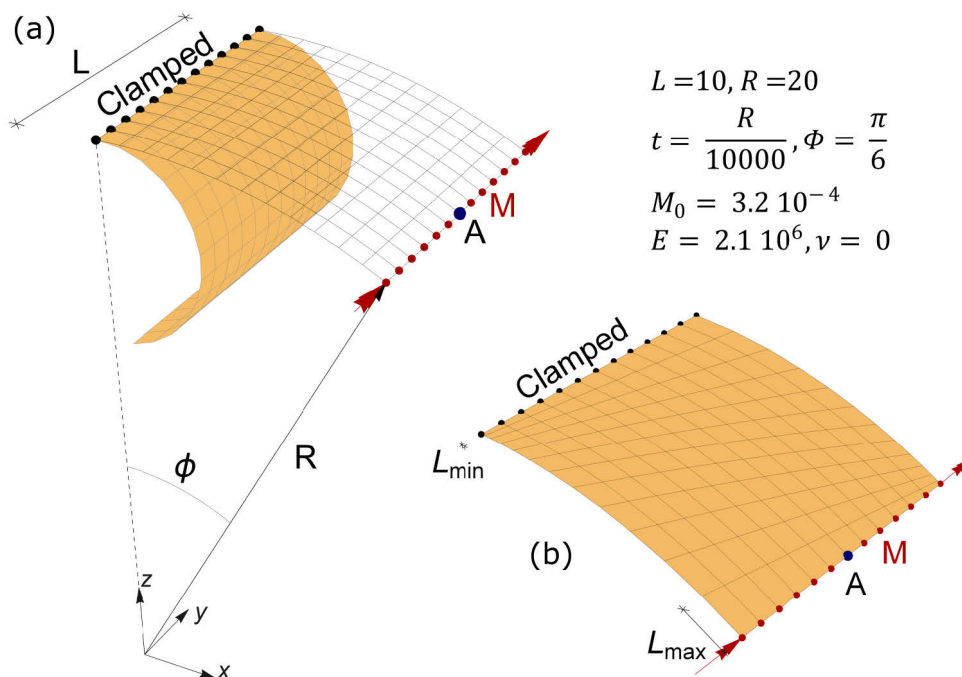
Figure 2.31: Cylindrical panel: (a) initial and final deformed configuration for regular mesh (MITC4) (b) distorted mesh.

Slika 2.31: Cilindrični panel: (a) začetna in deformirana konfiguracija za običajno mrežo (MITC4), (b) pokvarjena mreža.
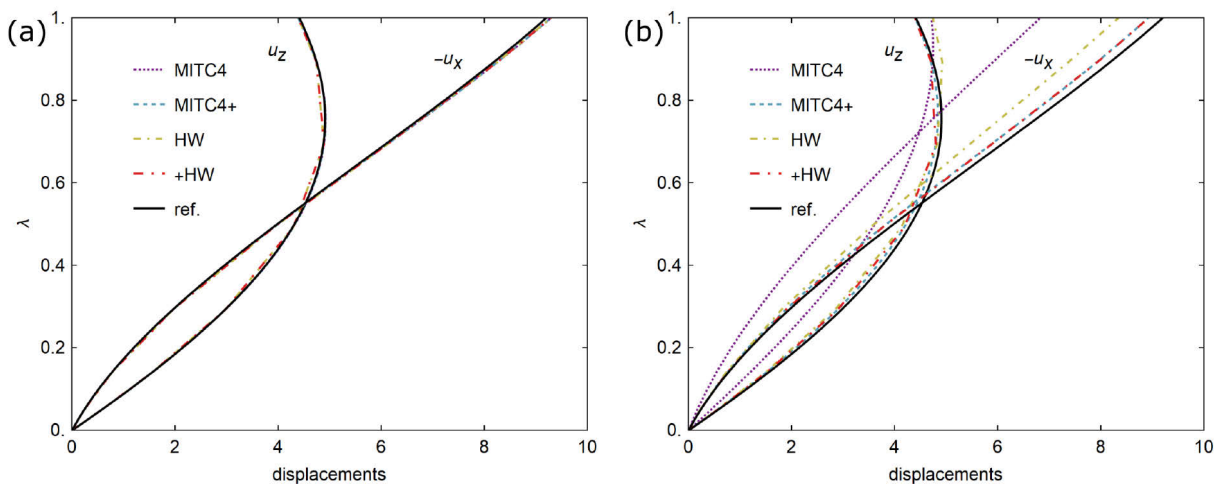
Figure 2.32: Cylindrical panel: response for (a) regular mesh and (b) distorted mesh.

Slika 2.32: Cilindrični panel: odziv za (a) običajno mrežo in (b) pokvarjeno mrežo.

Figure 2.32 shows the applied load versus displacements u_z and $-u_x$ of point A; the reference results obtained by regular mesh of 48×48 HW elements match perfectly those obtained for 32×32 regular mesh of MITC9 elements in [90]. The response of all formulations is practically the same for the regular mesh, see Figure 2.32 (a). For the distorted mesh, see Figure 2.32 (b), MITC4 is affected the most, HW shows reasonable results, while MITC4+ and +HW give similar results as for the regular mesh. The results indicate that for membrane locking remedy in pure bending case, MITC4+ is more effective than the mixed-hybrid treatment. The robustness and speed of the formulations are compared in Table 2.16.

Table 2.16: Cylindrical panel: computational details for $M = M_0$ for regular mesh (top) and distorted mesh (bottom); $u_{x,ref} = -9.21$.

Preglednica 2.16: Cilindrični panel: računske podrobnosti za $M = M_0$ za običajno mrežo (zgoraj) in pokvarjeno mrežo (spodaj); $u_{x,ref} = -9.21$.

FE	MITC4	MITC4+	HW	+HW
Displacement $-u_x$ $(\frac{-u_x}{-u_{x,ref}}[\%])$	9.30 (101)	9.30 (101)	9.30 (101)	9.30 (101)
Normalized CPU time	1.00	0.89	0.23	0.23
Req. no. of load increments	22	22	7	7
Number of total iterations	205	205	41	41
Number of back-steps	0	0	0	0
Displacement $-u_x$ $(\frac{-u_x}{-u_{x,ref}}[\%])$	6.83 (74)	8.92 (97)	8.35 (91)	8.93 (97)
Normalized CPU time	1.00	0.95	0.19	0.33
Req. no. of load increments	22	35	7	7
Number of total iterations	220	370	41	41
Number of back-steps	1	1	0	0

2.5.4.8 Doubly twisted beam

We consider a modified version of the twisted beam-like shell problem considered in e.g. [90], [91], [164] and Section 2.5.4.4. The beam is clamped at one edge and subjected to two forces, $P = \lambda P_y = \lambda P_z$, at the opposite end. The twist is 2π. The shell undergoes considerable bending, which is followed by stretching, see Figure 2.33 (b). Thus, this is a test for membrane-bending shell behavior.

In Figure 2.34, displacements u_z and u_y of point A are shown versus P; reference results were obtained by regular mesh of 20×60 HW elements. Regular and distorted meshes were used, with 12×4 and 6×20 elements, respectively, and ratio $L_{min}/L_{max} = 1/2$, see Figure 2.33 (a). Despite a coarse regular mesh, there is almost no difference in response between the formulations, which match well the reference results, see Figure 2.34 (a). Mesh distortion, see Figure 2.34 (b), greatly affects MITC4 (the results are far from the reference solution and useless), the HW solution is affected considerably, while MITC4+ and +HW show incredibly little sensitivity to mesh distortion. Table 2.17 shows that HW and +HW are the fastest, do not require back-steps and take large load increments.
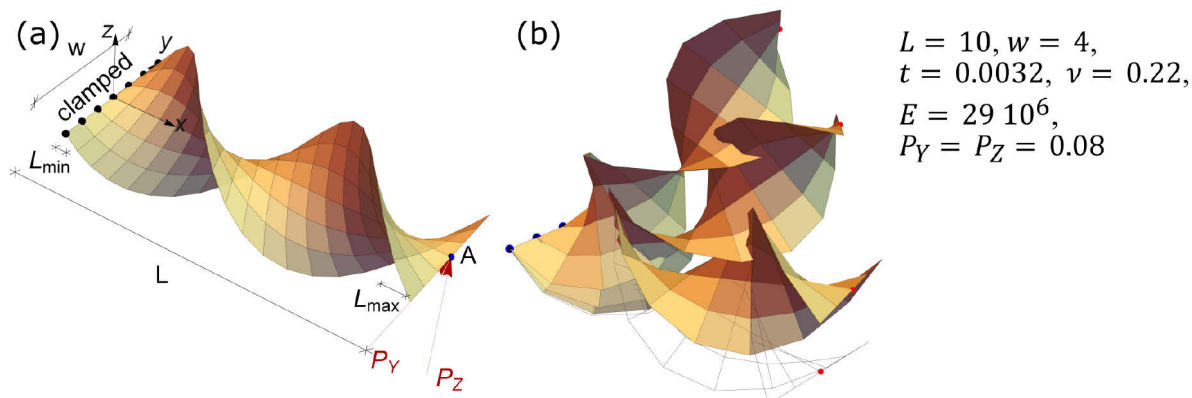
Figure 2.33: Doubly twisted beam: (a) problem data and distorted mesh (b) initial and three deformed
configurations for +HW (regular mesh).

Slika 2.33: Dvojno zavit nosilec: (a) podatki o problemu in pokvarjena mreža, (b) začetna in tri deformirane
konfiguracije za +HW (običajna mreža).
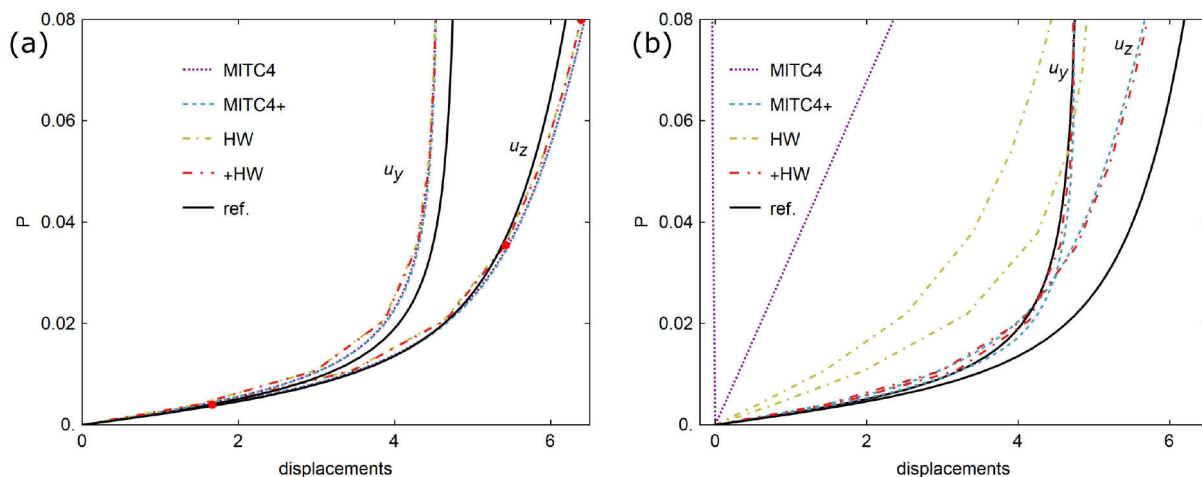
Figure 2.34: Doubly twisted beam: load-displacement curves for (a) regular mesh and (b) distorted mesh. Red
dots mark deformed configurations in Figure 2.33 (b).

Slika 2.34: Dvojno zavit nosilec: krivulje obtežba-pomik za (a) običajno mrežo in (b) pokvarjeno mrežo. Rdeče
pike označujejo deformirane konfiguracije na sliki 2.33 (b).

The twisted beam was also chosen to check for a possible undesirable hysteresis because of the
configuration dependent weighting factors (2.49) applied in MITC4+ and +HW. We chose the twist of
$\pi/8$ and distorted mesh with ratio $L_{max}/L_{min} = 4$, see Figure 2.35. The uniformly distributed load
$P = \lambda P_X$ was increased until $\lambda = 1$, which produced large membrane strains, and then decreased to $P =
0$. Figure 2.35 shows no hysteresis effect, which confirms that the weighting factors in (2.49) were
carefully calibrated.

Table 2.17: Doubly twisted beam: computational details for $P = 0.08$ for regular mesh (top) and distorted mesh (bottom); $u_{y,ref} = 4.75$.

Preglednica 2.17: Dvojno zavit nosilec: računske podrobnosti za $P = 0.08$ za običajno mrežo (zgoraj) in pokvarjeno mrežo (spodaj); $u_{y,ref} = 4.75$.

FE	MITC4	MITC4+	HW	+HW
Displacement u_y ($\frac{u_y}{u_{y,ref}}$[%])	4.52 (95)	4.53 (95)	4.52 (95)	4.53 (95)
Normalized CPU time	1.00	1.37	0.10	0.09
Req. no. of load increments	61	78	7	7
Total number of iterations	664	802	43	43
Number of back-steps	10	14	0	0
Displacement u_y ($\frac{u_y}{u_{y,ref}}$[%])	-0.04 (-1)	4.74 (100)	4.91 (103)	4.73 (100)
Normalized CPU time	1.00	13.5	0.93	1.71
Req. no. of load increments	7	56	7	7
Total number of iterations	51	585	41	43
Number of back-steps	0	9	0	0

$L = 10, w = 4, t = 0.1, \nu = 0.22,$
$E = 29\ 10^6, P_X = 5\ 10^7$
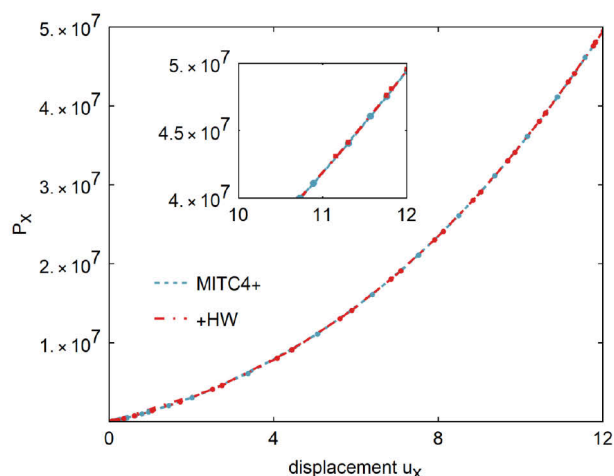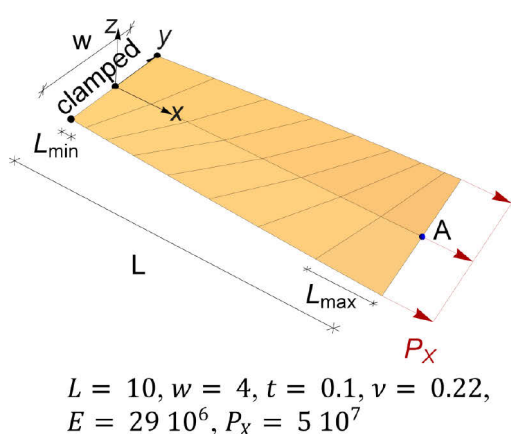
Figure 2.35: Beam with the twist of $\pi/8$ (left) and hysteresis response (right).
Slika 2.35: Nosilec, ukrivljen za $\pi/8$ (levo), in histerezni odziv (desno).

2.5.4.9 Thick deployable ring

The thick deployable ring example, see Figure 2.36 (a), was studied in detail in [54] and was recomputed by isogeometric Reissner-Mindlin (RM) and Kirchhoff-Love (KL) shell formulations in [122]. The example has similarities with the thin deployable ring example in Section 2.5.4.6, but the orientation of the rotation is different. The ring is clamped along the bottom cross-section and subjected to imposed rotation $\Phi = \lambda\Phi_0$ along the top cross-section. We used meshes of 80×1, 1200×1 and 1200×4 elements. Because our formulations do not have drilling rotation, the meshes were in the plane of the ring. This is in contrast to the mentioned isogeometric computations in [122], where the elements were oriented perpendicular to the plane of the ring and drilling rotation was applied. For this reason, our results do not match closely those from [122]. According to [54], at $\Phi = 2\pi$, the ring deploys into three circles with a radius $R/3$, and its initial shape is regained at $\Phi = 4\pi$. The example is a test for coupling of bending and twisting, with large parts of the ring exhibiting almost rigid-body motion.
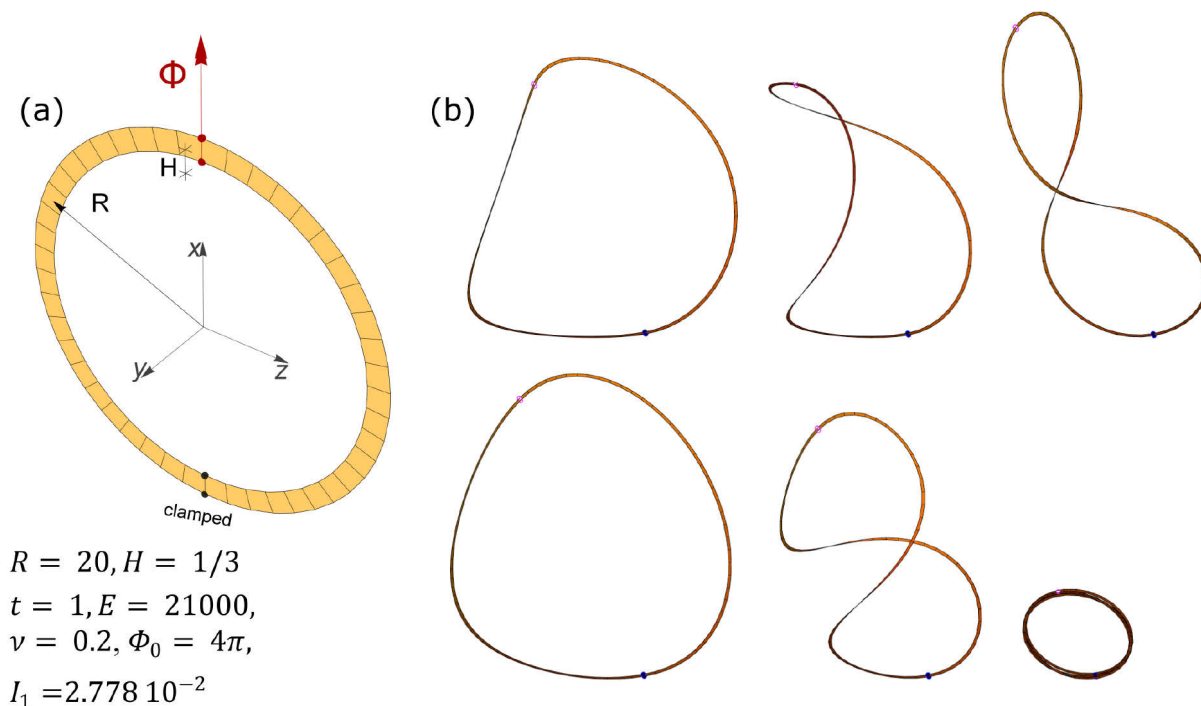
Figure 2.36: Thick deployable ring: (a) problem data; (b) 80×1 mesh; deformed configurations at points marked in Figure 2.37 for MITC4 (top) and for +HW (bottom).

Slika 2.36: Debel zložljiv obroč: (a) podatki o problemu, (b) 80×1 mreža; deformirane konfiguracije ob različnih točkah, označenih na sliki 2.37, za MITC4 (zgoraj) in za +HW (spodaj).
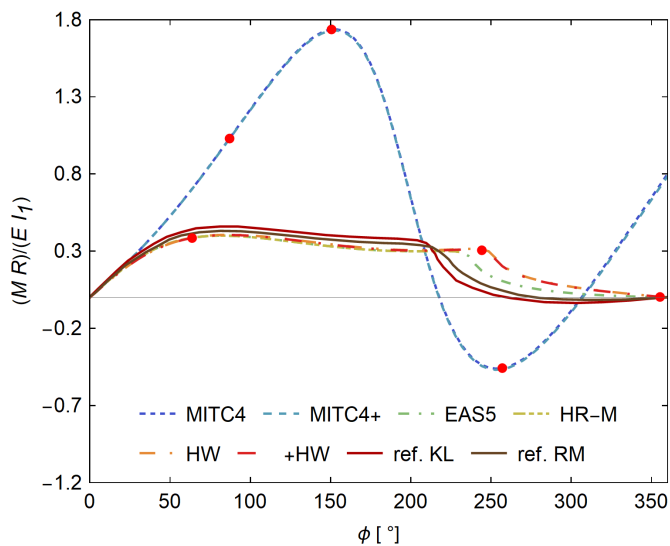
Figure 2.37: Thick deployable ring: load-displacement curves for 80×1 mesh; red dots mark deformed configurations in Figure 2.36 (b).

Slika 2.37: Debel zložljiv obroč: krivulje obtežba-pomik za mrežo 80×1; rdeče pike označujejo deformirane konfiguracije na sliki 2.36 (b).

The results are given in Figures 2.37 and 2.38, where moment-rotation curves are shown; M is the sum of reactions at nodes with imposed rotation. Figure 2.37 shows that MITC4 and MITC4+ exhibit severe membrane locking for the coarser mesh and predict a completely deviating solution. It seems that the solution is non-physical, because at $\Phi \approx 2\pi$ the elements cross each other, see Figure 2.36 (b). The

Lavrenčič, M. 2020. Numerical Procedures for Nonlinear Static and Dynamic Analyses of Shell Systems of Various Sizes.
PhD Th. Ljubljana, UL FGG, Third cycle doctoral study Built Environment.

59

present ANS membrane treatment has no effect for this example, because MITC4 and MITC4+ behave in the same way.

The HW and +HW formulations predict solutions that are qualitatively close to those presented in [122] and [54] and their results change only slightly with mesh refinement. For the 1200×1 mesh, the results of all formulations almost coincide; however, MITC4 and MITC4+ fail to converge at $\Phi \approx 2.6\pi$, see Figure 2.38 (a). For the 1200×4 mesh, the formulations provide the same response up to the final rotation $\Phi = 4\pi$, see Figure 2.38 (b). Here we show the number of negative pivots (NP) on the solution path; a change on NP indicates the occurrence of critical (i.e. limit or bifurcation) point. It is interesting that the formulations do not predict critical points at the same configurations. Moreover, MITC4 and MITC4+ detect two more than HW and +HW.
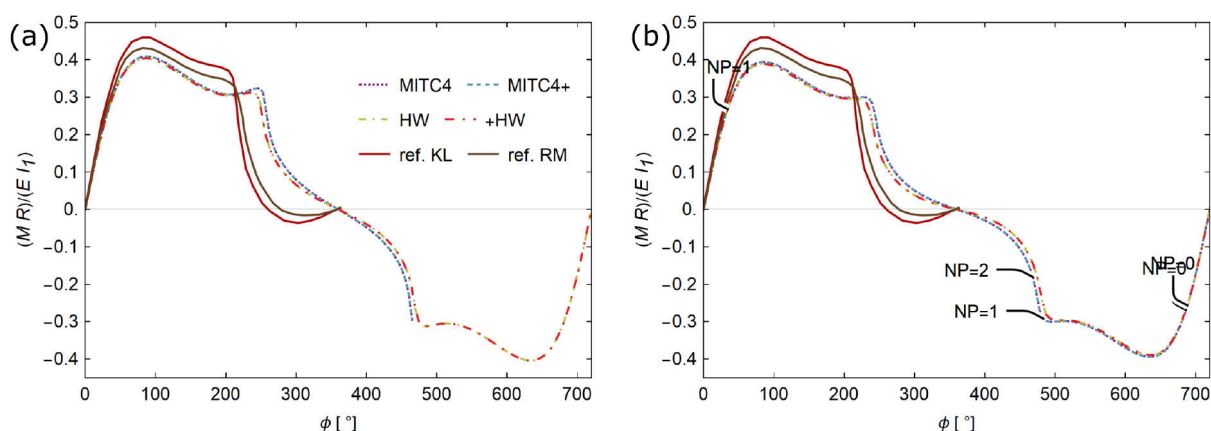
Figure 2.38: Thick deployable ring: load-displacement curves for (a) 1200×1 and (b) 1200×4 mesh.
Slika 2.38: Debel zložljiv obroč: krivulje obtežba-pomik za (a) mrežo 1200×1 in (b) mrežo 1200×4.

2.5.4.10 Pinched cylinder

The cylinder is clamped at one edge and subjected to two opposite vertical forces $P = \lambda P_0$ at the other edge, see Figure 2.39 (a). Due to the symmetry, only one fourth of the cylinder is modeled and symmetrical boundary conditions are considered. Initial and deformed meshes of 8×8 and 20×14 elements are shown in Figure 2.39 (a) and (b), respectively. Reference solution is taken from [152], where a 32×32 mesh was used. We applied the path-following method [150] to compute the complete response that included the snap-troughs and snap-backs, see Figure 2.40. The latter were associated with artificial mesh-dependent localized buckling due to sharp configuration changes of one or several elements, see Figure 2.39 (b) and (c). For this particular example, the problem of artificial mesh-dependent buckling was already reported in [44], see also [22]. As can be seen from Figure 2.40 (a) and (b), MITC4+ and +HW are somehow more prone to catching artificial buckling than MITC4 and HW, although the equilibrium path is non-smooth for all of the formulations. Nonetheless, when a finer mesh of 16×24 elements is used (not shown here), all the results coincide with the reference solution.

$R = 1.016, L = 3R,$
$t = 0.03, P_0 = 2000,$
$E = 2.0685 \ 10^7, v = 0.3$
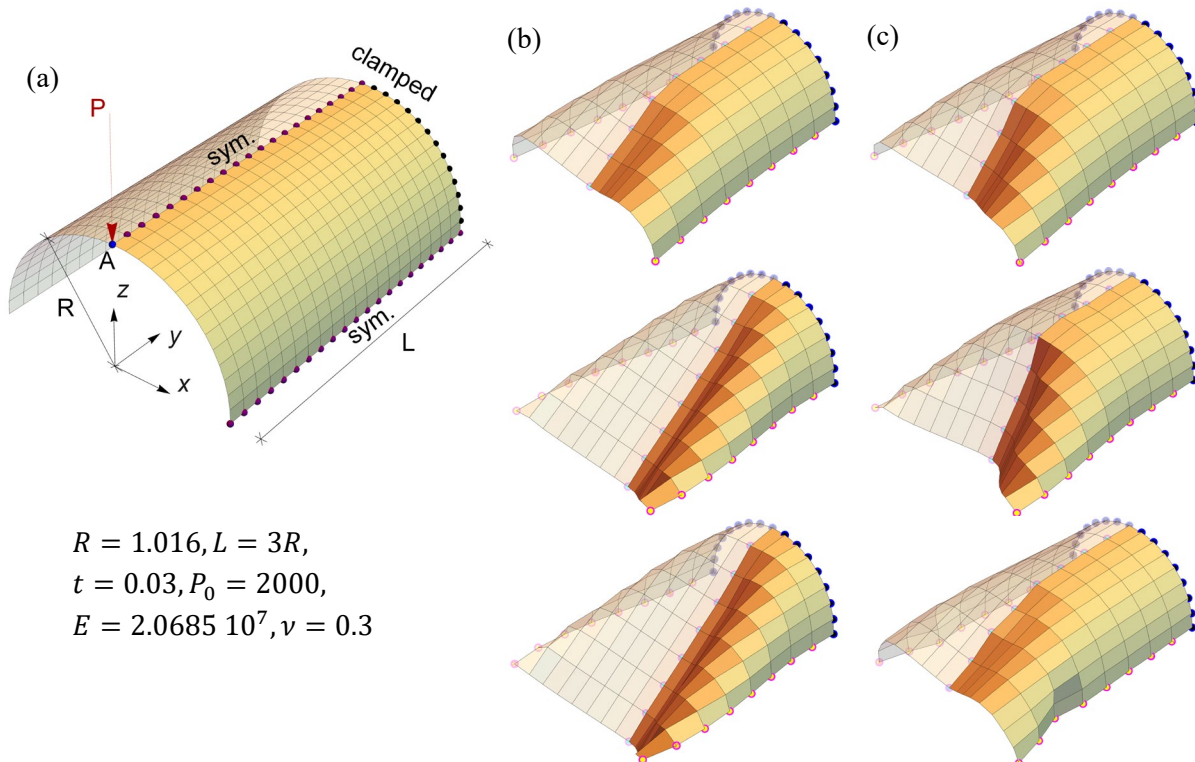
Figure 2.39: Pinched cylinder: (a) initial, (b) MITC4 deformed configurations, and (c) +HW deformed configuration at points marked in Figure 2.40 (a).
Slika 2.39: Preščipljen cilinder: (a) začetna, (b) MITC4 deformirane konfiguracije in (c) +HW deformirane konfiguracije na točkah, označenih na sliki 2.40 (a).
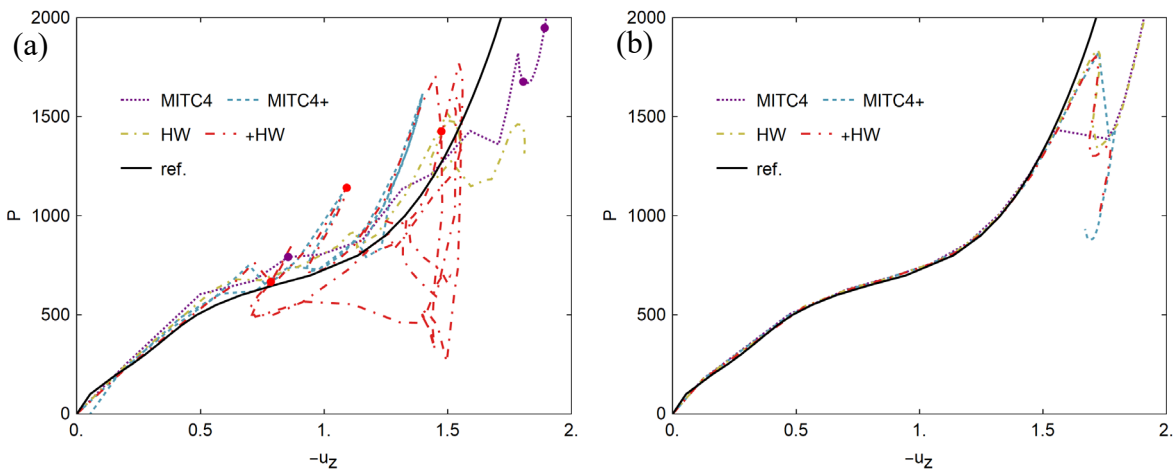
Figure 2.40: Pinched cylinder: load-displacement curves for (a) 8×8 mesh and (b) 14×20 mesh.
Slika 2.40: Preščipljen cilinder: krivulje obtežba-pomik za (a) 8×8 mrežo in (b) 14×20 mrežo.

2.6   Chapter conclusions

In this chapter a review of some widely used and other novel mixed shell finite elements was conducted. We described the implementation details for all the used formulations, as well as for the different rotation algorithms that can be used for the 5-dof inextensible director shell model. As for large rotation treatment, we conclude that the quaternion-based update greatly improves the robustness and in case of

incremental or iterative rotations also the speed of the algorithm. The additive total rotation algorithm can encounter a singularity, but this was not the case in any of the presented examples.

Although all of the used formulations pass the basic patch and conditioning number test, their performance is vastly different when it comes to some more demanding examples. It was shown that the 6-dof rotation-less formulation (D-ANS) is as effective as the MITC4 formulation. Nevertheless, the deficiencies of both, which had been known already, see e.g. [22], [89], [104], [159], were again highlighted by our diverse set of numerical tests.

It is now understood theoretically (see e.g. [114]) and has been confirmed by numerical experiments (see, e.g., [159] and the examples in this chapter) that the use of mixed-hybrid formulations is essential to get finite elements that allow for large solution steps. For the theoretical discussion on the ability of mixed formulations to take large solution steps, we refer to [114], where this issue is discussed for nonlinear mixed solid finite elements and the Hellinger-Reissner functional, but the conclusions are applicable also for the Hu-Washizu functional and shell finite elements. The main conclusion in [114] is that for mixed HR elements, the tangent stiffness matrix in the current iteration is much closer to the secant stiffness matrix of the current increment (than for the displacement-based elements). The reason is better iterative approximation of the converged incremental stresses. As a consequence, mixed formulations allow for larger solution steps and smaller number of iterations in comparison with the displacement-based formulations.

We used different variations of the mixed-hybrid element formulations, based on the Helliger-Reissner (HR) or Hu-Washizu (HW) functionals. It has been shown that not only a full HR or HW functional can be used, but a partial functional can also be the starting point of for the formulation of an elements. Only the membrane part or the combination of membrane and bending parts of the functional do not offer any great improvements. Great improvements are, however, observed if shear and membrane treatment are applied. Thus, the HR-M and HR-MB elements are not ideal candidates for use, while the HR-MS, HW, HW and HWEAS elements all produce good improvements compared to the MITC4 formulation. They are robust, converge fast and can take very large solution steps, thus allowing for very fast computations, as was shown in e.g. [59], [60], [159], [104] and confirmed by our extensive numerical experiments.

Unfortunately, the mixed-hybrid shell finite element formulations do not completely remove membrane and transverse shear locking. It was shown in [159] that it is possible to cure the transverse-shear locking in mixed-hybrid shell element by applying the ANS interpolations on the top of the Hu-Washizu interpolations for the stress resultants and strains. However, such mixed-hybrid shell element still remains sensitive to membrane locking for distorted meshes, as has been clearly shown by our numerical examples. On the other hand, the same numerical examples have demonstrated that the mesh distortion sensitivity can be effectively reduced by assumed natural strain interpolation of membrane strains, in particular by the recent MITC4+ version derived in [90].

Numerical examples show that the MITC4+ shell element converges fast and displays little sensitivity to mesh distortion. However, its weak spots are flat finite element meshes, since the membrane ANS enhancement has no effect on flat elements. Thus, MITC4+ behaves as MITC4. The formulation is also unable to compute large load increments; thus, it is not among the fastest.

As for the enhanced assumed strain (EAS) elements, it has been shown that at least 5 independent parameters are required to sufficiently improve the behavior of the elements, see also e.g. [22], [2]. The EAS5 and EAS7 elements provide good results in terms of convergence behavior, but they are sensitive to mesh distortion and are not capable of computing very long increments.

Based on [104], and confirmed by the numerical experiments here, the optimal choice for a formulation when computing a difficult shell problem is any of the formulations that combine the incredible features of MITC4+ and HW. We have demonstrated here that such a combination is easy to achieve and it results in robust elements that allow for large increments, show fast convergence and are low sensitive to mesh distortion.

3   NUMERICALLY DISSIPATIVE TIME-STEPPING SCHEMES FOR STRUCTURAL DYNAMICS

Chapter abstract

In this chapter we move on to dynamic analysis. We revisit some existing time-stepping schemes for structural dynamics with algorithmic dissipation, which fall either into the class of generalized-α methods or the class of energy-decaying (and momentum-conserving) methods. Some of the considered schemes are designed for the second-order and some for the first-order form of the differential equations of motion. We perform a comparison (for linear dynamics) of their characteristics and we study how these features extend to nonlinear dynamics, by performing numerical tests on examples of shell structures. For the considered schemes we illustrate their ability to decay/dissipate energy, their ability to fully/approximately conserve the angular momentum, and we estimate the nonlinear order of accuracy by error indicators. Let us finally note that this chapter is an extract of an article by Lavrenčič and Brank [105].

Nonlinear numerical examples in this chapter are computed using the dynamic extension of previously analysed MITC4 finite element, see Table 2.2 and Sections 2.2.1, 2.3.1 and 2.4.1, using the rotation algorithm IQ, see Table 2.7 and Section 2.2.2.

3.1   Chapter introduction

Compared to the static analysis, which was addressed in the previous chapter, dynamic analysis provides an alternative environment in which to perform difficult nonlinear calculation, with the effects of inertial forces taken into account. In the following chapter the characteristics of some implicit time integration schemes will be investigated and a theoretical and numerical comparison of the chosen schemes that fall either in the group of α-methods or the energy-decaying methods will be conducted. Most of the used schemes are designed to dissipate the unnatural higher structural frequencies that arise in the finite element models as a direct consequence of spatial discretization, as it was recognized very early that in order to truthfully represent the behavior of the structure, these spurious modes should be damped.

Among the α-methods mentioned above, the classical and popular ones are the HHT scheme of Hilber, Hughes and Taylor [65], the Wood-Bossak-Zienkiewicz scheme [170] (hereinafter called BAM), and the Chung and Hulbert scheme [38] (hereinafter called GAM). A more recent α-method is the JWH scheme of Jansen, Whiting and Hulbert [77]. A comparison of JWH against the composite Bathe scheme [7] performed in [80] suggested that JWH is among the best one-step α-methods. In the rest of this chapter (as in [96]), the four above mentioned α-methods (HHT, BAM, GAM and JWH) will be collectively called the generalized-α schemes (G-α). For linear dynamics, the G-α schemes are unconditionally stable, high-frequency dissipative and second-order accurate [49], but (except JWH) with poor overshoot performance [80].

The unconditional stability of the time-stepping schemes is well defined for linear dynamics by the spectral radius [67], [69], while in the nonlinear regime several criteria exist, see [49], among which energy preservation is arguably the most important. According to the energy criterion, the scheme is said to be unconditionally stable in nonlinear elasto-dynamics if for free motions $(V_{n+1} - V_n) +$

$(K_{n+1} - K_n) \leq 0$ is valid for a time step $[t_n, t_{n+1}]$, where V and K are potential and kinetic energies, respectively. This equation is in general not satisfied for the α-methods, even for small time steps. Moreover, the α-methods fail to conserve linear and angular momentum, see e.g. [131], [5]. Thus, the α-methods do not preserve physical constants of the motion of the underlying nonlinear continuous system. Subsequently, its structure is lost in a numerical solution. As a consequence, the (predominantly) good features of the α-methods in linear dynamics do not necessarily transfer to nonlinear dynamics. In general, these schemes may show undesirable energy fluctuations and the study in [49] indicates that the G-α schemes show oscillations in the intermediate frequency range. Despite this, it was reported in [96] that the G-α schemes can perform well for nonlinear problems, even for numerically stiff ones, as shown in [158] for BAM. However, for some other numerically stiff cases, the algorithmic failure of the G-α schemes was reported [108].

The energy-momentum conserving scheme, introduced by Simo and Tarnow [146], [145], on the other hand, fulfils the energy criterion for nonlinear elasto-dynamics. Due to its design it conserves the total mechanical energy of the system, which renders it unsuitable for some nonlinear applications, such as stability problems, see e.g. [102] and [108]. These kinds of observations were a motivation for the extension of the energy-momentum conserving scheme that includes algorithmic dissipation. In fact, a very elegant way of numerical dissipation was found that enables energy decay in nonlinear elasto-dynamics in a sense that $(V_{n+1} - V_n) + (K_{n+1} - K_n) + \Delta\mathcal{D} = 0$ for free motions, where $\Delta\mathcal{D} \geq 0$ is numerical dissipation in the time step, [4], [5], [26]. This energy-decaying property nicely coincides with the basic indicator of the stability in the nonlinear regime.

In this chapter, we analyze and compare the generalized-α and energy-decaying schemes in both linear and nonlinear settings. For linear dynamics, we compare the accuracy, dissipation, dispersion, as well as the overshoot behavior. For nonlinear dynamics, we compare the results of numerical tests on shell-like examples. They are a difficult test for dynamic schemes, because numerically stiff equations have to be solved as a result of a large difference between the bending (and shear) and the membrane deformation modes that coexist in shells. On the basis of these examples, we compare the ability of the dissipation/decaying of the energy, the ability to fully/approximately conserve the angular momentum, and we estimate the nonlinear order of accuracy by different error indicators. Let us mention that for the nonlinear version of the generalized-α schemes, we apply the algorithmic evaluation of the stresses, the idea taken from the energy-momentum conserving concept [96]. Besides the illustrative comparison on numerically stiff problem, the novelty of this chapter is also the application of the JWH scheme for shells, which has not been reported yet.

The rest of the chapter is organized as follows. In Section 3.2, the governing equations of the motion of a discrete system are summarized, which is followed by the description of the generalized-α schemes (in Section 3.3) and energy-decaying schemes (in Section 3.4). In these three sections, we do not elaborate on any particular solid or structural model, with its specific details, but we rather keep the equations in a generic (and simple) form, providing the essential information about the schemes. Sections 3.5 and 3.6 are devoted to the analysis of the schemes in linear and nonlinear settings, respectively, and the findings are summarized in Section 3.7.

3.2   Space-discrete equations of motion

For a nonlinear solid or structural model, which is discretized in space by the standard finite element method (and has n_{dof} nodal degrees of freedom, excluding those with the essential boundary conditions), the equation of motion and the initial conditions may be written as

$$\boldsymbol{G}_{dyn}\big(\boldsymbol{u}(t)\big) = \boldsymbol{F}_{ine}\big(\boldsymbol{u}(t), \ddot{\boldsymbol{u}}(t)\big) + \boldsymbol{C}\dot{\boldsymbol{u}}(t) + \boldsymbol{F}_{int}\big(\boldsymbol{u}(t)\big) - \boldsymbol{F}_{ext}(t) = \boldsymbol{0},$$
$$\boldsymbol{u}(0) = \boldsymbol{u}_0, \qquad \dot{\boldsymbol{u}}(0) = \dot{\boldsymbol{u}}_0. \tag{3.1}$$

Here, $\boldsymbol{u} \colon [0, t_f > 0] \to \mathbb{R}^{n_{dof}}$ is vector of n_{dof} unknown functions in time that represent nodal generalized displacements (i.e. displacements and rotations if the latter are included in the model), $t \in [0, t_f]$ denotes time on the interval of interest, and superimposed dot denotes time derivative, i.e. $\dot{\boldsymbol{u}} = d\boldsymbol{u}/dt$ and $\ddot{\boldsymbol{u}} = d^2\boldsymbol{u}/dt^2$. Furthermore, $\boldsymbol{F}_{ine}$ is a vector of nodal inertial forces (which depend, for a structural model with large rotations, not only on acceleration and initial density ρ_0 but also on configuration because of the gyroscopic effect caused by the rotation of e.g. beam cross-section frame or shell director, see e.g. [146], [23]), $\boldsymbol{C}$ is a positive semi-definite matrix that models damping (which is in many cases an artificial damping rather than a physical damping), $\boldsymbol{F}_{ext}$ is a vector of nodal external loading (which are considered in this work as conservative), and $\boldsymbol{F}_{int}$ is a vector of nodal internal forces.

The second-order differential equation (3.1) can be reduced to the first-order equation by introducing an additional unknown $\boldsymbol{v} \colon [0, t_f > 0] \to \mathbb{R}^{m_{dof}}$, which is a vector of m_{dof} unknown functions in time (with m_{dof} not necessarily equal to n_{dof}) that represent nodal generalized velocities (i.e. velocities associated with translations and rotations if the latter are included in the model). In this case, the equation of motion and the initial conditions may be written as

$$\widetilde{\boldsymbol{G}}_{dyn}\big(\boldsymbol{u}(t), \boldsymbol{v}(t)\big) = \boldsymbol{F}_{ine}\big(\boldsymbol{u}(t), \dot{\boldsymbol{v}}(t)\big) + \boldsymbol{C}\boldsymbol{v}(t) + \boldsymbol{F}_{int}\big(\boldsymbol{u}(t)\big) - \boldsymbol{F}_{ext}(t) = \boldsymbol{0},$$
$$\boldsymbol{v}(t) = \dot{\boldsymbol{u}}(t) \text{ or } \boldsymbol{v}(t) \overset{\overset{\text{weak equality}}{\approx}}{} \dot{\boldsymbol{u}}(t), \tag{3.2}$$
$$\boldsymbol{u}(0) = \boldsymbol{u}_0, \qquad \boldsymbol{v}(0) = \boldsymbol{v}_0.$$

As indicated, Eq. $(3.2)_2$ can be fulfilled either in a strong form (when time derivatives of generalized nodal displacements equal generalized nodal velocities) or in a weak form over the discretized spatial domain.

Eq. $(3.1)_1$ and Eq. $(3.2)_1$ represent equilibrium at the nodes of the finite element mesh time for any $t \in [0, t_f]$, i.e. the inertial, viscous and internal nodal forces are in equilibrium with the external nodal forces. It is worth noting that above we have assumed a standard spatial finite element discretization, with only nodal degrees of freedom. This assumption includes nonlinear solid/structural finite element formulations that are locking-free because of the locking remedies that do not extend the number of degrees of freedom, such as the B-bar method or the assumed natural strain method. Therefore, the mixed finite element formulations based on e.g. Hu-Washizu or Hellinger-Reissner variational principles, which are characterized by additional degrees of freedom and additional equations, are not covered by (3.1) and (3.2). For the mixed finite element formulations, see e.g. [104], [107], many of the below considered schemes, especially those belonging to the class of energy-decaying/conserving (and momentum conserving) methods, have to be reformulated, see e.g. [13]. We address this challenge in Chapter 4, where we derive energy-decaying schemes for some mixed-hybrid formulations.

In what follows, we will assume elastic material and $\boldsymbol{C} = \boldsymbol{0}$. The solution of (3.1) or (3.2) will be searched for at the discrete time points $0 = t_0, t_1, \cdots, t_n, t_{n+1}, \cdots, t_f$ by an implicit time-stepping scheme with an algorithmic (i.e. numerical) dissipation.

3.3   Generalized-α methods

3.3.1   Some generalized-α methods for the second-order system

A class of implicit time-stepping schemes, denoted as generalized-α (G-α) methods (see e.g. [38]), was designed for an optimal numerical dissipation while maintaining the second-order algorithmic accuracy. However, these features are valid for linear dynamics and do not necessarily extend to nonlinear dynamics.

The G-α methods use colocation points, $t_{n+\alpha_f}$ and $t_{n+\alpha_m}$ on a generic time interval $[t_n, t_{n+1}]$, which are defined as

$$t_{n+\alpha_f} = \alpha_f\, t_{n+1} + (1 - \alpha_f)t_n, \qquad t_{n+\alpha_m} = \alpha_m\, t_{n+1} + (1 - \alpha_m)t_n, \tag{3.3}$$

where α_f and α_m are free parameters. For known initial values, $\boldsymbol{u}_n = \boldsymbol{u}(t_n)$, $\dot{\boldsymbol{u}}_n = \dot{\boldsymbol{u}}(t_n)$, and $\ddot{\boldsymbol{u}}_n = \ddot{\boldsymbol{u}}(t_n)$, the G-$\alpha$ scheme computes solution of Eq. (3.1) on the time interval $[t_n, t_{n+1}]$, which is $\boldsymbol{u}_{n+1} = \boldsymbol{u}(t_{n+1})$, by satisfying

$$\boldsymbol{F}_{\text{ine}}\!\left(\boldsymbol{u}_{n+\alpha_m}, \ddot{\boldsymbol{u}}_{n+\alpha_m}\right) + \boldsymbol{F}_{\text{int},n+\alpha_f} - \boldsymbol{F}_{\text{ext}}\!\left(t_{n+\alpha_f}\right) = \boldsymbol{0}, \tag{3.4}$$

(note that $\boldsymbol{C} = \boldsymbol{0}$ was assumed) and applying the following convex combinations

$$\boldsymbol{u}_{n+\alpha} = \alpha\, \boldsymbol{u}_{n+1} + (1 - \alpha)\boldsymbol{u}_n \text{ for } \alpha = \alpha_f, \alpha_m, \qquad \ddot{\boldsymbol{u}}_{n+\alpha_m} = \alpha_m\, \ddot{\boldsymbol{u}}_{n+1} + (1 - \alpha_m)\ddot{\boldsymbol{u}}_n. \tag{3.5}$$

Here, one can choose the definition of the vector of internal nodal forces $\boldsymbol{F}_{\text{int},n+\alpha_f}$. It can be defined either as (*i*):

$$\boldsymbol{F}_{\text{int},n+\alpha_f} = \alpha_f\, \boldsymbol{F}_{\text{int},n+1} + (1 - \alpha_f)\boldsymbol{F}_{\text{int},n} = \alpha_f\, \boldsymbol{F}_{\text{int}}(\mathbf{u}_{n+1}) + (1 - \alpha_f)\boldsymbol{F}_{\text{int}}(\mathbf{u}_n), \tag{3.6}$$

or as (*ii*):

$$\boldsymbol{F}_{\text{int},n+\alpha_f} = \boldsymbol{F}_{\text{int}}\!\left(\boldsymbol{u}_{n+\alpha_f}\right), \tag{3.7}$$

or yet as (*iii*) with the algorithmic stresses as proposed e.g. in [146], [80] and [96]. For the total Lagrangian formulation with the 2nd Piola-Kirchhoff stresses (collected in vector $\boldsymbol{S}$), the option (*iii*) reads as:

$$\boldsymbol{F}_{\text{int},n+\alpha_f} = \mathbb{A}_{e=1}^{n_{el}} \boldsymbol{F}_{\text{int},n+\alpha_f}^e, \qquad \boldsymbol{F}_{\text{int},n+\alpha_f}^e = \int_{V^e} \boldsymbol{B}_{n+\alpha_f}^{e,T}\, \boldsymbol{S}_{alg}^e\, dV, \tag{3.8}$$

where $\mathbb{A}$ is the finite element assembly operator, n_{el} is the number of elements in the mesh, V^e is the initial volume of the element, $\boldsymbol{F}_{\text{int},n+\alpha_f}^e$ is the vector of the internal nodal forces of the element, $\boldsymbol{B}_{n+\alpha_f}^e = \boldsymbol{B}^e\!\left(\boldsymbol{u}_{n+\alpha_f}^e\right)$ is a matrix that relates the variation of the element's strain field at $t_{n+\alpha_f}$ with the variation of the nodal displacements of the element, and $\boldsymbol{S}_{alg}^e$ is a vector of the algorithmic stresses of the element

$$\boldsymbol{S}_{alg}^e = \alpha_f \boldsymbol{S}_{n+1}^e + (1 - \alpha_f)\boldsymbol{S}_n^e = \alpha_f \boldsymbol{S}^e(\boldsymbol{u}_{n+1}^e) + (1 - \alpha_f)\boldsymbol{S}^e(\boldsymbol{u}_n^e). \tag{3.9}$$

Here the superscript e again denotes element related quantities. It denotes both nodal values of the element as well as scalar, vector or matrix fields over the element (the types of quantities will be obvious from the context).

Option (*iii*) for the computation of $F_{\text{int},n+\alpha_f}$ will be chosen for the G-α schemes (and also for all other schemes) considered in this work. Note that for linear dynamics the three ways of computing $F_{\text{int},n+\alpha_f}$, i.e. (3.6), (3.7) and (3.8), are identical.

Table 3.1: Parameters of the considered Newmark schemes (NTR, NMD), G-α schemes (BAM, HHT, GAM, JWH), and energy-momentum-conserving scheme (EMC) expressed by spectral radius, see e.g. [38], [96], [77].
Preglednica 3.1: Parametri obravnavanih Newmarkovih shem (NTR, ND), G-α shem (BAM, HHT, GAM, JWH) in sheme, ki ohranja energijo, gibalno in vrtilno količino (EMC), izraženi kot funkcija spektralnega radija, glej npr. [38], [96], [77].

Scheme	α_m	α_f	β	γ	ρ_∞	Description
NTR	1	1	$\dfrac{1}{(\rho_\infty+1)^2}$	$\dfrac{3-\rho_\infty}{2\rho_\infty+2}$	1	Trapezoidal rule
NMD					$\in [0,1)$	Dissipative Newmark
BAM	$\dfrac{2}{\rho_\infty+1}$	1			$\in [0,1)$	Wood-Bossak-Zienkiewicz
HHT	1	$\dfrac{2\rho_\infty}{\rho_\infty+1}$	$\dfrac{1}{4}(1-\alpha_f+\alpha_m)^2$	$\dfrac{1}{2}-\alpha_f+\alpha_m$	$\in [\frac{1}{2},1)$	Hilber-Hughes-Taylor
GAM	$\dfrac{2-\rho_\infty}{1+\rho_\infty}$	$\dfrac{1}{1+\rho_\infty}$			$\in [0,1)$	Chung-Hulbert
EMC					1	Energy-momentum conserving
JWH	$\dfrac{3-\rho_\infty}{2(1+\rho_\infty)}$	$\dfrac{1}{1+\rho_\infty}$	$/$	$\dfrac{1}{2}+\alpha_m-\alpha_f$	$\in [0,1)$	Jansen-Whiting-Hulbert

A G-α scheme for Eq. (3.1) is completed by an approximation of nodal accelerations and velocities at t_{n+1}. To this end, the Newmark approximations [118] are the usual choice

$$\dot{u}_{n+1} = \frac{\gamma}{\beta\Delta t}(u_{n+1}-u_n) - \frac{\gamma-\beta}{\beta}\dot{u}_n - \frac{\gamma-2\beta}{2\beta}\Delta t\,\ddot{u}_n,$$
$$\ddot{u}_{n+1} = \frac{1}{\beta\Delta t^2}(u_{n+1}-u_n) - \frac{1}{\beta\Delta t}\dot{u}_n - \frac{1-2\beta}{2\beta}\ddot{u}_n,$$

(3.10)

where $\Delta t = t_{n+1}-t_n$ is a time step, and β and γ are two free parameters. Note that the initial conditions (3.1)$_2$ define the initial accelerations as $\ddot{u}_0 = M^{-1}\big(F_{\text{ext}}(0)-F_{\text{int}}(u_0)\big)$. Applying the above presented equations in (3.4) yields a nonlinear system of equations for u_{n+1}, which is solved iteratively by the Newton-Raphson method that requires spatial linearization of Eq. (3.4).

The free parameters of the G-α algorithms, α_m, α_f, β and γ, become mutually dependent after the enforcement of the conditions that maximize accuracy, optimize algorithmic dissipation, and provide unconditional stability. For linear dynamics, these conditions were studied in detail in e.g. [38], [64], [170], and the conditions for the second-order accuracy were assessed also for nonlinear dynamics in [49]. When the arguments from the above mentioned references are taken into account, α_m, α_f, β and γ become functions of a single (user-defined) parameter, which is spectral radius of the amplification matrix at infinity denoted as $\rho_\infty \in [0,1]$. The spectral radius controls the amount of the algorithmic dissipation in a sense that smaller ρ_∞ means larger dissipation, and for $\rho_\infty = 1$ there is no dissipation. It is worth noting that the dissipation of the G-α method relates to the decaying of the norm of the discrete solution and not to the decaying of the kinetic and/or potential energy of solid/structure.

These choices for α_m, α_f, β and γ in Table 3.1 for the three G-α schemes, denoted as GAM, BAM and HHT, provide unconditional stability, minimize low-frequency dissipation, maximize high-frequency dissipation and guarantee the second-order accuracy for at least displacements and velocities (all of the above applies for linear dynamics and does not necessarily extend to nonlinear dynamics). Remember that BAM denotes the Bossak-α method (sometimes referred to as WBZ, see e.g. [170]), HHT is Hilber-Hughes-Taylor method [65], and GAM is the method of Chung and Hulbert [38] (sometimes also referred to as CH).

3.3.2   Generalized-α method for the first-order system

The G-α schemes described above are based on the second order system of equations (3.1). For the first-order system of equations (3.2), Kadapa et al. [80] proposed a G-α scheme, referred to as JWH. The JWH was initially developed for fluid dynamics by Jansen et al. [77], while Kadapa et al. [80] recently adapted it for structural dynamics, see also [79].

For known initial values for the time interval $[t_n, t_{n+1}]$, $\boldsymbol{u}_n = \boldsymbol{u}(t_n)$, $\dot{\boldsymbol{u}}_n = \dot{\boldsymbol{u}}(t_n)$ and $\boldsymbol{v}_n = \boldsymbol{v}(t_n)$, JWH computes solution of Eq. (3.2) at t_{n+1}, which are nodal generalized displacements $\boldsymbol{u}_{n+1}$, by satisfying

$$\boldsymbol{F}_{\text{ine}}(\boldsymbol{u}_{n+\alpha_m}, \dot{\boldsymbol{v}}_{n+\alpha_m}) + \boldsymbol{F}_{\text{int},n+\alpha_f} - \boldsymbol{F}_{\text{ext}}(t_{n+\alpha_f}) = \boldsymbol{0}, \tag{3.11}$$

(note that $\boldsymbol{C} = \boldsymbol{0}$) and assuming strong equality of Eq. (3.2)$_1$ as

$$\boldsymbol{v}_{n+\alpha_f} = \dot{\boldsymbol{u}}_{n+\alpha_m}. \tag{3.12}$$

Approximations of displacement time derivatives, velocities, and velocity derivatives at t_{n+1} in terms of $\boldsymbol{u}_{n+1}$ are for JWH given by an algorithmic parameter γ as (see [77] and [80] for details)

$$\dot{\boldsymbol{u}}_{n+1} = \frac{1}{\gamma \Delta t}(\boldsymbol{u}_{n+1} - \boldsymbol{u}_n) + \frac{\gamma - 1}{\gamma}\dot{\boldsymbol{u}}_n,$$

$$\boldsymbol{v}_{n+1} = \frac{\alpha_m}{\alpha_f \gamma \Delta t}(\boldsymbol{u}_{n+1} - \boldsymbol{u}_n) + \frac{\gamma - \alpha_m}{\gamma \alpha_f}\dot{\boldsymbol{u}}_n + \frac{\alpha_f - 1}{\alpha_f}\boldsymbol{v}_n, \tag{3.13}$$

$$\dot{\boldsymbol{v}}_{n+1} = \frac{\alpha_m}{\alpha_f \gamma^2 \Delta t^2}(\boldsymbol{u}_{n+1} - \boldsymbol{u}_n) - \frac{1}{\alpha_f \gamma \Delta t}\boldsymbol{v}_n + \frac{\gamma - 1}{\gamma}\dot{\boldsymbol{v}}_n + \frac{\gamma - \alpha_m}{\gamma^2 \alpha_f \Delta t}\dot{\boldsymbol{u}}_n.$$

In addition to the combinations (3.5)$_1$, the following convex combinations apply:

$$\dot{\boldsymbol{u}}_{n+\alpha_m} = \alpha_m\,\dot{\boldsymbol{u}}_{n+1} + (1 - \alpha_m)\dot{\boldsymbol{u}}_n,$$
$$\boldsymbol{v}_{n+\alpha_f} = \alpha_f\,\boldsymbol{v}_{n+1} + (1 - \alpha_f)\boldsymbol{v}_n, \tag{3.14}$$
$$\dot{\boldsymbol{v}}_{n+\alpha_m} = \alpha_m\,\dot{\boldsymbol{v}}_{n+1} + (1 - \alpha_m)\dot{\boldsymbol{v}}_n.$$

According to the studies [77] and [80], JWH is (for linear dynamics and for the parameters from Table 3.1) second-order accurate, unconditionally stable, dissipative in the high-frequency range, and with negligible dissipation in the low-frequency range.

3.4   Energy-decaying methods

Several other (classical) schemes can also be obtained for specific values of α_m, α_f, β and γ in terms of ρ_∞, see e.g. [96] and [97]. Three of them (NTR, NMD and EMC) are presented in Table 3.1. NTR denotes classical non-dissipative ($\rho_\infty = 1$) Newmark trapezoidal rule with $\beta = 1/4$ and $\gamma = 1/2$, and NMD is dissipative Newmark scheme of the first-order accuracy [67]. The energy and momentum

conserving scheme (EMC) is non-dissipative ($\rho_\infty = 1$), with $\alpha_m = \alpha_f = \gamma = 1/2$ and $\beta = 1/4$, which collapses to the mid-point rule for linear dynamics.

3.4.1   Energy and momentum conserving scheme

The energy and momentum conserving (EMC) scheme basically consists of: (i) the application of the mid-point rule in Eq. (3.4) as

$$\boldsymbol{F}_{\text{ine}}\left(\boldsymbol{u}_{\text{n+1/2}}, \underbrace{\frac{\dot{\boldsymbol{u}}_{\text{n+1}} - \dot{\boldsymbol{u}}_{\text{n}}}{\Delta t}}_{\ddot{\boldsymbol{u}}_{\text{n+1/2}}}\right) + \boldsymbol{F}_{\text{int}}\left(\boldsymbol{u}_{\text{n+1/2}}, \boldsymbol{S}_{\text{alg}}^e\right) - \boldsymbol{F}_{\text{ext}}\left(t_{\text{n+1/2}}\right) = \boldsymbol{0}, \qquad e = 1, n_{el} \qquad (3.15)$$

where

$$\boldsymbol{u}_{\text{n+1/2}} = \frac{1}{2}\left(\boldsymbol{u}_{\text{n+1}} + \boldsymbol{u}_{\text{n}}\right),$$

$$\dot{\boldsymbol{u}}_{\text{n+1/2}} = \frac{\boldsymbol{u}_{\text{n+1}} - \boldsymbol{u}_{\text{n}}}{\Delta t} = \frac{1}{2}\left(\dot{\boldsymbol{u}}_{\text{n+1}} + \dot{\boldsymbol{u}}_{\text{n}}\right) \Rightarrow \dot{\boldsymbol{u}}_{\text{n+1}} = \frac{2\left(\boldsymbol{u}_{\text{n+1}} - \boldsymbol{u}_{\text{n}}\right)}{\Delta t} - \dot{\boldsymbol{u}}_{\text{n}}, \qquad (3.16)$$

and (ii) the algorithmic evaluation of stresses in (3.15) as (see (3.9))

$$\boldsymbol{S}_{\text{alg}}^e = \left(\boldsymbol{S}_{n+1}^e + \boldsymbol{S}_n^e\right)/2. \qquad (3.17)$$

The importance of EMC lies in the following relation (which was proven e.g. in [146], [4] and [13]) for the time increment $\Delta t = t_{n+1} - t_n$ with no external loading:

$$(V_{n+1} - V_n) + (K_{n+1} - K_n) = 0, \qquad (3.18)$$

where V and K are the potential and kinetic energy. In fact, the design of algorithmic stresses (3.17) enables energy conservation (independently of Δt) for a nonlinear elastic structure for an increment with no external forces. Thus, EMC is energy-conserving algorithm. As an aside, it should be noted that the stress formula (3.17) is valid for the St. Venant-Kirchhoff hyperelasticity, while the other hyperelastic models require its modification, see e.g. [130]. It is also worth noting that EMC conserves the momenta because of the desirable property of the mid-point rule, which is conservation of the linear and (more importantly) angular momentum, see e.g. [146] and [67].

Despite these advantageous features of EMC, the need was recognized for an extension of EMC in a sense of a controlled numerical dissipation in the high-frequency range in order to gain the robustness necessary to solve stiff problems. Namely, for the numerically stiff problems, EMC tends to compute highly oscillatory response with large error in the high-frequency range, see e.g. [102], [108], which diminishes its applicability for stiff structural dynamics problems. The energy conserving/decaying schemes considered in this work are summarized in Table 3.2.

Table 3.2: Energy-conserving/decaying schemes, see e.g. [4], [5].
Preglednica 3.2: Sheme, ki ohranjajo/disipirajo energijo, glej npr. [4], [5].

Scheme	Linear dynamics notation	α_{ED}	β_{ED}	Angular momentum conservation	Description
EMC	EMC	0	0	Yes	Energy-momentum conserving
ED1	ED1	$= \beta_{ED} > 0$	$= \alpha_{ED} > 0$	No	Energy-decaying, first-order
EDMC1	ED1	$= \beta_{ED} > 0$	$= \alpha_{ED} > 0$	Yes	Energy-decaying, momentum conserving, first-order
EDMC2	ED2	> 0	\	Yes	Energy-decaying, momentum conserving, second-order

3.4.2   Energy-decaying scheme of the first-order

It was shown in e.g. [4], [5], [26], [18] and [132] that EMC can be adapted to become numerically dissipate in a very favorable way by producing a controllable decaying of the total energy in time. To this end, two modifications of EMC need to be performed. The first modification changes the mid-point velocity approximation $(3.16)_2$ by introducing a term $\dot{\boldsymbol{u}}_{dis}$ that produces dissipation of the kinetic energy. The dissipative term is applied in the computation of the mid-point velocity simply as

$$\dot{\boldsymbol{u}}_{n+1/2} = \frac{\boldsymbol{u}_{n+1} - \boldsymbol{u}_n}{\Delta t} = \frac{1}{2}(\dot{\boldsymbol{u}}_{n+1} + \dot{\boldsymbol{u}}_n) + \underbrace{\beta_{ED}\frac{1}{2}(\dot{\boldsymbol{u}}_{n+1} - \dot{\boldsymbol{u}}_n)}_{\dot{\boldsymbol{u}}_{dis}} \Rightarrow$$
$$\dot{\boldsymbol{u}}_{n+1} = \frac{2(\boldsymbol{u}_{n+1} - \boldsymbol{u}_n) - \dot{\boldsymbol{u}}_n\Delta t(1 - \beta_{ED})}{\Delta t(1 + \beta_{ED})}. \tag{3.19}$$

The inclusion of velocity-dissipation via $\dot{\boldsymbol{u}}_{dis}$ in approximation of $\dot{\boldsymbol{u}}_{n+1/2}$ in (3.19) makes the latter depart from the direction of the mid-point rule $(\dot{\boldsymbol{u}}_{n+1} + \dot{\boldsymbol{u}}_n)/2$, which is the one that guaranties the conservation of angular momentum. Thus, the loss of the conservation of angular momentum is a price to pay for introducing the dissipation in the kinetic energy. The second modification changes the algorithmic stresses (3.17) by including the term $\boldsymbol{S}^e_{dis}$ which triggers dissipation of the potential energy. This dissipative term is applied as

$$\boldsymbol{S}^e_{alg} = \frac{(\boldsymbol{S}^e_{n+1} + \boldsymbol{S}^e_n)}{2} + \underbrace{\frac{\alpha_{ED}(\boldsymbol{S}^e_{n+1} - \boldsymbol{S}^e_n)}{2}}_{\boldsymbol{s}^e_{dis}}. \tag{3.20}$$

By inserting $\dot{\boldsymbol{u}}_{n+1}$ from (3.19) and $\boldsymbol{S}^e_{alg}$ from (3.20) into the equilibrium equation (3.15), one gets a scheme that decays energy in a controllable manner. In particular, the following holds for free motions:

$$(V_{n+1} - V_n) + (K_{n+1} - K_n) + \mathcal{D} = 0, \qquad \mathcal{D} \geq 0, \tag{3.21}$$

where $\mathcal{D}$ is dissipation of the total energy (i.e. the sum of kinetic and potential energies) within the time-step interval. The newly introduced free parameters α_{ED} and β_{ED} control dissipation in the kinetic and potential energy, respectively. They multiply the difference between successive values of unknowns within the time step, which is more likely smaller for the low-frequency than for the high-frequency modes. Thus, the scheme is expected to be more dissipative in the high-frequency range than in the low-frequency range, especially for small Δt.

In what follows, this time-stepping algorithm will be referred to as energy-decaying (ED1) scheme. It follows from (3.21) that ED1 enables the total energy to decay in time when the loading is not applied. It is worth noting that relation (3.21) does not hold for the G-α schemes from Section 3.3. Consequently, the incremental change of the energy dissipation for the G-α scheme can be negative, which is an undesirable and non-physical result. The reason is that the numerical dissipation for the G-α schemes relies on the decaying of the norm of the discrete solution rather than on the decaying of the energy, as will be illustrated in Section 3.6.

However, the above described extension of EMC, which lead to ED1, lowers the second-order accuracy of EMC to the first-order accuracy of ED1, and destroys the preservation of the angular momentum. The reason for the former is the first order difference in dissipation functions $\dot{\boldsymbol{u}}_{\text{dis}}$ and $\boldsymbol{S}^e_{\text{dis}}$, i.e. $\dot{\boldsymbol{u}}_{\text{dis}} \sim O(\Delta t)$ and $\boldsymbol{S}^e_{\text{dis}} \sim O(\Delta t)$. The reason for the latter is the departure from the direction of the mid-point rule velocity approximation (3.19) by including the dissipative term $\dot{\boldsymbol{u}}_{\text{dis}}$.

3.4.3   Energy-decaying momentum-conserving scheme of the first-order

It was recognized in e. g. [13], [56], [50], [132] and many other works that the conservation of momenta is an important feature that makes a given time integration method numerically successful. The conservation of the angular momentum can be regained for the energy-decaying scheme, if the velocity dissipation vector is designed so that it has the direction of the mid-point rule velocity approximation, which is $\boldsymbol{v}_{\text{n+1/2}} = (\boldsymbol{v}_{\text{n+1}} + \boldsymbol{v}_{\text{n}})/2$. Let us apply this idea for the first-order system of equations (3.11). In this case, the governing equations are

$$\boldsymbol{F}_{\text{ine}}\left(\boldsymbol{u}_{\text{n+1/2}}, \underbrace{\frac{\boldsymbol{v}_{\text{n+1}} - \boldsymbol{v}_{\text{n}}}{\Delta t}}_{\dot{\boldsymbol{v}}_{\text{n+1/2}}}\right) + \boldsymbol{F}_{\text{int}}\left(\boldsymbol{u}_{\text{n+1/2}}, \boldsymbol{S}^e_{\text{alg}}\right) - \boldsymbol{F}_{\text{ext}}\left(t_{\text{n+1/2}}\right) = \boldsymbol{0}, \qquad (3.22)$$

with $\boldsymbol{S}^e_{\text{alg}}$ as in (3.20). Moreover, another equation applies, enforcing the weak form of the equality between $\dot{\boldsymbol{u}}_{\text{n+1/2}}$ and $\boldsymbol{v}_{\text{n+1/2}} + \boldsymbol{v}_{\text{dis}}$, where the velocity dissipation vector $\boldsymbol{v}_{\text{dis}}$ (that produces dissipation in the kinetic energy) has the direction of $\boldsymbol{v}_{\text{n+1/2}} = (\boldsymbol{v}_{\text{n+1}} + \boldsymbol{v}_{\text{n}})/2$. The weak form is

$$\mathbb{A}_{e=1}^{n_{el}} \int_{V^e} \delta \boldsymbol{v}^e \left(\rho_0 \left(\frac{\boldsymbol{u}^e_{\text{n+1}} - \boldsymbol{u}^e_{\text{n}}}{\Delta t} - \left(1 + \underbrace{\beta_{ED} \frac{(v^e_{\text{n+1}} - v^e_{\text{n}})^2}{(v^e_{\text{n+1}})^2 - (v^e_{\text{n}})^2}}_{g^e_{\text{dis}}} \right) \frac{\boldsymbol{v}^e_{\text{n+1}} + \boldsymbol{v}^e_{\text{n}}}{2} \right) \right) = \boldsymbol{0}, \qquad (3.23)$$

where, $\boldsymbol{u}^e$ denotes the interpolation of generalized displacements field over the element by using interpolation functions and nodal values of the element $\overline{\boldsymbol{u}}^e$ (this kind of notation is used also for others interpolated quantities in (3.23)), $\delta \boldsymbol{v}^e$ denoted the variations of generalized velocities, $v^e = \|\boldsymbol{v}^e\|$ is Euclidean norm of $\boldsymbol{v}^e$, and $\boldsymbol{v}^e_{\text{dis}} = g^e_{\text{dis}} \boldsymbol{v}^e_{\text{n+1/2}}$ is the dissipative part of the approximation of velocity. Note that the degrees of freedom of the element are now en$_{\text{dof}}$ + em$_{\text{dof}}$, with $\mathbb{R}^{\text{en}_{\text{dof}}} \ni \overline{\boldsymbol{u}}^e \subset \boldsymbol{u} \in \mathbb{R}^{\text{n}_{\text{dof}}}$ for generalized displacements and $\mathbb{R}^{\text{em}_{\text{dof}}} \ni \overline{\boldsymbol{v}}^e \subset \boldsymbol{v} \in \mathbb{R}^{\text{m}_{\text{dof}}}$ for generalized velocities.

Expressions (3.22) and (3.23) restore the direction of the mid-point rule velocity approximation that conserves angular momentum. We will call such scheme energy-decaying and momentum-conserving scheme of the first-order accuracy and denote it as EDMC1, after [4].

3.4.4 Energy-decaying momentum-conserving scheme of the second-order

The extension of EDMC1 to the second-order accuracy, namely to EDMC2, is a rather demanding task. A possible approach, presented in [5] and [131] for solids and in [132] for shells, is summarized below. The idea is to extend the dissipative part of the algorithmic stresses, $\boldsymbol{S}^e_{\text{dis}}$ from (3.20), and velocity $\boldsymbol{v}^e_{\text{dis}}$, see (3.23), to be of the order $O(\Delta t^2)$. To this end, the quasi-intermediate parameters (marked with $\sim$) are introduced as

$$\boldsymbol{S}^e_{\text{dis}} = (\tilde{\boldsymbol{S}}^e_{\text{n}} - \boldsymbol{S}^e_{\text{n}})/2, \qquad \tilde{\boldsymbol{S}}^e_{\text{n}} = \boldsymbol{S}^e_{\text{n}} + \beta(\boldsymbol{S}^e_{\text{n+1}} - \boldsymbol{S}^e_{\text{n}}) \Rightarrow \boldsymbol{S}^e_{\text{dis}} = \beta(\boldsymbol{S}^e_{\text{n+1}} - \boldsymbol{S}^e_{\text{n}})/2 \tag{3.24}$$

and

$$g^e_{\text{dis}} = \frac{(\tilde{v}^e_{\text{n}} - v^e_{\text{n}})(v^e_{\text{n+1}} - v^e_{\text{n}})}{(v^e_{\text{n+1}})^2 - (v^e_{\text{n}})^2}, \tag{3.25}$$

where β is a parameter (yet to be given), and $\widetilde{(\cdot)}_n$ needs to be designed for the second-order approximations as $\widetilde{(\cdot)}_n = (\cdot)_n + O(\Delta t^2)$. The latter can be achieved by a cross-coupling of the stresses and velocities as

$$\beta = \alpha_{\text{ED}} \frac{\Delta t}{h}(\tilde{v}^e_{\text{n}} - v^e_{\text{n+1}}) \tag{3.26}$$

and

$$\tilde{v}^e_{\text{n}} = v^e_{\text{n}} - \frac{\Delta t}{\rho_0 h}\alpha_{\text{ED}}(\beta - 1)\underbrace{(\boldsymbol{S}^e_{\text{n+1}} - \boldsymbol{S}^e_{\text{n}}) \cdot (\boldsymbol{\varepsilon}^e_{\text{n+1}} - \boldsymbol{\varepsilon}^e_{\text{n}})}_{\Delta s}, \tag{3.27}$$

where h is a suitable geometric constant, with the role to provide dimensionally consistent expressions, and $\boldsymbol{\varepsilon}$ are deformations. Note that here α_{ED} controls dissipation of both kinetic and potential energy. Equations (3.26) and (3.27) form a linear system of two equations for β and $\tilde{v}^e_{\text{n}}$ at each integration point, which can be pre-solved in a closed form that expresses the quasi-intermediate parameters in terms of the basic variables, $\boldsymbol{u}_{\text{n+1}}$ and $\boldsymbol{v}_{\text{n+1}}$, which appear in $v^e_{\text{n+1}}$, $\boldsymbol{S}^e_{\text{n+1}}$ and $\boldsymbol{\varepsilon}^e_{\text{n+1}}$. The solution of this linear system is straightforward to compute.

Because of the cross-coupling, a (considerably) more involved linearization of governing equations is required for EDMC2. It was shown in [5] that EDMC2 obeys the energy relation (3.21) unconditionally in Δt, and is second-order accurate. The incremental dissipation in total energy, $\mathcal{D}$, which is the sum of dissipations in kinetic and potential energy, is always positive or zero.

3.5 Comparison of schemes in linear setting

In this section, the features of the considered time-stepping algorithms are revisited on a linear, undamped, unforced, single-degree-of-freedom system with mass m and stiffness k. Its motion is described by

$$\ddot{u} + \omega^2 u = 0 \iff \dot{v} + \omega^2 u = 0, \ \dot{u} = v \tag{3.28}$$

where u is displacement, v is velocity, and $\omega = \sqrt{k/m}$ is natural frequency with time period $T = 2\pi/\omega$. This equation can be seen as one of the modal equations of a multi-dimensional system. Although ω characterizes physical response of the system, ratio $\Delta t/T = \Delta t\omega/(2\pi) = \Omega/(2\pi)$ is used when analyzing a time stepping algorithm.

3.5.1   Amplification matrices

The exact solution of Eq. (3.28) for the initial conditions $u(0) = u_0$, $\dot{u}(0) = \dot{u}_0$ is, see e.g. [67], $u(t) = c_{11}\cos(\omega t) + c_{12}\sin(\omega t)$, where c_{11} and c_{12} are constants expressed by u_0 and $\dot{u}_0$. By defining $X(t) = \{u(t), \dot{u}(t), \ddot{u}(t)\}^T$, one has

$$X(t) = \mathbf{c}_1\cos(\omega t) + \mathbf{c}_2\sin(\omega t), \tag{3.29}$$

where $\mathbf{c}_1$ and $\mathbf{c}_2$ are vectors of constants. A numerical solution of (3.28) can be written in a recursive, one-step form as

$$X_{n+1} = \mathbf{A}X_n, \forall n \in [0,1, \dots, N-1], \tag{3.30}$$

where N is the number of discrete time-points, $\mathbf{A}$ is the amplification matrix, and X_i, $i \in [0,1, \dots, N-1]$, is

$$X_{i,NG-\alpha} = \{u_i, \dot{u}_i, \ddot{u}_i\}^T, X_{i,JWH} = \{u_i, v_i, \dot{u}_i, \dot{v}_i\}^T, X_{i,ED} = \{u_i, v_i\}^T. \tag{3.31}$$

Here, $NG - \alpha$={NTR, NMD, BAM, HHT, GAM, EMC} and ED={ED1, ED2}, see Table 3.1 and Table 3.2. An alternative form of (3.30) is

$$\widehat{X}_{n+1} = \widehat{\mathbf{A}}\widehat{X}_n, \forall n \in [0,1, \dots, N-1], \tag{3.32}$$

where

$$\widehat{X}_{i,NG-\alpha} = \{u_i, \Delta t \dot{u}_i, \Delta t^2 \ddot{u}_i\}^T, \widehat{X}_{i,JWH} = \{u_i, \Delta t v_i, \Delta t \dot{u}_i, \Delta t^2 \dot{v}_i\}^T, \widehat{X}_{i,ED} = \{u_i, \Delta t \dot{u}_i\}^T, \tag{3.33}$$

and the alternative version of amplification matrix $\widehat{\mathbf{A}}$ is obtained by transformation

$$\widehat{\mathbf{A}} = \mathbf{Q}\mathbf{A}\mathbf{Q}^{-1}, \tag{3.34}$$

where $\mathbf{Q}$ has the following forms for the $NG - \alpha$, JWH, and ED

$$\mathbf{Q} = \text{DIAG}[1, \Delta t, \Delta t^2], \qquad \mathbf{Q} = \text{DIAG}[1, \Delta t, \Delta t, \Delta t^2], \qquad \mathbf{Q} = \text{DIAG}[1, \Delta t]. \tag{3.35}$$

Note that the terms of $\widehat{\mathbf{A}}$ depend on $\Omega = \omega\Delta t = 2\pi \Delta t/T$.

The amplification matrix $\mathbf{A}$ for the $NG - \alpha$ can be obtained if Eqs. (3.4)-(3.10) are used to numerically solve (3.1). For JWH and ED, (3.11)-(3.14) and (3.19)-(3.27) are applied, respectively. The forms of the amplification matrix are:

$$\mathbf{A}_{NG-\alpha} = \frac{1}{D_{G-\alpha}} \begin{bmatrix} \alpha_m + (\alpha_f - 1)\beta\Omega^2 & \alpha_m\Delta t & \frac{1}{2}(\alpha_m - 2\beta)\Delta t^2 \\ -\gamma\Omega\omega & (\beta - \gamma)\Omega^2\alpha_f + \alpha_m & \left(\beta - \frac{\gamma}{2}\right)\Delta t\Omega^2\alpha_f + \Delta t(\alpha_m - \gamma) \\ -\omega^2 & -\alpha_f\Omega\omega & -1 + \frac{1}{2}(2\beta - 1)\Omega^2\alpha_f + \alpha_m \end{bmatrix}, \tag{3.36}$$

$$\mathbf{A}_{JWH} = \frac{1}{D_{JWH}} \begin{bmatrix} \alpha_m^2 + \widehat{D}\gamma^2\Omega^2 & \alpha_m\gamma\Delta t & \Delta t\alpha_m(\alpha_m - \gamma) & \gamma\Delta t^2\alpha_f(\alpha_m - \gamma) \\ -\gamma\Omega\omega\alpha_m & \gamma^2\Omega^2\widehat{D} + \alpha_m^2 & \gamma\Omega^2\alpha_f(\gamma - \alpha_m) & \Delta t\alpha_m(\alpha_m - \gamma) \\ -\gamma\Omega\omega\alpha_f & \alpha_m & (\gamma^2 - \gamma)\Omega^2\alpha_f^2 + \widehat{D} & \Delta t\alpha_f(\alpha_m - \gamma) \\ -\omega^2\alpha_m & -\gamma\Omega\omega\alpha_f & \Omega\omega\alpha_f(\gamma - \alpha_m) & (\gamma^2 - \gamma)\Omega^2\alpha_f^2 + \widecheck{D} \end{bmatrix}, \tag{3.37}$$

$$\mathbf{A}_{ED1} = (\mathbf{A}_1)^{-1}\mathbf{A}_2, \tag{3.38}$$

and

$$\mathbf{A}_{ED2} = (\mathbf{A}_3 - \mathbf{A}_4(\mathbf{A}_5)^{-1}\mathbf{A}_6)^{-1}(1 - \mathbf{A}_4(\mathbf{A}_5)^{-1}), \tag{3.39}$$

where

$$D_{NG-\alpha} = \alpha_m + \alpha_f \beta \Omega^2,$$
$$D_{JWH} = \alpha_m^2 + \alpha_f^2 \gamma^2 \Omega^2, \qquad \widehat{D} = (\alpha_f^2 - \alpha_f), \qquad \widecheck{D} = (\alpha_m^2 - \alpha_m)$$
$$D_{ED1} = 4 + \Omega^2 + 2\Omega^2 (\beta_{ED} + \alpha_{ED}(1 + 2\beta_{ED})), \tag{3.40}$$

$$\mathbf{A}_1 = \frac{1}{2}\begin{bmatrix} 2 & -\Delta t(1 + \beta_{ED}) \\ \Delta t \omega^2 (1 + \alpha_{ED}) & 2 \end{bmatrix}, \qquad \mathbf{A}_2 = \frac{1}{2}\begin{bmatrix} 2 & \Delta t(1 - \beta_{ED}) \\ -\Delta t \omega^2 (1 - \alpha_{ED}) & 2 \end{bmatrix},$$

and

$$\mathbf{A}_3 = \frac{1}{2}\begin{bmatrix} 2 & -\Delta t \\ \Delta t \omega^2 & 2 \end{bmatrix}, \mathbf{A}_4 = \frac{1}{2}\begin{bmatrix} 0 & -\Delta t \\ \Delta t \omega^2 & 0 \end{bmatrix} = \frac{-1}{2\alpha_{ED}}\mathbf{A}_6, \mathbf{A}_5 = \begin{bmatrix} 1 & -\alpha_{ED}\Delta t \\ \alpha_{ED}\Delta t \omega^2 & 1 \end{bmatrix}. \tag{3.41}$$

A remark on the amplification matrix for EMC is needed. The accelerations in EMC are obtained by post-processing and do not directly enter the formulation. Therefore, for EMC, $\mathbf{A}_{NG-\alpha}$ should reduce to $\mathbf{A}_{EMC}$, consisting of the first two rows and columns of $\mathbf{A}_{NG-\alpha}$. For EMC, $A_{NG-\alpha}(1,3) = A_{NG-\alpha}(2,3) = 0$, and the first two eigenvalues of $\mathbf{A}_{NG-\alpha}$ equal those of $\mathbf{A}_{EMC}$, which is the reason why $\mathbf{A}_{NG-\alpha}$ is also applicable for EMC.

3.5.2   Numerical dissipation and spectral radius

For linear dynamics, the stability condition follows from the spectral analysis of the amplification matrix. A spectral radius of an algorithm is defined as

$$\rho = \max(|\lambda_i|), \tag{3.42}$$

where λ_i is the i-th eigenvalue of $\widehat{\mathbf{A}}$. A scheme is said to be unconditionally stable in linear dynamics if $\rho \leq 1$ for any $\Omega \in [0, \infty)$, see e.g. [27]. Notation $\rho_\infty = \lim_{\Omega \to \infty} \rho$ is also used. The restrictions on the parameters of G-α and JWH to achieve unconditional stability in linear dynamics are given in e.g. [38], [49], [67] and [77].
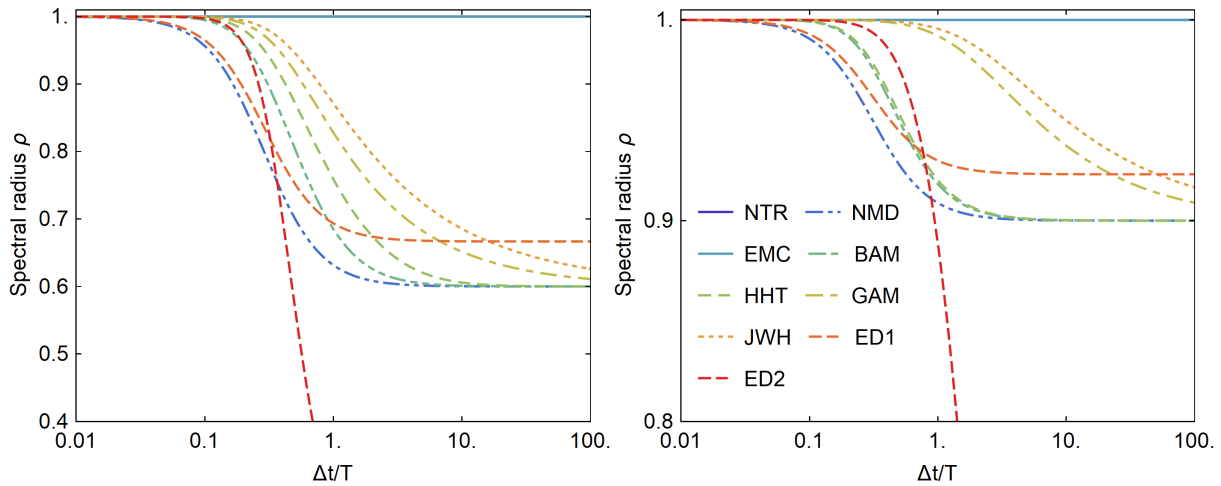
Figure 3.1: Spectral radius versus $\Delta t/T$. Left: $\alpha_{ED} = \beta_{ED} = 0.2$ (i.e. $\rho_\infty = 0.67$ for ED1) and $\rho_\infty = 0.6$. Right: $\alpha_{ED} = \beta_{ED} = 0.04$ (i.e. $\rho_\infty = 0.92$ for ED1) and $\rho_\infty = 0.9$.

Slika 3.1: Spektralni radij v odvisnosti od $\Delta t/T$. Levo: $\alpha_{ED} = \beta_{ED} = 0.2$ (oz. $\rho_\infty = 0.67$ za ED1) in $\rho_\infty = 0.6$. Desno: $\alpha_{ED} = \beta_{ED} = 0.04$ (oz. $\rho_\infty = 0.92$ za ED1) in $\rho_\infty = 0.9$.

In order to assess numerical dissipation, we will perform spectral analysis of amplification matrices (3.36)-(3.39). Let us recall that an algorithm is said to be convergent if for a fixed t_n and n = $t_n/\Delta t$, an

algorithmic solution of (3.28), which is denoted as u_n, converges towards exact solution $u(t_n)$ as $\Delta t \to 0$. For a convergent algorithm, the first two eigenvalues of amplification matrix are complex conjugate for any $\Omega \in [0, \infty)$, see e.g. [38], [182], [186]. These two, λ_1 and λ_2, are called the principal roots, while λ_3 (and also λ_4, if applicable) is called the spurious root.

The magnitude of ρ indicates the amount of numerical dissipation; the smaller the spectral radius, the higher the numerical dissipation. To represent the physical behavior of the structure as realistically as possible, the low frequencies (i.e. the basic structural modes) should be preserved. Thus, for $\Delta t/T \to 0$ an algorithm should provide $\rho = 1$. On the other hand, it is desirable that high frequencies are damped out; thus, for $\Delta t/T \to \infty$, an algorithm should provide $\rho_\infty < 1$. For a smooth decrease of ρ while Ω increases, the condition $|\lambda_3| \leq |\lambda_{1,2}|$ (and $|\lambda_4| \leq |\lambda_{1,2}|$, if applicable) has to hold for any $\Omega \in [0, \infty)$, see e.g. [38]. A violation of this results in a cusp, such that with Ω also ρ increases. Such an algorithm possesses more numerical dissipation for frequencies near the cusp than in the high-frequency range. Note that ED1 exhibits such a cusp if $\alpha_{ED} \neq \beta_{ED}$, see e.g. [5].

Provided that the algorithm is convergent, the principal roots of $\widehat{\mathbf{A}}$ can be written as, see e.g. [65],
$$\lambda_{1,2} = A \pm Bi = \exp(\overline{\Omega}(-\bar{\xi} \pm i)), \tag{3.43}$$
where $i = \sqrt{-1}$, $\bar{\xi}$ is the algorithmic damping ratio, and $\overline{\Omega} = \overline{\omega}\Delta t = 2\pi\,\Delta t/\overline{T}$, where $\overline{\omega}$ is algorithmic natural frequency with algorithmic time period $\overline{T} = 2\pi/\overline{\omega}$. According to [38], high-frequency dissipation is maximized if
$$\lim_{\Omega \to \infty} B(\Omega) = 0. \tag{3.44}$$
For the G-α schemes, an optimal dissipation was discussed in [38] and more recently revisited in [49]. Condition (3.44) holds also for ED1 and ED2, as can be straightforwardly checked by looking at the principal roots of the corresponding amplification matrices.

Figure 3.1 presents spectral radius versus $\Delta t/T$ for different values of user-defined dissipation parameters ρ_∞ and $\alpha_{ED} = \beta_{ED}$. Note that, according to [5],
$$\rho_\infty = \max\left[\frac{|1 - \alpha_{ED}|}{1 + \alpha_{ED}}, \frac{|1 - \beta_{ED}|}{1 + \beta_{ED}}\right] \tag{3.45}$$
for ED1 and $\rho_\infty = 0$ for ED2. One possible interpretation of the spectral radius function is the following: The later the drop of the function and the sharper it is, the better dissipation features the scheme has. Figure 3.1 shows that JWH and GAM have the latest drop; thus they preserve frequencies in the low and also in the middle range. In contrast, NMD and ED1 have the fastest drop, thus dissipating already in the low frequency range. Other schemes are in-between these two extremes, except NTR and EMC, which are non-dissipative with constant $\rho = 1$. ED2 is an exception, since it yields $\rho_\infty = 0$ for any choice of α_{ED}, with the latter influencing only the beginning of the drop, see also [5] and [132].

3.5.3 Numerical dissipation and algorithmic damping ratio, dispersion

Following standard exercise, see e.g. [65], the algorithmic solution of undamped system (3.28) can be written in a form that resembles the analytical solution of a damped system
$$u_n = \exp\left(-\bar{\xi}\overline{\omega}t_n\right)(c_1 \cos(\overline{\omega}t_n) + c_2 \sin(\overline{\omega}t_n)) + c_3 \lambda_3^n, \tag{3.46}$$
where

$$\bar{\omega} = \bar{\Omega}/\Delta t, \bar{\Omega} = \arctan(B/A),$$
$$\bar{\xi} = -\ln(A^2 + B^2)/2\bar{\Omega}.$$

(3.47)

Numerical dissipation can now be presented by the algorithmic damping ratio $\bar{\xi}$. Moreover, the algorithmic dispersion can be illustrated by a relative error in the period elongation $(\bar{T} - T)/T$, where $T = 2\pi/\omega$ and $\bar{T} = 2\pi/\bar{\omega}$, see e.g. [65].

The results are shown in Figures 3.2 and 3.3. Period elongation error in Figure 3.2 demonstrates that longer time steps cause artificial elongations of the periods. Lower frequencies with longer periods are less affected by longer time step than higher frequencies with shorter periods. Of the G-α schemes, BAM and HHT exhibit the highest error in period elongation. ED1 behaves similarly to EMC, whereas ED2 shows much less error than the other schemes. Figure 3.2 (right) shows that for a small dissipation the schemes yield practically the same error in period elongation, with the exception of HHT and BAM, which still suffer slightly more than others from this phenomenon, and ED2, which shows considerably less error than the other schemes.
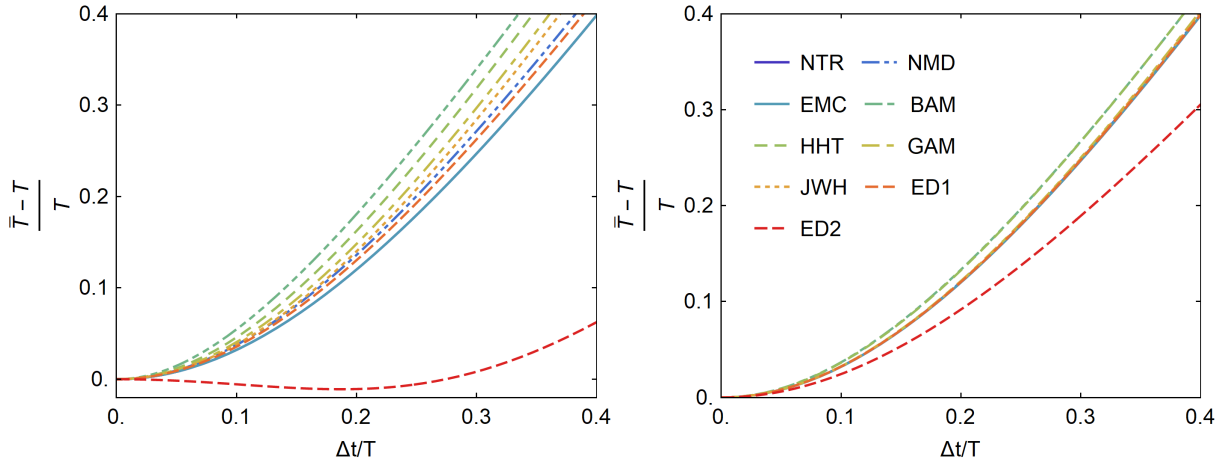
Figure 3.2: Error in period elongation versus $\Delta t/T$. Left: $\alpha_{\text{ED}} = \beta_{\text{ED}} = 0.2$ and $\rho_\infty = 0.6$. Right: $\alpha_{\text{ED}} = \beta_{\text{ED}} = 0.04$ and $\rho_\infty = 0.9$.

Slika 3.2: Napaka v podaljšanju nihajnega časa v odvisnosti od $\Delta t/T$. Levo: $\alpha_{\text{ED}} = \beta_{\text{ED}} = 0.2$ in $\rho_\infty = 0.6$.
Desno: $\alpha_{\text{ED}} = \beta_{\text{ED}} = 0.04$ in $\rho_\infty = 0.9$.

Algorithmic damping in Figure 3.3 presents the results from Figure 3.1 in a different view. It is confirmed again that in the low-frequency range, ED1 and NMD have much stronger damping in comparison with the other schemes and their first-order accuracy is reflected in nonzero slope at $\Delta t/T = 0$, see also [5]. They converge quicker to the final level of dissipation, thus affecting the middle and higher frequencies in the same manner. GAM and JWH, on the other hand, reach the final damping level gradually, so that the intermediate frequencies are less affected in comparison with the higher frequencies. Moreover, they leave low frequencies practically intact even for a considerable dissipation. ED2 is again a special case, since its dissipation starts gradually, but continues to rise as $\Delta t/T \to \infty$, which is in contrast to all other schemes that always converge to a certain $\bar{\xi}_\infty = \lim_{\Delta t/T \to \infty} \bar{\xi}$.
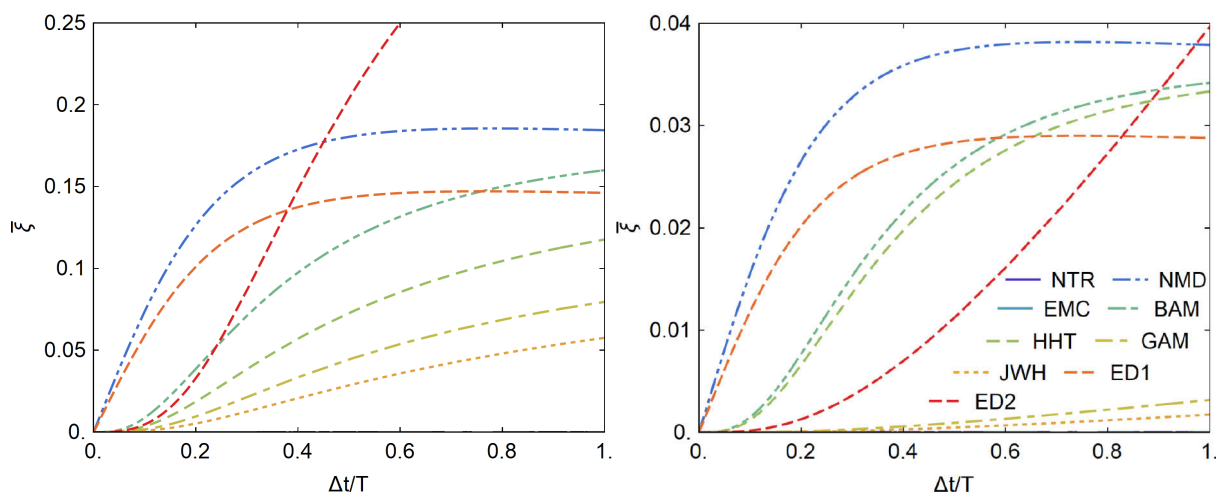
Figure 3.3: Algorithmic damping ratio versus $\Delta t/T$. Left: $\alpha_{ED} = \beta_{ED} = 0.2$ and $\rho_\infty = 0.6$. Right: $\alpha_{ED} = \beta_{ED} = 0.04$ and $\rho_\infty = 0.9$.

Slika 3.3: Razmerje algoritmičnega dušenja v odvisnosti od $\Delta t/T$. Levo: $\alpha_{ED} = \beta_{ED} = 0.2$ in $\rho_\infty = 0.6$. Desno: $\alpha_{ED} = \beta_{ED} = 0.04$ in $\rho_\infty = 0.9$.

3.5.4   Overshoot analysis

A tendency to significantly overshoot the exact solution in the early response was discovered in [55] and later investigated in e.g. [64], [80] and [49] (the latter for GAM, BAM and HHT). The overshoot is independent of the algorithmic stability. Tamma et al. [153] classified a method that suffers from m^{th}-order displacement overshooting and n^{th}-order velocity overshooting as the $[Um, Vn]$-algorithm. According to this classification, GAM, BAM and HHT are $[U0, V1]$-algorithms, while two families of algorithms developed in [81] and [186] that do not suffer from overshoot are classified as $[U0, V0]$.
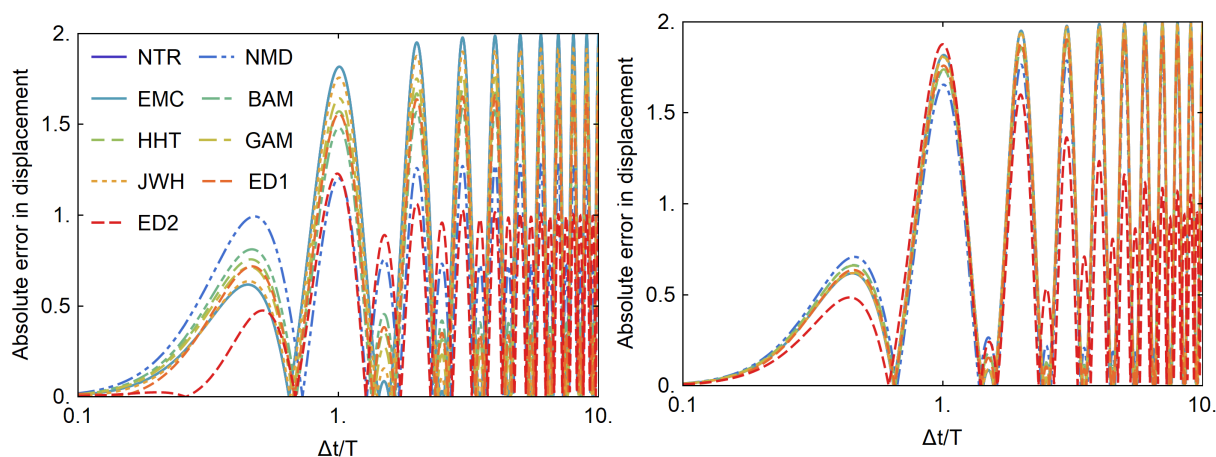
Figure 3.4: Overshoot analysis. Absolute error in displacement at first time step. Left: $\alpha_{ED} = \beta_{ED} = 0.2$ and $\rho_\infty = 0.6$. Right: $\alpha_{ED} = \beta_{ED} = 0.04$ and $\rho_\infty = 0.9$.

Slika 3.4: Analiza prekoračitve. Absolutna napaka v pomiku po prvem časovnem koraku. Levo: $\alpha_{ED} = \beta_{ED} = 0.2$ in $\rho_\infty = 0.6$. Desno: $\alpha_{ED} = \beta_{ED} = 0.04$ in $\rho_\infty = 0.9$.
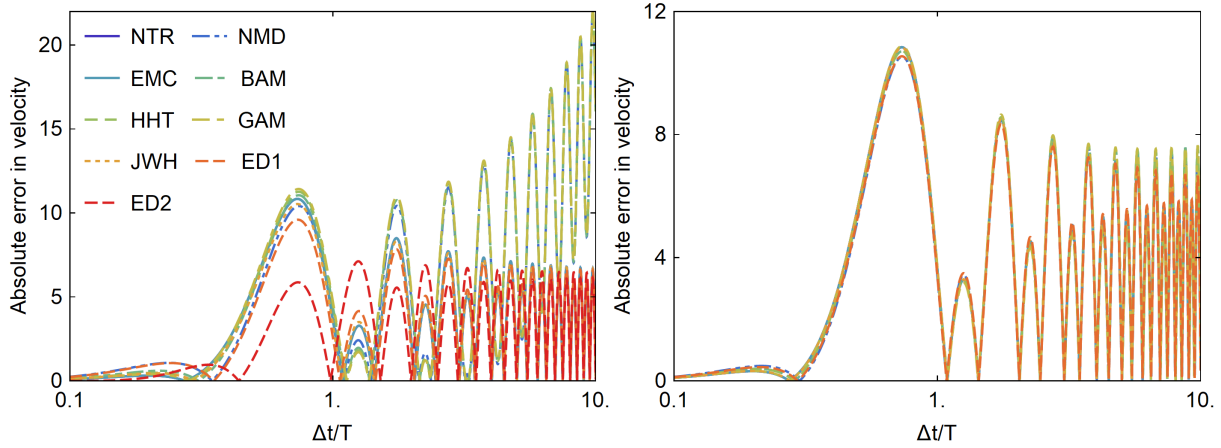
Figure 3.5: Overshoot analysis. Absolute error in velocity at first time step. Left: $\alpha_{\text{ED}} = \beta_{\text{ED}} = 0.2$ and $\rho_\infty = 0.6$. Right: $\alpha_{\text{ED}} = \beta_{\text{ED}} = 0.04$ and $\rho_\infty = 0.9$.

Slika 3.5: Analiza prekoračitve. Absolutna napaka v hitrosti po prvem časovnem koraku. Levo: $\alpha_{\text{ED}} = \beta_{\text{ED}} = 0.2$ in $\rho_\infty = 0.6$. Desno: $\alpha_{\text{ED}} = \beta_{\text{ED}} = 0.04$ in $\rho_\infty = 0.9$.
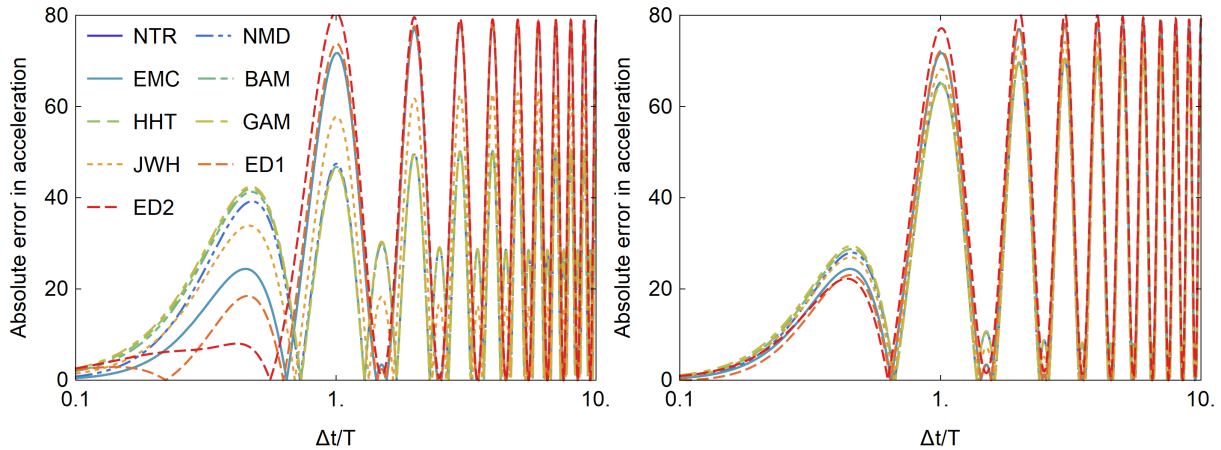
Figure 3.6: Overshoot analysis. Absolute error in acceleration at first time step. Left: $\alpha_{\text{ED}} = \beta_{\text{ED}} = 0.2$ and $\rho_\infty = 0.6$. Right: $\alpha_{\text{ED}} = \beta_{\text{ED}} = 0.04$ and $\rho_\infty = 0.9$.

Slika 3.6: Analiza prekoračitve. Absolutna napaka v pospešku po prvem časovnem koraku. Levo: $\alpha_{\text{ED}} = \beta_{\text{ED}} = 0.2$ in $\rho_\infty = 0.6$. Desno: $\alpha_{\text{ED}} = \beta_{\text{ED}} = 0.04$ in $\rho_\infty = 0.9$.

In this work, we assess the overshoot behavior of the schemes by studying the problem (3.28) with $m = 1$, $T = 1$, $u_0 = 1$, and $\dot{u}_0 = 0$. Displacement, velocity and acceleration are considered after one time-step and compared to the analytical solution. Absolute errors in time $t = \Delta t$ are shown in Figures 3.4 – 3.6. They indicate that stronger damping results in larger errors, and that an overshoot in velocity is observed for NMD, GAM, BAM and HHT, see Figure 3.5 (left). This confirms the known characteristic of these schemes, which is numerical amplification of high frequencies for $\Delta t/T \gg 1$. The other considered schemes do not exhibit overshoot in velocity. Moreover, none of the considered schemes exhibits overshoot in displacement or acceleration, see Figures 3.4 and 3.6.

3.5.5   Accuracy analysis

In this section, we numerically investigate global and local solution errors, in order to determine the order of accuracy of the considered schemes. Local errors for the system (3.28) can be collected in a vector as

$$e_{n+1} = \{e_{u_{n+1}}, e_{\dot{u}_{n+1}}, e_{\ddot{u}_{n+1}}\}^{\mathrm{T}}, \tag{3.48}$$

where $e_{u_{n+1}}, e_{\dot{u}_{n+1}}, e_{\ddot{u}_{n+1}}$ are local displacement, velocity and acceleration errors, respectively. Note that for JWH, vector e_{n+1} also includes the error in auxiliary variable v, $e_{v_{n+1}}$, while for EMC and ED, no acceleration error is included, because the schemes evaluate acceleration by post-processing. The local errors at t_{n+1} can be expressed as

$$e_{n+1} = X(t_{n+1}) - AX(t_n). \tag{3.49}$$

where $X(t_{n+1})$ and $X(t_n)$ are exact solutions at t_{n+1} and t_n, respectively, see e.g. [182]. The global error at t_{n+1} is defined as difference of exact and algorithmic solution at that time-point:

$$E_{n+1} = \{E_{u_{n+1}}, E_{\dot{u}_{n+1}}, E_{\ddot{u}_{n+1}}\}^{\mathrm{T}} = X(t_{n+1}) - X_{n+1}. \tag{3.50}$$

Substituting Eq. (3.49) into (3.50) and by recursively using the obtained expression, global error at t_{n+1} is expressed by local errors as:

$$E_{n+1} = \sum_{i=0}^{n} A^{n-i} e_i + A^{n+1} E_0, \tag{3.51}$$

where E_0 is the initial error, see [70] and [182]. Following [182], we set the initial error to be zero for the analysis bellow.

Let us study the local and global errors by analyzing the problem (3.28) subjected to non-zero initial conditions, as proposed in [70] and [182]. We choose the following data:

$$\omega = 2\pi, T = 1, u_0 = \dot{u}_0 = 1. \tag{3.52}$$

Both local and global errors were evaluated at time $t_{n+1} = 0.4 + \Delta t$. The algorithmic order of accuracy was estimated by using different time steps in the range from 10^{-4} to 0.1. Two levels of dissipation were considered: parameters $\alpha_{\mathrm{ED}} = \beta_{\mathrm{ED}} = 0.02$ and $\rho_\infty = 0.9$ for small dissipation, see Figure 3.7, and parameters $\alpha_{\mathrm{ED}} = \beta_{\mathrm{ED}} = 0.35$ and $\rho_\infty = 0.5$. The latter is the lowest ρ_∞ applicable to all schemes, see Figure 3.8, for large dissipation. The orders of accuracy are visible from the error graphs in Figures 3.7 and 3.8, as they correspond to the slopes of the lines. They are given in Table 3.3, which shows that they are equal for both levels of dissipation, as expected. For JWH, we show the results for velocity v rather than for $\dot{u}$. The order of accuracy for the former is $O(\Delta t^2)$ and for the latter it is $O(\Delta t)$, for both local and global errors. Note that the errors for some schemes change the slope in the interval of the considered values for Δt, however, in Table 3.3, the minimum approximate slope is taken into account. Table 3.3 shows that of the considered G-α schemes BAM, HHT, GAM and JWH are second-order accurate in displacement and velocity, and first-order accurate in acceleration, while NTR and NMD are second- and first-order accurate, respectively. As for the energy-momentum schemes, EMC and ED2 are second-order while ED1 is first-order accurate.
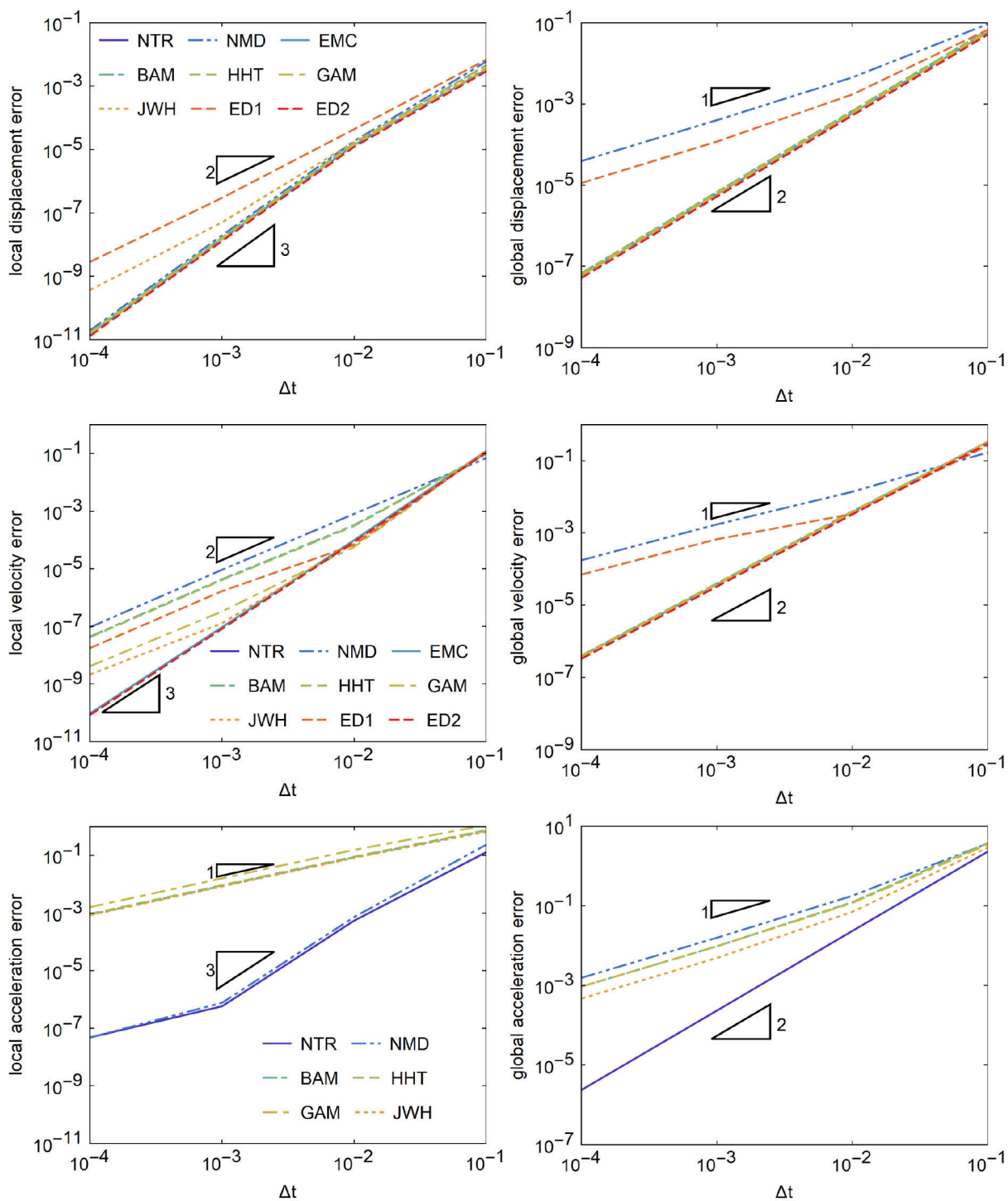
Figure 3.7: Displacement, velocity and acceleration error for $\alpha_{ED} = \beta_{ED} = 0.02$ and $\rho_\infty = 0.9$.
Slika 3.7: Napaka v pomikih, hitrostih in pospeških za $\alpha_{ED} = \beta_{ED} = 0.02$ in $\rho_\infty = 0.9$.
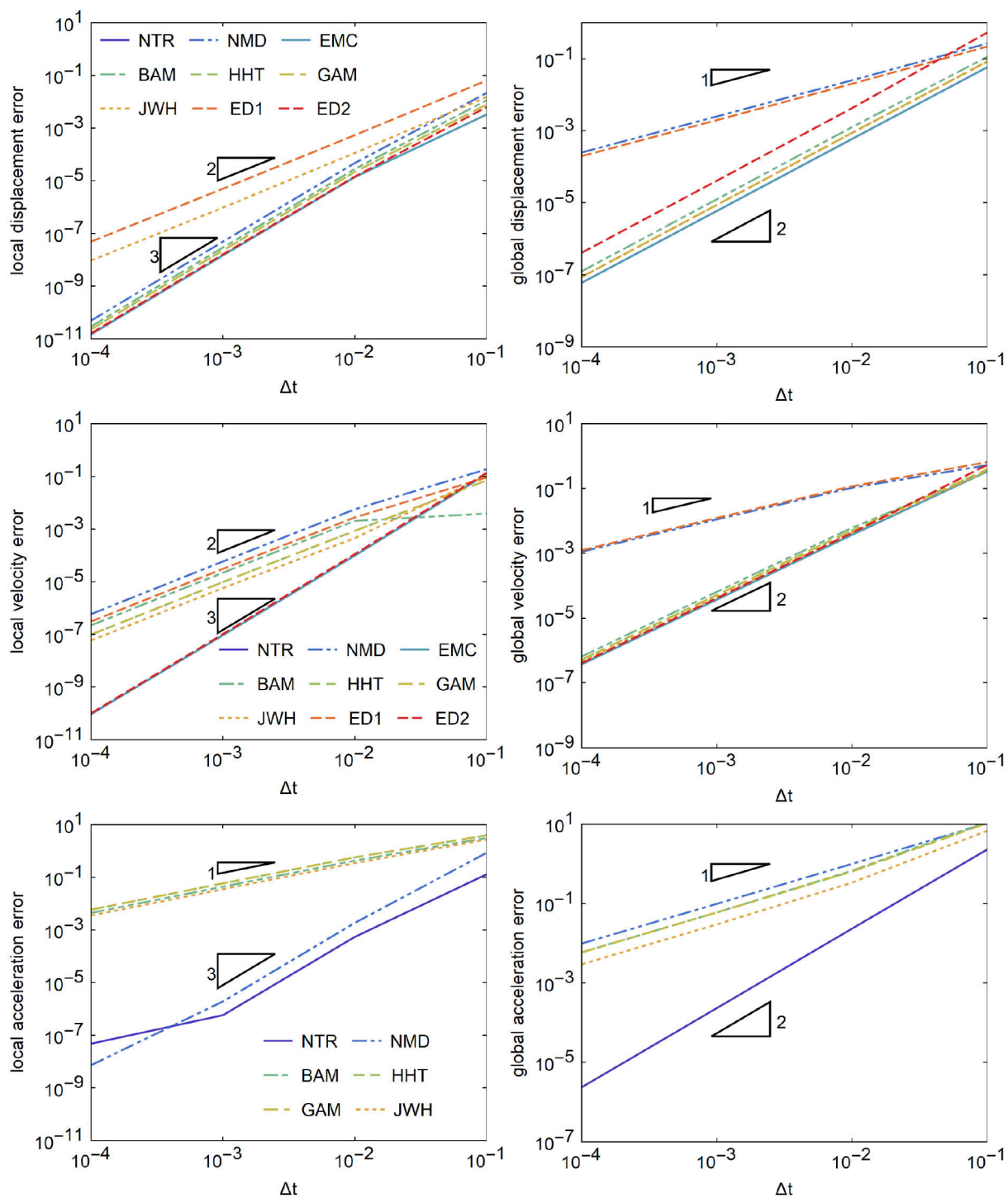
Figure 3.8: Displacement, velocity and acceleration error for $\alpha_{ED} = \beta_{ED} = 0.35$ and $\rho_\infty = 0.5$.

Slika 3.8: Napaka v pomikih, hitrostih in pospeških za $\alpha_{ED} = \beta_{ED} = 0.35$ in $\rho_\infty = 0.5$.

Table 3.3: Order of accuracy for considered schemes (displacements, velocity, acceleration).
Preglednica 3.3: Red natančnosti za obravnavane sheme (pomiki, hitrosti, pospeški).

Scheme	$\alpha_{ED} = \beta_{ED} = 0.02, \rho_\infty = 0.9$		$\alpha_{ED} = \beta_{ED} = 0.35, \rho_\infty = 0.5$	
	Local error	Global error	Local error	Global error
NTR	(3,3,1)	(2,2,2)	(3,3,3)	(2,2,2)
NMD	(3,2,1)	(1,1,1)	(3,2,3)	(1,1,1)
BAM	(3,2,1)	(2,2,1)	(3,2,1)	(2,2,1)
HHT	(3,2,1)	(2,2,1)	(3,2,1)	(2,2,1)
GAM	(3,2,1)	(2,2,1)	(3,2,1)	(2,2,1)
EMC	(3,3)	(2,2)	(3,3)	(2,2)
JWH	(2,2,1)	(2,2,1)	(2,2,1)	(2,2,1)
ED1	(2,2)	(1,1)	(2,2)	(1,1)
ED2	(3,3)	(2,2)	(3,3)	(2,2)

3.5.6   Linear example

We compare the considered schemes for problem (3.28) with $m = 1, T = 1, k = (2\pi/T)^2 m = 4\pi^2$ and the initial conditions $u_0 = 1, \dot{u}_0 = 0$.
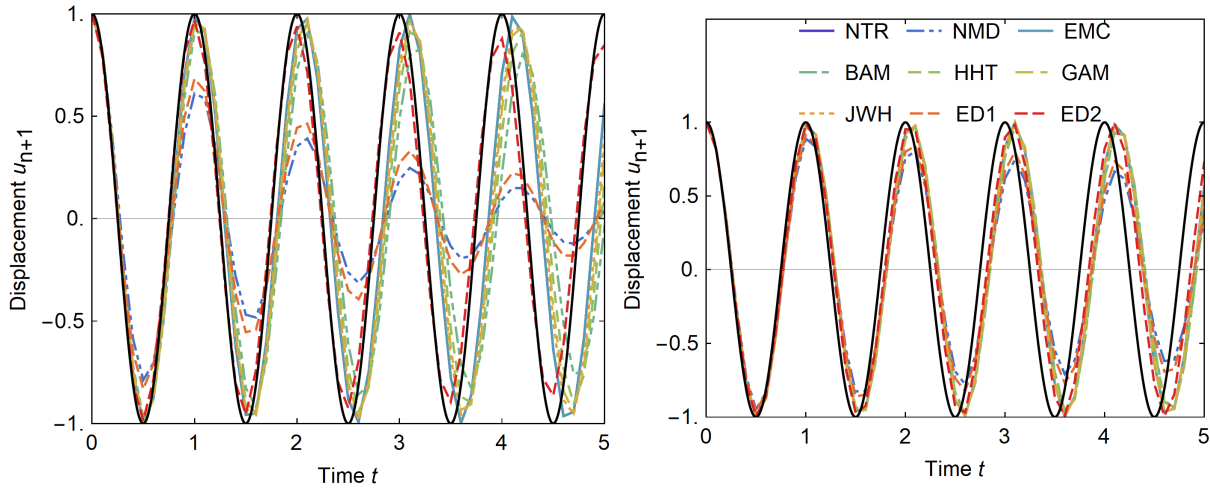
Figure 3.9: Model response for $\Delta t = T/10$, analytical solution is in black. Left: displacement for $\alpha_{ED} = \beta_{ED} = 0.2$ and $\rho_\infty = 0.6$. Right: displacement for $\alpha_{ED} = \beta_{ED} = 0.04$ and $\rho_\infty = 0.9$.
Slika 3.9: Modelni odziv za $\Delta t = T/10$, analitična rešitev je označena s črno. Levo: pomiki za $\alpha_{ED} = \beta_{ED} = 0.2$ in $\rho_\infty = 0.6$. Desno: pomiki za $\alpha_{ED} = \beta_{ED} = 0.04$ in $\rho_\infty = 0.9$.

Different levels of numerical dissipation and time step lengths Δt are used, to demonstrate the influence of both values on the response of the system. Figures 3.9 and 3.10 show that for a longer time step $\Delta t = T/10$, displacement response is much more strongly damped, compared with a shorter time step $\Delta t = T/100$. This is directly correlated to Figure 3.1, where for $\Delta t/T = 0.01$, no drop is yet observed on all the curves, with the exceptions of ED1 and NMD, while for $\Delta t/T = 0.1$ all the curves display at least a slight drop. As before, for the same values of dissipation parameters ρ_∞, NMD exhibits the strongest dissipation, while NTR and EMC both yield identical response with no dissipation. Period elongation is also evident, if we compare the considered schemes with the analytical solution, but it is more noticeable for a longer time step, while for a shorter time step, no elongation is observed even at the final time $t_f =$

$20s$. A noticeable exception is ED2 for $\alpha_{ED} = 0.2$, where the period elongation is less evident even for a longer time step, which is directly correlated to the ED2 curve in Figure 3.2.
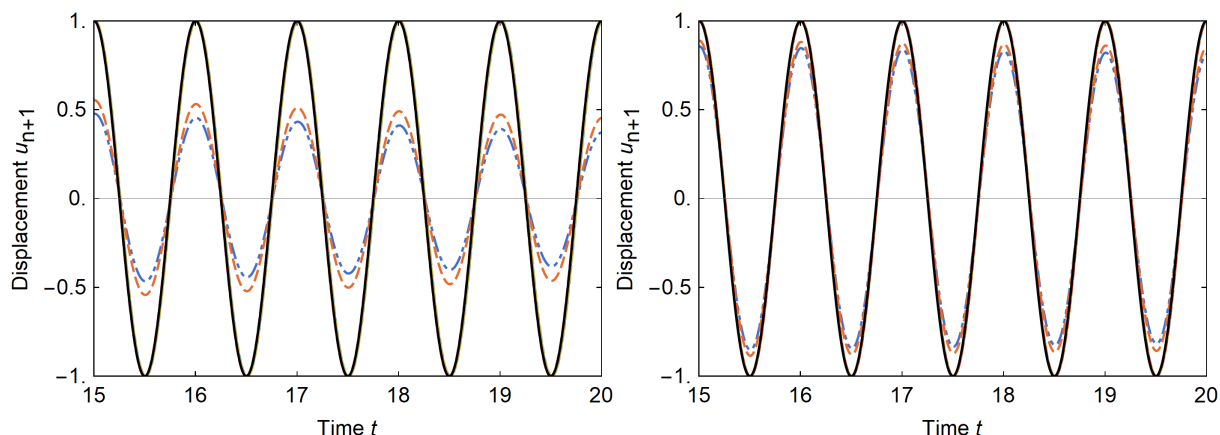
Figure 3.10: Model response for $\Delta t = T/100$, analytical solution is in black. Left: displacement for $\alpha_{ED} = \beta_{ED} = 0.2$ and $\rho_\infty = 0.6$. Right: displacement for $\alpha_{ED} = \beta_{ED} = 0.04$ and $\rho_\infty = 0.9$.
Slika 3.10: Modelni odziv za $\Delta t = T/100$, analitična rešitev je označena s črno. Levo: pomiki za $\alpha_{ED} = \beta_{ED} = 0.2$ in $\rho_\infty = 0.6$. Desno: pomiki za $\alpha_{ED} = \beta_{ED} = 0.04$ in $\rho_\infty = 0.9$.

3.6   Comparison of the schemes for nonlinear stiff equations

In this section, we analyze the performance of the above considered schemes in nonlinear elasto-dynamics. To this end, we implemented the schemes for a geometrically exact, inextensible director shell model with large rotations with Reissner-Mindlin kinematics, presented in detail e.g. in [23], [28], [140] and [142]. In particular, the implementation was carried out for the four-node, isoparametric, shell finite element, with the assumed natural strain formulation of Bathe and Dvorkin [48] for the transverse shear strains, and with the stress-resultant material model of the Saint-Venant Kirchhoff type. The rotations of the shell director are treated by an additive approach (iterative components of rotation vector are added in order to get incremental rotation vector), update of reference configuration frame at the end of each increment, and a quaternion regulation of the current rotation matrix at each increment (algorithm IQ from Table 2.7), see e.g. [26], [27], [104]. Thus, the description of the shell director rotation is singularity-free. Used shell formulation is described in detail for static formulations in Chapter 2, where it is denoted as MITC4.

Because of a large difference between the bending and the membrane deformation modes, see e.g. [104], [107], the shell finite element formulations yield numerically stiff equations. The numerical stiffness presents a significant challenge in computing the dynamic response and is therefore a demanding test for the time-stepping algorithms. Consequently, the numerical examples below will illustrate how the above considered schemes perform for the nonlinear stiff problems.

Let us mention that our shell formulations for NTR, NMD, GAM, HHT, BAM, JWH, EMC and ED1 have 5 nodal degrees of freedom (3 displacements of the mid-surface and 2 rotations of the inextensible shell director), and that our shell formulations for EDMC1 and EDMC2 have 11 nodal degrees of freedom (3 mid-surface displacements, 2 rotations of the shell director, 3 mid-surface velocities and 3

shell director velocities). We will omit a more detailed description of these finite element models and their implementations in this section. Nevertheless, we refer to Chapter 2 for description of static formulation and Chapters 4, 5 and 6 for its expansion to dynamics. Furthermore, let us recall the basic references:

(i)   For NTR, we refer to [27].

(ii)   For G-α (GAM, HHT, BAM) and NMD, we refer to [97], [96].

(iii)   For EMC, we refer to [146], [23] and [26].

(iv)   For ED1, we refer to [26].

(v)   For EDMC1 and EDMC2, we refer to [4], [5] and [132].

(vi)   To our best knowledge, a JHW shell formulation (of any kind) has not been applied so far, but we omit its description as well.

We may also mention a few additional useful references for shells: [102], where NTR, NMD, GAM, HHT, BAM, EMC and ED1 are implemented for a rotation-free shell with 6 kinematic parameters, [158], where NTR, BAM and EMC are implemented for a solid shell with enhanced assumed strains and [37], where NTR and EMC are implemented for a shell finite element with the drilling degree of freedom.

3.6.1   Vibration of a clamped S-shaped plate
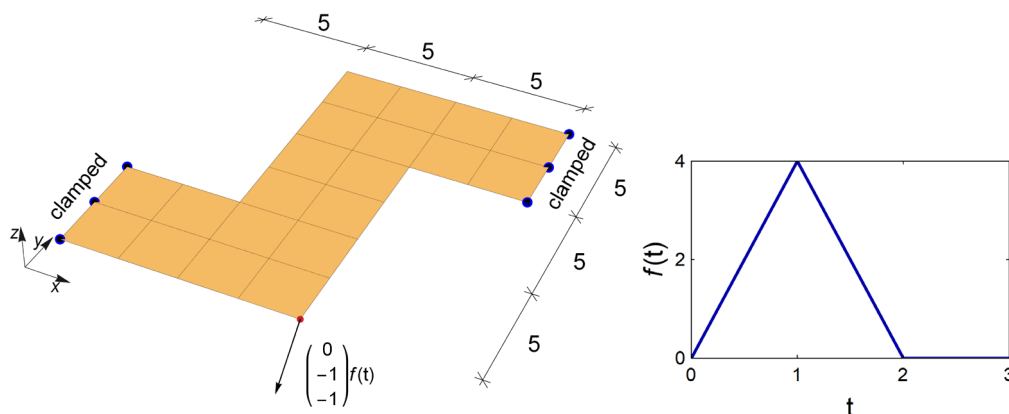
Figure 3.11: Clamped S-shaped plate problem.
Slika 3.11: Problem vpete plošče S oblike.

Let us consider a vibration of an S-shaped plate, presented in Figure 3.11, which was previously analyzed in e.g. [132]. The plate is clamped at two edges and subjected to an impulsive corner force as shown in Figure 3.11. The plate data are: thickness $h = 0.05$, material density $\rho = 5$, Young's modulus $E = 2 \, 10^5$, and Poisson's ratio $\nu = 0.3$. The plate is at rest at $t = 0$. Its dynamic response was computed up to $t_f = 10$ by using constant time steps $\Delta t = 2 \, 10^{-N}$ for $N \in [1, 2, 3, 4, 5]$. Thus, the difference between the largest and the smallest time step is 10^5. Two different levels of dissipation were considered: (i) smaller dissipation with $\rho_\infty = 0.9$ (for the dissipative schemes from Table 3.1) and $\alpha_{\mathrm{ED}} = \beta_{\mathrm{ED}} = 0.05$ (for the energy-decaying schemes), and (ii) larger dissipation with $\rho_\infty = 0.6$ and $\alpha_{\mathrm{ED}} = \beta_{\mathrm{ED}} = 0.2$.
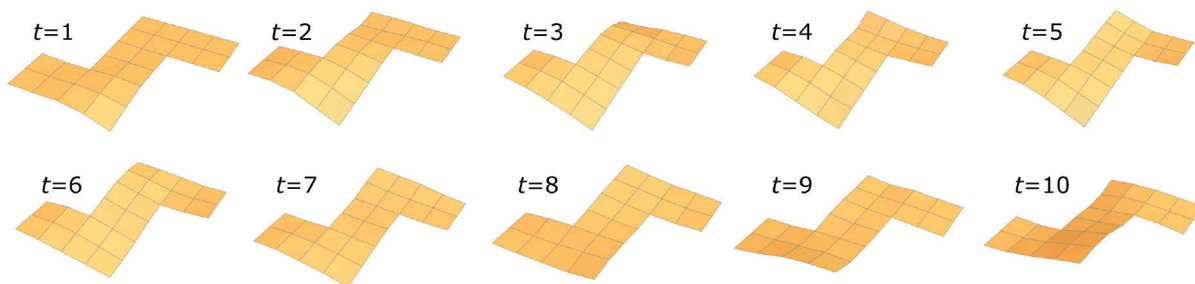
Figure 3.12: Clamped S: deformed meshes for EDMC2, $\alpha_{ED} = \beta_{ED} = 0.2$ and $\Delta t = 0.02$.
Slika 3.12: Vpeti S: deformirane mreže za EDMC2, $\alpha_{ED} = \beta_{ED} = 0.2$ in $\Delta t = 0.02$.
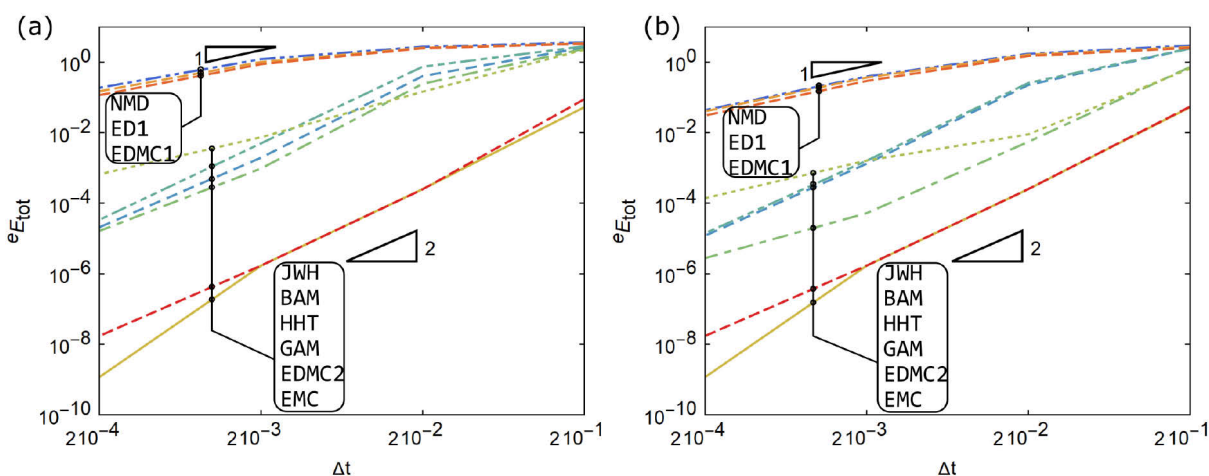
Figure 3.13: Clamped S: total energy error. Left: $\alpha_{\mathrm{ED}} = \beta_{\mathrm{ED}} = 0.2$ or $\rho_\infty = 0.6$. Right: $\alpha_{\mathrm{ED}} = \beta_{\mathrm{ED}} = 0.05$ or $\rho_\infty = 0.9$.

Slika 3.13: Vpeti S: napaka v celotni energiji. Levo: $\alpha_{\mathrm{ED}} = \beta_{\mathrm{ED}} = 0.2$ ali $\rho_\infty = 0.6$. Desno: $\alpha_{\mathrm{ED}} = \beta_{\mathrm{ED}} = 0.05$ ali $\rho_\infty = 0.9$.
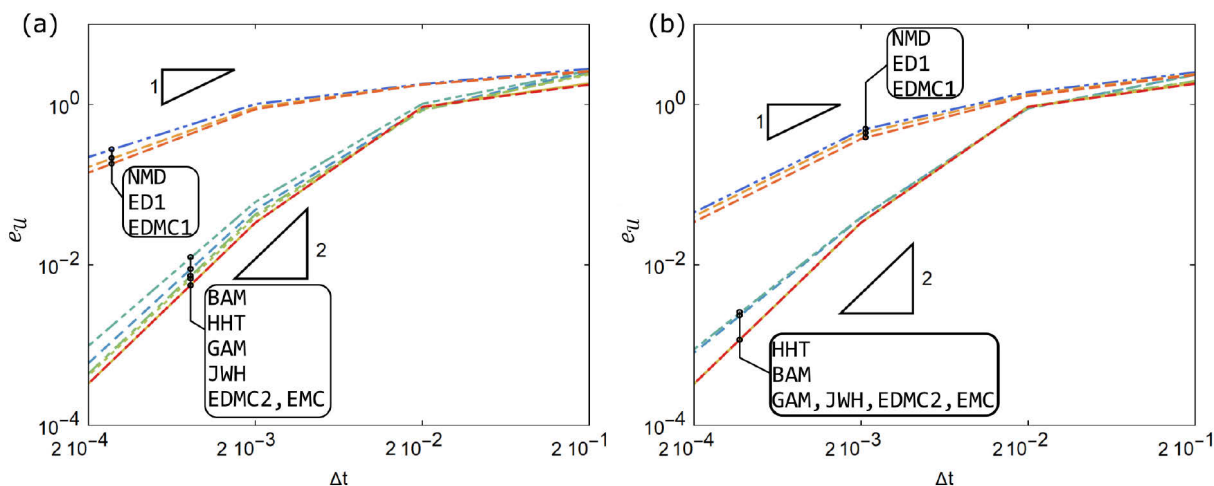
Figure 3.14: Clamped S: displacement error. Left: $\alpha_{\mathrm{ED}} = \beta_{\mathrm{ED}} = 0.2$ or $\rho_\infty = 0.6$. Right: $\alpha_{\mathrm{ED}} = \beta_{\mathrm{ED}} = 0.05$ or $\rho_\infty = 0.9$.

Slika 3.14: Vpeti S: napaka v pomikih. Levo: $\alpha_{\mathrm{ED}} = \beta_{\mathrm{ED}} = 0.2$ ali $\rho_\infty = 0.6$. Desno: $\alpha_{\mathrm{ED}} = \beta_{\mathrm{ED}} = 0.05$ ali $\rho_\infty = 0.9$.

The results are presented in Figures 3.12 – 14. Note that the non-dissipative NTR was not able to compute a solution for any of the chosen Δt. Figure 3.12 presents some deformed configurations, showing that out-of-plane deformations (associated with the lower-frequency bending modes) are accompanied by some in-plane deformations (related to the higher-frequency membrane modes).

In Figure 3.13, a relative error in the total energy (which is the sum of the kinetic and the potential energies) is shown with respect to Δt for the final time of the analysis t_f. For each considered scheme, the error was computed as

$$e_{E_{\text{tot}}} = \left| E_{tot} - E_{tot,lim} \right|, \tag{3.53}$$

where $E_{\text{tot,lim}}$ is the total energy computed for the smallest chosen time step $\Delta t = 2\ 10^{-5}$ (for a considered scheme). The slopes of the lines in Figure 3.13 indicate the order of accuracy of the schemes in an energy sense. Recall that the kinetic and potential energies are complicated expressions of the solution itself, i.e. of generalized displacements (and velocities) and their time derivatives. From Figure 3.13, one can conclude that:

- for the second-order schemes EDMC2 and EMC, the energy-convergence is of order two,
- for the second-order schemes HHT and BAM, the energy-convergence is of order two for small Δt and of order one for large Δt,
- for the second-order scheme GAM, the energy-convergence jumps between orders one and two,
- for the second-order schemes JWH, the energy-convergence is of order one (except for small dissipation and small Δt where it is of order two),
- for the first-order schemes NMD, ED1 and EDMC1, the energy-convergence is of order one for small Δt and less (almost constant) for large Δt.

Thus, only the slopes of the EDMC2 and EMC energy lines do not depend neither on Δt nor on dissipation, and the slope of the JWH energy line depends only slightly on Δt for small dissipation. For the other schemes, the slope of the energy line is Δt-dependent.

Figure 3.14 shows the norm of a generalized displacement error (following [132]), which is calculated on the basis of nodal differences at t_f as

$$e_u = \left[\sum_{a=1}^{n_{\text{node}}} \left(\left\| \boldsymbol{u}_{t_f}^a - \boldsymbol{u}_{t_f,lim}^a \right\| \right)^2 \right]^{1/2}. \tag{3.54}$$

Here, $\boldsymbol{u}^a$ are generalized displacements at node a, and $\boldsymbol{u}_{lim}^a$ are the values obtained for $\Delta t = 2\ 10^{-5}$. Error e_u is computed for each of the considered schemes. One can see that the slopes in Figures 3.13 and 3.14 do not match. Nevertheless, some similarities can be observed. In Figure 3.14, there are basically two sets of curves: one for the first-order schemes and one for the second-order ones. The displacement-convergence of the first-order schemes is approximately of order one (for small Δt) or less (for large Δt), and the displacement-convergence of the second-order schemes is approximately of order two (for small Δt) or less (for large Δt). Thus, the displacement-error of all the schemes is Δt-dependent.

Note that our results are in approximate accordance with [49] (i.e. only for $\Delta t < 2\ 10^{-2}$) where they state that GAM, BAM and HHT are second-order accurate for displacements and velocities also in nonlinear regime.

3.6.2   Flying L-shaped plate
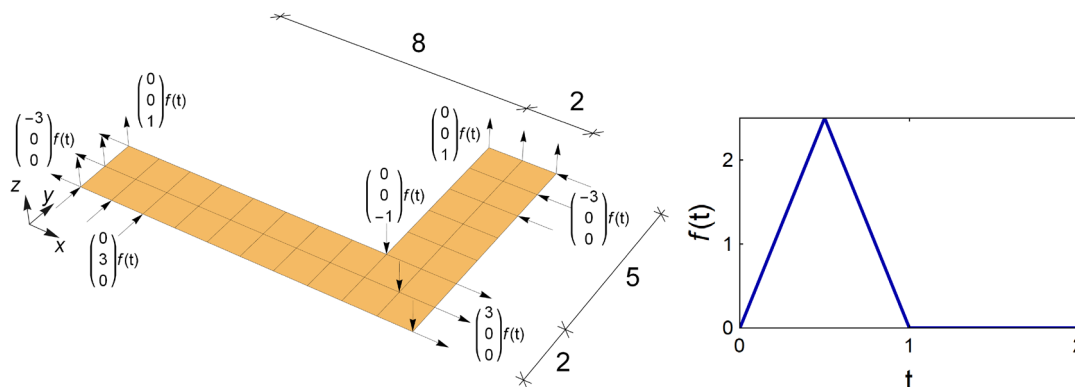
Figure 3.15: Flying L problem: mesh N = 2 with 2 elements per width.
Slika 3.15: Problem letečega L: mreža N = 2 z 2 elementoma po širini.

Let us consider an L-shaped plate from Figure 3.15, which is tossed in space by a set of impulsive nodal forces producing large bending and membrane deformations. The plate has thickness $h = 0.1$, material density $\rho = 1$, Young's modulus $E = 5 \; 10^5$ and Poisson's ratio $\nu = 0.3$. At $t = 0$, it stays at rest. The dynamics of the plate is analysed until $t_f = 20$ by using the time steps $\Delta t \in [2 \; 10^{-2}, 10^{-2}, 10^{-3}, 10^{-4}]$. The chosen damping factors are: $\rho_\infty = 0.6$ (for the dissipative schemes from Table 1) and $\alpha_{ED} = \beta_{ED} = 0.2$ (for the energy-decaying schemes).
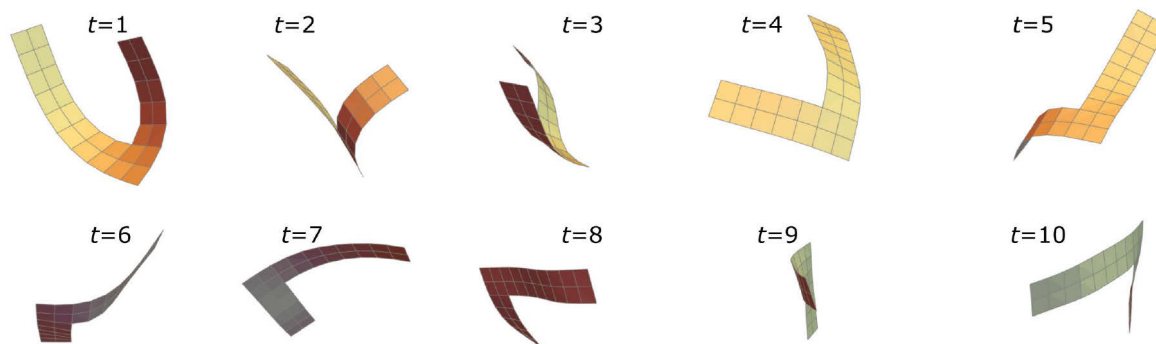
Figure 3.16: Flying L: deformed configurations (N = 2) for EDMC1, $\alpha_{ED} = \beta_{ED} = 0.2$ and $\Delta t = 0.001$.
Slika 3.16: Leteči L: deformirane konfiguracije (N = 2) za EDMC1, $\alpha_{ED} = \beta_{ED} = 0.2$ in $\Delta t = 0.001$.

The results are presented in Figures 3.16 – 3.18. Figure 3.16 shows some deformed configurations illustrating considerable vibrations during the plate motion. The dissipative schemes, which damp high-frequency stiff membrane vibrations and preserve low-frequency bending vibrations are able to compute a response for the chosen time steps. An exception is EDMC2, which falls for $\Delta t = 0.02$. On the other hand, non-dissipative EMC cannot compute responses for $\Delta t = 0.02$ and $\Delta t = 0.01$, and non-dissipative NTR is not able to compute a solution for any of the chosen Δt.
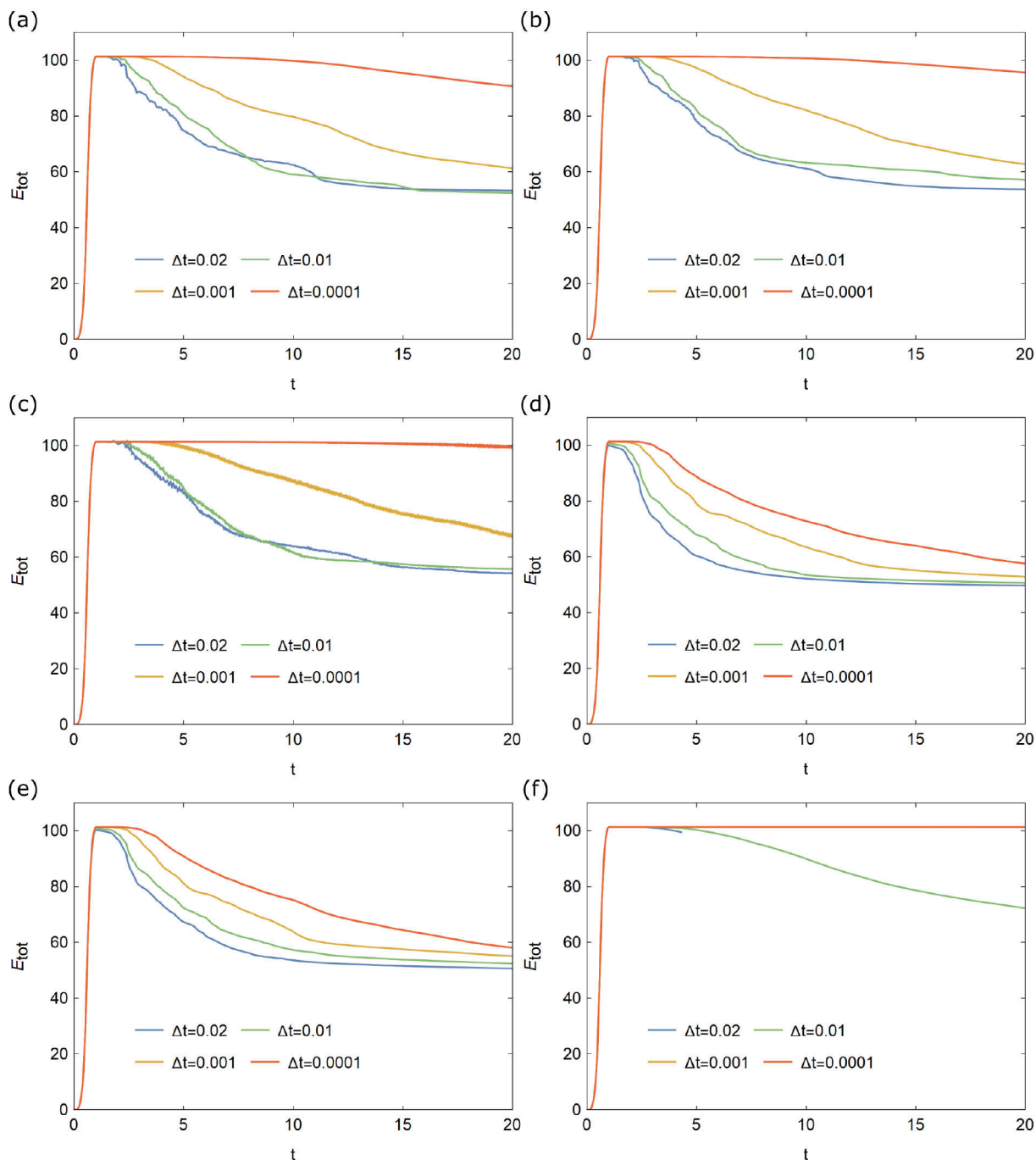
Figure 3.17: Flying L: evolution of the total energy for (a) BAM, (b) HHT, (c) JWH, (d) ED1, (e) EDMC1 and (f) EDMC2.

Slika 3.17: Leteči L: sprememba celotne energije za (a) BAM, (b) HHT, (c) JWH, (d) ED1, (e) EDMC1 in (f) EDMC2.

Figure 3.17 show evolution of the total energy with time for chosen time steps. After the end of the load application, the deformations are predominantly bending ones, i.e. low frequency modes, which are not dissipated, and the schemes compute almost constant energy. After that, high frequency vibrations, associated with small patches of elements, are observed, which are damped by the dissipative schemes (the amount depends on the properties of the scheme) and the energy begins to decrease. After effective dumping of these high-frequency vibrations, the energy becomes again almost constant. A similarity of curves can be noticed for G-α schemes, BAM, HHT and JWH. A similarity of curves can be also noticed

for the first-order energy-decaying schemes, ED1 and EDMC1, but the latter curves differ from those of G-α schemes. ED1 and EDMC1 start with considerable dissipation earlier than G-α schemes. We note that the chosen dissipation parameters for ED1 and EDMC1 equal $\rho_\infty = 0.67$ (see (3.45)), which is more than $\rho_\infty = 0.6$ that was chosen for G-α schemes. Second-order schemes tend to "flatten" the energy curved by reducing Δt, with this being most clearly expressed in EDMC2. There is no such effect for the first-order schemes.
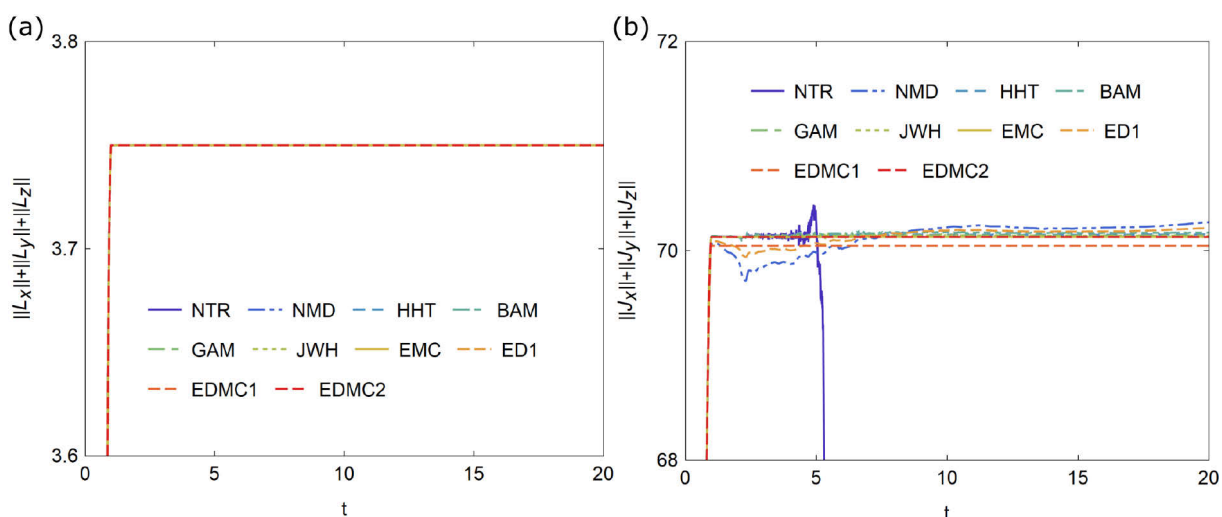
Figure 3.18: Flying L: evolution of (a) linear and (b) angular momentum for $\Delta t = 0.01$.
Slika 3.18: Leteči L: sprememba (a) gibalne količine in (b) vrtilne količine.

Table 3.4: Flying L: maximal linear momentum change in one time step after $t > 1$.
Preglednica 3.4: Leteči L: največja sprememba gibalne količine v enem koraku po času $t > 1$.

Δt	$\max\left(\dfrac{\|\boldsymbol{L}_{n+1}\| - \|\boldsymbol{L}_n\|}{\|\boldsymbol{L}_n\|}\right)$ [%]			
	BAM	GAM	JWH	NTR, NMD, EMC, HHT, ED1, EDMC1, EDMC2
$2\ 10^{-2}$	$1\ 10^{-4}$	$2\ 10^{-6}$	$7\ 10^{-6}$	0
10^{-2}	$3\ 10^{-5}$	$6\ 10^{-7}$	$2\ 10^{-6}$	0
10^{-3}	$3\ 10^{-7}$	0	$2\ 10^{-8}$	0
10^{-4}	$1\ 10^{-8}$	0	0	0

Table 3.5: Flying L: maximal angular momentum change in one time step after $t > 1$.
Preglednica 3.5: Leteči L: največja sprememba vrtilne količine v enem koraku po času $t > 1$.

Δt	$\max\left(\dfrac{\|\boldsymbol{J}_{n+1}\| - \|\boldsymbol{J}_n\|}{\|\boldsymbol{J}_n\|}\right)$ [%]							
	NTR	NMD	BAM	HHT	GAM	JWH	ED1	EMC, EDMC1, EDMC2
$2\ 10^{-2}$	1.5	0.06	0.10	0.1	0.04	0.06	0.03	0
10^{-2}	0.29	0.02	0.02	0.01	0.01	0.02	0.01	0
10^{-3}	0.002	$2\ 10^{-4}$	$4\ 10^{-4}$	$4\ 10^{-4}$	$3\ 10^{-4}$	$5\ 10^{-4}$	$1\ 10^{-4}$	0
10^{-4}	0.03	$5\ 10^{-6}$	$1\ 10^{-5}$	$5\ 10^{-6}$	$2\ 10^{-6}$	$3\ 10^{-6}$	$3\ 10^{-6}$	0

Figure 3.18 present evolution of the linear and angular momentum, L and J, respectively. The ordinate axes on Figure 3.18 (a) and (b) show the norms $\sum_{i=1}^{3} |L_i|$ and $\sum_{i=1}^{3} |J_i|$, correspondingly. Figure 3.18 (a) and Table 3.4 illustrate that NTR, NMD, EMC, HHT, ED1, EDMC1, EDMC2 exactly conserve linear momentum, and that also BAM, GAM and JWH (i.e. G-α schemes with $\alpha_m \neq 1$) have good properties in linear momentum conservation (they preserve it almost exactly). More importantly, Figure 3.18 (b) and Table 3.5 show that EMC, EDMC1 and EDMC2 also exactly conserve the angular momentum, whereas the other schemes do not possess this conservation property for J (the deviations from 0 are much larger than in the case of L, especially for NMD and ED1). The G-α schemes manage to conserve angular momentum only approximately (the conservation is improved though if small time steps are used). NTR performs the worst of the considered schemes with a large jump in the angular momentum just before its blow up. We note that 0 in Tables 3.4 and 3.5 means that the value is less than 10^{-9}.

In order to check dependency of results on the mesh, two additional meshes presented in Figure 3.19 were chosen. The deformed configurations for the finer mesh are given in Figure 3.20, and evolution of the total energy in time is shown in Figure 3.21. We note that self-contact can be observed in Figure 3.20, as we did not implement any procedures to avoid its occurrence. Figure 3.21 shows that there is smaller difference in energy curves for ED1 and EDMC1 than in the case of HHT and JWH.
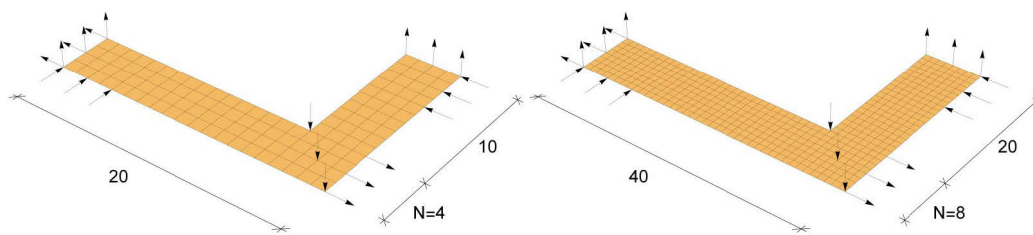
Figure 3.19: Flying L: refined meshes (N = 4 and N = 8) with 4 and 8 elements per width.
Slika 3.19: Leteči L: zgoščene mreže (N = 4 in N = 8) s 4 in 8 elementi po širini.
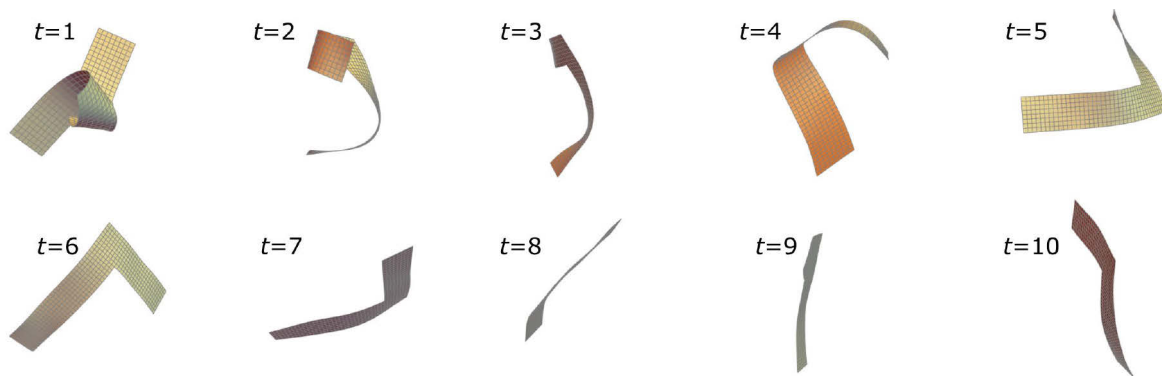
Figure 3.20: Flying L: deformed configurations (N = 8) for EDMC1, $\alpha_{ED} = \beta_{ED} = 0.2$ and $\Delta t = 0.001$.
Slika 3.20: Leteči L: deformirane konfiguracije (N = 8) za EDMC1, $\alpha_{ED} = \beta_{ED} = 0.2$ in $\Delta t = 0.001$.
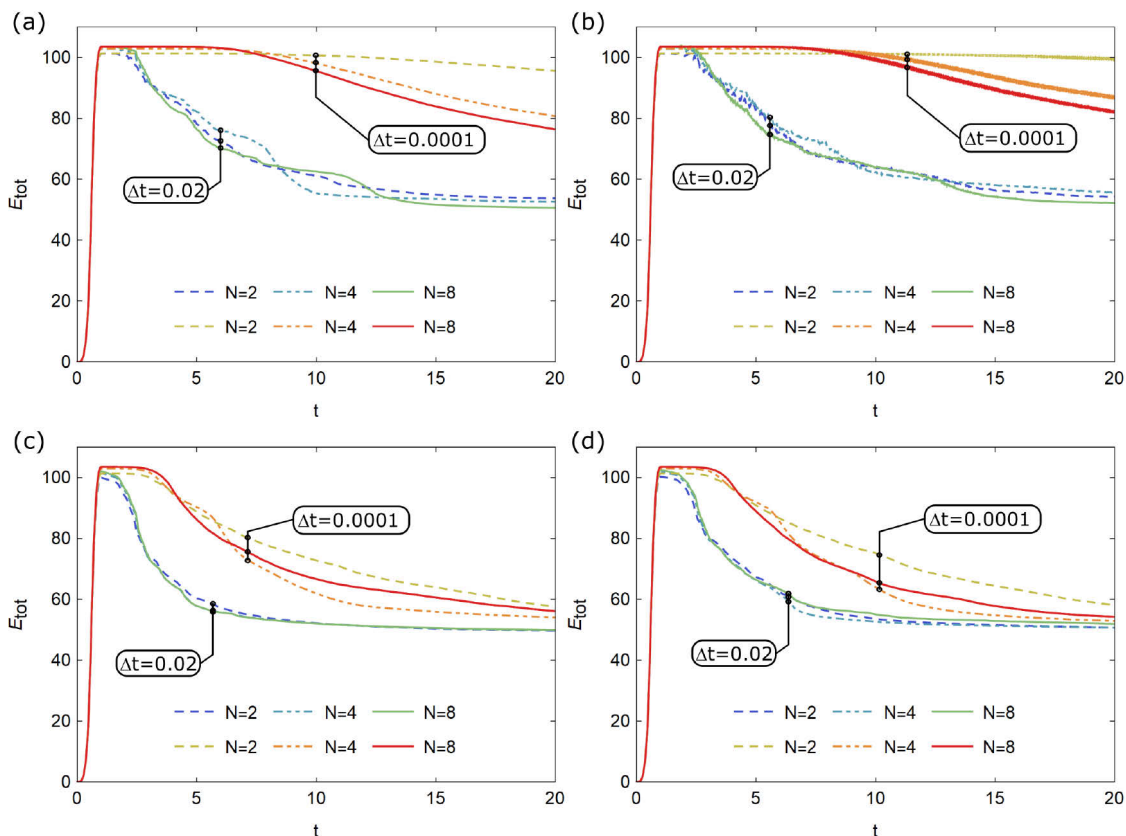
Figure 3.21: Flying L: evolution of the total energy for different mesh densities for (a) HHT, (b) JWH, (c) ED1 and (d) EDMC1.

Slika 3.21: Leteči L: Sprememba celotne energije za različne gostote mrež za (a) HHT, (b) JWH, (c) ED1 in (d) EDMC1.

3.6.3 Flying short cylinder
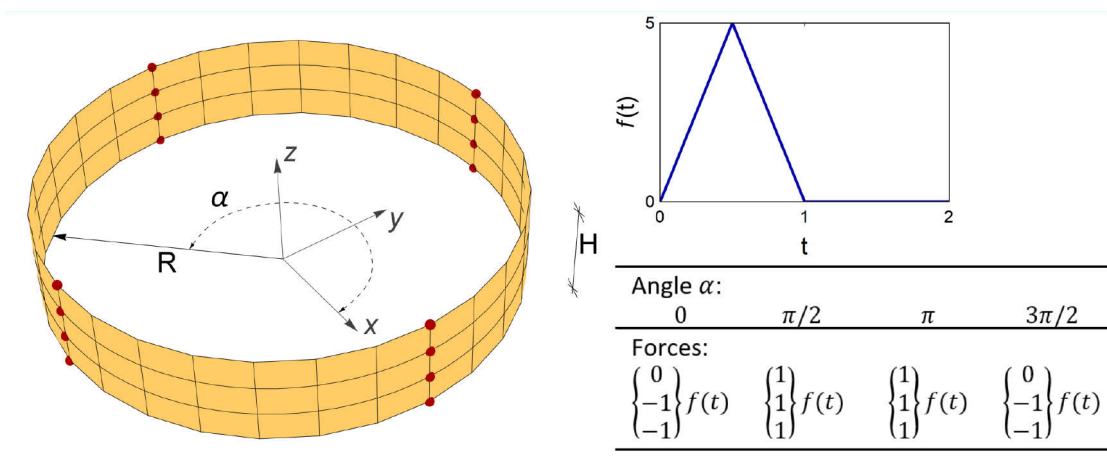
Figure 3.22: Short cylinder: geometry and loading.
Slika 3.22: Kratek cilinder: geometrija in obtežba.

We compute a classical example for shell dynamics, the flying cylinder, see Figure 3.22 and e.g. [23], [26], [50] and [146]. The data are: $R = 7.5$, $H = 3$, thickness $h = 0.02$, density $\rho = 1$, elastic modulus $E = 2\,10^8$ and Poisson's ratio $\nu = 0.3$. The cylinder is loaded by impulsive forces acting at the nodes

marked in Figure 3.22. At $t = 0$, the cylinder is at rest, and for $t > 1$, the cylinder exhibits free motion. The example was computed for different time steps, $\Delta t \in [2\ 10^{-2}, 10^{-2}, 5\ 10^{-3}, 10^{-3}, 10^{-4}]$, and two versions of dissipation parameters, $\rho_\infty \in [0.6, 0.9]$ and $\alpha_{\text{ED}} = \beta_{\text{ED}} \in [0.05, 0.2]$. Of special interest are results for $t > 1$, where we monitor kinetic, potential and total energy of the cylinder, as well as the linear and angular momentum.
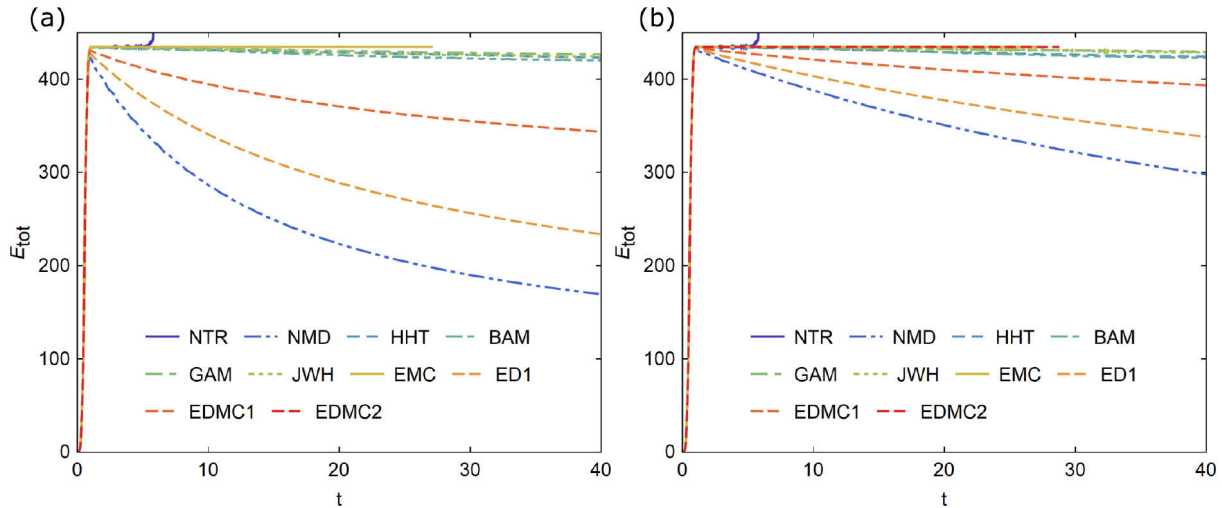
Figure 3.23: Short cylinder: total energy evolution for $\Delta t = 0.02$. Left: $\alpha_{\text{ED}} = \beta_{\text{ED}} = 0.2$ or $\rho_\infty = 0.6$. Right: $\alpha_{\text{ED}} = \beta_{\text{ED}} = 0.05$ or $\rho_\infty = 0.9$.

Slika 3.23: Kratek cilinder: spreminjanje celotne energije za $\Delta t = 0.02$. Levo: $\alpha_{\text{ED}} = \beta_{\text{ED}} = 0.2$ ali $\rho_\infty = 0.6$. Desno: $\alpha_{\text{ED}} = \beta_{\text{ED}} = 0.05$ ali $\rho_\infty = 0.9$.

Figure 3.23 shows energy evolution for both chosen levels of dissipation for time interval $[0, t_f = 40]$. A large difference can be observed between the results of the first order NMD, ED1 and EDMC1 and the second order schemes: the dissipation is much larger for the first-order schemes and the difference between the results in Figure 3.23 (a) and (b) is considerable for the first order schemes. The difference for the second-order schemes is less noticeable. For EDMC2 and $\Delta t = 0.02$, algorithmic failure occurred at $t \approx 1$ and $t \approx 29$, see Figure 3.23 (a) and (b), respectively, whereas NTR (because of blow-ups) and EMC (because of algorithmic failures) did not manage to provide results for the complete time period of interest.
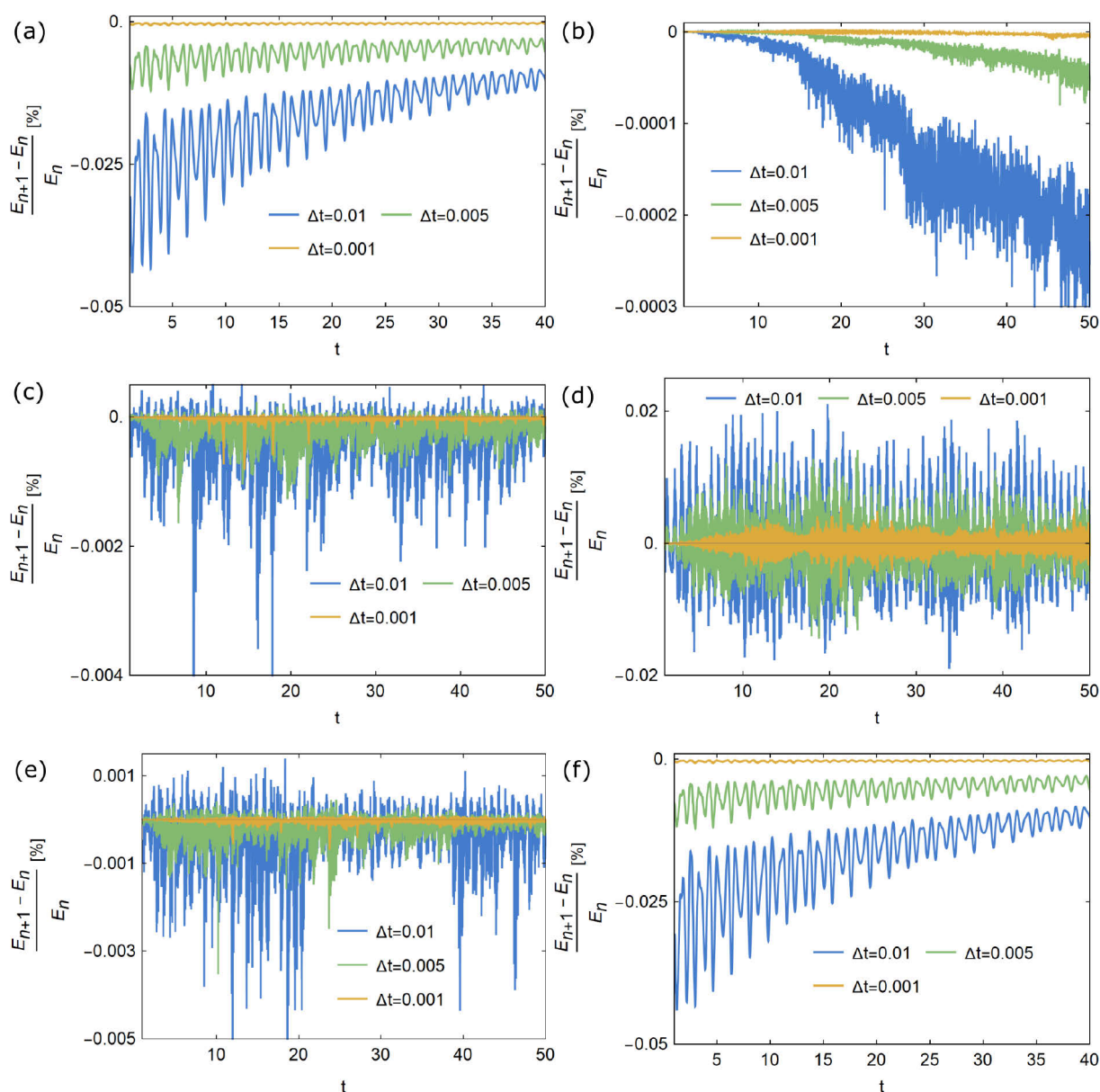
Figure 3.24: Short cylinder: step by step change of total energy for $t > 1$ and $\rho_\infty = 0.6$, $\alpha_{ED} = \beta_{ED} = 0.2$: (a) EDMC1, (b) EDMC2, (c) GAM, (d) JWH, (e) HHT and (f) NMD.

Slika 3.24: Kratek cilinder: sprememba celotne energije po posameznih korakih za $t > 1$ in $\rho_\infty = 0.6$ in $\alpha_{ED} = \beta_{ED} = 0.2$: (a) EDMC1, (b) EDMC2, (c) GAM, (d) JWH, (e) HHT in (f) NMD.

Let us recall that the energy-decaying in nonlinear elasto-dynamics is a basic indicator of an algorithmic stability in the nonlinear regime. To this end, Figure 3.24 and Table 3.6 show normalized incremental changes in total energy. Negative values on ordinates in Figure 3.24 (and in Table 3.6) are associated with positive incremental energy dissipation, whereas positive values denote negative incremental energy dissipation (which is non-physical). As in the previous example, the influence of the time step on the level of dissipation is clearly seen. The results in Figure 3.24 are presented only for $\Delta t \in [10^{-2}, 5\ 10^{-2}, 10^{-3}]$, but the trend is the same for the other chosen time steps shown in Table 3.6. For GAM, JWH, BAM and HHT, the total energy can increase substantially from one time step to another, indicating negative incremental energy dissipation, see Figure 3.24 (c) and (d) and Table 3.6. In this regard, JWH performs the worst among all G-α schemes. Although JWH performs well in the linear

dynamics, it seems that it is outperformed by the other G-α schemes in the nonlinear setting. Surprisingly, NMD performs well and computes positive incremental energy dissipation for all time steps. On the other hand, ED1, EDMC1 and EDMC2 are designed to dissipate the total energy. Therefore, it is not surprising that their incremental energy dissipations are always positive, see Figure 3.24 (a) and (b) and Table 3.6. The EMC exactly conserves the energy. Although not shown in the previous example, note that the same conclusions on energy dissipations can be made for the flying L example.
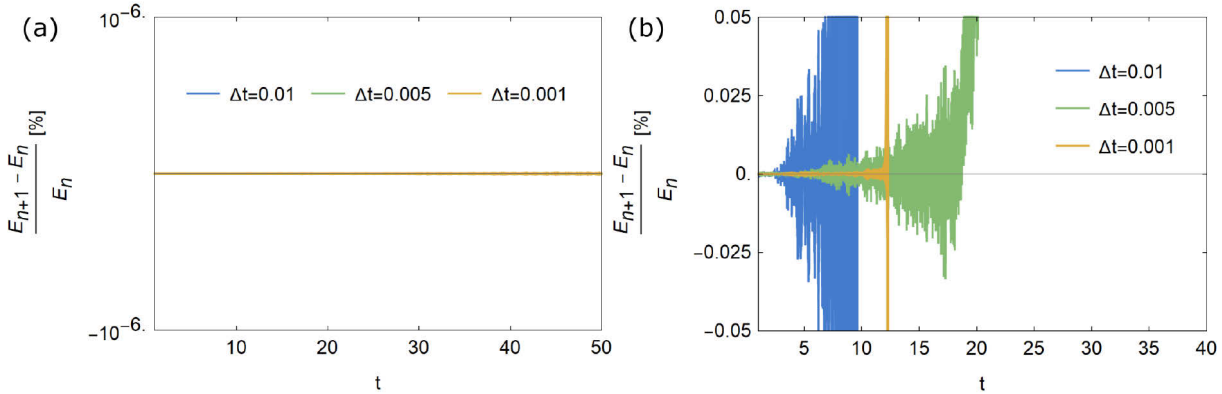
Figure 3.25: Short cylinder: step by step change of total energy for $t > 1$ and $\rho_\infty = 1$: (a) EMC, GAM, JWH, (b) NTR, NMD, HHT, BAM.

Slika 3.25: Kratek cilinder: sprememba celotne energije po posameznih korakih za $t > 1$ in $\rho_\infty = 1$: (a) EMC, GAM, JWH, (b) NTR, NMD, HHT, BAM.

In Figure 3.25, we present normalized incremental changes in total energy for $\rho_\infty = 1$. For this case, the schemes JWH and GAM conserve the energy and also the linear and angular momentum. The energy conservation is due to the application of the algorithmic stress resultants. This would not have been the case for any other type of computation of stress resultants. Namely, for all considered schemes, the algorithmic stress resultants are chosen to be computed as a combination of stress resultants at t_n and t_{n+1}, see Eq. (3.8), (3.9) and text below (3.9). The conservation of linear and angular momentum is because for $\rho_\infty = 1$ one gets $\alpha_f = \alpha_m = 1/2$ for GAM and JWH, i.e. the mid-point rule, see Table 3.1. This makes GAM for $\rho_\infty = 1$ equal to EMC, and JWH becomes an energy and momentum conserving scheme with displacements and velocities as unknowns. The second conclusion from the results for $\rho_\infty = 1$ is that NMD, BAM and HHT transform to NTR, as can also be checked from Table 3.1 and Figure 3.25 (b). Thus, the schemes in Figure 3.25 (a) exactly conserve the energy for $\rho_\infty = 1$, while the schemes in Figure 3.25 (b) show a blow up of energy, which causes the schemes to fail.

In Figure 3.26, we show the error (3.53) in total energy for different Δt. We look at the total energy at time $t = 5$, where $E_{\text{tot,lim}}$ in (3.53) is computed for each scheme for $\Delta t = 10^{-4}$. The approximate second order inclination of the lines in Figure 3.26 is seen for NTR, EMC and EDMC2, whereas for BAM and HHT the energy-error changes between first order and second order. The latter is also valid for JWH and GAM, although with the predominant energy-error of the first order. NMD, ED1 and EDMC1 clearly show approximate first order inclination of energy lines. Note that the slopes of the lines match well with the S-shaped plate example. Table 3.7 shows the CPU time for different Δt for the considered schemes, except for NTR, which fails to compute complete response for all time steps.

Note that the schemes need a similar CPU time to arrive at the final configuration. The exceptions are ED1, which is approx. 15% faster, and EDMC1, which is approx. 20% slower, compared to GAM.

Table 3.6: Short cylinder: maximal total energy change in one step after $t > 1$ for $\rho_\infty = 0.9$ or $\alpha_{ED} = \beta_{ED} = 0.05$.
Preglednica 3.6: Kratek cilinder: največja sprememba celotne energije v enem koraku po $t > 1$ za $\rho_\infty = 0.9$ ali $\alpha_{ED} = \beta_{ED} = 0.05$.

Δt	$\max\left(\dfrac{E_{n+1} - E_n}{E_n}\right)$ [%]							
	NMD	BAM	HHT	GAM	JWH	ED1	EDMC1	EDMC2
$2\ 10^{-2}$	-0.009	0.023	0.029	0.067	0.245	-0.008	-0.002	$-3\ 10^{-7}$
10^{-2}	-0.003	0.003	0.004	0.011	0.037	-0.003	$-7\ 10^{-4}$	$-5\ 10^{-9}$
$5\ 10^{-3}$	$-8\ 10^{-4}$	0.001	0.001	0.002	0.012	$-8\ 10^{-4}$	$-2\ 10^{-4}$	$-8\ 10^{-11}$
10^{-3}	$-4\ 10^{-5}$	$2\ 10^{-4}$	$3\ 10^{-4}$	$7\ 10^{-5}$	0.006	$-5\ 10^{-5}$	$-1\ 10^{-5}$	$2\ 10^{-13}$
10^{-4}	$-4\ 10^{-7}$	$3\ 10^{-5}$	$2\ 10^{-5}$	$2\ 10^{-5}$	0.004	$-5\ 10^{-7}$	$-2\ 10^{-7}$	$1\ 10^{-11}$
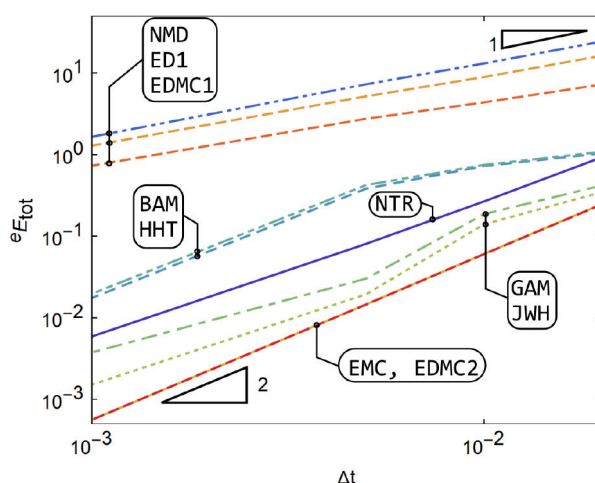
Figure 3.26: Short cylinder: total energy error at $t = 5$ for $\rho_\infty = 0.9$, $\alpha_{ED} = \beta_{ED} = 0.05$.
Slika 3.26: Kratek cilinder: napaka v celotni energiji ob času $t = 5$ za $\rho_\infty = 0.9$, $\alpha_{ED} = \beta_{ED} = 0.05$.

Table 3.7: Short cylinder: CPU time [s] for $\rho_\infty = 0.6$ or $\alpha_{ED} = \beta_{ED} = 0.2$.
Preglednica 3.7: Kratek cilinder: računski čas [s] za $\rho_\infty = 0.6$ ali $\alpha_{ED} = \beta_{ED} = 0.2$.

Δt	NMD	BAM	HHT	GAM	JWH	EMC	ED1	EDMC1	EDMC2
$2\ 10^{-2}$	16	17	18	18	17	/	14	21	/
10^{-2}	29	30	30	31	35	33	24	37	33
$5\ 10^{-3}$	53	53	54	53	57	57	48	71	57
10^{-3}	196	221	236	237	241	264	203	299	249
10^{-4}	3136	3309	3239	3206	3275	3170	3018	3621	3233

3.7   Chapter conclusions

In this chapter we revisited some generalized-α and energy-decaying schemes. Many of the former schemes are popular choices for commercial and research finite element codes, whereas the latter schemes are unnecessarily neglected in this regard. We made a condensed, yet comprehensive and illustrative comparison of these schemes, both in linear and nonlinear regime, in order to highlight their advantages and disadvantages.

For linear dynamics, the JWH scheme shows the best dissipative properties of all. It also does not suffer from overshoot in velocity like other generalized-α schemes (NMD, GAM, BAM and HHT). On the other hand, the dissipative properties of the second-order energy-decaying scheme deviate from the others in the sense that its spectral radius at infinity is zero and it completely removes higher-frequency modes.

For nonlinear dynamics, the momentum conservation plays a key role in achieving physically correct discrete representation of a problem. While most of the generalized-α schemes achieve an approximate conservation of linear momentum, none can conserve the angular momentum, which is accomplished only by the energy-momentum conserving and some of the energy-decaying schemes (if generalized velocities are used as additional degrees of freedom). The generalized-α methods do not decay the sum of potential and kinetic energies, although Erlicher et al. [49] reported that generalized-α methods show asymptotic energy stability in their nonlinear tests for large amounts of dissipation. The JWH scheme performs the worst of the G-α schemes in this sense, as its energy oscillations are the biggest. On the other hand, the energy-momentum conserving scheme ensures strict conservation of energy and momentum, but algorithmic failure can still occur because of non-damped oscillations. The energy-decaying and momentum-conserving schemes seem as a natural choice for nonlinear problems, because they preserve momenta and controllably dissipate the energy. Their deficit is that EDMC1 is only first-order accurate, while EDMC2 can fail for longer time steps.

To the best of our knowledge, JWH has not yet been analyzed in such detail in the nonlinear setting. It has been reported before that the properties of JWH in linear dynamics are excellent [80], but this study shows that JWH does not extend these properties to nonlinear dynamics. Among the considered generalized-α schemes, JWH is no better that the other generalized-α schemes in nonlinear regime. Moreover, for larger time steps and small chosen dissipation, JWH may easily fail, which is also the case for HHT. Furthermore, the nonlinear numerical examples show that the level of energy dissipation in general depends on the scheme accuracy (a lot), the chosen values for user controlled dissipation parameters, and the density of the chosen mesh.

The energy-decaying (and momentum-conserving) schemes seem to be the best option for nonlinear dynamics, because the fundamental structure of non-discretized equations is preserved and the decay of the energy can be controlled. However, the second-order accurate energy-decaying scheme that is considered in this chapter is obviously not optimal, and a better version should be searched for. Moreover, it demands generalized velocities as additional degrees of freedom, which complicates its implementation for the standard finite element formulations.

4 ENERGY-DECAYING AND MOMENTUM-CONSERVING SCHEMES FOR TRANSIENT SIMULATIONS WITH MIXED SHELL QUADRILATERALS

Chapter abstract

We present the four-field and the three-field mixed functionals that can be used to derive in an elegant way the energy-decaying and momentum-conserving (EDMC) time-stepping schemes for transient simulations with mixed finite elements. The functionals are applied for derivation of EDMC schemes for the previously identified high-performance mixed-hybrid shell finite elements that combine the assumed natural strain concept and mixed interpolations of Hu-Washizu or Hellinger-Reissner type. functionals are extended to the transient regime, where their robustness is preserved. The superior properties of these shell finite elements that are reflected in statics by very large solution steps and low-sensitivity to mesh distortion are through the four-field and the three-field mixed functionals extended to transient simulations. The content of this chapter is taken from the yet unpublished article [106].

Nonlinear numerical examples in this chapter are computed using the dynamic extensions (EDMC1 and EDMC2 schemes) of previously analysed finite elements MITC4, MITC4+, EAS5, +HW and +HR, see Tables 2.2 – 2.5 and Sections 2.2.1, 2.3.1 and 2.4.1 – 2.4.4. Furthermore, the rotation algorithm IQ was applied in all elements, see Table 2.7 and Section 2.2.2.

4.1 Chapter introduction

When investigating shell structures, a long-term time-domain analysis involving large displacements, rotations and strains due to dynamic loads is a difficult task. This is a consequence of the fact that discrete equations of shells are very stiff but also owing to the existence of conservation laws that should be appropriately represented in the mechanical model, including the conservation of momenta and energy under the proper boundary conditions. These properties are fundamental to the underlying physical system and have motivated the development of many works that inherit them. See e.g. [146] for the description of energy and momentum conserving (EMC) scheme and [23] for the implementation details of the EMC scheme for shell quadrilaterals.

On the other hand, for structural dynamic problems discretized with finite elements, it has often proven desirable or even necessary for the time-stepping schemes to controllably dissipate the unresolved high-frequency modes, so that their adverse effects on the numerical solution can be avoided, see e.g. [102], [108]. Therefore, a time integration scheme with controllable numerical dissipation in high-frequency modes and at the same time with less numerical dissipation in the low-frequency range is desirable. To this end, many single-step schemes with numerical damping have been proposed as an extension of the Newmark method. Such schemes are e.g. various α-methods proposed in [38], [65], [170] for linear dynamics and extended to nonlinear dynamics in [97], among many others.

Algorithms that are unconditionally stable for linear dynamics often lose this stability in the nonlinear case. Therefore, energy criterion is used to evaluate the scheme stability in the nonlinear regime, see e.g. [97], [105], [132], stating that a scheme is unconditionally stable in nonlinear elasto-dynamics if for free motion $(V_{n+1} - V_n) + (K_{n+1} - K_n) \leq 0$ is valid for a time step $[t_n, t_{n+1}]$, where V and K are potential and kinetic energies, respectively. This equation is in general not satisfied for the α-methods,

even for small time steps, see e.g. Chapter 3 or [132], [105]. It was also recognized, see e.g. [97], [132], [102], [105], that in order to achieve robustness, a time integration scheme must not only have some numerical (i.e. algorithmic) damping, but at the same time ensure the preservation of the underlying physic, i.e. the conservation of momenta, which the α-methods fail to achieve, see e.g. [105], [132]. The energy-decaying, momentum-conserving (EDMC) schemes, proposed in [4], [5], [132] or [51], on the other hand, manage to conserve these properties, which brings them to the focus of our attention.

We listed in Section 2.1 properties that an almost "optimal" finite element should possess and later extensively tested a large assortment of mixed formulations that improve the underlying displacement-based finite element. Let us list some of the most prominent again: (i) assumed natural strain (ANS) technique, see e.g. [48] and [89] for the treatment of transverse shear and membrane strains, respectively; (ii) enhanced assumed strain (EAS) technique, see e.g. [22], [12] and [143]; (iii) mixed-hybrid formulations based on the Hu-Washizu (HW) or Hellinger-Reissner (HR) functional, see e.g. [59], [60] and [159]. In Chapter 2, as well as in articles [104] and [107], we have concluded that in order to obtain a near optimal quadrilateral shell finite element, one should combine the ANS and hybrid HW or HR formulations.

Since some frequently applied techniques, such as ANS, EAS or reduced integration, do not affect the design of the EMC or EDMC schemes, their use has often been reported also in the shell dynamics field. The ANS for transverse shear strains, proposed by Dvorkin and Bathe in [48], has been widely applied to the shell elements in dynamics. On the other hand, the more recent ANS for membrane strains, proposed by Ko et al. in [89], has not yet been used in a shell dynamics formulation to the best of our knowledge. Vu-Quoc and Tan [158] developed a mixed Hu-Washizu type variational formulation, employing the EAS method for the solid shell element and EMC time-stepping scheme. Gebhardt and Rolfes [50] further developed a mixed EAS formulation for extensible director rotation-less shell formulation and applied the energy-decaying scheme following the ideas of [4], [5], [132].

Possible applications of the Hellinger-Reissner- or Hu-Washizu-based mixed-hybrid formulations in the domain of shell dynamics is, on the other hand, still rather unexplored. The first truly mixed-hybrid formulation for shell dynamics was developed by Betsch and Janz [13], who extended the Hu-Washizu type variational formulation for inextensible director shell finite elements for the energy-momentum conserving (EMC) time-stepping scheme.

In this chapter we aim to present variational formulation and time discretization that yield an energy-decaying, momentum-conserving scheme for mixed-hybrid formulations, based on the Hu-Washizu or Hellinger-Reissner functional.

The rest of the chapter is organized as follows. In Section 4.2 we introduce the proposed approach to design the EDMC integrator on a simple spring pendulum model. We start by the development of variational formulation and then develop the discretization in time for which we derive discrete balance laws. This is done separately for the formulations based on the Hu-Washizu and Hellinger-Reissner variational formulations in Sections 4.2.2 and 4.2.3, respectively. In Section 4.3, the presented formulations are then developed in the framework of mixed-hybrid shells. Section 4.4 is devoted to numerical examples, while conclusions are drawn in Section 4.5.

4.2   Spring pendulum formulation

Following the disposition in [13], we study mixed dynamic formulations for spring pendulum in order to prepare a foundation for a more demanding problem, namely mixed dynamic formulations for shells, which will be addressed in Section 4.3.
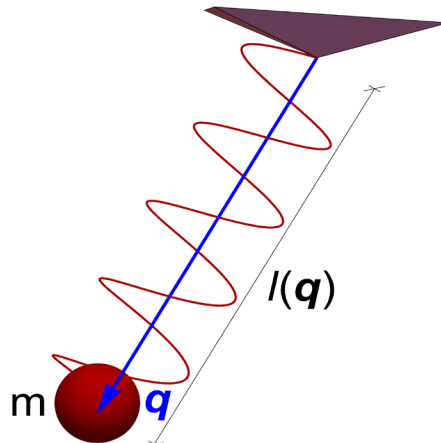
Figure 4.1: Simple spring pendulum.
Slika 4.1: Preprosto vzmetno nihalo.

4.2.1   2-field formulation

For the spring pendulum from Figure 4.1, the equations of motion can be derived by imposing the stationarity of the following function, see e.g. [13]

$$G(\boldsymbol{q}, \boldsymbol{v}) = \int_{t_0}^{t_e} (L(\boldsymbol{q}, \boldsymbol{v}) + (\dot{\boldsymbol{q}} - \boldsymbol{v}) \cdot \partial_v L(\boldsymbol{q}, \boldsymbol{v})) dt \,, \tag{4.1}$$

where $(\boldsymbol{q}, \boldsymbol{v}) \in \mathbb{R}^3 \times \mathbb{R}^3$ are space-state coordinates in time interval $[t_0, t_e]$, denoting the position vector and velocity of the particle with mass m, respectively. $(\dot{\ })$ denotes the time derivative and $L(\boldsymbol{q}, \boldsymbol{v}) = K(\boldsymbol{v}) - V(\boldsymbol{q})$ is the Lagrangian, defined as the difference between the kinetic energy

$$K = \frac{1}{2} \boldsymbol{v} \cdot \boldsymbol{M} \boldsymbol{v}, \tag{4.2}$$

where $\boldsymbol{M} = \text{DIAG}(m, m, m)$ is the mass matrix, and the potential energy. The latter is the sum of the deformation energy and the potential of external forces as

$$V = V_{int} + V_{ext}, \tag{4.3}$$

where $V_{int} = C\epsilon^2/2$, C is a material constant, and ϵ represents the Green-Lagrange strain $\epsilon = (l^2(\boldsymbol{q}) - l_0^2)/(2l_0^2)$, where $l(\boldsymbol{q}) = \sqrt{\boldsymbol{q} \cdot \boldsymbol{q}}$ is illustrated in Figure 4.1 and $l_0 = l(t_0)$. Inserting (4.2) and (4.3) into functional (4.1), the latter can be rewritten as

$$G(\boldsymbol{q}, \boldsymbol{v}) = \int_{t_0}^{t_e} \left(\left(\dot{\boldsymbol{q}} - \frac{1}{2} \boldsymbol{v} \right) \cdot \boldsymbol{M} \boldsymbol{v} - V_{int}(\epsilon(\boldsymbol{q})) - V_{ext}(\boldsymbol{q}) \right) dt \,, \tag{4.4}$$

and its stationarity is

$$\delta G(\boldsymbol{q}, \boldsymbol{v}; \delta \boldsymbol{q}, \delta \boldsymbol{v}) =$$
$$\int_{t_0}^{t_e} (\delta \dot{\boldsymbol{q}} \cdot \boldsymbol{M} \boldsymbol{v} + (\dot{\boldsymbol{q}} - \boldsymbol{v}) \cdot \boldsymbol{M} \delta \boldsymbol{v} - \delta \epsilon D V_{int}(\epsilon) + \delta \boldsymbol{q} \cdot \boldsymbol{f}_{ext}) dt = 0 \,. \tag{4.5}$$

Here, $\delta(\cdot)$ denotes the variation of $(\cdot)$, and the following notation is used: $DV_{int}(\epsilon) = dV_{int}(\epsilon)/d\epsilon$, $\delta\epsilon = D\epsilon(\boldsymbol{q}) \cdot \delta\boldsymbol{q}$, where $D\epsilon(\boldsymbol{q}) = d\epsilon(\boldsymbol{q})/d\boldsymbol{q}$, and $\boldsymbol{f}_{ext} = -dV_{ext}(\boldsymbol{q})/d\boldsymbol{q}$ encompasses conservative external forces acting on spring pendulum.

4.2.2   4-field Hu-Washizu formulation

Let us introduce strain ϵ^{HW} and spring force σ^{HW} besides the position $\boldsymbol{q}$ and velocity $\boldsymbol{v}$, as well as the constraint

$$\epsilon(\boldsymbol{q}) - \epsilon^{HW} = 0. \tag{4.6}$$

As shown in [13], one can extend the functional (4.4) by using σ^{HW} as the Lagrange multiplier for enforcing (4.6). This results in a 4-field Hu-Washizu-type functional

$$G_{HW}\left(\boldsymbol{q}, \boldsymbol{v}, \epsilon^{HW}, \sigma^{HW}\right) =$$

$$\int_{t_0}^{t_e} \left(\left(\dot{\boldsymbol{q}} - \frac{1}{2}\boldsymbol{v}\right) \cdot \boldsymbol{Mv} - \left(V_{int}(\epsilon^{HW}) + V_{ext}(\boldsymbol{q}) + \sigma^{HW}(\epsilon(\boldsymbol{q}) - \epsilon^{HW})\right)\right) dt. \tag{4.7}$$

Its stationarity reads as

$$\delta G_{HW}(\boldsymbol{q}, \boldsymbol{v}, \epsilon^{HW}, \sigma^{HW}; \delta\boldsymbol{q}, \delta\boldsymbol{v}, \delta\epsilon^{HW}, \delta\sigma^{HW}) = \int_{t_0}^{t_e} (\delta\dot{\boldsymbol{q}} \cdot \boldsymbol{Mv} + \boldsymbol{M}\delta\boldsymbol{v} \cdot (\dot{\boldsymbol{q}} - \boldsymbol{v})$$

$$-\delta\epsilon^{HW} DV_{int}(\epsilon^{HW}) + \delta\boldsymbol{q} \cdot \boldsymbol{f}_{ext} - \delta\sigma^{HW}(\epsilon(\boldsymbol{q}) - \epsilon^{HW})$$

$$-\delta\epsilon\, \sigma^{HW} + \delta\epsilon^{HW}\sigma^{HW})dt = 0, \tag{4.8}$$

Integrating per-partes the first product on the right hand side of (4.8) and taking into account that $\delta\boldsymbol{q} = \boldsymbol{0}$ at the end-points t_0 and t_e, we arrive at

$$\delta G_{HW}\left(\boldsymbol{q}, \boldsymbol{v}, \epsilon^{HW}, \sigma^{HW}; \delta\boldsymbol{q}, \delta\boldsymbol{v}, \delta\epsilon^{HW}, \delta\sigma^{HW}\right) =$$

$$\int_{t_0}^{t_e} (\delta\boldsymbol{q} \cdot (-\boldsymbol{M}\dot{\boldsymbol{v}} + \boldsymbol{f}_{ext} - D\epsilon(\boldsymbol{q})\sigma^{HW}) + \boldsymbol{M}\delta\boldsymbol{v} \cdot (\dot{\boldsymbol{q}} - \boldsymbol{v})$$

$$+ \delta\epsilon^{HW}\left(\sigma^{HW} - DV_{int}(\epsilon^{HW})\right) - \delta\sigma^{HW}(\epsilon(\boldsymbol{q}) - \epsilon^{HW})\right) dt = 0. \tag{4.9}$$

Considering that the variations $\delta\boldsymbol{q}$, $\delta\boldsymbol{v}$, $\delta\epsilon^{HW}$ and $\delta\sigma^{HW}$ are arbitrary, we arrive at the Euler-Lagrange expressions

$$\boldsymbol{M}\dot{\boldsymbol{v}} + D\epsilon(\boldsymbol{q})\sigma^{HW} = \boldsymbol{f}_{ext},$$
$$\epsilon(\boldsymbol{q}) = \epsilon^{HW},$$
$$\dot{\boldsymbol{q}} = \boldsymbol{v},$$
$$\sigma^{HW} = DV_{int}(\epsilon^{HW}), \tag{4.10}$$

where the first equation represents the equilibrium of inertial, internal and external forces, the second equation is constraint (4.8), the third equation provides relation between the velocity and time derivative of position, and the last equation is the constitutive one. These equations of motion are supplemented by the initial conditions for $\dot{\boldsymbol{v}}$, $\dot{\boldsymbol{q}}$, ϵ^{HW} and σ^{HW}, which have to be consistent with the initial $\boldsymbol{q}$ and $\boldsymbol{v}$ according to $(4.10)_2$ and $(4.10)_3$.

4.2.2.1   Balance laws

We can now check if the basic constants of the spring pendulum motion, which are the total energy, linear momentum and angular momentum, defined as

$$E = K + V, \qquad \boldsymbol{L} = \boldsymbol{Mv}, \qquad \boldsymbol{J} = \boldsymbol{M}(\boldsymbol{q} \times \boldsymbol{v}) \tag{4.11}$$

respectively, are preserved by the derived equations. To this end, let us multiply $(4.10)_1$ and $(4.10)_4$ by variations and make the sum as

$$\delta \boldsymbol{q} \cdot (\boldsymbol{M}\dot{\boldsymbol{v}} - \boldsymbol{f}_{ext} + D\epsilon(\boldsymbol{q})\sigma^{HW}) + \delta\epsilon^{HW}(DV_{int}(\epsilon^{HW}) - \sigma^{HW}) = 0. \qquad (4.12)$$

This kind of representation of Eqs. $(4.10)_1$ and $(4.10)_4$ does not introduce any changes in their strength. We further differentiate $(4.10)_2$ with respect to time to get the consistency condition, see [13]

$$\dot{\epsilon} = D\epsilon(\boldsymbol{q}) \cdot \dot{\boldsymbol{q}} = \dot{\epsilon}^{HW}. \qquad (4.13)$$

Thus, the four equations of motion in (4.10) are replaced with (4.12), (4.13) and $(4.10)_3$, for the purpose of the mentioned check. For later use, let us write the time derivative of kinetic and potential energy, (4.2) and (4.3), as

$$\dot{K} = \boldsymbol{M}\boldsymbol{v} \cdot \dot{\boldsymbol{v}}$$
$$\dot{V} = \underbrace{DV_{int}(\epsilon^{HW})\,\dot{\epsilon}^{HW}}_{\epsilon^{HW}\,C\,\dot{\epsilon}^{HW}} - \boldsymbol{f}_{ext} \cdot \dot{\boldsymbol{q}}, \qquad (4.14)$$

and the time derivative of linear and angular momentum, $(4.11)_2$ and $(4.11)_3$, as

$$\dot{\boldsymbol{L}} = \boldsymbol{M}\dot{\boldsymbol{v}}$$
$$\dot{\boldsymbol{J}} = \boldsymbol{M}(\dot{\boldsymbol{q}} \times \boldsymbol{v} + \boldsymbol{q} \times \dot{\boldsymbol{v}}) \stackrel{(4.10)_3}{\triangleq} \boldsymbol{M}(\boldsymbol{q} \times \dot{\boldsymbol{v}}) \qquad (4.15)$$

The conservation of the total energy can be checked by choosing $(\delta\boldsymbol{q}, \delta\epsilon^{HW}) = (\dot{\boldsymbol{q}}, \dot{\epsilon}^{HW})$ for admissible variations. By inserting the choice in (4.12), we get

$$\dot{\boldsymbol{q}} \cdot \boldsymbol{M}\dot{\boldsymbol{v}} - \dot{\boldsymbol{q}} \cdot \boldsymbol{f}_{ext} + \dot{\boldsymbol{q}} \cdot D\epsilon(\boldsymbol{q})\,\sigma^{HW} + \dot{\epsilon}^{HW}\,DV_{int}(\epsilon^{HW}) - \dot{\epsilon}^{HW}\,\sigma^{HW} = 0. \qquad (4.16)$$

By using the remaining two Eqs. $(4.10)_3$ and (4.13) in (4.16), we obtain

$$\underbrace{\boldsymbol{M}\boldsymbol{v} \cdot \dot{\boldsymbol{v}}}_{\dot{K}} + \underbrace{\underbrace{(-\dot{\boldsymbol{q}} \cdot \boldsymbol{f}_{ext})}_{\dot{V}_{ext}} + \underbrace{\dot{\epsilon}^{HW}DV_{int}(\epsilon^{HW})}_{\dot{V}_{int}}}_{\dot{V}} + \sigma^{HW}\underbrace{(\dot{\boldsymbol{q}} \cdot D\epsilon(\boldsymbol{q}) - \dot{\epsilon}^{HW})}_{=0,\ \ see(4.13)} = 0$$
$$\Rightarrow \dot{K} + \dot{V} = \dot{E} = 0 \qquad (4.17)$$

Eq. (4.17) shows that the total energy is preserved in time, i.e. the power of external forces $-\dot{V}_{ext} = \boldsymbol{f}_{ext} \cdot \dot{\boldsymbol{q}}$ equals the changes of kinetic and deformation energy $\dot{K} + \dot{V}_{int}$. We may also choose $(\delta\boldsymbol{q}, \delta\epsilon^{HW}) = (\dot{\boldsymbol{q}}, \dot{\epsilon}^{HW}) = (\boldsymbol{c}, 0)$ for admissible variations for $\forall \boldsymbol{c} \in \mathbb{R}^3$, and assume zero external forces (i.e. $\boldsymbol{f}_{ext} = \boldsymbol{0}$). From (4.13) it follows that this choice leads to $0 = \dot{\epsilon}^{HW} = \dot{\epsilon} = D\epsilon(\boldsymbol{q}) \cdot \boldsymbol{c}$ and allows for simplification of Eq. (4.16) into

$$\boldsymbol{c} \cdot \boldsymbol{M}\dot{\boldsymbol{v}} = \boldsymbol{c} \cdot \dot{\boldsymbol{L}} = 0 \Rightarrow \dot{\boldsymbol{L}} = \boldsymbol{0} \qquad (4.18)$$

which shows the conservation of linear momentum. In order to prove the conservation of angular momentum, let us choose $(\delta\boldsymbol{q}, \delta\epsilon^{HW}) = (\dot{\boldsymbol{q}}, \dot{\epsilon}^{HW}) = (\boldsymbol{c} \times \boldsymbol{q}, 0)$ and again assume a motion with zero external forces. One has $0 = D\epsilon(\boldsymbol{q}) \cdot (\boldsymbol{c} \times \boldsymbol{q})$ from (4.13), and simplification of Eq. (4.16) into $(\boldsymbol{c} \times \boldsymbol{q}) \cdot \boldsymbol{M}\dot{\boldsymbol{v}} = 0$. By using the scalar triple product rule, and the fact that $\boldsymbol{M} = m\boldsymbol{I}$, where $\boldsymbol{I}$ is unit matrix, one gets

$$\boldsymbol{M}(\boldsymbol{q} \times \dot{\boldsymbol{v}}) \cdot \boldsymbol{c} = 0 \Rightarrow \dot{\boldsymbol{J}} = \boldsymbol{0} \qquad (4.19)$$

which shows conservation of angular momentum. We can conclude that the 4-field formulation yields equations that conserve the fundamental constants of the spring pendulum motion.

4.2.2.2   Discretization in time

Let the time interval $[t_0, t_e]$ consists of $N + 1$ discrete time points, such that $0 = t_0 < \cdots t_n < t_{n+1} < \cdots t_N = t_e$. In this way, the time step $\Delta t = t_{n+1} - t_n$ is defined, which is not necessarily constant over the time interval $[t_0, t_e]$. We will study a generic time interval $[t_n, t_{n+1}]$ and denote the algorithmic

approximation of $(\cdot)$ at t_n and t_{n+1} as $(\cdot)_n$ and $(\cdot)_{n+1}$. Furthermore, introducing parameter $\theta \in [0,1]$, we will denote the combination $(\cdot)_{n+\theta} = \theta(\cdot)_{n+1} + (\theta - 1)(\cdot)_n$ with $(\cdot)_{n+\theta}$.

Let us perform time discretization of Eqs. (4.10) in a manner that enables controlled numerical dissipation of the total energy and that preserves linear and angular momentum. The following (mid-point) form for the discretization of (4.10), which comes from the ideas presented in [4], [5], [13] and [132], is adopted

$$M \frac{(v_{n+1} - v_n)}{\Delta t} + D\epsilon(q_{n+1/2})\sigma^{HW^*} = f_{ext,n+1/2},$$
$$\epsilon_{n+1} = \epsilon_{n+1}^{HW},$$
$$\frac{q_{n+1} - q_n}{\Delta t} = v^*,$$
$$\sigma_{n+1/2}^{HW} = DV_{int}(\epsilon_{n+1/2}^{HW}). \tag{4.20}$$

Here, v^* and σ^{HW^*} are the sum of conserving and dissipating parts

$$v^* = v_{cons} + v_{diss},$$
$$\sigma^{HW^*} = \sigma_{cons}^{HW} + \sigma_{diss}^{HW}, \tag{4.21}$$

where the conserving parts correspond to the middle-point approximations, i.e. $\sigma_{cons}^{HW} = \sigma_{n+1/2}^{HW}$, $v_{cons} = v_{n+1/2}$. The velocity and spring force terms with subscript *diss* are left undefined. They will be designed to generate controllable decay of kinetic and internal energy and to generate conservation of angular momentum.

4.2.2.3 Constants of motion for time discrete equations

Discrete counterparts of the balance laws, developed in Section 4.2.2.1, are derived below. Let us check whether the time discrete Eqs. (4.20) and (4.21) conserve the fundamental constants of motion. For this purpose, we multiply (4.20)$_1$ and (4.20)$_4$ with variations, make their sum and take (4.21)$_2$ into account, to get the discrete version of Eq. (4.12):

$$\delta q \cdot \left(M \frac{(v_{n+1} - v_n)}{\Delta t} - f_{ext,n+1/2} + D\epsilon(q_{n+1/2})(\sigma_{n+1/2}^{HW} + \sigma_{diss}^{HW}) \right)$$
$$+ \delta\epsilon^{HW}(DV_{int}(\epsilon_{n+1/2}^{HW}) - \sigma_{n+1/2}^{HW}) = 0. \tag{4.22}$$

By using (4.20)$_2$, we arrive at the discrete version of the consistency condition (4.13)

$$\dot{\epsilon}_{n+1/2} = D\epsilon(q_{n+1/2}) \cdot \frac{q_{n+1} - q_n}{\Delta t} = \dot{\epsilon}_{n+1/2}^{HW} = \frac{\epsilon_{n+1}^{HW} - \epsilon_n^{HW}}{\Delta t}. \tag{4.23}$$

Eq. (4.23) follows from the mid-point rule and equality (4.20)$_2$ (applied at the beginning and at the end of the time step):

$$\epsilon_{n+1} = \epsilon_{n+1}^{HW} \implies \epsilon_n + \dot{\epsilon}_{n+1/2}\Delta t = \epsilon_n^{HW} + \dot{\epsilon}_{n+1/2}^{HW}\Delta t \implies \dot{\epsilon}_{n+1/2} = \dot{\epsilon}_{n+1/2}^{HW} \tag{4.24}$$

Eqs. (4.22), (4.23), (4.20)$_3$ and (4.21)$_1$ will be used to prove that the chosen time discretization preserves the constants of motion.

To check for the energy, we use $(\delta q, \delta\epsilon^{HW}) = (q_{n+1} - q_n, \epsilon_{n+1}^{HW} - \epsilon_n^{HW})$ for admissible variations that recast (4.22) as

$$(\boldsymbol{q}_{n+1} - \boldsymbol{q}_n) \cdot \left(\boldsymbol{M} \frac{\boldsymbol{v}_{n+1} - \boldsymbol{v}_n}{\Delta t} - \boldsymbol{f}_{ext,n+1/2} + D\epsilon(\boldsymbol{q}_{n+1/2}) \left(\sigma_{n+1/2}^{HW} + \sigma_{diss}^{HW} \right) \right)$$
$$+(\epsilon_{n+1}^{HW} - \epsilon_n^{HW}) \left(DV_{int}(\epsilon_{n+1/2}^{HW}) - \sigma_{n+1/2}^{HW} \right) = 0 \tag{4.25}$$

Considering the consistency condition (4.23), the expression (4.25) can be simplified as

$$(\boldsymbol{q}_{n+1} - \boldsymbol{q}_n) \cdot \left(\boldsymbol{M} \frac{(\boldsymbol{v}_{n+1} - \boldsymbol{v}_n)}{\Delta t} - \boldsymbol{f}_{ext,n+1/2} \right) + (\epsilon_{n+1}^{HW} - \epsilon_n^{HW}) DV_{int}(\epsilon_{n+1/2}^{HW})$$
$$+\sigma_{diss}^{HW}(\epsilon_{n+1}^{HW} - \epsilon_n^{HW}) = 0. \tag{4.26}$$

By taking into account the remaining two Eqs. (4.20)₃ and (4.21)₁, we finally arrive at

$$\underbrace{\boldsymbol{v}_{n+1/2} \cdot \boldsymbol{M}(\boldsymbol{v}_{n+1} - \boldsymbol{v}_n)}_{K_{n+1} - K_n} - \underbrace{(\boldsymbol{q}_{n+1} - \boldsymbol{q}_n) \cdot \boldsymbol{f}_{ext,n+1/2}}_{\Delta W} + \underbrace{(\epsilon_{n+1}^{HW} - \epsilon_n^{HW}) \, DV_{int}(\epsilon_{n+1/2}^{HW})}_{V_{int,n+1} - V_{int,n}}$$
$$+ \underbrace{\boldsymbol{v}_{diss} \cdot \boldsymbol{M}(\boldsymbol{v}_{n+1} - \boldsymbol{v}_n) + \sigma_{diss}^{HW}(\epsilon_{n+1}^{HW} - \epsilon_n^{HW})}_{\Delta \mathcal{D}} = 0 \tag{4.27}$$
$$\Rightarrow K_{n+1} - K_n - \Delta W + V_{int,n+1} - V_{int,n} + \Delta \mathcal{D} = 0,$$

where

$$DV_{int}(\epsilon_{n+1/2}^{HW}) (\epsilon_{n+1}^{HW} - \epsilon_n^{HW}) = V_{int}(\epsilon_{n+1}^{HW}) - V_{int}(\epsilon_n^{HW}) \tag{4.28}$$

was applied, which follows from the quadratic form of V_{int}, see (4.4). In (4.27), ΔW represents the incremental work of external loading, and $\Delta \mathcal{D}$ is energy dissipation. Note that $\boldsymbol{v}_{diss}$ and σ_{diss}^{HW} have to be such that $\Delta \mathcal{D} \geq 0$, because the dissipation should not be negative. For $\Delta W = 0$, the energy at t_{n+1} equals $E_{n+1} = E_n - \Delta \mathcal{D}$. Thus, the energy is decaying. For $\Delta W = \Delta \mathcal{D} = 0$, one has $E_{n+1} = E_n$.

To check for the preservation of linear momentum, let us choose $(\delta \boldsymbol{q}, \delta \epsilon^{HW}) = (\boldsymbol{q}_{n+1} - \boldsymbol{q}_n, \epsilon_{n+1}^{HW} - \epsilon_n^{HW}) = (\boldsymbol{c}, 0)$ for $\forall \boldsymbol{c} \in \mathbb{R}^3$, and assume zero external loading (i.e. rigid body translation of the system). The consistency condition (4.23) for this choice indicates no change in the strain state because

$$0 = \epsilon_{n+1}^{HW} - \epsilon_n^{HW} = D\epsilon(\boldsymbol{q}_{n+1/2}) \cdot (\boldsymbol{q}_{n+1} - \boldsymbol{q}_n) \tag{4.29}$$

and Eq. (4.26) simplifies to

$$\boldsymbol{c} \cdot \boldsymbol{M} \frac{(\boldsymbol{v}_{n+1} - \boldsymbol{v}_n)}{\Delta t} = \boldsymbol{c} \cdot \frac{1}{\Delta t}(\boldsymbol{L}_{n+1} - \boldsymbol{L}_n) = 0 \Rightarrow \boldsymbol{L}_{n+1} = \boldsymbol{L}_n, \tag{4.30}$$

yielding the discrete conservation of linear momentum. In order to check for the conservation of angular momentum, we use $(\delta \boldsymbol{q}, \delta \epsilon^{HW}) = (\boldsymbol{q}_{n+1} - \boldsymbol{q}_n, \epsilon_{n+1}^{HW} - \epsilon_n^{HW}) = (\boldsymbol{c} \times \boldsymbol{q}_{n+1/2}, 0)$ at zero external loading (i.e. rigid body rotation of the system). Because Eq. (4.29) remains valid, we can now recast (4.26) as

$$\boldsymbol{c} \cdot \frac{1}{\Delta t} \boldsymbol{q}_{n+1/2} \times \boldsymbol{M}(\boldsymbol{v}_{n+1} - \boldsymbol{v}_n) = 0 \tag{4.31}$$

where we have already applied the scalar triple product rule. It can be shown that the change of the angular momentum can be written as

$$\boldsymbol{J}_{n+1} - \boldsymbol{J}_n = \boldsymbol{q}_{n+1/2} \times \boldsymbol{M}(\boldsymbol{v}_{n+1} - \boldsymbol{v}_n) - \boldsymbol{M}\boldsymbol{v}_{n+1/2} \times (\boldsymbol{q}_{n+1} - \boldsymbol{q}_n). \tag{4.32}$$

By comparing (4.31) and (4.32), we can conclude that the conservation of angular momentum is ensured if the second term on the right-hand side of (4.32) is zero, which holds for $\boldsymbol{v}_{n+1/2} \parallel (\boldsymbol{q}_{n+1} - \boldsymbol{q}_n)$. In view of (4.20)₃ and (4.21)₁, $\boldsymbol{v}_{diss} \parallel \boldsymbol{v}_{n+1/2}$ is demanded, which is another constraint on $\boldsymbol{v}_{diss}$. Thus, any $\boldsymbol{v}_{diss}$ with $\boldsymbol{v}_{diss} \cdot \boldsymbol{v}_{n+1/2} = \boldsymbol{0}$ guarantees the proposed scheme to conserve angular momentum.

4.2.3   3-field Hellinger-Reissner formulation

Let us introduce spring force σ^{HR} as an independent variable along with position vector $\boldsymbol{q}$ and velocity $\boldsymbol{v}$. This allows for the extension of the functional (4.4) as

$$G_{HR}\left(\boldsymbol{q},\boldsymbol{v},\sigma^{HR}\right) = \int_{t_0}^{t_e}\left(\left(\dot{\boldsymbol{q}}-\frac{1}{2}\boldsymbol{v}\right)\cdot\boldsymbol{M}\boldsymbol{v}-\underbrace{\left(\epsilon(\boldsymbol{q})\,\sigma^{HR}-\frac{1}{2}\sigma^{HR}\,C^{-1}\,\sigma^{HR}\right)}_{V_{int}(\dot{q},\sigma^{HR})}-V_{ext}(\boldsymbol{q})\right)dt. \quad (4.33)$$

Its stationarity has the following form

$$\delta G_{HR}\left(\boldsymbol{q},\boldsymbol{v},\sigma^{HR};\delta\boldsymbol{q},\delta\boldsymbol{v},\delta\sigma^{HR}\right) = \int_{t_0}^{t_e}(\delta\dot{\boldsymbol{q}}\cdot\boldsymbol{M}\boldsymbol{v}+\boldsymbol{M}\delta\boldsymbol{v}\cdot(\dot{\boldsymbol{q}}-\boldsymbol{v})$$
$$-\delta\epsilon(\boldsymbol{q})\sigma^{HR}+\delta\sigma^{HR}\left(C^{-1}\sigma^{HR}-\epsilon(\boldsymbol{q})\right)-\delta\boldsymbol{q}\cdot\boldsymbol{f}_{ext})dt = 0 \quad (4.34)$$

which can be rearranged by following the same steps as in Section 4.2.2 to get

$$\delta G_{HR}\left(\boldsymbol{q},\boldsymbol{v},\sigma^{HR};\delta\boldsymbol{q},\delta\boldsymbol{v},\delta\sigma^{HR}\right) = \int_{t_0}^{t_e}(\delta\boldsymbol{q}\cdot(-\boldsymbol{M}\dot{\boldsymbol{v}}+\boldsymbol{f}_{ext}-D\epsilon(\boldsymbol{q})\sigma^{HR})$$
$$+\boldsymbol{M}\delta\boldsymbol{v}\cdot(\dot{\boldsymbol{q}}-\boldsymbol{v})+\delta\sigma^{HR}\cdot\left(C^{-1}\sigma^{HR}-\epsilon(\boldsymbol{q})\right)\Big)dt = 0. \quad (4.35)$$

Thus, the following Euler-Lagrange equations of motions can be obtained

$$\boldsymbol{M}\dot{\boldsymbol{v}}+D\epsilon(\boldsymbol{q})\sigma^{HR} = \boldsymbol{f}_{ext},$$
$$\dot{\boldsymbol{q}} = \boldsymbol{v}, \quad (4.36)$$
$$C^{-1}\sigma^{HR} = \epsilon(\boldsymbol{q}).$$

The first equation in (4.36) represents the equilibrium of inertial, internal and external forces, the second equation relates velocity to the derivative of position vector, and the third equation is the constitutive one. Eqs. (4.36) are supplemented by the initial conditions for $\dot{\boldsymbol{v}}, \dot{\boldsymbol{q}}$ and σ^{HR}, which have to be consistent with the initial $\boldsymbol{q}$ and $\boldsymbol{v}$ according to (4.36)₂ and (4.36)₃.

4.2.3.1   Balance laws

In order to check if Eqs. (4.36) conserve the total energy, linear momentum and angular momentum, we multiply (4.36)₁ with variation

$$\delta\boldsymbol{q}\cdot(\boldsymbol{M}\dot{\boldsymbol{v}}-\boldsymbol{f}_{ext}+D\epsilon(\boldsymbol{q})\sigma^{HR}) = 0, \quad (4.37)$$

and introduce the consistency condition, which comes from time derivation of (4.36)₃

$$C^{-1}\dot{\sigma}^{HR} = \dot{\epsilon}(\boldsymbol{q}) = D\epsilon(\boldsymbol{q})\cdot\dot{\boldsymbol{q}}. \quad (4.38)$$

Thus, Eqs. (4.37), (4.38) and (4.36)₂ will be used for the check. Note that the time derivative of potential energy $V = V_{int}+V_{ext}$ is

$$\dot{V} = \underbrace{\dot{\boldsymbol{q}}\cdot D\epsilon(\boldsymbol{q})\sigma^{HR}+\epsilon(\boldsymbol{q})\,\dot{\sigma}^{HR}-\sigma^{HR}\,C^{-1}\,\dot{\sigma}^{HR}}_{=\,\epsilon(\boldsymbol{q})\,\dot{\sigma}^{HR},\ \text{see (4.38)}}-\boldsymbol{f}_{ext}\cdot\dot{\boldsymbol{q}} \quad (4.39)$$

Choosing $\delta\boldsymbol{q} = \dot{\boldsymbol{q}}$ for admissible variation in (4.37), yields

$$\dot{\boldsymbol{q}}\cdot\boldsymbol{M}\dot{\boldsymbol{v}}-\dot{\boldsymbol{q}}\cdot\boldsymbol{f}_{ext}+\dot{\boldsymbol{q}}\cdot D\epsilon(\boldsymbol{q})\sigma^{HR} = 0. \quad (4.40)$$

Taking into account (4.36)₂ in (4.40) gives

$$\underbrace{\boldsymbol{M}\boldsymbol{v}\cdot\dot{\boldsymbol{v}}}_{\dot{K}}+\underbrace{\underbrace{(-\dot{\boldsymbol{q}}\cdot\boldsymbol{f}_{ext})}_{\dot{V}_{ext}}+\underbrace{\overbrace{\dot{\boldsymbol{q}}\cdot D\epsilon(\boldsymbol{q})\sigma^{HR}}^{=\,\epsilon(\boldsymbol{q})\,\dot{\sigma}^{HR},\ \text{see (4.38), (4.36)}_3}}_{=\,\dot{V}_{int},\ \text{see (4.39)}}}_{\dot{V}} = 0 \Rightarrow \dot{K}+\dot{V} = 0. \quad (4.41)$$

Eq. (4.41) shows that the power of external forces equals the sum of changes of kinetic and deformation energy. In order to check for the preservation of linear momentum, we choose $\delta q = \dot{q} = c$, i.e. rigid translation of the system for which $\dot{\sigma}^{HR} = 0$, assume zero external loading and apply (4.38), which changes Eq. (4.40) into

$$c \cdot M\dot{v} = c \cdot \dot{L} = 0 \Rightarrow \dot{L} = 0 \tag{4.42}$$

showing the conservation of linear momentum. To check for the angular momentum, we may choose $\delta q = \dot{q} = c \times q$ for admissible variations at zero external loading, i.e. rigid rotation of the system. Eq. (4.38) still holds and Eq. (4.40) gives

$$(c \times q) \cdot M\dot{v} = 0 \tag{4.43}$$

With the triple scalar product rule, the expression in (4.43) can be rewritten as for the Hu-Washizu formulation, demonstrating the conservation of angular momentum $\dot{J} = 0$.

4.2.3.2 Discretization in time

Let us adopt the following (mid-point) approximations for the time discretization of Eqs. (4.36)

$$M\frac{(v_{n+1} - v_n)}{\Delta t} + D\epsilon(q_{n+1/2})\sigma^{HR^*} = f_{ext,n+1/2},$$

$$\frac{q_{n+1} - q_n}{\Delta t} = v^*, \tag{4.44}$$

$$C^{-1}\sigma_{n+1}^{HR} = \epsilon_{n+1},$$

where v^* and σ^{HR^*} are again assumed as the sum of two parts

$$v^* = v_{cons} + v_{diss}$$
$$\sigma^{HR*} = \sigma_{cons}^{HR} + \sigma_{diss}^{HR} \tag{4.45}$$

where the conserving parts correspond to the middle-point approximations, while v_{diss} and σ_{diss}^{HR} are left undefined. The motivation behind the discretization in (4.44) and (4.45) is the construction of a time-stepping scheme that allows for numerical decay of the total energy and preservation of linear and angular momentum.

4.2.3.3 Constants of motion for time discrete equations

Let us check if the discretized counterparts (4.44) and (4.45) of Eqs. (4.36) preserve the constants of motion. To this end, we multiply (4.44)₁ with variation and take into account (4.45)₂ to get

$$\delta q \cdot \left(M\frac{v_{n+1} - v_n}{\Delta t} + D\epsilon(q_{n+1/2})\left(\sigma_{n+1/2}^{HR} + \sigma_{diss}^{HR}\right) - f_{ext,n+1/2}\right) = 0. \tag{4.46}$$

The application of (4.44)₃ (at the beginning and at the end of the time step), along with the mid-point rule, gives an expression, which is the discrete version of the consistency condition (4.38)

$$C^{-1}\dot{\sigma}_{n+1/2}^{HR} = C^{-1}\frac{(\sigma_{n+1}^{HR} - \sigma_n^{HR})}{\Delta t} = \frac{\epsilon_{n+1} - \epsilon_n}{\Delta t} = \dot{\epsilon}_{n+1/2} = D\epsilon(q_{n+1/2}) \cdot \frac{(q_{n+1} - q_n)}{\Delta t}. \tag{4.47}$$

In order to check for the energy, let us use $\delta q = (q_{n+1} - q_n)$ in (4.46) to get

$$(q_{n+1} - q_n) \cdot M\frac{v_{n+1} - v_n}{\Delta t} + \underbrace{(q_{n+1} - q_n) \cdot D\epsilon(q_{n+1/2})}_{=\epsilon_{n+1}-\epsilon_n, \text{ see } (4.47)}\left(\sigma_{n+1/2}^{HR} + \sigma_{diss}^{HR}\right)$$
$$-(q_{n+1} - q_n) \cdot f_{ext,n+1/2} = 0. \tag{4.48}$$

By noting that

$$V_{int,n+1} - V_{int,n} = \epsilon_{n+1}\,\sigma_{n+1}^{HR} - \frac{1}{2}\sigma_{n+1}^{HR}\,C^{-1}\sigma_{n+1}^{HR}$$

$$-\left(\epsilon_n\,\sigma_n^{HR} - \frac{1}{2}\sigma_n^{HR}\,C^{-1}\sigma_n^{HR}\right) \overset{(4.44)_3}{\;\hat{=}\;} \frac{1}{2}\epsilon_{n+1}\,\sigma_{n+1}^{HR} - \frac{1}{2}\epsilon_n\,\sigma_n^{HR},$$

(4.49)

and considering $(4.44)_2$, $(4.44)_3$ and $(4.45)_1$ in (4.48), we obtain

$$\underbrace{\boldsymbol{v}_{n+1/2}\cdot\boldsymbol{M}(\boldsymbol{v}_{n+1}-\boldsymbol{v}_n)}_{K_{n+1}-K_n} + \underbrace{\frac{1}{2}\epsilon_{n+1}\,\sigma_{n+1}^{HR} - \frac{1}{2}\epsilon_n\,\sigma_n^{HR}}_{V_{int,n+1}-V_{int,n}}$$

$$-\underbrace{(\boldsymbol{q}_{n+1}-\boldsymbol{q}_n)\cdot\boldsymbol{f}_{ext,n+1/2}}_{\Delta W} + \underbrace{\boldsymbol{v}_{diss}\cdot\boldsymbol{M}(\boldsymbol{v}_{n+1}-\boldsymbol{v}_n) + \sigma_{diss}^{HR}(\epsilon_{n+1}-\epsilon_n)}_{\Delta\mathcal{D}} = 0$$

(4.50)

$$\Rightarrow K_{n+1} - K_n + V_{int,n+1} - V_{int,n} - \Delta W + \Delta\mathcal{D} = 0.$$

In (4.50), $\Delta\mathcal{D}$ is energy dissipation, which has the same structure as in Section 4.2.2, and ΔW is incremental work of external loading. The undefined terms $\boldsymbol{v}_{diss}$ and σ_{diss}^{HR} should yield $\Delta\mathcal{D} \geq 0$.

To check for the linear momentum, let us choose $\delta\boldsymbol{q} = \boldsymbol{q}_{n+1} - \boldsymbol{q}_n = \boldsymbol{c}$ at zero external loading, i.e. rigid translation of the system, for which $\sigma_{n+1}^{HR} - \sigma_n^{HR} = 0$. In this case, Eq. (4.48) simplifies to

$$\boldsymbol{c}\cdot\boldsymbol{M}\frac{\boldsymbol{v}_{n+1}-\boldsymbol{v}_n}{\Delta t} = \boldsymbol{c}\cdot\frac{1}{\Delta t}(\boldsymbol{L}_{n+1}-\boldsymbol{L}_n) = 0,$$

(4.51)

demonstrating conservation of linear momentum. To check for the angular momentum, let us apply $\delta\boldsymbol{q} = (\boldsymbol{q}_{n+1} - \boldsymbol{q}_n) = (\boldsymbol{c}\times\boldsymbol{q}_{n+1/2})$ at zero external loading, i.e. rigid body rotation of the system, which simplifies Eq. (4.48) into

$$\boldsymbol{c}\cdot\frac{1}{\Delta t}\boldsymbol{q}_{n+1/2}\times\boldsymbol{M}(\boldsymbol{v}_{n+1}-\boldsymbol{v}_n) = 0.$$

(4.52)

Following the same line of reasoning as for the Hu-Washizu formulation, we can show that angular momentum is conserved for the chosen discretization in time if $\boldsymbol{v}_{diss}\parallel\boldsymbol{v}_{n+1/2}$.

4.3   Shell formulations

In this section, we derive mixed dynamic formulations for the inextensible-director, large rotation shell model with Reissner-Mindlin kinematics, the detailed description of which is given in Section 2.2.1., by using the procedures illustrated in the previous section for the spring pendulum.

4.3.1   Shell model and 2-field formulation

As the detailed description of the considered static shell formulation was given in Section 2.2.1, we will only highlight here the relations that play a significant role in the development of dynamic formulation.

The position vectors at the initial and deformed configurations are the following functions of convected curvilinear coordinates $(\xi^1,\xi^2)\in M\subset\mathbb{R}^2$, through-the-thickness coordinate $\xi^3\in[-t/2,t/2]$, and time $t_0\leq t\leq t_e$

$$\boldsymbol{X}(\xi^1,\xi^2,\xi^3) = \boldsymbol{X}_0(\xi^1,\xi^2) + \xi^3\boldsymbol{D}(\xi^1,\xi^2)\;\; \text{at } t_0,$$

$$\boldsymbol{x}(\xi^1,\xi^2,\xi^3) = \underbrace{\boldsymbol{X}_0(\xi^1,\xi^2) + \boldsymbol{u}(\xi^1,\xi^2)}_{\boldsymbol{x}_0(\xi^1,\xi^2)} + \xi^3\boldsymbol{d}(\xi^1,\xi^2)\;\text{at } t > t_0.$$

(4.53)

Here, M is given parametric domain that is mapped by $\boldsymbol{X}_0$ and $\boldsymbol{x}_0$ into shell mid-surface, and t is the initial shell thickness. Furthermore, $\boldsymbol{u}$ is mid-surface displacement vector, $\boldsymbol{D}$ is unit normal vector to the

initial mid-surface, called shell director, and $\boldsymbol{d}$ is its mapping at deformed configuration, which is generated by no-drill rotation $\boldsymbol{\Lambda}(\boldsymbol{\vartheta})$ as $\mathbb{R}^2 \ni \boldsymbol{\vartheta} \mapsto \boldsymbol{d} = \boldsymbol{\Lambda}(\boldsymbol{\vartheta})\boldsymbol{e}_3 \in \mathbb{R}^3$, where $\boldsymbol{\vartheta}$ are large rotation parameters and $\boldsymbol{e}_3 = [0,0,1]^T$. As $\boldsymbol{X}_0$ and $\boldsymbol{D}$ are given, shell motion is described through the configuration and velocity spaces with elements $\boldsymbol{\Phi} = [\boldsymbol{u}^T, \boldsymbol{d}^T]^T : M \mapsto \mathbb{R}^3 \times S^2$ and $\boldsymbol{V} = [\boldsymbol{v}^T, \boldsymbol{\omega}^T]^T :$ $M \mapsto \mathbb{R}^3 \times T_d S^2$, where $\boldsymbol{v}$ is mid-surface velocity and $\boldsymbol{\omega}$ is velocity of shell director. The unit sphere and its tangent space are defined as $S^2 := \{\boldsymbol{d} \in \mathbb{R}^3 \mid \parallel \boldsymbol{d} \parallel = 1\}$ and $T_d S^2 := \{\boldsymbol{\omega} \in \mathbb{R}^3 \mid \boldsymbol{\omega} \cdot \boldsymbol{d} = 0\}$.

The "in-plane" covariant components of the Green-Lagrange strain tensor (dependent on $\boldsymbol{\Phi}$) are expressed with respect to the contravariant base vectors, see (2.6). They can be further transformed to the previously defined Cartesian basis $\{\hat{\boldsymbol{e}}_1, \hat{\boldsymbol{e}}_2, \hat{\boldsymbol{e}}_3 \equiv \boldsymbol{D}\}$, see (2.9), and collected into three vectors of Cartesian membrane, bending and transverse shear strains $\boldsymbol{\varepsilon} = [\hat{\varepsilon}_{11}, \hat{\varepsilon}_{22}, 2\hat{\varepsilon}_{12}]^T$, $\boldsymbol{\kappa} = [\hat{\kappa}_{11}, \hat{\kappa}_{22}, 2\hat{\kappa}_{12}]^T$ and $\boldsymbol{\gamma} = [2\hat{\varepsilon}_{13}, 2\hat{\varepsilon}_{23}]^T$, respectively, where $\widehat{}$ is used to denote the Cartesian component. Let us adopt the Saint Venant-Kirchhoff shell material model, which allows us to easily define the energy conjugated second Piola-Kirchhoff shell stress resultants with respect to the local Cartesian basis at the mid-surface point under consideration. The constitutive stress resultants are grouped into vectors of membrane forces, bending moments, and transverse shear forces as $\boldsymbol{N} = \left[\widehat{N}_{11}, \widehat{N}_{22}, \widehat{N}_{12}\right]^T$, $\boldsymbol{M} = \left[\widehat{M}_{11}, \widehat{M}_{22}, \widehat{M}_{12}\right]^T$ and $\boldsymbol{Q} = \left[\widehat{Q}_{13}, \widehat{Q}_{23}\right]^T$, respectively. The following relations apply: $\boldsymbol{N} = \mathbf{C}^m \boldsymbol{\varepsilon}$, $\boldsymbol{M} = \mathbf{C}^b \boldsymbol{\kappa}$, $\boldsymbol{Q} = \mathbf{C}^s \boldsymbol{\gamma}$, where $\mathbf{C}^m$, $\mathbf{C}^b$ and $\mathbf{C}^s$ are the standard membrane, bending and transverse shear constitutive matrices for the inextensible-director shell model, respectively, found in Section 2.2.1. The shell strains and the constitutive stress resultants can be written as

$$\begin{aligned} \boldsymbol{\epsilon} &= \boldsymbol{\epsilon}(\boldsymbol{\Phi}) = [\boldsymbol{\varepsilon}^T, \boldsymbol{\kappa}^T, \boldsymbol{\gamma}^T]^T, \\ \boldsymbol{\sigma} &= \boldsymbol{\sigma}(\boldsymbol{\Phi}) = [\boldsymbol{N}^T, \boldsymbol{M}^T, \boldsymbol{Q}^T]^T, \end{aligned} \tag{4.54}$$

where the following relation applies $\boldsymbol{\sigma} = \partial W / \partial \boldsymbol{\epsilon} = \mathbf{C}\,\boldsymbol{\epsilon}$, where $W(\boldsymbol{\epsilon})$ denotes the strain energy function of quadratic form $W(\boldsymbol{\epsilon}) = \boldsymbol{\epsilon} \cdot \boldsymbol{C}\boldsymbol{\epsilon}/2$ and $\mathbf{C} = \mathrm{DIAG}[\mathbf{C}^m, \mathbf{C}^b, \mathbf{C}^s]$.

The 2-field functional is given as

$$G(\boldsymbol{\Phi}, \boldsymbol{V}) = \int_{t_0}^{t_e} \int_M \left(\left(\dot{\boldsymbol{\Phi}} - \frac{1}{2}\boldsymbol{V} \right) \cdot \boldsymbol{M}_{\rho 0} \boldsymbol{V} - W\big(\boldsymbol{\epsilon}(\boldsymbol{\Phi})\big) \right) dA dt - \int_{t_0}^{t_e} V_{ext}(\boldsymbol{\Phi}) dt, \tag{4.55}$$

where the potential of the external loads V_{ext} is defined as Π_{ext} in (2.14). $\boldsymbol{M}_{\rho 0}$ is the mass matrix

$$\boldsymbol{M}_{\rho 0} = \begin{bmatrix} A_{\rho 0}\boldsymbol{I} & \mathbf{0} \\ \mathbf{0} & I_{\rho 0}\boldsymbol{I} \end{bmatrix}, \tag{4.56}$$

with A_0 and I_0 as the middle surface mass density and the inertia of the shell director, respectively, given as

$$A_0 = \int_{-t/2}^{t/2} \rho_0 \, d\xi^3 = \rho\, t, \qquad I_0 = \int_{-t/2}^{t/2} \rho_0 \, (\xi^3)^2 d\xi^3 = \rho_0 \frac{t^3}{12} \tag{4.57}$$

and ρ_0 is the initial mass density. By imposing the stationarity condition $\delta G = 0$ on (4.55), we arrive at the following Euler-Lagrange equations (see e.g. [132] for details)

$$\int_M \big(\delta\boldsymbol{\Phi} \cdot \boldsymbol{M}_{\rho 0} \dot{\boldsymbol{V}} + \delta\boldsymbol{\epsilon} \cdot \boldsymbol{\sigma}\big) dA = -V_{ext}(\delta\boldsymbol{\Phi}),$$

$$\int_M \delta\boldsymbol{V} \cdot \big(\dot{\boldsymbol{\Phi}} - \boldsymbol{V}\big) dA = 0. \tag{4.58}$$

where $\delta\boldsymbol{\Phi} = [\delta\boldsymbol{u}^T, \delta\boldsymbol{d}^T]^T$, $\delta\boldsymbol{V} = [\delta\boldsymbol{v}^T, \delta\boldsymbol{\omega}^T]^T$ and $\delta\boldsymbol{\epsilon} = d/d\chi[\boldsymbol{\epsilon}(\boldsymbol{\Phi} + \chi\delta\boldsymbol{\Phi})]_{\chi=0}$. We note that the constraint $\delta\boldsymbol{d} \in T_{\boldsymbol{d}}S^2$, thus $\delta\boldsymbol{d} \cdot \boldsymbol{d} = 0$, apply.

4.3.1.1   Discretization in time

For the above described formulation, the balance laws have been derived in e.g. [132], and we refrain from further detailing. However, for the sake of comparison with the time discrete versions of the Hu-Washizu and Hellinger-Reissner formulations that will be presented in sections below, let us give the time discrete counterparts of Eqs. (4.58) that are based on the mid-point rule

$$\int_M \left(\delta\boldsymbol{\Phi} \cdot \boldsymbol{M}_{\rho 0} \frac{\boldsymbol{V}_{n+1} - \boldsymbol{V}_n}{\Delta t} + \delta\boldsymbol{\epsilon}(\boldsymbol{\Phi}_{n+1/2}, \delta\boldsymbol{\Phi}) \cdot \boldsymbol{\sigma}^* \right) dA = -V_{ext}(\delta\boldsymbol{\Phi}),$$

$$\int_M \delta\boldsymbol{V} \cdot \left(\frac{\boldsymbol{\Phi}_{n+1} - \boldsymbol{\Phi}_n}{\Delta t} - \boldsymbol{V}^* \right) dA = 0,$$

$$\tag{4.59}$$

with external loading in $V_{ext}(\delta\boldsymbol{\Phi})$ evaluated at $t_{n+1/2}$, and $\boldsymbol{V}^*$ and $\boldsymbol{\sigma}^*$ of the following form

$$\boldsymbol{V}^* = \boldsymbol{V}_{cons} + \boldsymbol{V}_{diss},$$
$$\boldsymbol{\sigma}^* = \boldsymbol{\sigma}_{cons} + \boldsymbol{\sigma}_{diss}.$$

$$\tag{4.60}$$

The conserving parts refer to the midpoint approximations used for the energy conserving scheme $\boldsymbol{\sigma}_{cons} = \boldsymbol{\sigma}_{n+1/2}$, $\boldsymbol{V}_{cons} = \boldsymbol{V}_{n+1/2}$. The terms with $diss$ in (4.60) are left undefined for the moment, having in mind that they will be used to ensure the desired dissipation and conservation properties of the time-stepping algorithm. It is worth noting that the variations $\delta\boldsymbol{\Phi}$ in (4.59) are associated with the mid-point, thus $\delta\boldsymbol{d} \in T_{\overline{\boldsymbol{d}}_{n+1/2}}S^2$, where $\overline{\boldsymbol{d}}_{n+1/2} = \boldsymbol{d}_{n+1/2}/\|\boldsymbol{d}_{n+1/2}\|$ is of unit length, which implies the constraint $\delta\boldsymbol{d} \cdot \boldsymbol{d}_{n+1/2} = 0$. As for the variation of strains in (4.59), $\delta\boldsymbol{\epsilon}(\boldsymbol{\Phi}_{n+1/2}, \delta\boldsymbol{\Phi}) = d/d\chi[\boldsymbol{\epsilon}(\boldsymbol{\Phi}_{n+1/2} + \chi\delta\boldsymbol{\Phi})]_{\chi=0}$, which leads to the following result (see (2.7)–(2.16))

$$\delta\boldsymbol{\epsilon} = \boldsymbol{T} \left(\frac{\partial\boldsymbol{\epsilon}_{n+1/2}}{\partial\boldsymbol{\Phi}_{n+1/2}}\delta\boldsymbol{\Phi} + \sum_{\beta=1}^{2} \frac{\partial\boldsymbol{\epsilon}_{n+1/2}}{\partial(\boldsymbol{\Phi}_{n+1/2})_{,\beta}}\delta\boldsymbol{\Phi}_{,\beta} \right),$$

$$\tag{4.61}$$

where (the notation $\boldsymbol{x}_{0_{n+1/2}} = \boldsymbol{x}_0$ and $\boldsymbol{d}_{n+1/2} = \boldsymbol{d}$ is used here)

$$\frac{\partial\boldsymbol{\epsilon}_{n+1/2}}{\partial\boldsymbol{\Phi}_{n+1/2}} = \begin{bmatrix} \boldsymbol{0}_{3\times3} & \boldsymbol{0}_{3\times3} \\ \boldsymbol{0}_{3\times3} & \boldsymbol{0}_{3\times3} \\ \boldsymbol{0}_{2\times3} & \begin{bmatrix} \boldsymbol{x}_{0,1}^T \\ \boldsymbol{x}_{0,2}^T \end{bmatrix} \end{bmatrix}, \quad \frac{\partial\boldsymbol{\epsilon}_{n+1/2}}{\partial(\boldsymbol{\Phi}_{n+1/2})_{,1}} = \begin{bmatrix} \boldsymbol{x}_{0,1}^T & \boldsymbol{0}^T \\ \boldsymbol{0}^T & \boldsymbol{0}^T \\ \boldsymbol{x}_{0,2}^T & \boldsymbol{0}^T \\ \boldsymbol{d}_{,1}^T & \boldsymbol{x}_{0,1}^T \\ \boldsymbol{0}^T & \boldsymbol{0}^T \\ \boldsymbol{d}_{,2}^T & \boldsymbol{x}_{0,2}^T \\ \boldsymbol{d}^T & \boldsymbol{0}^T \\ \boldsymbol{0}^T & \boldsymbol{0}^T \end{bmatrix}, \quad \frac{\partial\boldsymbol{\epsilon}_{n+1/2}}{\partial(\boldsymbol{\Phi}_{n+1/2})_{,2}} = \begin{bmatrix} \boldsymbol{0}^T & \boldsymbol{0}^T \\ \boldsymbol{x}_{0,2}^T & \boldsymbol{0}^T \\ \boldsymbol{x}_{0,1}^T & \boldsymbol{0}^T \\ \boldsymbol{0}^T & \boldsymbol{0}^T \\ \boldsymbol{d}_{,2}^T & \boldsymbol{x}_{0,2}^T \\ \boldsymbol{d}_{,1}^T & \boldsymbol{x}_{0,1}^T \\ \boldsymbol{0}^T & \boldsymbol{0}^T \\ \boldsymbol{d}^T & \boldsymbol{0}^T \end{bmatrix}. \tag{4.62}$$

$\boldsymbol{0}^T = [0,0,0]$ and $\boldsymbol{T}$ performs transformation of the covariant strains to the local Cartesian strains, as was shown in Sections 0 and 2.4 for different mixed formulations. The proof that the above time discretization conserves/decays total energy and preserves linear and angular momentum will be omitted (see e.g. [132] for details).

4.3.2   4-field Hu-Washizu formulation

Following the procedure outlined in Section 4.2.2, the 4-field Hu-Washizu functional for the considered shell model is

$$G_{HW}(\boldsymbol{\Phi}, \boldsymbol{V}, \boldsymbol{\epsilon}^{HW}, \boldsymbol{\sigma}^{HW}) =$$

$$\int_{t_0}^{t_e} \int_M \left(\left(\dot{\boldsymbol{\Phi}} - \frac{1}{2}\boldsymbol{V} \right) \cdot \boldsymbol{M}_{\rho 0}\boldsymbol{V} - W(\boldsymbol{\epsilon}^{HW}) - \boldsymbol{\sigma}^{HW} \cdot (\boldsymbol{\epsilon}(\boldsymbol{\Phi}) - \boldsymbol{\epsilon}^{HW}) \right) dAdt - \int_{t_0}^{t_e} V_{ext}(\boldsymbol{\Phi})dt, \qquad (4.63)$$

where we introduced the strain and stress resultant vectors

$$\boldsymbol{\epsilon}^{HW} = [\boldsymbol{\varepsilon}^{HW,T}, \boldsymbol{\kappa}^{HW,T}, \boldsymbol{\gamma}^{HW,T}]^T, \qquad \boldsymbol{\sigma}^{HW} = [\boldsymbol{N}^{HW,T}, \boldsymbol{M}^{HW,T}, \boldsymbol{Q}^{HW,T}]^T, \qquad (4.64)$$

respectively, that are composed of membrane, bending and transverse shear contributions. By using the ideas from Section 4.2.2 and imposing the stationarity condition $\delta G_{HW} = 0$ on (4.63), we arrive at the following Euler-Lagrange equations of motion

$$\int_M \delta\boldsymbol{\Phi} \cdot \boldsymbol{M}_{\rho 0}\dot{\boldsymbol{V}} + \delta\boldsymbol{\epsilon}(\delta\boldsymbol{\Phi}, \boldsymbol{\Phi}) \cdot \boldsymbol{\sigma}^{HW} dA = -V_{ext}(\delta\boldsymbol{\Phi}),$$

$$\int_M \delta\boldsymbol{\sigma}^{HW} \cdot (\boldsymbol{\epsilon}(\boldsymbol{\Phi}) - \boldsymbol{\epsilon}^{HW})dA = 0,$$

$$\int_M \delta\boldsymbol{V} \cdot (\dot{\boldsymbol{\Phi}} - \boldsymbol{V})dA = 0, \qquad\qquad (4.65)$$

$$\int_M \delta\boldsymbol{\epsilon}^{HW} \cdot (\boldsymbol{\sigma}^{HW} - DW(\boldsymbol{\epsilon}^{HW})dA = 0.$$

The first equation in (4.65) is the weak form of the equilibrium of inertial, internal and external forces, and the other three equations are the weak enforcements of kinematic, constitutive and velocity equations. These equations are supplemented by generalized displacements boundary conditions and initial conditions for $\dot{\boldsymbol{V}}, \dot{\boldsymbol{\Phi}}, \boldsymbol{\epsilon}^{HW}$ and $\boldsymbol{\sigma}^{HW}$ that have to be consistent with initial $\boldsymbol{V}$ and $\boldsymbol{\Phi}$ in view of (4.65).

4.3.2.1 Balance laws

Total linear momentum $\boldsymbol{L}$, total angular momentum $\boldsymbol{J}$ and total energy E are defined as

$$\boldsymbol{L}(\boldsymbol{V}) = \int_M A_{\rho 0}\boldsymbol{v}dA,$$

$$\boldsymbol{J}(\boldsymbol{\Phi}, \boldsymbol{V}) = \int_M \left(A_{\rho 0}\boldsymbol{x}_0 \times \boldsymbol{v} + I_{\rho 0}\boldsymbol{d} \times \boldsymbol{\omega} \right)dA, \qquad (4.66)$$

$$E(\boldsymbol{\Phi}, \boldsymbol{V}, \boldsymbol{\epsilon}^{HW}) = \int_M \left(\frac{1}{2}\boldsymbol{M}_{\rho 0}\boldsymbol{V} \cdot \boldsymbol{V} + W(\boldsymbol{\epsilon}^{HW}) \right)dA + V_{ext}(\boldsymbol{\Phi}).$$

By introducing kinetic energy K and deformation energy V_{int} as

$$K(\boldsymbol{V}) = \int_M \frac{1}{2}\boldsymbol{M}_{\rho 0}\boldsymbol{V} \cdot \boldsymbol{V}dA, \qquad V_{int}(\boldsymbol{\epsilon}^{HW}) = \int_M W(\boldsymbol{\epsilon}^{HW})dA, \qquad (4.67)$$

the total energy can be given as

$$E(\boldsymbol{\Phi}, \boldsymbol{V}, \boldsymbol{\epsilon}^{HW}) = K(\boldsymbol{V}) + \underbrace{V_{int}(\boldsymbol{\epsilon}^{HW}) + V_{ext}(\boldsymbol{\Phi})}_{V(\boldsymbol{\epsilon}^{HW}, \boldsymbol{\Phi})}, \qquad (4.68)$$

where V is the potential energy.

Let us rearrange the Euler-Lagrange equations (4.65) in a manner that proved advantageous for checking conservation of the constants of the motion in Section 4.2.2. To that end, let us make the sum of (4.65)$_1$ and (4.65)$_4$ as

$$\int_M \left(\delta\boldsymbol{\Phi} \cdot \boldsymbol{M}_{\rho 0}\dot{\boldsymbol{V}} + \boldsymbol{\sigma}^{HW} \cdot (\delta\boldsymbol{\epsilon}(\delta\boldsymbol{\Phi}, \boldsymbol{\Phi}) - \delta\boldsymbol{\epsilon}^{HW}) + \delta\boldsymbol{\epsilon}^{HW} \cdot DW(\boldsymbol{\epsilon}^{HW}) \right)dA = -V_{ext}(\delta\boldsymbol{\Phi}), \qquad (4.69)$$

and take the time derivative of (4.65)$_2$ to get the consistency condition

$$\int_M \delta\boldsymbol{\sigma}^{HW} \cdot (\dot{\boldsymbol{\epsilon}} - \dot{\boldsymbol{\epsilon}}^{HW}) dA = 0. \tag{4.70}$$

The rearrangement enables the replacement of the four integral equations in (4.70) with the following three: (4.69), (4.70) and (4.65)$_3$. As shown in Section 4.2.2, this kind of reformulation of the basic equations of the 4-field Hu-Washizu functional allows to prove the balance laws.

By defining the time derivative of the kinetic and deformation energy as (see (4.67))

$$\dot{K} = \int_M \boldsymbol{M}_{\rho 0}\boldsymbol{V} \cdot \dot{\boldsymbol{V}} dA, \qquad \dot{V} = \int_M \dot{\boldsymbol{\epsilon}}^{HW} \cdot DW(\boldsymbol{\epsilon}^{HW}) dA + V_{ext}(\dot{\boldsymbol{\Phi}}), \tag{4.71}$$

where we have taken into account that for the conservative loads $\dot{V}_{ext}(\boldsymbol{\Phi}) = V_{ext}(\dot{\boldsymbol{\Phi}})$, the conservation of the total energy can be proven in the following way. By choosing $(\delta\boldsymbol{\Phi}, \delta\boldsymbol{\epsilon}^{HW}) = (\dot{\boldsymbol{\Phi}}, \dot{\boldsymbol{\epsilon}}^{HW})$ in (4.69), we arrive at

$$\int_M \left(\dot{\boldsymbol{\Phi}} \cdot \boldsymbol{M}_{\rho 0}\dot{\boldsymbol{V}} + \boldsymbol{\sigma}^{HW} \cdot (\dot{\boldsymbol{\epsilon}} - \dot{\boldsymbol{\epsilon}}^{HW}) + \dot{\boldsymbol{\epsilon}}^{HW} \cdot DW(\boldsymbol{\epsilon}^{HW})\right) dA = -V_{ext}(\dot{\boldsymbol{\Phi}}), \tag{4.72}$$

where

$$\delta\boldsymbol{\epsilon} = (\partial\boldsymbol{\epsilon}/\partial\boldsymbol{\Phi})\delta\boldsymbol{\Phi} + \sum_{\beta=1}^{2} \frac{\partial\boldsymbol{\epsilon}}{\partial\boldsymbol{\Phi}_{,\beta}}\delta\boldsymbol{\Phi}_{,\beta} \stackrel{\delta\boldsymbol{\Phi}=\dot{\boldsymbol{\Phi}}}{\triangleq} (\partial\boldsymbol{\epsilon}/\partial\boldsymbol{\Phi})\dot{\boldsymbol{\Phi}} + \sum_{\beta=1}^{2} \frac{\partial\boldsymbol{\epsilon}}{\partial\boldsymbol{\Phi}_{,\beta}}\dot{\boldsymbol{\Phi}}_{,\beta} = \dot{\boldsymbol{\epsilon}}, \tag{4.73}$$

was taken into account. By further applying $\delta\boldsymbol{\sigma}^{HW} = \boldsymbol{\sigma}^{HW}$ in (4.70), and inserting the result in (4.72), one gets

$$\int_M \left(\dot{\boldsymbol{\Phi}} \cdot \boldsymbol{M}_{\rho 0}\dot{\boldsymbol{V}} + \dot{\boldsymbol{\epsilon}}^{HW} \cdot DW(\boldsymbol{\epsilon}^{HW})\right) dA = -V_{ext}(\dot{\boldsymbol{\Phi}}). \tag{4.74}$$

Finally, by choosing $\delta\boldsymbol{V} = \boldsymbol{M}_{\rho 0}\dot{\boldsymbol{V}}$ for the admissible variation in (4.65)$_3$ and subtracting the result from (4.74), we obtain an expression for the conservation of the total energy

$$\underbrace{\int_M \boldsymbol{M}_{\rho 0}\boldsymbol{V} \cdot \dot{\boldsymbol{V}} dA}_{\dot{K}} + \underbrace{\underbrace{\int_M \dot{\boldsymbol{\epsilon}}^{HW} \cdot DW(\boldsymbol{\epsilon}^{HW}) dA + V_{ext}(\dot{\boldsymbol{\Phi}})}_{\dot{V}_{int}}}_{\dot{V}} = 0 \tag{4.75}$$

$$\Rightarrow \dot{K} + \dot{V} = \dot{E} = 0.$$

Let us choose $(\delta\boldsymbol{\Phi}, \delta\boldsymbol{\epsilon}^{HW}) = (\dot{\boldsymbol{\Phi}}, \dot{\boldsymbol{\epsilon}}^{HW}) = ((\dot{\boldsymbol{u}}, \dot{\boldsymbol{d}}), \boldsymbol{0}) = ((\boldsymbol{c}, \boldsymbol{0}), \boldsymbol{0})$ in (4.74), use $\boldsymbol{0} = \dot{\boldsymbol{\epsilon}} = \dot{\boldsymbol{\epsilon}}^{HW}$ (see (4.70)), and assume no external loading, to get

$$\boldsymbol{c} \cdot \int_M \left(A_{\rho 0}\dot{\boldsymbol{v}}\right) dA = 0. \tag{4.76}$$

Because the change of the linear momentum in time is defined as

$$\dot{\boldsymbol{L}} = \int_M A_{\rho 0}\dot{\boldsymbol{v}} dA, \tag{4.77}$$

and $\boldsymbol{c}$ is an arbitrary vector, Eq. (4.76) shows that $\dot{\boldsymbol{L}} = \boldsymbol{0}$. In a similar fashion, the choice $(\delta\boldsymbol{\Phi}, \delta\boldsymbol{\epsilon}^{HW}) = (\dot{\boldsymbol{\Phi}}, \dot{\boldsymbol{\epsilon}}^{HW}) = ((\boldsymbol{c} \times \boldsymbol{x}_0, \boldsymbol{c} \times \boldsymbol{d}), \boldsymbol{0})$ for admissible variations in (4.74) at zero external loads yields

$$\boldsymbol{c} \cdot \int_M \left(A_{\rho 0}\boldsymbol{x}_0 \times \dot{\boldsymbol{v}} + I_{\rho 0}\boldsymbol{d} \times \dot{\boldsymbol{\omega}}\right) dA = 0. \tag{4.78}$$

As $\boldsymbol{c}$ is an arbitrary vector and

$$\dot{\boldsymbol{J}} = \int_M \left(A_{\rho 0}\boldsymbol{x}_0 \times \dot{\boldsymbol{v}} + I_{\rho 0}\boldsymbol{d} \times \dot{\boldsymbol{\omega}}\right) dA, \tag{4.79}$$

it follows from (4.78) that the chosen formulation preserves angular momentum, i.e. $\dot{\boldsymbol{J}} = \boldsymbol{0}$.

4.3.2.2   Discretization in time

Time discretization of equations of motion (4.65) that preserves linear and angular momentum and enables user-controlled energy dissipation is based on the mid-point rule

$$\int_M \left(\delta\boldsymbol{\Phi} \cdot \boldsymbol{M}_{\rho 0} \frac{\boldsymbol{V}_{n+1} - \boldsymbol{V}_n}{\Delta t} + \delta\boldsymbol{\epsilon}\left(\delta\boldsymbol{\Phi}, \boldsymbol{\Phi}_{n+1/2}\right) \cdot \boldsymbol{\sigma}^{HW*} \right) dA = -V_{ext}(\delta\boldsymbol{\Phi}),$$

$$\int_M \delta\boldsymbol{\sigma}^{HW} \cdot \left(\boldsymbol{\epsilon}_{n+1} - \boldsymbol{\epsilon}_{n+1}^{HW}\right) dA = 0,$$

$$\int_M \delta\boldsymbol{V} \cdot \left(\frac{\boldsymbol{\Phi}_{n+1} - \boldsymbol{\Phi}_n}{\Delta t} - \boldsymbol{V}^* \right) dA = 0, \tag{4.80}$$

$$\int_M \delta\boldsymbol{\epsilon}^{HW} \cdot \left(\boldsymbol{\sigma}_{n+1/2}^{HW} - DW\left(\boldsymbol{\epsilon}_{n+1/2}^{HW}\right) dA = 0, \right.$$

where $\boldsymbol{V}^*$ and $\boldsymbol{\sigma}^{HW*}$ are

$$\boldsymbol{V}^* = \boldsymbol{V}_{cons} + \boldsymbol{V}_{diss},$$
$$\boldsymbol{\sigma}^{HW*} = \boldsymbol{\sigma}_{cons}^{HW} + \boldsymbol{\sigma}_{diss}^{HW}. \tag{4.81}$$

The conserving parts are again defined by the midpoint approximations $\boldsymbol{\sigma}_{cons}^{HW} = \boldsymbol{\sigma}_{n+1/2}^{HW}$, $\boldsymbol{V}_{cons} = \boldsymbol{V}_{n+1/2}$, while the expressions with subscript $diss$ will be defined below.

4.3.2.3   Constants of motion for time discrete equations

To prove that (4.80) and (4.81) conserve the constants of the motion, we start by writing the sum of (4.80)$_1$ and (4.80)$_4$ and taking into account (4.81)$_2$ as

$$\int_M \left(\delta\boldsymbol{\Phi} \cdot \boldsymbol{M}_{\rho 0} \frac{\boldsymbol{V}_{n+1} - \boldsymbol{V}_n}{\Delta t} + \boldsymbol{\sigma}_{n+1/2}^{HW} \cdot \left(\delta\boldsymbol{\epsilon}\left(\delta\boldsymbol{\Phi}, \boldsymbol{\Phi}_{n+1/2}\right) - \delta\boldsymbol{\epsilon}^{HW} \right) + \delta\boldsymbol{\epsilon}^{HW} \cdot DW\left(\boldsymbol{\epsilon}_{n+1/2}^{HW}\right) \right) dA$$
$$+ \int_M \boldsymbol{\sigma}_{diss}^{HW} \cdot \delta\boldsymbol{\epsilon}\left(\delta\boldsymbol{\Phi}, \boldsymbol{\Phi}_{n+1/2}\right) dA = -V_{ext}(\delta\boldsymbol{\Phi}). \tag{4.82}$$

Differentiating (4.80)$_2$ with respect to time and using the mid-point rule leads to the discrete form of the consistency condition

$$0 = \int_M \delta\boldsymbol{\sigma}^{HW} \cdot \left(\dot{\boldsymbol{\epsilon}}_{n+1/2} - \dot{\boldsymbol{\epsilon}}_{n+1/2}^{HW} \right) dA = \frac{1}{\Delta t} \int_M \delta\boldsymbol{\sigma}^{HW} \cdot \left((\boldsymbol{\epsilon}_{n+1} - \boldsymbol{\epsilon}_n) - (\boldsymbol{\epsilon}_{n+1}^{HW} - \boldsymbol{\epsilon}_n^{HW}) \right) dA \tag{4.83}$$
$$\Rightarrow (\boldsymbol{\epsilon}_{n+1} - \boldsymbol{\epsilon}_n) = (\boldsymbol{\epsilon}_{n+1}^{HW} - \boldsymbol{\epsilon}_n^{HW})$$

To prove the conservation of the constants of motion, we will use (4.82) and (4.83) along with (4.80)$_3$ and (4.81)$_1$.

In order to check for the energy, let us choose $(\delta\boldsymbol{\Phi}, \delta\boldsymbol{\epsilon}^{HW}) = (\boldsymbol{\Phi}_{n+1} - \boldsymbol{\Phi}_n, \boldsymbol{\epsilon}_{n+1}^{HW} - \boldsymbol{\epsilon}_n^{HW})$ for admissible variations in (4.82) to get

$$\int_M \left((\boldsymbol{\Phi}_{n+1} - \boldsymbol{\Phi}_n) \cdot \boldsymbol{M}_{\rho 0} \frac{\boldsymbol{V}_{n+1} - \boldsymbol{V}_n}{\Delta t} + \boldsymbol{\sigma}_{n+1/2}^{HW} \cdot \left((\boldsymbol{\epsilon}_{n+1} - \boldsymbol{\epsilon}_n) - (\boldsymbol{\epsilon}_{n+1}^{HW} - \boldsymbol{\epsilon}_n^{HW}) \right) \right) dA$$
$$\int_M \left((\boldsymbol{\epsilon}_{n+1}^{HW} - \boldsymbol{\epsilon}_n^{HW}) \cdot DW\left(\boldsymbol{\epsilon}_{n+1/2}^{HW}\right) + \boldsymbol{\sigma}_{diss}^{HW} \cdot (\boldsymbol{\epsilon}_{n+1} - \boldsymbol{\epsilon}_n) \right) dA = -V_{ext}(\boldsymbol{\Phi}_{n+1} - \boldsymbol{\Phi}_n), \tag{4.84}$$

where the following relation was applied

$$\delta\boldsymbol{\epsilon}\left(\boldsymbol{\Phi}_{n+1} - \boldsymbol{\Phi}_n, \boldsymbol{\Phi}_{n+1/2}\right) = \boldsymbol{\epsilon}(\boldsymbol{\Phi}_{n+1}) - \boldsymbol{\epsilon}(\boldsymbol{\Phi}_n) = \boldsymbol{\epsilon}_{n+1} - \boldsymbol{\epsilon}_n, \tag{4.85}$$

which can be proved by using (4.61) and (4.62). With the choice $\delta\boldsymbol{\sigma}^{HW} = \boldsymbol{\sigma}^{HW}_{n+1/2}$ in (4.83), and by subtracting the result from (4.84), we get

$$\int_M \left(\frac{\boldsymbol{\Phi}_{n+1} - \boldsymbol{\Phi}_n}{\Delta t} \cdot \boldsymbol{M}_{\rho 0}(\boldsymbol{V}_{n+1} - \boldsymbol{V}_n) + (\boldsymbol{\epsilon}^{HW}_{n+1} - \boldsymbol{\epsilon}^{HW}_n) \cdot DW(\boldsymbol{\epsilon}^{HW}_{n+1/2}) \right) dA$$
$$+ \int_M \sigma^{HW}_{diss} \cdot (\boldsymbol{\epsilon}_{n+1} - \boldsymbol{\epsilon}_n) dA = -V_{ext}(\boldsymbol{\Phi}_{n+1} - \boldsymbol{\Phi}_n). \tag{4.86}$$

Furthermore, with $\delta\boldsymbol{V} = \boldsymbol{M}_{\rho 0}(\boldsymbol{V}_{n+1} - \boldsymbol{V}_n)$ in (4.80)₃ and by using (4.81)₁, we arrive at

$$\int_M \frac{\boldsymbol{\Phi}_{n+1} - \boldsymbol{\Phi}_n}{\Delta t} \cdot \boldsymbol{M}_{\rho 0}(\boldsymbol{V}_{n+1} - \boldsymbol{V}_n) dA = \int_M \boldsymbol{V}^* \cdot \boldsymbol{M}_{\rho 0}(\boldsymbol{V}_{n+1} - \boldsymbol{V}_n) dA$$
$$= \int_M \left(\boldsymbol{V}_{n+1/2} \cdot \boldsymbol{M}_{\rho 0}(\boldsymbol{V}_{n+1} - \boldsymbol{V}_n) + \boldsymbol{V}_{diss} \cdot \boldsymbol{M}_{\rho 0}(\boldsymbol{V}_{n+1} - \boldsymbol{V}_n) \right) dA. \tag{4.87}$$

Finally, by inserting (4.87) in Eq. (4.86), the conservation of the energy follows as

$$\underbrace{\int_M \boldsymbol{V}_{n+1/2} \cdot \boldsymbol{M}_{\rho 0}(\boldsymbol{V}_{n+1} - \boldsymbol{V}_n) dA}_{K_{n+1} - K_n}$$
$$+ \underbrace{\underbrace{\int_M (\boldsymbol{\epsilon}^{HW}_{n+1} - \boldsymbol{\epsilon}^{HW}_n) \cdot DW(\boldsymbol{\epsilon}^{HW}_{n+1/2}) dA}_{V_{int,n+1} - V_{int,n}} + \underbrace{V_{ext}(\boldsymbol{\Phi}_{n+1} - \boldsymbol{\Phi}_n)}_{\Delta W}}_{V_{int,n+1} - V_{int,n} - \Delta W}$$
$$+ \underbrace{\int_M \left(\sigma^{HW}_{diss} \cdot (\boldsymbol{\epsilon}_{n+1} - \boldsymbol{\epsilon}_n) + \boldsymbol{V}_{diss} \cdot \boldsymbol{M}_{\rho 0}(\boldsymbol{V}_{n+1} - \boldsymbol{V}_n) \right) dA = 0}_{\Delta\mathcal{D}}$$
$$\Rightarrow K_{n+1} - K_n + V_{int,n+1} - V_{int,n} - \Delta W + \Delta\mathcal{D} = 0 \tag{4.88}$$

where $\Delta\mathcal{D}$ is dissipation defined in terms of $\boldsymbol{V}_{diss}$ and σ^{HW}_{diss} that should generate $\Delta\mathcal{D} \geq 0$, and ΔW is incremental work of external loading.

We now turn to check the preservation of linear momentum. Assuming no external loading, and choosing $(\delta\boldsymbol{\Phi}, \delta\boldsymbol{\epsilon}^{HW}) = (\boldsymbol{\Phi}_{n+1} - \boldsymbol{\Phi}_n, \boldsymbol{\epsilon}^{HW}_{n+1} - \boldsymbol{\epsilon}^{HW}_n) = ((\boldsymbol{u}_{n+1} - \boldsymbol{u}_n, \boldsymbol{d}_{n+1} - \boldsymbol{d}_n), \boldsymbol{0}) = ((\boldsymbol{c}, \boldsymbol{0}), \boldsymbol{0})$ as admissible variations for $\forall \boldsymbol{c} \in \mathbb{R}^3$, implies $\boldsymbol{\epsilon}_{n+1} - \boldsymbol{\epsilon}_n = \boldsymbol{0}$ (see (4.83)) and (see (4.84))

$$\boldsymbol{c} \cdot A_{\rho 0}(\boldsymbol{v}_{n+1} - \boldsymbol{v}_n) = \boldsymbol{c} \cdot (\boldsymbol{L}_{n+1} - \boldsymbol{L}_n) = 0, \tag{4.89}$$

which gives the balance law for linear momentum. As for the balance law for angular momentum, it can be shown that its discrete change can be written as

$$\boldsymbol{J}_{n+1} - \boldsymbol{J}_n = \left(A_{\rho 0} \boldsymbol{x}_{0_{n+1/2}} \times (\boldsymbol{v}_{n+1} - \boldsymbol{v}_n) + I_{\rho 0} \boldsymbol{d}_{n+1/2} \times (\boldsymbol{\omega}_{n+1} - \boldsymbol{\omega}_n) \right)$$
$$- \left(A_{\rho 0} \boldsymbol{v}_{n+1/2} \times (\boldsymbol{x}_{0_{n+1}} - \boldsymbol{x}_{0_n}) + I_{\rho 0} \boldsymbol{\omega}_{n+1/2} \times (\boldsymbol{d}_{n+1} - \boldsymbol{d}_n) \right). \tag{4.90}$$

The assumption of no external loading and the choice $(\delta\boldsymbol{\Phi}, \delta\boldsymbol{\epsilon}^{HW}) = (\boldsymbol{\Phi}_{n+1} - \boldsymbol{\Phi}_n, \boldsymbol{\epsilon}^{HW}_{n+1} - \boldsymbol{\epsilon}^{HW}_n) = \left((\boldsymbol{x}_{0_{n+1}} - \boldsymbol{x}_{0_n}, \boldsymbol{d}_{n+1} - \boldsymbol{d}_n), \boldsymbol{0} \right) = \left((\boldsymbol{c} \times \boldsymbol{x}_{0_{n+1/2}}, \boldsymbol{c} \times \boldsymbol{d}_{n+1/2}), \boldsymbol{0} \right)$ give $\boldsymbol{\epsilon}_{n+1} - \boldsymbol{\epsilon}_n = \boldsymbol{0}$ (see (4.83)) and (see (4.84))

$$\boldsymbol{c} \cdot \int_M A_{\rho 0} \boldsymbol{x}_{0_{n+1/2}} \times (\boldsymbol{v}_{n+1} - \boldsymbol{v}_n) + I_{\rho 0} \boldsymbol{d}_{n+1/2} \times (\boldsymbol{\omega}_{n+1} - \boldsymbol{\omega}_n) dA = 0. \tag{4.91}$$

Comparing (4.91) and (4.90), we conclude that in order for angular momentum to be conserved, the second term on the r.h.s. of (4.90) should be $\boldsymbol{0}$, which holds for $\boldsymbol{v}_{n+1/2} \parallel (\boldsymbol{x}_{0_{n+1}} - \boldsymbol{x}_{0_n})$ and $\boldsymbol{\omega}_{n+1/2} \parallel (\boldsymbol{d}_{n+1} - \boldsymbol{d}_n)$. From (4.80)₃ we note that $\frac{(\boldsymbol{x}_{0_{n+1}} - \boldsymbol{x}_{0_n})}{\Delta t} = \boldsymbol{v}^*$ and $\frac{(\boldsymbol{d}_{n+1} - \boldsymbol{d}_n)}{\Delta t} = \boldsymbol{\omega}^*$, which means that the

conservation of angular momentum is ensured if $\boldsymbol{v}_{n+1/2} \parallel \boldsymbol{v}^* = \boldsymbol{v}_{n+1/2} + \boldsymbol{v}_{diss}$ and $\boldsymbol{\omega}_{n+1/2} \parallel \boldsymbol{\omega}^* = \boldsymbol{\omega}_{n+1/2} + \boldsymbol{\omega}_{diss}$. Thus, $\boldsymbol{v}_{diss}$ and $\boldsymbol{\omega}_{diss}$ should take directions of $\boldsymbol{v}_{n+1/2}$ and $\boldsymbol{\omega}_{n+1/2}$, respectively.

4.3.3   3-field Hellinger-Reissner formulation

Following the developments from Section 4.2.3, the 3-Hellinger-Reissner functional for the considered shell model can be written as

$$G_{HR}\left(\boldsymbol{\Phi}, \boldsymbol{V}, \boldsymbol{\sigma}^{HR}\right) =$$

$$\int_{t_0}^{t_e}\left(\int_M \left(\dot{\boldsymbol{\Phi}} - \frac{1}{2}\boldsymbol{V}\right) \cdot \boldsymbol{M}_{\rho 0}\boldsymbol{V}dA - \underbrace{\int_M\left(\boldsymbol{\epsilon}(\boldsymbol{\Phi})\cdot\boldsymbol{\sigma}^{HR} - \frac{1}{2}\boldsymbol{\sigma}^{HR}\cdot\boldsymbol{C}^{-1}\boldsymbol{\sigma}^{HR}\right)dA}_{V_{int}}\right)dt - \int_{t_0}^{t_e}V_{ext}dt, \quad (4.92)$$

where we introduced the stress resultant vector $\boldsymbol{\sigma}^{HR}$. Following the procedure from Section 4.2.3 and imposing the stationarity condition $\delta G_{HR} = 0$ on (4.92), we arrive at the following Euler-Lagrange equations of motion

$$\int_M \left(\delta\boldsymbol{\Phi}\cdot\boldsymbol{M}_{\rho 0}\dot{\boldsymbol{V}} + \delta\boldsymbol{\epsilon}(\delta\boldsymbol{\Phi}, \boldsymbol{\Phi})\cdot\boldsymbol{\sigma}^{HR}\right)dA = -V_{ext}(\delta\boldsymbol{\Phi}),$$

$$\int_M \delta\boldsymbol{V}\cdot\left(\dot{\boldsymbol{\Phi}} - \boldsymbol{V}\right)dA = 0, \quad (4.93)$$

$$\int_M \delta\boldsymbol{\sigma}^{HR}\cdot\left(\boldsymbol{C}^{-1}\boldsymbol{\sigma}^{HR} - \boldsymbol{\epsilon}(\boldsymbol{\Phi})\right)dA = 0,$$

which are supplemented by generalized displacements boundary conditions and initial conditions for $\dot{\boldsymbol{V}}, \dot{\boldsymbol{\Phi}}$ and $\boldsymbol{\sigma}^{HR}$ that have to be consistent with initial $\boldsymbol{V}$ and $\boldsymbol{\Phi}$ in view of (4.93).

4.3.3.1   Balance laws

In this section, we show that Eqs. (4.93) preserve linear momentum $\boldsymbol{L}$, angular momentum $\boldsymbol{J}$ and total energy E, given in (4.66)-(4.68). To that end, we write (4.93)$_1$ as

$$\int_M \left(\delta\boldsymbol{\Phi}\cdot\left(\boldsymbol{M}_{\rho 0}\dot{\boldsymbol{V}}\right) + \delta\boldsymbol{\epsilon}(\delta\boldsymbol{\Phi}, \boldsymbol{\Phi})\cdot\boldsymbol{\sigma}^{HR}\right)dA = -V_{ext}(\delta\boldsymbol{\Phi}), \quad (4.94)$$

and obtain the consistency condition by differentiating (4.93)$_3$ with respect to time

$$0 = \int_M \delta\boldsymbol{\sigma}^{HR}\cdot\left(\boldsymbol{C}^{-1}\dot{\boldsymbol{\sigma}}^{HR} - \dot{\boldsymbol{\epsilon}}\right)dA \Rightarrow \boldsymbol{C}^{-1}\dot{\boldsymbol{\sigma}}^{HR} = \dot{\boldsymbol{\epsilon}} \quad (4.95)$$

Note that the time derivative of the potential energy in (4.92) is

$$\dot{V} = \int_M \left(\underbrace{\dot{\boldsymbol{\epsilon}}\cdot\boldsymbol{\sigma}^{HR} + \boldsymbol{\epsilon}(\boldsymbol{\Phi})\cdot\dot{\boldsymbol{\sigma}}^{HR} - \boldsymbol{\sigma}^{HR}\cdot\boldsymbol{C}^{-1}\dot{\boldsymbol{\sigma}}^{HR}}_{=\boldsymbol{\epsilon}(\boldsymbol{\Phi})\cdot\dot{\boldsymbol{\sigma}}^{HR}, \text{ see } (4.95)}\right)dA + V_{ext}(\dot{\boldsymbol{\Phi}}). \quad (4.96)$$

where we have taken into account that for the conservative loading $\dot{V}_{ext}(\boldsymbol{\Phi}) = V_{ext}(\dot{\boldsymbol{\Phi}})$.

Let us choose $\delta\boldsymbol{\Phi} = \dot{\boldsymbol{\Phi}}$ for admissible variations in (4.94) to get

$$\int_M \left(\dot{\boldsymbol{\Phi}}\cdot\boldsymbol{M}_{\rho 0}\dot{\boldsymbol{V}} + \underbrace{\delta\boldsymbol{\epsilon}(\dot{\boldsymbol{\Phi}}, \boldsymbol{\Phi})}_{\substack{=\dot{\boldsymbol{\epsilon}}=\boldsymbol{C}^{-1}\dot{\boldsymbol{\sigma}}^{HR} \\ \text{see } (4.73),(4.95)}}\cdot\boldsymbol{\sigma}^{HR}\right)dA = -V_{ext}(\dot{\boldsymbol{\Phi}}) \quad (4.97)$$

Choosing $\delta V = M_{\rho 0}\dot{V}$ in $(4.93)_2$, $\delta\sigma^{HR} = \dot{\sigma}^{HR}$ and subtracting the two resulting Eqs. from (4.97), we can now recast it as

$$\underbrace{\int_M M_{\rho 0}V \cdot \dot{V}dA}_{\dot{K}} + \underbrace{\int_M (\epsilon(\Phi) \cdot \dot{\sigma}^{HR})dA + V_{ext}(\dot{\Phi})}_{\dot{V}_{int}} = 0 \tag{4.98}$$

$$\Rightarrow \dot{K} + \dot{V} = \dot{E} = 0,$$

showing the conservation of total energy in time.

We choose $\delta\Phi = \dot{\Phi} = (c, 0)$ for $\forall c \in \mathbb{R}^3$ and no external loading, which corresponds to rigid body translation and no change in strain field, see (4.62). (4.95) now gives

$$0 = C^{-1}\dot{\sigma}^{HR} = \dot{\epsilon} \tag{4.99}$$

and Eq. (4.97) changes into

$$c \cdot \underbrace{\int_M (A_{\rho 0}\dot{v})dA}_{\dot{L}} = 0 \tag{4.100}$$

showing conservation of linear momentum. We may further choose $\delta\Phi = \dot{\Phi} = (c \times x_0, c \times d)$ as admissible variations at no external virtual work. Eq. (4.99) still holds, and Eq. (4.97) gives

$$c \cdot \underbrace{\int_M A_{\rho 0}x_0 \times \dot{v} + I_{\rho 0}d \times \dot{\omega}dA}_{\dot{j}} = 0 \tag{4.101}$$

which presents the conservation of angular momentum.

4.3.3.2   Discretization in time

Let us adopt the following (mid-point) time discretization of equations of motion (4.93)

$$\int_M \left(\delta\Phi \cdot M_{\rho 0}\frac{V_{n+1} - V_n}{\Delta t} + \delta\epsilon(\delta\Phi, \Phi_{n+1/2}) \cdot \sigma^{HR*} \right)dA = -V_{ext}(\delta\Phi),$$

$$\int_M \delta V \cdot \left(\frac{\Phi_{n+1} - \Phi_n}{\Delta t} - V^* \right)dA = 0, \tag{4.102}$$

$$\int_M \delta\sigma^{HR} \cdot (C^{-1}\sigma^{HR}_{n+1} - \epsilon_{n+1})dA = 0,$$

where

$$\sigma^{HR*} = \sigma^{HR}_{cons} + \sigma^{HR}_{diss} \tag{4.103}$$
$$V^* = V_{cons} + V_{diss}$$

and $\sigma^{HR}_{cons} = \sigma^{HR}_{n+1/2}$, $V_{cons} = V_{n+1/2}$, while the σ^{HR}_{diss} and V_{diss} are left undefined for now.

4.3.3.3   Constants of motion for time discrete equations

Let us write Eq. $(4.102)_1$ by using $(4.103)_1$ as

$$\int_M \left(\delta\Phi \cdot \left(M_{\rho 0}\frac{V_{n+1} - V_n}{\Delta t} \right) + \delta\epsilon(\delta\Phi, \Phi_{n+1/2}) \cdot \left(\sigma^{HR}_{n+1/2} + \sigma^{HR}_{diss} \right) \right)dA = -V_{ext}(\delta\Phi), \tag{4.104}$$

and get the discrete version of consistency condition by differentiating $(4.102)_3$ with respect to time as

$$0 = \int_M \delta\sigma^{HR} \cdot \left(C^{-1}\dot{\sigma}^{HR}_{n+1/2} - \dot{\epsilon}_{n+1/2} \right) = \frac{1}{\Delta t}\int_M \delta\sigma^{HR} \cdot (C^{-1}(\sigma^{HR}_{n+1} - \sigma^{HR}_n)$$

$$-\epsilon_{n+1} - \epsilon_n)dA \quad \Rightarrow (\epsilon_{n+1} - \epsilon_n) = C^{-1}(\sigma^{HR}_{n+1} - \sigma^{HR}_n) \tag{4.105}$$

Eqs. (4.102)$_{2,3}$ and (4.104) along with (4.103)$_2$ and (4.105) will be used to check the algorithmic preservation of motion.

Let us use $\delta\boldsymbol{\Phi} = \boldsymbol{\Phi}_{n+1} - \boldsymbol{\Phi}_n$ and apply (4.85) in (4.104) to get

$$\int_M \left((\boldsymbol{\Phi}_{n+1} - \boldsymbol{\Phi}_n) \cdot \boldsymbol{M}_{\rho 0} \frac{\boldsymbol{V}_{n+1} - \boldsymbol{V}_n}{\Delta t} + \boldsymbol{\sigma}_{n+1/2}^{HR} \cdot (\boldsymbol{\epsilon}_{n+1} - \boldsymbol{\epsilon}_n) \right.$$
$$\left. + \boldsymbol{\sigma}_{diss}^{HR} \cdot (\boldsymbol{\epsilon}_{n+1} - \boldsymbol{\epsilon}_n) \right) dA = -V_{ext}(\boldsymbol{\Phi}_{n+1} - \boldsymbol{\Phi}_n). \tag{4.106}$$

Choosing $\delta\boldsymbol{V} = \boldsymbol{M}_{\rho 0}(\boldsymbol{V}_{n+1} - \boldsymbol{V}_n)$ in (4.102)$_2$, $\delta\boldsymbol{\sigma}^{HR} = (\boldsymbol{\sigma}_{n+1}^{HR} - \boldsymbol{\sigma}_n^{HR})$ in (4.102)$_3$ and subtracting the two resulting equations from (4.104) while taking into account the consistency condition (4.105), we obtain

$$\underbrace{\int_M \boldsymbol{V}_{n+1/2} \cdot \boldsymbol{M}_{\rho 0}(\boldsymbol{V}_{n+1} - \boldsymbol{V}_n) dA}_{K_{n+1} - K_n}$$
$$+ \underbrace{\int_M \left((\boldsymbol{\sigma}_{n+1}^{HR}\boldsymbol{\epsilon}_{n+1} - \boldsymbol{\sigma}_n^{HR}\boldsymbol{\epsilon}_n) - \frac{1}{2}(\boldsymbol{\sigma}_{n+1}^{HR} \cdot \boldsymbol{C}^{-1}\boldsymbol{\sigma}_{n+1}^{HR} - \boldsymbol{\sigma}_n^{HR} \cdot \boldsymbol{C}^{-1}\boldsymbol{\sigma}_n^{HR}) \right) dA}_{V_{int,n+1} - V_{int,n}}$$
$$+ \underbrace{V_{ext}(\boldsymbol{\Phi}_{n+1} - \boldsymbol{\Phi}_n)}_{\Delta W} + \underbrace{\int_M \left(\boldsymbol{\sigma}_{diss}^{HR} \cdot (\boldsymbol{\epsilon}_{n+1} - \boldsymbol{\epsilon}_n) + \boldsymbol{V}_{diss} \cdot \boldsymbol{M}_{\rho 0}(\boldsymbol{V}_{n+1} - \boldsymbol{V}_n) \right) dA}_{\Delta\mathcal{D}} = 0 \tag{4.107}$$
$$\Rightarrow K_{n+1} - K_n + V_{int,n+1} - V_{int,n} - \Delta W + \Delta\mathcal{D} = 0$$

where $\Delta\mathcal{D}$ is energy dissipation governed by $\boldsymbol{\sigma}_{diss}^{HR}$ and $\boldsymbol{V}_{diss}$, which should be chosen to provide $\Delta\mathcal{D} \geq 0$. Eq. (4.107) shows preservation of total energy for $\Delta W = 0$ and $\Delta\mathcal{D} = 0$.

We choose $\delta\boldsymbol{\Phi} = \boldsymbol{\Phi}_{n+1} - \boldsymbol{\Phi}_n = (\boldsymbol{c}, \boldsymbol{0})$ as admissible variations for $\forall\boldsymbol{c} \in \mathbb{R}^3$ and no external loading, which corresponds to rigid body translation and no change in strain field, see (4.62). (4.105) now gives

$$0 = \boldsymbol{C}^{-1}(\boldsymbol{\sigma}_{n+1}^{HR} - \boldsymbol{\sigma}_n^{HR}), \tag{4.108}$$

and (4.104) changes to

$$\boldsymbol{c} \cdot A_{\rho 0}(\boldsymbol{v}_{n+1} - \boldsymbol{v}_n) = \boldsymbol{c} \cdot (\boldsymbol{L}_{n+1} - \boldsymbol{L}_n) = 0, \tag{4.109}$$

implying conservation of linear momentum. We may further choose $\delta\boldsymbol{\Phi} = \boldsymbol{\Phi}_{n+1} - \boldsymbol{\Phi}_n = \left(\boldsymbol{c} \times \boldsymbol{x}_{0_{n+1/2}}, \boldsymbol{c} \times \boldsymbol{d}_{n+1/2} \right)$ as admissible variations at no external virtual work. Eq. (4.108) still holds, and Eq. (4.104) gives

$$\boldsymbol{c} \cdot \int_M A_{\rho 0}\boldsymbol{x}_{0_{n+1/2}} \times (\boldsymbol{v}_{n+1} - \boldsymbol{v}_n) + I_{\rho 0}\boldsymbol{d}_{n+1/2} \times (\boldsymbol{\omega}_{n+1} - \boldsymbol{\omega}_n) dA = 0. \tag{4.110}$$

Following the reasoning from Section 4.3.2.3, we can again conclude that the conservation of angular momentum is ensured if $\boldsymbol{v}_{diss}$ and $\boldsymbol{\omega}_{diss}$ have the directions of $\boldsymbol{v}_{n+1/2}$ and $\boldsymbol{\omega}_{n+1/2}$, respectively.

4.3.4   Dissipation variables

We can now elaborate on dissipation terms $\boldsymbol{V}_{diss} = \{\boldsymbol{v}_{diss}, \boldsymbol{\omega}_{diss}\}$, and $\bar{\boldsymbol{\sigma}}_{diss} \in \{\boldsymbol{\sigma}_{diss}, \boldsymbol{\sigma}_{diss}^{HW}, \boldsymbol{\sigma}_{diss}^{HR}\}$. According to the above derivations, the followings has to be considered:
* The numerical dissipation of the time-stepping scheme from Section 4.3.1 should always be positive or zero, which is also demanded for the scheme from Section 4.3.2 (for the 4-field Hu-

Washizu formulation) and for the scheme from Section 4.3.3 (for the 3-field Hellinger-Reissner formulation). In other words, $\Delta\mathcal{D} \geq 0$ in (4.88) and (4.107).

- Moreover, according to the discussion after Eq. (4.91) and Eq. (4.109), for the considered schemes $\boldsymbol{v}_{diss}$ should be parallel to $\boldsymbol{v}_{n+1/2}$ and $\boldsymbol{\omega}_{diss}$ should be parallel to $\boldsymbol{\omega}_{n+1/2}$ to generate the preservation of angular momentum.

4.3.4.1   Defining dissipation terms for the first order scheme

The choice that takes the above constraints into account and yields a first order accurate EDMC1 scheme is (see also [4] and [132])

$$
\boldsymbol{v}_{diss} = \beta_{ED} \underbrace{\frac{(v_{n+1} - v_n)^2}{(v_{n+1})^2 - (v_n)^2}}_{g_{v,diss}} \boldsymbol{v}_{n+1/2},
$$

$$
\boldsymbol{\omega}_{diss} = \beta_{ED} \underbrace{\frac{(\omega_{n+1} - \omega_n)^2}{(\omega_{n+1})^2 - (\omega_n)^2}}_{g_{\omega,diss}} \boldsymbol{\omega}_{n+1/2},
$$
$$
\overline{\boldsymbol{\sigma}}_{diss} = \alpha_{ED}(\overline{\boldsymbol{\sigma}}_{n+1} - \overline{\boldsymbol{\sigma}}_n)/2,
$$
(4.111)

where $v = \|\boldsymbol{v}\|$ and $\omega = \|\boldsymbol{\omega}\|$. Dissipation can be controlled by user defined factors $[\alpha_{ED}, \beta_{ED}] \geq 0$, where choosing the value 0 represents no dissipation and values (0,1) are usually applied. Here, α_{ED} controls the dissipation of potential and β_{ED} of kinetic energy. In the presented examples, $\alpha_{ED} = \beta_{ED}$ will always be used. This option was shown in [4] and [105] to result in the dissipation in higher frequencies.

4.3.4.2   Defining dissipation terms for the second order scheme

Defining a second order accurate scheme EDMC2 is a more demanding task. We adopt here the idea presented in [5] and [132], where the dissipative terms are extended to be of order $O(\Delta t^2)$. To this end, the quasi-intermediate parameters (marked with $\widetilde{(\cdot)}_n$) are introduced as

$$
\overline{\boldsymbol{\sigma}}_{diss} = (\widetilde{\overline{\boldsymbol{\sigma}}}_n - \overline{\boldsymbol{\sigma}}_n)/2, \qquad \widetilde{\overline{\boldsymbol{\sigma}}}_n = \left[\widetilde{\overline{\boldsymbol{N}}}_n^T, \widetilde{\overline{\boldsymbol{M}}}_n^T, \widetilde{\boldsymbol{Q}}_n^T \right]^T,
$$
(4.112)

with

$$
\widetilde{\overline{\boldsymbol{N}}}_n = \overline{\boldsymbol{N}}_n + \beta_m(\overline{\boldsymbol{N}}_{n+1} - \overline{\boldsymbol{N}}_n), \qquad \widetilde{\overline{\boldsymbol{M}}}_n = \overline{\boldsymbol{M}}_n + \beta_b(\overline{\boldsymbol{M}}_{n+1} - \overline{\boldsymbol{M}}_n),
$$
$$
\widetilde{\overline{\boldsymbol{Q}}}_n = \overline{\boldsymbol{Q}}_n + \beta_s(\overline{\boldsymbol{Q}}_{n+1} - \overline{\boldsymbol{Q}}_n),
$$
(4.113)

and

$$
\boldsymbol{v}_{diss} = \underbrace{\frac{(\tilde{v}_n - v_n)(v_{n+1} - v_n)}{(v_{n+1})^2 - (v_n)^2}}_{g_{v,diss}} \boldsymbol{v}_{n+1/2},
$$

$$
\boldsymbol{\omega}_{diss} = \underbrace{\frac{(\widetilde{\omega}_n - \omega_n)(\omega_{n+1} - \omega_n)}{(\omega_{n+1})^2 - (\omega_n)^2}}_{g_{\omega,diss}} \boldsymbol{\omega}_{n+1/2},
$$
(4.114)

where $\beta_m, \beta_b, \beta_s$ are dimensionless parameters (yet to be given), and $\widetilde{(\cdot)}_n$ needs to be designed for the second-order approximations as $\widetilde{(\cdot)}_n = (\cdot)_n + O(\Delta t^2)$. The latter can be achieved by cross-coupling of the stresses and velocities as

$$\beta_m = \alpha_{ED,mv} \frac{\Delta t}{h} (\tilde{v}_n - v_{n+1}) + \alpha_{ED,m\omega} \frac{\Delta t}{h} r_\rho (\tilde{\omega}_n - \omega_{n+1}),$$

$$\beta_b = \alpha_{ED,bv} \frac{\Delta t}{h} (\tilde{v}_n - v_{n+1}) + \alpha_{ED,b\omega} \frac{\Delta t}{h} r_\rho (\tilde{\omega}_n - \omega_{n+1}), \qquad (4.115)$$

$$\beta_s = \alpha_{ED,sv} \frac{\Delta t}{h} (\tilde{v}_n - v_{n+1}) + \alpha_{ED,s\omega} \frac{\Delta t}{h} r_\rho (\tilde{\omega}_n - \omega_{n+1}),$$

and

$$\tilde{v}_n = v_n - \frac{\Delta t}{A_0 h} \big(\alpha_{ED,mv}(\beta_m - 1)(\bar{N}_{n+1} - \bar{N}_n) \cdot (\varepsilon_{n+1} - \varepsilon_n) + \alpha_{ED,bv}(\beta_b - 1)$$

$$(\bar{M}_{n+1} - \bar{M}_n) \cdot (\kappa_{n+1} - \kappa_n) + \alpha_{ED,sv}(\beta_s - 1)(\bar{Q}_{n+1} - \bar{Q}_n) \cdot (\gamma_{n+1} - \gamma_n) \big)$$

$$\tilde{\omega}_n = \omega_n - \frac{\Delta t}{I_0 h} r_0 \big(\alpha_{ED,m\omega}(\beta_m - 1)(\bar{N}_{n+1} - \bar{N}_n) \cdot (\varepsilon_{n+1} - \varepsilon_n) + \alpha_{ED,b\omega}(\beta_b - 1)$$

$$(\bar{M}_{n+1} - \bar{M}_n) \cdot (\kappa_{n+1} - \kappa_n) + \alpha_{ED,s\omega}(\beta_s - 1)(\bar{Q}_{n+1} - \bar{Q}_n) \cdot (\gamma_{n+1} - \gamma_n) \big)$$

$$(4.116)$$

where h is a suitable geometric constant with the role to provide dimensionally consistent expressions, and $r_0 = \sqrt{I_0/A_0}$. Note that we have here six α_{ED} parameters to control the dissipation. This allows for more flexibility on dissipation through different components of shell deformations. Following [132], we assume hereinafter $\alpha_{ED,m\omega} = 0$ and $\alpha_{ED,mv} = \alpha_{ED,bv} = \alpha_{ED,sv} = \alpha_{ED,b\omega} = \alpha_{ED,s\omega} = \alpha_{ED}$. Eqs. (4.115) and (4.116) form a linear system of equations for β's, $\tilde{v}_n$ and $\tilde{\omega}_n$ at each integration point, which can be pre-solved in a closed form that expresses the quasi-intermediate parameters in terms of the basic variables, $\boldsymbol{\Phi}_{n+1}$ and $\boldsymbol{V}_{n+1}$.

4.4   Numerical examples

Five static finite element shell formulations for four-node quadrilateral were taken as the starting point for dynamic formulations. The elements that were tested extensively for static problems in Section 2.5.4 and [104], [107] (and several other works) are:

(i)   MITC4 formulation that employs the assumed natural strain method for transverse shear strains, see [48].

(ii)   MITC4+ formulation that employs the ANS concept for transverse shear and membrane strains, see [89], [90].

(iii) Enhanced assumed strain formulation EAS5, where 5 parameters are used to enhance the membrane part of the strains, see e.g. [22].

(iv)   Mixed-hybrid formulation (hereinafter called +HW) that is based on the Hu-Washizhu functional (with 28 parameters in total for the interpolation of strains and stress resultants). On top of that it uses the ANS concepts of MITC4+ for the membrane and the transverse shear strains (it was introduced in [104] as an improvement of the ideas of [159] and [90]).

(v)   Mixed-hybrid functional (hereinafter called +HR) that is based on the Hellinger-Reissner functional (with 14 parameters in total for stress resultants). On top of that it uses the ANS concepts of MITC4+ for the membrane and the transverse shear strains (it was introduced in [107] as an improvement of the ideas from [90] and [59]).

We refrain here from giving any detailed descriptions of element implementation, and refer the reader to Chapter 2 or the above-mentioned references. We should only note that the weighting factors used in

the implementation of membrane ANS in (2.49) are here not configuration dependent, as was the case for static formulation. They are rather expressed in the initial configuration.

The results for three numerical examples are presented below, where we try to determine whether or not the features of the used formulations will translate from static to dynamic analysis. Where adaptive time-stepping was used, function (2.81) was applied with $I_0 = 8$ and $N = 15$ as the desired and maximal allowed number of incremental iterations, respectively. If convergence was not reached in 15 iterations, the time-step was re-computed with $\Delta t/2$. The convergence tolerance was set to 10^{-8} for all examples.

4.4.1   Flying L-shaped plate

Let us again consider an L-shaped plate from Figure 3.15, which is tossed in space by a set of impulsive nodal forces producing large bending and membrane deformations. At $t = 0$, it stays at rest and exhibits free motion after $t > 1$. The plate has thickness $h = 0.1$, material density $\rho = 1$, Young's modulus $E = 10^6$ and Poisson's ratio $\nu = 0.3$. The response of the plate is analysed until $t_f = 20$, using constant time steps $\Delta t \in \{2\,10^{-2}, 10^{-3}\}$. Two damping factors were chosen to enforce minor and major damping $\alpha_{ED} = \beta_{ED} \in \{0.05, 0.4\}$.

The total energy evolution for different combinations of damping factors and time steps is given in Figure 4.2. The results show (slight) differences between the elements. Figure 4.2 (a) – (d) display that for larger dissipation parameters, the differences between the elements are very small, while for the smaller dissipation parameters, the differences get larger. For the case with no dissipation, there is a difference in the energy level, see Figure 4.2 (e) – (f). However, all the elements exactly conserve the energy, which is reflected by the fact that the computed values for energy for $t \in (1,20]$ vary in the range of 10^{-11}. All the elements also exactly preserve linear and angular momentum, see Figure 4.3, with the computed values varying in the range of 10^{-12} for $t \in (1,20]$. It is nevertheless interesting to note that while the level of linear momentum after $t = 1$ is the same for all the formulations and for both schemes, see Figure 4.3 (a), the level of angular momentum can slightly differ from one element to another and also between the EDMC1 and EDMC2 schemes, see Figure 4.3 (b), where notation $L = \left[L_x, L_y, L_z\right]^T$ and $J = \left[J_x, J_y, J_z\right]^T$ is used.

An error analysis was performed next, using constant time steps of $\Delta t \in \{0.02, 10^{-2}, 10^{-3}, 10^{-4}\}$. Figure 4.4 shows an error in generalized displacements, which is calculated on the basis of nodal differences at $t_e = 5$ as shown in (3.54), with limit values obtained for $\Delta t = 10^{-5}$ (for each element). The slopes of the lines indicate the order of accuracy of the schemes in a solution sense. In Figure 4.4 (b), a relative error in the total energy at $t_e = 5$ is shown with respect to Δt, as shown in (3.53) where $E_{\text{tot,lim}}$ is the total energy computed for $\Delta t = 10^{-5}$ (for each element). The slopes of the lines are similar and indicate the order of accuracy of the schemes in an energy sense. EDMC2 results are not shown for $\Delta t = 0.02$ as only +HR and MITC4 managed to compute the complete solution. Both error indicators show, that the accuracy of the underlying scheme is independent of the used element formulation.
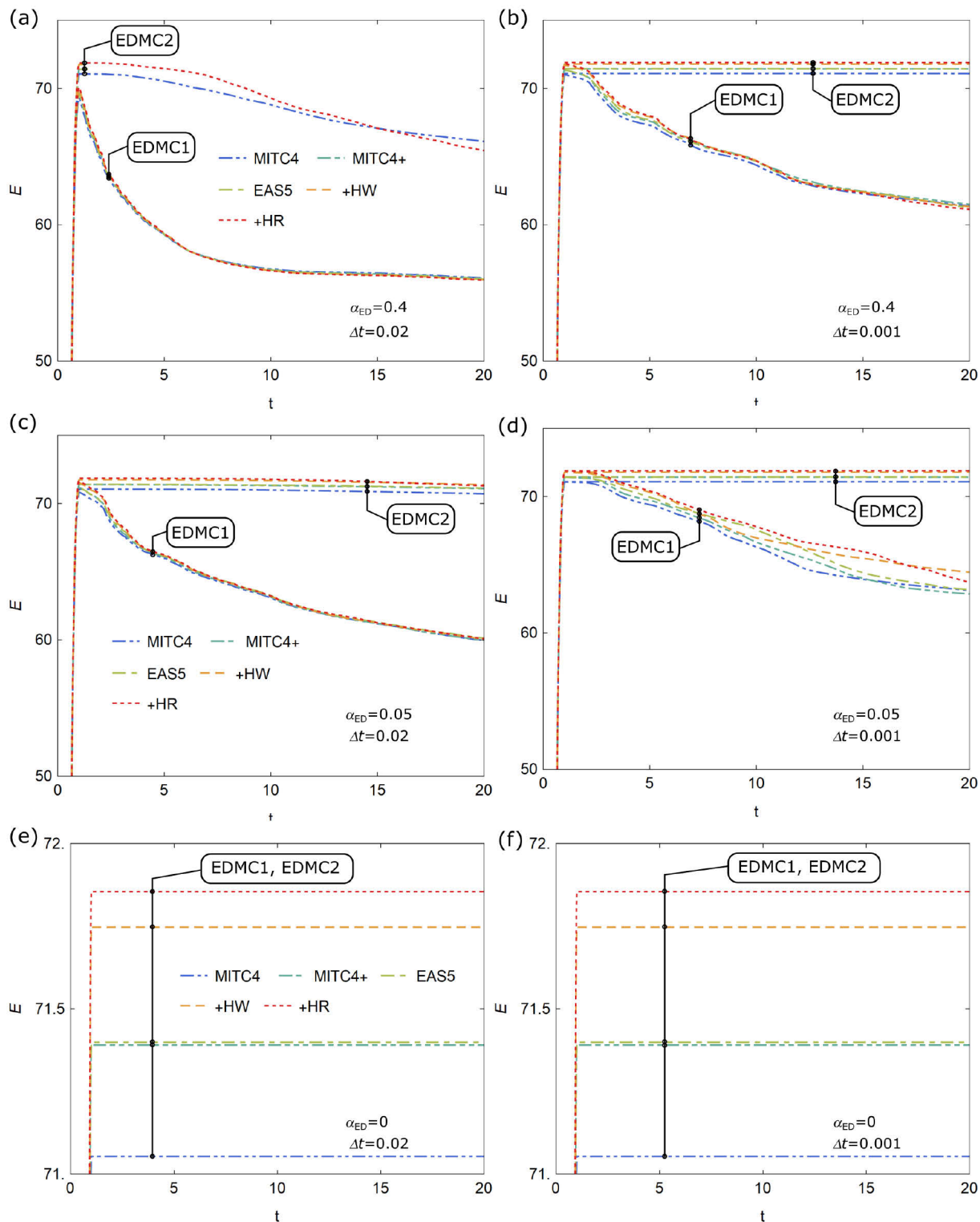
Figure 4.2: Flying L: energy evolution for different time steps and dissipation parameters.
Slika 4.2: Leteči L: spreminjanje energije za različne časovne korake in disipacijske parametre.
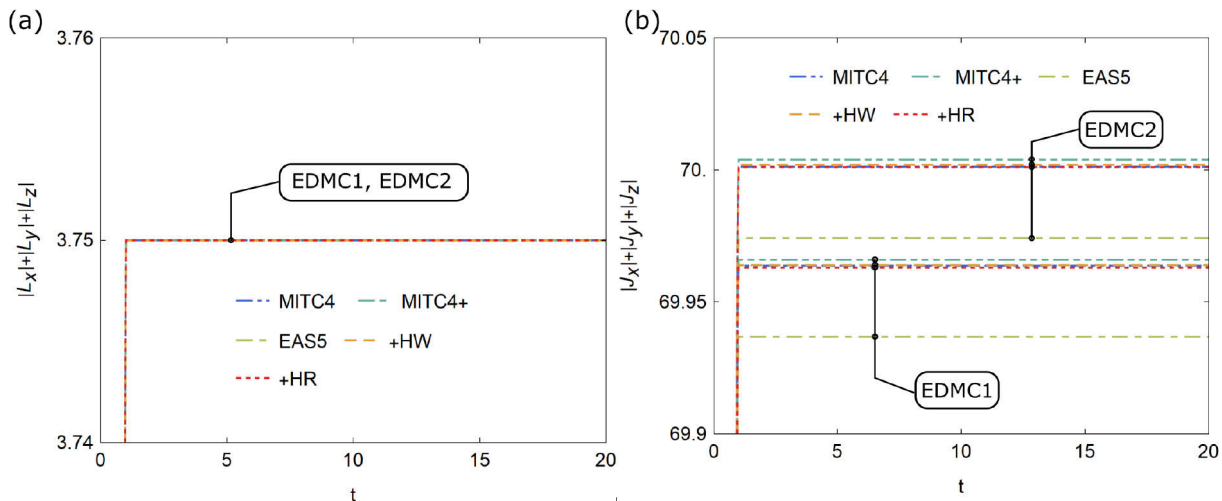
Figure 4.3: Flying L: energy evolution for different time steps and dissipation parameters.

Slika 4.3: Leteči L: spreminjanje gibalne in vrtilne količine za $\alpha_{ED} = 0.4$ in $\Delta t = 0.02$.
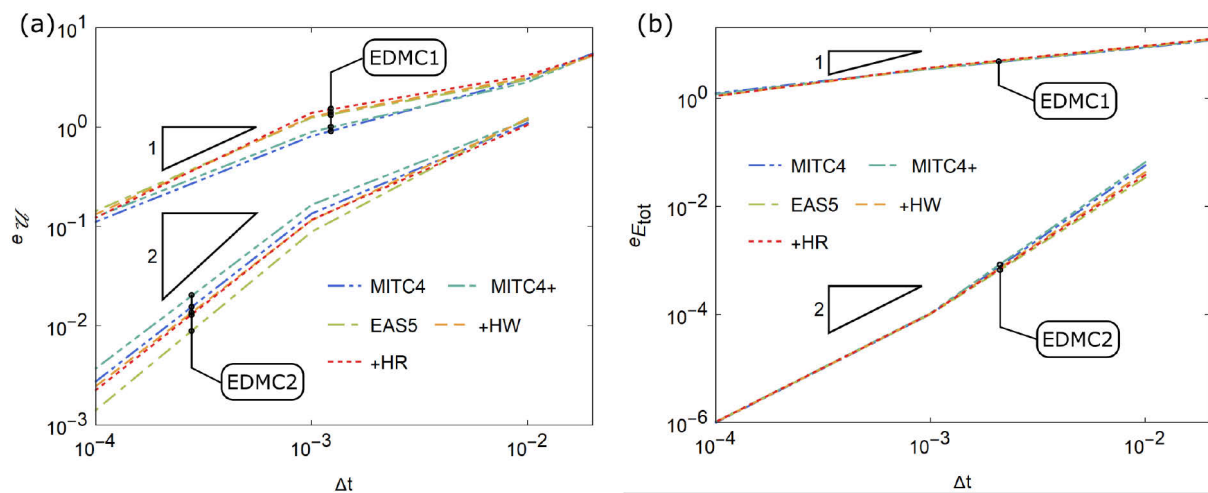
Figure 4.4: Flying L: (a) displacement error, (b) energy error for $\alpha_{ED} = 0.4$.

Slika 4.4: Leteči L: (a) napaka v pomikih, (b) napaka v energiji za $\alpha_{ED} = 0.4$.

4.4.2   Flying short cylinder

We recompute a classical example for shell dynamics, the flying short cylinder, see Figure 3.22 and e.g. [23], [26], [146]. The data are: $R = 7.5$, $H = 3$, thickness $h = 0.02$, density $\rho = 1$, elastic modulus $E = 2 \, 10^8$ and Poisson's ratio $\nu = 0.3$. The cylinder is loaded by impulsive forces and is at rest at $t = 0$, while for $t > 1$, the cylinder exhibits free motion. An adaptive time-stepping scheme (2.81) was used and dissipation factors $\alpha_{ED} \in \{0.05, 0.6\}$ were applied. We look here at the long-term response for time up to $t_f = 500$. For the time-stepping function, $\Delta t_1 = 0.1$, $\Delta t_{min} = 10^{-3}$, $\Delta t_{max} = \begin{cases} 0.1, & 0 \le t \le 1 \\ 5, & 1 < t \end{cases}$.

Table 4.1 shows that EDMC2 scheme requires shorter load increments compared with the EDMC1, which results in a longer CPU time. However, for both schemes, +HW and +HR elements can take larger time increments, which can considerably shorten the computational time. MITC4, MITC4+ and EAS5 elements take approximately the same CPU time to compute the complete response, while the +HW and +HR elements shorten that CPU time for approximately 90% for EDMC1 and 50% for EDMC2. This

kind of time reduction is in agreement with results for statics presented in [104] and [107], where it is shown that +HW and +HR elements can take very large solution steps in static analyses. Figure 4.5 shows that longer steps taken by +HW and +HR are reflected in larger dissipation of the total energy for both EDMC1 and EDMC2. For the EDMC1 scheme, the computed energies gradually converge to the approximately same level for all elements for a large time, indicating that at large t the higher-order vibration modes have been (almost) completely damped and that the motion of cylinder is accompanied (almost) only by low-order vibrations that remain untouched by dissipative procedure. For a short-time response, however, the difference is considerable, because the schemes are only first order accurate. As EDMC2 is second order accurate, the difference in energy levels is not visible in the short-time response, but gradually increases in time due to large load increments taken by +HW and +HR elements.

Table 4.1: Short cylinder: computational details.
Preglednica 4.1: Kratek cilinder: računske podrobnosti.

Formulation	Scheme	$\alpha_{\text{ED}} = 0.6$			$\alpha_{\text{ED}} = 0.05$		
		Normalized CPU time	Number of increments	Avg. no. of iterations in increment	Normalized CPU time	Number of increments	Avg. no. of iterations in increment
MITC4	EDMC1	1	1340	11.0	1	3250	10.6
	EDMC2	21.07	18435	10.3	8.78	31120	9.5
MITC4+	EDMC1	0.96	1246	11.1	0.99	3206	10.7
	EDMC2	21.95	19286	10.3	10.34	37468	9.5
EAS5	EDMC1	1.17	1328	11.0	1.12	3347	10.6
	EDMC2	21.50	18226	10.3	8.96	31155	9.5
+HW	EDMC1	0.13	199	8.9	0.08	350	8.8
	EDMC2	10.06	13071	7.5	5.10	20758	7.9
+HR	EDMC1	0.12	199	8.9	0.07	342	8.9
	EDMC2	9.73	13346	7.5	4.95	21575	7.9

Figure 4.6 shows that for each of the schemes and for constant Δt all elements give the same energy curves and that the differences in results in Figure 4.5 is only due to the adaptive time step algorithm which assigns different time steps to the elements. It further shows that EDMC2 often fails to compute full response when constant Δt is used. In Figure 4.7, we present displacement $u_x - kt$, where $u_x = \boldsymbol{u} \cdot [1,0,0]^T$ and k is a suitable constant, of the mid-surface point initially located at $\{R, 0, 0\}$. For EDMC1 scheme, the effect of large dissipation ($\alpha_{ED} = \beta_{ED} = 0.6$) is seen in lower number of waves, which are smooth because of the considerable damping. More waves are observed in the same time interval for lower dissipation ($\alpha_{ED} = \beta_{ED} = 0.05$) and their shapes vary more. On the other hand, the EDMC2 scheme yields results that are in very good agreement for all the elements and are not affected by the choice of damping. The effect of the error for first order accurate EDMC1 scheme for +HW and +HR elements, which is caused by the larger time steps, can be observed on Figure 4.7. In conclusion, +HW and +HR elements can take large time steps, but due to the low accuracy of the derived EDMC1 schemes, this can be fully exploited only when EDMC2 is used.
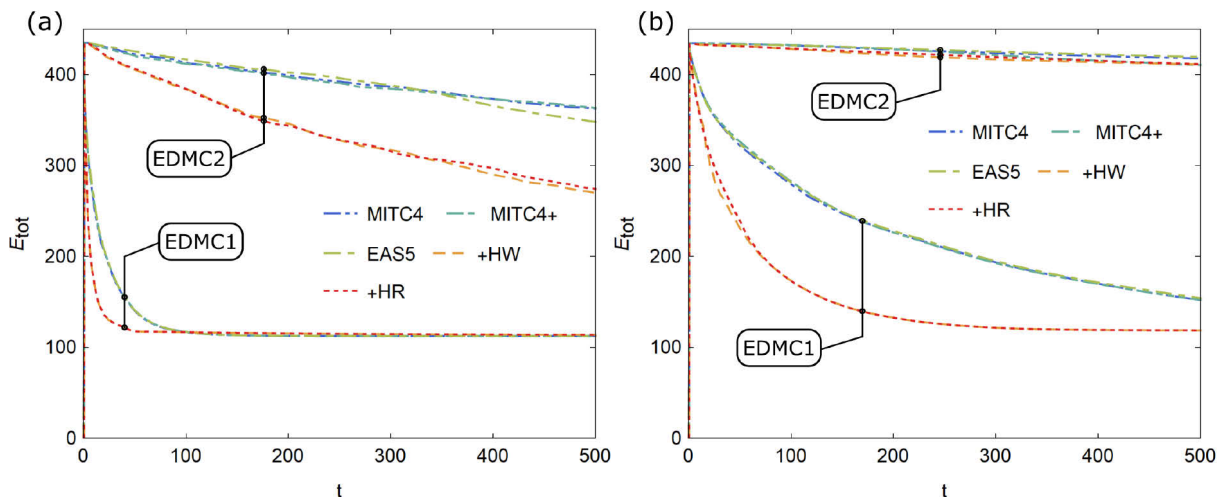
Figure 4.5: Short cylinder: total energy for (a) $\alpha_{ED} = 0.6$ and (b) $\alpha_{ED} = 0.05$.

Slika 4.5: Kratek cilinder: celotna energija za (a) $\alpha_{ED} = 0.6$ in (b) $\alpha_{ED} = 0.05$.
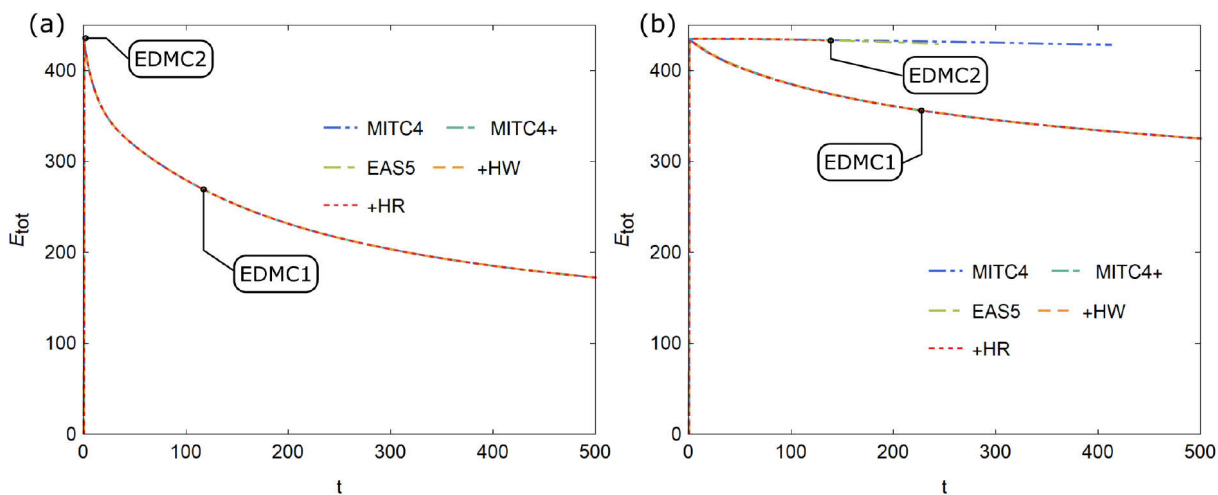
Figure 4.6: Short cylinder: total energy for (a) $\alpha_{ED} = 0.6$ and (b) $\alpha_{ED} = 0.05$, computed with $\Delta t = 0.05$.

Slika 4.6: Kratek cilinder: celotna energija za (a) $\alpha_{ED} = 0.6$ in (b) $\alpha_{ED} = 0.05$, izračunana za $\Delta t = 0.05$.
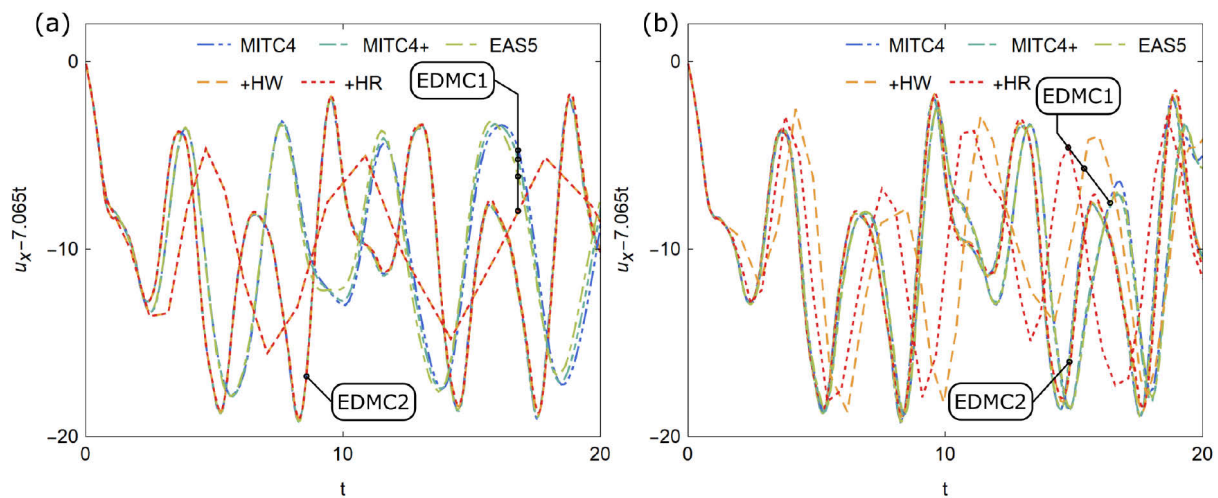
Figure 4.7: Short cylinder: displacement response for (a) $\alpha_{ED} = 0.6$ and (b) $\alpha_{ED} = 0.05$.

Slika 4.7: Kratek cilinder: pomik za (a) $\alpha_{ED} = 0.6$ in (b) $\alpha_{ED} = 0.05$.

4.4.3 Raasch's hook in dynamics

We look here at the classical static benchmark test from Section 2.5.4.2 and modify it to make it more demanding in dynamic analysis. The geometry of the hook still consists of two arches with different radii of curvature, see Figure 4.8, but the boundary conditions are changed. It is pinned at one end and subjected to uniform line forces $F(t)$ and $2F(t)$ at the other end. Thickness $t = 0.02$, width $w = 20$, $E = 3300$ and $v = 0.3$ data were taken as for the nonlinear static example and material density $\rho = 10^{-4}$ was used. The shell was analyzed with meshes of $(2N + 3N) \times N$ elements, where $N \in \{4, 16\}$. Here, N is the number of elements in the width, and $2N$ and $3N$ are the numbers of elements for the first and second arch, respectively. In addition to regular meshes, we also used distorted meshes with pattern shown in Figure 2.15. The ratio between the longest and the shortest element edge (in the curvilinear direction) L_{max}/L_{min} was set to 1.5 and 2 for the first and the second arch, respectively. This has proven a very demanding test for distorted meshes already for static formulations, as was shown in [104] and [107]. In the response graphs, we show the displacement of point A, see Figure 4.8.

A dissipation factor $\alpha_{ED} = \beta_{ED} = 0.1$ was used for all analyses. Reference results were obtained by MITC4+ elements (MITC4 gives the same results) for a fine mesh $N = 32$ by using small time steps for EDMC1 and EDMC2 separately.

The other results were obtained with the adaptive time-stepping function (2.81), with time steps of $\Delta t_1 = 0.5, \Delta t_{min} = 10^{-4}, \Delta t_{max} = \begin{cases} 0.5, & 0 \leq t \leq 12 \\ 10, & 12 < t \end{cases}$.
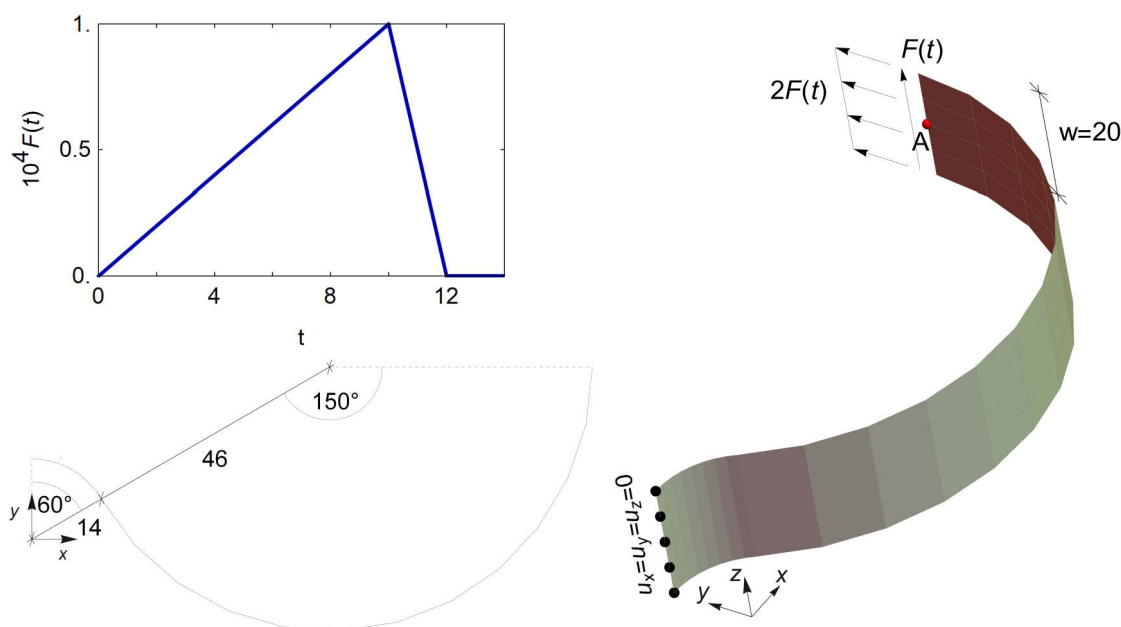
Figure 4.8: Raasch's hook in dynamics: loading function, initial geometry and boundary conditions for mesh $N = 4$.

Slika 4.8: Raascheva kljuka v dinamiki: obtežna funkcija, začetna geometrija in robni pogoji za mrežo $N = 4$.

Figures 4.9 and 4.10 show how mesh distortion effects the results for EDMC1 and EDMC2 schemes, respectively. For the coarse mesh $N = 4$, MITC4+, +HW, +HR (that all employ the membrane ANS

concept) perform much better than MITC4 and EAS5, especially for distorted mesh. This is the case for both EDMC1 and EDMC2 scheme. The response of EAS5 is better than that of MITC4, but the improvement is not very significant. Nonetheless, none of the elements manage to describe the response very well for the course, distorted mesh. For the mesh $N = 16$, all elements perform good, except MITC4 for distorted mesh. As shown in Figure 4.9, the difference between the MITC4+, +HW and +HR for EDMC1 is in a slight shift of the latter two, which is because larger time steps were taken by +HW and +HR. This results in shorter computational time and less iterations are needed in each time steps (see Table 4.2). Time steps taken by +HW and +HR were almost always equal to the maximum allowed time step and the computational time was reduced for approximately 45% comparing to MITC4. It could have been reduced even more if bigger Δt_{max} would had been used, however, this would cause a bigger phase shift in the response, see e.g. [105] for an explanation of this phenomena. As for EDMC2 scheme, all the formulations take shorter time steps and the shift for +HW and +HR is not observed in Figure 4.10. However, see Table 4.3, they still manage to take longer time steps and require less iterations per step, compared with other formulations. We can conclude that excellent properties of +HW and +HR regarding low-sensitivity to mesh distortion prolong from statics to dynamics.
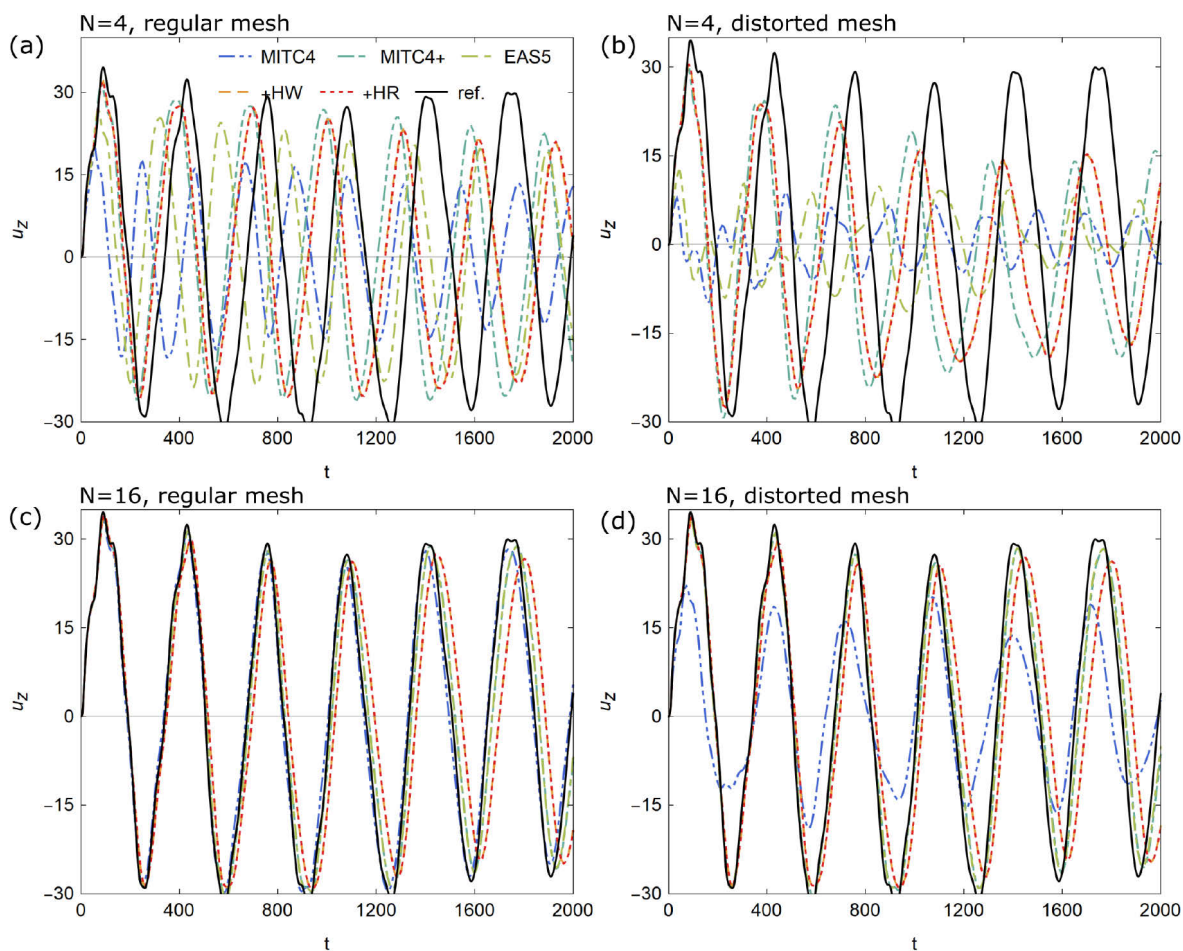
Figure 4.9: Raasch's hook in dynamics: response for regular and distorted mesh for EDMC1.
Slika 4.9: Raascheva kljuka v dinamiki: odziv za običajno in pokvarjeno mrežo za EDMC1.
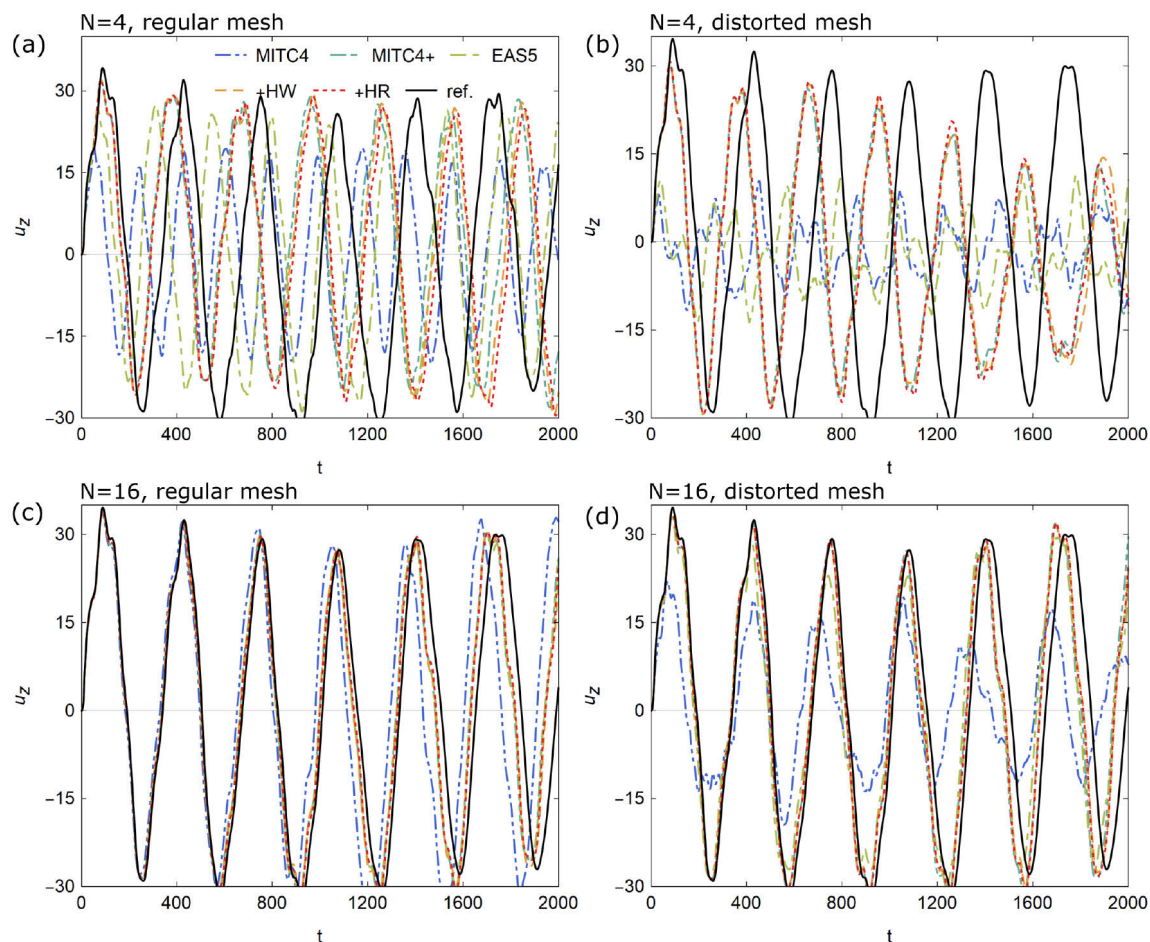
Figure 4.10: Raasch's hook in dynamics: response for regular and distorted mesh for EDMC2.

Slika 4.10: Raascheva kljuka v dinamiki: odziv za običajno in pokvarjeno mrežo za EDMC2.

Table 4.2: Raasch's hook in dynamics: computational details for regular and distorted mesh $N = 16$ for EDMC1.

Preglednica 4.2: Raascheva kljuka v dinamiki: računske podrobnosti za običajno in pokvarjeno mrežo $N = 16$ za EDMC1.

Formulation	Regular mesh			Distorted mesh		
	Normalized CPU time	Number of increments	Avg. no. of iterations in increment	Normalized CPU time	Number of increments	Avg. no. of iterations in increment
MITC4	1.00	355	9.1	1.00	316	9.1
MITC4+	1.01	354	9.1	1.12	354	9.1
EAS5	1.07	348	9.2	1.17	348	9.1
+HW	0.45	224	5.5	0.50	224	5.5
+HR	0.42	224	5.5	0.46	224	5.5

Table 4.3: Raasch's hook in dynamics: computational details for regular and distorted mesh $N = 16$ for EDMC2.
Preglednica 4.3: Raascheva kljuka v dinamiki: računske podrobnosti za običajno in pokvarjeno mrežo $N = 16$ za EDMC2.

Formulation	Regular mesh			Distorted mesh		
	Normalized CPU time	Number of increments	Avg. no. of iterations in increment	Normalized CPU time	Number of increments	Avg. no. of iterations in increment
MITC4	1	3714	8.9	1	6977	9.4
MITC4+	1.04	3937	9.1	0.44	3152	9.3
EAS5	1.33	4669	8.9	0.52	3779	9.3
+HW	0.8	2083	7.5	0.26	2619	7.5
+HR	0.9	2571	7.6	0.09	2485	7.6

4.5 Chapter conclusions

In this chapter we have presented a family of mixed variational formulations for nonlinear structural dynamics and their time discretization that enables user-controlled dissipation of higher structural frequencies.

We have confirmed here also for shell dynamics, as was shown in [107] for static regime, that the EAS formulations offer only a slight improvement of elements' behavior while being computationally slightly more demanding. The ANS+ formulation, on the other hand, offers a great improvement of elements' response for static and also dynamic regime, while the computational performance is not affected. Applying the combination of the ANS+ and hybrid formulations, the computational costs are greatly reduced, while the mesh sensitivity is also reduced.

The EDMC formulations presented in [132] add additional computational cost compared to the classical G-α schemes, due to introduction of velocities as independent nodal dofs. This additional cost can be circumvented by implementing the special implementation procedure proposed in [132], but we have demonstrated here that by using the +HW and +HR formulations, the computational cost is significantly reduced and surpasses even the cost of displacement-based formulations with 5 dofs. Furthermore, the element robustness is greatly improved in comparison to the MITC4 formulation that is typically employed for such simulations.

The first order accuracy of EDMC1 is a serious deficit, but as was demonstrated above the EDMC2 schemes suffers from other deficiencies, such as requiring much shorter load increments. It also has troubles computing the complete response when a constant time step is used. By applying adaptive time stepping algorithms, however, we can overcome some of its flaws.

5   SIMULATION OF SHELL BUCKLING BY IMPLICIT DYNAMICS

Chapter abstract

In this chapter we study shell buckling process by applying implicit structural dynamic time-stepping schemes with numerical dissipation. We are interested in the assessment of the ability of these schemes to handle complex buckling and post-buckling processes of thin shells (even for cases when static path-following methods fail). The computed numerical examples include some classical shell buckling problems where we illustrate that (high-frequency) numerical dissipation is absolutely necessary for an efficient implicit dynamic simulation of complex shell buckling and post-buckling processes. The dynamic results are compared with the static ones that were computed by the path-following method. Finally, it should be noted that the content of this chapter is an extract of the article by Lavrenčič and Brank [102].

All nonlinear numerical examples in this chapter are computed using the dynamic extension of previously analysed 6-parameter, extensible director finite element D-ANS, see Table 2.6 and Sections 2.2.3, 2.3.2 and 2.4.1. Dynamic schemes NTR, NMD, BAM, HHT, GAM, EMC, ED1 are used.

5.1   Chapter introduction

As recognized in the previous chapters, implicit dynamic analysis can be an effective tool to address some difficult problems. In this chapter we will focus on the difficult problem of shell buckling, using the time-stepping schemes from Table 3.1 and Table 3.2 (excluding the EDMC and JWH). Other than EMC and NTR, they all exhibit high-frequency dissipation for linear elastodynamics. Let us recall however, that the dissipative/conservation properties of the above-mentioned schemes are not preserved in nonlinear elastodynamics, as was clearly demonstrated in Chapter 3, see also e.g. [4]. We again stress that for nonlinear elastodynamics, the time-discretization that deviates from the mid-point approximation introduces error in the solution, e.g. [99], and for this reason, the nonlinear stability criterion is not satisfied for the generalized-α schemes. In such case, uncontrollable growth of energy and algorithmic failure can be observed. For numerically stiff problems, which are typical in structural dynamics, the Energy-momentum conserving scheme may produce highly oscillatory response, thus adding to the above mentioned error in the high-frequency range, e.g. [20], [26]. Non-damped and by error polluted higher frequencies may demand ever smaller time steps for Energy-momentum method, until the steps become prohibitively small and the scheme fails. As an extension of the Energy-momentum method, the Energy-decaying scheme is designed to numerically dissipate energy (i.e. both kinematic and potential energies) in a controllable manner, which makes the Energy-decaying scheme a very attractive choice.

In this chapter, we revisit the modified generalized-α method, the Energy-momentum conserving method and the first-order accurate Energy-decaying scheme for the shell model under consideration. We use a 6-parameter, stress-resultant, extensible director shell model, which incorporates the thickness stretch, described for statics in Section 2.2.3 and denoted as D-ANS in Section 2.5 (the considered model should not be confused with the 6-parameter finite rotation model, e.g. [72], [75]). We avoid the transverse locking by enforcing condition $M_{33} = 0$ and by implementing the assumed natural strain (ANS) interpolation for the transverse normal strain [15]. The transverse shear locking is avoided by the

ANS interpolation of the transverse shear strains, suggested by [48]. For benchmark tests presented in Section 2.5 (see also e.g. [152]), the derived 6-parameter quadrilateral element yields practically identical results as the widely adopted 5-parameter MITC4 element presented in Section 2.2.1 (see also e.g. [28] and [47]) or the 7-parameter element from e.g. [19], [24]. As shown in Section 2.5.2.2, the conditioning numbers of linear stiffness matrices of the 6-parameter rotation-less and the 5-parameter element with rotations are of the same order. This indicates that the above mentioned error in the high-frequency range, which is related to the mechanical model, is of the same order for both elements.

The computed numerical examples range from a snap-through and shell collapse to the buckling of perfect and imperfect cylinder under axial load. They demonstrate that the chosen implicit schemes with numerical dissipation are very suitable for the buckling simulation of elastic shell-like structures (which have in many cases little internal dissipation). Implicit structural dynamics can provide very reasonable solutions, even when static path-following methods fail. Moreover, in dynamics, one does not need to deal with the critical (limit and bifurcation) points. Let us finally recall that when considering shell buckling, one should keep in mind the imperfections, which have for many shells strong influence on the buckling load and modes and also on the post-buckling response. The influence of geometric imperfections on cylinder buckling is studied in Section 5.3.6.2. However, a more detailed treatment of shell imperfections is outside the scope of this work. For recent discussions on geometric imperfections we refer to [61] and [62].

5.2   Dynamic shell finite element formulation

5.2.1   Shell model

We model a shell with its middle surface and a field of extensible unit directors, as described in Section 2.2.3. We highlight here only the differences from the D-ANS model and derive its extension to dynamics.

As before, strains and stress resultants are collected in vectors, Saint-Venant-Kirchhoff hyperelastic model is adopted to define the constitutive relations and the value for shell correction factor is set to 5/6. The weak form of the equilibrium equations (i.e. the virtual work equation) can be written as

$$G_{\text{dyn}}(\boldsymbol{u}, \boldsymbol{w}; \delta\boldsymbol{u}, \delta\boldsymbol{w}) = \delta\Pi(\boldsymbol{u}, \boldsymbol{w}; \delta\boldsymbol{u}, \delta\boldsymbol{w}) + A_0 \int_M \delta\boldsymbol{u} \cdot \ddot{\boldsymbol{u}}\, dA + I_0 \int_M \delta\boldsymbol{w} \cdot \ddot{\boldsymbol{w}}\, dA$$
$$- \int_M \delta\boldsymbol{u} \cdot \boldsymbol{n}^{def}\, p\, dA = 0, \tag{5.1}$$

where $\delta\Pi(\boldsymbol{u}, \boldsymbol{w}; \delta\boldsymbol{u}, \delta\boldsymbol{w})$ is defined in (2.15). Acceleration of the middle surface point is denoted as $\ddot{\boldsymbol{u}}$, acceleration of shell director vector is $\ddot{\boldsymbol{d}} = \ddot{\boldsymbol{w}}$, and A_0 and I_0 are the middle surface mass density and inertia of the shell director, respectively, defined in (4.64). The deformation-dependent pressure p, having direction of normal to deformed middle surface $\boldsymbol{n}^{def} = (\boldsymbol{r}_\xi \times \boldsymbol{r}_\eta)/\| \boldsymbol{r}_\xi \times \boldsymbol{r}_\eta \| = \boldsymbol{n}^{def}(\boldsymbol{u})$, is considered in (5.1). For thin shell $\boldsymbol{n}^{def} \approx \boldsymbol{t}/\| \boldsymbol{t} \| = \boldsymbol{n}^{def}(\boldsymbol{w})$, since the negligible transverse shear strains in thin shell keep the deformed shell director (almost) perpendicular to the deformed middle surface. This approximation will be adopted in this work. We further refer to Sections 2.2.3. and 3 for more detailed explanation of the used notation.

Functional (5.1) incorporates three sets of equations that define any structural model: (weak) equilibrium equations, kinematic equations, and constitutive equations. It provides a system of nonlinear equations after using finite element method for its discretization in space and an implicit dynamics time-stepping scheme for its discretization in time, which will be only briefly addressed in the next two sections, respectively.

5.2.2 Discretization in space

Over the element domain A_e, the interpolation of the shell initial and deformed configurations, defined by middle surface and shell director, is performed following Eqs. (3.4)-(3.6) from Section 2.3.2. Membrane and bending strains, ε_{ab}^h and κ_{ab}^h, respectively, are expressed at a Gauss integration point using local Cartesian basis. The approximation of transverse shear and normal strains on the other hand rely on the assumed natural strain (ANS) concepts described in Sections 2.4.1.1 and 2.4.1.3.

Taking into account the spatial discretization, relations between the mesh and element degrees-of-freedom, kinematic admissibility of nodal virtual displacements, and displacement boundary conditions, functional (5.1) becomes an assembly of finite element contributions with mesh nodal values as the unknowns

$$G_{\text{dyn}}^h = \mathbb{A}_{e=1}^{n_{el}} G_{\text{dyn}}^e(\delta \boldsymbol{u}_a, \delta \boldsymbol{w}_a; \boldsymbol{u}_a, \boldsymbol{w}_a) =$$

$$\mathbb{A}_{e=1}^{n_{el}} \int_{A_e} \left(\delta \boldsymbol{\varepsilon}^h \cdot \boldsymbol{N}^h + \delta \boldsymbol{\kappa}^h \cdot \boldsymbol{M}^h + \delta \boldsymbol{\gamma}^h \cdot \boldsymbol{Q}^h \right) dA + \mathbb{A}_{e=1}^{n_{el}} \int_{A_e} \left(A_0 \delta \boldsymbol{u}^h \cdot \ddot{\boldsymbol{u}}^h + I_0 \delta \boldsymbol{w}^h \cdot \ddot{\boldsymbol{w}}^h \right) dA \quad (5.2)$$

$$-\mathbb{A}_{e=1}^{n_{el}} \int_{A_e} \left(\delta \boldsymbol{u}^h \cdot \overline{\boldsymbol{b}} + \delta \boldsymbol{u}^h \cdot \boldsymbol{n}^{def,h} \, p \right) dA - \mathbb{A}_{e=1}^{n_{el}} \int_{\Gamma_{\bar{t},e}} \delta \boldsymbol{u}^h \cdot \bar{\boldsymbol{t}} \, ds = 0.$$

5.2.3 Discretization in time

Following the development from 4.3, we partition the time interval of interest $[t_0, T]$ into a number of sub-intervals $[t_0, T] = \bigcup_{n=0}^{N}[t_n, t_{n+1}]$. Let $(\cdot)_{a,n}$ denote the given value of $(\cdot)_a$ at t_n, and let $(\cdot)_{a,n+1}$ denote the corresponding value at t_{n+1}. We choose the Newmark approximations [118] to express nodal accelerations and velocities at t_{n+1}

$$\dot{\boldsymbol{u}}_{a,n+1} = \frac{\gamma}{\beta \Delta t}\left(\boldsymbol{u}_{a,n+1} - \boldsymbol{u}_{a,n}\right) - \frac{\gamma - \beta}{\beta}\dot{\boldsymbol{u}}_{a,n} - \frac{\gamma - 2\beta}{2\beta}\Delta t \, \ddot{\boldsymbol{u}}_{a,n},$$

$$\ddot{\boldsymbol{u}}_{a,n+1} = \frac{1}{\beta \Delta t^2}\left(\boldsymbol{u}_{a,n+1} - \boldsymbol{u}_{a,n}\right) - \frac{1}{\beta \Delta t}\dot{\boldsymbol{u}}_{a,n} - \frac{1 - 2\beta}{2\beta}\ddot{\boldsymbol{u}}_{a,n}, \quad (5.3)$$

$$\dot{\boldsymbol{w}}_{a,n+1} = \frac{\gamma}{\beta \Delta t}\left(\boldsymbol{w}_{a,n+1} - \boldsymbol{w}_{a,n}\right) - \frac{\gamma - \beta}{\beta}\dot{\boldsymbol{w}}_{a,n} - \frac{\gamma - 2\beta}{2\beta}\Delta t \, \ddot{\boldsymbol{w}}_{a,n},$$

$$\ddot{\boldsymbol{w}}_{a,n+1} = \frac{1}{\beta \Delta t^2}\left(\boldsymbol{w}_{a,n+1} - \boldsymbol{w}_{a,n}\right) - \frac{1}{\beta \Delta t}\dot{\boldsymbol{w}}_{a,n} - \frac{1 - 2\beta}{2\beta}\ddot{\boldsymbol{w}}_{a,n}. \quad (5.4)$$

To approximate nodal values within the interval $[t_n, t_{n+1}]$ we will use linear interpolations, e.g. [38], so the approximation of nodal acceleration at $t_{n+\alpha_m}$ and nodal displacement and external loading at $t_{n+\alpha_f}$ goes as

$$\ddot{\boldsymbol{u}}_{a,n+\alpha_m} = \alpha_m\,\ddot{\boldsymbol{u}}_{a,n+1} + (1-\alpha_m)\ddot{\boldsymbol{u}}_{a,n}, \qquad \ddot{\boldsymbol{w}}_{a,n+\alpha_m} = \alpha_m\,\ddot{\boldsymbol{w}}_{a,n+1} + (1-\alpha_m)\ddot{\boldsymbol{w}}_{a,n},$$

$$\boldsymbol{u}_{a,n+\alpha_f} = \alpha_f\,\boldsymbol{u}_{a,n+1} + (1-\alpha_f)\boldsymbol{u}_{a,n}, \qquad \boldsymbol{w}_{a,n+\alpha_f} = \alpha_f\,\boldsymbol{w}_{a,n+1} + (1-\alpha_f)\boldsymbol{w}_{a,n}, \qquad (5.5)$$

$$\overline{\boldsymbol{b}}_{n+\alpha_f} = \alpha_f\,\overline{\boldsymbol{b}}_{n+1} + (1-\alpha_f)\overline{\boldsymbol{b}}_n, \qquad \overline{\boldsymbol{t}}_{n+\alpha_f} = \alpha_f\,\overline{\boldsymbol{t}}_{n+1} + (1-\alpha_f)\overline{\boldsymbol{t}}_n,$$

where $t_{n+\alpha_m} = \alpha_m t_{n+1} + (1-\alpha_m)t_n$, $t_{n+\alpha_f} = \alpha_f t_{n+1} + (1-\alpha_f)t_n$. Research on the conservation of energy and momentum, e.g. [23], [96], [146], motivates the use of the same linear interpolation to approximate the internal forces at $t_{n+\alpha_f}$

$$\boldsymbol{N}_{n+\alpha_f}^h = \alpha_f \boldsymbol{N}_{n+1}^h + (1-\alpha_f)\boldsymbol{N}_n^h = \boldsymbol{C}^m \cdot \left[\alpha_f\,\boldsymbol{\varepsilon}_{n+1}^h + (1-\alpha_f)\boldsymbol{\varepsilon}_n^h\right],$$

$$\boldsymbol{M}_{n+\alpha_f}^h = \alpha_f \boldsymbol{M}_{n+1}^h + (1-\alpha_f)\boldsymbol{M}_n^h = \boldsymbol{C}^b \cdot \left[\alpha_f\,\boldsymbol{\kappa}_{n+1}^h + (1-\alpha_f)\boldsymbol{\kappa}_n^h\right], \qquad (5.6)$$

$$\boldsymbol{Q}_{n+\alpha_f}^h = \alpha_f \boldsymbol{Q}_{n+1}^h + (1-\alpha_f)\boldsymbol{Q}_n^h = \boldsymbol{C}^s \cdot \left[\alpha_f\,\boldsymbol{\gamma}_{n+1}^h + (1-\alpha_f)\boldsymbol{\gamma}_n^h\right].$$

Approximation (5.3), (5.4) and interpolations (5.5), (5.6) can be used for time-discretization of functional (5.2) as

$$\delta\mathrm{G}_{dyn}^h = \mathbb{A}_{e=1}^{nel}\delta\mathrm{G}^e\big(\delta\boldsymbol{u}_a, \delta\boldsymbol{w}_a; \boldsymbol{u}_{a,n+1}, \boldsymbol{w}_{a,n+1}\big) =$$

$$\mathbb{A}_{e=1}^{nel}\int_{A_e}\left(\delta\boldsymbol{\varepsilon}^h\cdot\boldsymbol{N}_{n+\alpha_f}^h + \delta\boldsymbol{\kappa}^h\cdot\boldsymbol{M}_{n+\alpha_f}^h + \delta\boldsymbol{\gamma}^h\cdot\boldsymbol{Q}_{n+\alpha_f}^h\right)dA$$

$$+\mathbb{A}_{e=1}^{nel}\int_{A_e}\left(A_0\delta\boldsymbol{u}^h\cdot\ddot{\boldsymbol{u}}_{n+\alpha_m}^h + I_0\delta\boldsymbol{w}^h\cdot\ddot{\boldsymbol{w}}_{n+\alpha_m}^h\right)dA \qquad (5.7)$$

$$-\mathbb{A}_{e=1}^{nel}\int_{A_e}\left(\delta\boldsymbol{u}^h\cdot\overline{\boldsymbol{b}}_{n+\alpha_f} + \delta\boldsymbol{u}^h\cdot\boldsymbol{n}_{n+\alpha_f}^{def,h}\,p_{n+\alpha_f}\right)dA - \mathbb{A}_{e=1}^{nel}\int_{\Gamma_{\bar{t},e}}\delta\boldsymbol{u}^h\cdot\overline{\boldsymbol{t}}_{n+\alpha_f}\,ds = 0,$$

where accelerations are applied at $t_{n+\alpha_m}$, and loadings and internal forces are applied at $t_{n+\alpha_f}$. Note that $\boldsymbol{n}_{n+\alpha_f}^{def,h} = \boldsymbol{n}_{n+\alpha_f}^{def,h}\big(\boldsymbol{w}_{a,n+\alpha_f}\big)$.

Several implicit time-stepping schemes that fall into class of generalized-α method [96] can be obtained by varying α_m, α_f, β and γ in (5.8). They are summarized in Table 3.1, where parameters α_m, α_f, β and γ are given as functions of spectral radius at infinity $\rho_\infty \in [0,1]$, which controls the amount of numerical dissipation. Listed parameters are optimal for α-methods (in linear elastodynamics) for minimizing low-frequency and maximizing high-frequency dissipations [38].

Besides the schemes from Table 3.1 (with the exception of JWH) we will also use the first-order accurate modification of EMC scheme, namely the Energy-decaying scheme (ED1 from Table 3.2) that we denote here as ED, e.g. [26], [132]. It is important to note that dissipation parameters defined in this section follow the development from [26], so a slight modification compared to the ED1 scheme from Section 3.4, is applied. The interval of validity for the dissipation parameters is modified from the original values $\alpha_{ED}, \beta_{ED} \in [0,1]$ to $\alpha_{ED}, \beta_{ED} \in [0,0.5]$. Namely values $\alpha_{ED} = \beta_{ED} = 0.5$ now correspond to the same level of dissipation that was achieved in Chapter 3 using values $\alpha_{ED} = \beta_{ED} = 1$. This change is visible also in the expressions (5.8) and (5.9).

The EMC can be modified to dissipate high frequencies by: (i) replacing (5.6) with

$$\boldsymbol{N}_{n+\alpha_f} = \boldsymbol{C}^m \cdot \left[\alpha_f\,\boldsymbol{\varepsilon}_{n+1} + (1-\alpha_f)\boldsymbol{\varepsilon}_n + \alpha_{ED}(\boldsymbol{\varepsilon}_{n+1} - \boldsymbol{\varepsilon}_n\,)\right],$$

$$\boldsymbol{M}_{n+\alpha_f} = \boldsymbol{C}^b \cdot \left[\alpha_f\,\boldsymbol{\kappa}_{n+1} + (1-\alpha_f)\boldsymbol{\kappa}_n + \alpha_{ED}(\boldsymbol{\kappa}_{n+1} - \boldsymbol{\kappa}_n\,)\right], \qquad (5.8)$$

$$\boldsymbol{Q}_{n+\alpha_f} = \boldsymbol{C}^s \cdot \left[\alpha_f\,\boldsymbol{\gamma}_{n+1} + (1-\alpha_f)\boldsymbol{\gamma}_n + \alpha_{ED}(\boldsymbol{\gamma}_{n+1} - \boldsymbol{\gamma}_n\,)\right],$$

where α_{ED} controls dissipation in potential energy, (ii) replacing Newmark approximations for velocities in (5.4) with (note that $\beta = 1/4$ and $\gamma = 1/2$)

$$\frac{(\boldsymbol{u}_{a,n+1} - \boldsymbol{u}_{a,n})}{\Delta t} = \frac{1}{2}(\dot{\boldsymbol{u}}_{a,n} + \dot{\boldsymbol{u}}_{a,n+1}) + \beta_{ED}(\dot{\boldsymbol{u}}_{a,n+1} - \dot{\boldsymbol{u}}_{a,n})$$

$$\Rightarrow \dot{\boldsymbol{u}}_{a,n+1} = \frac{1}{(\Delta t/2 + \beta_{ED}\Delta t)}(\boldsymbol{u}_{a,n+1} - \boldsymbol{u}_{a,n}) - \dot{\boldsymbol{u}}_{a,n}(\Delta t/2 - \beta_{ED}\Delta t)),$$

$$\frac{(\boldsymbol{w}_{a,n+1} - \boldsymbol{w}_{a,n})}{\Delta t} = \frac{1}{2}(\dot{\boldsymbol{w}}_{a,n} + \dot{\boldsymbol{w}}_{a,n+1}) + \beta_{ED}(\dot{\boldsymbol{w}}_{a,n+1} - \dot{\boldsymbol{w}}_{a,n})$$

$$\Rightarrow \dot{\boldsymbol{w}}_{a,n+1} = \frac{1}{(\Delta t/2 + \beta_{ED}\Delta t)}(\boldsymbol{w}_{a,n+1} - \boldsymbol{w}_{a,n} - \dot{\boldsymbol{w}}_{a,n}(\Delta t/2 - \beta_{ED}\Delta t)),$$

(5.9)

where β_{ED} controls dissipation in kinetic energy, and (iii) replacing accelerations in (5.5) with

$$\ddot{\boldsymbol{u}}_{a,n+1/2} = \frac{\dot{\boldsymbol{u}}_{a,n+1} - \dot{\boldsymbol{u}}_{a,n}}{\Delta t}, \qquad \ddot{\boldsymbol{w}}_{a,n+1/2} = \frac{\dot{\boldsymbol{w}}_{a,n+1} - \dot{\boldsymbol{w}}_{a,n}}{\Delta t},$$

(5.10)

thus completing the description of ED scheme for the extensible director shell model.

5.3   Numerical examples

We have already shown in Section 2.5.2 that the proposed 6-parameter element passes the basic Patch test and although it has 13 nonzero eigenvalues, compared to the 9 nonzero eigenvalues of the 5-parameter elements, they have the conditioning number of the same order. This indicates that 6-parameter element might produce some more high-frequency modes in dynamics, but the frequency range of these modes will be the same for both elements.

Static analyses were performed either by the path-following method described in [150] (hereinafter denoted as AL) or by the displacement-control (hereinafter denoted as DC). The chosen path-following method is in fact cylindrical arc-length [41]. For AL, the maximal and minimal allowed incremental arc-lengths were $\Delta\gamma_{max} = 0.5$ and $\Delta\gamma_{min} = 10^{-8}$, respectively.

Table 5.1: Minimal and maximal allowed Δt.
Preglednica 5.1: Najmanjši in največji dovoljeni Δt.

Example	Δt_{min} [s]	Δt_{max} [s]	$\Delta t_{initial}$ [s]
5.3.2	10^{-4}	10^{-1}	10^{-2}
5.3.3.1	10^{-5}	$2 \cdot 10^{-3}$ *	$2 \cdot 10^{-3}$
5.3.3.2	10^{-5}	10^{-2}	$2 \cdot 10^{-3}$
5.3.4	10^{-6}	10^{-2}	$2 \cdot 10^{-3}$
5.3.5	10^{-6}	10^{-2}	$2 \cdot 10^{-3}$
5.3.6	10^{-8}	$2 \cdot 10^{-3}$ **	10^{-2}

* Around buckling initiation, $\Delta t_{max} = 5 \cdot 10^{-4}$ s.

** Until $t = 0.28$ s, $\Delta t_{max} = 10^{-2}$ s.

For dynamic analyses, the adaptive time-step-size function (2.81) was used, with the desired and maximal allowed number of incremental iterations set to $I_0 = 8$ and $N = 25$, respectively. Minimal and maximal allowed time steps, as well as the initial one, are presented in Table 5.1 for all examples. For examples 5.3.2 – 5.3.5, spectral radius $\rho_\infty = 0.9$ was chosen. For example 5.3.6, values of ρ_∞ are given

in Section 5.3.6. The chosen parameters for ED scheme were $\alpha_{ED} = 0.02$ and $\beta_{ED} = 0.02$. The convergence tolerance was 10^{-8}.

5.3.1 Static benchmark tests

We have already tested extensively the derived element in static settings in Section 2.5, where we denoted it as D-ANS. Here we present two additional benchmark tests to demonstrate that the derived 6-parameter shell element performs well for standard shell problems. The data is given in Figure 5.1. The tests were also computed by the 5-parameter large rotation shell element from [28] and [47], denoted as MITC4 in Section 2.5. The results of both elements match well with each other and also with [152], who used Abaqus S4R element, see Figure 5.2. This indicates that the performance of the derived 6-parameter rotation-less element is indeed comparable to the 5-parameter large rotation elements. We note that example in Figure 5.1 (a) differs from the pinched cylinder example from Figure 2.39.
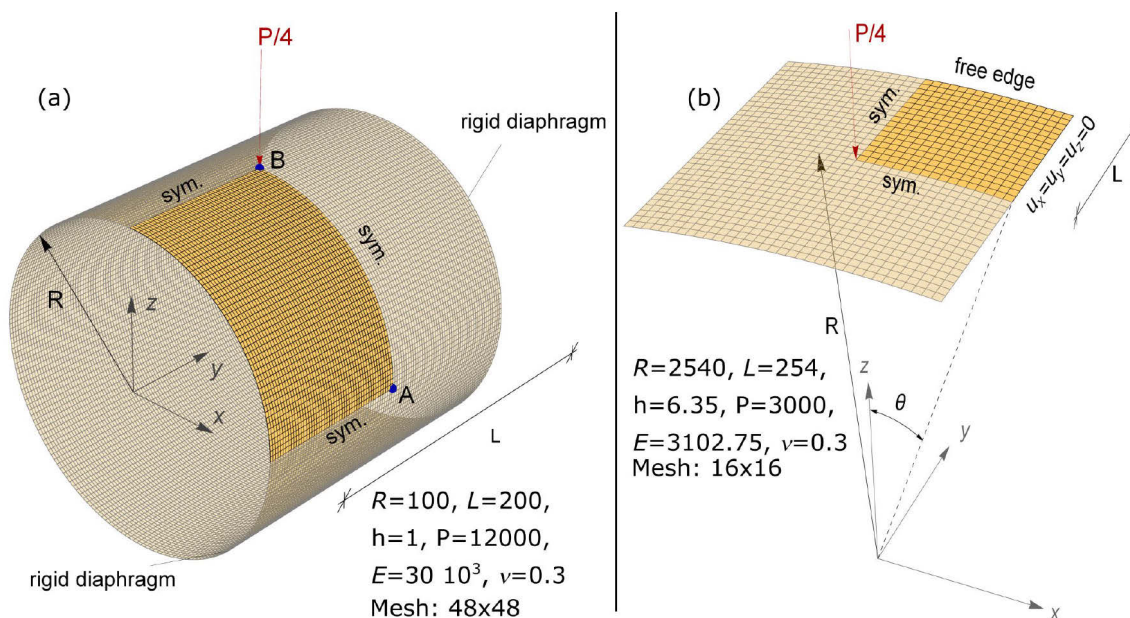
Figure 5.1: Data for (a) pinched cylindrical shell with end rigid diaphragms, (b) hinged cylindrical panel.
Slika 5.1: Podatki za (a) preščipljen cilinder s končnimi diafragmami, (b) členkast cilindrični panel.
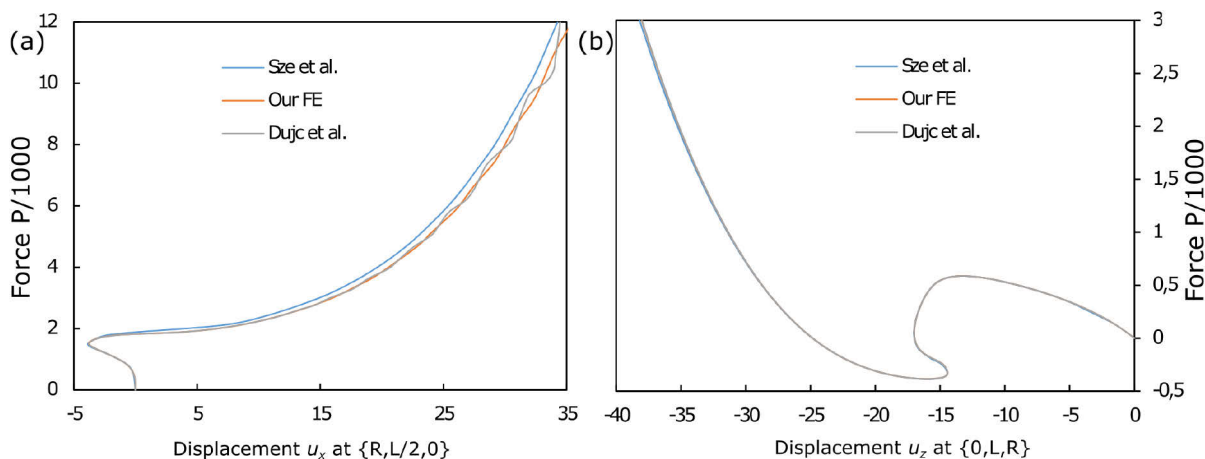
Figure 5.2: Load-deflection curves for (a) pinched cylindrical shell and (b) hinged cylindrical panel.
Slika 5.2: Krivulje odziva za (a) preščipljen cilinder in (b) členkast cilindrični panel.

5.3.2   Dynamic benchmark test

In order to illustrate the performance of the dynamic formulation for the D-ANS element with the implicit time-stepping schemes, a dynamic benchmark test of the flying short cylinder is executed, see Section 3.6.3 and Figure 3.22 for example details. Let us repeat that the cylinder is loaded by a set of impulsive nodal forces and for $t > 1$ exhibits free motion. Adaptive time-stepping is used here, as opposed to the constant time increments, used in 3.6.3 and the level of introduced dissipation is low.
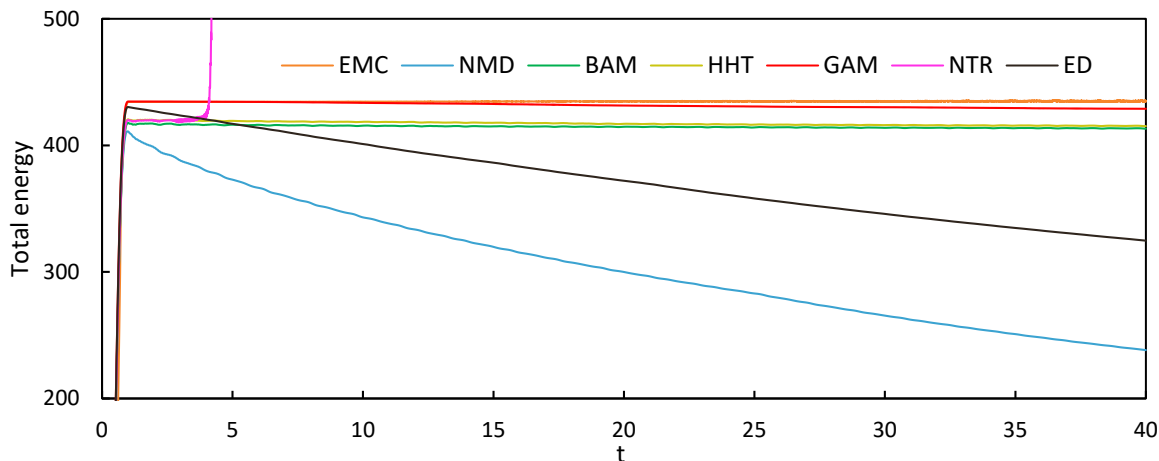
Figure 5.3: Short cylinder: energy evolution in time.
Slika 5.3: Kratek cilinder: razvoj energije v času.
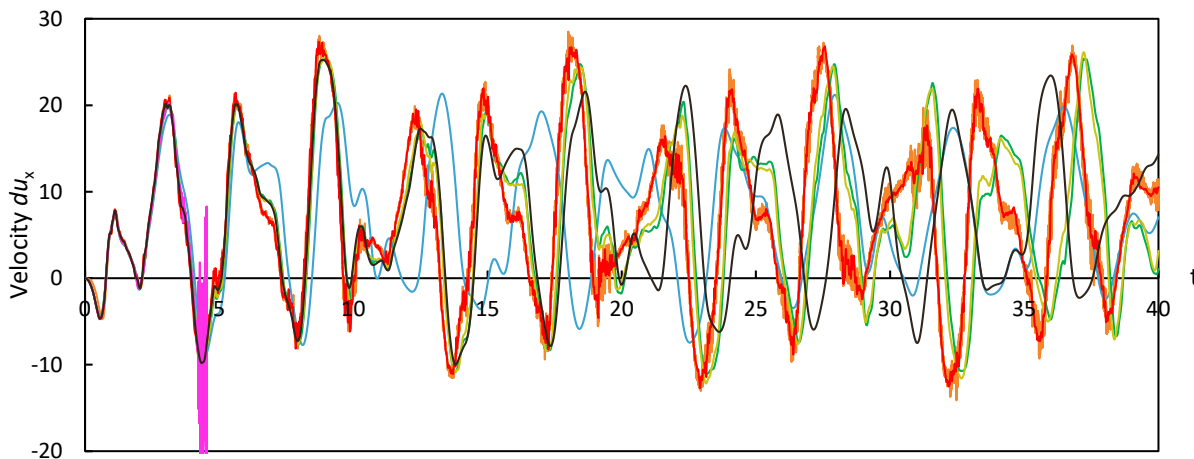
Figure 5.4: Short cylinder: middle surface node velocity versus time.
Slika 5.4: Kratek cilinder: hitrost vozlišča na srednji ploskvi.

Figure 5.3 shows that after $t > 1$ EMC exactly preserves structural energy, and GAM, BAM and HHT predict almost constant energy. GAM energy line is only slightly below the EMC line and BAM and HHT energies are further below. The dissipation of the first-order accurate NMD and ED seems to be exaggerated. NTR analysis blows up at approximately $t \approx 4\ s$. Figure 5.4 shows the time oscillation of velocity in x direction of the middle surface node initially located at $\{R, 0, 0\}$. The dissipative schemes introduce phase shifts in velocity, the larger the dissipation the larger the shift. Results in Figure 5.4 are almost identical for EMC and GAM on one hand and for BAM and HHT on the other hand, with difference between the two pairs increasing with time. NMD produces shift already from the beginning.

Also ED shows considerable phase shift. Figure 5.5 illustrates the tumbling of cylinder; configurations for every 25th step are shown for NMD. Let us note that only EMC ensures exact conservation of linear and angular momentum, whereas some other schemes show only small deviations, which is in agreement with the results for the 5-parameter shell model in Section 3.6.3.
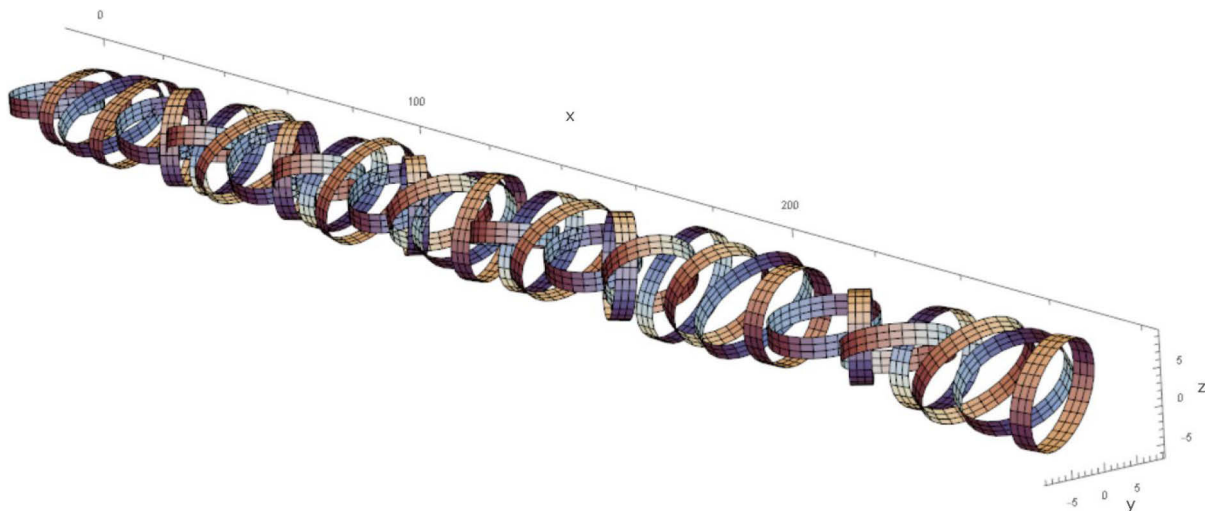
Figure 5.5: Short cylinder: sequence of deformed configurations.
Slika 5.5: Kratek cilinder: zaporedje deformiranih konfiguracij.

5.3.3   Snap-through of a conical shell
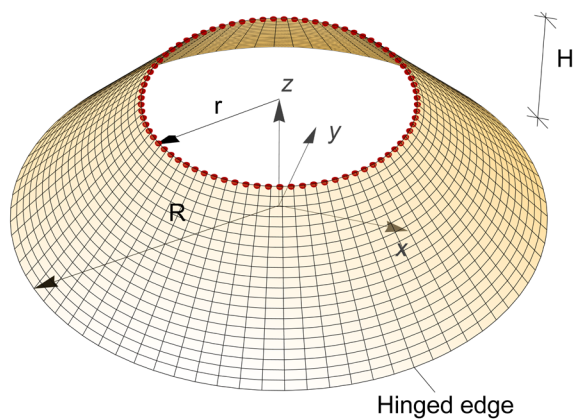
$H = 1$ m, $R = 2$ m, $r = 1$ m,
$h = 0.01$ m, $\rho = 7.8\,\mathrm{t/m^3}$,
$E = 206.9 \cdot 10^6$ kN/m^2, $\nu = 0.29$

Mesh: $80x20$
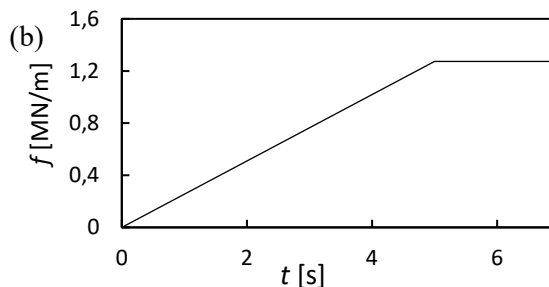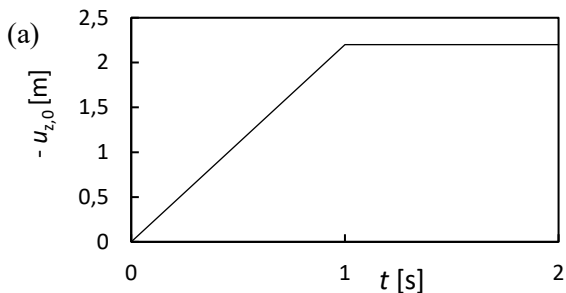
Figure 5.6: Conical shell data.
Slika 5.6: Podatki o stožčasti lupini.

The geometric, material and loading data for this example are shown in Figure 5.6. Two load cases are considered: (a) imposed displacement, and (b) imposed line force, both acting at the top edge in –z direction. The displacements of the bottom edge are constrained. The force-displacement curves in figures below are for the node with initial coordinates $\{0, -r, H\}$.

5.3.3.1   Imposed displacement case

In Figure 5.7, the reaction force versus imposed displacement curve is given. Figure 5.8 shows some deformed configurations, and Figure 5.10 presents energy change with time. The snap-through starts at $t \approx 0.05$ s, when $u_z \approx -0.1$ m. Due to the imposed displacements, the snap-through is controlled and the fully inversed configuration is reached slowly at $t \approx 1$ s, when $u_z \approx -2$ m. Figure 5.7 shows that the matching between the schemes is close until $u_z \approx -1.7$ m, excluding NTR, which blows up at $u_z \approx -0.7$ m. The results start to oscillate at $u_z \approx -1.85$ m, when the shell is just about to fully inverse. EMC displays large oscillations, and also the dissipative schemes produce considerable oscillations between $u_z \approx -1.85$ m and $u_z \approx -2$ m. Figure 5.8 shows that the oscillations relate to the turn-over of the bottom ring just before the full inverse. Four configurations are presented in Figure 5.8 for BAM, with (b1) and (b2) showing configurations before the oscillations and (c) showing configuration after the oscillations are damped.

Figure 5.7 also contains the results of two static analyses: the one based on the displacement control (DC), and the other based on the arc-length (AL). Let us note that the results of dynamic and static analyses do not differ too much until $u_z \approx -1.9$ m. However, both static analyses fail to compute the final part of the force-displacement curve from $u_z \approx -1.9$ m on. Figure 5.7 shows only the first part of the AL computed response. More of it is in Figure 5.9 (left), where the red dot marks the point at which the computation was stopped. Even after several "cycles", the AL analysis did not take the path towards the fully inversed configuration computed by all time-stepping schemes except NTR.

Table 5.2: Buckling loads for displacement imposed case.
Preglednica 5.2: Uklonske sile za primer vsiljevanja pomika.

Integration scheme	Dynamic analyses							Static analyses	
	NMD	ED	BAM	HHT	GAM	EMC	NTR	DC	AL
Buckling load [kN]	9971	10067	10030	10021	10247	10293	10574	9961	9960
Buckling time [s]	0.047	0.048	0.047	0.047	0.048	0.058	0.062	0.050	0.051
load / load (DC) [%]	100.1	101.1	100.7	100.6	102.9	103.3	106.2	100.0	100.0

For comparison of elastic and elasto-plastic static analyses, Figure 5.9 (right) shows the results of static elasto-plastic analysis for Ilyushin stress resultant elasto–plasticity [47], with yield strength $f_y = 355$ MPa and stress-resultant isotropic hardening $H = 2$ MPa. The force, at which the snap-through starts, is for elasto-plastic cone considerably smaller than for elastic one. Figure 5.9 (right) shows that for elasto-plastic static analyses, both DC and AL give proper results. Table 5.2 shows the results for the buckling load. The schemes with dissipation compute almost identical buckling time, while the EMC buckling time is larger. The results of NTR differ most from the rest.
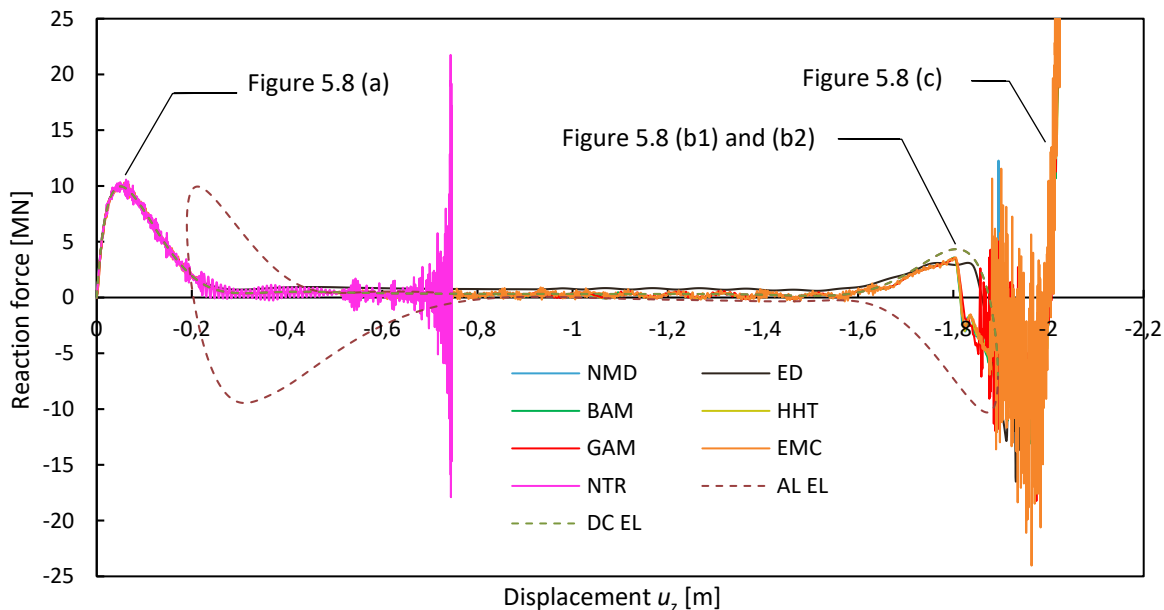
Figure 5.7: Conical shell: reaction force vs. imposed displacement.
Slika 5.7: Stožčasta lupina: reakcijska sila v odvisnosti od vsiljenega pomika.
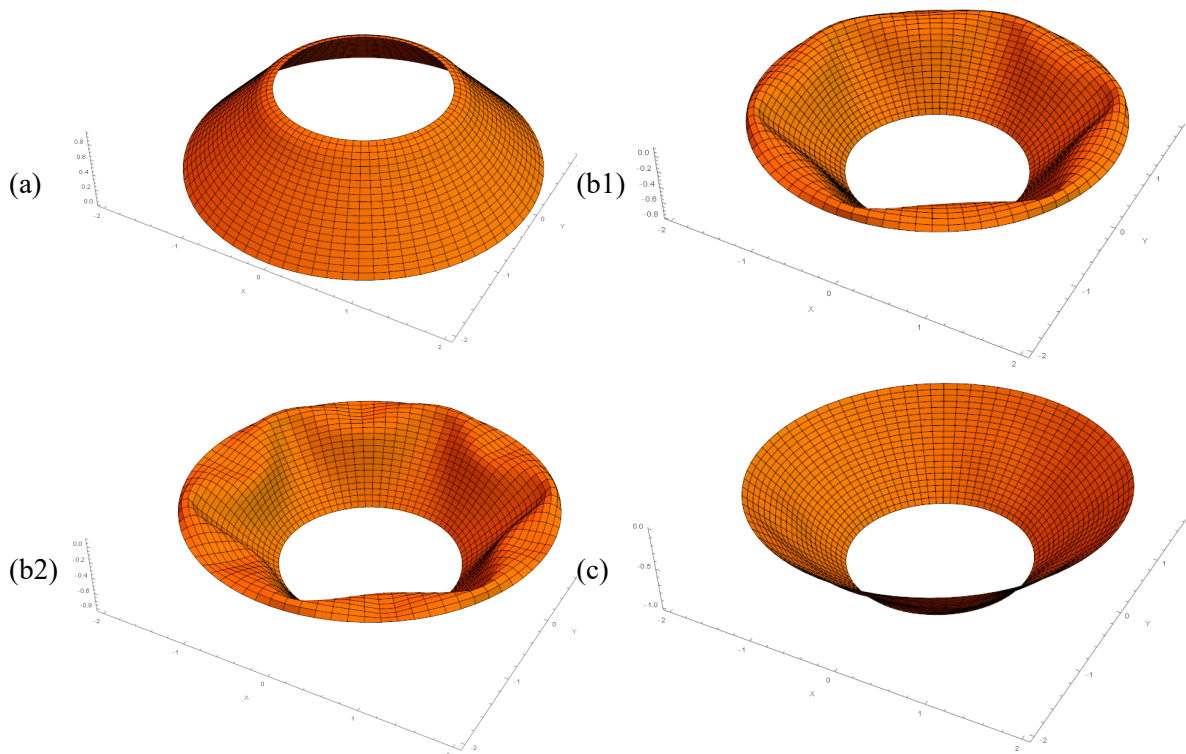
Figure 5.8: Conical shell: deformed shapes for imposed displacement case (BAM).
Slika 5.8: Stožčasta lupina: deformirane konfiguracije za primer vsiljevanja pomika (BAM).

The time-change of total energy is given in Figure 5.10. At the beginning of the snap-through (at $t \approx$ 0.11 s and $u_z \approx -0.22$ m), the energy slowly increases until mark I in Figure 5.10 (see configurations at I in Figure 5.8 (b1) and (b2)), when it starts decreasing until the shell is fully inversed (at $t \approx 1$ s and $u_z = -2$ m). The schemes damp oscillations in different manners, which is the reason that the curves differ after $t \approx 0.85$ s. The large final increase in the energy, marked with II in Figure 5.10, is due to

cone stretching after snap-through. Let us note that NTR energy blows up at $t \approx 0.3$ s and that EMC fails to produce results for the total time of interest. Figure 5.11 shows how the time step changes because of (2.81). ED can use Δt_{max} throughout the entire time of interest. On the other hand, EMC requires extremely short time steps after $t \approx 0.85$ s.
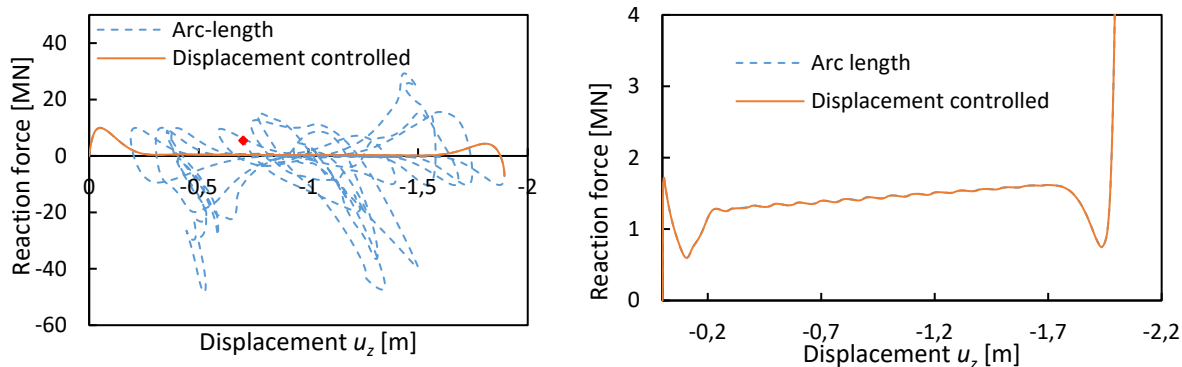
Figure 5.9: Conical shell: results for elastic (left) and elasto-plastic (right) static analysis.
Slika 5.9: Stožčasta lupina: rezultati za elastično (levo) in elasto-plastično (desno) statično analizo.
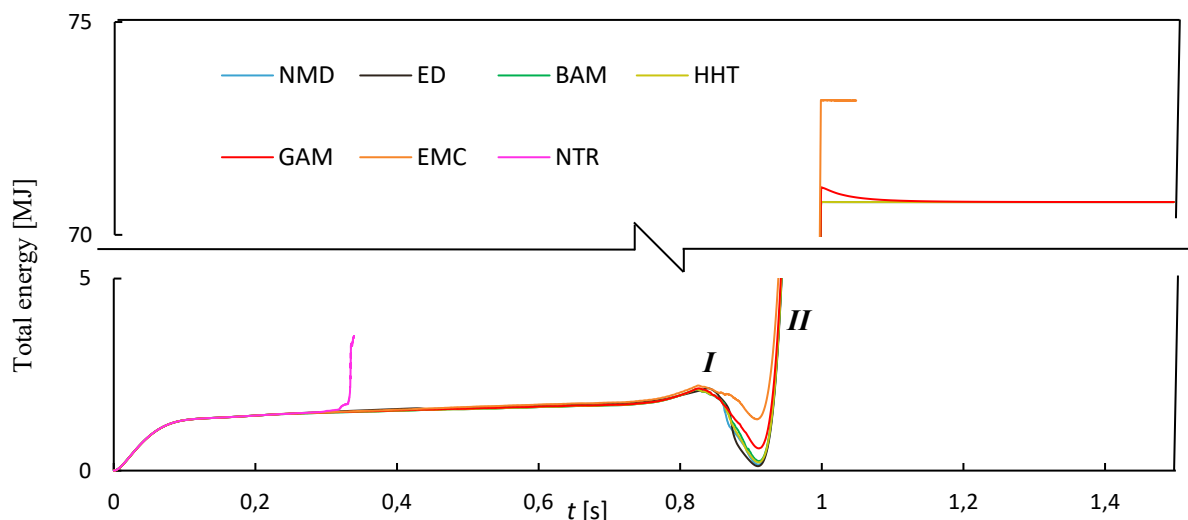
Figure 5.10: Conical shell: total energy evolution in time.
Slika 5.10: Stožčasta lupina: sprememba celotne energije v času.
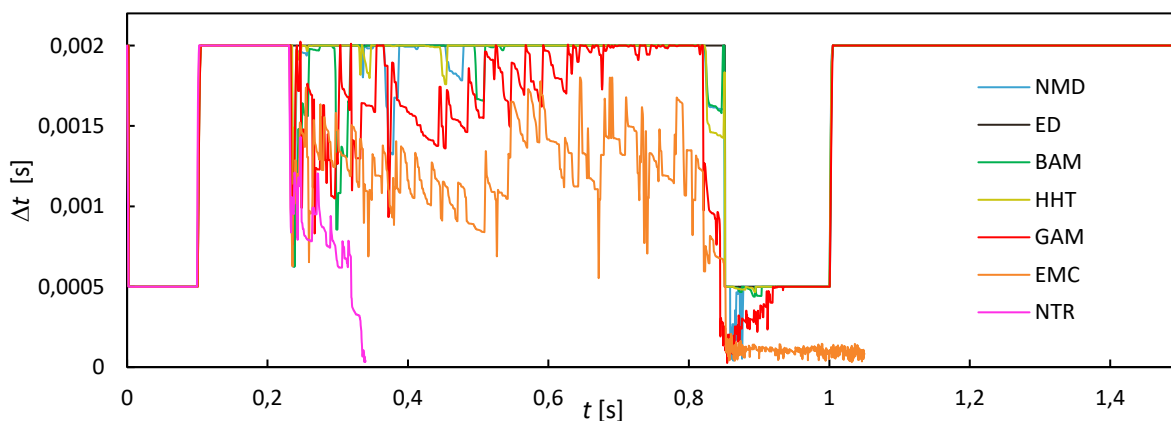
Figure 5.11: Conical shell: time step versus time.
Slika 5.11: Stožčasta lupina: dolžina časovnega koraka v odvisnosti od časa.

5.3.3.2   Imposed force case

A line force is applied on the upper edge of the cone according to the loading function in Figure 5.6 (b), with the final value $f = 1.273$ MN/m. In this load case, the dead load is taken into account, in contrast to the imposed displacement case. The snap-through starts at $t \approx 1$ s (except for ED that predicts it sooner) and it is (almost) instantaneous, contrary to the first load case. Heavy oscillations in displacements and energy occur during and after the snap-through, see Figures 5.12 – 5.14.

Figure 5.12 shows the time evolution of vertical displacement of the node with initial coordinates $\{0, -r, H\}$, and Figure 5.13 shows the time evolution of the energy. Both figures illustrate how the schemes handle the oscillations. ED scheme damps the oscillations quickly and efficiently (although the chosen parameters might produce too much damping). BAM and EMC predict large oscillations (EMC oscillations are extremely large) and the on-going vibrations of the cone, which eventually leads to computational failure due to too small Δt (EMC fails much sooner than BAM). It seems that GAM damping is the most reasonable. Figure 5.14 shows some deformed configurations. Figure 5.15 presents the time step changes due to (2.81). ED can use large time steps for most of the time. NMD, GAM and HHT can also use reasonably large time steps. The imposed force load case is more demanding for dynamic computations than the imposed displacement one, because only NMD, ED, HHT and GAM produce results until the final time $t = 6$ s (the other schemes fail before). For these schemes, the total energy is almost constant after $t = 5$ s, when the external loading is constant.
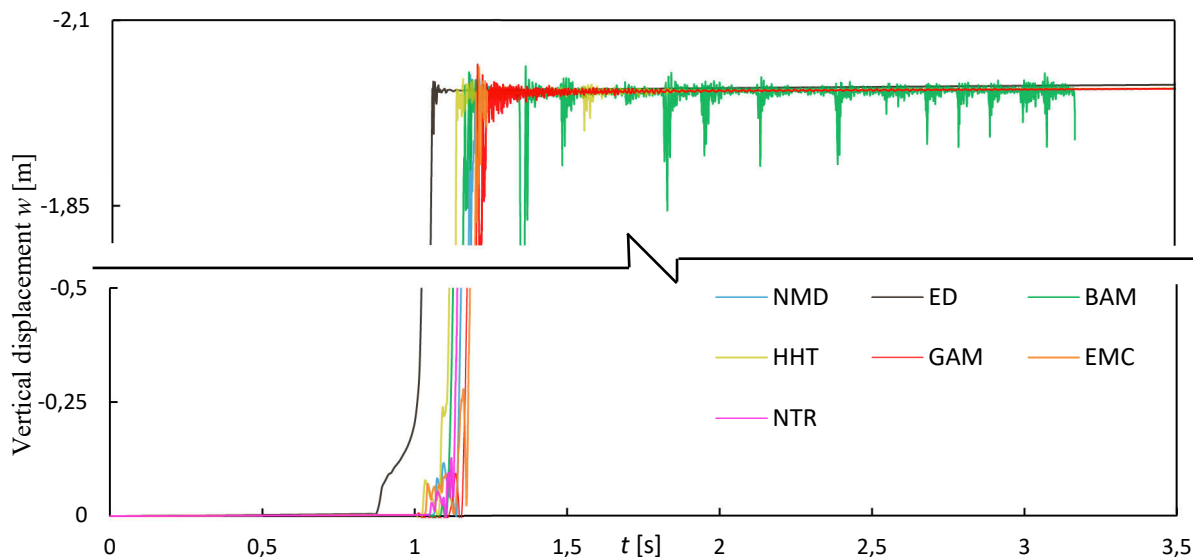
Figure 5.12: Conical shell, line force: vertical displacement of node $\{0, -r, H\}$.
Slika 5.12: Stožčasta lupina, linijska sila: vertikalni pomik vozlišča $\{0, -r, H\}$.
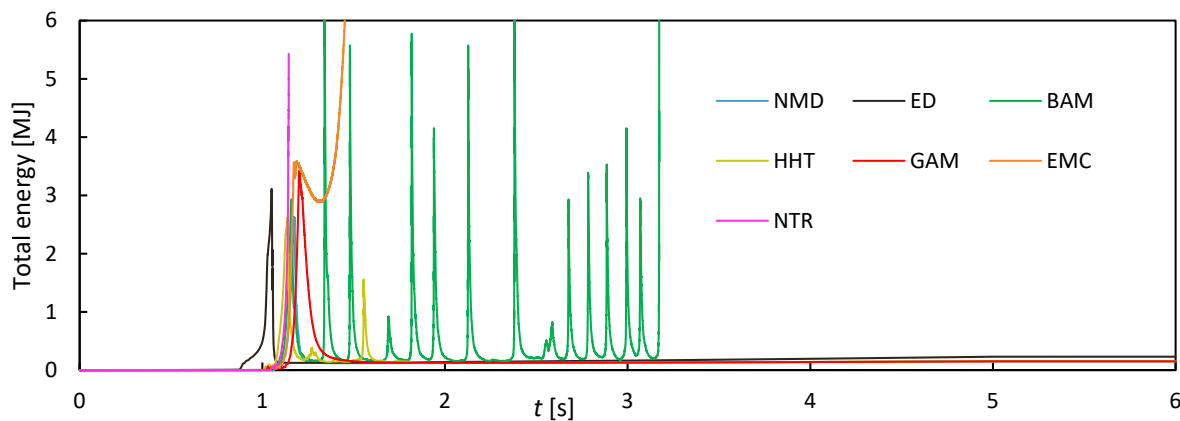
Figure 5.13: Conical shell, line force: total energy evolution in time.
Slika 5.13: Stožčasta lupina, linijska sila: sprememba celotne energije v času.
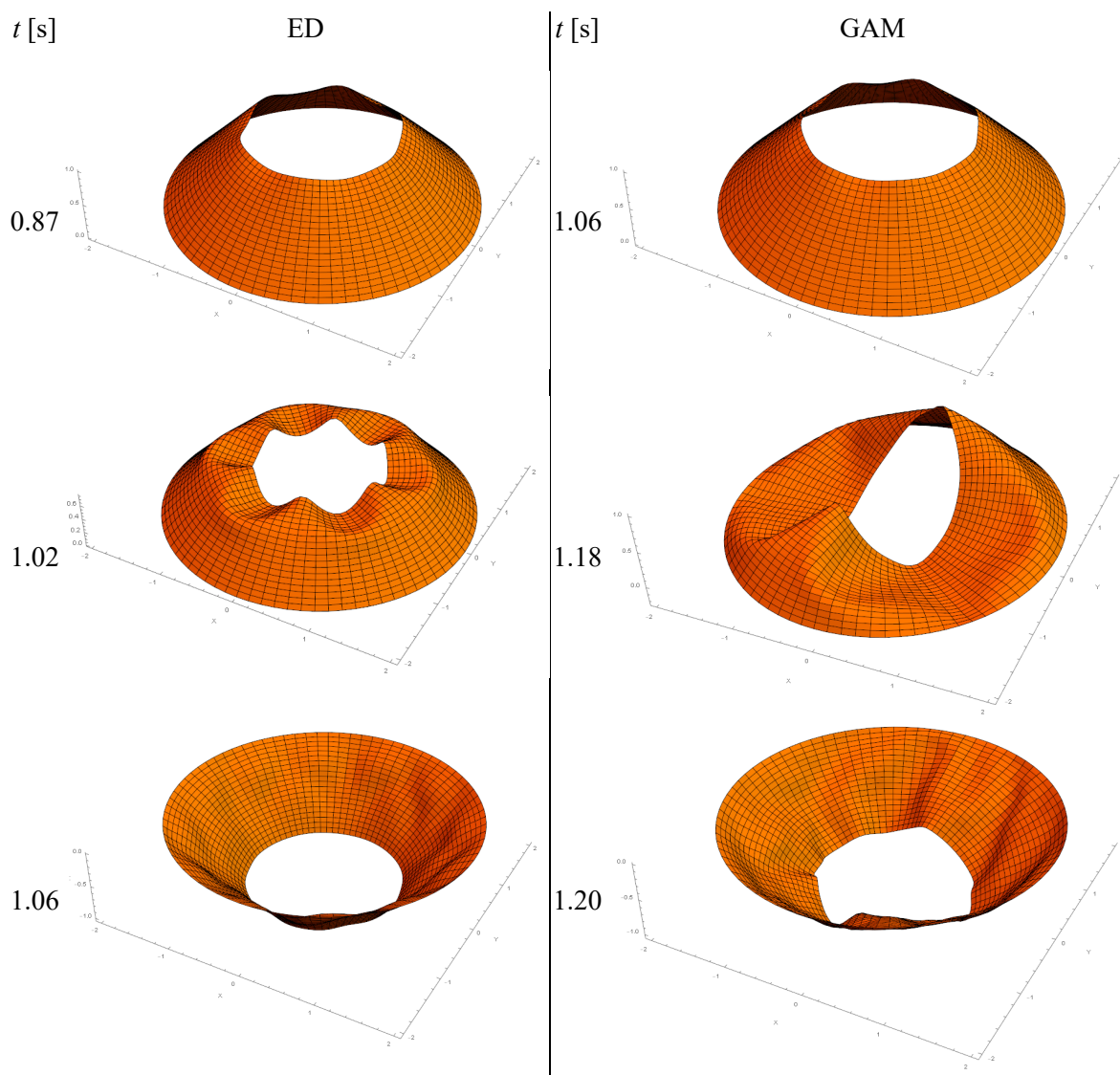
Figure 5.14: Conical shell, line force: deformed shapes.
Slika 5.14: Stožčasta lupina, linijska sila: deformirane konfiguracije.
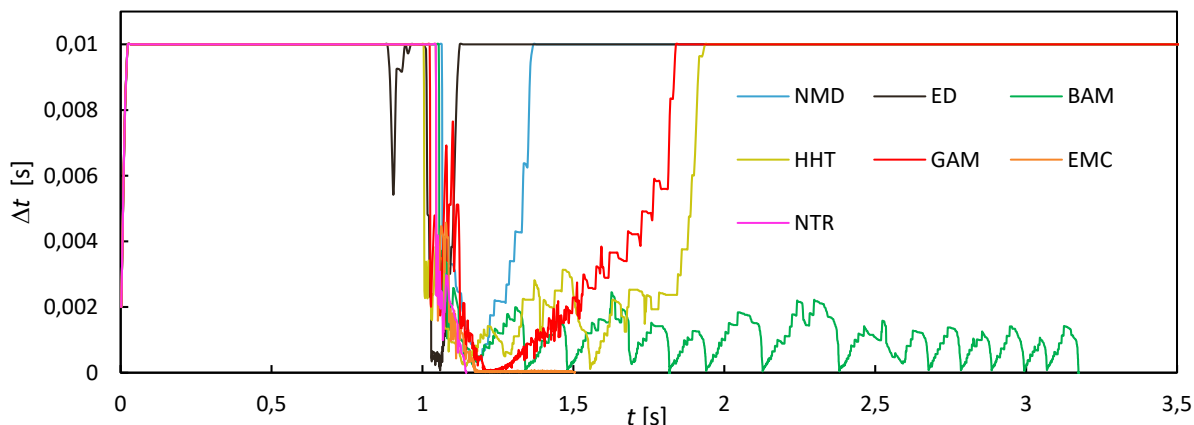
Figure 5.15: Conical shell, line force: time step versus time.
Slika 5.15: Stožčasta lupina, linijska sila: dolžina časovnega koraka v odvisnosti od časa.

5.3.4   Snap-through of thin cylindrical panel

Very thin cylindrical panel ($h/R = 1/4000$) is considered, with geometry, material and loading data as shown in Figure 5.16. Previous examples indicate that the dissipative schemes handle the snap-through problems much better than EMC. Thus, we chose for this example only BAM and GAM. The static arc-length (AL) analysis for $P = \lambda P_0$, where λ is load multiplier, and the static displacement-control analysis are also done. Let us note that the latter failed soon due to the heavy snap-backs in the static load-displacement curve, Figure 5.18.

$R = 4000$ mm, $L = 1600$ mm,
$\rho = 7.8\ 10^{-6}$ kg/mm^3, $h = 1$ mm,
$E = 210\ 10^3$ MPa,
$\nu = 0.3$, $\theta = 2 \arcsin[L/(2R)]$
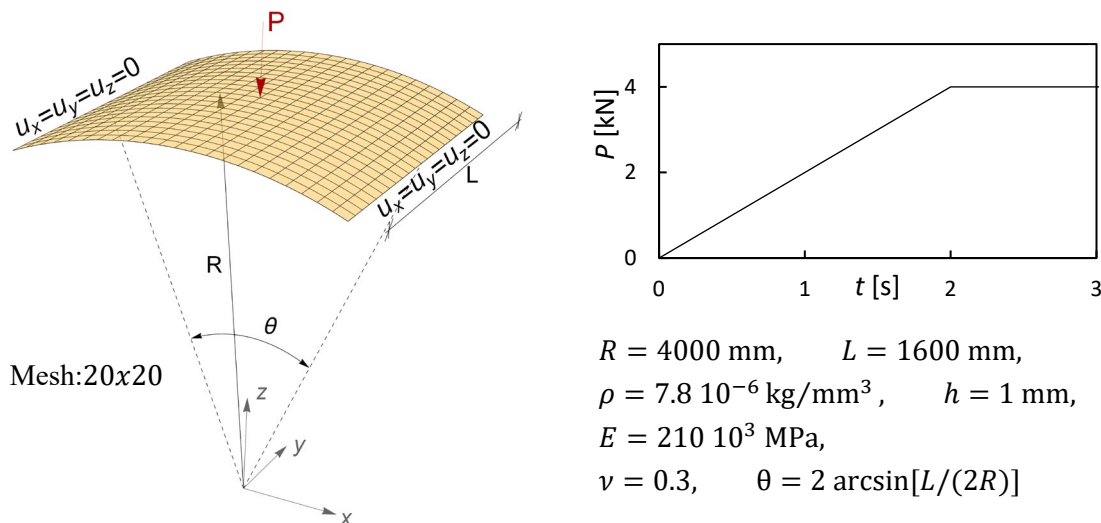
Figure 5.16: Thin panel data.
Slika 5.16: Podatki za tanek panel.

Figure 5.17 shows that the beginning of buckling (snap-through), up to $u_z \approx -20$ mm, is adequately captured by all analyses. Both BAM and GAM predict a considerable push-back of the shell before the snap-through is completed, Figure 5.17. The dissipation smooths oscillations during the snap-through and in the shell inverse configuration. Two deformed configurations are shown in Figure 5.17. They relate to the blue dots in the load-displacement curve. The complete results of the static AL analysis are presented in Figure 5.18. The AL makes many loops, changing considerably the waving pattern of

deformation, but never reaches the complete inverse configuration shown in Figure 5.17. The red dot in Figure 5.18 marks the point where the analysis was stopped. We can conclude that for this example the complete snap-through process can only be computed by dynamic analysis using an energy dissipative scheme. The static analyses fail to compute the complete buckling process.
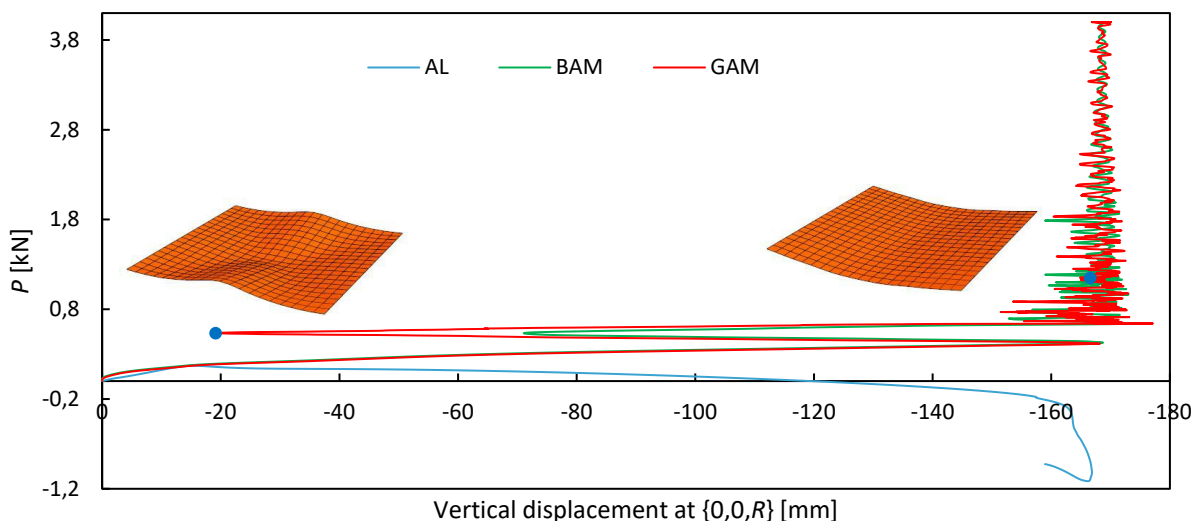
Figure 5.17: Thin panel: vertical displacement versus load.
Slika 5.17: Tanek panel: vertikalni pomik v odvisnosti od obtežbe.
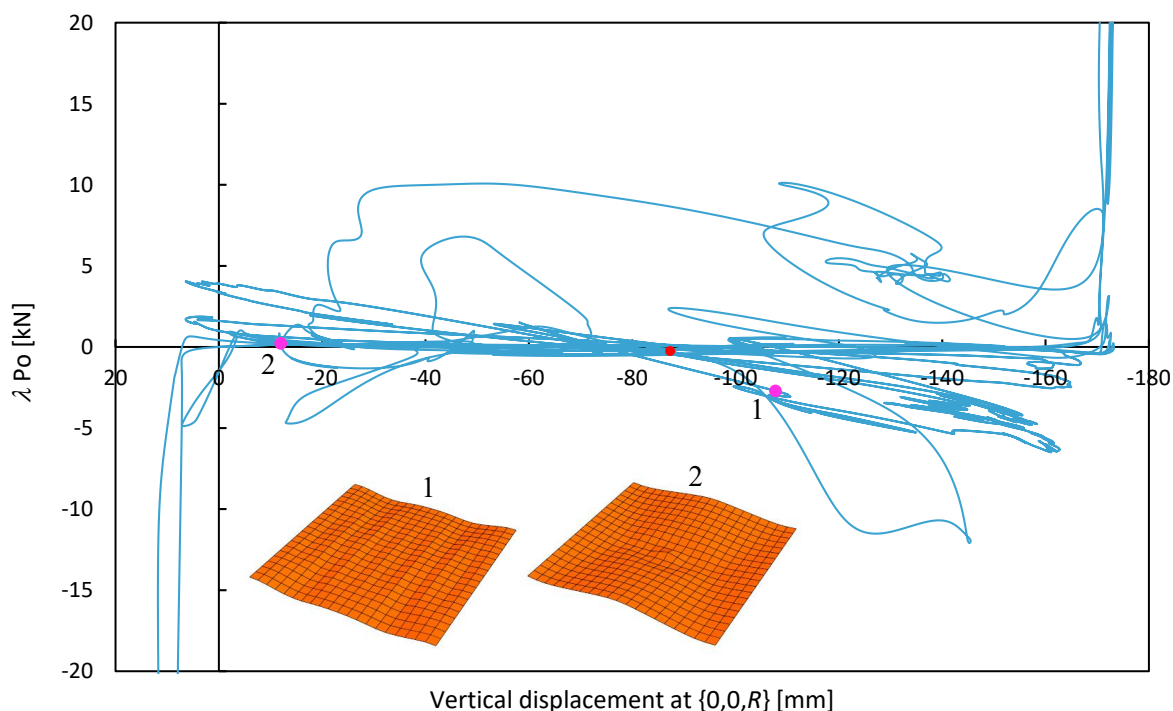
Figure 5.18: Thin panel: vertical displacement versus load for static arc-length analysis.
Slika 5.18: Tanek panel: vertikalni pomik v odvisnosti od obtežbe za statično analizo z metodo ločne dolžine.

5.3.5   Collapse of half-sphere under pressure

Let us consider a half-sphere under external pressure. The geometric, material and loading data are shown in Figure 5.19. The mesh is obtained by mapping a mesh defined on one half of a cube onto the half-sphere. The conservative surface pressure $p(t)$ acts on the outer surface. The problem was analyzed by GAM and BAM and by static AL analysis performed for surface pressure $\lambda(t)\, p_0$.

$R = 1000$ mm, $\rho = 7.8\ 10^{-6}$ kg/mm^3,
$h = 5$ mm, $E = 210\ 10^3$ MPa,
$\nu = 0.3$, $p_0 = 10$ N/mm^2,

Mesh: 2700 elements
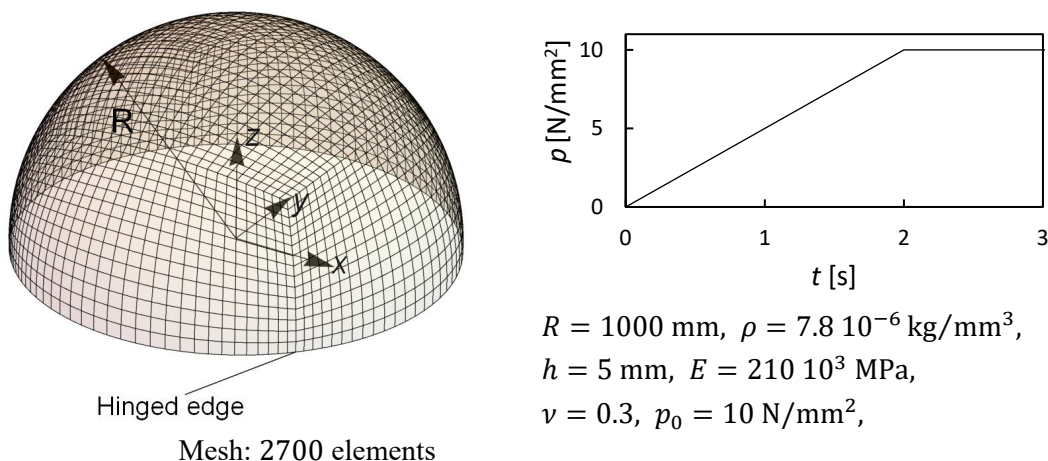
Figure 5.19: Half-sphere data.
Slika 5.19: Podatki za polkroglo.

Figure 5.20 shows pressure versus deflection curves for the upper-most point of the half-sphere. The buckling of the half-sphere under pressure is practically instantaneous. It starts with the appearance of dimples (i.e. wrinkling) that break the half-sphere symmetry (see configurations related to time-point 1 in Figure 5.20). The dimples appear around the lines, which are maps of the edges of the half-cube. This indicates that the location of the dimples relates to small disturbances introduced by spatial discretization. GAM and BAM predict wrinkling formation almost at the same load levels, which are very close to the static buckling load, see Table 5.3. After the initial wrinkling formation, the shell collapses very quickly.

One can observe that the dynamic load-displacement curves are different from the static one. This is because in the load-imposed dynamics the load decrease is not possible, while it is possible in the static arc-length analysis. For dynamic computations, the analysis stops just after the start of buckling (point 1 in Figure 5.20), because no solution for a load higher than the buckling load exists. The schemes compute several deformed configurations just after the start of buckling and then stop (see configurations at points 2 and 3). Note that the time difference between the buckling start (point 1) and point 3 is only $\Delta t \approx 0.005$ s. For static arc-length analysis, the computations can proceed after the buckling load. The load can be reduced in the arc-length analysis, and therefore a new, stable configuration can be found for a much lower load than the buckling load (see configuration at point 5). For this reason, one should not compare configurations 2 and 3 with configurations 4 and 5.
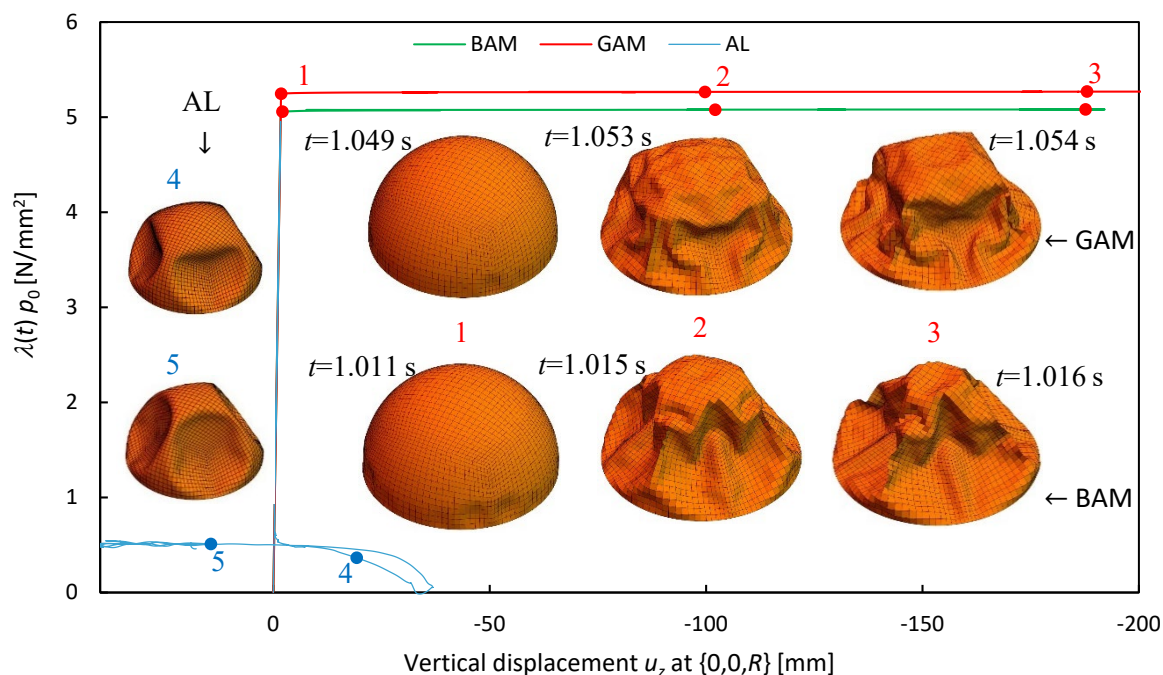
Figure 5.20: Half-sphere: force – displacement curve with deformed meshes at $u_z \approx [-2, -100, -190]$.
Slika 5.20: Polkrogla: krivulja sila-pomik z deformiranimi konfiguracijami pri $u_z \approx [-2, -100, -190]$.

Table 5.3: Half-sphere: buckling loads.
Preglednica 5.3: Polkrogla: uklonske sile.

	Dynamic analyses		Static analysis
Integration scheme	BAM	GAM	AL
Buckling load [N]	5.05	5.24	4.95
load / load(AL) [%]	101.9	105.8	100.0

5.3.6   Buckling of axially loaded cylinder

Let us consider the classical shell problem, elastic buckling of cylinder under axial compression. We refer to [92], who recomputed test specimen Z=500 of Yamaki experiments [175]. The input data (see Figure 5.21) and the experimental results are taken from [175] (see p. 230/Figure 3.52d (a), and p. 433/Figure 5.24b (i)), who tested cylinders made of polyethylene terephthalate, which were carefully manufactured in order to remove (as much as possible) geometric imperfections. Theoretical critical stress for elastic axially compressed cylinder (for axisymmetric buckling mode) is $\sigma_{cr} = \frac{E}{\sqrt{3(1-\nu^2)}} \frac{h}{R}$, e.g. [83]. For the considered cylinder $\sigma_{cr} = 8.31$ MPa and the theoretical critical axial force $P_{cr} = 1290$ N.

$R = 100$ mm, $L = 113.9$ mm,

$\rho = 1.38 \cdot 10^{-6} \text{ kg/mm}^3$, $h = 0.247$ mm,

$E = 5560$ MPa, $\nu = 0.3$

Mesh: $400x80$
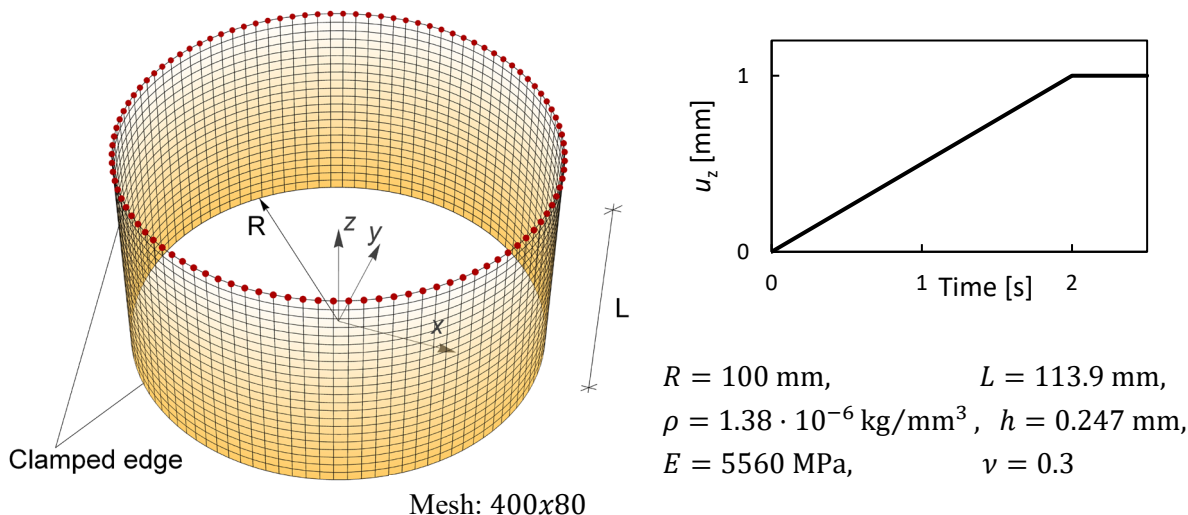
Figure 5.21: Cylinder data.
Slika 5.21: Podatki o cilindru.

The experimental buckling mode was a diamond-like mode with both axial and circumferential waves. The number of waves in the post-buckling changed abruptly several times during the increase of axial displacement. The experimental results are shown in Figure 5.22 (along with the results of our computations). They are labelled as "Asymmetric" and "Symmetric", where the asymmetry and symmetry relate to the shape of buckling mode (i.e. pattern) with respect to the cross-section at the middle-height of the cylinder. The asymmetric patterns (and the related load-displacement curve) were obtained by increasing and decreasing the edge axial displacement, which was imposed during the experiment. On the other hand, the symmetric patterns (and the related curves) were obtained by applying small point-wise disturbance forces (in the shell-normal direction) at certain time-points (by using fingers). One can note that the experimental buckling load in Figure 5.22 is significantly lower than the theoretical one.

Our computations were performed by imposing axial displacement at the upper edge according to function in Figure 5.21. Hereinafter, the number of axial half-waves will be denoted as *m* and the number of circumferential full waves as *n*.

5.3.6.1   Cylinder without geometric imperfections

Cylinder without geometric imperfections was computed with BAM (for $\rho_\infty = 0.6$), GAM (for. $\rho_\infty = 0.8$), and ED (for $\alpha_{ED} = \beta_{ED} = 0.02$). The results are compared with the experiment in Figure 5.22. BAM results match very well with the experiment, except for the buckling load. BAM computes the transition of asymmetric buckling mode into the diamond-like mode, as observed in the experiment (see configurations A-D in Figure 5.22). Moreover, three changes of the wave numbers *m* and *n* match exactly the experimental observations (see configurations E-G in Figure 5.22). ED results match the first experimental buckling modes (A-D), including asymmetric D mode, whereas further ED results coincide with symmetric experimental curves rather than with asymmetric ones. The ED changing of wave numbers is nonetheless in agreement with the experiment. GAM fails to catch the first post-buckling branch with mode D. The cylinder oscillates when the transition to mode D should happen, but

then it skips mode D and jumps into mode E. Figure 5.22 shows that all three schemes can accurately simulate the buckling pattern transition; except GAM, which missed out mode D ($n = 12, m = 2$), and ED preferred symmetric modes instead of asymmetric. For videos of complete responses see [101].

The computed response depends on the amount of numerical dissipation, dictated by ρ_∞ (the smaller ρ_∞ the larger dissipation). Figure 5.23 shows BAM and GAM responses for different values of ρ_∞. For $\rho_\infty = 0.6$ and $\rho_\infty = 0.8$. The BAM results are in very good agreement with the experiment in the post-buckling regime. For larger ρ_∞, the BAM results are completely polluted by higher frequencies. Such pollution is much smaller for GAM results, which, however, always miss out one post-buckling mode. Let us note that small ρ_∞ elongates the buckling-load plateau. Table 5.4 shows that for larger ρ_∞ the required time-step gets shorter and the computational time gets longer.

In order to show the influence of imposed displacement velocity, Figure 5.24 presents results for several load functions for BAM with $\rho_\infty = 0.6$. The load function in Figure 5.21, where the final imposed displacement is reached at $t = 2$ s, is replaced with the load functions where the final imposed displacement is reached at 0.5, 2, 5 and 10 s. Figure 5.24 shows that short loading times result in a long plateau in the force-displacement chart. On this plateau, the axisymmetric pattern forms, which is not observed experimentally. For longer loading time (e.g. $t = 5$ s or $t = 10$ s), with very small inertial forces, the plateau is very short or does not appear at all.
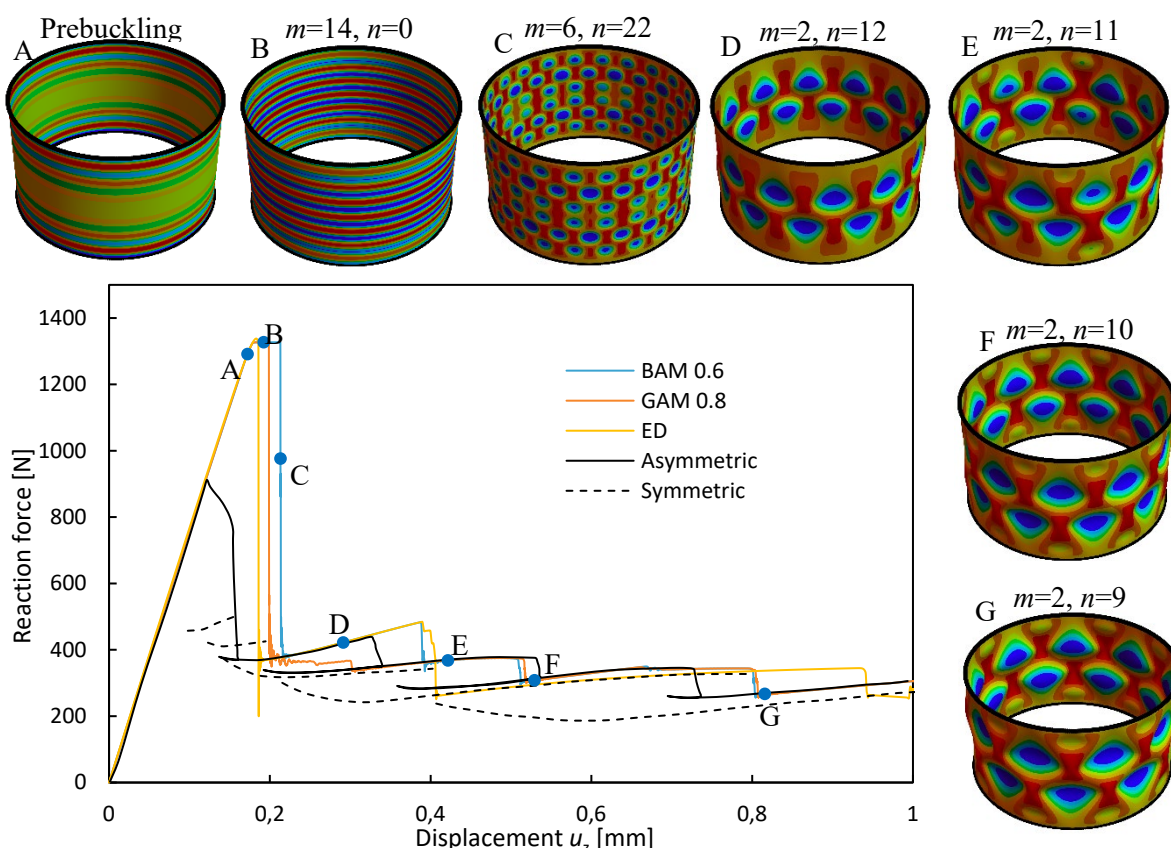
Figure 5.22: Ideal cylinder: force-displacement curves.
Slika 5.22: Idealen cilinder: krivulje sila-pomik.

Table 5.4: Buckling of ideal cylinder: number of time steps for different values of spectral radius.

Preglednica 5.4: Uklon idealnega cilindra: število časovnih korakov za različne vrednosti spektralnega radija.

Time integration scheme	BAM	BAM	BAM	GAM	GAM	GAM	GAM	ED
Spectral radius ρ_∞	0.6	0.8	0.9	0.6	0.8	0.9	0.95	/
Number of time steps	1152	1278	4875	1327	1691	2101	3092	1008
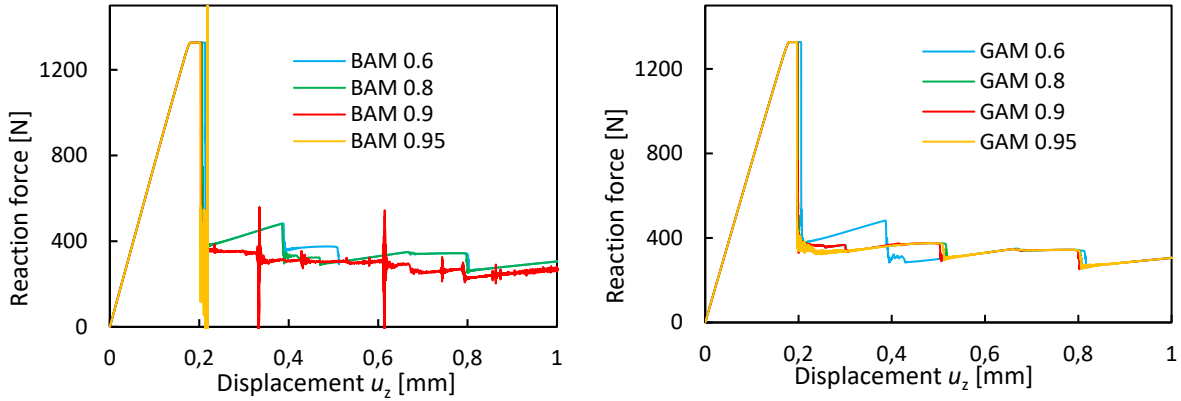
Figure 5.23: Ideal cylinder: response curves for different values of spectral radius.

Slika 5.23: Idealen cilinder: krivulje odziva za različne vrednosti spektralnega radija.
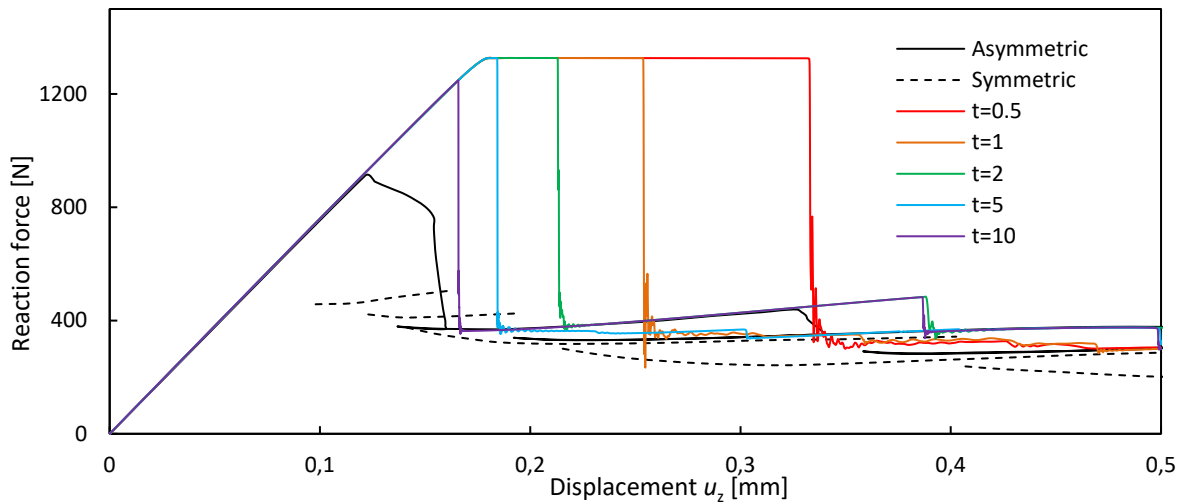
Figure 5.24: Ideal cylinder: response curves for different loading time, for BAM and $\rho_\infty = 0.6$.

Slika 5.24: Idealen cilinder: krivulje odziva za različna trajanja nanašanja obtežbe, za BAM in $\rho_\infty = 0.6$.

5.3.6.2 Cylinder with geometric imperfections

Initial geometric imperfections were added to the considered cylinder. Kobayashi [92] performed linearized buckling analysis to compute cylinder eigenmodes, and then used factorized sum of the first 18 eigenmodes to simulate geometric imperfections. They reported that the first 18 computed eigenmodes could be described by the following half-wave and wave numbers: $m = 13$ and $n = 0, \dots, 7$, and $m = 12$ and $n = 0, \dots, 9$. We adopt the approach of [92]. Moreover, we mimic factorized sum of the first 18 eigenmodes by the following function

$$\Delta R(\theta, z) = \frac{h}{100}\left(\sum_{m=12}^{13} \sin\left[\frac{m\pi z}{L}\right] + \sum_{n=1}^{7} \sin[n\theta] \sin\left[\frac{13\,\pi z}{L}\right] + \sum_{n=1}^{9} \sin[n\theta] \mathrm{Sin}\left[\frac{12\,\pi z}{L}\right] \right) \quad (5.11)$$

where 1% of the cylinder thickness was chosen for the amplitude, as suggested by [92]. Let us note that ΔR was added to the cylinder radius R when the mesh was generated.

Results of the analyses of cylinder with geometric imperfections are given in Figure 5.25. The imperfections reduce the computed buckling load (with respect to ideal cylinder) and make it comparable with experimental buckling load. The primary buckling patterns change (with respect to ideal cylinder), see configurations A-D in Figure 5.25. However, once the first diamond-like post-buckling mode is reached (configuration E with $n = 12, m = 2$), further buckling pattern transition is exactly the same as for the ideal cylinder and experiment. Moreover, GAM does not miss out mode with $n = 12, m = 2$, which was the case for ideal cylinder. Let us note that there is a difference between BAM and GAM results only in the first part of post-buckling curves in Figure 5.25. Comparison of results for ideal and imperfect cylinder show that a difference is up to the buckling mode with $n = 12, m = 2$, and that after that load-displacement curves do not differ much.
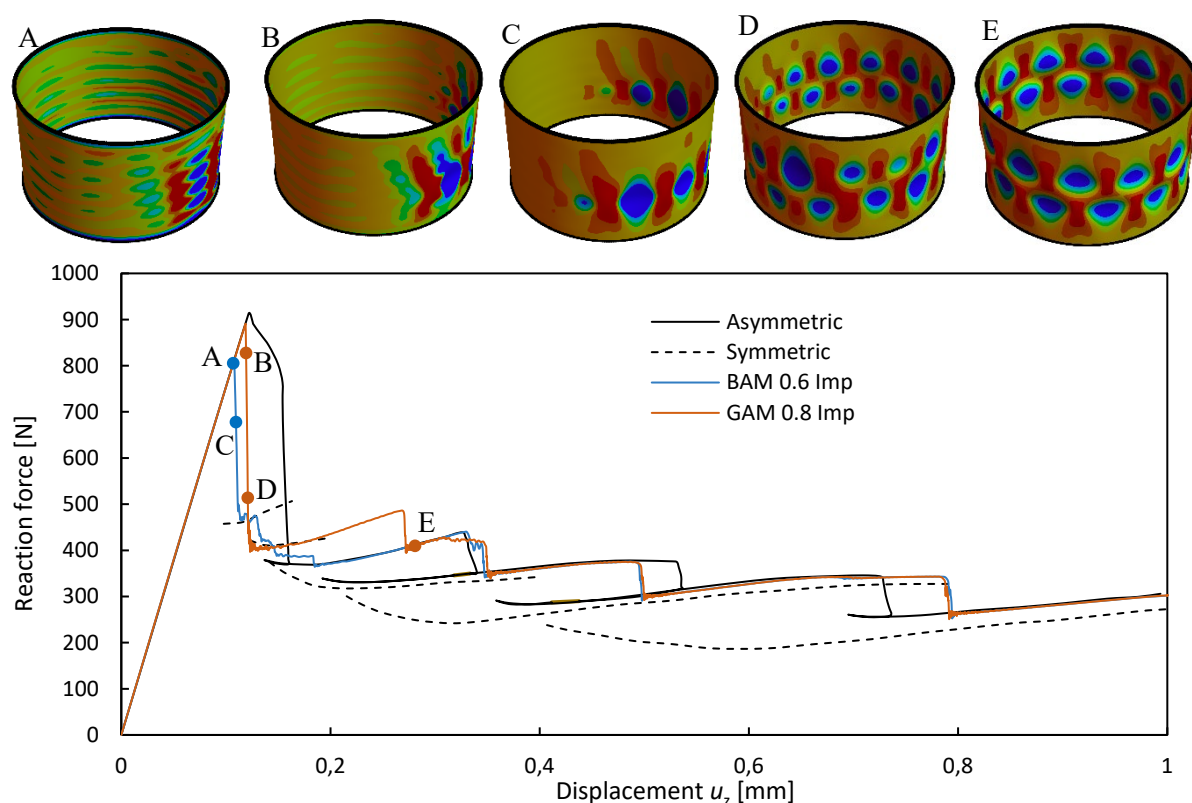
Figure 5.25: Imperfect cylinder: force-displacement curves.
Slika 5.25: Cilinder z nepopolnostmi: krivulje sila-pomik.

5.4   Chapter conclusions

In this chapter, we investigated the applicability of five implicit schemes of structural dynamics with (controllable) numerical dissipation, which belong either to the class of generalized-α methods, or Energy-decaying method, for simulating complex buckling processes of elastic shells. Beside five numerically dissipative schemes, the Energy-momentum conserving scheme and the Newmark's trapezoidal rule were also investigated. These seven implicit schemes were applied for the computation of classical shell buckling problems: snap-through, complete collapse and cylinder under axial load. The

following comparison of computed results was performed: characteristic displacement versus time curves, energy versus time curves and required time-step length versus time curves. The convergence abilities of the schemes, i.e. how far they can go before they fail and why they fail, have also been assessed. In this manner, some empirical knowledge about the suitability of a particular scheme to handle complex shell buckling problems has been built up.

We can conclude that most of the applied implicit schemes for structural dynamics that possess (controllable) numerical damping (in the high-frequency range) are suitable for the simulation of shell buckling. These are the modified Generalized alpha (GAM), Bossak (BAM) and HHT schemes (the word "modified" is used to reflect different computation of internal forces with respect to the original versions), as well as the Energy-decaying scheme (ED). They provided favorable results for the computed examples related to complex buckling processes of shell-like structures and systems, including the transition of buckling patterns. On the other hand, the following schemes do not seem to be suitable for the shell buckling analysis: Newmark's trapezoidal rule (NTR), first-order dissipative Newmark's scheme (NMD) and Energy-momentum conserving scheme (EMC). Newmark's trapezoidal rule can quickly fail due to sudden increase in energy. Also, the dissipative Newmark's scheme (NMD) can fail due to its first-order accuracy and uncontrollable numerical dissipation. The results of energy-conserving scheme (EMC) may be polluted by artificial higher frequencies or heavy vibrations that can easily lead to the scheme's computational failure.

The inadequacy of the path-following static methods for certain structural applications with complex post-critical equilibrium paths has been recognized before, e.g. [43], and it is confirmed in this work. Numerical examples show that the proposed dynamic approach to shell buckling analysis can be superior to the static path-following analysis. In some computed cases, when the static path-following analysis failed, the implicit numerically dissipative schemes were able to find the solution.

It is sometimes difficult to compare the results of nonlinear static and dynamic analyses. For this reason, we illustrate the difference between static and dynamic load versus characteristic displacements curves in Figure 5.26. It illustrates (left) the results of a collapse analysis, with a solid curve representing a path-following (i.e. arc-length) static solution, and dashed curves representing imposed load and imposed displacement dynamic solutions (the dynamics solutions may oscillate at some regions, which is not shown). Figure 5.26 (right) illustrates the results of a snap-through problem.
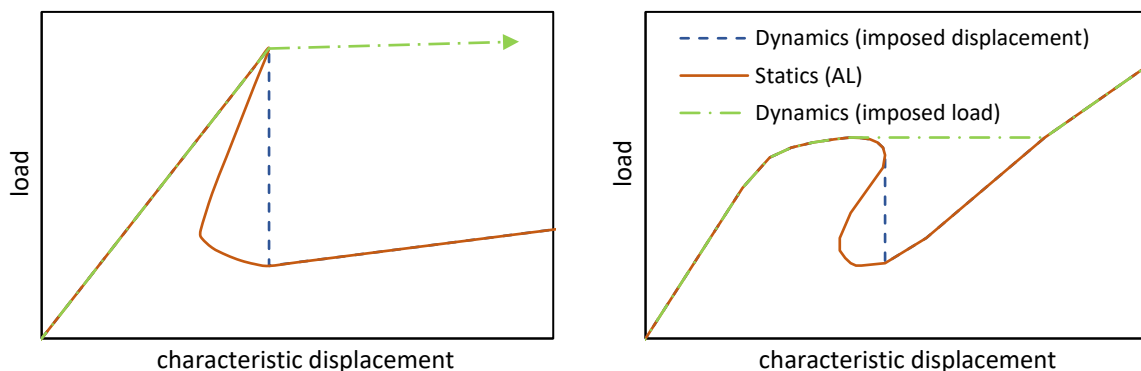
Figure 5.26: Dynamic versus static results.
Slika 5.26: Rezultati za dinamično ali statično analizo.

6   WRINKLING OF SHELL-SUBSTRATE SYSTEMS

Chapter abstract

In this chapter we propose three efficient computational models for predicting the surface wrinkling in compressed shell-substrate composites. To capture the transitions between the wrinkling modes, we use implicit dynamics in a combination with elastic foundation that represents the substrate. We first focus on axially compressed bi-layer cylindrical shell-substrate composites. In this context we apply the generalized-α and energy-decaying time stepping schemes presented in the previous sections. Next, we focus on the surface wrinkling of core-shell spherical systems under external pressure. In this context we apply the energy-decaying time stepping scheme. The content of this chapter is adopted from articles [108] and [157] where cylindrical and spherical examples were addressed.

Numerical examples of axially compressed cylinders are computed using the dynamic extension of previously analysed 6 – parameter extensible director finite element D-ANS, see Table 2.6 and Sections 2.2.3, 2.3.2 and 2.4.1. On the other hand, examples of pressurized spheres are computed using the dynamic extension of previously analysed MITC4 finite element, see Table 2.2 and Sections 2.2.1, 2.3.1 and 2.4.1, using rotation algorithm IQ, see Table 2.7 and Section 2.2.2. Dynamic schemes NTR, BAM, HHT, GAM, EMC, ED1 are used.

6.1   Chapter introduction

The common approach in tackling the extremely difficult problem of surface wrinkling is to perform a numerical nonlinear static stability analysis. For problems where such methods fail, nonlinear structural dynamics or pseudo-dynamic relaxation methods can be used, [102], [173]. In dynamics, explicit schemes are preferred to implicit ones, as they make up for the lack of accuracy due to the relatively easy implementation. Based on our experience in the field of shell dynamics, we propose to use implicit dynamics schemes in combination with a relatively simple shell model.

Two specific shapes of shell-core composites are addressed. We will focus first on the cylindrical systems, where the motivation is provided by the works of Zhao et al. [182] and Xu and Potier-Ferry [173]. In [182] they reported a combined experimental and theoretical investigation of the cylindrical system that was subjected to axial compression. They showed that, irrespective of the system properties, the first wrinkling mode is always axisymmetric and periodic along the longitudinal axis of the cylinder. With some parameter settings they observed the transitions of the wrinkle patterns from axisymmetric to diamond-like patterns. They also found that the main role in this wrinkling mode transition is played by the ratio of the elastic moduli E_s/E_f and the geometric ratio R/t_f, where R and t_f are the cylinder radius and the cylinder thickness, respectively (here, subscript f refers to the film (shell) and subscript s to the substrate). Based on the work of Zhao et al. [182] and their own analysis, Xu and Potier-Ferry [173] proposed a coefficient

$$C = E_s/E_f\left(R/t_f\right)^{3/2}, \tag{6.1}$$

with the critical value $C_{crit} \approx 0.88$ and showed that for systems with $C > C_{crit}$ only the axisymmetric wrinkling mode occurs, whereas for systems with $C < C_{crit}$ the transition from the axisymmetric to the diamond-like wrinkling mode is expected. An experimental and theoretical analysis of a similar problem

was also carried out by Shao et al. [135] to investigate hierarchical wrinkling patterns and to confirm these results.

Various numerical approaches have been considered in the past to analyze this difficult problem. In [182] and [78], axially compressed cylinders on substrates were analyzed in Abaqus [1] by a very dense mesh of 3D solid finite elements and a convenient initial geometric imperfection to trigger the wrinkling transition. The analyses were carried out in a static framework by pseudo-dynamic regularization. Such a model is to a certain extent tailored to reproduce the wrinkling transition and is computationally extremely costly. In [173] they investigated the wrinkling transition numerically by performing a static analysis using an advanced path-following method and a small perturbation force to trigger the transition to the secondary branch at the bifurcation points. They used a 3D finite element model consisting of an 8-node nonlinear shell element with 7 parameters, 8-node linear 3D solid elements and kinematic constraints between solid and shell degrees of freedom.

Other shell-substrate systems that we are interested in are the spherical composites. The motivation for our work is provided in the recent articles by Veldin et al. [156] and Xu et al. [174]. While the first authors performed systematic static analyses on spheroidal systems to predict the buckling and post-buckling behavior, the latter conducted experimental and numerical investigation on micro-scale spheres, suggesting the validity of parameter (6.1) also for spheres. They observed that for a relatively soft core ($C < 1.3$) local dimples can be observed on the sphere. With a larger coefficient ($1.3 < C < 15$), buckyball patterns can be observed and by increasing the coefficient ($C > 15$), distorted patterns involving polygon and labyrinth modes appear. In [156], the analyses were performed by modeling the substrate as elastic foundation and by using the path-following technique. In [174], numerical investigation was again performed in Abaqus [1], using eight-node elements for the substrate and thin shell elements for the surface layer and adopting dynamic relaxation method.

After briefly presenting the numerical models at the beginning of this chapter, we next focus on the surface wrinkling of axially compressed cylinders adhering to soft substrates and the transitions between the wrinkling modes. Several popular implicit dynamic time integration schemes that fall into the class of generalized-α methods [49] are tested to solve the problem, see Table 3.1. In particular, GAM, see e.g. [38], [96], [97], HHT [65], and BAM, see e.g. [158], [170]. In addition, classical NTR, see e.g. [118], [21], EMC, see e.g. [146], [23], [26], and ED1 (here denoted as ED), see e.g. [4], [26], [132], are also considered, see Table 3.2. As for the cylinder, we model the shell by the 6-parameter stress-resultant extensible director shell model presented in e.g., [144], [102] and in Chapter 4. The substrate is modeled as an elastic foundation, see e.g. [63], [185] and [100]. Our computational model does not require any geometric imperfections or perturbation forces to trigger the transitions between wrinkling modes. The number of finite elements in the mesh is significantly lower compared to the 3D solid models. We identify which schemes are capable of capturing the complete buckling and post-buckling phenomena and find that they yield results that are similar to what was observed in experiments [185].

In the next part of this chapter, implicit dynamics is applied to study the surface wrinkling of spheres on soft substrates subjected to external pressure, where we again try to capture the transitions between the wrinkling modes. Two computational models are proposed and tested on a set of three spherical examples. Energy-decaying scheme ED1 (here denoted as ED) was used in combination with the $5-$

parameter stress-resultant inextensible director shell model representing the shell and elastic foundation representing the substrate. Static formulation of the used shell model was already presented in Section 2.2 and was extended to a special case of 11 – parameter dynamic formulation in Section 4.3.1. Here, the straightforward 5 – parameter extension to dynamics will be briefly addressed, which represents the first of the two used models. The second computational model is obtained by reducing the kinematics so that only the radial displacements are considered, significantly simplifying the kinematic description of the shell.

6.2   Dynamic finite element formulations for stiff-shell-soft-core composites

6.2.1   Extensible-director shell on elastic foundation

Let us start the development with the extensible-director shell model presented in Section 2.2.3 for statics and extended to dynamics in Section 5.2. The weak form of the equilibrium equations, introduced in (5.1) is here extended, to account for the spring stiffness of the substrate, as

$$G_{dyn}(\boldsymbol{u}, \boldsymbol{w}; \delta\boldsymbol{u}, \delta\boldsymbol{w}) = \int_M (\delta\boldsymbol{\varepsilon} \cdot \boldsymbol{N} + \delta\boldsymbol{\kappa} \cdot \boldsymbol{M} + \delta\boldsymbol{\gamma} \cdot \boldsymbol{Q})dA + A_0 \int_M \delta\boldsymbol{u} \cdot \ddot{\boldsymbol{u}} \, dA +$$

$$I_0 \int_M \delta\boldsymbol{w} \cdot \ddot{\boldsymbol{w}} \, dA - \int_M \delta\boldsymbol{u} \cdot \overline{\boldsymbol{b}} \, dA - \int_{\Gamma_{\overline{t}}} \delta\boldsymbol{u} \, \overline{\boldsymbol{t}} \, ds - \int_M \delta\boldsymbol{u} \cdot \boldsymbol{n}^{def} \left(-K_s \boldsymbol{u} \cdot \boldsymbol{n}^{def} \right) dA = 0. \tag{6.2}$$

In Eq. (6.2), K_S is the linear area spring stiffness of the substrate and we refer to Sections 2.2.3 and 5.2 for detailed explanation of the rest of notation.

The contribution of the elastic foundation is introduced in Eq. (6.2) through the area spring stiffness K_s acting in the direction of the normal to the deformed middle surface

$$\boldsymbol{n}^{def} = \frac{\boldsymbol{x}_{0,\alpha} \times \boldsymbol{x}_{0,\beta}}{\left\| \boldsymbol{x}_{0,\alpha} \times \boldsymbol{x}_{0,\beta} \right\|}. \tag{6.3}$$

In this work, the substrate is modelled as a Winkler elastic foundation using the expression for stiffness K_S from [182]

$$K_S = \frac{1}{2} \bar{E}_s \frac{\sqrt{p_0^2 + q_0^2}}{R}, \tag{6.4}$$

where $\bar{E}_s = E_s/(1 - v_s^2)$ is the plane-strain elastic modulus of the core, and p_0 and q_0 are the critical wrinkling wavelengths in the axial and circumferential directions, respectively. Note that a similar formula from [100] gives practically the same value of K_S. According to [182], knowing that the initial wrinkling pattern is always axisymmetric, we assume $q_0 = 0$ and obtain p_0 by solving

$$-2 + \frac{t_f^2}{6(1 - v^2)R^2} p_0^4 - \frac{3R}{6(1 - v^2)t_f} \frac{\bar{E}_s}{\bar{E}_f} p_0 = 0, \tag{6.5}$$

where $\bar{E}_f = E_f/(1 - v_f^2)$. The authors in [82] and [173] propose a slightly different expression for the substrate stiffness, but we observed that there is practically no difference in the numerical values of the coefficient obtained by either of the formulae.

6.2.1.1   Spatial and temporal discretization

Spatial and temporal discretization is accomplished by following the procedure from Sections 5.2.2 and 5.2.3. Space- and time-discrete version of the functional (6.2) can be written as

$$G_{dyn}^h = \mathbb{A}_{e=1}^{n_{el}} G_{dyn}^e \left(\delta \boldsymbol{u}_a, \delta \boldsymbol{w}_a ; \boldsymbol{u}_{a,n+1}, \boldsymbol{w}_{a,n+1} \right) =$$

$$\mathbb{A}_{e=1}^{n_{el}} \int_{A_e} \left(\delta \boldsymbol{\varepsilon}^h \cdot \boldsymbol{N}_{n+\alpha_f}^h + \delta \boldsymbol{\kappa}^h \cdot \boldsymbol{M}_{n+\alpha_f}^h + \delta \boldsymbol{\gamma}^h \cdot \boldsymbol{Q}_{n+\alpha_f}^h \right) dA$$

$$+ \mathbb{A}_{e=1}^{n_{el}} \int_{A_e} \left(A_0 \delta \boldsymbol{u}^h \cdot \ddot{\boldsymbol{u}}_{n+\alpha_m}^h + I_0 \delta \boldsymbol{w}^h \cdot \ddot{\boldsymbol{w}}_{n+\alpha_m}^h \right) dA \qquad (6.6)$$

$$- \mathbb{A}_{e=1}^{n_{el}} \int_{A_e} \left(\delta \boldsymbol{u}^h \cdot \overline{\boldsymbol{b}}_{n+\alpha_f} + \delta \boldsymbol{u}^h \cdot \boldsymbol{n}_{n+\alpha_f}^{def,h} \left(-K_S \boldsymbol{u}_{n+\alpha_f}^h \cdot \boldsymbol{n}_{n+\alpha_f}^{def,h} \right) \right) dA$$

$$- \mathbb{A}_{e=1}^{n_{el}} \int_{\Gamma_{\bar{t},e}} \delta \boldsymbol{u}^h \cdot \overline{\boldsymbol{t}}_{n+\alpha_f} \, ds = 0,$$

where the notable difference from the functional (5.2) is the introduction of the spring stiffness, representing the Winkler foundation. Eq. (6.6) yields a system of nonlinear equations for nodal displacements at t_{n+1}, which we solve with the Newton-Raphson method.
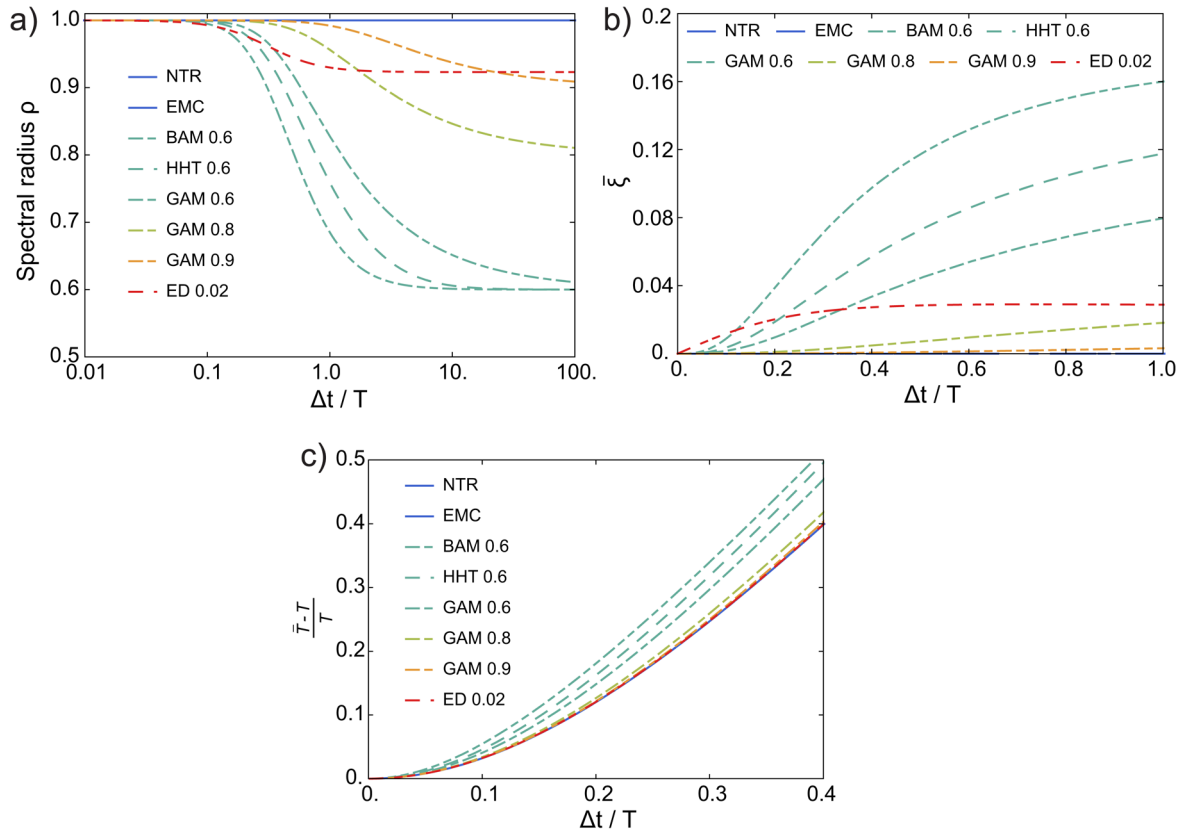
Figure 6.1: Properties of used time integration schemes: a) spectral radius, b) damping coefficient and c) period elongation versus $\Delta t / T$.

Slika 6.1: Lastnosti uporabljenih integracijskih shem: a) spektralni radij, b) koeficient dušenja in c) podaljšanje nihajnega časa v odvisnosti od $\Delta t / T$.

Several implicit time-stepping schemes from the family of generalized-α methods, presented in Table 3.1, are obtained by varying parameters α_m, α_f, β and γ in the proposed discretization. For the cylindrical shell examples, the following were used: NTR, BAM, HHT, GAM and EMC. Furthermore, the energy-decaying scheme, more specifically the ED1 scheme, was also applied, see Table 3.2.

Our experience with the buckling analysis of axially compressed cylinders with no core, presented in Section 5.3.6, see also [102], indicates that considerable algorithmic dissipation is needed to capture the mode jumps (matching experimental results from [175]) in the post-buckling regime for the GAM, HHT, BAM and ED schemes. Even though dissipation properties of the adopted schemes are already extensively analyzed in Chapter 3, we show in Figure 6.1 the spectral radius, damping coefficient and period elongation for the considered schemes, where dissipation factors used for the analyses of the cylindrical systems in Section 6.3 are applied. In Figure 6.1 a) GAM 0.6 denotes GAM with $\rho_\infty = 0.6$, see Table 3.1, ED 0.02 denotes ED1 with $\alpha_{ED} = \beta_{ED} = 0.02$, see Table 3.2, etc.

Comparison of ED 0.02 and GAM 0.6 curves in Figure 6.1 a) shows that the latter starts with the damping at $\Delta t/T \approx 0.1$ and the former starts even sooner. However, ED 0.02 damping is stronger in the intermediate-frequency range (up to $\Delta t/T \approx 0.35$), and significantly weaker in the high-frequency range. GAM 0.8 and GAM 0.9 do not dissipate the intermediate frequencies, but rather only the higher ones (after $\Delta t/T \approx 0.3$ and $\Delta t/T \approx 0.9$, respectively). The algorithmic damping is also illustrated in Figure 6.1 b) where a measure of numerical dissipation is damping coefficient $\bar{\xi}$. Figure 6.1 b) clearly shows that ED 0.02 exhibits damping for all frequencies and is stronger than the one of GAM 0.6 up to $\Delta t/T \approx 0.35$. Damping coefficient for GAM 0.8 or GAM 0.9 is considerably smaller than for GAM 0.6 or ED 0.02. Figure 6.1 c) shows the elongation of the time periods due to the applied algorithm and dissipation, where $\bar{T}$ is the algorithmic time period. ED 0.02 error is the same as for NTR and EMC schemes, but smaller than the one of GAM 0.6. The conclusions that were outlined here for the GAM scheme can be very straightforwardly applied also to the BAM and HHT schemes.

It should be noted that the generalized-α schemes do not fulfill the energy criterion for the unconditional stability in nonlinear dynamics. Furthermore, according to [49] and our test in Section 5.3, GAM, HHT and BAM may exhibit strong energy oscillations in the intermediate-frequency range, which was also observed in numerical simulations presented in the next section. These oscillations were not observed to the same extent for the ED1 scheme, which was shown in Section 3.6 to be unconditionally stable in nonlinear dynamics. Finally, note that the validity interval for the dissipation parameters of the ED scheme is $\alpha_{ED}, \beta_{ED} \in [0,0.5]$, as was presented in Chapter 5 for the extensible director shell model.

6.2.2   Inextensible-director shell on elastic foundation

The inextensible-director shell model presented in Chapter 2 for statics (denoted therein as MITC4) is extended here to account for the inertial and substrate effects. The weak form (2.13) is thus expanded as

$$G_{dyn}(\boldsymbol{u}, \boldsymbol{d}; \delta\boldsymbol{u}, \delta\boldsymbol{d}) = \delta\Pi - \int_M \delta\boldsymbol{u} \cdot \boldsymbol{n} \, (-K_s \boldsymbol{u} \cdot \boldsymbol{n}) \, dA$$
$$+ A_0 \int_M \delta\boldsymbol{u} \cdot \ddot{\boldsymbol{u}} \, dA + I_0 \int_M \delta\boldsymbol{d} \cdot \ddot{\boldsymbol{d}} \, dA = 0. \tag{6.7}$$

Here, K_S is again the linear area spring stiffness of the substrate, but unlike the extensible director model, we presume here that it is acting in the direction of the normal to the undeformed middle surface. The rest of the notations are explained in detail in Sections 2.2.1 and 4.3. The expression for stiffness K_S is again taken from [182], see Eq. (6.4).

Let us note that the complexities of implementation of implicit schemes are of the same order for the 5 – parameter element with rotational degrees of freedom and for the 6 – parameter element with only displacement degrees of freedom, presented in Section 5.2. This is due to the fact that here, the time-interpolation of the shell director, rather than of the rotations, is adopted. Thus, the time update of the shell director has in this case exactly the same form as the time update of the displacements. This is not the case in some rare situations when the time update of rotations is performed, e.g. [27].

6.2.2.1 Spatial and temporal discretization

Spatial discretization follows the procedure from Sections 2.3.1 and 5.2.2. Membrane and bending strains, ε_{ab}^h and κ_{ab}^h, respectively, are expressed at a Gauss integration point using local Cartesian basis. The approximation of transverse shear strains, on the other hand, relies on the assumed natural strain (ANS) concepts described in Section 2.4.1.1. Temporal discretization follows the lines presented in Sections 4.3 and 5.2.3, where the discretization for the energy-decaying scheme is presented. Note that the validity interval for the dissipation parameters for the ED scheme is $\alpha_{ED}, \beta_{ED} \in [0,1]$, as was presented in Chapter 3. Space- and time-discretization of the functional (6.7) can be written as

$$
\begin{aligned}
G_{dyn}^h = \mathbb{A}_{e=1}^{n_{el}} G_{dyn}^e \left(\delta \boldsymbol{u}_a, \delta \boldsymbol{d}_a; \boldsymbol{u}_{a,n+1}, \boldsymbol{d}_{a,n+1} \right) = \\
\mathbb{A}_{e=1}^{n_{el}} \int_{A_e} \left(\delta \boldsymbol{\varepsilon}^h \cdot \boldsymbol{N}_{n+\alpha_f}^h + \delta \boldsymbol{\kappa}^h \cdot \boldsymbol{M}_{n+\alpha_f}^h + \delta \boldsymbol{\gamma}^h \cdot \boldsymbol{Q}_{n+\alpha_f}^h \right) dA \\
+ \mathbb{A}_{e=1}^{n_{el}} \int_{A_e} \left(A_0 \delta \boldsymbol{u}^h \cdot \ddot{\boldsymbol{u}}_{n+\alpha_m}^h + I_0 \delta \boldsymbol{d}^h \cdot \ddot{\boldsymbol{d}}_{n+\alpha_m}^h \right) dA \\
- \mathbb{A}_{e=1}^{n_{el}} \int_{A_e} \left(\delta \boldsymbol{u}^h \cdot \overline{\boldsymbol{b}}_{n+\alpha_f} + \delta \boldsymbol{u}^h \cdot \boldsymbol{n}_{n+\alpha_f}^h \left(-K_S \boldsymbol{u}_{n+\alpha_f}^h \cdot \boldsymbol{n}_{n+\alpha_f}^h \right) \right) dA \\
- \mathbb{A}_{e=1}^{n_{el}} \int_{\Gamma_{\bar{t},e}} \delta \boldsymbol{u}^h \cdot \overline{\boldsymbol{t}}_{n+\alpha_f} \, ds = 0.
\end{aligned}
\tag{6.8}
$$

We will here denote the derived formulation as RM-5 (Reissner-Mindlin shell with 5 dof per node). In Section 6.4, we also use a second computational model, a dynamic finite element formulation called QKQ-3 (as quasi-Kirchhof quadrilateral element with 3 dof per node), which is based on a reduced-order version of the above described shell theory. It applies a simplification that neglects the tangential displacements and thus assumes

$$
\boldsymbol{u} = u_{normal} \boldsymbol{d}, \qquad u_{normal} = \boldsymbol{u} \cdot \boldsymbol{d}.
\tag{6.9}
$$

This considerably simplifies the kinematics of the geometrically exact shell model. Since this assumption does not fit well with the shear deformable model, we further apply a quasi-Kirchhoff-Love simplification by using a large value for $\boldsymbol{C}^s$ (of the order $\approx 10^5$) in Eq. (2.11), which plays the role of the penalty number in the computations and allows only negligible transverse shear strains. The spatial and temporal discretization of QKQ-3 is the same as for RM-5. The difference between QKQ-3 and RM-5 is that the former formulation uses kinematic constraint (6.9) and mimics the Kirchhoff-Love solution, whereas the latter does not use any simplifications or modifications, see also Table 6.1.

Table 6.1: Finite elements used for the analysis of spheres.
Preglednica 6.1: Končna elementa, uporabljena za analizo sfer.

Element	Kinematics	Reduction of tangential displacements	Large shear modulus (as penalty parameter)
RM-5	Reissner-Mindlin	No	No
QKQ-3	Reissner-Mindlin	Yes	Yes

6.3   Cylindrical shell examples

We considered four cylinders, CS1-CS4, with geometric and material properties adopted from reference [173] (we collect them in Table 6.2 for convenience). The first three examples CS1-CS3 have $C < C_{crit}$, and the CS4 has $C > C_{crit}$. The restraints $u_x = u_z = w_x = w_z = 0$ were applied on both ends of the cylinder, along with the prescribed axial displacement (see Figure 6.2). The cylinder was at rest at $t = 0$. No geometrical imperfections or perturbation forces were imposed.

The aforementioned time-stepping schemes were used with an adaptive time-step function (2.81), where the desired and maximal allowed numbers of incremental iterations are set to $I_0 = 8$ and $N = 25$, respectively. Minimal and maximal allowed time steps were set to $\Delta t_{min} = 10^{-8}$ s and $\Delta t_{max} = 0.01$ s. If convergence was not achieved within 25 iterations, the increment was re-computed with $\Delta t/2$. The initial time step was $\Delta t = 0.01$ s and the convergence tolerance for the norm of the iterative displacement vector was set to 10^{-12}.

In the following figures, u_y denotes the imposed axial displacement and "reaction force" the sum of nodal axial reactions at one end. The colors on the deformed configurations relate to the radial displacements, which are magnified two times to show greater contrast between the wrinkling patterns (the same scaling applies for all configurations).

Table 6.2: Geometric and material data for cylinders CS1–CS4. Symbols E, ν, K_s, R, L and ρ denote the elastic modulus, Poisson ratio, spring coefficient, radius, length and density of the cylinder, respectively.
Preglednica 6.2: Geometrijski in materialni podatki za cilindre CS1–CS4. Simboli E, ν, K_s, R, L in ρ označujejo elastični modul, Poissonov količnih, koeficient togosti vzmeti, radij, dolžino in gostoto cilindra, v tem vrstnem redu.

System	E_f [MPa]	E_s [MPa]	$K_s \left[\dfrac{N}{mm^3}\right]$	ν_f	ν_s	t_f [mm]	R [mm]	L [mm]	$\rho_f \left[\dfrac{g}{mm^3}\right]$	C
CS1	$2.16 \cdot 10^4$	1.8	127.6	0.4	0.48	10^{-3}	0.3	0.3	10^{-3}	0.43
CS2	$2.16 \cdot 10^4$	1.8	198.8	0.4	0.48	10^{-3}	0.113	0.15	10^{-3}	0.10
CS3	$2.16 \cdot 10^5$	1.8	196.3	0.4	0.48	10^{-3}	0.113	0.3	10^{-3}	0.01
CS4	$1.3 \cdot 10^3$	1.8	211.6	0.4	0.48	10^{-3}	0.2	0.2	10^{-3}	3.92
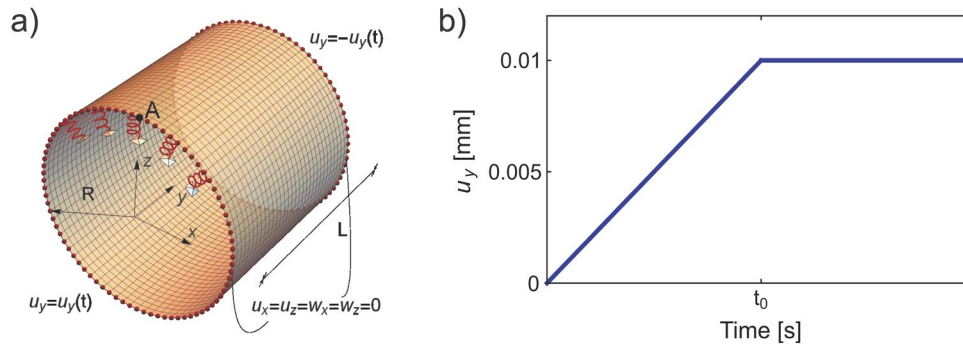
Figure 6.2: a) Finite element model (the springs are distributed across the entire inner surface). b) Loading function.

Slika 6.2: a) Model končnih elementov (vzmeti so razporejene po celotni notranji površini). b) Obtežna funkcija.

6.3.1 System CS1

We analyzed system CS1 ($C = 0.43$) using a 240×120 element mesh, the loading time $t_0 = 10$ s and the damping factors (where applicable) $\rho_\infty = 0.6$ and $\alpha_{ED} = \beta_{ED} = 0.02$. The results of the analyses depicting the reaction force as a function of the axial displacement and all identified patterns (A-I) according to different dynamic schemes are shown in Figure 6.3.

Figure 6.3 a) shows that ED and GAM predicted multiple pattern transitions in the post-buckling regime. ED predicted 5 pattern transitions and GAM predicted 3. The first pattern transition identified by ED corresponds to the transition from a smooth (shown in configuration O in Figure 6.3 c), to an axisymmetric pattern (shown in configuration A) with 6 waves (12 half-waves) along the length of the cylinder. Next, the transition from the axisymmetric pattern in configuration A to the (symmetric) diamond-like dimple pattern in configuration B is found, with 5 bands of dimples along the length of the cylinder and 17 dimples along the circumference (comprising each band) of the cylinder. Both mode jumps are known from the experiments of Zhao et al. [185] and numerical analysis of Zhao et al. [185] and Xu and Potier-Ferry [173] on axially compressed shell-core cylinders. In addition to the two studies, our computational model based on ED reveals new mode jumps when the load is further increased. First, the dimple pattern in configuration B transforms into another diamond-like dimple pattern shown in configuration C, with a slightly different number of dimples. In this configuration, we count 5 bands of dimples along the length and 15 dimples along the circumference of the cylinder. Similar to this mode jump, another one is observed at approximately $u_y = 0.002$ mm. At this load, the pattern jumps into a different (also symmetric) diamond-like dimple pattern, shown in configuration D, which has 3 bands of fully developed dimples at the mid-length of the cylinder and two bands of partially developed dimples near the boundary. Each band is comprised of 9 dimples along the circumference of the cylinder, which is a drastic decrease in the characteristic wavelength of the pattern. Interestingly, the mode jumps we find in this example are similar to those observed on cylindrical shells without substrate support (see Section 5.3.6 or e.g. Yamaki [175] for experimental and Lavrenčič and Brank [102] for numerical analysis). As far as we know, these results have not yet been recorded in the known literature on axially compressed shell-core cylinders.

The final (fifth) mode jump that occurred after $u_y = 0.003$ mm was due to excessive vibrations that ED could not damp out (due to the very small Δt required by the adaptive time stepping scheme in this region), which eventually caused the analysis to fail because the time step became prohibitively small.

The transition from a smooth to an axisymmetric pattern was also found by GAM (the obtained configuration is similar to A, not shown here). The next pattern GAM predicted is shown in configuration E. It was similar to the one found in configuration D by ED. We found that the pattern in configuration E has 4 bands of dimples along the length and 10 dimples along the circumference of the cylinder (recall, configuration D has 3 fully and 2 half-developed bands with 9 dimples). We attribute the difference between the results of both schemes to different dissipative properties, as shown in Figure 6.1 a)-c). Similar to ED, also GAM was unable to damp out the excessive vibrations and failed around $u_y = 0.003$ mm.
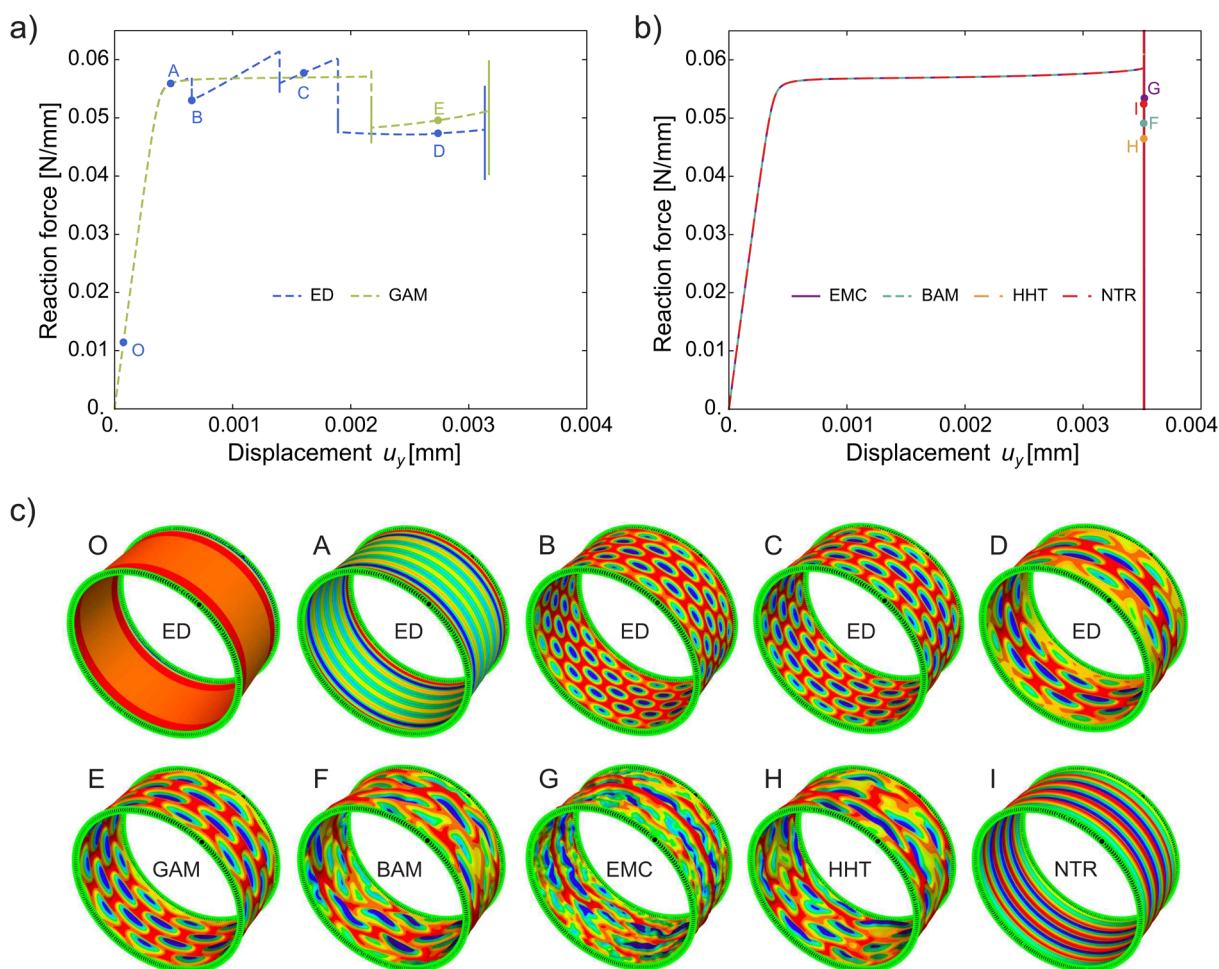
Figure 6.3: System CS1: a) force-displacement response for ED and GAM, b) force-displacement response for EMC, BAM, HHT and NTR, c) deformed shell configurations at various points on the above diagrams. Patterns in configurations F-I are oscillating due to the un-damped vibrations.

Slika 6.3: Sistem CS1: a) odziv sila-pomik za ED in GAM, b) odziv sila-pomik za EMC, BAM, HHT in NTR, c) deformirane konfiguracije iz različnih točk na zgornjih diagramih. Vzorci na konfiguracijah F-I nihajo zaradi nepodušenih vibracij.

EMC, BAM and HHT first found the axisymmetric wrinkling mode (as in configuration A) and then, at $u_y \approx 0.0035$ mm (see Figure 6.3 b)), implied that the wrinkling mode should jump to the diamond-like pattern, as shown in configurations F, G and H in Figure 6.3 c). However, none of them could "freeze" the pattern due to strong vibrations that the schemes were unable to damp. Nevertheless, as configurations F, G and H confirm, the precursors of the diamond-like wrinkling mode were found. NTR, on the other hand, predicted a jump, but the pattern remained axisymmetric (and oscillating), as shown in configuration I.
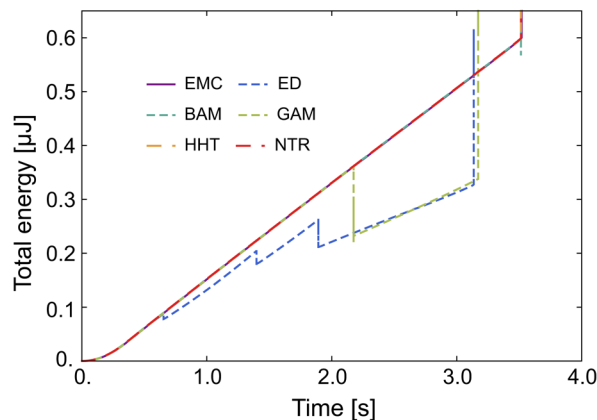
Figure 6.4: Total energy versus time for the CS1 system.
Slika 6.4: Celotna energija v odvisnosti od časa za sistem CS1.

Next, we show in Figure 6.4 the total energy (the sum of kinetic and potential energies) versus time. At mode jumps, the total energy drops due to the redistribution of the membrane part of the potential energy to the bending part. This is not the case at the uncompleted final mode jump, where the kinetic energy increases considerably due to the un-damped vibrations. It is interesting to note that despite the difference in configurations D and E, after GAM transitions the total energy for ED and GAM is very similar to the diamond-like mode.

6.3.2   System CS2

We analyzed system CS2 ($C = 0.1$), using a mesh of 220×100 elements, the loading time $t_0 = 10$ s and the damping factors (where applicable) $\rho_\infty = 0.6$ and $\alpha_{ED} = \beta_{ED} = 0.02$. The results, which are qualitatively similar to those of the CS1 case, are presented in Figures 6.5 and 6.6.

Figure 6.5 a) shows that ED and GAM predicted multiple pattern transitions in the post-buckling regime, 5 and 3, respectively, as before. All distinct patterns (configurations A-D) obtained by ED at different levels of imposed displacements are given in Figure 6.5 c). The characteristic findings are the same as in the CS1 case: i.e. pattern transition from smooth (configuration O) to axial wrinkling (configuration A); pattern transition from axial to diamond-like dimples (configuration B); jumps between different diamond-like dimple patterns to obtain fewer and larger dimples (configurations C and D); configurations D (for ED) and F (for GAM) are almost identical but not the same (due to different algorithmic properties, as shown in Figure 6.1 a) – c)); after a certain displacement, in this case $u_y \approx 0.007$ mm, both ED and GAM failed because of excessive undamped vibrations.

Furthermore, the results for BAM, HHT and NTR (configurations H, I and J in Figure 6.5 c)) show that these schemes did not find any transitions from the axisymmetric to the diamond-like pattern (see also Figure 6.5 b). It is also interesting to note that non-dissipative EMC started with the transition to the diamond-like pattern (configuration G), but the process was not completed because of the high vibrations that led to an analysis failure due to $\Delta t < \Delta t_{min}$ in adaptive algorithm (2.81). The high-frequency contamination is seen in the deformed configuration G.

Figure 6.6 shows the total energy versus time. An increase in total energy at the last uncompleted jump reflects an increase in kinetic energy due to strong vibrations. Note that ED and GAM have virtually the same total energy in the branches with configurations D and F, but there is a difference in the levels of the membrane and bending parts of the potential energy (not shown). ED (configuration D) has higher membrane energy and GAM (configuration F) has higher bending energy, similar to what we observe in the CS1 case.
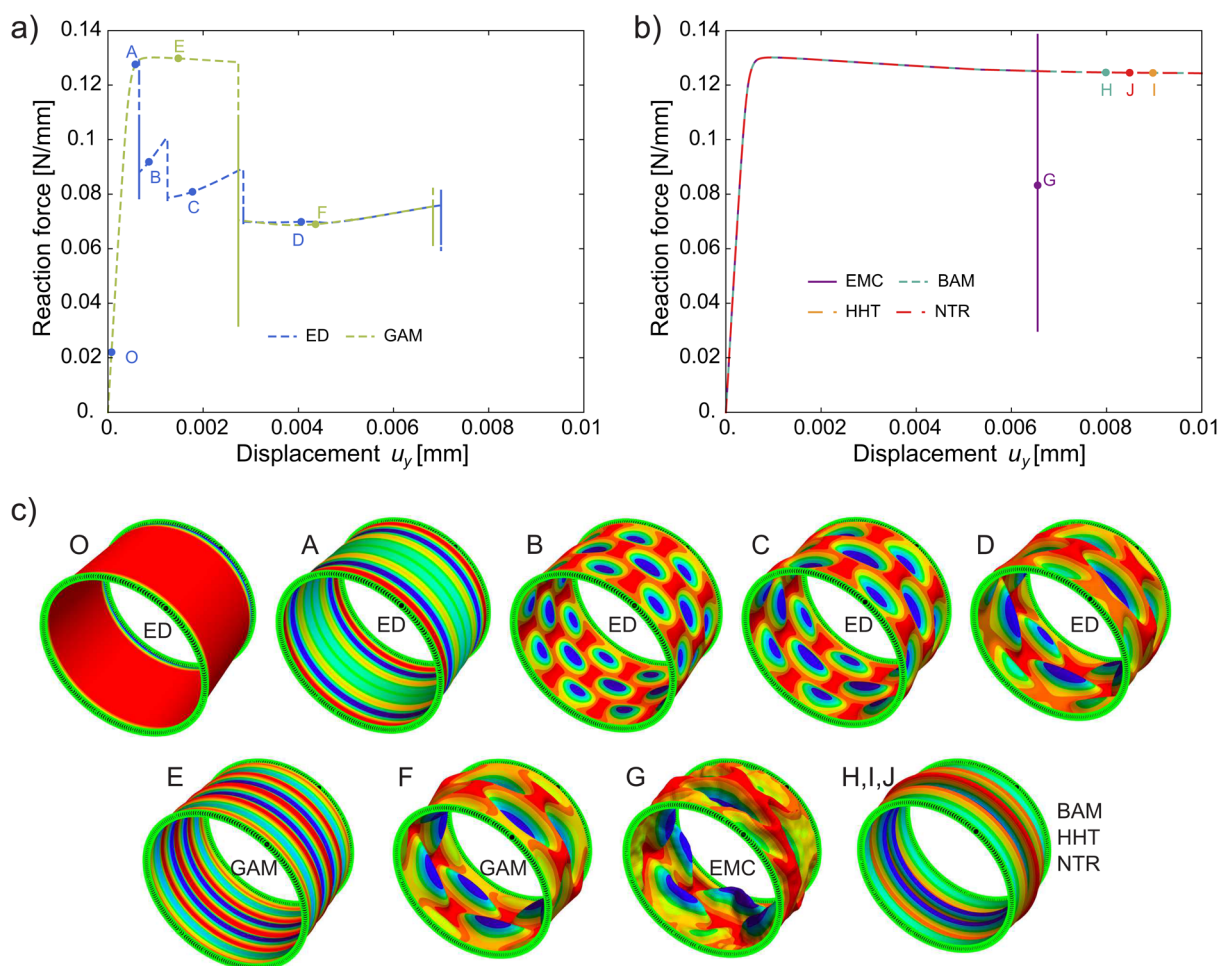
Figure 6.5: System CS2: a) force-displacement response for ED and GAM, b) force-displacement response for EMC, BAM, HHT and NTR, c) deformed shell configurations at various points on the above diagrams. Pattern in configuration G is oscillating due to the un-damped vibrations.
Slika 6.5: Sistem CS2: a) odziv sila-pomik za ED in GAM, b) odziv sila-pomik za EMC, BAM, HHT in NTR, c) deformirane konfiguracije iz različnih točk na zgornjih diagramih. Vzorec na konfiguraciji G niha zaradi nepodušenih vibracij.
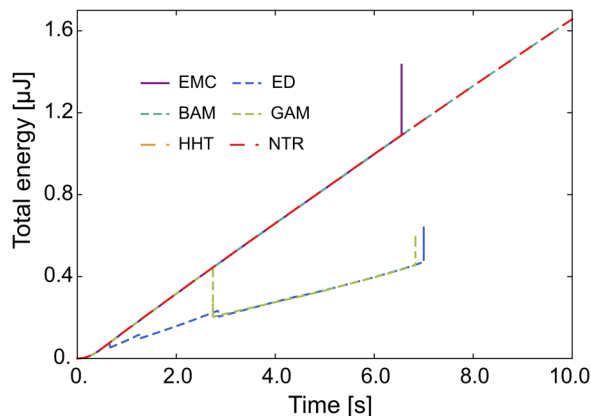
Figure 6.6: Total energy versus time for the CS2 system.
Slika 6.6: Celotna energija v odvisnosti od časa za sistem CS2.

6.3.3   System CS3

We analyzed system CS3 ($C = 0.01$) using a mesh of 160×200 elements, the loading time $t_0 = 10$ s and the damping factors (where applicable) $\rho_\infty = 0.6$ and $\alpha_{ED} = \beta_{ED} = 0.02$. The results are presented in Figures 6.7 and 6.8.

Figure 6.7 a) shows multiple post-buckling pattern transitions predicted by ED (more than in the CS1 and CS2 cases). All the patterns detected by ED are shown as configurations O-G in Figure 6.7 c). Note that the value of parameter C is less than critical, the same as in the first two cases, but much smaller. We first detect the transition from a smooth (configuration O) to an axisymmetric wrinkling pattern (configuration A), followed by the transition to the dimple mode wrinkling (from B to C), as predicted by the theory of Xu and Potier-Ferry [173] for sub-critical C. However, in this case, we observe a two-step transition to the diamond-like dimple pattern across the entire surface. We observe that the dimple pattern localizes first at the mid-length of the cylinder (see configuration B), where the stiffness of the shell is slightly lower than at both edges, and spreads across the whole surface only at the next jump (see configuration C). Also note that the diamond-like mode presented in configuration C is symmetric with respect to the mid-length cross-section of the cylinder, with 3 fully developed bands of dimples and 2 bands (one at each edge) of onsetting dimples, each comprised of 6 dimples in the circumferential direction. Multiple localized bucklings are then observed, with pattern D showing one of these stages. The cylinder reaches configuration E, in which 3 fully developed bands of dimples and 2 bands (one at each edge) of onsetting dimples are observed in the axial direction, each comprised of 5 dimples in the circumferential direction. Localized buckling is again observed in configuration F, and finally, mode G with an antisymmetric diamond-like pattern with 4 dimples in the axial and 4 in the circumferential direction is found.
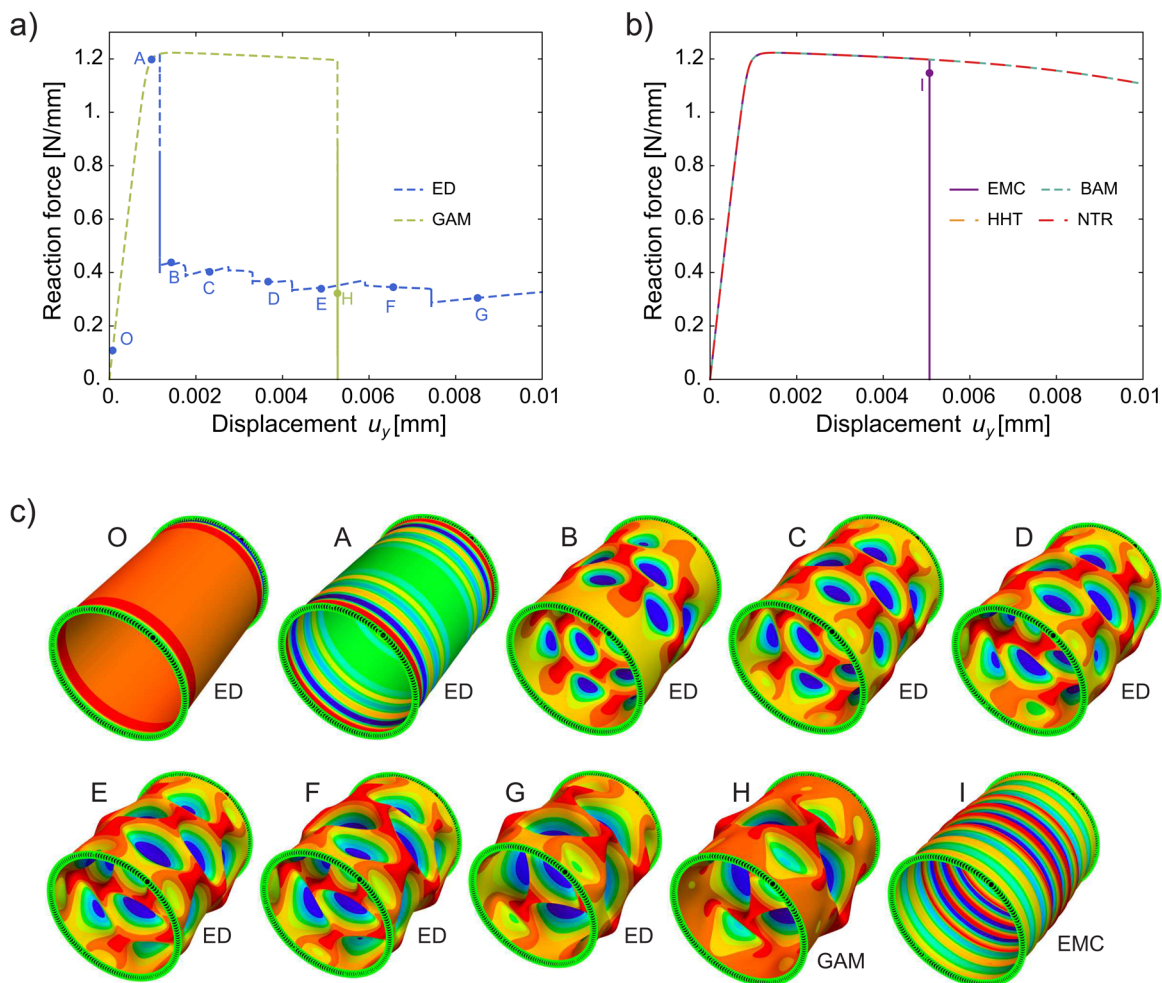
Figure 6.7: System CS3: a) force-displacement response for ED and GAM, b) force-displacement response for EMC, BAM, HHT and NTR, c) deformed shell configurations at various points on the above diagrams.
Slika 6.7: Sistem CS3: a) odziv sila-pomik za ED in GAM, b) odziv sila-pomik za EMC, BAM, HHT in NTR, c) deformirane konfiguracije iz različnih točk na zgornjih diagramih.

Figure 6.7 a) also shows that a transition for GAM began to form at $u_y \approx 0.005$ mm (see configuration H), but was never completed due to strong vibrations and the resulting failure of the analysis. For this reason, the obtained deformed configuration is not similar to either E or F. According to [49], GAM exhibits strong energy oscillations in the intermediate-frequency range, which may also have occurred in this example. Recall also that ED dissipates in the intermediate-frequency range, see Figure 6.1 a) and b) for comparison.

In Figure 6.7 b) we present the results of other schemes, BAM, HHT and NTR, which did not detect the pattern transition (as in the CS2 example), while non-dissipative EMC did, but only to start the transition to another axisymmetric mode (see configuration I), which was not completed due to undamped vibrations.
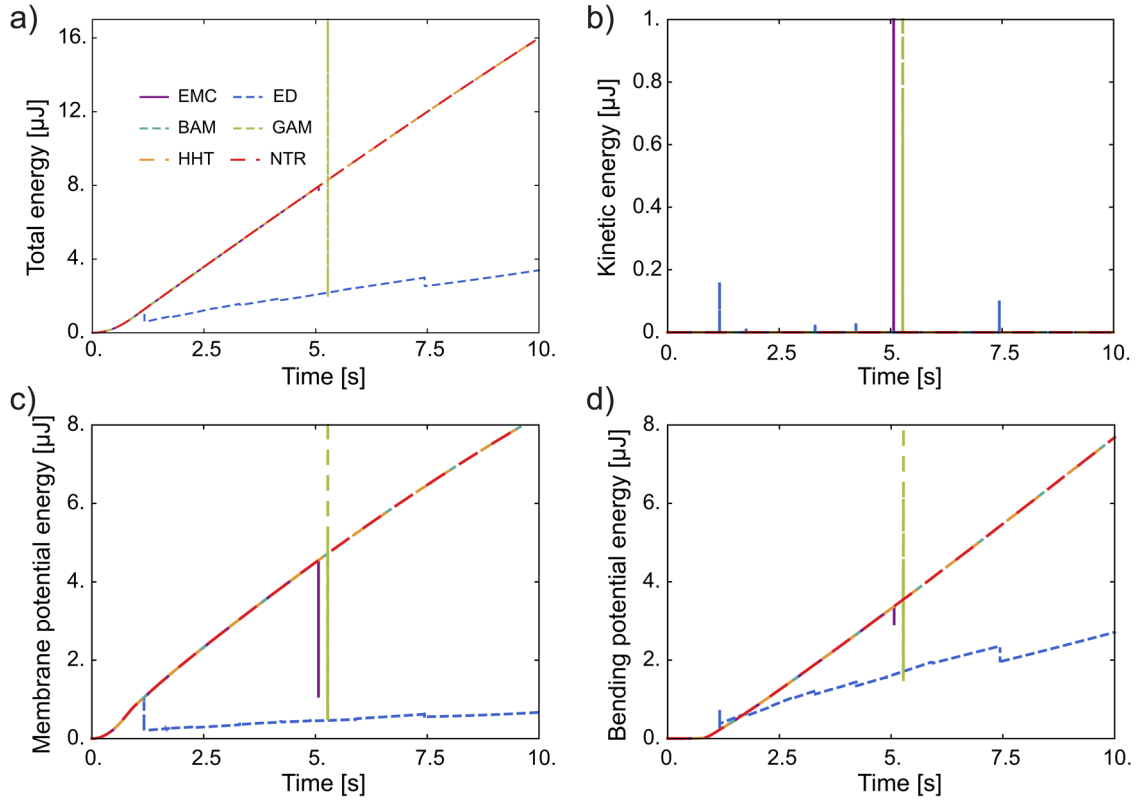
Figure 6.8: Energy evolution in time for CS3 system.
Slika 6.8: Spreminjanje energije v času za sistem CS3.

In Figure 6.8 we show the diagrams of the total and kinetic energies, as well as the membrane and bending parts of the potential energy as a function of time (the transverse shear part of the potential energy is negligible). The kinetic energy makes up a very small part of the total energy. However, it increases suddenly at the time of the pattern transition until the vibrations associated with the transition are damped out. GAM and EMC show a large increase in kinetic energy at their failures when attempting to complete the mode jump, which was associated with strong vibrations (note also the oscillations of the membrane and the bending parts of potential energy at the same time). The membrane part of the potential energy is large in the initial axisymmetric buckling mode. It is interesting that for ED, the membrane part of the potential energy drops significantly at the first mode jump and remains almost constant, and that subsequent jumps are mainly related to the change of the bending part of the potential energy, which is consistent with the observations in [82].

6.3.4   System CS4

We analyzed system CS4 ($C = 3.92$) using a mesh of 100×200 elements, the loading time $t_0 = 10$ s and the damping factors (where applicable) $\rho_\infty = 0.6$ and $\alpha_{ED} = \beta_{ED} = 0.02$. The results are presented in Figure 6.9.
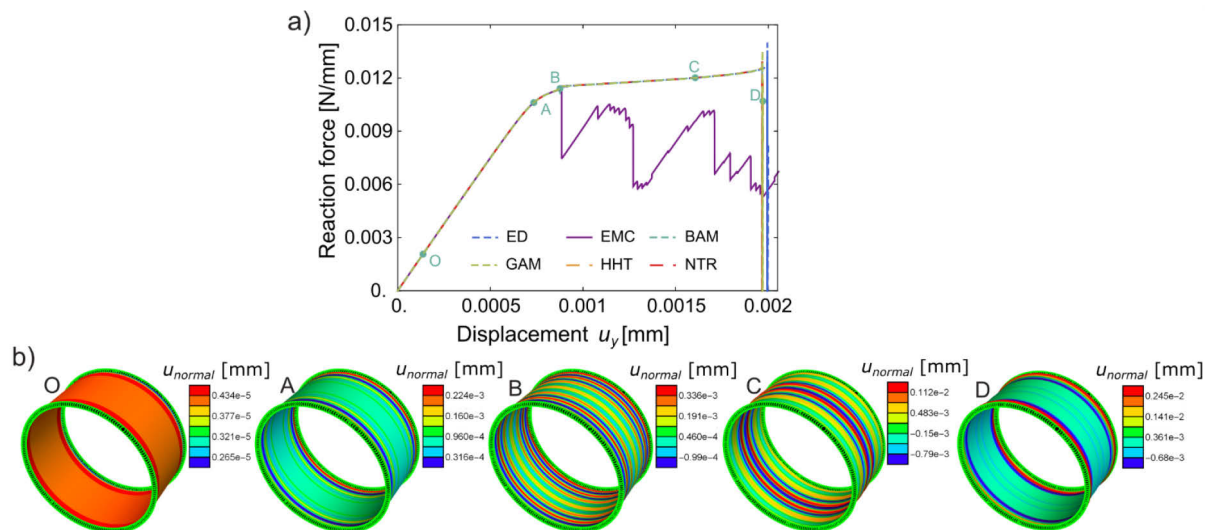
Figure 6.9: System CS4: a) force-displacement response, b) deformed shell configurations at various points on the above diagrams.

Slika 6.9: Sistem CS4: a) odziv sila-pomik, b) deformirane konfiguracije iz različnih točk na zgornjih diagramih.

In contrast to the CS1-CS3 systems, system CS4 buckles only in axisymmetric patterns, as predicted by the theory, because the value of parameter C is supercritical, cf. Eq. (6.1). In this case, all schemes (except EMC) predicted practically identical responses. In Figure 6.9, we show 5 configurations (O-D) of the cylinder found at different imposed displacements u_y. Only one transition of the pattern was found, as the initially smooth surface (configuration O) buckled into axisymmetric wrinkles. The buckling was gradual; first the axisymmetric wrinkling occurred at the edges of the system (see configuration A) and then gradually, with the increase of compression, emanated towards the mid-length of the cylinder (configuration B) and fully developed in configuration C. The same response of the shell was also reported in [173]. Moreover, at $u_y \approx 0.002$ mm, the next jump was predicted by all tested dynamic schemes (except EMC), but only towards a new axisymmetric pattern (see configuration D). This transition was never completed due to strong oscillations.

6.3.5   Critical axial force

The critical axial force at the onset of the axisymmetric wrinkling $f_{cr,dy}$ for each configuration of the cylindrical shell can be found from the diagrams in Figures 6.3, 6.5, 6.7 and 6.9. We list the values we find in Table 6.3 and compare them with the analytical critical axial force $f_{cr} = \sigma_{cr} t_f$, where σ_{cr} is the critical stress, calculated from the following expression

$$\sigma_{cr} = E_f \left[\frac{1}{p_0^2} + \frac{t_f^2 p_0^2}{4c^2 R^2} + \frac{3R\bar{E}_s}{2c^2 t_f \bar{E}_f p_0} \right], \qquad (6.10)$$

see e.g. [182] for the derivation. Here $c = \sqrt{3(1 - \nu^2)}$. According to [182], knowing that the initial wrinkling pattern is always axisymmetric, one can assume $q_0 = 0$ and obtain p_0 by solving Eq. (6.5).

In addition to the analytical and our numerical values of the critical buckling force, Table 6.3 also contains the results obtained by Xu and Potier-Ferry [173] by their numerical analysis (denoted as

$f_{cr,Xu}$). It can be seen that the results for f_{cr}, $f_{cr,dy}$ and $f_{cr,Xu}$ are in good agreement and that our prediction is on average slightly better than that of [173].

Table 6.3: Critical load for axisymmetric buckling.
Preglednica 6.3: Kritična sila za osnosimetrični uklon.

Case	CS1	CS2	CS3	CS4
f_{cr} [N/mm]	0,060	0,134	1,27	0,0130
$f_{cr,dy}$ [N/mm] $(f_{cr,dy}/f_{cr}\,\%)$	0,056 (93 %)	0,129 (96 %)	1,23 (97 %)	0,0115 (88 %)
$f_{cr,Xu}$ [N/mm] $(f_{cr,Xu}/f_{cr}\,\%)$	0,065 (108 %)	0,112 (84 %)	0,91 (72 %)	0,013 (100 %)

6.4   Spherical shell examples

Three specific spherical shell-core systems are selected in order to evaluate the two used computational models and compare the computer response with the experimental results, obtained by [174]. The characteristics of the spheres were chosen following the results from Xu et al. [174], in an attempt to see different wrinkling patterns emerging in the loading process. Their material and geometric properties are listed in Table 6.4.

No restraints were applied on the spheres, which were at rest at $t = 0$. Pressure was applied using a load speed of $0.01\,\text{MPa/s}$ which helped to ensure that the complex wrinkling patterns could form. No geometrical imperfections or perturbation forces were imposed. During the analysis we monitored the pressure level p versus radial displacement u_{normal} of a particular node of the mesh. The colors on the displayed deformed configurations relate to the radial displacements, which are magnified two times to show greater contrast between the wrinkling patterns.

Table 6.4: Geometric and material data for spheres S1–S3. Symbols E, ν, K_s, R and ρ denote the elastic modulus, Poisson ratio, spring coefficient, radius and density of the sphere, respectively.
Preglednica 6.4: Geometrijski in materialni podatki za sfere S1–S3. Simboli E, ν, K_s, R in ρ označujejo elastični modul, Poissonov količnih, koeficient togosti vzmeti, radij in gostoto sfere, v tem vrstnem redu.

System	E_f [MPa]	E_s [MPa]	$K_s\left[\dfrac{\text{N}}{\text{mm}^3}\right]$	ν_f	ν_s	t_f [mm]	R [mm]	$\rho_f\left[\dfrac{\text{g}}{\text{cm}^3}\right]$	C
S1	250	2.5	1.3525	0.3	0.49	0.4	20	0.965	3.5
S2	2.1	0.23	0.17378	0.49	0.49	0.6	20	0.965	21.2
S3	2.1	0.23	0.52223	0.49	0.49	0.2	20	0.965	109.5

Of the aforementioned time-stepping schemes, only the first order accurate energy-decaying scheme (ED1) was used and the adaptive time-step function (2.81) was applied, where the desired and maximal allowed numbers of incremental iterations were set to $I_0 = 8$ and $N = 25$, respectively. Minimal and maximal allowed time steps were set to $\Delta t_{min} = 5\,10^{-7}$ s and $\Delta t_{max} = 0.5$ s. If convergence was not achieved within 25 iterations, the increment was re-computed with $\Delta t/2$. The initial time step was $\Delta t = 0.5$ s and the convergence tolerance for the norm of the iterative displacement vector was set to 10^{-8}.

User defined parameters that control the numerical dissipation were set to $\alpha_{ED} = \beta_{ED} = 0.5$, which introduced a high-level of numerical dissipation into the algorithm. This level of dissipation allowed a smoother development of wrinkles throughout the sphere and a smoother continuation of the analysis after the initial wrinkling pattern was formed.

We used highly non-structured meshes with $n_{el} = (52431; 89855; 148512)$ elements, which give the characteristic length of the quadrilateral element $l_{avg} = (0.32; 0.24; 0.16)$ mm for each $C = (3.5; 21.2; 109.5)$. The number of elements was chosen based on the convergence analysis performed in [156] and our preliminary prediction of wrinkling patterns using the values of factor C. Namely, dimples with shorter wavelengths, which demand the use of finer mesh, were expected to form in spheres with larger C.

The results of the analyses are shown in Figures $6.10 - 6.13$ where pressure p versus displacement u_{normal} is displayed. In all cases, the panels show the transition from an initially uniform spherical deformation (smooth surface) to a deformation with dimples. In two cases ($C = 21.2$ and $C = 109.5$), RM-5 predicts a further (secondary) transition to a deformation pattern with channels (labyrinthine pattern). From Figure 6.13 it can also be seen that with increasing C the number of dimples increases (and the characteristic wavelength decreases).
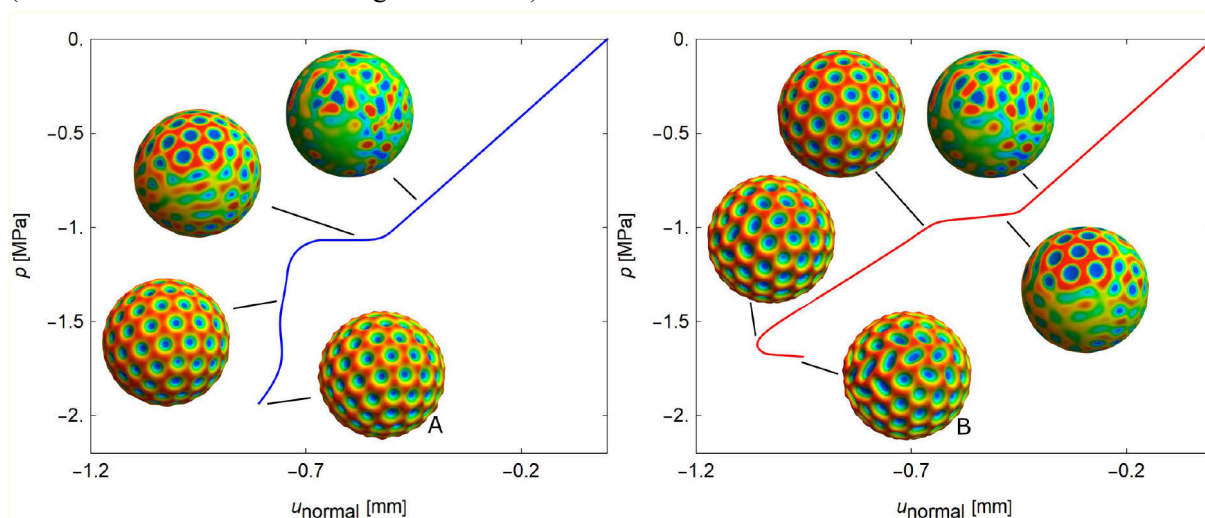
Figure 6.10: System S1: pressure-displacement response QKQ-3 (left) and RM-5 (right). Deformed shell configurations are displayed at various points. Marks A and B correspond to the final configurations, shown in Figure 6.13.

Slika 6.10: Sistem S1: odziv pritisk-pomik za QKQ-3 (levo) in RM-5 (desno). Deformirane konfiguracije so prikazane na različnih točkah. Oznaki A in B se nanašata na končni konfiguraciji, prikazani tudi na sliki 6.13.

For systems S2 and S3, we observe that a transition from dimple-like to labyrinthine pattern occurs. While the RM-5 formulation is capable of fully describing this transformation, the QKQ-3 formulation struggles to transition to the second pattern. At one point, the pattern seems to resemble the one from RM-5, but the kinematic simplification seems to restrict the elements from fully describing the labyrinthine pattern. Nonetheless, both models successfully predict a significant difference between the forming processes of systems S1 – S3. While large dimples can be observed for system S1 already at the beginning of the wrinkling process, the initial creases of the shell for the S3 system are significantly smaller.
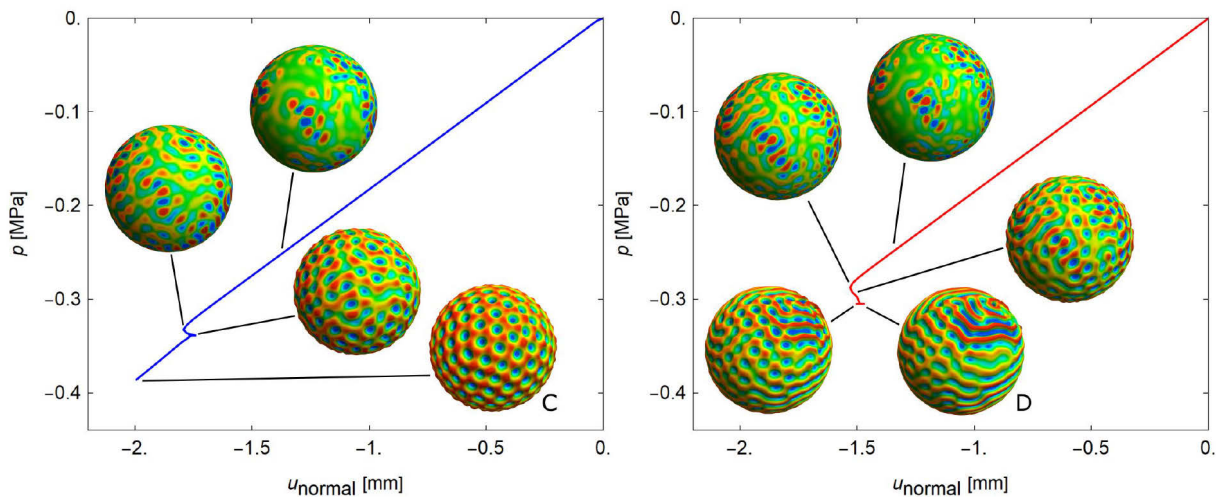
Figure 6.11: System S2: pressure-displacement response QKQ-3 (left) and RM-5 (right). Deformed shell configurations are displayed at various points. Marks C and D correspond to the final configurations, shown in Figure 6.13.

Slika 6.11: Sistem S2: odziv pritisk-pomik za QKQ-3 (levo) in RM-5 (desno). Deformirane konfiguracije so prikazane na različnih točkah. Oznaki C in D se nanašata na končni konfiguraciji, prikazani tudi na sliki 6.13.
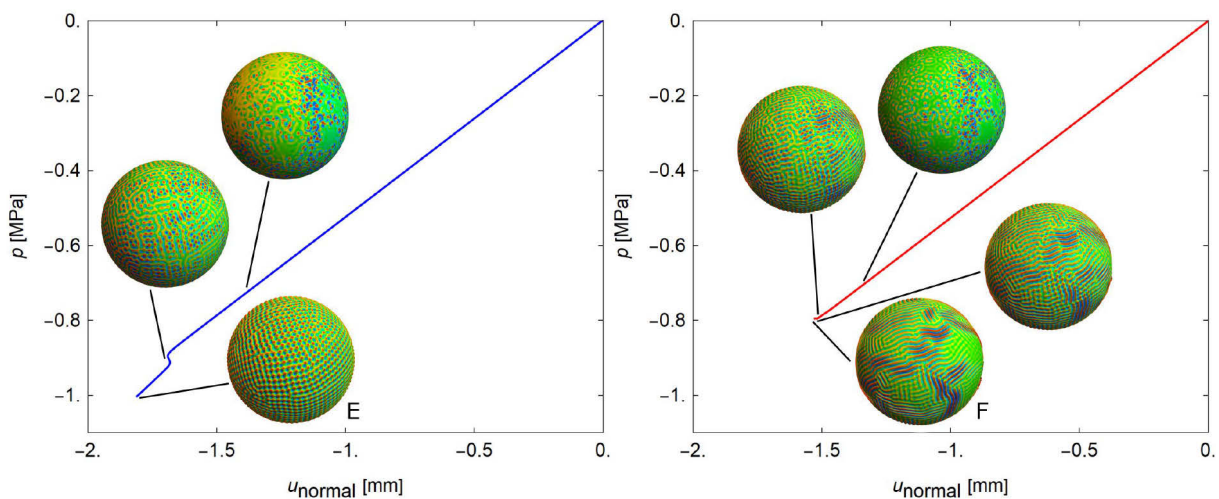
Figure 6.12: System S3: pressure-displacement response QKQ-3 (left) and RM-5 (right). Deformed shell configurations are displayed at various points. Marks E and F correspond to the final configurations, shown in Figure 6.13.

Slika 6.12: Sistem S3: odziv pritisk-pomik za QKQ-3 (levo) in RM-5 (desno). Deformirane konfiguracije so prikazane na različnih točkah. Oznaki E in F se nanašata na končni konfiguraciji, prikazani tudi na sliki 6.13.

Figure 6.13 a) – c) compare the load-displacement curves and the final wrinkling patterns for each system S. A complete agreement between the load-displacement curves for both models is obtained before buckling, but there is a noticeable difference in the initial buckling load. Furthermore, it can be observed that the post-buckling paths do not match. The reason for this stems from the fact that the wrinkling pattern predicted by a certain formulation is slightly distorted compared to the wrinkling pattern predicted by another formulation. Namely, a dimple can occur at a different location.
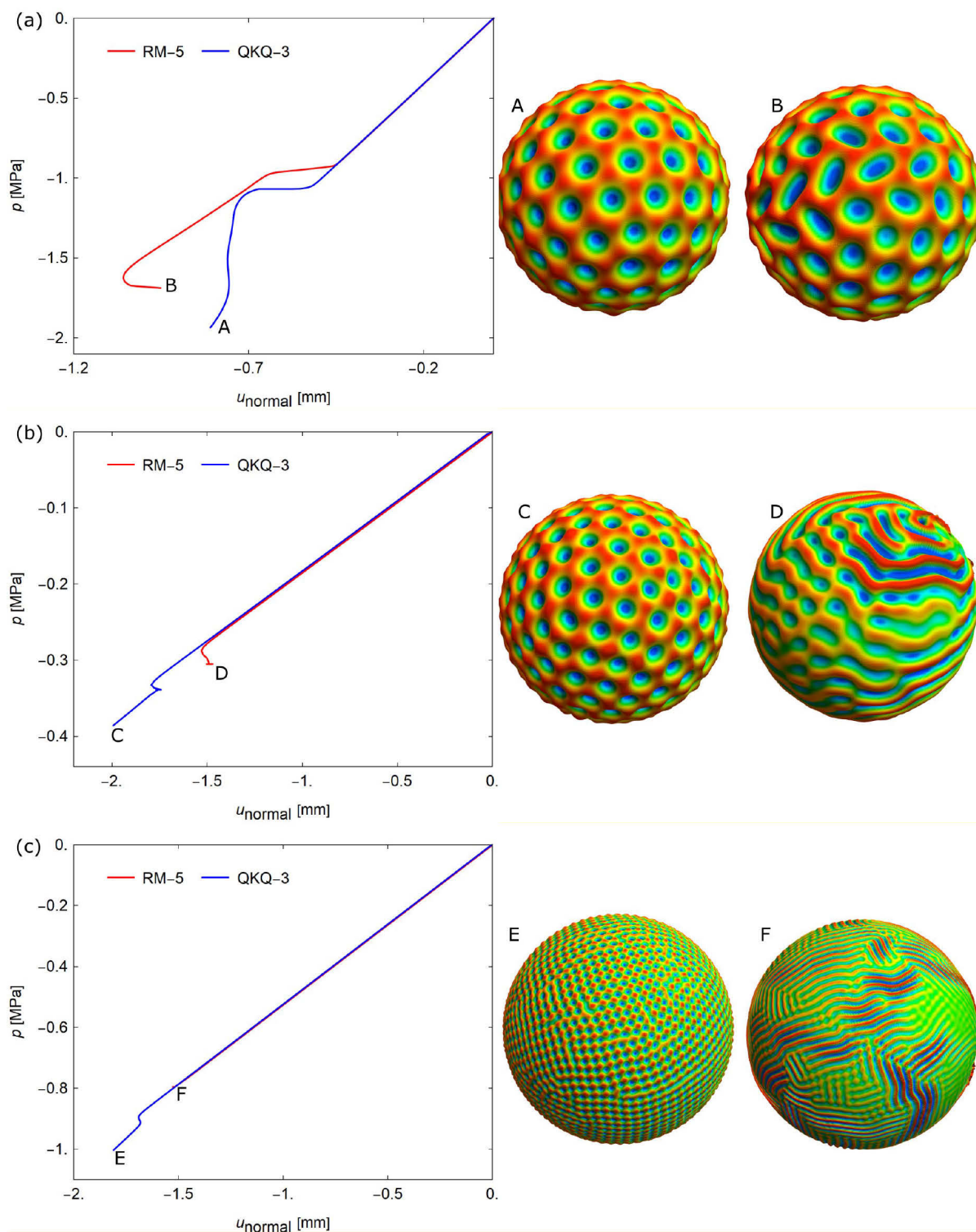
Figure 6.13: A comparison of load-displacement curves for all three shell-core systems and both computational models (left). Comparison of fully developed wrinkling patterns (right).

Slika 6.13: Primerjava med krivuljami pritisk-pomik za vse tri sisteme lupina-jedro in oba računska modela (levo). Primerjava polno razvitih vzorcev gubanja (desno).

A more detailed comparison between the fully developed patterns is shown in Figure 6.13 (right). Good agreement between the number of dimples was observed for system S1, while for systems S2 and S3 the QKQ-3 is unable to describe to labyrinthine pattern that the RM-5 model finds. The results obtained

by the latter are in good agreement with the experimental and numerical results found by Xu et al. [174], proving that the simple dynamic models presented here can also be applied for spherical systems.

6.5   Chapter conclusions

We have shown that the geometrically exact, nonlinear shell finite elements on an elastic foundation and the implicit structural dynamics can be successfully applied to investigate primary buckling and secondary mode transitions in the post-buckling regime of curved shell/substrate composites.

In the study of cylindrical systems, six time stepping schemes (GAM, BAM, HHT, NTR, EMC, ED1) were applied. We have shown that a combination of the ED1 scheme and an adaptive time-stepping algorithm comprises an efficient solution procedure for this remarkably difficult problem. However, other schemes (except GAM in some cases) cannot make a definite prediction of the pattern due to insufficient damping of strong high-modes-vibrations at buckling mode jumps. The classical implicit schemes, HHT, BAM and NTR, which are default schemes in commercial finite element codes, have not been successful in solving the problems considered in this work (the same applies to the non-dissipative EMC scheme).

Our numerical experiments on four shell composites (named as CS1-CS4) showed that our computational model can reproduce the experimentally observed phenomena from [182] and the numerical predictions from [173]. A good agreement between the theoretical [185], numerical [173] and the results of our computations was found for both the primary buckling load and the pattern prediction. We confirmed that, as predicted in the two studies, the system with the supercritical value of the critical parameter C (in our case CS4) has only one axisymmetric wrinkling mode, whereas for the subcritical C (in our case CS1-CS3) a system should show first the transition from the initially smooth to the axisymmetric wrinkling mode and, when the load is further increased, the secondary transition to the diamond-like wrinkling mode.

In addition to these known results, our numerical model shows the existence of multiple mode jumps in the post-buckling regime. In the CS3 configuration, for example, we observe that the secondary transition is gradual. First, the dimple diamond-like wrinkling pattern is localized at the mid-length of the shell and then gradually spreads towards the edges of the cylindrical system. For the CS1 and CS2 configurations, our computational model based on the ED scheme reveals new mode jumps when the load is further increased. We discover that the first observed diamond-like dimple pattern jumps with each jump into diamond-like dimple patterns with a smaller number of dimples. The difference between the first and last dimple mode can be significant (see CS1 in Figure 6.3 c). It is interesting that the mode jumps we found are similar to those found on cylindrical shells without substrate support, see e.g. [175] for experimental and [102], [92] for numerical analyses. To our best knowledge, these results have not yet been recorded in the known literature on axially compressed cylindrical shell/substrate composites, neither experimentally nor numerically.

For the analysis of spherical systems, we applied only the ED1 scheme, which proved to be the most effective in the case of cylinders. In combination with adaptive time-stepping algorithm it again provides a good solution procedure for this difficult (and highly sensitive) problem. Our numerical experiments

on three shell composites (named S1-S3) showed that the used computational models can reproduce experimentally and numerically observed phenomena from [174].

We compared two computational models, of which one has simplified kinematics. The reduced-order formulation has proven effective for small and medium values of the characteristic parameter C, but is less effective for larger values, where the transition to the second pattern was observed by the RM-5 formulation and also in the results by Xu et al. [174]. The predicted initial buckling load differs for both used formulations, but the results are still similar and are also in good agreement with those obtained from static analysis, see [156] and [157].

Let us finally note that in the qualitative prediction of wrinkle patterns we obtain a good agreement between our results and those of Xu et al. [174], where experimental results and numerical results based on one-eight symmetry were reported. In our case, we used external pressure to stimulate the system and the reference results are obtained by thermal shrinkage, which, in turn, shows that the wrinkle mechanism is universal and independent of the external stimulus.

7   CONCLUSIONS

The thesis addresses a variety of topics related to shell structures and nonlinear shell analysis. In the field of mixed formulations for shell quadrilaterals, we first identified five criteria that an "optimal" shell element should fulfill. These helped us to choose appropriate numerical tests, with which a comparison of some existing finite elements and a group of new formulations was conducted. All of the established formulations seemed to lack in one or more of the performance areas, which motivated us to combine the Hu-Washizu element from [159] (and the Hellinger-Reissner element from [59]) with the ANS interpolations for the membrane strains from [90]. This resulted in a group of novel elements, which are low-sensitive to mesh distortion and allow for large solution steps. Although the difference between our elements and the original formulations may seem very small, the effects in numerical results are far from small and very beneficial, as has been clearly demonstrated by a set of representative numerical examples.

In our opinion, the development of classical theory-based "optimal" nonlinear shell finite element is of great practical interest and thus worth investigating. The presented work can definitely be seen as a step towards the optimal low order (4-node) shell nonlinear finite element (that is based on classical shell theory with transverse shear effects). We speculate, however, that with continuous development of different mixed and hybrid shell elements, a new formulation that is even more effective and robust will emerge in the future.

In Chapter 3 we studied structural dynamics, focusing on implicit dynamic time integration schemes from the groups of generalized-α and energy-decaying schemes, which are suitable to be implemented with shell finite elements. We assessed the selected schemes first in the linear dynamics setting, where we compared their stability, dispersion and accuracy properties. Furthermore, following the development from [80], we looked into the overshoot behavior and we showed that none of the considered schemes overshoots in the displacement, while an overshoot in velocity is observed for NMD, GAM, BAM and HHT. For NTR, EMC, JWH, ED1 and ED2 no overshot is observed. Local and global errors were computed in Section 3.5.5, following the example of [182]. Next, we illustrate all of the finding on a SDOF problem in Section 3.5.6. All but one of the considered schemes are well known and adopted in many research or commercial software programs, so their details and the findings from Section 3.5 can be confirmed in e.g. [5], [38], [65], [170]. We must note, however, that the majority of the listed references deal only with a few of the selected schemes, while our aim was to create a condensed but still comprehensive review of a much wider group of schemes. Furthermore, the JWH scheme [80] has, to the best of our knowledge, not yet been extensively analyzed, and we hope to have contributed here to its understanding.

Next, we implemented these schemes for a nonlinear shell finite element and compared their properties also in the case of nonlinear analysis. We demonstrated that although some characteristics do transfer from linear to nonlinear regime, the generalized-α schemes, which are unconditionally stable in linear dynamics, do not fulfill the stability criterion for nonlinear dynamics. While the energy-decaying schemes manage to fulfill this criterion, there emerge other unfavorable traits, concerning the first order-accuracy of ED(MC)1 or a difficult implementation process for EDMC2. While JWH exhibits the best

characteristics in linear dynamics, it is considerably outperformed by energy-decaying schemes in nonlinear dynamics.

In Chapter 4 we aimed to merge the favorable characteristics of some mixed-hybrid formulations that were shown to be near optimal in Chapter 2, with the energy-decaying momentum-conserving time integration schemes EDMC1 and EDMC2 that proved to be stable in nonlinear dynamic analysis in Chapter 3. We first derived the extended Hu-Washizu and Hellinger-Reissner functionals on a simple spring pendulum example and later extended it to shell dynamics. Time discretization and discrete balance laws were derived for both novel formulations. In the numerical examples section, we considered the classical MITC4 formulation, as well as the MITC4+, EAS5 and the novel +HW and +HR formulations, all adapted for shell dynamics. We performed 3 tests, where it was shown that the favorable properties of these formulations extend nicely from static to the dynamic regime. We argue that these developments are the most important contribution of our work.

The term structural buckling is usually associated with the first critical point (i.e. with the first limit or bifurcation point) on the structural equilibrium path obtained by nonlinear static analysis. For many practical engineering shell structures, the buckling load (i.e. the load at the first critical point) is the only needed outcome of the stability analysis. Only in recent years the mechanical instabilities of shell structures have been exploited as platforms for advanced functionality and superior physical properties. For such advanced use of shell-like structures and systems, a systematic knowledge of the buckling process including development and evolution of the buckling pattern is mandatory. As illustrated in Chapter 5, the implicit time-integration schemes for structural dynamics, with controllable numerical dissipation of high-frequency modes and at the same time little numerical dissipation in the low-frequency range, are suitable for such task. They can be used to analyze the buckling process of shell-like structures and systems, including the transition of the buckling patterns during the buckling process.

Numerical tests show that the schemes that numerically dissipate high-frequency modes are the most appropriate for the shell buckling analysis. Newmark trapezoidal rule (NTR) is very inaccurate and fails quickly. The results of energy-conserving scheme (EMC) may be polluted by artificial higher frequencies that can lead to computational failure. The best results were obtained by schemes with controllable algorithmic dissipation of higher frequencies, such as energy-decaying scheme (ED), and the generalized-α method with high frequency dissipation (GAM). It turns out that the implicit dynamic analysis with (high-frequency) numerical dissipation is considerably more robust and efficient than the arc-length static analysis for several computed examples, including snap trough problems and buckling of cylinder under axial load.

The wrinkling (i.e. buckling) of curved systems composed of thin hard film and thick soft substrate has recently attracted a considerably attention, since it may be related to diverse phenomena in nature and technology. The analysis of wrinkling pattern transition of such systems has been of particular interest. It turned out that the numerical stability analysis of curved film-substrate systems, along with analysis of wrinkling transition, is far from the trivial task. In Chapter 6, we showed that the implicit structural dynamics can be used to study the transition of the wrinkling pattern in curved film-substrate systems. It was shown that a good qualitative analysis of wrinkling patterns of curved film-substrate systems,

including the transition of the wrinkling patterns, can be obtained by some implicit time stepping schemes.

In Chapter 6 we showed that 3D (static) computational models of [182], [78], [173] and [174] can be complemented by a relatively simple and fast procedure that provides practically the same results in pattern prediction. We proposed three efficient computational models that are based on the shell models presented in Chapters 4 and 5. We first focused on axially compressed bi-layer cylindrical shell-substrate composites. Of the previously considered time stepping schemes, we applied some of the generalized-α and energy-decaying time stepping schemes presented in Chapter 3. Next, we focused on the surface wrinkling of core-shell sphere systems under external pressure. In this context we applied only the energy-decaying time stepping scheme.

As far as the cylindrical composites are concerned, our numerical model can also predict mode jumps in the far post-buckling regime, which the authors of the previously mentioned studies did not observe. Of course, only experiments can confirm our numerical prediction of mode jumps. To the best of our knowledge, no (very) precise experiments have been designed yet to test the post-critical mode transitions for axially loaded cylinders on soft substrates. The experimental research in [185] was pioneering, but it mainly focused on relating different wrinkling patterns with geometrical and material properties. Due to fabrication limitations that cause imperfections, it would be quite a challenge to design an experiment to observe all the transitions. However, from the similarity between our results and several sharp jumps associated with mode transitions reported in classical texts on experiments on axially loaded cylinders without an inner core, see e.g. [175], we speculate that the mode transitions found with our computational model are real.

A full and a reduced shell model are used for the analysis of wrinkling on spheres. We find good agreement between the reported experimental results and the emerging wrinkling patterns obtained for the full model. The reduced model is blind to the transformation from the dimple-like to the labyrinthine pattern, but the overall results still match well with the experimental and numerical results obtained by [174].

8   RAZŠIRJENI POVZETEK

Lupinaste konstrukcije in sistemi se uporabljajo na mnogih tehniških področjih, tudi v gradbeništvu. Omogočajo optimalno konstrukcijsko zasnovo z vidika razmerja med težo in nosilnostjo. Zaradi skoraj neomejenih možnosti oblikovanja ukrivljenih oblik in sposobnosti, da prečno obtežbo prenašajo z ravninskimi mehanizmi, so zelo pogosto uporabljeni konstrukcijski elementi v tehniki.

Za numerično reševanje nelinearnih problemov v tehniki se je uveljavila metoda končnih elementov. Statični inženirski problem prevede na sistem nelinearnih enačb (kjer so neznanke diskretne prostorske vrednosti spremenljivk problema), ki se rešuje z Newtonovo iteracijsko metodo (npr. [42]). Če se obravnava dinamični problem, postane sistem nelinearnih enačb tudi časovno odvisen, zato sta, poleg prostorske, potrebna še časovna diskretizacija in algoritem za časovno korakanje (t. i. časovne integracijske sheme). Moderne časovne integracijske sheme za nelinearno dinamiko konstrukcij so zasnovane na zahtevah, da morajo znati algoritmično ohranjati fizikalne količine, ki se ohranjajo pri gibanju določenih dinamičnih sistemov. To so npr. energija sistema, gibalna in vrtilna količina, neelastična materialna disipacija in podobno.

Zahteve, ki se pojavljajo pri numeričnem modeliranju nelinearnega odziva lupin, so med drugim povezane s točnim opisom kinematike, posebej velikih rotacij, točnim opisom prečnih strižnih napetosti ter preprečevanjem pojavljanja različnih parazitnih napetosti (tj. blokiranja), npr. [164]. Končni elementi za lupine so raznovrstni, saj so mnogi lupinasti končni elementi namenjeni simulaciji specifičnih problemov. V zadnjem času se pojavljajo različne nove numerične formulacije za analizo lupin, med katerimi so za nas najzanimivejši geometrijsko preprosti, hibridni končni elementi, ki kljub preprosti geometriji kažejo veliko robustnost in dobro natančnost pri reševanju specifičnih nelinearnih lupinastih problemov. Izraz hibridni elementi je v tem delu uporabljen po definiciji, ki jo je predstavil Crisfield [42]. Elemente, ki imajo vse prostostne stopnje (pomike, rotacije in dodatne prostostne stopnje) definirane v vozliščih, je poimenoval kot mešane. Nadalje je elemente, ki kondenzirajo dodatne prostostne stopnje na nivoju elementa, klasificiral kot hibridne oziroma mešane–hibridne. Opomnimo le, da taka terminologija ni splošno uveljavljena.

Z lupinastimi končnimi elementi se simulira cela vrsta pojavov, ki segajo od mega velikosti (npr. uklon tankih jeklenih silosov [76] ali obnašanje armiranobetonskih hladilnih stolpov) prek mikro velikosti (npr. gubanja trdih filmov na mehkih jedrih [31]), pa vse do nano velikosti (npr. deformiranje in uklon nano struktur).

V disertaciji smo z namenom napredka znanja in razpoložljivih orodij na področju analize lupinastih konstrukcij z uporabo metode končnih elementov obravnavali spekter različnih tem. Najprej smo pozornost namenili mešanim in hibridnim elementom za statiko, pri čemer smo izdelali obsežen povzetek obstoječih formulacij in predlagali nekaj novih, zelo učinkovitih končnih elementov. Nadalje smo analizirali implicitne sheme za časovno korakanje v dinamiki, ki jih je mogoče aplicirati na končne elemente za lupine. V nadaljevanju smo formulirali posebno shemo, ki omogoča združitev visoko učinkovitih hibridnih elementov in sposobnosti disipiranja energije, ter izpeljali vse pripadajoče ravnotežne zakone. Različne modele lupin smo v kombinaciji z implicitno dinamiko nato uporabili za račun kompleksnih stabilnostnih problemov, ki vključujejo uklon in gubanje.

8.1   Mešani hibridni končni elementi za lupine

»Skoraj optimalen« 4-vozliščni, nelinearni končni element za lupine mora: (i) prestati vse osnovne teste, (ii) izkazati skoraj optimalno konvergenco, (iii) biti neobčutljiv na popačenje mreže, (iv) omogočiti dolge obtežne korake, (v) biti računsko hiter. Poleg tega mora biti opremljen z učinkovitim opisom velikih rotacij. Osnovna formulacija, ki temelji na posplošenih pomikih (pomikih in morebitnih rotacijah), ne izpolnjuje vseh zgoraj navedenih meril, zato smo pozornost usmerili na mešane in hibridne formulacije iz skupin ANS (Assumed Natural Strain), EAS (Enhanced Assumed Strain), hibridnih HW (Hu-Washizu) in hibridnih HR (Hellinger-Reissner) formulacij. V poglavju 2 smo opisali postopek implementacije za 15 mešanih ali mešanih–hibridnih formulacij, ki omogočajo neodvisno interpolacijo deformacij in/ali napetosti, in primerjali njihovo numerično učinkovitost. Dva modela lupine sta pri tem uporabljena kot osnova; 5 – parametrični model z velikimi rotacijami in neraztegljivim smernikom, npr. [139], [24]; in 6 – parametrični model brez rotacij in z raztegljivim smernikom, npr. [17].

8.1.1   Model z neraztegljivim smernikom in opis rotacij

Lupina je modelirana kot površina, opremljena z neraztegljivim smernikom, ki se nahaja v trirazsežnem prostoru s fiksno, ortonormirano bazo e_i, $i = 1,2,3$. Pozicijski vektor do začetne konfiguracije lupine je podan kot

$$X(\xi^1, \xi^2, \zeta) = X_0(\xi^1, \xi^2) + \zeta D(\xi^1, \xi^2), \quad \zeta \in [-t/2, t/2], \quad (\xi^1, \xi^2) \in \mathcal{A}, \quad \|D\| = 1,$$

kjer sta ξ^1, ξ^2 krivočrtni koordinati, ζ pa je koordinata po višini. $X_0(\xi^1, \xi^2)$ določa položaj srednje ploskve, $D(\xi^1, \xi^2)$ je polje normal na srednjo ploskev, imenovanih smerniki, t je debelina lupine in $\mathcal{A}$ je območje parametrizacije. Naj bo

$$D(\xi^1, \xi^2) = \Lambda_0(\xi^1, \xi^2)e_3,$$

kjer je $\Lambda_0(\xi^1, \xi^2)$ tenzor, ki ga poimenujemo začetna rotacija. V deformirani legi je pozicija materialne točke podana kot

$$x(\xi^1, \xi^2, \zeta) = \underbrace{[X_0(\xi^1, \xi^2) + u(\xi^1, \xi^2)]}_{x_0(\xi^1, \xi^2)} + \zeta d(\xi^1, \xi^2), \quad \|d\| = 1,$$

kjer je d smernik, ki ni nujno pravokoten na deformirano srednjo ploskev, in u pomik srednje ploskve. Smernik v deformirani legi je definiran kot

$$d = \Lambda e_3,$$

kjer je Λ rotacija, ki zavrti e_3 v d brez upoštevanja rotacije okrog lastne osi in je parametrizirana z rotacijskim parametrom ϑ. Kovariantni krivočrtni bazni vektorji v začetni in deformirani legi so tako definirani kot

$$G_\alpha = \frac{\partial X}{\partial \xi^\alpha}, \qquad R_\alpha = \frac{\partial X_0}{\partial \xi^\alpha}, \qquad \alpha = 1,2$$

$$g_\alpha = \frac{\partial x}{\partial \xi^\alpha}, \qquad r_\alpha = \frac{\partial x_0}{\partial \xi^\alpha}.$$

Z zgornjimi količinami lahko zapišemo Green-Lagrangeeve deformacije kot

$$E = \frac{1}{2}(g_i \cdot g_j - G_i \cdot G_j)G^i \otimes G^j = E_{ij}G^i \otimes G^j \approx E_{ij}R^i \otimes R^j.$$

Ko upoštevamo nekaj poenostavitev, glej izraz (2.6), lahko zgornje deformacije zapišemo v treh vektorjih, kjer so zbrane membranske, strižne in upogibne deformacije

$$\varepsilon_{\alpha\beta} = \frac{1}{2}\big(\boldsymbol{r}_\alpha \cdot \boldsymbol{r}_\beta - \boldsymbol{R}_\alpha \cdot \boldsymbol{R}_\beta\big), \qquad 2\varepsilon_{\alpha3} = \gamma_\alpha = \boldsymbol{r}_\alpha \cdot \boldsymbol{d} - \boldsymbol{R}_\alpha \cdot \boldsymbol{D},$$

$$\kappa_{\alpha\beta} = \frac{1}{2}\big(\boldsymbol{r}_\alpha \cdot \boldsymbol{d}_{,\beta} + \boldsymbol{r}_\beta \cdot \boldsymbol{d}_{,\alpha} - \boldsymbol{R}_\alpha \cdot \boldsymbol{D}_{,\beta} - \boldsymbol{R}_\beta \cdot \boldsymbol{D}_{,\alpha}\big),$$

kjer velja $(\circ)_{,\alpha} = \partial(\circ)/\partial\xi^\alpha$. Green-Lagrangeevim deformacijam so energijsko konjugirane druge Piola-Kirchhoffove rezultante napetosti $\boldsymbol{n}$, $\boldsymbol{m}$ in $\boldsymbol{q}$. Nadalje uvedemo ortonormirano bazo $\hat{\boldsymbol{e}}_i$, kjer velja $\hat{\boldsymbol{e}}_3 \equiv \boldsymbol{D}$, $\hat{\boldsymbol{e}}_1 \perp \hat{\boldsymbol{e}}_3$, $\|\hat{\boldsymbol{e}}_1\| = 1$ in $\hat{\boldsymbol{e}}_2 = \hat{\boldsymbol{e}}_3 \times \hat{\boldsymbol{e}}_1$. Tako lahko deformacije in njim pripadajoče rezultante napetosti zapišemo v navedeni bazi kot

$$\boldsymbol{\epsilon} = [\hat{\varepsilon}_{11}, \hat{\varepsilon}_{22}, 2\hat{\varepsilon}_{12}]^T, \qquad \boldsymbol{\kappa} = [\hat{\kappa}_{11}, \hat{\kappa}_{22}, 2\hat{\kappa}_{12}]^T, \qquad \boldsymbol{\gamma} = [\hat{\gamma}_1, \hat{\gamma}_2]^T,$$

$$\boldsymbol{n} = [\hat{n}_{11}, \hat{n}_{22}, \hat{n}_{12}]^T, \qquad \boldsymbol{m} = [\hat{m}_{11}, \hat{m}_{22}, \hat{m}_{12}]^T, \qquad \boldsymbol{q} = [\hat{q}_1, \hat{q}_2]^T.$$

Za opis obnašanja materiala smo privzeli Saint-Venant-Kirchhoffov izotropični hiperelastični materialni model, ki upošteva predpostavko o ničelnih napetostih izven ravnine ($\hat{n}_{33} = \hat{m}_{33} = 0$). To pripelje do naslednjih izrazov za konstitutivne zakone

$$\boldsymbol{n} = \boldsymbol{C}^m \boldsymbol{\varepsilon}, \qquad \boldsymbol{m} = \boldsymbol{C}^b \boldsymbol{\kappa}, \qquad \boldsymbol{q} = \boldsymbol{C}^s \boldsymbol{\gamma}, \qquad \boldsymbol{C}^m = t\overline{\overline{\boldsymbol{C}}}, \qquad \boldsymbol{C}^b = t^3/12\overline{\overline{\boldsymbol{C}}},$$

kjer je $\overline{\overline{\boldsymbol{C}}}$ standardna konstitutivna matrika za ravninsko napetostno stanje.

Energijski potencial lupine, ki je obremenjena z zunanjim pritiskom $\overline{\boldsymbol{b}}$ in silami $\overline{\boldsymbol{t}}$, lahko zapišemo kot

$$\Pi(\boldsymbol{u}, \boldsymbol{d}) = \Pi_{\text{int}}(\boldsymbol{u}, \boldsymbol{d}) - \Pi_{\text{ext}}(\boldsymbol{u}, \boldsymbol{d}) =$$

$$\int_M \frac{1}{2}\big(\boldsymbol{\varepsilon} \cdot \boldsymbol{C}^m \boldsymbol{\varepsilon} + \boldsymbol{\kappa} \cdot \boldsymbol{C}^b \boldsymbol{\kappa} + \boldsymbol{\gamma} \cdot \boldsymbol{C}^s \boldsymbol{\gamma}\big)\, dA - \left(\int_M \boldsymbol{u} \cdot \overline{\boldsymbol{b}}\, dA + \int_{\Gamma_{\overline{t}}} \boldsymbol{u} \cdot \overline{\boldsymbol{t}}\, ds\right),$$

kjer je M začetna srednja ploskev in $\Gamma_{\overline{t}}$ predstavlja tisti del lupine, ki je obremenjen s predpisano silo. Lupina je v ravnotežju, ko je energijski potencial v minimumu, kar zapišemo z izrazom za virtualno delo

$$\delta\Pi(\boldsymbol{u}, \boldsymbol{d}; \delta\boldsymbol{u}, \delta\boldsymbol{d}) = \int_M \big(\delta\boldsymbol{\epsilon} \cdot \boldsymbol{C}^m \boldsymbol{\varepsilon} + \delta\boldsymbol{\kappa} \cdot \boldsymbol{C}^b \boldsymbol{\kappa} + \delta\boldsymbol{\gamma} \cdot \boldsymbol{C}^s \boldsymbol{\gamma}\big)\, dA - \delta\Pi_{\text{ext}}(\delta\boldsymbol{u}, \delta\boldsymbol{d}) = 0,$$

kjer $\delta\Pi$ predstavlja variacijo potencialne energije, $\delta\boldsymbol{u}$ in $\delta\boldsymbol{d}$ sta kinematično sprejemljivi variaciji pomika $\boldsymbol{u}$ in smernika $\boldsymbol{d}$, $\delta\Pi_{\text{ext}}$ je variacija potenciala zunanje obtežbe, $\delta\boldsymbol{\epsilon}$, $\delta\boldsymbol{\kappa}$ in $\delta\boldsymbol{\gamma}$ pa so variacije membranskih, upogibnih in strižnih deformacij.

V obravnavanem modelu za opis rotacij uporabimo rotacijsko matriko $\boldsymbol{\Lambda}$ iz izraza (2.4). To rotacijo lahko razdelimo na dva dela, tako da izrazimo smernik $\boldsymbol{d}$ kot

$$\boldsymbol{d} = \boldsymbol{\Lambda}_0 \widetilde{\boldsymbol{\Lambda}}(\boldsymbol{\vartheta}_T)\boldsymbol{e}_3 = \widetilde{\boldsymbol{\Lambda}}(\boldsymbol{\theta}_T)\boldsymbol{\Lambda}_0\boldsymbol{e}_3 = \widetilde{\boldsymbol{\Lambda}}(\boldsymbol{\theta}_T)\boldsymbol{D},$$

kjer $\boldsymbol{\vartheta}_T$ in $\boldsymbol{\theta}_T$ predstavljata totalni materialni oziroma prostorski parameter rotacije. V našem delu se odločimo za materialno parametrizacijo, ki sledi Rodriguezovi formuli

$$\widetilde{\boldsymbol{\Lambda}}(\boldsymbol{\vartheta}_T) = \cos\vartheta_T \boldsymbol{I} + \frac{\sin\vartheta_T}{\vartheta_T}\widehat{\boldsymbol{\vartheta}}_T + \frac{1 - \cos\vartheta_T}{\vartheta_T^2}\boldsymbol{\vartheta}_T \otimes \boldsymbol{\vartheta}_T,$$

kjer je $\boldsymbol{I}$ matrika identitete, $\vartheta_T = \|\boldsymbol{\vartheta}_T\|$, $\widehat{\boldsymbol{\vartheta}}_T \boldsymbol{b} = \boldsymbol{\vartheta}_T \times \boldsymbol{b}$ za $\forall \boldsymbol{b}$ in za poševno simetrično matriko $\widehat{\boldsymbol{\vartheta}}_T$, $\otimes$ pa predstavlja tenzorski produkt. Ker $\boldsymbol{\vartheta}_T$ zavrti $\boldsymbol{e}_3$ v $\boldsymbol{d}$ brez rotacije okrog lastne osi, ima le dve neničelni komponenti, kar posledično poenostavi izraz na

$$\boldsymbol{d} = \boldsymbol{\Lambda}_0 \widetilde{\boldsymbol{\Lambda}}(\boldsymbol{\vartheta}_T)\boldsymbol{e}_3 = \boldsymbol{\Lambda}_0\left(\cos\vartheta_T \boldsymbol{e}_3 + \frac{\sin\vartheta_T}{\vartheta_T}\boldsymbol{\vartheta}_T \times \boldsymbol{e}_3\right).$$

V zgornjem izrazu pride do singularnosti v primeru, ko je $\vartheta_T = \pi$, zato je smiselno rotacijo $\mathbf{\Lambda}_0$, ki je povezana z začetno konfiguracijo, nadomestiti z rotacijo, ki je povezana s konfiguracijo med začetno in trenutno. To lahko storimo z rotacijo $\mathbf{\Lambda}_n$, ki je povezana z zadnjo konvergirano konfiguracijo, ali pa z rotacijo $\mathbf{\Lambda}_n^{k-1}$, povezano s konfiguracijo v zadnji iteraciji. Ti dve rotaciji sta parametrizirani z rotacijskima vektorjema $\boldsymbol{\vartheta}_I$ oziroma $\boldsymbol{\vartheta}_{n+1}^k$, ki ju lahko namesto rotacijskega vektorja $\boldsymbol{\vartheta}_T$ uporabimo v zgornjih izrazih, glej sliko 2.1.

Alternativo opisu zasuka z rotacijsko matriko predstavljajo rotacijski kvaternioni $\hat{q}$, dobljeni iz zasukov kot

$$\hat{q} = \left[\cos\left(\frac{\vartheta}{2}\right), \frac{\boldsymbol{\vartheta}}{\vartheta}\sin\left(\frac{\vartheta}{2}\right)\right]^T.$$

Prednost takega zapisa v primerjavi z rotacijsko matriko je to, da je med računom treba shraniti 4 skalarne vrednosti, medtem ko jih je pri rotacijski matriki treba shraniti 9. Smernik v deformirani legi lahko dobimo z uporabo izrazov (2.23)–(2.27).

8.1.2   Model z raztegljivim smernikom

V modelu z raztegljivim smernikom se izognemo uporabi rotacij, pri čemer pozicijski vektor nedeformirane materialne točke zapišemo enako kot v primeru modela z neraztegljivim smernikom. Pozicijski vektor materialne točke v deformirani legi pa zapišemo kot

$$\boldsymbol{x} = \underbrace{[\boldsymbol{X}_0 + \boldsymbol{u}]}_{\boldsymbol{x}_0} + \zeta\boldsymbol{d}, \qquad \boldsymbol{d} = \boldsymbol{D} + \boldsymbol{w},$$

kjer $\boldsymbol{d}$ ni več nujno enotske dolžine in $\boldsymbol{w}$ označuje vektor pomika smernika. Za opis deformacij uporabimo komponente Green-Lagrangeevega tenzorja, za rezultante napetosti pa drugi Piola-Kirchhoffov tenzor. Poleg komponent, opisanih v prejšnjem poglavju, se v obravnavanem modelu dodatno pojavijo še deformacije v smeri debeline, definirane kot

$$\varepsilon_{33} = \frac{1}{2}\left(\boldsymbol{x}_{,3} \cdot \boldsymbol{x}_{,3} - \boldsymbol{X}_{,3} \cdot \boldsymbol{X}_{,3}\right) = \frac{1}{2}\left(\boldsymbol{d} \cdot \boldsymbol{d} - \underbrace{\boldsymbol{D} \cdot \boldsymbol{D}}_{1}\right),$$

kjer je $(\circ)_{,3} = \partial(\circ)/\partial\zeta$. Deformacije in napetosti lahko spet zapišemo v vektorski obliki in izražene v ortonormirani bazi

$$\bar{\boldsymbol{\varepsilon}} = [\hat{\varepsilon}_{11}, \hat{\varepsilon}_{22}, \hat{\varepsilon}_{33}, 2\hat{\varepsilon}_{12}]^T, \qquad \boldsymbol{\kappa} = [\kappa_{11}, \kappa_{22}, 2\kappa_{12}]^T, \qquad \boldsymbol{\gamma} = [\hat{\gamma}_1, \hat{\gamma}_2]^T,$$
$$\bar{\boldsymbol{n}} = [\hat{n}_{11}, \hat{n}_{22}, \hat{n}_{33}, \hat{n}_{12}]^T, \qquad \boldsymbol{m} = [\hat{m}_{11}, \hat{m}_{22}, \hat{m}_{12}]^T, \qquad \boldsymbol{q} = [\hat{q}_1, \hat{q}_2]^T.$$

Za materialni model je uporabljen specializirani Saint-Venant-Kirchhoffov hiperelastični konstitutivni zakon, kjer velja $\bar{\boldsymbol{n}} = \overline{\boldsymbol{C}}^m\bar{\boldsymbol{\varepsilon}}, = \boldsymbol{C}^b\boldsymbol{\kappa}$ in $\boldsymbol{q} = \boldsymbol{C}^s\boldsymbol{\gamma}$. Tu je $\overline{\boldsymbol{C}}^m = t\overline{\boldsymbol{C}}$, pri čemer $\overline{\boldsymbol{C}}$ predstavlja standardno 3d konstitutivno matriko.

Funkcional potencialne energije lahko zdaj zapišemo kot

$$\Pi(\boldsymbol{u}, \boldsymbol{w}) = \int_M \frac{1}{2}\left(\bar{\boldsymbol{\varepsilon}}^T\overline{\boldsymbol{C}}^m\bar{\boldsymbol{\varepsilon}} + \boldsymbol{\kappa}^T\boldsymbol{C}^b\boldsymbol{\kappa} + \boldsymbol{\gamma}^T\boldsymbol{C}^s\boldsymbol{\gamma}\right)dA - \Pi_{\text{ext}}(\boldsymbol{u}, \boldsymbol{w}),$$

njegovo šibko obliko pa

$$\delta\Pi(\boldsymbol{u}, \boldsymbol{w}; \delta\boldsymbol{u}, \delta\boldsymbol{w}) = \int_M \left(\delta\bar{\boldsymbol{\varepsilon}}^T\bar{\boldsymbol{n}} + \delta\boldsymbol{\kappa}^T\boldsymbol{m} + \delta\boldsymbol{\gamma}^T\boldsymbol{q}\right)dA - \delta\Pi_{\text{ext}}(\delta\boldsymbol{u}, \delta\boldsymbol{w}) = 0.$$

8.1.3 Implementacija za štirivozliščni končni element

Začetno srednjo ploskev M diskretiziramo z n_{el} izoparametričnimi štirivozliščnimi končnimi elementi, tako da velja $M \approx \bigcup_{e=1}^{n_{el}} A_e$. Na površini A_e so začetne koordinate in začetni smernik opisani kot

$$X_0^h(\xi, \eta) = \sum_{a=1}^{4} N_a(\xi, \eta) X_{0a}, \qquad D^h = \sum_{a=1}^{n_4} N_a(\xi, \eta) D_a, \qquad \|D_a\| = 1,$$

kjer podpis $(\cdot)_a$ označuje vrednosti v vozliščih, nadpis h označuje aproksimacijo funkcije (ali funkcionala), ξ, η pa sta izoparametrični koordinati, ki parametrizirata srednjo ploskev elementa. $N_a(\xi, \eta)$ so bilinearne Lagrangeeve interpolacijske funkcije, definirane na površini kvadrata $\mathcal{A}_e = [-1, 1] \times [-1, 1]$. Deformirana konfiguracija je za $5-$parametrični model aproksimirana kot

$$x_0^h = X_0^h + u^h, \qquad u^h(\xi, \eta) = \sum_{a=1}^{n_{en}} N_a(\xi, \eta) u_a, \qquad d^h = \sum_{a=1}^{n_{en}} N_a(\xi, \eta) d_a.$$

Za $6-$parametrični model je interpolacija srednje ploskve enaka kot zgoraj, medtem ko je smernik interpoliran kot

$$d^h = D^h + w^h, \qquad w^h(\xi, \eta) = \sum_{a=1}^{n_{en}} N_a(\xi, \eta) w_a.$$

Funkcional potencialne energije lahko v diskretni obliki zdaj napišemo kot

$$\Pi^h = \mathbb{A}_{e=1}^{n_{el}} \Pi^{e,h}(u^h, d^h) = \mathbb{A}_{e=1}^{n_{el}} \left(\Pi_{\text{int}}^{e,h}(u^h, d^h) - \Pi_{\text{ext}}^{e,h}(u^h, d^h) \right),$$

kjer $\mathbb{A}$ označuje operator združevanja končnih elementov.

Da postopek implementacije opišemo v celoti, je treba definirati še transformacije, ki preslikajo količine iz krivočrtnega koordinatnega sistema v lokalni kartezični koordinatni sistem, ki je definiran v Gaussovi točki ali v središču elementa. Osnovne transformacijske matrike so definirane v izrazih (2.40)–(2.41). Pri opisu mešanih formulacij se v tem povzetku izognemo prikazu posameznih transformacij, so pa te podrobno opisane v poglavjih $2.4.1 - 2.4.4$.

8.1.4 Mešani končni elementi

V disertaciji smo predstavili nekaj najpogosteje uporabljenih mešanih formulacij za štirivozliščne končne elemente za lupine. Razdelimo jih lahko v več družin, ki so na kratko opisane v naslednjih poglavjih.

8.1.4.1 ANS elementi

ANS koncept temelji na neodvisni interpolaciji deformacij po elementu. V izbranih točkah, glej sliko 2.3, so deformacije izvrednotene z uporabo standardnih izrazov, te vrednosti pa so nato interpolirane po elementu z ustreznimi interpolacijskimi funkcijami. Z uporabo ANS formulacij se lahko zelo učinkovito izognemo strižnemu, debelinskemu ali membranskemu blokiranju, ki je pogosto razlog za slabše obnašanje elementa.

Strižnemu blokiranju se lahko izognemo z uporabo strižnega ANS koncepta iz [48]

$$\begin{bmatrix} \tilde{\gamma}_1 \\ \tilde{\gamma}_2 \end{bmatrix} = \frac{1}{2} \begin{bmatrix} (1-\eta)\gamma_1^A + (1+\eta)\gamma_1^C \\ (1-\xi)\gamma_2^D + (1+\xi)\gamma_2^B \end{bmatrix},$$

kjer so oznake A, B, C in D povezane s točkami na sliki 2.3. Te deformacije nato transformiramo v lokalni kartezični koordinatni sistem in jih uporabimo v funkcionalu potencialne energije, da pridemo do formulacije, poimenovane kot MITC4.

Membranskemu blokiranju se lahko izognemo z uporabo interpolacijskih funkcij, ki so bile definirane za element, poimenovan MITC4+, glej [89] in [90]. Membranske deformacije so dane z izrazi

$$\tilde{\varepsilon}_{11} = (-1 + \eta^2)\big(a_B \varepsilon_{11}^B + a_D \varepsilon_{11}^D + a_E \varepsilon_{12}^E\big) +$$

$$\frac{1}{2}(1 - 2a_A - \eta + 2a_A \eta^2)\varepsilon_{11}^A + \frac{1}{2}(1 - 2a_C + \eta + 2a_C \eta^2)\varepsilon_{11}^C,$$

$$\tilde{\varepsilon}_{22} = (-1 + \xi^2)\big(a_A \varepsilon_{22}^A + a_C \varepsilon_{22}^C + a_E \varepsilon_{12}^E\big) +$$

$$\frac{1}{2}(1 - 2a_B + \xi + 2a_B \xi^2)\varepsilon_{22}^B + \frac{1}{2}(1 - 2a_D - \xi + 2a_D \xi^2)\varepsilon_{22}^D,$$

$$\tilde{\varepsilon}_{12} = \frac{1}{4}(-\xi + 4a_A \xi\eta)\varepsilon_{11}^A + \frac{1}{4}(\xi + 4a_C \xi\eta)\varepsilon_{11}^C +$$

$$\frac{1}{4}(\eta + 4a_B \xi\eta)\varepsilon_{22}^B + \frac{1}{4}(-\eta + 4a_D \xi\eta)\varepsilon_{22}^D + (1 + a_E \xi\eta)\varepsilon_{12}^E,$$

pri čemer so točke A, B, C, D in E prikazane na sliki 2.3, deformacije pa so v teh točkah izvrednotene z uporabo standardnega izraza (2.7). V zgornjih izrazih nastopajo tudi utežni faktorji, ki so povezani z zadnjo konvergirano lego in so razloženi v izrazih (2.49)–(2.51). Deformacije so spet transformirane v lokalni kartezični koordinatni sistem in skupaj s strižnimi ANS deformacijami uporabljene v funkcionalu potencialne energije, da prispemo do MITC4+ elementa.

Blokiranju v smeri debeline, ki lahko nastane pri 6 – parametričnem modelu z raztegljivim smernikom, se lahko izognemo, če uporabimo ANS koncept iz [15], tako da so vrednosti deformacije ε_{33} izvrednotene v vozliščih in interpolirane po elementu z uporabo standardnih interpolacijskih funkcij, kot

$$\tilde{\varepsilon}_{33} = \sum_{a=1}^{n_{en}} N_a(\xi, \eta)\, \varepsilon_{33a}.$$

8.1.4.2   EAS formulacije

EAS formulacije izvirajo iz Hu-Washizujevega funkcionala, kjer je polje deformacij reparametrizirano kot

$$\boldsymbol{\epsilon}^{EAS} = \boldsymbol{\epsilon}^h + \hat{\tilde{\boldsymbol{\epsilon}}},$$

pri čemer je $\boldsymbol{\epsilon}^h$ polje deformacij, povezanih s pomiki, $\hat{\tilde{\boldsymbol{\epsilon}}}$ pa so dodatne deformacije, ki obogatijo osnovno polje. Tak pristop lahko uporabimo za izboljšavo membranskih, upogibnih in strižnih deformacijah, a je bilo v [22] pokazano, da je računsko upravičena le izboljšava membranskega dela, ki smo jo zato obravnavali v tej disertaciji. Pomembna predpostavka, ki je veljavna ob izpeljavi EAS formulacij, je ortogonalnost med poljem rezultant napetosti in poljem dodatnih deformacij $\tilde{\boldsymbol{\epsilon}}$. Iz tega sledi, da lahko osnovni Hu-Washizujev funkcional poenostavimo v

$$\Pi_{EAS}^{e,h}(\boldsymbol{u}^h, \boldsymbol{d}^h, \hat{\tilde{\boldsymbol{\epsilon}}}) = \int_{A_e} \left(\frac{1}{2}\boldsymbol{\epsilon}^{EAS} \cdot (\boldsymbol{C}\,\boldsymbol{\epsilon}^{EAS}) \right) dA - \Pi_{ext}^{e,h}(\boldsymbol{u}^h, \boldsymbol{d}^h),$$

kjer je $\boldsymbol{C} = \mathrm{DIAG}[\mathbf{C}^m, \mathbf{C}^b, \mathbf{C}^s]$.

Polje membranskih deformacij lahko izboljšamo z uporabo 4, 5 ali 7 neodvisnih parametrov, ki jih interpoliramo po elementu z uporabo izraza

$$\tilde{\boldsymbol{\varepsilon}} = \boldsymbol{\Gamma}\,\widetilde{\boldsymbol{\alpha}},$$

pri čemer so interpolacijske funkcije za elemente s 4, 5 ali 7 neodvisnimi parametri $\boldsymbol{\alpha}$ definirane kot

$$\boldsymbol{\Gamma} = \begin{bmatrix} \xi & 0 & 0 & 0 \\ 0 & \eta & 0 & 0 \\ 0 & 0 & \xi & \eta \end{bmatrix}, \qquad \boldsymbol{\Gamma} = \begin{bmatrix} \xi & 0 & 0 & 0 & 0 \\ 0 & \eta & 0 & 0 & 0 \\ 0 & 0 & \xi & \eta & \xi\eta \end{bmatrix}, \qquad \boldsymbol{\Gamma} = \begin{bmatrix} \xi & 0 & 0 & 0 & \xi\eta & 0 & 0 \\ 0 & \eta & 0 & 0 & 0 & \xi\eta & 0 \\ 0 & 0 & \xi & \eta & 0 & 0 & \xi\eta \end{bmatrix}.$$

Te deformacije so nato transformirane v lokalni koordinatni sistem z uporabo izraza (2.63), s čimer pridemo do končne izpeljave končnih elementov EAS4, EAS5 in EAS7.

8.1.4.3   Hibridne Hellinger-Reissner formulacije

Hellinger-Reissnerjev (HR) funkcional ima naslednjo obliko

$$\Pi_{\mathrm{HR}}^{e,h}\big(\boldsymbol{u}^h, \boldsymbol{d}^h, \boldsymbol{\sigma}^{HR}\big) = \int_{A_e} \left[\boldsymbol{\epsilon}^h \cdot \boldsymbol{\sigma}^{HR} - \frac{1}{2}\boldsymbol{\sigma}^{HR} \cdot \boldsymbol{C}^{-1}\boldsymbol{\sigma}^{HR} \right] dA - \Pi_{\mathrm{ext}}^{e,h}\big(\boldsymbol{u}^h, \boldsymbol{d}^h\big),$$

kjer smo v formulacijo uvedli polje neodvisnih rezultant napetosti $\boldsymbol{\sigma}^{HR} = [\boldsymbol{n}^{HR,T}, \boldsymbol{m}^{HR,T}, \boldsymbol{q}^{HR,T}]^T$. Interpolacijske funkcije za neodvisne napetosti so zapisane kot

$$\boldsymbol{n}^{HR} = \begin{bmatrix} \bar{n}^{11} \\ \bar{n}^{22} \\ \bar{n}^{12} \end{bmatrix} = \begin{bmatrix} \bar{\beta}_1 + (\eta - \bar{\eta})\bar{\beta}_9 \\ \bar{\beta}_2 + (\xi - \bar{\xi})\bar{\beta}_{10} \\ \bar{\beta}_3 \end{bmatrix}, \qquad \boldsymbol{m}^{HR} = \begin{bmatrix} \bar{m}^{11} \\ \bar{m}^{22} \\ \bar{m}^{12} \end{bmatrix} = \begin{bmatrix} \bar{\beta}_4 + (\eta - \bar{\eta})\bar{\beta}_{11} \\ \bar{\beta}_5 + (\xi - \bar{\xi})\bar{\beta}_{12} \\ \bar{\beta}_6 \end{bmatrix}$$

$$\boldsymbol{q}^{HR} = \begin{bmatrix} \bar{q}^{13} \\ \bar{q}^{23} \end{bmatrix} = \begin{bmatrix} \bar{\beta}_7 + (\eta - \bar{\eta})\bar{\beta}_{13} \\ \bar{\beta}_8 + (\xi - \bar{\xi})\bar{\beta}_{14} \end{bmatrix},$$

kjer je $\overline{\boldsymbol{\beta}} = \left[\bar{\beta}_1, \cdots, \bar{\beta}_{14}\right]^T$ vektor neodvisnih parametrov, $\bar{\xi}$ in $\bar{\eta}$ pa sta konstanti, ki določata koordinate težišča elementa. Zgoraj določene rezultante napetosti in deformacije je treba transformirati v lokalni koordinatni sistem v središču elementa, kot je opisano v izrazih (2.70)–(2.71), s čimer zagotovimo, da element izpolni osnovni »patch test«. Pri implementaciji HR elementov lahko poleg zgoraj zapisanega funkcionala uporabimo tudi delni oz. nepopolni HR funkcional, kot je npr. zapisan v (2.67), kjer so uvedene neodvisne interpolacije za membranski, upogibni ali strižni del posebej (ali v izbrani medsebojni kombinaciji). S tem zmanjšamo število neodvisnih parametrov na ravni elementa in posledično skrajšamo računski čas.

8.1.4.4   Hibridne Hu-Washizu formulacije

Poleg neodvisnih rezultant napetosti $\boldsymbol{\sigma}^{HW}$, ki so interpolirane enako kot zgoraj opisane $\boldsymbol{\sigma}^{HR}$, se v Hu-Washizujevem (HW) funkcionalu pojavijo tudi neodvisne deformacije $\boldsymbol{\epsilon}^{HW}$

$$\Pi_{\mathrm{HW}}^{e,h}\big(\boldsymbol{u}^h, \boldsymbol{d}^h, \boldsymbol{\epsilon}^{HW}, \boldsymbol{\sigma}^{HW}\big) = \int_{A_e} \left[\frac{1}{2}\boldsymbol{\epsilon}^{HW} \cdot \boldsymbol{C}\boldsymbol{\epsilon}^{HW} + \boldsymbol{\sigma}^{HW} \cdot \big(\boldsymbol{\epsilon}^h - \boldsymbol{\epsilon}^{HW}\big) \right] dA - \Pi_{\mathrm{ext}}^{e,h}\big(\boldsymbol{u}^h, \boldsymbol{d}^h\big).$$

Deformacije $\boldsymbol{\epsilon}^{HW}$ se po elementu interpolirajo z uporabo enakih funkcij, kot so zgoraj uporabljene za rezultante napetosti, pri čemer so neodvisni parametri zapisani v vektorju $\boldsymbol{\alpha}$. Ta lahko ima v našem primeru 14 ali 20 členov. Druga opcija je uporabljena v primeru, ko v Hu-Washizujevo formulacijo vključimo še dodatnih 6 EAS parametrov (ki so pravokotni na neodvisne rezultante napetosti $\boldsymbol{\sigma}^{HW}$).

Neodvisne napetosti in deformacije ter deformacije, izpeljane iz pomikov, je, enako kot za HR elemente, treba transformirati v lokalni koordinatni sistem v središču elementa.

8.1.4.5   Nove hibridne formulacije

V disertaciji smo predstavili tudi nove hibridne formulacije, ki uspešno združijo pozitivne lastnosti zgoraj opisanih hibridnih HR ali HW formulacij in ANS formulacije za membranske deformacije. Izkaže se, da se lahko take formulacije izpeljejo tako, da v Hu-Washizujevem ali Hellinger-Reissnerjevem funkcionalu zamenjamo deformacije ϵ^h z ANS deformacijami ϵ^{ANS}, ki jih je treba ustrezno transformirati. Taka implementacija je relativno preprosta, razlika, ki se pojavi v numeričnih rezultatih, pa je zelo velika in govori novi formulaciji v prid.

8.1.5   Numerični primeri

V poglavju z numeričnimi primeri smo najprej primerjali obnašanje vseh uporabljenih algoritmov za račun velikih rotacij v elementu s 5 parametri, glej preglednico 2.7, tem pa smo dodali še odziv elementa s 6 parametri, glej sliki 2.5 in 2.6. Ugotovili smo, da obe osnovni formulaciji izračunata enake odzive, razlike pa se pojavijo med različnimi algoritmi za rotacije v 5 – parametričnem elementu. Te so najvidnejše v odzivu za primer s prostorskimi rotacijami, kjer so spremljani pomiki različni za vsakega izmed algoritmov, medtem ko so pomiki za primere z ravninskimi rotacijami enaki za vse algoritme. Izkazalo se je, da uporaba rotacijskih kvaternionov izboljša numerične lastnosti elementa, saj se pri algoritmih I in M med računom »izgubi« ortogonalnost rotacijskih matrik, medtem ko se to pri kvaternionih ne zgodi. Glede na računsko hitrost sta najugodnejša algoritma T in IQ.

Nadalje smo z linearnimi različicami elementov izvedli dve verziji »patch testa«, glej sliko 2.7, ki so ju uspešno prestali vsi obravnavani elementi, našteti v preglednicah 2.2–2.6. Izvedli smo test lastnih vrednosti in izračunali koeficient pogojenosti, glej slike 2.8–2.10, kjer vsi elementi dajo primerljive rezultate. Manjše razlike, ki se pojavijo, so posledica uporabe prej opisanih izboljšav v posamezni formulaciji. Izvedli smo še dva dodatna linearna testa, kjer pa razlike v odzivu med elementi niso tako očitne kot pri nelinearnih testih, ki smo jih izračunali v nadaljevanju.

V seriji 10 numeričnih primerov, glej poglavje 2.5.4, smo pokazali obnašanje obravnavanih elementov v nelinearni analizi. Elementi MITC4, EAS4 in D-ANS izračunajo primerljive odzive, ki pa so natančni le, če je uporabljena relativno gosta in nepopačena mreža. MITC4+ element se je izkazal kot izredno neobčutljiv na popačenje mreže, hibridni HW in HR pa kot računsko hitri elementi, ki so sposobni izračunati zelo dolge obtežne inkremente. Elementi +HW in +HR, ki smo jih predstavili v tem delu, so uspešno združili vse naštete pozitivne lastnosti, brez da bi ohranili katero izmed negativnih. Lahko zaključimo, da edini izmed uporabljenih elementov izpolnijo vseh pet zahtev, ki jih želimo od »optimalnega« štirivozliščnega elementa.

8.2   Implicitne sheme za časovno integracijo

V nadaljevanju disertacije smo obravnavali implicitne sheme za časovno korakanje v dinamiki konstrukcij. Osredotočili smo se na sheme iz skupin posplošenih α (G-α) metod in metod, ki omogočajo

Lavrenčič, M. 2020. Numerical Procedures for Nonlinear Static and Dynamic Analyses of Shell Systems of Various Sizes.
PhD Th. Ljubljana, UL FGG, Third cycle doctoral study Built Environment.

181

kontrolirano sipanje energije (ED). Iz skupine prvih smo uporabili klasične sheme, kot so HHT [65], BAM [170] in GAM [38], pa tudi novejšo JWH shemo [77]. Razen zadnje za račun vse uporabijo Newmarkove predpostavke, ki so uporabljene tudi v NMD in NTR shemah, glej npr. [27], [97], [96]. V linearni dinamiki so naštete sheme brezpogojno stabilne in (razen NTR) omogočajo disipacijo višjih frekvenc. Opozoriti pa je treba, da se njihove dobre lastnosti ne nujno vedno prenesejo iz linearne v nelinearno dinamiko.

V nelinearni dinamiki je pogoj za stabilnost sheme definiran v smislu energije. Shema je brezpogojno stabilna, če za prosto gibanje znotraj poljubnega časovnega koraka $[t_n, t_{n+1}]$ velja $(V_{n+1} - V_n) + (K_{n+1} - K_n) \leq 0$, kjer sta V in K potencialna in kinetična energija. G-α metode tega pogoja v splošnem ne izpolnjujejo, hkrati pa tudi ne omogočajo ohranjanja gibalne in vrtilne količine. Pri analizi v nelinearni dinamiki se lahko izkaže, da pride pri G-α shemah do nenadzorovanega nihanja energije in posledično tudi odpovedi računa. V disertaciji, poleg že omenjenih G-α metod, obravnavamo tudi shemo EMC, glej [146] in [145], ki je zasnovana tako, da ohranja energijo ter gibalno in vrtilno količino. Ohranjanje fizikalnih lastnosti, kot sta gibalna in vrtilna količina, je zaželena lastnost, obstaja pa kopica problemov, pri katerih je za uspešen izračun odziva potrebna disipacija energije. Take lastnosti izkazujejo ED(MC) sheme, kjer z razširitvijo EMC sheme omogočimo kontrolirano disipacijo energije, pri čemer je izpolnjen pogoj za brezpogojno stabilnost in je, ob upoštevanju določenih pogojev, zagotovljeno tudi ohranjanje gibalne in vrtilne količine.

Enačbo dinamičnega ravnotežja lahko za nelinearno telo, ki je v prostoru diskretizirano s končnimi elementi, zapišemo v obliki diferencialne enačbe drugega reda s pripadajočimi robnimi pogoji

$$\boldsymbol{G}_{\text{dyn}}\big(\boldsymbol{u}(t)\big) = \boldsymbol{F}_{\text{ine}}\big(\boldsymbol{u}(t), \ddot{\boldsymbol{u}}(t)\big) + \boldsymbol{C}\dot{\boldsymbol{u}}(t) + \boldsymbol{F}_{\text{int}}\big(\boldsymbol{u}(t)\big) - \boldsymbol{F}_{\text{ext}}(t) = \boldsymbol{0},$$
$$\boldsymbol{u}(0) = \boldsymbol{u}_0, \qquad \dot{\boldsymbol{u}}(0) = \dot{\boldsymbol{u}}_0.$$

Tu $\boldsymbol{u}$ predstavlja posplošene pomike (pomike in rotacije), $t \in [0, t_f]$ označuje čas znotraj izbranega intervala, nadpisane pike pa označujejo odvod te količine po času. $\boldsymbol{F}_{\text{ine}}$ je vektor vozliščnih inercijskih sil, $\boldsymbol{C}$ je matrika dušenja, $\boldsymbol{F}_{\text{int}}$ in $\boldsymbol{F}_{\text{ext}}$ pa vozliščne notranje in zunanje sile. Do drugačne oblike zapisa pridemo, če zgornji izraz zapišemo v obliki diferencialne enačbe prvega reda

$$\widetilde{\boldsymbol{G}}_{\text{dyn}}\big(\boldsymbol{u}(t), \boldsymbol{v}(t)\big) = \boldsymbol{F}_{\text{ine}}\big(\boldsymbol{u}(t), \dot{\boldsymbol{v}}(t)\big) + \boldsymbol{C}\boldsymbol{v}(t) + \boldsymbol{F}_{\text{int}}\big(\boldsymbol{u}(t)\big) - \boldsymbol{F}_{\text{ext}}(t) = \boldsymbol{0},$$
$$\boldsymbol{v}(t) = \dot{\boldsymbol{u}}(t) \text{ ali } \boldsymbol{v}(t) \overset{\text{šibka enakost}}{\approx} \dot{\boldsymbol{u}}(t),$$
$$\boldsymbol{u}(0) = \boldsymbol{u}_0, \qquad \boldsymbol{v}(0) = \boldsymbol{v}_0.$$

Če kot iztočnico vzamemo diferencialno enačbo drugega reda, lahko izpeljemo mnogo shem za časovno integracijo iz skupine G-α. Te so zasnovane tako, da se ravnotežje izvrednoti v pomožnih časovnih točkah $t_{n+\alpha_m}$ oziroma $t_{n+\alpha_f}$, kjer izvrednotimo inercijske oziroma notranje sile, tako da ravnotežna enačba postane

$$\boldsymbol{F}_{\text{ine}}\big(\boldsymbol{u}_{n+\alpha_m}, \ddot{\boldsymbol{u}}_{n+\alpha_m}\big) + \boldsymbol{F}_{\text{int},n+\alpha_f} - \boldsymbol{F}_{\text{ext}}\big(t_{n+\alpha_f}\big) = \boldsymbol{0}.$$

Pri tem sta α_m in α_f parametra, ki ju določi uporabnik. Notranje sile so v vseh implementiranih shemah izražene z uporabo izraza

$$\boldsymbol{F}_{int,n+\alpha_f} = \mathbb{A}_{e=1}^{n_{el}} \boldsymbol{F}_{int,n+\alpha_f}^e, \qquad \boldsymbol{F}_{int,n+\alpha_f}^e = \int_{V^e} \boldsymbol{B}_{n+\alpha_f}^{e,T} \boldsymbol{S}_{alg}^e dV,$$

kjer $\mathbb{A}$ predstavlja operator, ki sestavi mrežo končnih elementov, n_{el} je število elementov, V^e pa začetni volumen elementa. $\boldsymbol{F}^e_{int,n+\alpha_f}$ je vektor notranjih vozliščnih sil v elementu, $\boldsymbol{B}^e_{n+\alpha_f} = \boldsymbol{B}^e\left(\boldsymbol{u}^e_{n+\alpha_f}\right)$ je matrika, ki poveže variacije deformacij v času $t_{n+\alpha_f}$ z variacijami vozliščnih pomikov, in $\boldsymbol{S}^e_{alg}$ je vektor algoritmičnih napetosti

$$\boldsymbol{S}^e_{alg} = \alpha_{\mathrm{f}}\boldsymbol{S}^e_{n+1} + (1 - \alpha_{\mathrm{f}})\boldsymbol{S}^e_n = \alpha_{\mathrm{f}}\boldsymbol{S}^e(\boldsymbol{u}^e_{n+1}) + (1 - \alpha_{\mathrm{f}})\boldsymbol{S}^e(\boldsymbol{u}^e_n).$$

Zaradi upoštevanja zgornjih izrazov poimenujemo obravnavane sheme tudi modificirane G-α sheme, saj notranje sile niso izračunane neposredno iz pomikov v času $t_{n+\alpha_f}$. G-α sheme pri računu privzamejo Newmarkove predpostavke za hitrosti in pospeške

$$\dot{\boldsymbol{u}}_{n+1} = \frac{\gamma}{\beta\Delta t}(\boldsymbol{u}_{n+1} - \boldsymbol{u}_n) - \frac{\gamma - \beta}{\beta}\dot{\boldsymbol{u}}_n - \frac{\gamma - 2\beta}{2\beta}\Delta t\,\ddot{\boldsymbol{u}}_n,$$

$$\ddot{\boldsymbol{u}}_{n+1} = \frac{1}{\beta\Delta t^2}(\boldsymbol{u}_{n+1} - \boldsymbol{u}_n) - \frac{1}{\beta\Delta t}\dot{\boldsymbol{u}}_n - \frac{1 - 2\beta}{2\beta}\ddot{\boldsymbol{u}}_n,$$

kjer sta γ in β Newmarkova parametra. Te predpostavke so uporabljene tudi v Newmarkovih shemah brez disipacije (NTR) in z disipacijo (NMD). Posebno mesto med shemami zaseda EMC, ki zagotavlja ohranjanje energije ter gibalne in vrtilne količine. Izpeljemo jo lahko tudi kot poseben primer GAM sheme, kjer je $\rho_\infty = 1$.

Diferencialna enačba prvega reda je iztočnica za formiranje sheme JWH, kjer je enakost med hitrostmi $\boldsymbol{v}$ in odvodi pomikov $\dot{\boldsymbol{u}}$ strogo zagotovljena. Newmarkove predpostavke so tu zamenjane s spodnjimi izrazi

$$\dot{\boldsymbol{u}}_{n+1} = \frac{1}{\gamma\Delta t}(\boldsymbol{u}_{n+1} - \boldsymbol{u}_n) + \frac{\gamma - 1}{\gamma}\dot{\boldsymbol{u}}_n,$$

$$\boldsymbol{v}_{n+1} = \frac{\alpha_{\mathrm{m}}}{\alpha_{\mathrm{f}}\gamma\Delta t}(\boldsymbol{u}_{n+1} - \boldsymbol{u}_n) + \frac{\gamma - \alpha_m}{\gamma\alpha_f}\dot{\boldsymbol{u}}_n + \frac{\alpha_f - 1}{\alpha_f}\boldsymbol{v}_n,$$

$$\dot{\boldsymbol{v}}_{n+1} = \frac{\alpha_{\mathrm{m}}}{\alpha_{\mathrm{f}}\gamma^2\Delta t^2}(\boldsymbol{u}_{n+1} - \boldsymbol{u}_n) - \frac{1}{\alpha_f\gamma\Delta t}\boldsymbol{v}_n + \frac{\gamma - 1}{\gamma}\dot{\boldsymbol{v}}_n + \frac{\gamma - \alpha_m}{\gamma^2\alpha_f\Delta t}\dot{\boldsymbol{u}}_n.$$

V preglednici 3.1 smo podali izraze za parametre, ki omogočajo, da zgoraj naštete α sheme izkazujejo optimalno disipacijo in so brezpogojno stabilne. Ob upoštevanju teh izrazov postanejo parametri α_{m}, α_{f}, β in γ medsebojno odvisni ter določeni z izbiro spektralnega radija v neskončnosti, ρ_∞.

Shemo EMC lahko modificiramo, da omogoča kontrolirano disipacijo energije, in tako pridemo do skupine shem, ki sipajo energijo (ED). To storimo z modificiranjem izrazov za hitrosti in notranje sile, kjer členom EMC sheme dodamo disipativne člene, v katerih količino disipacije nadziramo s parametroma α_{ED} in β_{ED}. Implementacija za shemo prvega reda natančnosti ED1 je relativno preprosta in izhaja iz osnovne diferencialne enačbe ravnotežja drugega reda. Implementacija shem, ki omogočajo ohranjanje gibalne in vrtilne količine, pa zahteva za izhodišče diferencialno enačbo prvega reda, kjer je enakost med hitrostmi $\boldsymbol{v}$ in odvodi pomikov $\dot{\boldsymbol{u}}$ zagotovljena v šibki obliki. Shema EDMC1, ki je prvega reda natančnosti, je kljub temu po obliki enaka shemi ED1, pri čemer ohranjanje vrtilne količine zagotovimo tako, da disipativnemu členu pripišemo smer hitrosti $\boldsymbol{v}_{n+1/2}$. Implementacija sheme EDMC2 je nekoliko zahtevnejša, saj so disipativne količine medsebojno povezane z namenom, da se doseže drugi red natančnosti, kot je prikazano v izrazih (3.24)–(3.27), pri čemer je disipacija odvisna le od parametra α_{ED}.

8.2.1   Primerjava v linearnem okolju

Sheme smo v linearnem okolju primerjali na osnovi odziva nedušenega sistema z 1 prostostno stopnjo z maso m in togostjo k, katerega gibanje opiše izraz

$$\ddot{u} + \omega^2 u = 0 \;\; \Leftrightarrow \; \dot{v} + \omega^2 u = 0, \;\; \dot{u} = v,$$

kjer je u pomik, v hitrost in $\omega = \sqrt{k/m}$ naravna frekvenca z nihajnim časom $T = 2\pi/\omega$. Za opis lastnosti shem je največkrat uporabljeno razmerje med časovnim korakom v analizi in nihajnim časom $\Delta t/T$. Naj omenimo, da so tu obravnavane lastnosti neodvisne od sposobnosti sheme, da ohranjanja gibalno in vrtilno količino, zato smo za ED(MC) sheme v tem poglavju poenostavljeno uporabili le oznaki ED1 in ED2.

Numerično rešitev zgoraj navedenega izraza lahko za vsako izmed shem zapišemo v obliki

$$\boldsymbol{X}_{\text{n}+1} = \mathbf{A}\boldsymbol{X}_{\text{n}}, \forall \text{n} \in [0,1,\dots,\text{N}-1],$$

kjer je N število diskretnih časovnih točk, $\mathbf{A}$ amplifikacijska matrika in $\boldsymbol{X}_i$, $i \in [0,1,\dots,\text{N}-1]$ vektor, ki je definiran za skupine shem NG-α = {NTR, NMD, BAM, HHT, GAM, EMC}, JWH in ED = {ED1, ED2} kot

$$\boldsymbol{X}_{\text{i,NG}-\alpha} = \{u_{\text{i}}, \dot{u}_{\text{i}}, \ddot{u}_{\text{i}}\}^{\text{T}}, \boldsymbol{X}_{\text{i,JWH}} = \{u_{\text{i}}, v_{\text{i}}, \dot{u}_{\text{i}}, \dot{v}_{\text{i}}\}^{\text{T}}, \boldsymbol{X}_{\text{i,ED}} = \{u_{\text{i}}, v_{\text{i}}\}^{\text{T}}.$$

Z uporabo izrazov (3.4)–(3.10), (3.11)–(3.14) in (3.19)–(3.27) lahko zapišemo amplifikacijsko matriko za vsako izmed obravnavanih shem. Eksplicitno smo jih podali v izrazih (3.36)–(3.41).

Z analizo amplifikacijske matrike lahko določimo nekatere lastnosti shem v linearni dinamiki. Najprej smo izvedli spektralno analizo posameznih shem, kjer smo spektralni radij izračunali z izrazom

$$\rho = \max(|\lambda_{\text{i}}|),$$

pri čemer je λ_i i-ta lastna vrednost modificirane amplifikacijske matrike $\hat{\mathbf{A}}$, glej izraz (3.34). Shema je v linearni dinamiki brezpogojno stabilna, če velja $\rho \leq 1$ za vse $\Omega = 2\pi\Delta t/T \in [0,\infty)$. Naj omenimo, da od tod izhaja oznaka za spektralni radij v neskončnosti $\rho_\infty = \lim_{\Omega \to \infty} \rho$, ki je za skupino G-$\alpha$ shem parameter, ki ga poda uporabnik in z njim definira količino disipacije. Dobro zasnovana shema bo ohranila nižje, osnovne frekvence, medtem ko bo višje frekvence podušila. Tako želimo, da velja $\rho = 1$ za $\Delta t/T \to 0$ in $\rho < 1$ za $\Delta t/T \to \infty$. Na sliki 3.1 so prikazani poteki spektralnega radija za vse izbrane sheme pri določenih vrednostih parametrov disipacije. Od G-α shem izkazujeta GAM in JWH najboljše spektralne lastnosti, saj je spektralni radij $\rho = 1$ tudi za frekvence v srednjem območju, medtem ko druge sheme pri enakem predpisanem ρ_∞ podušijo tudi srednje frekvence, kar je še posebej opazno pri shemah ED1 in NMD. ED2 shema izkazuje drugačno obnašanje, saj pri njej velja $\rho_\infty = 0$ ne glede na izbran parameter dušenja, ki določi le, kdaj se bo zgodil padec s $\rho = 1$.

S pomočjo lastnih vrednosti amplifikacijske matrike lahko analiziramo tudi algoritmično dušenje $\bar{\bar{\xi}}$ in algoritmično podaljšanje nihajnega časa $(\bar{T} - T)/T$ za posamezno shemo. Rezultati so prikazani na slikah 3.2 in 3.3, kjer je vidno, da se s daljšanjem časovnega koraka Δt poveča tudi napaka v izračunanem nihajnem času. Najugodnejši potek $(\bar{T} - T)/T$ je viden za ED2 shemo, medtem ko so si rezultati za ostale sheme medsebojno zelo podobni. Razvidno je tudi, da imata NMD in ED1 zelo močno dušenje, natančnost prvega reda teh dveh shem pa se izraža v strmem naklonu funkcije $\bar{\bar{\xi}}$ že na samem začetku grafa.

Primerjali smo tudi nagnjenost shem k močni prekoračitvi analitične rešitve. Ta lastnost je bila prvič raziskana v [55], pozneje pa so avtorji v [153] klasificirali algoritme glede na njihovo nagnjenost k močni prekoračitvi rešitve za pomike, hitrosti ali pospeške. Za linearni sistem z $m = 1, T = 1, u_0 = 1$ in $\dot{u}_0 = 0$ smo preverili to nagnjenost tako, da smo primerjali algoritmično izračunane pomike, hitrosti in pospeške z analitičnimi vrednostmi teh količin. Izkazalo se je, da so sheme NMD, GAM, BAM in HHT nagnjene k močni prekoračitvi rešitve za hitrosti. Druge sheme pa ne izkazujejo te neželene lastnosti pri nobeni količini. S slik 3.4–3.6 je razvidno tudi, da je, vsaj v območju $\Delta t/T < 1$, napaka v rešitvi večja, če je izbrano večje dušenje.

V nadaljevanju smo analizirali lokalno in globalno napako, s katero smo ocenili red natančnosti posameznih shem. Napako smo dobili s primerjavo analitične in algoritmične rešitve, pri čemer smo obravnavali sistem z $\omega = 2\pi, T = 1, u_0 = \dot{u}_0 = 1$ in primerjali rešitev pri času $t = 0.4 + \Delta t$. Uporabili smo različne dolžine časovnih korakov in dva različna nivoja numerične disipacije; enega z veliko disipacijo $\alpha_{\text{ED}} = \beta_{\text{ED}} = 0.35$ in $\rho_\infty = 0.5$, enega za pa z majhno disipacijo $\alpha_{\text{ED}} = \beta_{\text{ED}} = 0.02$ in $\rho_\infty = 0.9$. Iz rezultatov na slikah 3.7–3.8 in v preglednici 3.3 je razvidno, da je napaka neodvisna od nivoja disipacije. Vse G-α sheme izkazujejo globalno napako prvega reda za pospeške ter napako drugega reda v pomikih in hitrostih. Shemi ED1 oziroma ED2 pa medtem izkazujeta globalno napako prvega oziroma drugega reda za pomike in hitrosti.

Končno smo primerjali še linearni odziv shem za preprost sistem z eno prostostno stopnjo. Tu smo prikazali, kako so vse prej obravnavane lastnosti vidne v odzivu preprostega sistema. Jasno je razvidna razlika med ED1 in NMD, ki sta prvega reda natančnosti, in vsemi ostalimi shemami, ki so drugega reda natančnosti.

8.2.2 Primerjava v nelinearnem okolju

Prej predstavljene sheme smo implementirali v 5 – parametrični končni element za lupine z velikimi rotacijami, poimenovan kot MITC4 v poglavju 2. Samega postopka implementacije nismo podrobno opisovali. Omeniti je treba le, da shemi EDMC1 in EDMC2, ki omogočata kontrolirano disipacijo energije ter hkrati ohranjanje gibalne in vrtilne količine, zahtevata uporabo končnega elementa z 11 prostostnimi stopnjami (3 pomiki srednje ploskve, 2 zasuka smernika, 3 hitrosti srednje ploskve in 3 kotne hitrosti smernika), medtem ko je za ostale sheme uporabljen osnovni element s 5 prostostnimi stopnjami (3 pomiki srednje ploskve, 2 zasuka smernika).

V prvem obravnavanem primeru smo računali vibriranje S plošče, glej sliko 3.11, pri čemer smo z uporabo energijskega kriterija (3.53) in kriterija posplošenih pomikov (3.54) ocenjevali napako uporabljenih shem v nelinearni dinamiki. Zaključili smo, da je napaka za shemi EMC in EDMC2 tudi v nelinearni dinamiki drugega reda, medtem ko je napaka za G-α sheme med prvim in drugim redom. Sheme NMD, ED1 in EDMC1, ki so v linearni dinamiki prvega reda natančnosti, ohranijo prvi red natančnosti tudi v nelinearni dinamiki.

Nadalje smo obravnavali primer leteče L plošče, glej sliko 3.15. Med prostim letom se plošča močno deformira, pojavi pa se kombinacija membranskih in upogibnih deformacij. Med odzivom smo

spremljali celotno energijo sistema in vpliv izbranega časovnega koraka Δt na njeno spreminjanje. Kot je zaradi izkazanih lastnosti v linearni dinamiki pričakovano, se tudi v nelinearni dinamiki količina disipirane energije pri vseh shemah poveča, če je uporabljen daljši časovni korak. Težave so se med analizo pojavile pri shemah NTR, kjer je račun odpovedal za vse uporabljene Δt, in EDMC2 ter EMC, kjer je račun odpovedal le za daljše Δt. Vse analizirane sheme vsaj približno ohranjajo gibalno količino, ohranjanje vrtilne količine pa je opazno le pri shemah EMC, EDMC1 in EDMC2. Preverili smo tudi vpliv gostote mreže elementov na rezultate, pri čemer se je izkazalo, da so razlike za shemi ED1 in EDMC1 manjše v primerjavi z rezultati za HHT in JWH, glej sliko 3.21.

Zadnji obravnavani primer je bil leteči kratek cilinder, glej sliko 3.22. Tu nas je še posebej zanimalo relativno spreminjanje energije med posameznimi časovnimi koraki, kar smo prikazali na sliki 3.24. Izkazalo se je, da nobena izmed G-α metod ne izpolnjuje pogoja za stabilnost v nelinearni dinamiki. Izpolnijo pa ga sheme NMD, EMC, ED1, EDMC1 in EDMC2. Nadalje smo na osnovi energijskega kriterija ocenili napako posameznih shem, zaključki pa se dobro ujemajo s tistimi za primer S plošče.

8.3 Aplikacija modernih shem za časovno integracijo na hibridnih končnih elementih

Zaradi velike togosti diskretnih enačb za lupinaste končne elemente, pa tudi zaradi želje po ohranjanju fizikalnih lastnosti, kot so celotna energija, gibalna in vrtilna količina, je dolgotrajna dinamična analiza lupinastih konstrukcij zelo težavna. V poglavju 3 smo pokazali, da je za uporabo v nelinearni dinamični analizi smiselno izbrati sheme za časovno integracijo, ki omogočajo disipacijo energije, hkrati pa zagotavljajo ohranjanje drugih fizikalnih količin. Tem merilom ustrezata shemi EDMC1 in EDMC2, ki izpolnjujeta tudi pogoj stabilnosti v nelinearni dinamiki., zato smo se v poglavju 4 osredotočili le nanju.

V poglavju 2 smo našteli lastnosti, ki jih mora izpolniti skoraj optimalen končni element za lupine. Elementi, ki so izpeljani le s pomiki in rotacijami, teh pogojev ne izpolnijo, lahko pa jih izboljšamo z uporabo različnih tehnik. Med mešane elemente, spadajo med drugim tudi ANS, EAS, hibridne HW in HR formulacije, ki smo jih obravnavali v našem delu. Od naštetih so se za najučinkovitejše izkazali hibridni HW ali HR elementi, ki istočasno upoštevajo tudi ANS metodo za prečne strižne in membranske deformacije, poimenovani +HW in +HR.

V poglavju 4 smo predstavili razvoj hibridne formulacije, pri čemer smo optimalne elemente iz poglavja 2 razširili v dinamiko. Medtem ko uporaba ANS in EAS tehnik ne vpliva na izpeljavo dinamične formulacije končnega elementa, zahtevajo HW in HR formulacije precej spremenjen pristop. V našem delu smo zato želeli sistematično izpeljati dve hibridni formulaciji, ki delujeta znotraj okvirov shem EDMC1 in EDMC2. Razvoj smo začeli na preprostem primeru vzmetnega nihala in izraze nato razširili za lupinaste končne elemente.

8.3.1 Formulacija vzmetnega nihala

Pri izpeljavi hibridnih formulacij za preprosto vzmetno nihalo, glej sliko 4.1, lahko izhajamo iz osnovnega funkcionala

$$G(\boldsymbol{q}, \boldsymbol{v}) = \int_{t_0}^{t_e} \left(\dot{\boldsymbol{q}} - \frac{1}{2}\boldsymbol{v}\right) \cdot \boldsymbol{M}\boldsymbol{v} - \left(V_{int}(\epsilon(\boldsymbol{q})) + V_{ext}\right)dt,$$

kjer so $(\boldsymbol{q}, \boldsymbol{v}) \in \mathbb{R}^3 \times \mathbb{R}^3$ prostostne stopnje, ki določajo pozicijo delca z maso m oziroma njegovo hitrost. $\boldsymbol{M}$ predstavlja masno matriko, V_{int} in V_{ext} pa notranjo in zunanjo potencialno energijo.

Hibridne Hu-Washizu formulacije vpeljejo neodvisno napetost in deformacijo σ^{HW} in ϵ^{HW}, s katerima lahko osnovni funkcional razširimo v novo obliko, njegovo šibko obliko pa zapišemo v obliki Euler-Lagrangeevih izrazov

$$\boldsymbol{M}\dot{\boldsymbol{v}} + D\epsilon(\boldsymbol{q})\sigma^{HW} = \boldsymbol{f}_{ext},$$
$$\epsilon(\boldsymbol{q}) = \epsilon^{HW},$$
$$\dot{\boldsymbol{q}} = \boldsymbol{v},$$
$$\sigma^{HW} = DV_{int}(\epsilon^{HW}).$$

V poglavju 4.2.2.1 smo nato s pametno izbiro kinematično dopustnih variacij dokazali ohranjanje energije, gibalne in vrtilne količine za tako formulacijo. Zgornje izraze smo nato zapisali v diskretni obliki

$$\boldsymbol{M}\frac{(\boldsymbol{v}_{n+1} - \boldsymbol{v}_n)}{\Delta t} + D\epsilon(\boldsymbol{q}_{n+1/2})\sigma^{HW^*} = \boldsymbol{f}_{ext,n+1/2},$$
$$\epsilon_{n+1} = \epsilon^{HW}_{n+1},$$
$$\frac{\boldsymbol{q}_{n+1} - \boldsymbol{q}_n}{\Delta t} = \boldsymbol{v}^*,$$
$$\sigma^{HW}_{n+1/2} = DV_{int}(\epsilon^{HW}_{n+1/2}),$$

kjer količini $\boldsymbol{v}^*$ in σ^{HW^*} vsebujeta člene, ki povzročajo disipacijo energije. V poglavju 4.2.2.3 so nato izpeljani še diskretni zakoni ohranjanja gibalne in vrtilne količine ter disipacije energije.

Nadalje smo zapisali še razširjeni Hellinger-Reissnerjev funkcional, pri katerem uvedemo neodvisno napetost σ^{HR}. Njegovo šibko obliko lahko zapišemo v obliki naslednjih Euler-Lagrangeevih izrazov

$$\boldsymbol{M}\dot{\boldsymbol{v}} + D\epsilon(\boldsymbol{q})\sigma^{HR} = \boldsymbol{f}_{ext},$$
$$\dot{\boldsymbol{q}} = \boldsymbol{v},$$
$$C^{-1}\sigma^{HR} = \epsilon(\boldsymbol{q}),$$

kjer je C posplošen materialni parameter. Ohranjanje energije, gibalne in vrtilne količine je za tako formulacijo dokazano v poglavju 4.2.3.1. Temu sledi časovna diskretizacija zgornjih enačb, ki jih zapišemo v obliki

$$\boldsymbol{M}\frac{(\boldsymbol{v}_{n+1} - \boldsymbol{v}_n)}{\Delta t} + D\epsilon(\boldsymbol{q}_{n+1/2})\sigma^{HR^*} = \boldsymbol{f}_{ext,n+1/2},$$
$$\frac{\boldsymbol{q}_{n+1} - \boldsymbol{q}_n}{\Delta t} = \boldsymbol{v}^*,$$
$$C^{-1}\sigma^{HR}_{n+1} = \epsilon_{n+1}.$$

Disipacija je v tem primeru prisotna prek količin $\boldsymbol{v}^*$ in σ^{HR^*}. Izpeljava diskretnih ravnotežnih zakonov ohranjanja gibalne, vrtilne količine in disipacije energije sledi korakom, predstavljenim v poglavju 4.2.3.3.

8.3.2   Formulacija za lupine

Pri izpeljavi hibridnih formulacij za lupine smo najprej izhajali iz funkcionala za formulacijo s posplošenimi pomiki in hitrostmi, ki ga lahko v šibki obliki zapišemo v obliki Euler-Lagrangeevega izraza

$$\int_M \delta\boldsymbol{\Phi} \cdot \boldsymbol{M}_{\rho 0}\dot{\boldsymbol{V}} + \delta\boldsymbol{\epsilon}(\delta\boldsymbol{\Phi}, \boldsymbol{\Phi}) \cdot \boldsymbol{\sigma} dA = -V_{ext}(\delta\boldsymbol{\Phi}),$$

$$\int_M \delta\boldsymbol{V} \cdot (\dot{\boldsymbol{\Phi}} - \boldsymbol{V})dA = 0.$$

Tu sta $\boldsymbol{\Phi}$ in $\boldsymbol{V}$ vektorja posplošenih pomikov in hitrosti, $\boldsymbol{M}_{\rho 0}$ pa masna matrika za lupino, kjer so zajeti tudi vplivi smernika.

Razširjeno hibridno Hu-Washizu formulacijo lahko po zgledu primera vzmetnega nihala zapišemo v Euler-Lagrangeevi obliki kot

$$\int_M \delta\boldsymbol{\Phi} \cdot \boldsymbol{M}_{\rho 0}\dot{\boldsymbol{V}} + \delta\boldsymbol{\epsilon}(\delta\boldsymbol{\Phi}, \boldsymbol{\Phi}) \cdot \boldsymbol{\sigma}^{HW} dA = -V_{ext}(\delta\boldsymbol{\Phi}),$$

$$\int_M \delta\boldsymbol{\sigma}^{HW} \cdot (\boldsymbol{\epsilon}(\boldsymbol{\Phi}) - \boldsymbol{\epsilon}^{HW})dA = 0,$$

$$\int_M \delta\boldsymbol{V} \cdot (\dot{\boldsymbol{\Phi}} - \boldsymbol{V})dA = 0,$$

$$\int_M \delta\boldsymbol{\epsilon}^{HW} \cdot (\boldsymbol{\sigma}^{HW} - DW(\boldsymbol{\epsilon}^{HW})dA = 0.$$

Ravnotežni zakoni so, ob pametni izbiri kinematično dopustnih variacij in drugačnem zapisu nekaterih spremenljivk, izpeljani v poglavju 4.3.2.1, ki mu sledi diskretizacija zgornjih izrazov, ki jih lahko zapišemo kot

$$\int_M \delta\boldsymbol{\Phi} \cdot \boldsymbol{M}_{\rho 0}\frac{\boldsymbol{V}_{n+1} - \boldsymbol{V}_n}{\Delta t} + \delta\boldsymbol{\epsilon}(\delta\boldsymbol{\Phi}, \boldsymbol{\Phi}_{n+1/2}) \cdot \boldsymbol{\sigma}^{HW^*} dA = -V_{ext}(\delta\boldsymbol{\Phi}),$$

$$\int_M \delta\boldsymbol{\sigma}^{HW} \cdot (\boldsymbol{\epsilon}_{n+1} - \boldsymbol{\epsilon}^{HW}_{n+1})dA = 0,$$

$$\int_M \delta\boldsymbol{V} \cdot \left(\frac{\boldsymbol{\Phi}_{n+1} - \boldsymbol{\Phi}_n}{\Delta t} - \boldsymbol{V}^*\right)dA = 0,$$

$$\int_M \delta\boldsymbol{\epsilon}^{HW} \cdot (\boldsymbol{\sigma}^{HW}_{n+1/2} - DW(\boldsymbol{\epsilon}^{HW}_{n+1/2})dA = 0.$$

Kot dokažemo v poglavju 4.3.2.3, tak zapis omogoča kontrolirano disipacijo energije ter hkratno ohranjanje gibalne in vrtilne količine.

Podoben postopek smo ponovili tudi za razširjeni Hellinger-Reissnerjev funkcional, ki ga lahko v Euler-Lagrangeevi obliki zapišemo kot

$$\int_M \delta\boldsymbol{\Phi} \cdot \boldsymbol{M}_{\rho 0}\dot{\boldsymbol{V}} + \delta\boldsymbol{\epsilon}(\delta\boldsymbol{\Phi}, \boldsymbol{\Phi}) \cdot \boldsymbol{\sigma}^{HR} dA = -V_{ext}(\delta\boldsymbol{\Phi}),$$

$$\int_M \delta\boldsymbol{V} \cdot (\dot{\boldsymbol{\Phi}} - \boldsymbol{V})dA = 0,$$

$$\int_M \delta\boldsymbol{\sigma}^{HR} \cdot (\boldsymbol{C}^{-1}\boldsymbol{\sigma}^{HR} - \boldsymbol{\epsilon}(\boldsymbol{\Phi}))dA = 0.$$

Po izpeljavi ravnotežnih zakonov v poglavju 4.3.3.1 zapišemo časovno diskretizirano različico zgornjih izrazov

$$\int_M \delta\boldsymbol{\Phi} \cdot \boldsymbol{M}_{\rho 0} \frac{\boldsymbol{V}_{n+1} - \boldsymbol{V}_n}{\Delta t} + \delta\boldsymbol{\epsilon}\big(\delta\boldsymbol{\Phi}, \boldsymbol{\Phi}_{n+1/2}\big) \cdot \boldsymbol{\sigma}^{HR^*} dA = -V_{ext}(\delta\boldsymbol{\Phi}),$$

$$\int_M \delta\boldsymbol{V} \cdot \left(\frac{\boldsymbol{\Phi}_{n+1} - \boldsymbol{\Phi}_n}{\Delta t} - \boldsymbol{V}^* \right) dA = 0,$$

$$\int_M \delta\boldsymbol{\sigma}^{HR} \cdot (\mathbf{C}^{-1}\boldsymbol{\sigma}^{HR}_{n+1} - \boldsymbol{\epsilon}_{n+1}) dA = 0,$$

za katere v poglavju 4.3.3.3 dokažemo, da zagotavljajo kontrolirano disipacijo energije ter ohranjanje gibalne in vrtilne količine.

Izognemo se podrobnemu opisu implementacije teh formulacij za štirivozliščne končne elemente, saj ta sledi enakim korakom, kot so bili predstavljeni že v poglavju 2. Poleg +HW in +HR končnih elementov, v poglavju 4.4, kjer so predstavljeni trije numerični testi, uporabimo tudi MITC4, MITC4+ in EAS5 formulacije.

Najprej smo ponovili test leteče L plošče iz poglavja 3.6.2. Tu pokažemo, da vse formulacije zagotovijo ohranjanje vrtilne in gibalne količine, glej sliko 4.3. Med njimi se sicer pojavijo razlike v poteku celotne energije, ki pa za EDMC1 shemo v vseh primerih s časom konvergira k enaki vrednosti. Za EDMC2 shemo ta konvergenca ni opazna. Prikazali smo, da so razlike v celotni energiji med formulacijami večje, če je uporabljena manjša disipacija, medtem ko so pri večji disipaciji te razlike manjše, glej sliko 4.2.

Na primeru letečega kratkega cilindra smo pokazali, da so hibridne formulacije +HW in +HR v primerjavi z ostalimi sposobne izračunati občutno daljše obtežne korake, za posamezen korak pa potrebujejo manj iteracij, glej preglednico 4.1. Njihov računski čas je tako nekajkrat krajši, kar smo pri hibridnih formulacijah opazili že v statični analizi. Za EDMC1 shemo se daljši koraki posledično izražajo tudi v večji disipaciji in zamiku v odzivu, ki je viden na sliki 4.7, kjer spremljamo pomik izbrane točke. Za EDMC2 shemo pa ta zamik ni viden.

Nazadnje smo izračunali še modificiran primer Raascheve kljuke, pri čemer smo uporabili tudi pokvarjeno mrežo. S tem smo pokazali, da se z uporabo membranskega ANS odpravi občutljivost na pokvarjeno mrežo. Enako kot smo zaključili za statično analizo, lahko tudi tu ugotovimo, da sta se, od uporabljenih končnih elementov, +HW in +HR izkazala za najrobustnejša in najhitrejša.

8.4   Stabilnostna analiza lupin z uporabo dinamike

V poglavju 5 smo dinamično analizo uporabili za simuliranje različnih stabilnostnih problemov lupinastih konstrukcij. Z izračunanimi primeri smo potrdili nekatere rezultate iz prejšnjih poglavij, med drugim pa smo ugotovili, da je disipacija energije nujna, če želimo uspešno analizirati težke stabilnostne probleme. Za račun smo uporabili sheme BAM, HHT in GAM iz družine posplošenih α metod, ED1 iz družine shem, ki sipajo energijo, EMC, ki ohranja energijo, in NTR ter NMD iz družine Newmarkovih shem. Ker EMC in NTR ne disipirata energije, sta se izkazali za najslabšo izbiro, medtem ko so G-α in ED1 sheme izračunale zelo zadovoljive rezultate.

Omenjene sheme smo implementirali za 6 – parametrični model lupine z raztegljivim smernikom, ki je za statično formulacijo podrobno opisan v poglavju 2.2.3, v poglavju 5.2 pa smo ga razširili za dinamično analizo.

Izračunani numerični primeri so pokazali, da so izbrane implicitne sheme z numerično disipacijo zelo primerne za simulacijo uklona elastičnih lupinastih konstrukcij. Implicitna dinamika konstrukcij lahko izračuna zelo uporabne rešitve, tudi kadar statičnim metodam tega ne uspe. Prednost takega načina računa je tudi v tem, da se ni treba ukvarjati s kritičnimi (limitnimi in bifurkacijskimi) točkami. Omenimo naj, da je pri analizi lupinastih konstrukcij treba imeti v mislih tudi nepopolnosti, ki pa smo jim namenili le krajši del poglavja o uklonu cilindra.

Z izpeljanim elementom smo najprej izračunali dva osnovna statična in dodaten osnovni dinamični test. Tu smo pokazali, da je obnašanje uporabljenega 6 – parametričnega elementa tako pri statični kot dinamični analizi primerljivo z obnašanjem 5 – parametričnega elementa. Od stabilnostnih problemov smo najprej analizirali preskok stožčaste lupine, glej sliko 5.7, ki ji na zgornjem robu vsiljujemo silo ali pomik. V primeru vsiljevanja pomikov je preskok bolj kontroliran, kljub temu pa se takoj po preskoku pojavijo vibracije, ki jih nekatere sheme uspešno podušijo, medtem ko drugim tega ne uspe. NTR odpove, že preden se pojavi končni preskok, EMC pa sicer izračuna odziv tudi po končnem preskoku, a odpove kmalu zatem, saj se v cilindru pojavijo nenaravne vibracije, ki jih shema ne poduši. Rezultate smo primerjali tudi s statično analizo, s katero pa nam ni uspelo izračunati celotnega odziva. Ujemanje med rezultati je sicer do trenutka preskoka zelo dobro, glej sliko 5.7, razlike med izračunanimi uklonskimi silami pa so za različne dinamične sheme minimalne.

Enak primer smo nato porаčunali še z vsiljevanjem sile, kar se je izkazalo za zahtevnejšo nalogo, saj so tudi nekatere G-α sheme odpovedale pred koncem analize. Enako kot za primer vsiljevanja pomika sta najprej odpovedali NTR in EMC shemi, pozneje pa še BAM. V primerjavi z vsiljevanjem pomikov se tu pojavijo občutnejše vibracije, ki so vidne na sliki 5.12, kar je v primeru večine algoritmov zahtevalo uporabo zelo kratkih časovnih korakov. Najmanj težav pa sta s takim načinom obremenitve izkazali shemi ED1 in NMD.

Nadalje smo obravnavali primer preskoka tankega cilindričnega panela, glej sliko 5.16. Rezultate smo ponovno primerjali s statično analizo, pri čemer smo za reševanje uporabili metodo ločne dolžine, s katero pa nam ni uspelo izračunati odziva po preskoku. Obe uporabljeni shemi za časovno korakanje v dinamiki (BAM in GAM) sta medtem brez težav izračunali celoten odziv in podušili vibracije, ki so se pojavile v trenutku preskoka. Temu je sledil račun primera zmečkanja polkrogle, obremenjene z zunanjim pritiskom, kjer smo za račun z dinamiko ponovno uporabili shemi BAM in GAM, statični račun pa smo izvedli z metodo ločne dolžine. Do trenutka, ko se začne mečkanje, je odziv za vse tri analize enak, razlike, ki nastanejo po tej točki, pa so prikazane na sliki 5.20.

Nazadnje smo obravnavali primer osno obremenjenega cilindra, glej sliko 5.21, kjer smo opazovali spreminjanje uklonskih oblik in jih primerjali z eksperimentalnimi rezultati iz [175]. Cilinder smo obremenili z vsiljenim pomikom, za analizo pa smo uporabili sheme BAM, GAM in ED1. Za primer cilindra brez dodanih nepopolnosti vse sheme predvidijo uklonsko silo, ki je občutno večja od eksperimentalno izmerjene. Ujemanje med eksperimentalnimi in numeričnimi rezultati po prvem uklonu

je kljub temu zelo dobro, saj nam je z izbranimi shemami uspelo opisati enake uklonske oblike, kot so se pojavile tudi v eksperimentu. Pri tem smo preverili tudi vpliv hitrosti obremenjevanja in uporabljene disipacije na rezultate, kar smo prikazali na slikah 5.23 in 5.24.

Obravnavali smo tudi nepopoln cilinder, pri čemer smo geometrijske nepopolnosti opisali s skalirano vsoto prvih 18 lastnih oblik. Tak pristop je povzročil, da se je izračunana začetna uklonska sila zelo približala eksperimentalno določeni sili, na sam potek uklonskih oblik v poznejšem območju pa ni zelo vplival.

8.5   Analiza gubanja

Običajen način analize gubanja ukrivljenih tankih površin je uporaba statičnih metod, kot je metoda ločne dolžine, pristopov, kot je dinamična relaksacija, ali pa uporaba eksplicitne dinamične analize. V poglavju 6 tega dela smo predlagali tri učinkovite računske modele za napovedovanje površinskega gubanja v stisnjenih kompozitnih lupinah, ki uporabijo implicitno dinamiko za izračun prehodov med različnimi oblikami gubanja, ki se lahko pojavijo. Za osnovo smo uporabili 5 – oziroma 6 – parametrični model lupine, vpliv substrata pa smo opisali kot delovanje elastične podlage. Analizirali smo več kompozitnih sistemov cilindrov in sfer, pri čemer smo za analizo prvih uporabili integracijske sheme, ki so bile uporabljene tudi za stabilnostno analizo lupin v poglavju 5, medtem ko smo za analizo sfer uporabili le ED1 shemo, ki se je izkazala kot najrobustnejša.

Avtorji v drugih delih so, da so dosegli preskok sistema v smiselno uklonsko obliko, navadno aplicirali neko manjšo perturbacijsko silo ali geometrijsko nepopolnost. Mehko jedro kompozita so običajno modelirali s 3d končnimi elementi, kar v kombinaciji z gosto mrežo zahteva veliko računsko moč. Naši računski modeli so v primerjavi z naštetimi preprostejši, saj ne zahtevajo aplikacije kakršnih koli nepopolnosti ali perturbacijske sile. Hkrati je tudi število končnih elementov v modelu občutno manjše.

Izhajali smo iz del [173] in [174], kjer so avtorji predlagali koeficient

$$C = E_s/E_f \left(R/t_f \right)^{3/2},$$

ki uspešno napove, katera vrsta gubanja se bo pojavila v cilindričnih ali sferičnih kompozitih. Tu podpis s predstavlja substrat, f pa film oziroma lupino. Pri cilindrih so avtorji opazili kritično vrednost koeficienta $C_{crit} \approx 0.88$, pri čemer za sisteme s $C < C_{crit}$ velja, da se pojavijo le osnosimetrične oblike gub, pri ostalih sistemih pa pride do preskoka med osnosimetričnimi in diamantno oblikovanimi gubami. Pri sferičnih sistemih je faktor C povezan z gubanjem tako, da pri manjših vrednostih napove pojav večjih vdolbin, pri večjih vrednostih faktorja pa so te vdolbine vedno manjše in na neki točki preskočijo v vzorec v obliki labirinta.

Najprej smo analizirali štiri primere cilindričnih kompozitov CS1–CS4 z vrednostmi faktorja $C = (0.43; 0.1; 0.01; 3.92)$, podatke za katere smo privzeli iz [173].

Pri analizi cilindra CS1 so vse uporabljene sheme izračunale, da je prva uklonska oblika osnosimetrična. Razen NTR so vse ostale uporabljene sheme tudi napovedale prehod iz osnosimetričnega v diamantni vzorec, a le shemama ED in GAM je uspelo podušiti vibracije, ki se zgodijo ob tem prehodu, kar je vidno na sliki 6.3. ED shemi je uspelo opisati več prehodov med različnimi oblikami gubanja, česar

nobeni drugi shemi ni uspelo. Oblike, ki jih opišejo vse sheme (razen NTR), so si podobne v tem, da je število valov, ki se pojavijo v osni smeri in v smeri obsega, približno enako.

Pri cilindru CS2 lahko na sliki 6.5 opazimo podobne rezultate kot prej, saj je spet le ED shema zaznala več prehodov med uklonskimi oblikami. GAM in EMC sta edini od ostalih shem, ki sta zaznali prehod iz osnosimetričnega vzorca v diamantni vzorec, a le GAM je uspešno podušila vibracije, ki so se pojavile ob tem prehodu.

Za cilinder CS3 tudi GAM ne uspe podušiti vibracij, ED pa tudi v tem primeru zazna več prehodov med uklonskimi oblikami. Za ta in za prejšnje primere smo prikazali tudi graf energije, glej sliko 6.8, kjer je vidno, da se ob vsakem preskoku uklonske oblike potencialna energija zmanjša, kinetična pa hipoma naraste.

Cilinder CS4 ima vrednost faktorja $C = 3.92 > C_{crit}$, zato tu ne pride do spremembe osnosimetrične oblike vzorca, ki vedno nastopi najprej. Preverili smo tudi izračunane uklonske sile in ugotovili dobro ujemanje tako z numeričnimi rezultati avtorjev iz [173] kot z analitično rešitvijo, glej preglednico 6.3.

V nadaljevanju smo analizirali 3 sferične kompozite, pri čemer smo z ustrezno izbiro geometrije in materiala vnaprej želeli zagotoviti, da se bodo pojavili različni tipi gubanja. Za analizo smo uporabili dva modela lupine, pri čemer je prvi, poimenovan RM-5, osnovni 5 – parametrični, pri drugem pa privzamemo kinematično poenostavitev, ki omogoča premik le v smeri radialno glede na lupino. Ta model ima tako le 3 prostostne stopnje, poimenujemo pa ga QKQ-3. Hkrati smo v drugem modelu s povečanjem strižnega modula zagotovili, da so strižne deformacije zanemarljive. Pri računu smo uporabili večje dušenje kot prej za cilindre, saj smo le tako lahko zagotovili bolj kontroliran prehod med oblikami gubanja.

Z obema uporabljenima modeloma smo nato analizirali tri sfere, z vrednostmi parametra $C = (3.5; 21.2; 109.5)$. Rezultati analiz so prikazani na slikah 6.10–6.13, kjer je v vseh primerih razviden prehod s prvotno gladke površine z enakomernimi sferičnimi deformacijami na površino z vdolbinami. V dveh primerih ($C = 21.2$ in $C = 109.5$) 5-parametrični model izračuna nadaljnjo spremembo v vzorcu gubanja s kanali (labirintni vzorec). Iz rezultatov je razvidno tudi, da se s povečanjem faktorja C poveča tudi število gub.

Medtem ko je 5 – parametrični model izračunal spremembo vzorca gubanja iz jamic v labirinte, 3 – parametrični model te spremembe ni bil sposoben opisati. Razlika med modeloma je vidna tudi v nivoju uklonske obtežbe, saj se prve gube pri 3 – parametričnem modelu pojavijo pozneje, pri večjem pritisku. Vseeno se rezultati za oba modela do točke uklona povsem ujemajo, sprememba števila jamic pa je usklajena s spremembo faktorja C.

8.6 Zaključek

V disertaciji smo obravnavali najrazličnejše teme, povezane z lupinastimi konstrukcijami in nelinearno analizo lupin. Na področju mešanih formulacij za štirivozliščne končne elemente za lupine smo najprej opredelili pet točk, ki jih mora izpolnjevati »optimalen« lupinasti končni element. Na osnovi teh meril

smo izbrali ustrezne numerične teste, pri čemer smo izvedli obsežno primerjavo nekaterih obstoječih in tudi novih formulacij. Nobeni od ustaljenih formulacij ne uspe izpolniti vseh meril za »optimalen« element, zato smo združili tehnike, uporabljene v Hu-Washizu elementih iz [159] (in Hellinger-Reissner elementu iz [59]), z ANS interpolacijami za membranske napetosti iz [90]. Tako je nastala skupina novih elementov, ki niso občutljivi na popačenje mreže in omogočajo izračun dolgih obtežnih korakov. Čeprav se na prvi pogled zdi, da je razlika med našimi elementi in izvirnimi formulacijami majhna, učinki, ki so vidni iz rezultatov številnih numeričnih testov, še zdaleč niso majhni in so zelo ugodni.

Menimo, da ima težnja po razvoju »optimalnega« nelinearnega končnega elementa za lupine, ki temelji na klasični teoriji, zelo praktično ozadje. Predstavljeno delo je take mogoče razumeti kot korak k optimalnemu (4 – vozliščnemu) nelinearnemu končnemu elementu za lupine (ki temelji na klasični lupinski teoriji s prečnimi strižnimi učinki). Zaradi nenehnega razvoja novih mešanih formulacij pa lahko gotovo ugotovimo, da se bo v prihodnosti pojavila še učinkovitejša in robustnejša formulacija.

V 3. poglavju smo obravnavali področje strukturne dinamike s poudarkom na implicitnih integracijskih shemah za časovno korakanje, ki so primerne za implementacijo v kombinaciji s končnimi elementi za lupine. Večina obravnavanih shem izhaja iz družin posplošenih α metod in metod, ki sipajo energijo. Izbrane sheme smo najprej primerjali na področju linearne dinamike, kjer smo primerjali njihove lastnosti stabilnosti, disperzije in natančnosti. Poleg tega smo po zgledu iz [80] pogledali tudi nagnjenost k močni prekoračitvi rešitve, kjer smo pokazali, da nobena od obravnavanih shem ne izkazuje takega obnašanja pri pomikih, medtem ko se za hitrost to opazi pri NMD, GAM, BAM in HHT shemah. Pri NTR, EMC, JWH, ED1 in ED2 ni opaziti prekoračitve. Nadalje smo po vzoru iz [182] izračunali tudi lokalno in globalno napako obravnavanih shem. Nato smo njihove lastnosti ponazorili na primeru problema z eno prostostno stopnjo. Vse obravnavane sheme, z izjemo JWH, so dobro znane in v uporabi v številnih raziskovalnih ali komercialnih programih, zato je mogoče naše ugotovitve potrditi v številnih referencah, npr. [4], [38], [65], [170]. Vendar moramo pripomniti, da velika večina referenc obravnava le posamezne izbrane sheme, zato smo si v disertaciji prizadevali za oblikovanje zgoščenega, a še vedno celovitega pregleda nekaterih najpogosteje uporabljenih.

Poleg tega smo navedene sheme implementirali tudi za nelinearne končne elemente za lupine in primerjali njihove lastnosti v nelinearni analizi. Pokazali smo, da se nekatere značilnosti prenesejo iz linearnega v nelinearni režim in da posplošene α sheme ne izpolnjujejo merila stabilnosti za nelinearno dinamiko. Na drugi strani smo obravnavali tudi sheme, ki sipajo energijo in izpolnjujejo merilo stabilnosti, a se pri njih pojavijo druge neugodne lastnosti, ki zadevajo natančnost le prvega reda ED(MC)1 oziroma zahteven postopek implementacije EDMC2. Kolikor nam je znano, shema JWH [80] še ni bila široko uporabljena in analizirana na področju dinamike lupinastih konstrukcij, in upravičeno upamo, da bo naše delo prispevalo k dodatni razlagi njenih lastnosti.

V 4. poglavju smo združili ugodne lastnosti nekaterih mešanih formulacij, ki so se v 2. poglavju izkazale za optimalne, s shemami za časovno integracijo, ki sipajo energijo in ohranjajo gibalno in vrtilno količino ter so se v nelinearni dinamični analizi izkazale za stabilne. Najprej smo na primeru preprostega vzmetnega nihala izpeljali lastnosti razširjenega Hu-Washizujevega in Hellinger-Reissnerjevega funkcionala, ki smo jih nato razširili na dinamiko lupin. Izvedli smo časovno diskretizacijo in za obe novi formulaciji izpeljali diskretne ravnotežne zakone. V poglavju z numeričnimi primeri smo primerjali

rezultate za MITC4, MITC4+, EAS5 in nove +HW in +HR formulacije za dinamiko lupin. Izvedli smo tri teste, pri čemer se je pokazalo, da se ugodne lastnosti teh formulacij lepo prenesejo iz statičnega v dinamični režim. Menimo, da ravno razvoj teh formulacij predstavlja najpomembnejši prispevek našega dela.

Fenomen uklona je po navadi povezan s prvo kritično točko na ravnotežni poti, dobljeno z nelinearno statično analizo. Za številne praktične konstrukcijske lupinaste konstrukcije je uklonska obremenitev (tj. obremenitev na prvi kritični točki) edini potrebni rezultat stabilnostne analize. Šele v zadnjih letih so mehanske nestabilnosti lupinastih konstrukcij začeli izkoriščati kot platforme za doseganje naprednih funkcionalnosti ali izboljšanih fizikalnih lastnosti. Za napredno uporabo lupinastih konstrukcij in sistemov je ključno sistematično poznavanje celotnega postopka uklona. V 5. poglavju smo pokazali, da so za tako nalogo primerne tudi implicitne sheme za časovno korakanje v dinamiki, ki omogočajo nadzorovano sipanje energije, ki izhaja iz višjih frekvenc, in hkrati ohranjajo frekvence v nižjem območju. Uporabljajo se lahko za analizo uklonskih procesov lupinastih konstrukcij in sistemov, vključno s spreminjanjem uklonskega vzorca. Številni v tej nalogi prikazani primeri kažejo, da so lahko implicitne dinamične analize boljše od statičnih analiz, izvedenih z metodo ločne dolžine.

Numerični testi kažejo, da so med uporabljenimi shemami za uklonsko analizo najprimernejše tiste, ki podušijo višje frekvence. Newmarkova trapezna shema (NTR) je zelo netočna in hitro odpove. Rezultati sheme, ki ohranja energijo (EMC), pa so lahko onesnaženi z umetnimi višjimi frekvencami, ki lahko privedejo do odpovedi računa. Najboljše rezultate smo dobili z uporabo shem z nadzorovano, algoritmično disipacijo višjih frekvenc, kot je shema, ki sipa energijo (ED), in posplošena α metoda z disipacijo visokih frekvenc (GAM). Za več računskih primerov, vključno s preskokom sistema in uklonom valja pod osno obremenitvijo, se je izkazalo, da je implicitna dinamična analiza z (visokofrekvenčno) numerično disipacijo bistveno robustnejša in učinkovitejša kot statična analiza.

Gube (tj. izbokline) ukrivljenih sistemov, sestavljenih iz tankega trdega filma in debele mehke podlage, so v zadnjem času pritegnile veliko pozornosti, saj so lahko povezane z različnimi naravnimi ali umetno povzročenimi pojavi. Izkazalo se je, da je numerična stabilnostna analiza ukrivljenih sistemov film-substrat, skupaj z analizo spreminjanja vzorca gub, daleč od trivialne naloge. V 6. poglavju smo pokazali, da se lahko implicitna strukturna dinamika uporablja za proučevanje spreminjanja takih vzorcev. Pokazalo se je, da je mogoče z nekaterimi implicitnimi shemami za časovno korakanje pridobiti dobro kvalitativno oceno vzorcev gubanja ukrivljenih sistemov film-substrat, vključno s prehodi med posameznimi vzorci.

Predlagali smo tri učinkovite računske modele, ki temeljijo na modelih lupin, predstavljenih v 4. in 5. poglavju, mehek substrat pa smo modelirali kot elastično podlago. Najprej smo se osredotočili na osno obremenjene, dvoslojne cilindrične kompozite, nato pa na površinsko gubanje sfer z jedrom, obremenjenih z zunanjim pritiskom. Pri obeh smo pokazali, da lahko namesto klasičnih 3D (statičnih) računskih modelov [78], [173], [174] in [186] uporabimo razmeroma preprost in hiter postopek, ki zagotavlja praktično enake rezultate pri napovedovanju vzorcev. Kar zadeva cilindrične kompozite, uporabljen numerični model napoveduje skoke uklonskih oblik globoko v postkritičnem območju, česar avtorji prej omenjenih študij niso opazili. Seveda lahko te numerične napovedi potrdijo samo eksperimenti. Toda iz podobnosti med rezultati za cilindre s polnilom in rezultati za cilindre brez polnila,

prikazanimi v 5. poglavju, domnevamo, da so prehodi med oblikami, ki jih najdemo z našim računskim modelom, resnični. Za analizo gubanja krogel lahko za oba uporabljena modela ponovno najdemo dobro ujemanje med nastalimi vzorci gub in eksperimentalnimi rezultati. Preprostejši model je sicer slep za preoblikovanje iz vzorca hribov in dolin v vzorec labirinta, vendar se, globalno gledano, rezultati dobro ujemajo z eksperimentalnimi in numeričnimi rezultati, pridobljenimi v [174].

REFERENCES

[1]   Abaqus. 2018. Abaqus Manuals, Dassoult Systems. Providence, RI, USA.

[2]   Andelfinger, U., Ramm, E. 1993. EAS-elements for two-dimensional, three-dimensional, plate and shell structures and their equivalence to HR-elements. Int J Numer Meth Engng 36: 1311-1337. https://doi.org/10.1002/nme.1620360805

[3]   Armero, F., Petocz, E. 1998. Formulation and analysis of conserving algorithms for frictionless dynamic contact/impact problems. Comput. Methods Appl. Mech. Engrg. 158: 269-300. https://doi.org/10.1016/S0045-7825(97)00256-9

[4]   Armero, F., Romero, I. 2001. On the formulation of high-frequency dissipative time-stepping algorithms for nonlinear dynamics. Part I: low-order methods for two model problems and nonlinear elastodynamics. Comput. Methods Appl. Mech. Engrg. 190: 2603-2649. https://doi.org/10.1016/S0045-7825(00)00256-5

[5]   Armero, F., Romero, I. 2001. On the formulation of high-frequency dissipative time-stepping algorithms for nonlinear dynamics. Part II: second-order methods. Comput. Methods Appl. Mech. Engrg. 190: 6783-6824. https://doi.org/10.1016/S0045-7825(01)00233-X

[6]   Bathe, K.J. 2014. Finite Element Procedures Second Edition. Watertown, Massachusetts, (selfpublished by Bathe, K.J.).

[7]   Bathe, K.J., Baig, M.M.I. 2005. On a composite implicit time integration procedure for nonlinear dynamics. Computers and Structures 83: 2513–24. https://doi.org/10.1016/j.compstruc.2005.08.001

[8]   Bathe, K.J., Iosilevich, A., Chapelle, D. 2000. An evaluation of the MITC shell elements. Computers and structures 75: 1-30. https://doi.org/10.1016/S0045-7949(99)00214-X

[9]   Baumann, M., Schweizerhof, K., Andrussow, S. 1994. An efficient mixed hybrid 4-node shell element with assumed stresses for membrane, bending and shear parts. Engineering Computations 11, 1: 69–80. https://doi.org/10.1108/02644409410799164

[10]   Bazzi, G., Anderheggen, E. 1982. The ρ-family of algorithms for time-step integration with improved numerical dissipation. Earthquake Eng. Struct. Dynam. 10: 537-550.

[11]   Belytschko, T., Schoeberle, D.F. 1975. On the unconditional stability of an implicit algorithm for nonlinear structural dynamics. J. Appl. Mech. 42: 865-869.

[12]   Betsch, P., Gruttmann, F., Stein, E. 1996 A 4-node finite shell element for the implementation of general hyperelastic 3D-elsticity at finite strains. Comput. Methods Appl. Mech. Engrg. 130, 1-2: 57-79. https://doi.org/10.1016/0045-7825(95)00920-5

[13]   Betsch, P., Janz, A. 2016. An energy-momentum consistent method for transient simulations with mixed finite elements developed in the framework of geometrically exact shells. Int. J. Numer. Meth. Engng. 108: 423-455.

[14]   Betsch, P., Menzel, A., Stein, E. 1998. On the parametrization of finite rotations in computational mechanics. A classification of concepts with application to smooth shells. Comput. Methods Appl. Mech. Engrg. 155: 273-305. https://doi.org/10.1016/S0045-7825(97)00158-8

[15]   Betsch, P., Stein, E. 1995. An assumed strain approach avoiding artificial thickness straining for a nonlinear 4-node shell element. Communications in Numerical Methods in Engineering 11: 899-909. https://doi.org/10.1002/cnm.1640111104

[16]   Betsch, P., Steinmann, P. 2000. Inherently energy conserving time finite elements for classical mechanics. J. Comput. Phys. 160: 88-116.

[17]   Bischoff, M., Ramm, E. 1997. Shear deformable shell elements for large strains and rotations. Int J Numer Meth Engng 40, 23: 4427-4449. https://doi.org/10.1002/(SICI)1097-0207(19971215)40:23<4427::AID-NME268>3.0.CO;2-9

[18]   Botasso, C.L., Bauchau, A.A., Choi, J.Y. 2002. An energy-decaying scheme for nonlinear dynamics of shells. Comput. Methods Appl. Mech. Engrg. 191: 3099-3121.

[19]   Brank B, Korelc J, Ibrahimbegovic A (2002) Nonlinear shell problem formulation accounting for through-the-thickness stretching and its finite element implementation. Computers and Structures 80(9-10):699-717. https://doi.org/10.1016/S0045-7949(02)00042-1

[20]   Brank, B. 2002. An energy conserving non-linear dynamic finite element formulation for flexible composite laminates. Computers and Structures 80: 677-689.

[21]   Brank, B. 2005. Nonlinear shell models with seven kinematic parameters. Comput. Methods Appl. Mech. Engrg. 194, 21-24: 2336-2362.

[22]   Brank, B., 2008. Assessment of 4-node EAS-ANS shell elements for large deformation analysis. Comput. Mech. 42: 39-51. https://doi.org/10.1007/s00466-007-0233-3

[23]   Brank, B., Briseghella, L., Tonello, N., Damjanić, F.B. 1998. On nonlinear dynamics of shells: Implementation of energy-momentum conserving algorithm for a finite rotation shell model. Int J Numer Meth Engng 42, 3: 409-442. https://doi.org/10.1002/(SICI)1097-0207(19980615)42:3<409::AID-NME363>3.0.CO;2-B

[24]   Brank, B., Damjanić, F.B., Perić, D. 1995. On implementation of a nonlinear four node shell finite element for thin multilayered elastic shells. Comput Mech 16, 5: 341-359.

[25]   Brank, B., Ibrahimbegovic, A. 2001. On the relation between different parametrizations of finite rotations for shells. Engineering Computations 18: 950-973. https://doi.org/10.1108/02644400110403984

[26]   Brank, B., Korelc, J., Ibrahimbegovic, A. 2003. Dynamics and time-stepping schemes for elastic shells undergoing finite rotations. Computers and Structures 81, 12: 1193–1210. https://doi.org/10.1016/S0045-7949(03)00036-1

[27]   Brank, B., Mamouri, S., Ibrahimbegovic, A. 2005. Constrained finite rotations in dynamics of shells and Newmark implicit time-stepping schemes. Engineering Computations 22, 5-6: 505-535. https://doi.org/10.1108/02644400510602998

[28]   Brank, B., Perić, D., Damjanić, F.B. 1997. On large deformations of thin elasto-plastic shells: Implementation of a finite rotation model for quadrilateral shell element. Int J Numer Meth Engng 40: 689-726. https://doi.org/10.1002/(SICI)1097-0207(19970228)40:4<689::AID-NME85>3.0.CO;2-7

[29]   Breid, D., Crosby, A.J. 2013. Curvature-controlled wrinkle morphologies. Soft Matter 9, 13: 3624-3630.

[30]   Brojan, M., Terwagne, D., Lagrange, R., Reis, P.M. 2015. Wrinkling crystallography on spherical surfaces. Proceedings of the National Academy of Sciences of the United States of America 112, 1: 14-19. https://doi.org/10.1073/pnas.1411559112

[31]   Budday, S., Andres, S., Walter, B., Steinmann, P., Kuhl, E. 2017. Wrinkling instabilities in soft bilayered systems. Phil. Trans. R. Soc. A 375: 20160163. http://dx.doi.org/10.1098/rsta.2016.0163

[32]   Cao, G., Chen, X., Li, C., Ji, A., Cao, Z. 2008. Self-Assembled Triangular and Labyrinth Buckling Patterns of Thin Films on Spherical Substrates. Phys. Rev. Lett. 100, 3: 036102(4).

[33]   Cao, Y.P., Li, B., Feng, X.Q. 2012. Surface wrinkling and folding of core-shell soft cylinders. Soft Matter 8: 556-562. https://doi.org/10.1039/C1SM06354E

[34]   César de Sá, J.M.A., Natal Jorge, R.M., Fontes Valente, R.A., Almeida Areias, P.M. 2002. Development of shear locking-free shell elements using an enhanced assumed strain formulation. Int. J. Numer. Meth. Engng. 53, 7: 1721–1750. https://doi.org/10.1002/nme.360

[35]   Chan, E.P., Smith, E.J., Hayward, R.C., Crosby, A.J. 2008. Surface Wrinkles for Smart Adhesion. Advanced Materials 20: 711–716.

[36]   Choi, C.K., Paik, J.G. 1996. An effective four node degenerated shell element for geometrically nonlinear analysis. Thin-Walled Structures 24, 3: 261–283. https://doi.org/10.1016/0263-8231(95)00037-2

[37]   Chróścielewski, J., Witkowski, W. 2018. Time-Stepping Algorithms in Nonlinear Resultant Shell Dynamics. In: Altenbach, H. (ed.), Öchsner, A. (ed.). Encyclopedia of Continuum Mechanics. Heidelberg, Berlin, Springer.

[38]   Chung, J., Hulbert, G.M. 1993. A time integration algorithm for structural dynamics with improved numerical dissipation – the generalized-alpha method. Journal of Applied Mechanics-Transactions of the Asme 60, 2: 371-375. https://doi.org/10.1115/1.2900803

[39]   Chung, J.Y., Youngblood, J.P., Stafford, C.M. 2007. Anisotropic wetting on tunable micro-wrinkled surfaces. Soft Matter 3: 1163-1169.

[40]   Combescure, A. 1986. Static and dynamic buckling of large thin shells – Design procedure, computation tools, physical understanding of the mechanisms, Nuclear Engineering and Design 92, 3: 339-354

[41]   Crisfield, M.A. 1991. Non-linear Finite Element Analysis of Solids and Structures, Vol. 1: Essentials. Chichester, John Wiley & Sons.

[42]   Crisfield, M.A., 1996. Non-linear finite element analysis of solids and structures, Volume 2: Advanced topics. Chichester, John Wiley & Sons.

[43]   Crisfield, M.A., Jelenic, G., Mi, Y., Zhong, H.G., Fan, Z. 1997. Some aspects of the non-linear finite element method. Finite elements in analysis and design 27: 19-40.
https://doi.org/10.1016/S0168-874X(97)00004-8

[44]   Crisfield, M.A., Peng, X. 1996. Instabilities induced by coarse meshes for a nonlinear shell problem. Engineering Computations 13, 6: 110-114.

[45]   Daszkiewicz, K., Witkowski, W., Burzyński, S., Chróścielewski, J. 2019. Robust four-node elements based on Hu–Washizu principle for nonlinear analysis of Cosserat shells. Continuum Mech. Thermodyn 31, 6: 1757. https://doi.org/10.1007/s00161-019-00767-1

[46]   Djermane, M., Zaoui, D., Labbaci, B., Hammadi, F. 2014. Dynamic buckling of steel tanks under seismic excitation: Numerical evaluation of code provisions. Engineering Structures 70: 181–196.

[47]   Dujc, J., Brank, B. 2012. Stress resultant plasticity for shells revisited. Comput. Methods Appl. Mech. Engrg. 247: 146-165. https://doi.org/10.1016/j.cma.2012.07.012

[48]   Dvorkin, E.N., Bathe, K.J. 1984. A continuum mechanics based four-node shell element for general nonlinear analysis. Engineering Computations 1, 1: 77-88. https://doi.org/10.1108/eb023562

[49]   Erlicher, S., Bonaventura, L., Bursi, O.S. 2002. The analysis of the Generalized-α method for nonlinear dynamic problems. Comput Mech 28: 83-104.

[50]   Gebhardt, C.G., Rolfes, R. 2017. On the nonlinear dynamics of shell structures: Combining a mixed finite element formulation and a robust integration scheme. Thin-Walled Structures 118: 56–72.
https://doi.org/10.1016/j.tws.2017.05.001

[51]   Gebhardt, C.G., Romero, I., Rolfes, R. 2020. A new conservative/dissipative time integration scheme for nonlinear mechanical systems. Comput Mech 65: 405–427.

[52]   Gee, M., Ramm, E., Wall, W.A. 2005. Parallel multilevel solution of nonlinear shell structures. Comput. Methods Appl. Mech. Engrg. 194: 2513–2533.
https://doi.org/10.1016/j.cma.2004.07.043

[53]   Gonzalez, O. 2000. Exact energy and momentum conserving algorithms for general models in nonlinear elasticity. Comput. Methods Appl. Mech. Eng. 190: 1763-1783.
https://doi.org/10.1016/S0045-7825(00)00189-4

[54]   Goto, Y., Watanabe, Y., Kasugai, T., Obata, M. 1992. Elastic buckling phenomenon applicable to deployable rings. Int. J. Solids Struct. 29, 7: 893-909. https://doi.org/10.1016/0020-7683(92)90024-N

[55]   Goudreau, G.L., Taylor, R.L. 1972. Evaluation of numerical integration methods in elastodynamics. Comput. Methods Appl. Mech. Engrg. 2: 69-97.

[56]   Graham, E., Jelenić, G. 2003. A general framework for conservative single-step time-integration schemes with higher-order accuracy for a central-force system. Comput. Methods Appl. Mech. Eng. 192: 3585–3618.

[57]   Greco, L., Cuomo, M., Contrafatto, L. 2018. A reconstructed local B formulation for isogeometric Kirchhoff-Love shells. Comput. Methods Appl. Mech. Engrg. 332: 462-487. https://doi.org/10.1016/j.cma.2018.01.005

[58]   Groh, R.M.J., Avitabile, D., Pirrera, A. 2018. Generalised path-following for well-behaved nonlinear structures. Comput. Methods Appl. Mech. Engrg. 331: 394–426.

[59]   Gruttmann, F., Wagner, W. 2005. A linear quadrilateral shell element with fast stiffness computation. Comp. Methods Appl. Mech. Engrg. 194: 4279-4300. https://doi.org/10.1016/j.cma.2004.11.005

[60]   Gruttmann, F., Wagner, W. 2006. Structural analysis of composite laminates using a mixed hybrid shell element. Comput Mech 37: 479–497. https://doi.org/10.1007/s00466-005-0730-1

[61]   Hao, P., Wang, B., Li, G., Meng, Z. 2015. Hybrid framework for reliability-based design optimization of imperfect stiffened shells. AIAA Journal 53, 10: 2878-2889.

[62]   Hao, P., Wang, B., Tian, K., Du, K., Zhang, X. 2015. Influence of imperfection distributions for cylindrical stiffened shells with weld lands. Thin-Walled Structures 93: 177-187.

[63]   Hetenyi, M. 1946. Beams on Elastic Foundations. Michigan, Ann Arbor, University of Michigan Press.

[64]   Hilber, H.M., Hughes, T.J.R. 1978. Collocation, dissipation and "overshoot" for time integration schemes in structural dynamics. Earthquake Eng. Struct. Dynam. 6: 99-117. https://doi.org/10.1002/eqe.4290060111

[65]   Hilber, H.M., Hughes, T.J.R., Taylor, R.L. 1977. Improved numerical dissipation for time integration algorithms in structural dynamics. Earthquake Eng. Struct. Dynam. 5, 3: 283-292. https://doi.org/10.1002/eqe.4290050306

[66]   Hilburger, M.W., Waas, A.M., Starnes Jr., J.H. 1997. Modeling the dynamics response and establishing post-buckling/post snap-thru equilibrium of discrete structures via a transient analysis. Journal of Applied Mechanics 64, 3: 590-595. https://doi.org/10.1115/1.2788933

[67]   Huges, T.J.R. 2000. The finite element method. Linear static and dynamic finite element analysis, Mineola, New York: Dover Publications.

[68]   Hughes, T.J.R., Caughey, T.K., Liw, W.K. 1978. Finite-element methods for nonlinear elastodynamics which conserve energy. J. Appl. Mech. Trans. ASME 45: 366-370.

[69]   Hulbert, G.M. 2017. Computational Structural Dynamics. In: Stein, E. (ed.), de Borst, R. (ed.), Hughes T.J.R., (ed.). Encyclopedia of Computational Mechanics Second Edition, Part 1. Solids and Structures. John Wiley & Sons, Ltd. https://doi.org/10.1002/9781119176817.ecm2028

[70]   Hulbert, G.M., Hughes, T.J.R. 1987. An error analysis of truncated starting conditions in step-by-step time integration: consequences for structural dynamics. Earthquake Eng. Struct. Dynam. 15, 7: 901–910. https://doi.org/10.1002/eqe.4290150710

[71]   Ibrahimbegovic, A 1997. On the choice of finite rotation parameters. Comput. Methods Appl. Mech. Eng. 149, 1–4: 49–71 https://doi.org/10.1016/S0045-7825(97)00059-5

[72]   Ibrahimbegovic, A. 1994. Stress Resultant Geometrically Nonlinear Shell Theory With Drilling Rotations. Part I: A Consistent Formulation. Comput. Methods Appl. Mech. Engrg. 118: 265-284.

[73]   Ibrahimbegovic, A., 2009. Nonlinear Solid Mechanics. Dordrecht, Springer Netherlands.

[74]   Ibrahimbegovic, A., Brank, B., Courtois, P. 2001. Stress resultant geometrically exact form of classical shell model and vector-like parameterization of constrained finite rotations. Int J Numer Meth Engng 52, 11: 1235-1252. https://doi.org/10.1002/nme.247

[75]   Ibrahimbegovic, A., Frey, F. 1994. Stress Resultant Geometrically Nonlinear Shell Theory With Drilling Rotations. Part II: Computational Aspects. Comput. Methods Appl. Mech. Engrg. 118: 285-308.

[76]   Iwicki, P., Tejchman, J., Chróścielewski, J. 2014. Dynamic FE simulations of buckling process in thin-walled cylindrical metal silos. Thin-Walled Structures 84: 344–359. https://doi.org/10.1016/j.tws.2014.07.011

[77]   Jansen, K.E., Whiting C.H., Hulbert, G.M. 2000. A generalized-a method for integrating filtered Navier-Stokes equations with a stabilized finite element method. Comput. Methods Appl. Mech. Eng. 190: 305–19. https://doi.org/10.1016/S0045-7825(00)00203-6

[78]   Jia, F., Li, B., Cao, Y.P., Xie, W.H., Feng X.Q. 2015. Wrinkling pattern evolution of cylindrical biological tissues with differential growth. Physical Review E 91: 012403-1-8.

[79]   Kadapa, C. 2019. Novel quadratic Bézier triangular and tetrahedral elements using existing mesh generators: Applications to linear nearly incompressible elastostatics and implicit and explicit elastodynamics. Int J Numer Meth Engng 117: 543-573. https://doi.org/10.1002/nme.5967

[80]   Kadapa, C., Dettmer, W.G., Perić, D. 2017. On the advantages of using the first-order generalised-alpha scheme for structural dynamic problems. Computers and Structures 193: 226-238. https://doi.org/10.1016/j.compstruc.2017.08.013

[81]   Kaiping,Y. 2008. A new family of generalized-α time integration algorithms without overshoot for structural dynamics. Earthquake Eng. Struct. Dynam. 37: 1389–1409.

[82]   Karam, G.N., Gibson, L.J. 1995. Elastic buckling of cylindrical shells with elastic cores – I Analysis. Int. J. Solids Struct. 32: 1259–1283.

[83]   Karman, T., Tsien, H.S. 1941. The buckling of thin cylindrical shells under axial compression. Journal of the Aeronautical Sciences 8, 8: 303-312.

[84]   Kirchhoff, G.R. 1850. Über das Gleichgewicht und die Bewegung einer elastischen Scheibe. Crelles Journal für die reine und angewandte Mathematik: 40, 51–88.

[85]   Klinkel, S., Gruttmann, F., Wagner, W. 2007. A mixed shell formulation accounting for thickness strains and finite strain 3d material models. Int. J. Numer. Meth. Engng. 74: 945–970. https://doi.org/10.1002/nme.2199

[86]   Knight, N.F. 1997. Raasch Challenge for Shell Elements. AIAA Journal 35, 2: 375-381. https://doi.org/10.2514/2.104

[87]   Ko, Y., Lee, P.S., Bathe, K.J. 2016. The MITC4+ shell element and its performance. Computers and Structures 169: 57-68. https://doi.org/10.1016/j.compstruc.2016.03.002

[88]   Ko, Y., Lee, P.S., Bathe, K.J. 2017. A new 4-node MITC element for analysis of two-dimensional solids and its formulation in a shell element. Computers and Structures 192: 34–49. https://doi.org/10.1016/j.compstruc.2017.07.003

[89]   Ko, Y., Lee, P.S., Bathe, K.J. 2017. A new MITC4+ shell element. Computers and Structures 182: 404-418. https://doi.org/10.1016/j.compstruc.2016.11.004

[90]   Ko, Y., Lee, P.S., Bathe, K.J. 2017. The MITC4+ shell element in geometric nonlinear analysis. Computers and Structures 185: 1-14. https://doi.org/10.1016/j.compstruc.2017.01.015

[91]   Ko, Y., Lee, Y., Lee, P.S., Bathe, K.J. 2017. Performance of the MITC3+ and MITC4+ shell elements in widely-used benchmark problems. Computers and Structures 193: 187-206. https://doi.org/10.1016/j.compstruc.2017.08.003

[92]   Kobayashi, T., Mihara, Y., Fujii, F. 2012. Path-tracing analysis for post-buckling process of elastic cylindrical shells under axial compression. Thin-walled structures 61: 180-187. https://doi.org/10.1016/j.tws.2012.05.018

[93]   Korelc, J. 2010 Direct computation of critical points based on Crouts elimination and diagonal subset test function. Computers and Structures 88, 3-4: 189–197. https://doi.org/10.1016/j.compstruc.2009.10.001

[94]   Korelc, J. 2020. AceGen manual, AceFEM manual. Available at http://symech.fgg.uni-lj.si/

[95]   Korelc, J., Wriggers, P. 2016. Automation of Finite Element Methods. Switzerland, Springer International Publishing.

[96]   Kuhl, D., Crisfield, M.A. 1999. Energy-conserving and decaying algorithms in nonlinear structural dynamics. Int J Numer Meth Engng 45, 5: 569-599. https://doi.org/10.1002/(SICI)1097-0207(19990620)45:5<569::AID-NME595>3.0.CO;2-A

[97]   Kuhl, D., Ramm, E. 1999. Generalized energy–momentum method for nonlinear adaptive shell dynamics. Comput. Methods Appl. Mech. Engrg. 178: 343-366. https://doi.org/10.1016/S0045-7825(99)00024-9

[98]   Kulikov, G.M., Plotnikova, S.V. 2010. A family of ANS four-node exact geometry shell elements in general convected curvilinear coordinates. Int J Numer Meth Engng 83, 10: 1376–1406. https://doi.org/10.1002/nme.2872

[99]   Lacoma, L.M., Romero, I. 2007. Error estimation for the HHT method in non-linear solid dynamics. Computers and Structures 85: 158–169.

[100]   Lagrange, R., Jimenez, F.L., Terwagne, D., Brojan, M., Reis, P.M. 2016. From wrinkling to global buckling of a ring on a curved substrate. Journal of the Mechanics and Physics of Solids 89: 77-95.

[101]   Lavrenčič, M. 2018. Complete animations of buckling processes http://fgg-web.fgg.uni-lj.si/~/mlavrenc/ (Accessed 10. 6. 2020)

[102]   Lavrenčič, M., Brank, B. 2018. Simulation of Shell Buckling by Implicit Dynamics and Numerically Dissipative Schemes. Thin-walled structures 132: 682-699. https://doi.org/10.1016/j.tws.2018.08.010

[103]   Lavrenčič, M., Brank, B. 2019. Hybrid-Mixed Shell Finite Elements and Implicit Dynamic Schemes for Shell Post-buckling. In: Altenbach, H. (ed.), Chróścielewski, J. (ed.), Eremeyev, V.A. (ed.), Wiśniewski, K. (ed.) Recent Developments in the Theory of Shells, Springer: 383–412 p.

[104]   Lavrenčič, M., Brank, B. 2020 Hybrid-mixed shell quadrilateral that allows for large solution steps and is low-sensitive to mesh distortion. Comput. Mech. 65: 177-192. https://doi.org/10.1007/s00466-019-01759-3

[105]   Lavrenčič, M., Brank, B. 2020. Comparison of numerically dissipative schemes for structural dynamics: generalized-alpha versus energy-decaying methods. Thin-walled structures 157: 107075. https://doi.org/10.1016/j.tws.2020.107075

[106]   Lavrenčič, M., Brank, B. 2020. Energy-decaying momentum-conserving schemes for dynamics of hybrid-mixed shell quadrilaterals. In editorial process.

[107]   Lavrenčič, M., Brank, B. 2020. Mixed low-order finite elements for geometrically exact shell models: overview and comparison. In editorial process.

[108]   Lavrenčič, M., Brank, B., Brojan, M. 2020. Multiple wrinkling mode transitions in axially compressed cylindrical shell-substrate in dynamics. Thin-Walled Structures 150: 106700. https://doi.org/10.1016/j.tws.2020.106700

[109]   Lee, P.S., Bathe, K.J. 2002. On the asymptotic behavior of shell structures and the evaluation in finite element solutions. Computers and Structures 80: 235-255. https://doi.org/10.1016/s0045-7949(02)00009-3

[110]   Li, B., Cao, Y.P., Feng, X.Q., Gao, H. 2011. Surface wrinkling of mucosa induced by volumetric growth: Theory, simulation and experiment. Journal of the Mechanics and Physics of Solids 59: 758-774.

[111]   Li, B., Fei, J., Cao, J.P., Feng, X.Q., Gao. H. 2011. Surface Wrinkling Patterns on a Core-Shell Soft Sphere. Phys. Rev. Lett. 106, 23: 234301(4). https://doi.org/10.1103/PhysRevLett.106.234301

[112]   Love, A.E.H. 1906. A Treatise on the Mathematical Theory of Elasticity (2nd ed.). Cambridge, University Press.

[113]   Macneal, R.H., Harder, R.L. 1985. A proposed standard set of problems to test finite element accuracy. Finite Elements in Analysis and Design 1, 1: 3–20. https://doi.org/10.1016/0168-874X(85)90003-4

[114]   Magisano, D., Leonetti, L., Garcea, G. 2017. Advantages of the mixed format in geometrically nonlinear analysis of beams and shells using solid finite elements. Int. J. Numer. Meth. Engng. 109: 1237–1262. https://doi.org/10.1002/nme.5322

[115]   Mäkinen, J. 2008. Rotation manifold SO(3) and its tangential vectors. Comput Mech 42, 6: 907–919. https://doi.org/10.1007/s00466-008-0293-z

[116]   Mamouri, S., Mourid, E., Ibrahimbegovic, A. 2015. Study of geometric nonlinear instability of 2D frame structures. European Journal of Computational Mechanics 24, 6: 256-278.

[117]   Mindlin, R.D. 1951. Influence of rotatory inertia and shear on flexural motions of isotropic elastic plates. Journal of Applied Mechanics Transactions of the ASME 18: 31–38.

[118]   Newmark, N.M. 1972. Method of computation for structural dynamics. Pressure Vessels Piping Design Anal 2: 1235-1264.

[119]   Nguyen, C.U., Ibrahimbegovic, A. 2020. Visco-plasticity stress-based solid dynamics formulation and time-stepping algorithms for stiff case. International Journal of Solids and Structures 196-197: 154-170. https://doi.org/10.1016/j.ijsolstr.2020.04.018

[120]   Noh, G., Bathe, K.J. 2019. For direct time integrations: A comparison of the Newmark and $\rho\infty$-Bathe schemes. Computers and Structures 225: 106079. https://doi.org/10.1016/j.compstruc.2019.05.015

[121]   Noh, G., Ham, S., Bathe, K.J. 2013. Performance of an implicit time integration scheme in the analysis of wave propagations. Computers and Structures 123: 93–105.

[122]   Oesterle, B., Sachse, R., Ramm, E., Bischoff, M. 2017. Hierarchic isogeometric large rotation shell elements including linearized transverse shear parametrization. Comput. Methods Appl. Mech. Engrg. 321: 383-405. https://doi.org/10.1016/j.cma.2017.03.031

[123]   Ota, N.S.N., Wilson, L., Neto, G.A., Pellegrino, S., Pimenta, P.M. 2016. Nonlinear dynamic analysis of creased shells. Finite Elements in Analysis and Design 121: 64–74. https://doi.org/10.1016/j.finel.2016.07.008

[124]   Patricio, P., Teixeira, P.I.C., Trindade, A.C., Godinho, M.H. 2014. Longitudinal versus polar wrinkling of core-shell fibers with anisotropic size mismatches. Physical Review E 89, 1: 012403(1-7).

[125]   Pian, T.H.H. 1964. Derivation of element stiffness matrices by assumed stress distributions. AIAA J. 2: 1333–1336. https://doi.org/10.2514/3.2546

[126]   Pian, T.H.H., Sumihara, K. 1984. Rational approach for assumed stress finite elements. Int. J. Numer. Meth. Engng. 20, 9: 1685-1695. https://doi.org/10.1002/nme.1620200911

[127]   Polat, C. 2010. A Parametric Study for Four Node Bilinear EAS Shell Elements. Journal of Mechanics 26, 04: 431–438. https://doi.org/10.1017/S1727719100004639

[128]   Ramm, E., Wall, W. A. 2004. Shell structures – a sensitive interrelation between physics and numerics. Int. J. Numer. Meth. Engng. 60: 381-427.

[129]   Reissner, E. 1944. On the theory of bending of elastic plates. Journal of Mathematics and Physics 23: 184–191.

[130]   Romero, I. 2012. An analysis of the stress formula for energy-momentum methods in nonlinear elastodynamics. Comput Mech 50: 603-610. https://doi.org/10.1007/s00466-012-0693-y

[131]   Romero, I. 2016. High Frequency Dissipative Integration Schemes for Linear and Nonlinear Elastodynamics. In: Betsch, P. (ed.). Structure-preserving Integrators in Nonlinear Structural Dynamics and Flexible Multibody Dynamics. Switzerland, Springer Nature: 1-31 p.

[132]   Romero, I., Armero, F. 2002. Numerical integration of the stiff dynamics of geometrically exact shells: an energy-dissipative momentum conserving scheme. Int. J. Numer. Meth. Engng 54: 1043-1086.

[133]   Saigal, S., Yang, T.Y., Kapania, R.K. 1987. Dynamic buckling of imperfection-sensitive shell structures. Journal of Aircraft 24, 10: 718-724.

[134]   Sansour, C., Wriggers, P., Sansour, J. 1997. Nonlinear dynamics of shells: theory, finite element formulation and integration schemes. Nonlinear Dynamics 13: 279–305.

[135]   Shao, Z.C., Zhao, Y., Zhang, W., Cao, Y., Feng X.Q. 2016. Curvature induced hierarchical wrinkling patterns in soft bilayers. Soft Matter 12: 7977-7982

[136]   Simitses, G.J., Sheinman, I. 1982. Dynamic buckling of shell structures: Concepts and applications. Acta Astronautica 9, 3: 179-182.

[137]   Simo J.C., Hughes, T.J.R. 1986. On the Variational Foundations of Assumed Strain Methods. Journal of Applied Mechanics 53, 1:51-54. https://doi.org/10.1115/1.3171737

[138]   Simo, J.C., Tarnow, N., Doblare, M. 1995. Non-linear dynamics of three-dimensional rods: exact energy and momentum conserving algorithms. Int J Numer Meth Engng 38: 1431–1473.

[139]   Simo, J.C., Armero, F. 1992. Geometrically non-linear enhanced strain mixed methods and the method of incompatible modes. Int. J. Numer. Meth. Engng. 33, 7: 1413-1449. https://doi.org/10.1002/nme.1620330705

[140]   Simo, J.C., Fox, D.D. 1989. On a stress resultant geometrically exact shell model. Part I: Formulation and optimal parametrization. Comput. Methods Appl. Mech. Engrg. 72: 267-304. https://doi.org/10.1016/0045-7825(89)90002-9

[141]   Simo, J.C., Fox, D.D., Rifai, M.S. 1989. On a stress resultant geometrically exact shell model. Part II: The linear theory; Computational aspects. Comput. Methods. Appl. Mech. Eng. 73: 53-92. https://doi.org/10.1016/0045-7825(89)90098-4

[142]   Simo, J.C., Fox, D.D., Rifai, M.S. 1990. On a stress resultant geometrically exact shell model. Part III: Computational aspects of the nonlinear theory. Comput. Methods Appl. Mech. Engrg. 79: 21-70. https://doi.org/10.1016/0045-7825(90)90094-3

[143]   Simo, J.C., Rifai, M.S. 1990. A class of mixed assumed strain methods and the method of incompatible modes. Int. J. Numer. Meth. Engng. 29: 1595-1638. https://doi.org/10.1002/nme.1620290802

[144]   Simo, J.C., Rifai, M.S., Fox, D.D. 1990. On a stress resultant geometrically exact shell model. Part IV: Variable thickness shells with through-the-thickness stretching. Comput. Methods Appl. Mech. Engrg. 81: 91-126.

[145]   Simo, J.C., Tarnow, N. 1992. The discrete energy-momentum method conserving algorithms for nonlinear dynamics. ZAMP 43: 757–792.

[146]   Simo, J.C., Tarnow, N. 1994. A new energy and momentum conserving algorithm for the nonlinear dynamics of shells. Int J Numer Meth Engng 37, 15: 2527-2549.

[147]   Simo, J.C., Wong, K. 1991. Unconditionally stable algorithms for rigid body dynamics that exactly preserve energy and momentum, Int J Numer Meth Engng 31, 19–52.

[148]   Soop, N., Lagrange, R., Terwagne, D., Reis, P.M., Dunkel, J. 2015. Curvature-induced symmetry breaking determines elastic surface patterns. Nature Materials 14, 337-342.

[149]   Stanić, A., Brank, B. 2017. A path-following method for elasto-plastic solids and structures based on control of plastic dissipation and plastic work. Finite Elements in Analysis and Design 123: 1-8. https://doi.org/10.1016/j.finel.2016.09.005

[150]   Stanić, A., Brank, B., Korelc, J. 2016. On path following methods for structural failure problems. Comput. Mech. 58, 2: 281–306 https://doi.org/10.1007/s00466-016-1294-y

[151]   Stoop, N., Lagrange, R., Terwagne, D., Reis, P.M., Dunkel. J. 2015. Curvature-induced symmetry breaking determines elastic surface patterns. Nat. Mater. 14: 337-342. https://doi.org/10.1038/nmat4202

[152]   Sze, K.Y., Liu, X.H., Lo, S.H. 2004 Popular benchmark problems for geometric nonlinear analysis of shells. Finite Elements in Analysis and Design 40: 1551-1569. https://doi.org/10.1016/j.finel.2003.11.001

[153]   Tamma, K.K., Zhou, X., Sha, D. 2000. The Time Dimension. A theory towards the evolution, classification, characterization and design of computational algorithms for transient dynamic applications. Archives of Computational Methods in Engineering 7, 2: 67-290. https://doi.org/10.1007/BF02736209

[154]   Taylor, M., Bertoldi, K., Steigmann, D.J. 2014. Spatial resolution of wrinkle patterns in thin elastic sheets at finite strain. Journal of the Mechanics and Physics of Solids 62: 163–180. https://doi.org/10.1016/j.jmps.2013.09.024

[155]   Terwagne, D., Brojan, M., Reis, P.M. 2014. Smart morphable surfaces for aerodynamic drag control. Advanced Materials 26, 38: 6608-6611. https://doi.org/10.1002/adma.201470262

[156]   Veldin, T., Brank, B., Brojan, M. 2019. Computational Finite Element Model for Surface Wrinkling of Shells on Soft Substrates. Communications in Nonlinear Science and Numerical Simulation 79, 104863: 1-117. https://doi.org/10.1016/j.cnsns.2019.104863

[157]   Veldin, T., Lavrenčič, M., Brank, B., Brojan, M. 2020. A comparison of computational models for wrinkling of pressurized core-shell systems. Int J Nonlin Mech. 127: 103611. https://doi.org/10.1016/j.ijnonlinmec.2020.103611

[158]   Vu-Quoc, L., Tan, X.G. 2003. Optimal solid shells for nonlinear analyses of multilayer composites. II: Dynamics. Comput. Methods Appl. Mech. Engrg. 192, 9-10: 1017-1059. https://doi.org/10.1016/S0045-7825(02)00336-5

[159]   Wagner, W., Gruttmann, F. 2005. A robust non-linear mixed hybrid quadrilateral shell element. Int. J. Numer. Meth. Engng. 64: 635-666. https://doi.org/10.1002/nme.1387

[160]   Wagner, W., Wriggers, P. 1988. A simple method for the calculation of postcritical branches. Engineering Computations 5: 103–109.

[161]   Washizu, K. 1982. Variational methods in elasticity and plasticity, 3rd edn. Oxford, Pergamon Press.

[162]   White, S.C, Weaver, P.M., Wu, K.C. 2015. Post-buckling analyses of variable-stiffness composite cylinders in axial compression. Composite Structures 123: 190–203. https://doi.org/10.1016/j.compstruct.2014.12.013

[163]   Wilson, E.L. 1968. A Computer Program for Dynamic Stress Analysis of Underground Structures. Berkeley, CA: SESM, University of California, Berkeley.

[164]   Wiśniewski, K. 2010. Finite Rotation Shells, Basic Equations and Finite Elements for Reissner Kinematics. Netherlands, Springer Netherlands.

[165]   Wiśniewski, K., Turska, E. 2008. Improved four-node Hellinger-Reissner elements based on skew coordinates. Int J Numer Meth Engng 76: 798–836. https://doi.org/10.1002/nme.2343

[166]   Wiśniewski, K., Turska, E. 2009. Improved 4-node Hu–Washizu elements based on skew coordinates. Comput. Struct. 87: 407–424. https://doi.org/10.1016/j.compstruc.2009.01.011

[167]   Wiśniewśki, K., Turska, E. 2017. Selected Topics on Mixed/Enhanced Four-Node Shell Elements with Drilling Rotation. In: Altenbach, H. (ed.), Eremeyev, V. (ed.). Shell-like Structures Advanced Theories and Applications, Switzerland, Springer Nature: 247-288 p.

[168]   Wiśniewski, K., Wagner, W., Turska, E., Gruttmann, F. 2010. Four-node Hu–Washizu elements based on skew coordinates and contravariant assumed strain. Comput. Struct. 88: 1278-1284. https://doi.org/10.1016/j.compstruc.2010.07.008

[169]   Wolfram Research, Inc. 2020. Mathematica Version 12.1. Wolfram Research, Inc., Champaign, Illinois.

[170]   Wood, W.L., Bossak, M., Zienkiewicz, O.C. 1980. An alpha-modification of Newmark method. Int J Numer Meth Engng 15, 10: 1562-1566. https://doi.org/10.1002/nme.1620151011

[171]   Wriggers P. 2008. Nonlinear finite element methods. New York, Springer.

[172]   Wriggers, P., Simo, J.C. 1990. A general procedure for the direct computation of turning and bifurcation points. Int J Numer Meth Engng 30: 155–167.

[173]   Xu, F., Potier-Ferry, M. 2016. On axisymmetric/diamond-like mode transitions in axially compressed core-shell cylinders. Journal of the Mechanics and Physics of Solids 94: 68-87. https://doi.org/10.1016/j.jmps.2016.04.025

[174]   Xu, F., Zhao, S., Lu, C., Potier-Ferry, M. 2020. Pattern selection in core-shell spheres. J. Mech. Phys. Solids 137: 103892. https://doi.org/10.1016/j.jmps.2020.103892

[175]   Yamaki, N. 1984. Elastic stability of circular cylindrical shells. Amsterdam, Netherlands, Elsevier Science publishers B.V.

[176]   Yang, J., Xia, P. 2019. Rotation vector and its complement parameterization for singularity-free corotational shell element formulations. Comput. Mech. 64: 789. https://doi.org/10.1007/s00466-019-01681-8

[177]   Yin, J., Chen, X. 2010. Buckling of anisotropic films on cylindrical substrates: insights for self-assembly fabrication of 3D helical gears. Journal of Physics D: Applied Physics 43, 1-7: 115402.

[178]   Yin, J., Han, X., Cao, Y., Lu, C. 2014. Surface Wrinkling on Polydimethylsiloxane Microspheres via Wet Surface Chemical Oxidation. Sci. Rep. UK 4, 8: 5710.

[179]   Yu, G., Xie, X., Carstensen, C. 2011. Uniform convergence and a posteriori error estimation for assumed stress hybrid finite element methods. Comput. Methods Appl. Mech. Engrg. 200: 2421-2433. https://doi.org/10.1016/j.cma.2011.03.018

[180]   Yuan, K.Y., Huang, Y.S., Pian, T.H.H. 1993. New strategy for assumed stresses for 4-node hybrid stress membrane element. Int. J. Numer. Meth. Engng. 36: 1747–1763. https://doi.org/10.1002/nme.1620361009

[181]   Zhang, H.M., Xing, Y.F., Ji, Y. 2020 An energy-conserving and decaying time integration method for general nonlinear dynamics. Int. J. Numer. Methods. Eng. 121: 925–944. https://doi.org/10.1002/nme.6251

[182]   Zhang, J., Liu, Y., Liu, D. 2017. Accuracy of a composite implicit time integration scheme for structural dynamics. Int. J. Numer. Meth. Engng. 109: 368-406. https://doi.org/10.1002/nme.5291

[183]   Zhang, J., Zhang, M., Tang, W., Wang, W., Wang, M. 2017. Buckling of spherical shells subjected to external pressure: A comparison of experimental and theoretical data. Thin-Walled Structures 111: 58–64. https://doi.org/10.1016/j.tws.2016.11.012

[184]   Zhang, X., Mather, P.T., Bowick, M.J., Zhang. T. 2019. Non-uniform curvature and anisotropic deformation control wrinkling patterns on tori. Soft Matter 15: 5204-5210. https://doi.org/10.1039/C9SM00235A

[185]   Zhao, Y., Cao, Y. P., Feng, X. Q., Ma, K. 2014. Axial compression-induced wrinkles on a core-shell soft cylinder: Theoretical analysis, simulations and experiments. Journal of the Mechanics and Physics of Solids 73: 212-227. https://doi.org/10.1016/j.jmps.2014.09.005

[186]   Zhou, X., Tamma, K.K. 2004. Design, analysis and synthesis of generalized single step single solve and optimal algorithms for structural dynamic. Int. J. Numer. Meth. Engng. 59, 5: 597-668. https://doi.org/10.1002/nme.873

[187]   Zupan, E., Saje, M., Zupan, D. 2009 The quaternion-based three-dimensional beam theory. Comput. Methods Appl. Mech. 198, 49–52: 3944–3956. https://doi.org/10.1016/j.cma.2009.09.002

»This page is intentionally blank«

APPENDIX A

The constants $\bar{\bar{\xi}}$ and $\bar{\eta}$ can be analytically integrated taking (2.5) and consider that the area of the shell mid-surface can be approximated in case of warped elements as, see supplement material of [159]

$$\left| \boldsymbol{R}_\xi \times \boldsymbol{R}_\eta \right| \approx \det \mathbf{J}_C^G, \tag{A.1}$$

with $\mathbf{J}_C^G$ defined in (2.41) and the determinant can be decomposed as

$$\det \mathbf{J}_C^G = j_0 + \xi j_1 + \eta j_2. \tag{A.2}$$

The components of (A.2) are further defined as

$$j_0 = \left| \boldsymbol{R}_\xi^0 \times \boldsymbol{R}_\eta^0 \right|, \qquad j_1 = \hat{\boldsymbol{e}}_3 \cdot \left(\boldsymbol{R}_\xi^0 \times \boldsymbol{R}^1 \right), \qquad j_2 = \hat{\boldsymbol{e}}_3 \cdot \left(\boldsymbol{R}^1 \times \boldsymbol{R}_\eta^0 \right), \tag{A.3}$$

where

$$\boldsymbol{R}_\xi^0 = \boldsymbol{R}_\xi|_{\eta \to 0}, \qquad \boldsymbol{R}_\eta^0 = \boldsymbol{R}_\eta|_{\xi \to 0},$$

$$\boldsymbol{R}_\xi = \boldsymbol{R}_\xi^0 + \eta \boldsymbol{R}^1, \qquad \boldsymbol{R}_\eta = \boldsymbol{R}_\eta^0 + \xi \boldsymbol{R}^1, \qquad \boldsymbol{R}^1 = \frac{\partial^2 \boldsymbol{X}_0}{\partial \eta \partial \xi}. \tag{A.4}$$

With $A_e = 4j_0$ and results (A.2) – (A.4), we can write (2.69) as

$$\bar{\bar{\xi}} = \frac{1}{A_e} \int_{A_e} \xi \, \mathrm{d}A = \frac{1}{3} \frac{j_1}{j_0}, \qquad \bar{\eta} = \frac{1}{A_e} \int_{A_e} \eta \, \mathrm{d}A = \frac{1}{3} \frac{j_2}{j_0}. \tag{A.5}$$

APPENDIX B

Bellow we derive the transformation between the contravariant and Cartesian coordinates for the membrane part of independent stress resultants and elaborate why this transformation must be performed in the element center. The contravariant components of membrane stress resultants can be written as

$$\begin{bmatrix} \tilde{n}^{11} \\ \tilde{n}^{22} \\ \tilde{n}^{12} \end{bmatrix} = \begin{bmatrix} \bar{\beta}_1 + (\eta - \bar{\eta})\bar{\beta}_9 \\ \bar{\beta}_2 + (\xi - \bar{\xi})\bar{\beta}_{10} \\ \bar{\beta}_3 \end{bmatrix}. \tag{B.1}$$

Using the transformation matrix, to express this in the element-center Cartesian coordinate system, gives us

$$\begin{bmatrix} \hat{n}^{11} \\ \hat{n}^{22} \\ \hat{n}^{12} \end{bmatrix} = \begin{bmatrix} (J_{C,11}^C)^2 & (J_{C,21}^C)^2 & 2J_{C,11}^C J_{C,21}^C \\ (J_{C,12}^C)^2 & (J_{C,22}^C)^2 & 2J_{C,12}^C J_{C,22}^C \\ J_{C,11}^C J_{0,12}^C & J_{C,21}^C J_{C,22}^C & J_{C,11}^C J_{C,22}^C + J_{C,21}^C J_{C,12}^C \end{bmatrix} \begin{bmatrix} \bar{\beta}_1 + (\eta - \bar{\eta})\bar{\beta}_9 \\ \bar{\beta}_2 + (\xi - \bar{\xi})\bar{\beta}_{10} \\ \bar{\beta}_3 \end{bmatrix} =$$

$$\begin{bmatrix} (\bar{\beta}_1 + (\eta - \bar{\eta})\bar{\beta}_9)(J_{C,11}^C)^2 + (\bar{\beta}_2 + (\xi - \bar{\xi})\bar{\beta}_{10})(J_{C,21}^C)^2 + \bar{\beta}_3\, 2J_{C,11}^C J_{C,21}^C \\ (\bar{\beta}_1 + (\eta - \bar{\eta})\bar{\beta}_9)(J_{C,12}^C)^2 + (\bar{\beta}_2 + (\xi - \bar{\xi})\bar{\beta}_{10})(J_{C,22}^C)^2 + \bar{\beta}_3\, 2J_{C,12}^C J_{C,22}^C \\ (\bar{\beta}_1 + (\eta - \bar{\eta})\bar{\beta}_9)J_{C,11}^C J_{C,12}^C + (\bar{\beta}_2 + (\xi - \bar{\xi})\bar{\beta}_{10})J_{C,21}^C J_{C,22}^C + \bar{\beta}_3(J_{C,11}^C J_{C,22}^C + J_{C,21}^C J_{C,12}^C) \end{bmatrix} = \tag{B.2}$$

$$\begin{bmatrix} \bar{\beta}_1(J_{C,11}^C)^2 + (\eta - \bar{\eta})\bar{\beta}_9(J_{C,11}^C)^2 + \bar{\beta}_2(J_{C,21}^C)^2 + (\xi - \bar{\xi})\bar{\beta}_{10}(J_{C,21}^C)^2 + \bar{\beta}_3\, 2J_{C,11}^C J_{C,21}^C \\ \bar{\beta}_1(J_{C,12}^C)^2 + (\eta - \bar{\eta})\bar{\beta}_9(J_{C,12}^C)^2 + \bar{\beta}_2(J_{C,22}^C)^2 + (\xi - \bar{\xi})\bar{\beta}_{10}(J_{C,22}^C)^2 + \bar{\beta}_3\, 2J_{C,12}^C J_{C,22}^C \\ \bar{\beta}_1 J_{C,11}^C J_{C,12}^C + (\eta - \bar{\eta})\bar{\beta}_9 J_{C,11}^C J_{C,12}^C + \bar{\beta}_2 J_{C,21}^C J_{C,22}^C + (\xi - \bar{\xi})\bar{\beta}_{10} J_{C,21}^C J_{C,22}^C + \bar{\beta}_3(J_{C,11}^C J_{C,22}^C + J_{C,21}^C J_{C,12}^C) \end{bmatrix}$$

We can now introduce three new stress parameters

$$\beta_1 = \bar{\beta}_1(J_{C,11}^C)^2 + \bar{\beta}_2(J_{C,21}^C)^2 + \bar{\beta}_3\, 2J_{C,11}^C J_{C,21}^C,$$
$$\beta_2 = \bar{\beta}_1(J_{C,12}^C)^2 + \bar{\beta}_2(J_{C,22}^C)^2 + \bar{\beta}_3\, 2J_{C,12}^C J_{C,22}^C, \tag{B.3}$$
$$\beta_3 = \bar{\beta}_1 J_{C,11}^C J_{C,12}^C + \bar{\beta}_2 J_{C,21}^C J_{C,22}^C + \bar{\beta}_3(J_{C,11}^C J_{C,22}^C + J_{C,21}^C J_{C,12}^C).$$

Using them, we can now rewrite expression (B.2) as

$$\begin{bmatrix} \hat{n}^{11} \\ \hat{n}^{22} \\ \hat{n}^{12} \end{bmatrix} = \begin{bmatrix} \beta_1 + (\eta - \bar{\eta})\bar{\beta}_9 (J_{C,11}^C)^2 + (\xi - \bar{\xi})\bar{\beta}_{10} (J_{C,21}^C)^2 \\ \beta_2 + (\eta - \bar{\eta})\bar{\beta}_9 (J_{C,12}^C)^2 + (\xi - \bar{\xi})\bar{\beta}_{10} (J_{C,22}^C)^2 \\ \beta_3 + (\eta - \bar{\eta})\bar{\beta}_9 J_{C,11}^C J_{C,12}^C + (\xi - \bar{\xi})\bar{\beta}_{10} J_{C,21}^C J_{C,22}^C \end{bmatrix} =$$

$$\begin{bmatrix} 1 & 0 & 0 & (J_{C,11}^C)^2(\eta - \bar{\eta}) & (J_{C,21}^C)^2(\xi - \bar{\xi}) \\ 0 & 1 & 0 & (J_{C,12}^C)^2(\eta - \bar{\eta}) & (J_{C,22}^C)^2(\xi - \bar{\xi}) \\ 0 & 0 & 1 & J_{C,11}^C J_{C,12}^C(\eta - \bar{\eta}) & J_{C,21}^C J_{C,22}^C(\xi - \bar{\xi}) \end{bmatrix} \begin{bmatrix} \beta_1 \\ \beta_2 \\ \beta_3 \\ \bar{\beta}_9 \\ \bar{\beta}_{10} \end{bmatrix}. \tag{B.4}$$

Performing the transformation in the element center enables this formulation to describe a constant stress state and to pass the patch test. Namely if the transformation was to be different in every Gauss point, the introduction of $\bar{\beta} \to \beta$ would not be possible and the value of $\hat{n}^{\alpha\beta}$ could be different in every Gauss point, even for a constant value of $\bar{\beta}$ parameters. The same straightforward procedure is used to derive the bending and shear stress resultants.